

REPORT DOCUMENTATION PAGE			Form Approved OMB No. 0704-0188	
<small>Public reporting burden for this collection of information is estimated to average 1 hour per response, including the time for reviewing instructions, searching existing data sources, gathering and maintaining the data needed, and completing and reviewing the collection of information. Send comments regarding this burden estimate or any other aspect of this collection of information, including suggestions for reducing this burden, to Washington Headquarters Services, Directorate for Information Operations and Reports, 1215 Jefferson Davis Highway, Suite 1204, Arlington, VA 22202-4302, and to the Office of Management and Budget, Paperwork Reduction Project (0704-0188), Washington, DC 20503.</small>				
1. AGENCY USE ONLY (Leave blank)		2. REPORT DATE 6/30/95		3. REPORT TYPE AND DATES COVERED Final May 1, 1993 - April 30, 1995
4. TITLE AND SUBTITLE The Development of Chemically Pumped Visible Lasers from Efficient Electronic Energy Transfer			5. FUNDING NUMBERS  DAAH04-93-G-0195	
6. AUTHOR(S)  James L. Gole			8. PERFORMING ORGANIZATION REPORT NUMBER  FINAL REPORT	
7. PERFORMING ORGANIZATION NAME(S) AND ADDRESS(ES)  School of Physics Georgia Institute of Technology Atlanta, Georgia 30332-0430			10. SPONSORING/MONITORING AGENCY REPORT NUMBER  ARO 30852.15-PH	
9. SPONSORING/MONITORING AGENCY NAME(S) AND ADDRESS(ES)  U.S. Army Research Office 4300 S. Miami Blvd. P.O. Box 12211 Research Triangle Park, N.C. 27709-2211			11. SUPPLEMENTARY NOTES  The view, opinions and/or findings contained in this report are those of the author and should not be construed as an official Department of the Army position, policy, or decision, unless so designated by other documentation.	
12a. DISTRIBUTION/AVAILABILITY STATEMENT  Approved for public release; distribution unlimited			12b. DISTRIBUTION CODE	
13. ABSTRACT (Maximum 200 words)  Visible chemical laser amplifiers have been generated in select wavelength regions near 527, 492, and 460 nm employing the highly efficient and selective formation of sodium dimer electronically excited states from the sodium trimer-halogen atom (X=Cl, Br, I) reactions. With a focus to increasing amplifier gain length and amplifying medium concentration, an extended path length slit source device has been constructed which created intersecting alkali and halogen sheaths forming the basis for the development of a visible chemical laser oscillator. This device has now revealed the first Raman pumping resulting entirely from a chemical reaction, the process being observed in the absence of an external light source. Extrapolations on the Na <sub>3</sub> -X amplifier concept involving Group IIA metal - F, Cl reactions are considered. Very near resonant energy transfers from selectively formed metastable states of SiO to receptor alkali atoms form sodium or potassium atom laser amplifiers, resulting in a gain condition at $\lambda = 569, 616, 819, \text{ and } 581 \text{ nm}$ . These results form the basis for full cavity oscillation in the Na system at 569 nm. Silane based thermolysis, thermolysis-discharge, and thermolysis-photolysis sources of SiO metastables have been developed and have been used to pump atomic sodium and molecular bromine. The thermolysis sources form highly reproducible SiO fluxes. The efficient energy transfer pumping of potential amplifying transitions in the lead (Pb), copper (Cu), and tin (Sn) systems is outlined.				
14. SUBJECT TERMS  Visible chemical lasers, ultrafast electronic energy transfer, SiO metastable production, pumping of atomic transitions, Raman pumping in the absence of an external light source.			15. NUMBER OF PAGES	
17. SECURITY CLASSIFICATION OF REPORT  UNCLASSIFIED			16. PRICE CODE	
18. SECURITY CLASSIFICATION OF THIS PAGE  UNCLASSIFIED			19. SECURITY CLASSIFICATION OF ABSTRACT  UNCLASSIFIED	
20. LIMITATION OF ABSTRACT  UL				

The Development of Chemically Pumped Visible Lasers from Efficient  
Electronic Energy Transfer

A report submitted to the Army Research Office

(Final Report May 1, 1993 - April 30, 1995)

by James L. Gole

High Temperature Laboratory

and

School of Physics

Georgia Institute of Technology

Atlanta, Georgia 30332

Accession For	
NTIS GRA&I	<input checked="" type="checkbox"/>
DTIC TAB	<input type="checkbox"/>
Unannounced	<input type="checkbox"/>
Justification	
By	
Distribution/	
Availability Codes	
Dist	Avail and/or Special
A-1	

Visible chemical laser amplifiers have been generated in select wavelength regions near 527, 492, and 460 nm employing the highly efficient and selective formation of sodium dimer electronically excited states from the sodium trimer-halogen atom ( $X = \text{Cl}, \text{Br}, \text{I}$ ) reactions. With a focus to increasing amplifier gain length and amplifying medium concentration, an extended path length slit source device has been constructed which creates intersecting alkali and halogen sheaths forming the basis for the development of a visible chemical laser oscillator. This device has now revealed the first Raman pumping resulting entirely from a chemical reaction, the process being observed in the absence of an external light source. Extrapolations on the  $\text{Na}_3\text{-X}$  amplifier concept involving Group IIA metal - F, Cl reactions are considered. Very near resonant energy transfers from selectively formed metastable states of SiO to receptor alkali atoms form sodium or potassium atom laser amplifiers, resulting in a gain condition at  $\lambda = 569, 616, 819,$  and  $581 \text{ nm}$ . These results form the basis for full cavity oscillation in the Na system at  $569 \text{ nm}$ . Silane based thermolysis, thermolysis - discharge, and thermolysis - photolysis sources of SiO metastables have been developed and have been used to pump atomic sodium and molecular bromine. The thermolysis sources form highly reproducible SiO fluxes. The efficient energy transfer pumping of potential amplifying transitions in the lead (Pb), copper (Cu), and tin (Sn) systems is outlined.

19950703 309

## TABLE OF CONTENTS

	page
1. FOREWORD. . . . .	1
2. CURVE CROSSINGS, ELECTRONIC ENERGY TRANSFER COLLISIONS, AND EFFICIENT CHEMICAL PUMPING. . . . .	4
3. A HIGHLY EFFICIENT AND SELECTIVE ELECTRON JUMP-HARPOON PROCESS. . .	4
4. EFFICIENT, FAST, INTRA- AND INTERMOLECULAR ENERGY TRANSFER PUMPING.	4
5. CONTINUOUS CHEMICAL LASER AMPLIFIERS IN THE VISIBLE REGION BASED ON HIGHLY EFFICIENT AND SELECTIVE REACTIONS . . . . .	6
- Formation of Amplifiers (Oscillators) Through Direct Chemical Reaction. . . . .	6
- Electronically Inverted Na <sub>2</sub> Produced from the Na <sub>3</sub> -X(Cl,Br,I) Reactions . . . . .	6
- Development of an Extended Path Length Na <sub>3</sub> -X(Cl,Br,I) Reaction Amplification Zone. . . . .	8
- Raman Pumping in the Absence of an External Light Source. . . . .	10
- Extension of the Na <sub>3</sub> -X(Cl,Br,I) Amplifier Concept . . . . .	13
- Long Range Collisional Stabilization and the Symmetry Constrained Dynamics of High Temperature Complex Formation. . . . .	14
6. NEAR RESONANT ENERGY TRANSFER FROM METASTABLE ENERGY STORAGE STATES OF SiO AND GeO TO FORM ATOM BASED LASER AMPLIFIERS. . . . .	16
- Full Cavity Measurements. . . . .	18
- Improvement of the Energy Transfer Based Configuration - Ultimate Goals . . . . .	19
A. Concentric Reactant Mixing. . . . .	19
B. Considering Self Absorption and Self Quenching. . . . .	20
C. Nitrogen vs. Argon Entrainment. . . . .	21
D. Output Coupling . . . . .	21
- System Modeling . . . . .	21
- Extension of Near Resonant Intermolecular Energy Transfer Concept to Additional Energy Transfer Pumped Atomic Receptors . . . . .	22
- Improving the Si Atom and SiO Metastable Source Configurations. .	24
REFERENCES. . . . .	28
PUBLICATIONS. . . . .	33
INVITED TALKS ON ARMY SPONSORED RESEARCH. . . . .	35
SCIENTIFIC PERSONNEL SUPPORTED BY THIS PROJECT (DEGREES AWARDED). .	36

- APPENDIX I      - The Unique Complexation and Oxidation of Metal-Based Clusters
- APPENDIX II     - Fluorine Hot Atom Oxidation of Bismuth Vapor. A Comment on the Evaluation of the BiF Bond Energy
- APPENDIX III    - Evidence for Continuous Visible Chemical Lasing From the Fast Near Resonant Energy Transfer Pumping of Atomic Sodium
- APPENDIX IV     - Chemically Driven Continuous Visible Laser Amplifiers and Oscillators Based on Metal Molecule - Halogen Atom Reactions
- APPENDIX V      - Chemically Driven Visible Laser Amplifiers and Oscillators Based on Fast Electronic Energy Transfer
- APPENDIX VI     - Laser Induced Fluorescence and Radiative Lifetimes of the Low-Lying Electronic States of Gaseous AgF
- APPENDIX VII    - A Chemiluminescent and Laser Induced Fluorescent Probe of A New Low-Lying  $A'^1\Omega_1$  State of Gaseous AgF
- APPENDIX VIII   - Raman Pumping in the Absence of an External Light Source
- APPENDIX IX     - The Expansion of Small Molecule Configuration Space: Highly Efficient Long Range Stabilization and Energy Transfer Involving Electronically Excited States
- APPENDIX X      - Chemically Induced Processes Evidencing Raman Gain
- APPENDIX XI     - Highly Efficient Collisional Stabilization and the Symmetry Constrained Dynamics of High Temperature Complex Formation
- APPENDIX XII    - Confirmation of Long-Range Collision Complex Stabilization Through The Controlled Relaxation of High Internal Excitation
- APPENDIX XIII   - What is the Ionization Potential of Silicon Dimer?
- APPENDIX XIV    - Spectroscopy of the  $H^3\Sigma_u^-$  Electronic State of  $Si_2$  Using a Combined Laser Vaporization-Rempy and Oven Based LIF Study
- APPENDIX XV     - A New and Simple Pyrolysis Source for the Controlled Formation of SiO Metastables

## Foreword

We have developed a wealth of evidence to suggest that surprisingly efficient collision induced energy transfers and collisional stabilization can be ascribed to small molecules and atoms present at elevated energies in high stress non-equilibrium environments. Apparent energy transfer and stabilization rates, which in some cases would appear to defy conventional kinetic models, are far in excess of those normally associated with the lowest vibrational-rotational levels of molecules and systems in their lowest or ground states at room temperature. This project has attempted to take advantage of these characteristics with a focus toward the development of the first visible chemical laser amplifiers and oscillators. Two novel approaches to form electronically inverted molecular diatomic and atomic configurations making use of (1) highly efficient and selective fast "electron jump" reactive encounters, and (2) highly efficient near resonant electronic energy transfer, have been employed to produce amplification and oscillation and to reveal several unusual characteristics of these inherently high temperature environments.

A primary approach to continuous visible chemical laser development has been signaled by the successful production of visible chemical laser amplifiers using the highly efficient and selective formation of sodium dimer, excited states from the fast sodium trimer-halogen atom ( $M_3 - X(Cl, Br, I)$ ) reactions. These chemical laser amplifiers have employed the extremely high cross section  $Na_n$  ( $n=2,3$ )- $X(Cl, Br, I)$  reactions to create a continuous electronic population inversion based on the chemical pumping of sodium dimer ( $Na_2$ ). Optical gain through stimulated emission has been demonstrated in select regions close to 527, 492, and 460 nm. A model, under development, which evokes the vibrational and rotational selectivity inherent to a dissociative ionic recombination process ( $Na_3^+ + X^- \rightarrow Na_2 + NaX$ ) in correlation with the coupling between select sodium dimer excited states, appears to provide a semiquantitative explanation of the observed behavior.

An assessment of the manner in which gain is generated in these fast reactive encounters has suggested that a considerable enhancement of the amplification can be obtained with a versatile long-path length source configuration. The considered amplifiers are therefore being optimized with a focus to increasing amplifier gain length and amplifying medium concentration using an upscaled device which has been designed to allow the ready movement

of extended path length alkali trimer and halogen atom slit sources relative to each other, creating adjustable intersecting reactive alkali and halogen atom flows. The controlled intersection of these reacting sheaths forms an extended reaction - amplification zone. It is this extended gain zone which we are employing to convert the created amplifiers to visible chemical laser oscillators. With this focus to the development of a long path length amplifying medium employing the trimer reactions, we have observed the first resonance Raman pumping of  $\text{Na}_2$  in the absence of an external light source. Here, the Na D-line emission which results from the  $\text{Na}_2\text{-Br}$  reaction is scattered by sodium dimers cooled, in supersonic expansion, so as to populate the lowest vibrational levels of the  $\text{Na}_2$  ground electronic state. An initial analysis suggests that we have observed the manifestation of resonance Raman progressions, however, the time scale for the Raman process may be considerably shorter than anticipated suggesting a surprisingly large cross section. This suggests a further long range interaction of the excited  $\text{Na}^2\text{P}$  atoms with those  $\text{Na}_2$  molecules which are Raman pumped. We are beginning to observe the manifestation of significant and surprising interactions. In concert with observations made on a number of additional systems, the current observations suggest that the  $\text{Na}_n\text{-X}$  reaction systems may also behave in response to a highly efficient funneling of the reaction energy via diffuse reactant and product electron density and that their study can serve as a model for more complex systems.

This report also suggests and begins to demonstrate extrapolations on the sodium trimer-halogen atom systems including the potential excimer forming  $\text{M}_3$  ( $\text{M}=\text{Mg}, \text{Ca}, \text{Sr}, \text{Ba}$ ) - F (Cl) reactions. Initial results for the  $\text{Mg}_x$  ( $x=2,3$ ) - F atom reactions are reported. Further, the course of these studies has also lead to a remarkable discovery concerning the stabilization of high temperature complexes. Through a combination of single and multiple collision chemiluminescence (CL) and laser induced fluorescence (LIF) spectroscopy, we have demonstrated the astonishing efficiency with which a high temperature reaction complex can be stabilized. We have obtained clear evidence for the stabilization of Group IIA  $\text{MX}_2$  ( $\text{M}=\text{Ca}, \text{Sr}, \text{Ba}, \text{X}=\text{Cl}, \text{Br}, \text{I}$ ) dihalide complexes, formed in concert with direct  $\text{M} + \text{X}_2 \rightarrow \text{MX}_2^*$  reactive encounters, through the extremely long range interaction with an additional halogen molecule. The onset of the monitored R3BR process at  $1 \times 10^{-6}$  Torr signals an enormous stabilization cross section ( $\sigma > 5000 \text{ \AA}^2$ ). The demonstrated efficiency is

certainly not explained within an RRKM framework, again suggesting that new models, which focus on long range energy flow as opposed to fragmentation, may be necessary to explain these efficient interactions. The data from this study begins to reveal a much broader range of interaction than has typically been associated with the collisional stabilization and energy transfer process. The enhanced interaction range of the dihalide complexes may also result from the influence of a diffuse electron density. The current results focus attention on the potential importance of collisionally stabilized radiative or non-radiative complexation processes at elevated temperatures. These efficient processes may influence gas-surface depositions which are strongly dependent upon formation of the gas phase constituency.

We also present the results of studies in which we have used a very near resonant energy transfer from selectively formed metastable states of SiO ( $a^3\Sigma^+$ ,  $b^3\Pi$ ) to select metal atoms in order to form sodium and potassium atom based laser amplifiers at  $\lambda = 535, 417, 569, 616, 819$ , and  $581$  nm. Metastable SiO has also been used to pump molecular bromine. The metastable triplet states are generated in high yield from a select group (Si-N<sub>2</sub>O, Si-NO<sub>2</sub>) of oxidation reactions. The energy stored in these generated triplet states is transferred in a highly efficient electronic energy transfer process to pump ground state Na, and K atoms to select excited states. So efficient are these transfers that they have been used to produce superfluorescence from Tl and Ga atoms at  $535$  and  $417$  nm<sup>15,16</sup> and amplified spontaneous emission (ASE) from Na atoms at  $569, 616$ , and  $819$  nm (Appendices III and V). Adopting a pumping sequence in which a premixed Group IVA metalloid-receptor atom combination is oxidized we have demonstrated full cavity oscillation in the Tl ( $535$  nm)<sup>15,16</sup> and Na ( $569$  nm - Appendices III and V) systems. The concepts employed to create amplification and oscillation in these systems also appear applicable to the efficient energy transfer pumping of potential amplifying transitions in the lead (Pb), copper (Cu - analog of Cu vapor laser), and tin (Sn) receptor atoms.

The outlined results, obtained with an oven based source of the Group IVA metalloid, require high source operating temperatures so as to obtain substantial Si or Ge atomic fluxes. In order to (1) greatly alleviate the temperature requirement and (2) generate higher metalloid concentrations for the pumping of appropriate atomic receptors, we have also been concerned with the development of considerably lower temperature silane (SiH<sub>4</sub>) based

thermolysis, thermolysis-discharge, and thermolysis-photolysis combination sources as a means of generating atomic silicon. These partially successful efforts are also summarized in this report.

## **Curve Crossings, Electronic Energy Transfer Collisions, and Efficient Chemical Pumping**

### **"A Highly Efficient and Selective Electron-Jump-Harpoon Process"**

The collision dynamics of processes proceeding on electronically excited surfaces is fundamental to the attainment of population inversions based on electronic transitions in the visible spectral region.<sup>1,2</sup> A particular subgroup of these electronic energy transfer processes involves metal atoms or molecules of low ionization potential. These species react very efficiently with atoms or molecules of significant electron affinity via what is termed the electron jump-harpoon process. **It is this process, specifically involving the reaction of metal trimers and forming the product metal dimer and metal halide, that may represent one of the few direct chemical routes to produce electronically inverted products.** The alkali trimer molecule,  $\text{Na}_3$ , readily provides an electron to harpoon a hungry halogen atom,  $\text{X}$ , producing a switch from the interaction of two neutral species to that of two ions ( $\text{Na}_3^+ + \text{X}^-$ ). The convergence, crossing, and interaction of the two potentials describing the neutral (covalent) and ionic (coulombic) constituencies allows an effective switch of the reactants (curve crossing). For  $\text{Na}_3$ , with its low ionization potential, the curve crossing occurs at very long range ( $> 10\text{\AA}$ ) leading to a high cross section for product  $\text{Na}_2$  formation. Based upon the experimental results obtained thusfar in our laboratory, the sodium trimer reactions show not only vibrational but also rotational selectivity as they create electronic population inversions in the product  $\text{Na}_2$ . Theoretical considerations (see also following sections) would suggest that these trimer reactions and their analogs represent key processes to yield electronically inverted products in direct chemical reaction.<sup>1,2</sup>

### **"Efficient, Fast, Intra- and Intermolecular Energy Transfer Pumping"**

The energy transfer based approach which we have used to develop the

first visible chemical laser amplifiers and oscillators has relied on our belief that the majority of successful electronic transition chemical lasers will require a two-step approach.<sup>3,4</sup> Chemical energy must be produced and stored in a first step and then transferred in a collision induced process to an appropriate lasing medium in a second step. Following this scheme, we can attempt to produce inversions using (1) "ultrafast" intramolecular energy transfer among the excited electronic states of small diatomic molecules<sup>5-8</sup> or (2) fast intermolecular transfer from electronically excited metastable storage states to readily lasing atomic receptors. Both processes inherently involve the curve crossing of electronic states which is basic to the creation of a highly efficient energy transfer route.

Electronically and highly vibrationally excited molecules, with their inherently diffuse electron densities and large amplitude vibrational motions simply interact more effectively than do ground state molecules in their lowest vibrational-rotational levels. We have determined that several diatomic metal monoxides including silicon and germanium oxide display collision induced electronic-to-electronic (E-E)<sup>5-9</sup> and vibrational-to-electronic (V-E)<sup>10</sup> intermolecular energy transfers which proceed at rates comparable to or far in excess of gas kinetic. Transfers from metastable to shorter lived excited states may proceed at rates which approach 500 times gas kinetic (cross sections in excess of  $4000 \text{ \AA}^2$ ). The low-lying electronic states of several simple high temperature molecules (the products of metal oxidation) interact with a collision partner which induces energy transfer with a much larger impact parameter than would have been previously anticipated on the basis of studies involving the lowest vibrational-rotational levels of their ground states. In a sense, we are dealing with "pseudo-macromolecules" which display many of the characteristics inherent to Rydberg states<sup>11</sup> with their large transfer and relaxation cross sections. In several cases the rates for the observed transfers may be comparable to the radiative rates associated with the usually shorter lived and potentially useful upper levels which the intramolecular transfer populates.<sup>12</sup> Rates of this magnitude, properly employed, can be competitive with optical pumping!

At some point, the distinction between fast intramolecular energy transfer processes, correlating with electronic state couplings and the periods of molecular vibrations (rotations), and intermolecular energy transfer, governed by the duration of collisions with electronically excited

states, is indistinguishable.<sup>1,2</sup> We have demonstrated that it is reasonable to expect certain near resonant intermolecular energy transfers to proceed with extremely high cross sections.<sup>13</sup> One might consider that an electronically excited molecule, with its diffuse electron density, has the ability to send out more feelers or interaction lines as it influences reaction and collision partners. The increased interaction rates which several experiments now suggest are most encouraging for the development of visible chemical lasers from energy transfer processes. It is precisely these very exciting results which we have already made use of in the initial development of several systems.

## **CONTINUOUS CHEMICAL LASER AMPLIFIERS IN THE VISIBLE REGION BASED ON HIGHLY EFFICIENT AND SELECTIVE CHEMICAL REACTIONS**

### **Formation of Amplifiers (Oscillators) Through Direct Chemical Reaction**

$\text{Na}_2$  chemical laser amplifiers have been developed<sup>14-16</sup> in our laboratory employing the high cross section  $\text{Na}_n$  ( $n = 2,3$ ) -  $\text{X}(\text{Cl}, \text{Br}, \text{I})$  electron jump reactions to create a continuous electronic population inversion based on the chemical pumping of sodium dimer ( $\text{Na}_2$ ). Sodium trimer molecules produced in supersonic expansion (see also Appendices I and IV) are reacted with halogen atoms to create the inversions on electronic transitions in  $\text{Na}_2$ . Optical gain through stimulated emission has been demonstrated in select regions close to 527, 492, and 460 nm with potential extension to the  $\sim 395$ ,  $\sim 365$ , and  $\sim 350$  nm regions. The observed gain (max. of 4% at  $\sim 527$  nm corres. to  $8 \times 10^{-3}/\text{cm}$  for individual rotational levels (see following)) can be enhanced considerably with a more versatile long path length source configuration. The development of this source configuration has been a major focus of our efforts over the last two years.

### **Electronically Inverted $\text{Na}_2$ Produced from the $\text{Na}_3$ - $\text{X}(\text{Cl}, \text{Br}, \text{I})$ Reactions**

Efficient chemical laser oscillators should be developed from the high cross section, highly exothermic  $\text{Na}_3$  -  $\text{X}(\text{Cl}, \text{Br}, \text{I})$  reactions which selectively form  $\text{Na}_2^*$  in a limited number of its excited electronic states (Fig. 1(a)). The optical signatures for the processes

Figure 1(a) Approximate potential curves for select states of  $\text{Na}_2$ .

Figure 1(b) Chemiluminescent emission resulting from the reaction  $\text{Na}_3 + \text{X} \rightarrow \text{Na}_2 + \text{NaX}$  with  $\text{X} = \text{Br}, \text{I}$ . The spectra display sharp fluorescence features in the visible at 527, 492, and 460.5 nm superimposed on a broader  $\text{Na}_2$  background emission.

Figure 1(c) Comparison of (a) observed and (b) calculated emission spectra for the  $\text{Na}_2$  B-X emission system. The experimental spectrum corresponds to the chemiluminescence from the  $\text{Na}_2$ -Br reaction. The calculated spectrum, which was obtained for a rotational temperature,  $T_{\text{rot}} \approx 1000\text{K}$ , represents an estimate of effective rotational temperatures in a system operated under single collision conditions and therefore not at equilibrium. Relative vibrational populations input for  $\text{Na}_2$  B-X,  $v' = 0.6$  were in the ratio 1.00:1.17:1.33:1.50:1.67:1.54.

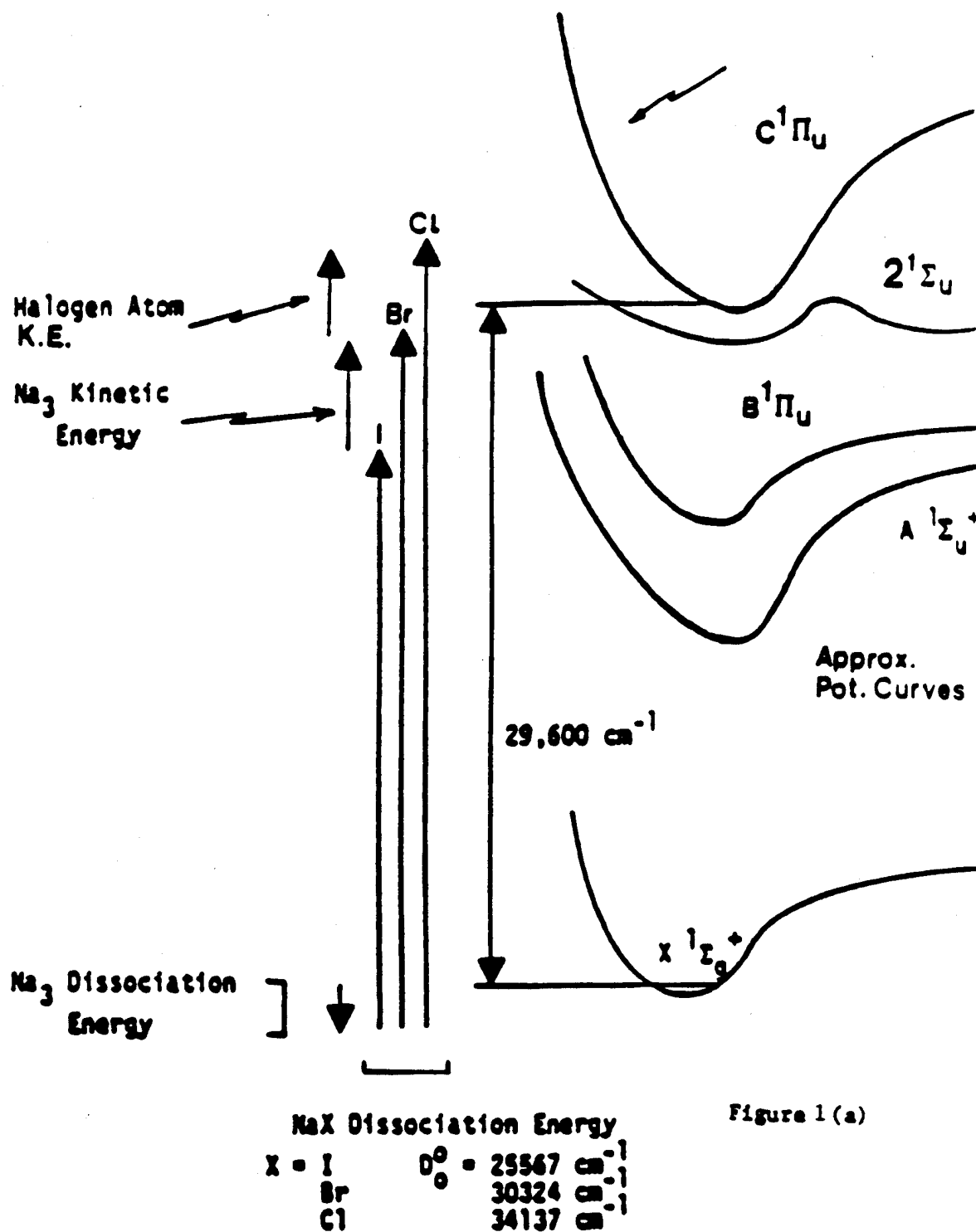


Figure 1(a)

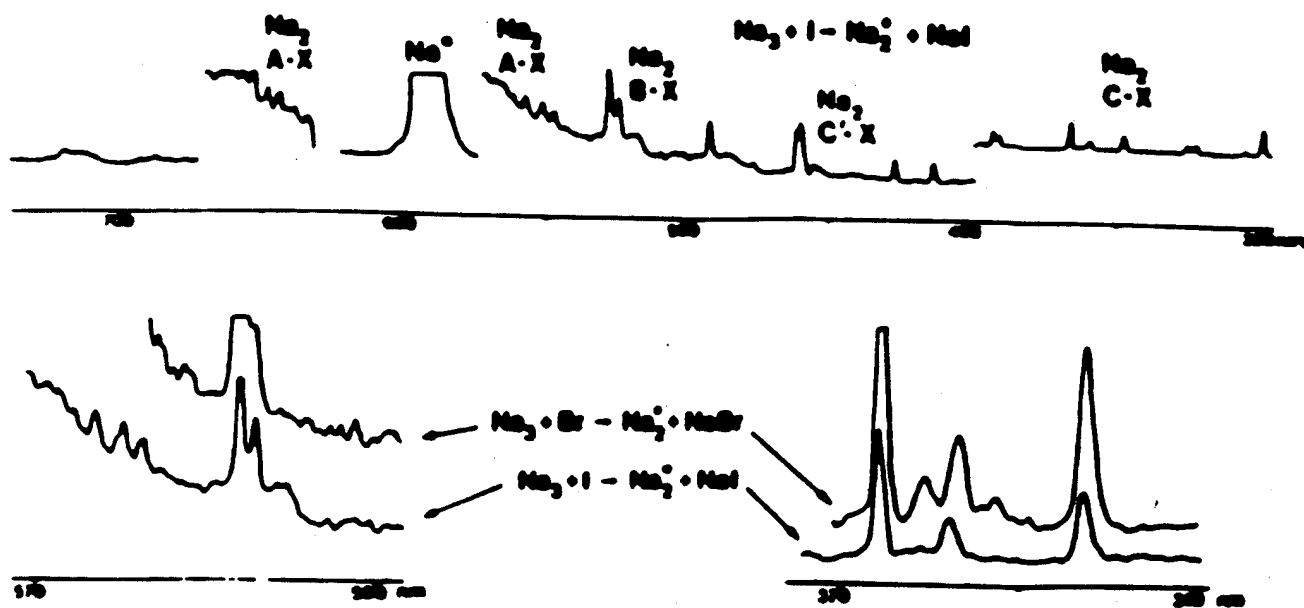


Figure 1(b)

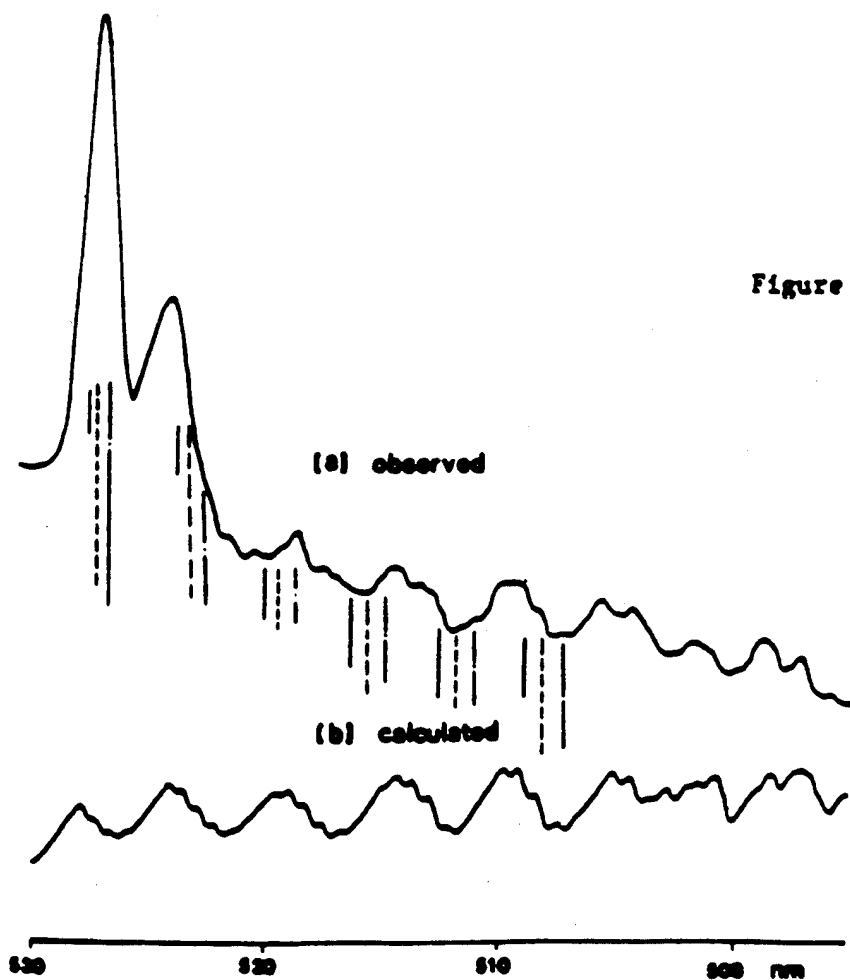
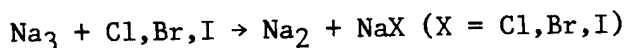


Figure 1(c)



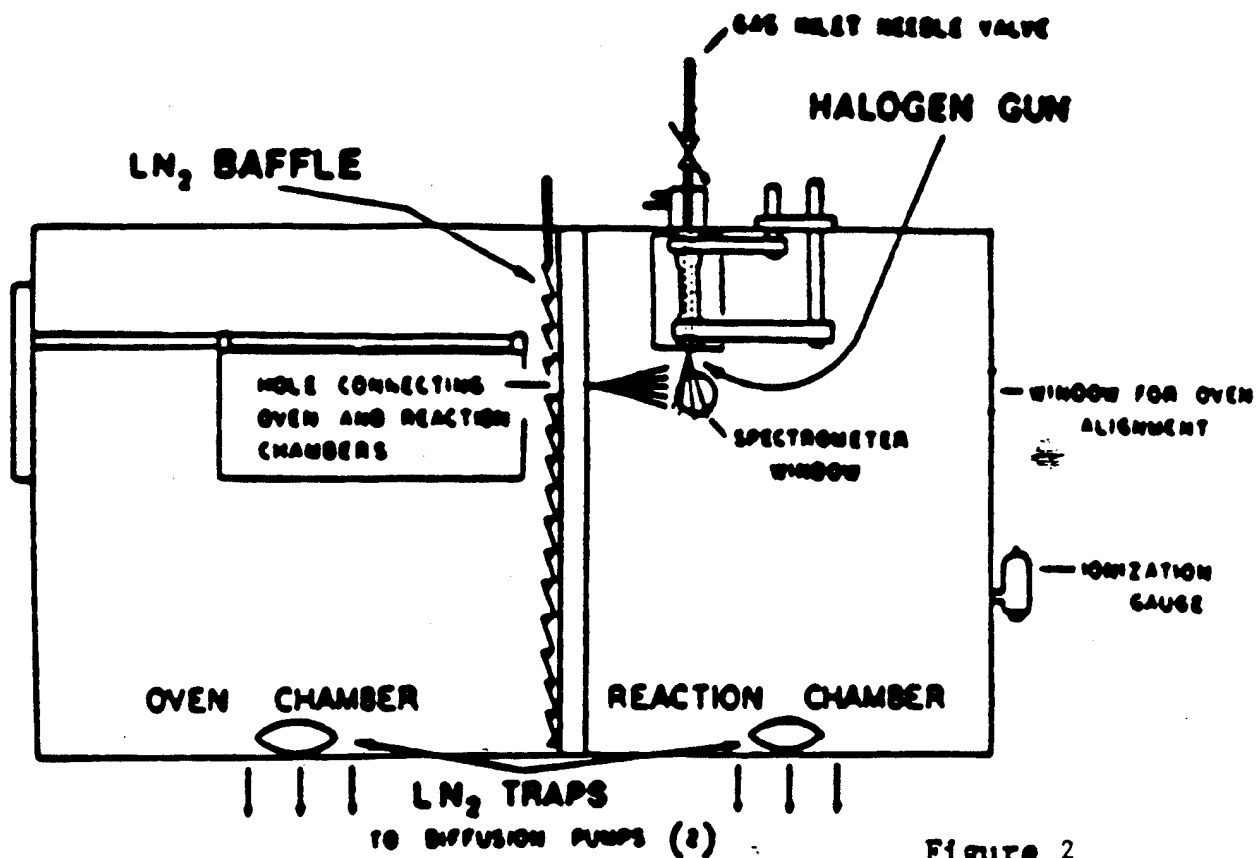
(1)

encompass emission from a limited number of  $\text{Na}_2$  band systems. Surprisingly, the observed emission is characterized by sharp well defined emission regions (Figs. 1(b), 1(c)) superimposed on a much weaker but perceptible and analyzable  $\text{Na}_2$  background fluorescence. As Fig. 1(c) demonstrates, these sharp emission features are not readily explained by invoking a purely fluorescent process.

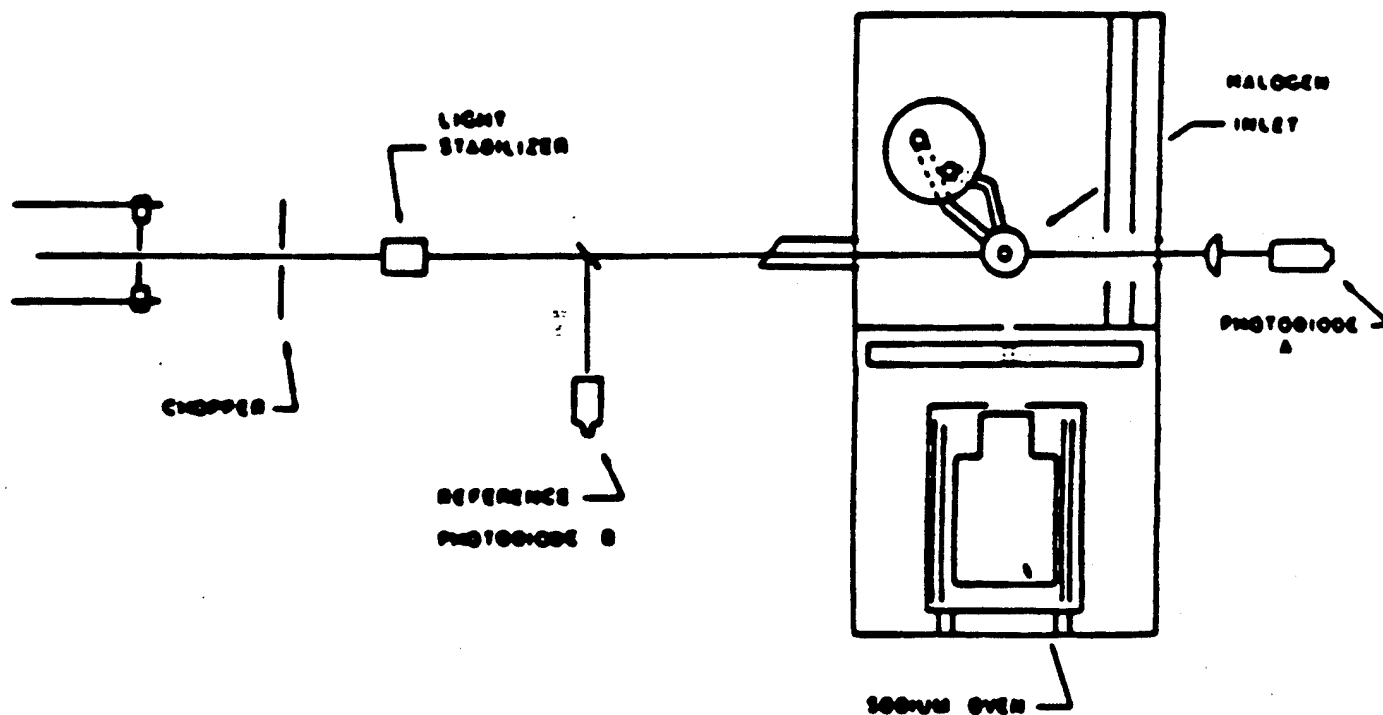
The sharp nature of several of the B-X, C-X, and C'-X  $\text{Na}_2$  fluorescence features (Figs. 1(b), 1(c)), their correlation in certain regions to the emission characteristic of optically pumped  $\text{Na}_2$  laser systems<sup>17</sup> (ex: 528.2 nm ( $\nu', \nu''$ ) = (6,14) B-X), and the near exponential growth of these features relative to the background  $\text{Na}_2$  fluorescence spectrum with increasing  $\text{Na}_3$  concentration, suggests that stimulated emission might be associated with certain of the emitting  $\text{Na}_2$  reaction products. Laser gain measurements were carried out to assess this possibility.

In order to do these gain studies, we further developed (Fig. 2(a)) a unique source configuration which allows the supersonic expansion of pure sodium vapor to create a  $\text{Na}_3$  concentration not previously attained in a reaction-amplification zone. Using argon ion laser pumped dye lasers to study the  $\text{Na}_3 + \text{Br}$  reaction we have scanned (Fig. 2(b)) the entire wavelength region from 420 to 600 nm (Figure 1(b)) in  $\sim 3$  nm intervals at  $0.5 \text{ cm}^{-1}$  resolution (FWHM) and the regions around 527 nm and 460 nm (Fig. 1(c)) at  $0.007 \text{ cm}^{-1}$  resolution.<sup>12-16</sup> We find that laser gain and hence amplification is associated with very limited regions of the spectrum. The observations suggest that several of the sharp emission features apparent in Figure 1 correspond to a stimulated emission process and the establishment of a population inversion. Optical gain through stimulated emission ( $0.5 \text{ cm}^{-1}$  resolution) in the regions close to 527 nm (1%), 492 nm (0.3%), and 460.5 nm (0.8% gain) correlates precisely with the reactive process and the relative intensities of those features observed while monitoring the light emitted from the  $\text{Na}_3\text{-Br}$  and  $\text{Na}_3\text{-I}$  reactions. High resolution ring dye laser scans in the 527 nm region indicate that the gain for the system is a minimum of 3.8% for an individual rovibronic transition with approximately four to seven individual rotational transitions showing gain. At 459.8 nm, we have measured an 2.3% gain for an individual rotational transition. The results

Figure 2: Schematic of (a) apparatus for the study of the chemiluminescent  $\text{Na}_3$  - X reactions and (b) the arrangement of the experimental configuration for measuring gain from the  $\text{Na}_3$  - X metathesis.



a



b

demonstrate the continuous amplifying medium for a visible chemical laser in at least three wavelength regions.<sup>14-16</sup> At no other scanned wavelengths have we observed gain. In fact, in scanning the 420-600 nm region, we generally observe losses relative to the incident laser photon flux due primarily to scattering (to only a negligible extent, absorption) on transit through the Na<sub>3</sub>-Br reaction zone. In the region of the sodium D-line, a substantial absorption and hence loss is monitored as a function of the trimer-halogen atom reaction.<sup>14-16</sup>

Because of the low Na<sub>3</sub> ionization potential and the high halogen electron affinities,<sup>18</sup> the Na<sub>3</sub>-halogen atom reactions are expected to proceed via an electron jump mechanism with extremely high cross sections,<sup>19</sup> producing substantial Na<sub>2</sub> excited state populations. The question of why the Na<sub>3</sub>-X reactions appear to demonstrate vibrational and rotational selectivity associated with certain wavelength regions may be dealt with by invoking a model for the dissociative ionic recombination,  $\text{Na}_3^+ + \text{X}^- \rightarrow \text{Na}_2^* + \text{NaX}$ , and the curve crossings which influence the distribution of product molecules for this process.<sup>20</sup> This model, coupled with an analysis of the electronic coupling between select sodium dimer excited states, may provide a semi-quantitative explanation for the created population inversions.

The population inversions monitored thusfar are thought to be sustained (1) by the large number of free halogen atoms reacting with Na<sub>2</sub> molecules in those ground state levels on which the transitions emanating from the Na<sub>2</sub> excited states terminate and (2) collisional relaxation of the ground state sodium dimer molecules. The cross section for reaction of vibrationally excited ground state Na<sub>2</sub> is expected to be at least comparable to the cross section for collision induced vibrational deactivation of the Na<sub>2</sub> manifold. Extremely efficient reactions greatly assist the depletion of the lower state levels in this system allowing one to sustain a continuous population inversion.

#### **Development of an Extended Path Length Na<sub>3</sub> - X (Cl,Br,I) Reaction - Amplification Zone**

A major focus of our efforts has been to considerably improve the magnitude of the amplification demonstrated for the sodium dimer amplifiers at ~527, ~492, and ~460 nm. The apparatus depicted in Figure 2 now produces a

substantial  $\text{Na}_3$  concentration ( $\geq 10^{13}/\text{cc}$ ) albeit in a limited reaction-amplification zone. In order to demonstrate continuous chemical laser oscillation, however, it is desirable to create an enhanced sodium trimer - halogen atom reaction zone not only in terms of reactant concentration but also with respect to the amplification zone path length. The overall apparatus design which we are developing, depicted in part schematically in Figures 3-5 and discussed in detail in Appendices IV, VIII, and X is meant to accommodate high intersecting reactant flows from both sodium trimer and (dual rotatable) halogen atom sources in order to produce an enhanced concentration of  $\text{Na}_2$  amplifiers over a significantly extended path length.

The apparatus outlined in Figs. 3-5 attempts to increase the  $\text{Na}_3$  reaction - amplification zone concentration by repositioning the trimer and halogen atom sources relative to each other and facilitating the halogenation process much closer to the alkali nozzle itself, in a gas dynamic configuration. We also have incorporated the facility for the in-situ adjustment of the alkali and halogen source positions. This includes the ability to rotate the dual alkali-trimer-flow-encompassing halogen atom slit sources (Figs. 3(b)) so as to optimize flow mixing. Further, as a means of increasing the reaction zone and gain length, we have developed and continue to test several continuous flow slit sources (Appendix IV for more detailed discussion).

In a pure sodium supersonic expansion, the  $\text{Na}_3$  constituency is dominated by a much larger atom and cold dimer concentration.<sup>21</sup> These constituencies do not absorb at the  $\text{Na}_2$  amplifier wavelengths characteristic of the  $\text{Na}_3$ -halogen atom reaction systems. However, it is desirable to minimize the atom and dimer while increasing the trimer concentration. The trimer concentration must be altered and improved through an appropriate adjustment of the supersonic expansion conditions shifting the distribution to higher sodium polymers. By seeding the expansion with helium, argon, or other noble gas atoms, several researchers<sup>22</sup> have demonstrated that the atom and dimer concentrations can be made quite small relative to the much larger sodium polymers.<sup>22</sup> Our ultimate goal is to develop a system which does not operate at these extreme expansion conditions but, rather, we seek a middle ground which will allow us to produce primarily the trimer and a few larger clusters.<sup>23</sup> This condition should be achieved through the appropriate adjustment of parameters which can be manipulated in the expansion including (1) the rear oven stagnation pressure (argon or helium + sodium), (2) the

frontal nozzle temperature, and (3) the ratio of the supersonic expansion source pressure to the overall expansion chamber pressure.

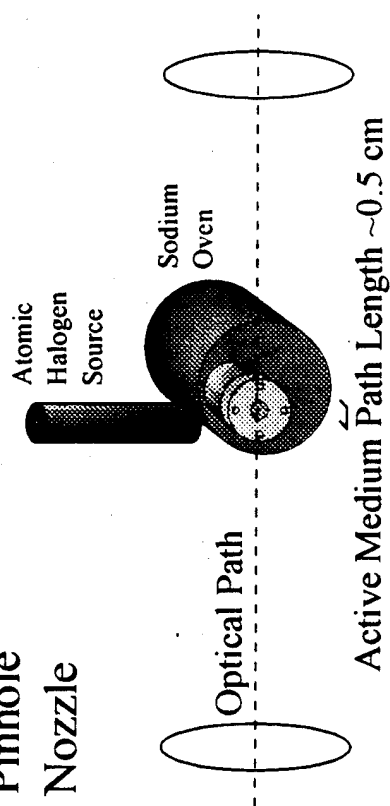
The sodium slit source is positioned relative to the dual halogen slit sources located above and below what can be envisioned as the position of an expanding alkali sheath created upon expansion from the alkali slit source. The reaction zone-cavity configuration is designed to allow for 1) short transit of the reactants  $\text{Na}_3$  and  $\text{X} = \text{Cl}, \text{Br}, \text{I}$  to the reaction - amplification zone, 2) flexible movement of these sources with respect to each other and with respect to the flow patterns created in the system and 3) minimal interaction of these reactants with laser cavity windows. To insure this , minimal interaction, self-cleaning optical windows<sup>24</sup> are used.

We have now carried out several experiments using the extended amplification zone device depicted in Figure 3. These studies are outlined in more detail in Appendices IV, VIII, and X, however, it is important to note the most important observations which we have made in these initial efforts. These include 1) what appears to be the first observation of Raman pumping in a purely chemical environment with the attendant measurement of gain associated with the Stokes scattering and 2) excited state chemical pumping which is the equivalent of that obtained with a substantial  $2\text{W}/\text{cm}^2$  laser pump of sodium vapor ( $\text{Na}_x$  @  $0.344 \text{ mm}/\text{Hg}$  - see Appendix IV). Thus, while we have not yet reached the necessary  $\text{Na}_3$  concentrations in our reactive zone to produce the inverted  $\text{Na}_2$  B-X features (Fig. 1), we have already observed an unusual and unexpected cooperative behavior associated with the longer path length configuration.

#### **Raman Pumping in the Absence of an External Light Source**

Using the configuration described in Figures 3-5 (Appendices IV, VIII, and X for additional detail) we have observed the first resonance Raman pumping generated in a purely chemical reactive environment in the absence of an external light source. The observations made in the present study bear a close analogy to those of Wellegehausen<sup>17</sup> and Bergmann and coworkers<sup>25-26</sup> in their analysis of optically pumped sodium dimer lasers operative on a stimulated Raman scattering process. Here, as Fig. 6 demonstrates, we observe a series of Raman-like Stokes and anti-Stokes features which (1) are associated primarily with the lowest vibrational levels of  $\text{Na}_2$ , (2) correlate

## Pinhole Nozzle



## Slit Nozzle

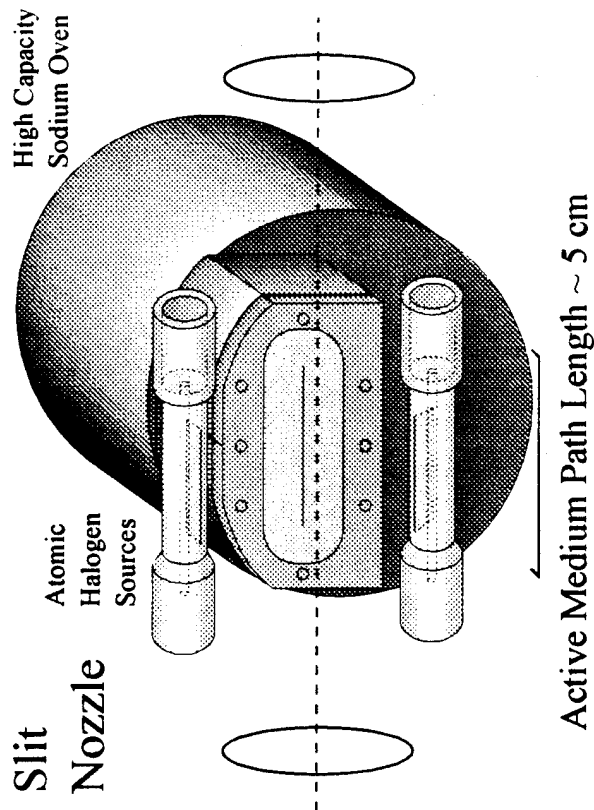
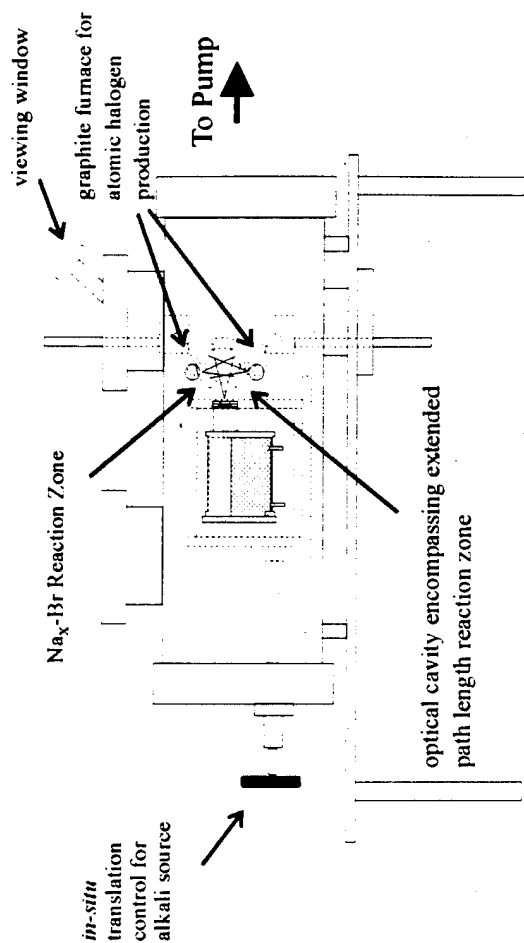


Figure 3

(a) Pinhole nozzle supersonic alkali metal source producing a  $\sim 1$  cm path length.  
 (b) Slit nozzle supersonic source producing an extended path length reaction zone.



Figures 4  
 Apparatus depicting placement of supersonic slit source

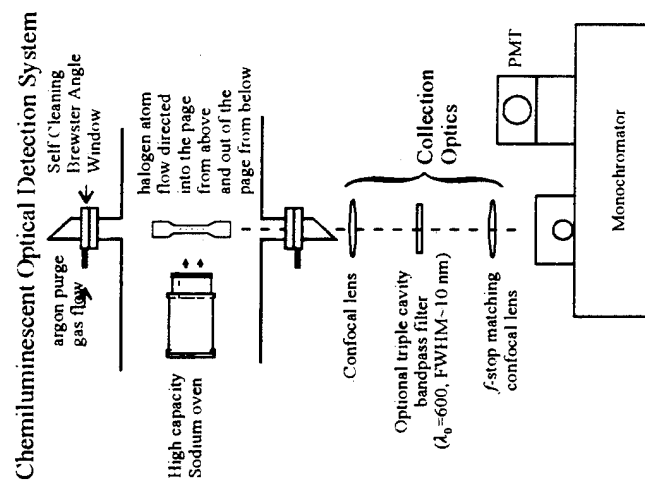


Figure 5:  
 Optical detection system for collecting  $\text{Na}_n - \text{X}$  ( $n = 2, 3$ ;  $\text{X} = \text{Br}, \text{Cl}$ ) chemiluminescence.

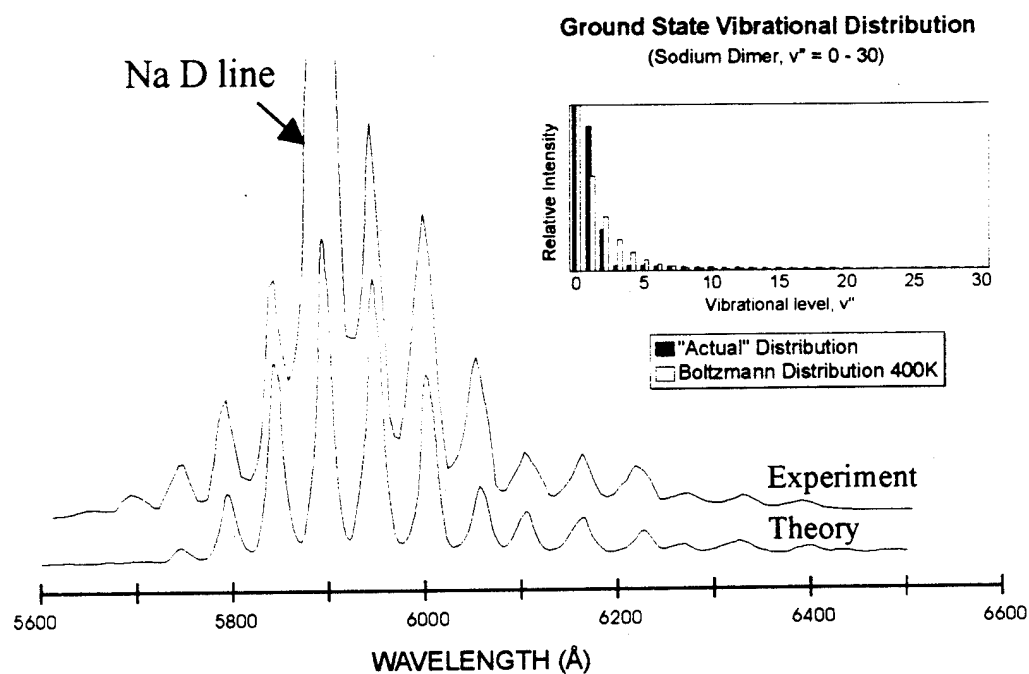


Figure 6  
Comparison of experimental spectrum with computer modelled distribution (res.  $\sim 5 \text{ \AA}$ ,  $T_{\text{oven}} \sim 875\text{K}$ ,  $T_{\text{nozzle}} \sim 935\text{K}$ ). Optimum agreement between calculation and experiment was found for the slightly nonthermal distribution depicted in the upper righthand corner of the figure. A Boltzmann distribution at 400K is included for comparison. See text for discussion.

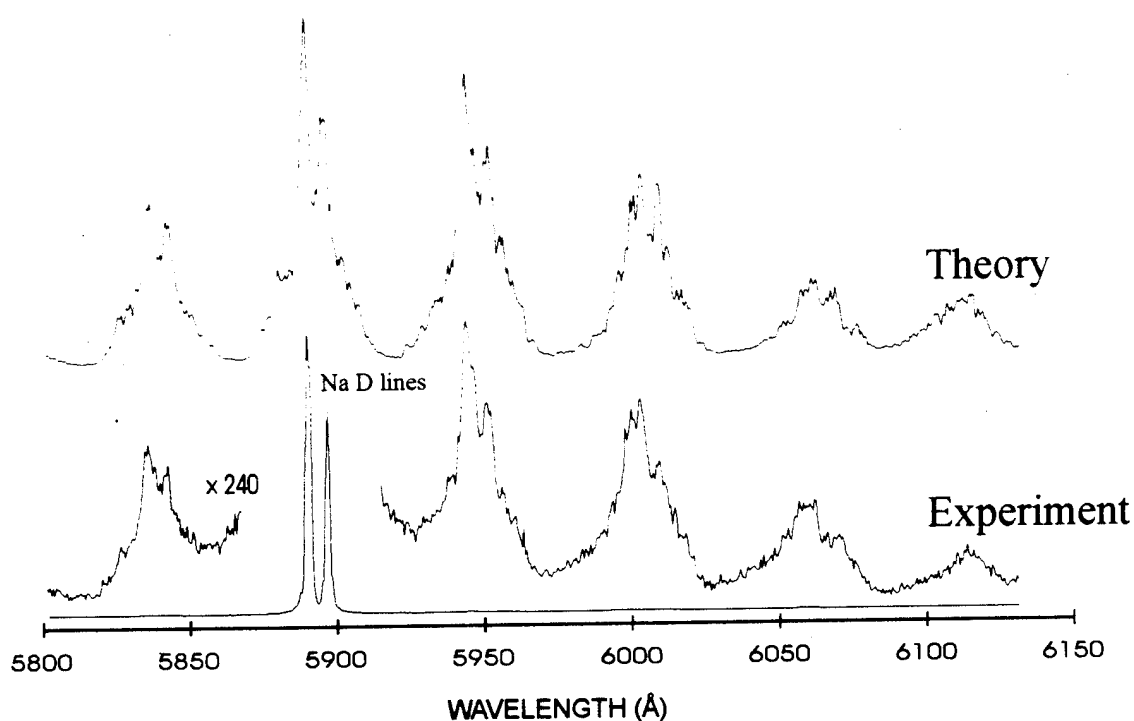
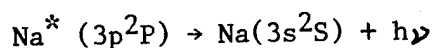
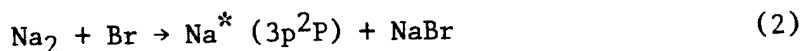


Figure 7  
Raman-like spectrum taken at a resolution of  $\sim 1.5 \text{ \AA}$  ( $T_{\text{oven}} \sim 875\text{K}$ ,  $T_{\text{nozzle}} \sim 935\text{K}$ ) depicting the two Na D-line components and the satellite Raman structure. The spin-orbit frequency difference of the two Na D-line components is reproduced in the scattered radiation. A simulated spectrum is presented for comparison ( $T_{\text{ROT}} \sim 400\text{K}$ ,  $\Gamma = 4 \text{ cm}^{-1}$ ). See text for discussion.

strongly with a scattering process involving the Na D-line components ( $3p^2P_{3/2,1/2} - 3s^2S_{1/2}$ ), clearly evident in Fig. 7, and (3) are created in the chemical reaction sequence



The Raman features depicted in Figures 6 and 7 are not readily generated by light from an external laser (Appendices VIII, X) tuned to the Na D-line resonance and appear to be enhanced by the environment of the reaction zone itself.

Any attempt to fit the observed structure (symmetric about the Na D-line) to a resonance fluorescent series appropriate to the experimental conditions fails completely. The D-line emission is scattered by cooled sodium dimers ( $\text{Na}_2$ ) generating multiple Stokes and anti-Stokes features. These are assigned as resonance Raman progressions and, as Figures 6 and 7 indicate, are well simulated on the basis of the resonance Raman theory outlined by Rousseau and Williams<sup>27</sup> and others.<sup>28</sup> Here, except at very low reactant concentrations, the intensity of the Raman scattering overwhelms any normal chemiluminescent emission from the reaction zone.

The results of initial gain studies (in which amplification has been observed on many of the Stokes and anti-Stokes components of the Raman spectrum) are suggestive of a stimulated Raman scattering process similar to that associated with optically pumped alkali dimer lasers. However, as Figure 8 demonstrates, the scattering linewidth,  $\Gamma$ , determined from a higher resolution fit ( $\sim 0.5 \text{ \AA}$ ) of the resonance Raman intensity expression (see Appendix X for definitions)

$$I_s(\nu_G, J_G, \nu_F, J_F) = \frac{32\pi^3 \omega_i^4 I_p}{9c^4 h^2} M(\xi_0)^4 e^{-E_0(J_0+1)hc/kT} N(\nu_G) \times \sum_{J_1} \left( 3S_{J_G} S_{J_F} \frac{|\langle \nu_F | \nu_1 \rangle \langle \nu_1 | \nu_G \rangle|^2}{(\omega_{G1} - \omega_{F1})^2 + \Gamma^2} + 2S_{J_G} S_{J_F} \frac{|\langle \nu_F | \nu_1 \rangle \langle \nu_1 | \nu_G \rangle|^2}{(\omega_{G1} - \omega_{F2})^2 + \Gamma^2} \right) \quad (3)$$

associated with the present process appears to be close to  $4 \text{ cm}^{-1}$ . This

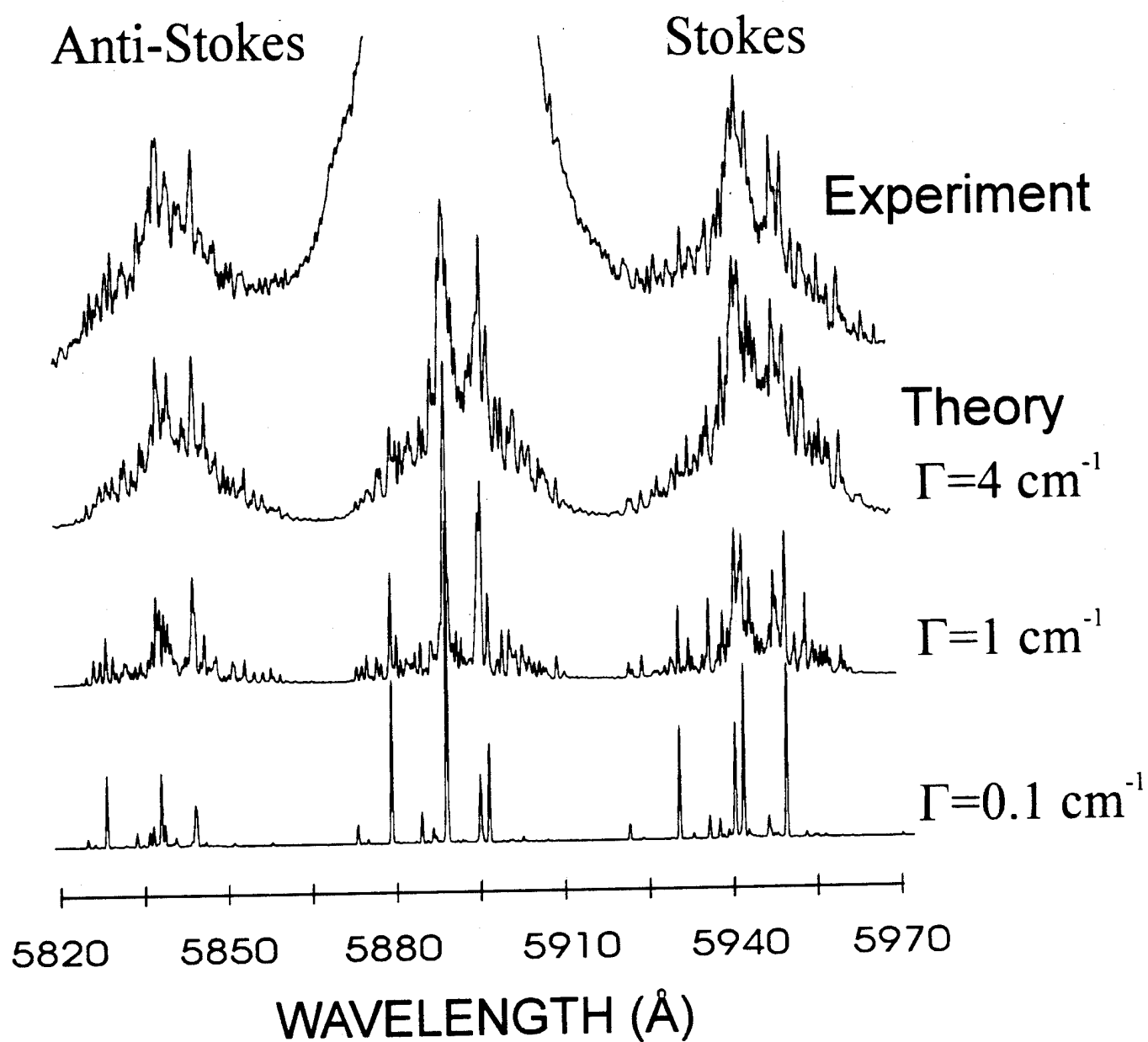


Figure 8

High resolution spectrum ( $\sim 0.5 \text{ \AA}$ ) and simulated spectra for  $\Gamma = 0.1, 1$ , and  $4 \text{ cm}^{-1}$  demonstrating the marked improvement in the fit to the experimental Raman-like features for increasing values of  $\Gamma$ . See text for discussion

result suggests that we have observed more than a "simple" Raman-like scattering process. In order to address this result we might consider a further long range interaction of the electronically excited sodium  $3p^2P$  atoms with those  $Na_2$  molecules which are Raman pumped, an interaction of the  $Na_2$  molecules with the Br atoms that induces a time varying enhancement of the dimer polarizability (hyperpolarizability), or (less likely) the presence of a large electric field created due to the reactive environment in the vicinity of the reaction zone. It would appear that this interaction leads to a much more efficient Raman-like scattering process which also is apparently chemically enhanced.

While further experiments will be necessary to clarify the mechanism for the scattering process, the long path length reaction zone employed in these experiments appears to have revealed the manifestation of a significant cooperative phenomena. The moderate Rydberg character of the  $Na\ 3p^2P$  excited state, with its diffuse electron density, may lend itself to a considerable long range interaction inducing cooperative effects. The assessment of these surprising cooperative effects should be the subject of continued study.

The intense "Raman" features depicted in Figures 6-8 have prompted preliminary experiments (Appendix X) to assess whether a stimulated Raman process might be operative. The path length of the active medium is in excess of 5 cm (considerably longer than most gas phase chemical reaction zones) and since the very intense D-line pumping is distributed virtually throughout the entire extent of this area, we attempted to assess the possible existence of a gain condition on any of the suspected Raman features (most likely the first Stokes line). It should be noted that gain would be predicted on the basis of the nonlinear treatment of the stimulated Raman effect, however, the gain condition might also be achieved for certain levels of the  $Na_2$  A-X transition through the resonance Raman effect if the  $Na_2$  ground state temperature is sufficiently low.

The layout of the gain measurement configuration used to conduct several preliminary gain measurements is depicted in Figure 9. In this experiment, a laser beam (HeNe laser) originating  $\sim 15$  ft from the expansion zone is directed through a small adjustable aperture and the reaction zone. The beam is subsequently reflected back through the aperture, thus ensuring that the normal of the reflector is perfectly parallel to the reaction zone. A light gathering lens is placed intermediate to the reaction zone and the adjustable

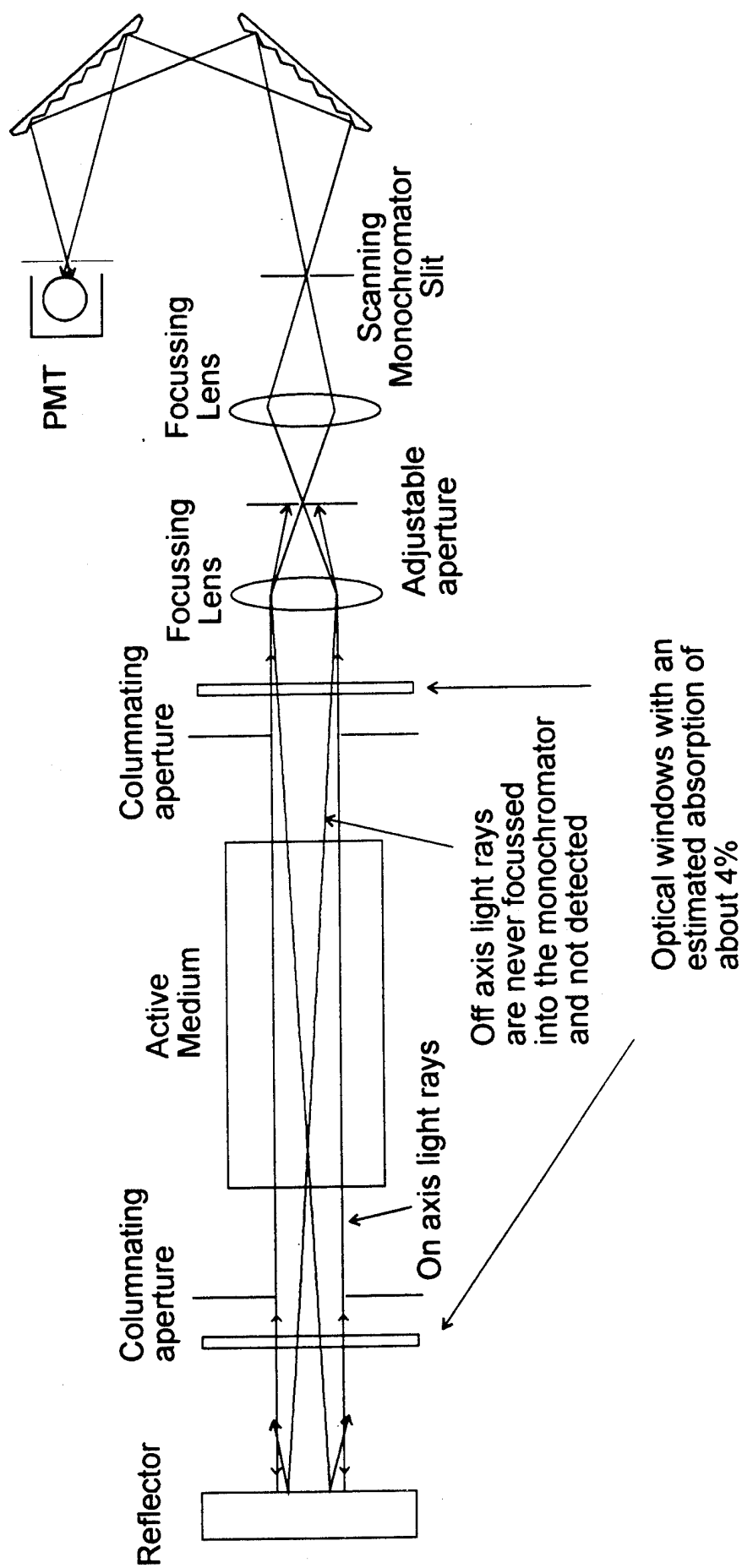


Figure 9

Schematic of gain measurement configuration. Intensities monitored with the PMT are measured with the high reflector blocked and unblocked. In the absence of gain or loss, the maximum ratio of those intensities that can be monitored can be no greater than two. The condition that we accept only light travelling parallel to the optical axis is necessary for the case in which the gain medium may not be uniform.

aperture so that light from the HeNe laser is reflected from the back mirror and focused onto the aperture. Establishing the geometry in this manner ensures that the optical system rejects off-axis light rays and accepts only radiation parallel to the optic axis. Consequently, observed output light intensities measured when the high reflector is blocked can be compared with intensities measured with the same reflector open to the reaction zone. Assuming that only on-axis radiation can be reflected from the mirror and subsequently detected, the maximum intensity ratio for the unblocked mirror ( $I_u$ ) to that observed with a blocked mirror ( $I_b$ ) can be no greater than two (neglecting the effects of gain and absorption in the reactive medium). The detection of a ratio ( $I_u/I_b$ ) greater than two is suggestive of the development of enough gain in the reactive medium to overcome any losses due to absorption or scattering. Although explicit measurements have not yet been performed, our glass optical windows usually absorb about 4% of the incident radiation per pass. Typically the distance between the mirror and the aperture is 1m, with the aperture narrowed to about 1 mm in diameter. The focal length of the lens was about 12 cm.

The described gain configuration was used to make several measurements at the first Stokes frequency ( $\sim 16830 \text{ cm}^{-1}$ ). The ratio,  $I_u/I_b$ , was consistently found to be in excess of 2.3. The measurements, performed on the remaining satellite peaks suggested ratios of order slightly greater than 2. Similar measurements performed on the Na D line components and several peaks of the thermally relaxed  $\text{Na}_2$  B-X emission system (Figure 5 - Appendix IV) showed intensity ratios much less than 2, the maximum intensity ratio monitored at the D-line being 1.3. Further discussion of the gain measurements can be found in Appendices IV and X.<sup>29</sup>

### **Extension of the $\text{Na}_3$ - X(Cl,Br,I) Amplifier Concept**

The  $\text{Na}_2$  amplifiers which we have characterized in the visible region operate on bound-bound transitions. It is not difficult to envision an extrapolation on the  $\text{Na}_3$ -X reaction concept which involves the alkaline earth metal trimers and the formation of excited state dimers which can undergo bound-free excimer transitions. With this focus, we have attempted to generate the  $\text{M}_2$  excimer analogs of the  $\text{Na}_2$  laser amplifiers discussed previously. The ground electronic state of  $\text{Mg}_2$  is very weakly bound.<sup>30</sup>

However, detailed calculations suggest the  $\text{Mg}_2$  - Mg bond strength may be on the order of 0.6 eV,<sup>31</sup> quite comparable to that of  $\text{Na}_3$ . We are now forming magnesium molecules, specifically  $\text{Mg}_2$  and  $\text{Mg}_3$ , and observing the excited state products of their oxidation with F and Cl atoms. A halogen atom discharge source which we have developed to study the  $\text{Bi}_2 + \text{F}$  reaction<sup>32</sup> (see also Appendix II) is being used to investigate the  $\text{Mg}_2\text{-F}$ ,  $\text{Mg}_3\text{-F}$ ,  $\text{Mg}_2\text{-Cl}$ , and  $\text{Mg}_3\text{-Cl}$  reactions.<sup>33</sup> These studies will soon be extrapolated to the heavier alkaline earths,  $\text{Ca}_x$  -  $\text{Ba}_x$ . To date, we have not observed strong  $\text{Mg}_2$  emission from the  $\text{Mg}_3$  - F, Cl reactions, however, surprisingly, preliminary results on this system signal the formation of excited state  $\text{Mg}_x\text{F}$  and  $\text{Mg}_x\text{Cl}$  charge transfer complexes where x is most likely two (Appendix IV). Although we have not yet demonstrated the potential for forming an  $\text{Mg}_2^*$  based excimer amplifier laser system, the creation of a long-lived  $\text{Mg}_x\text{F}$  complex suggests that, with some modification, this may be feasible.

#### Long Range Collisional Stabilization and the Symmetry Constrained Dynamics of High Temperature Complex Formation

As an off-shoot of our study of Group IIA cluster halogen atom reactions, in a study of Group IIA metal-halogen molecule reactions, we have now clearly demonstrated the highly efficient collisional stabilization of high temperature complexes of some considerable spatial extent.<sup>34</sup> In a series of near single collision and well-defined multiple collision CL and LIF studies extending over six decades of pressure (Appendices XI, XII), we demonstrate the stabilization of electronically excited Group IIA dihalide collision complexes via a radiative three body recombination (R3BR) process operative at microTorr pressures. Over the pressure range  $1 \times 10^{-6}$  -  $5 \times 10^{-4}$  Torr, a comparative study of the emission from  $\text{M}$  ( $\text{M} = \text{Ca}, \text{Sr}, \text{Ba}$ ) -  $\text{X}_2(\text{Cl}_2, \text{Br}_2, \text{I}_2)$  and  $\text{M-XY}(\text{ICl}, \text{IBr})$  reactive encounters identifies a symmetry constrained dynamics associated with the formation of the dihalide complexes (along a  $\text{C}_{2v}$  reaction coordinate) as they are stabilized by interaction with an additional halogen molecule. The symmetry constraint, indicated by a much weaker emission from the mixed halogen reactions (especially of barium and strontium), signals the dominance of an extremely efficient collisional stabilization. The onset of the monitored R3BR process at  $1 \times 10^{-6}$  Torr defines an extremely large stabilization cross section which cannot be readily explained within an RRKM

framework.

By relaxing the near continuous emissions (exemplified for the Sr reactions in Figure 10) observed for the complex formation under near single collision conditions, controlled multiple collision experiments establish the previously challenged stabilization mechanism<sup>35</sup> and show that the low pressure continua result from the overlap of a closely spaced, highly excited, rovibronic distribution. Further, as we demonstrate for the Sr-Cl<sub>2</sub> reaction in Figure 11, these multiple collision studies reveal the first vibronically resolved electronic emission for the dihalides. Comparative studies on several additional systems<sup>5,10,12</sup> of the resolved vibronic emission from the multiple collision experiments provide strong confirmation of the highly efficient collisional stabilization.

The observation of an R3BR process at pressures as low as  $1 \times 10^{-6}$  Torr is surprising. A steady-state treatment of the most reasonable mechanism for dihalide formation via collisional stabilization (within the RRKM framework) which models the chemiluminescence signal as a function of halogen concentration can be shown to be consistent with (1) an enormous stabilization cross section of order  $\sigma \sim 3000-5000 \text{ \AA}^2$ <sup>36</sup> and (2) an extremely long excited state radiative lifetime,  $\tau \sim 10^{-2}$  seconds. Within an RRKM framework, the collisional stabilization mechanism requires a radiative lifetime well in excess of  $10^{-5}$  seconds in order that emission from the complex compete favorably with the excited state dihalide loss mechanisms. However, experiments indicate that the process appears to be operative for much shorter lived excited states.

If we eliminate the requirement for a long-lived excited state, we must require a considerably larger stabilization cross-section and an extremely long range interaction involving the forming Group IIA dihalide excited states and their relaxing collision partner. It is clear that the stabilization process competes favorably with unimolecular decomposition for which RRKM calculations suggest a unimolecular lifetime (averaged over the distribution of energy and angular momentum) on the order of  $\tau \sim 10^{-7}$  seconds. These factors raise the question of whether association processes in these systems can be treated in a satisfactory fashion by employing some variant of unimolecular rate theory. A key question must be whether dissociative processes (well characterized by RRKM theory) or highly efficient energy transfer dominates these high temperature environments. We suggest that some

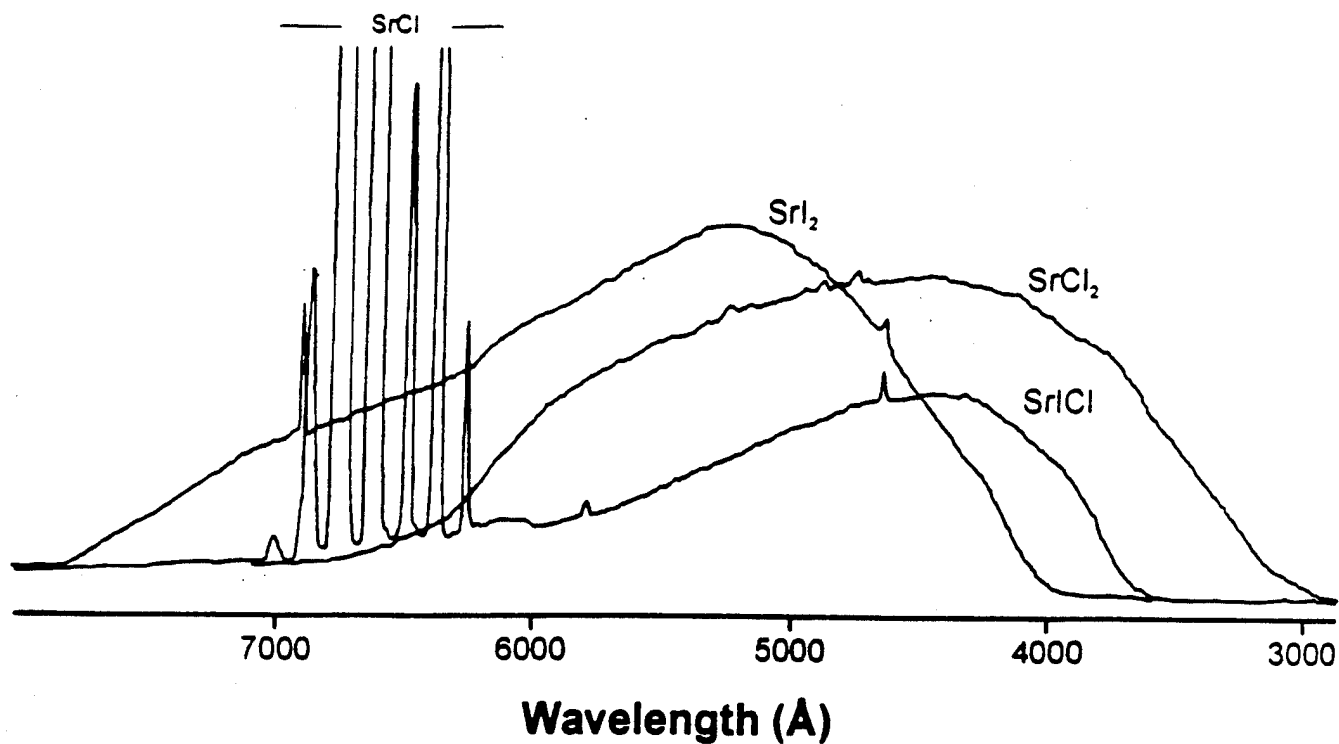


Figure 10

Continuum emission associated with the Strontium dihalides

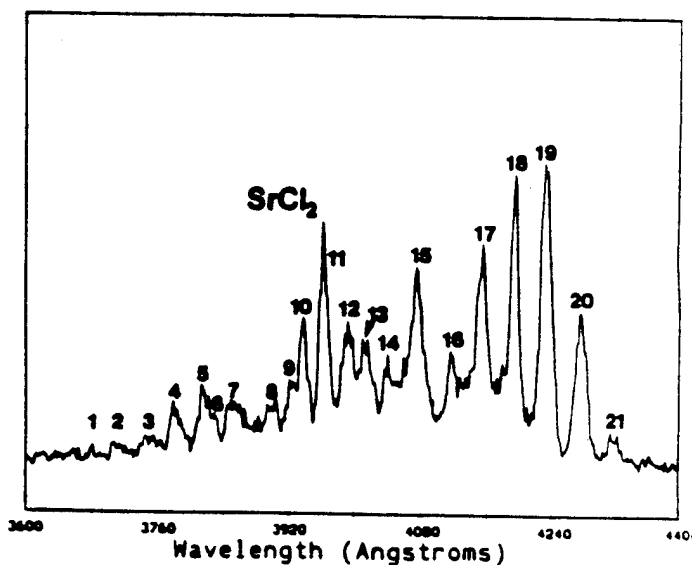
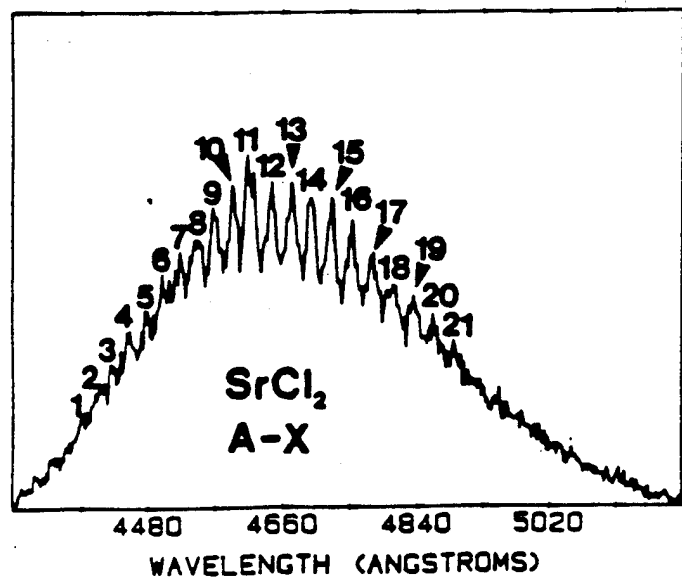
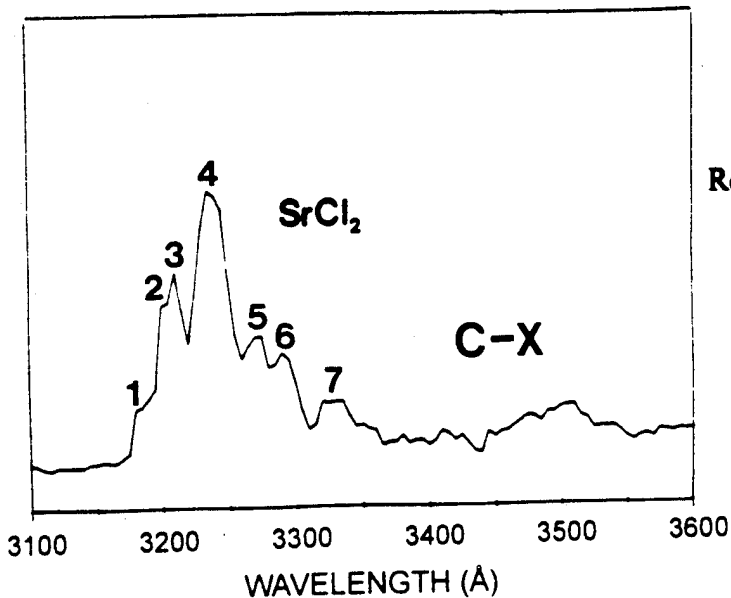


Figure 11

Resolved  $\text{SrCl}_2$  emission for the A-X, B-X, and C-X systems



answers to this question will be obtained by carefully monitoring the pressure dependence of the chemiluminescence over pressure ranges extending from the near single collision regime (e.g., Fig. 10) to the relaxed multiple collision regime (e.g., Fig. 11).

An expansion of the studies we have outlined, using a combination of CL and LIF techniques, can be employed to carefully define the periodicity of complex formation, and the importance of electronically induced pathways for energy flow. In the final analysis, these effects are associated with dihalide molecular electronic structure and its attendant effect on the dynamics of halide formation. They should, however, be manifest in all high temperature environments. A demonstrated collisional stabilization not readily explained within the RRKM framework suggests that new or highly modified models will be necessary to explain the efficient interaction of electronically excited states as well as highly vibrationally excited ground states. The data from this study now begin to provide important information on the efficient stabilization of excited state intermediate complexes, defining a much broader range of interaction than has typically been associated with collisional stabilization phenomena. The demonstrated interaction range of the dihalides (and the enhanced interaction of high temperature molecules in general) has direct implication for the understanding of molecular formation and energy transfer in those environments which characterize systems operating under extreme conditions. A neglect of these phenomena in models of chemical lasing, combustion, propulsion, or shock driven phenomena renders these descriptions unrealistic.

#### **NEAR RESONANT ENERGY TRANSFER FROM METASTABLE ENERGY STORAGE STATES OF SiO AND GeO TO FORM ATOM BASED LASER AMPLIFIERS**

We have found that certain near resonant intermolecular energy transfers proceed with extremely high cross sections. We have discovered an exciting family of reactions that efficiently transfer energy from the metastable triplet states of  $\text{SiO}^*$  and  $\text{GeO}^*$  to pump select excited states of several atoms. So efficient are these transfers that they have been used to produce superfluorescence from  $\text{Tl}^{37}$  and  $\text{Ga}^{37,38}$  atoms at 535 and 417 nm and amplified spontaneous emission (ASE) from Na atoms<sup>37</sup> at 569, 616, and 819 nm (Appendices III, V) and K atoms at 581 nm. The energy stored in the metastable triplet

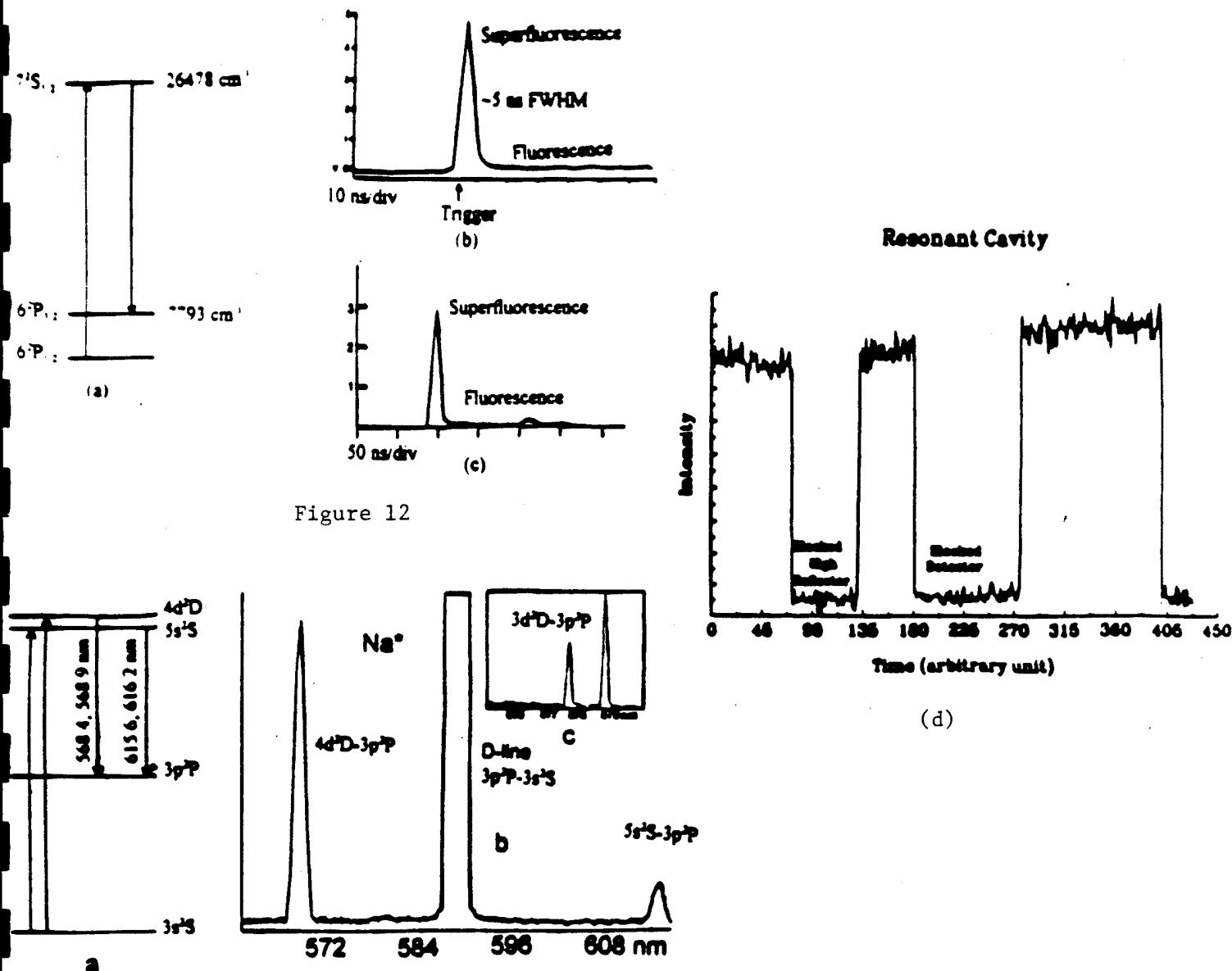


Figure 12

Figure 13

Figure 12(a): Tl atom energy levels.

Figure 12(b): Tl  $7^2S_{1/2} - 6^2P_{1/2}$  (535 nm) superfluorescence observed at a signal trigger level of 0.2V (fluorescent level  $\sim 0.45V$ ). The measured FWHM is  $< 5 \text{ ns}$  (compared to  $\tau \sim 7.5 \text{ ns}$ , the radiative lifetime of the  $7^2S_{1/2}$  level. A return to the fluorescence level is seen subsequent to the superfluorescence pulse. No superfluorescent pulse is associated with the Tl  $7^2S_{1/2} - 6^2P_{3/2}$  (377 nm) transition.

Figure 12(c): Tl  $7^2S_{1/2} - 6^2P_{3/2}$  (535 nm) superfluorescent oscillation observed with full laser cavity configuration. The superfluorescence/fluorescence ratio (fluorescence following termination of lasing action) is in excess of 100.

Figure 13(a): Na atom energy level scheme and pumping cycles to produce  $4d^2D$  and  $5s^2S$  excited states.

Figure 13(b): Typical energy transfer pumping spectrum for Na  $4d^2D - 3p^2P$  and  $5s^2S - 3p^2P$  transitions and  $3p^2P - 3s^2S$  sodium D-line emission. The D-line emission results both from direct energy transfer pumping from ground state  $N_2O$  and from fluorescence to the  $3p^2P$  level.

Figure 13(c): Energy transfer pumping spectrum corresponding to the Na  $3d^2D - 3p^2P$  transition.

Figure 13(d): Full cavity output created with  $\sim 0.2\%$  output coupling for the continuous Si-SiO ( $Si-N_2O$ ) - Na amplifier at  $569 \text{ nm}$ . The full cavity output is compared to that obtained with both a blocked high reflector and with the entire cavity isolated from the signal detection system. The ratio of the output obtained for the full cavity to that obtained with a blocked high reflector exceeds  $10^3/1$ .

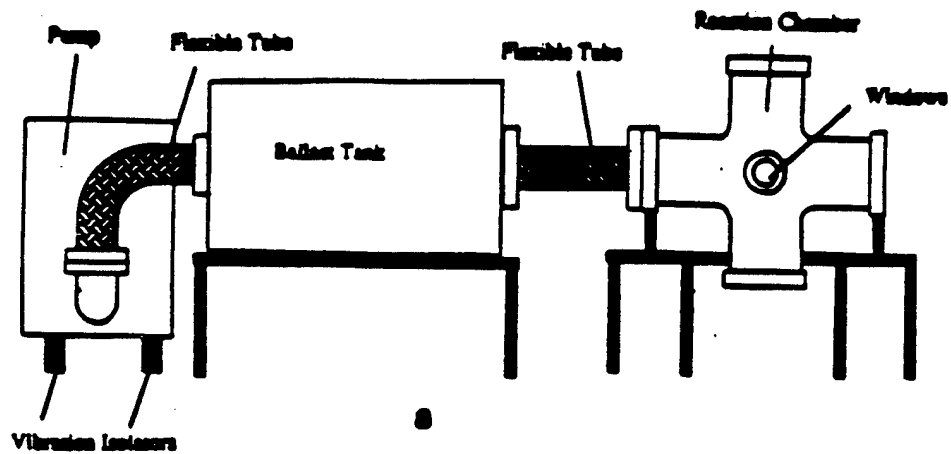
states, formed from the  $\text{Si}(^3\text{P}) + \text{NO}_2$ ,  $\text{N}_2\text{O}^{39,40}$  and  $\text{Ge}(^3\text{P}) + \text{O}_3^{41}$  reactions, is transferred to pump (Fig. 12)  $\text{X}^2\text{P}_{1/2}$  Tl atoms to their lowest lying  $^2\text{S}_{1/2}$  state<sup>37</sup> and (Fig. 13)  $\text{X}^2\text{S}_{1/2}$  Na atoms<sup>37</sup> to their excited  $3\text{d}^2\text{D}$ ,  $4\text{d}^2\text{D}$ , and  $5\text{s}^2\text{S}$  states. Adopting a pumping sequence in which a premixed Group IVA metalloid-receptor atom combination is oxidized, we observe a system temporal behavior which suggests the creation of a population inversion and gain condition in the Tl and Na systems, forming the basis for short pulse full cavity oscillation on the Tl  $7^2\text{S}_{1/2} - 6^2\text{P}_{3/2}$  transition at 535 nm and continuous oscillation on the Na  $4\text{d}^2\text{D} - 3\text{p}^2\text{P}$  transition at 569 nm. The continuous oscillation associated with the sodium system (Appendices III, V), in particular, demonstrates an astounding energy transfer efficiency.

One might envision the SiO and GeO " $\text{a}^3\Sigma^+$ " and " $\text{b}^3\Pi$ " states forming a combined metastable triplet state reservoir which is, at best, weakly coupled to the ground electronic  $\text{X}^1\Sigma^+$  state (minimal nonradiative transfer). This reservoir can be maintained and can transfer its energy to pump the atom of interest if a near resonant energy transfer is feasible. This approach is outlined in more detail in Appendices III and V.

We have used SiO metastables formed in the Si- $\text{N}_2\text{O}$  reaction, to successfully energy transfer pump Na atoms to their low-lying  $5\text{s}^2\text{S}$  and  $4\text{d}^2\text{D}$  levels from which they subsequently emit radiation at  $\lambda \approx 616$  nm and 569 nm as they undergo transition to the  $3\text{p}^2\text{P}$  levels. The accessed Na cycle with its  $50^{42}$  ( $4\text{d}^2\text{D} - 3\text{p}^2\text{P}$ ) to  $\sim 100$  nanosecond upper state radiative lifetimes (vs. for example Tl  $^2\text{S}_{1/2}$  at  $\sim 7_{\text{nsec}}$ .<sup>43</sup>) and short-lived terminal laser level would appear ideally suited to obtain higher duty cycle laser amplifiers and oscillators. We also obtain evidence for the energy transfer pump of the Na  $3\text{d}^2\text{D}$  level with which is associated an atomic emission at  $\lambda \approx 819$  nm ascribed to the Na  $3\text{d}^2\text{D} - 3\text{p}^2\text{P}$  transition.

In order to study amplification in the sodium and potassium systems, we have constructed a relatively versatile device (Fig. 14) (see also Appendices III and V) which allows us to obtain a moderately long amplification path length.<sup>16</sup> This construction can take advantage of three entrainment flow configurations for silicon or germanium in the cycle producing SiO and GeO metastables, one of which is depicted in Fig. 14. These flow configurations produce the longest path length SiO metastable flame (5 + cm) yet obtained. The entrainment flow configuration must be designed to create large concentrations of SiO (GeO) metastables which are intersected at  $\sim 90^\circ$ , in

Figure 14: (a) Schematic of reaction chamber and windows defining optical train, ballast tank to moderate pumping fluctuations, and pumping configuration, for extended path lengths Si-SiO (Si-N<sub>2</sub>O)-Na reaction amplification zone. (b),(c) Side and overhead views of reaction chamber showing positioning of Si oven source, relative locations of Si and Na oven sources, oxidant injection system, and relative positions of these devices with respect to the optical train. (d),(e) Closeup view of silicon and sodium oven assemblies. (f) Schematic overview of reaction chamber-amplification zone, ballast, and pump for extended path length Si-SiO(Si-N<sub>2</sub>O)-Na gain medium. The figure indicates the course alignment path (~ 15 ft) for the HeNa laser and its correlation with the optical train surrounding the reaction zone and terminating at the monochromator.



Overall Apparatus Configuration

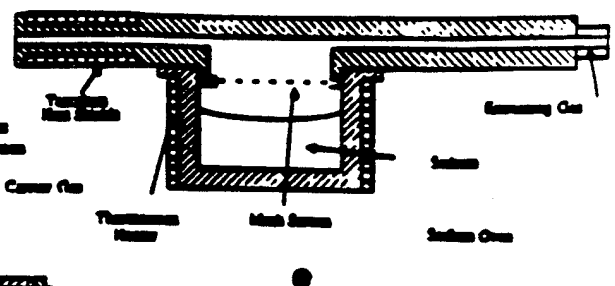
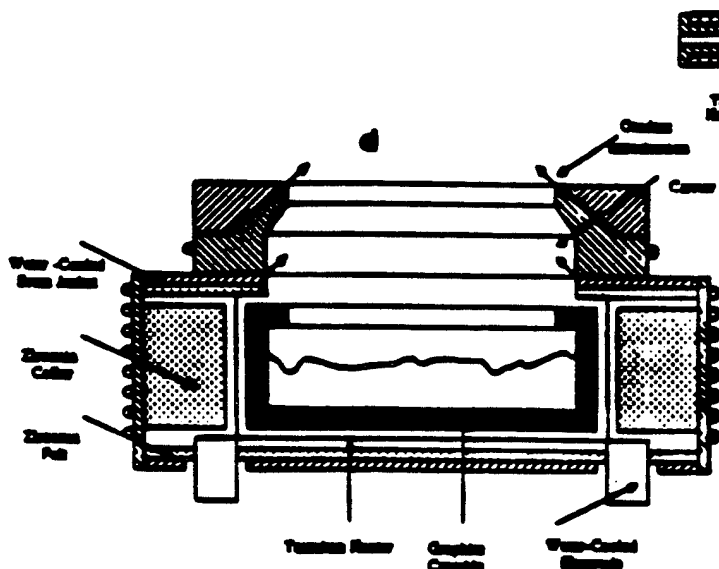
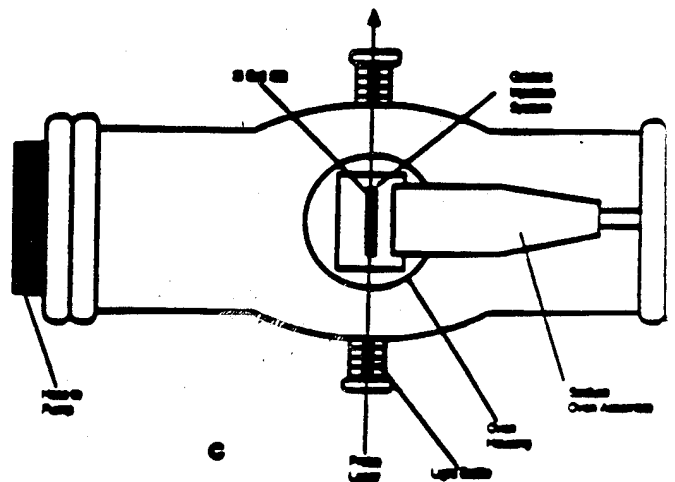
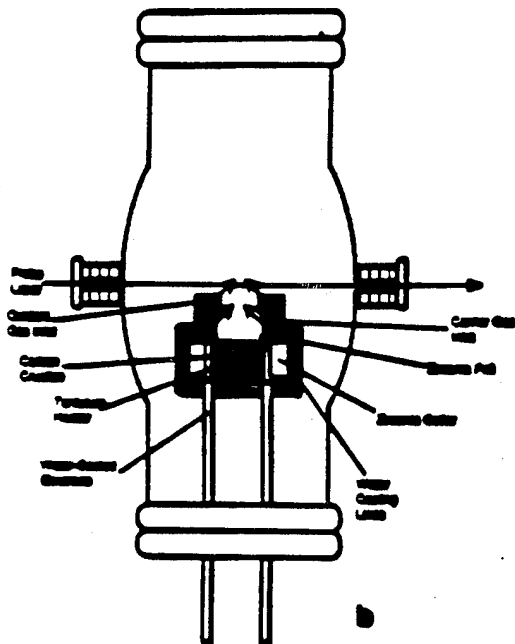


Figure 14

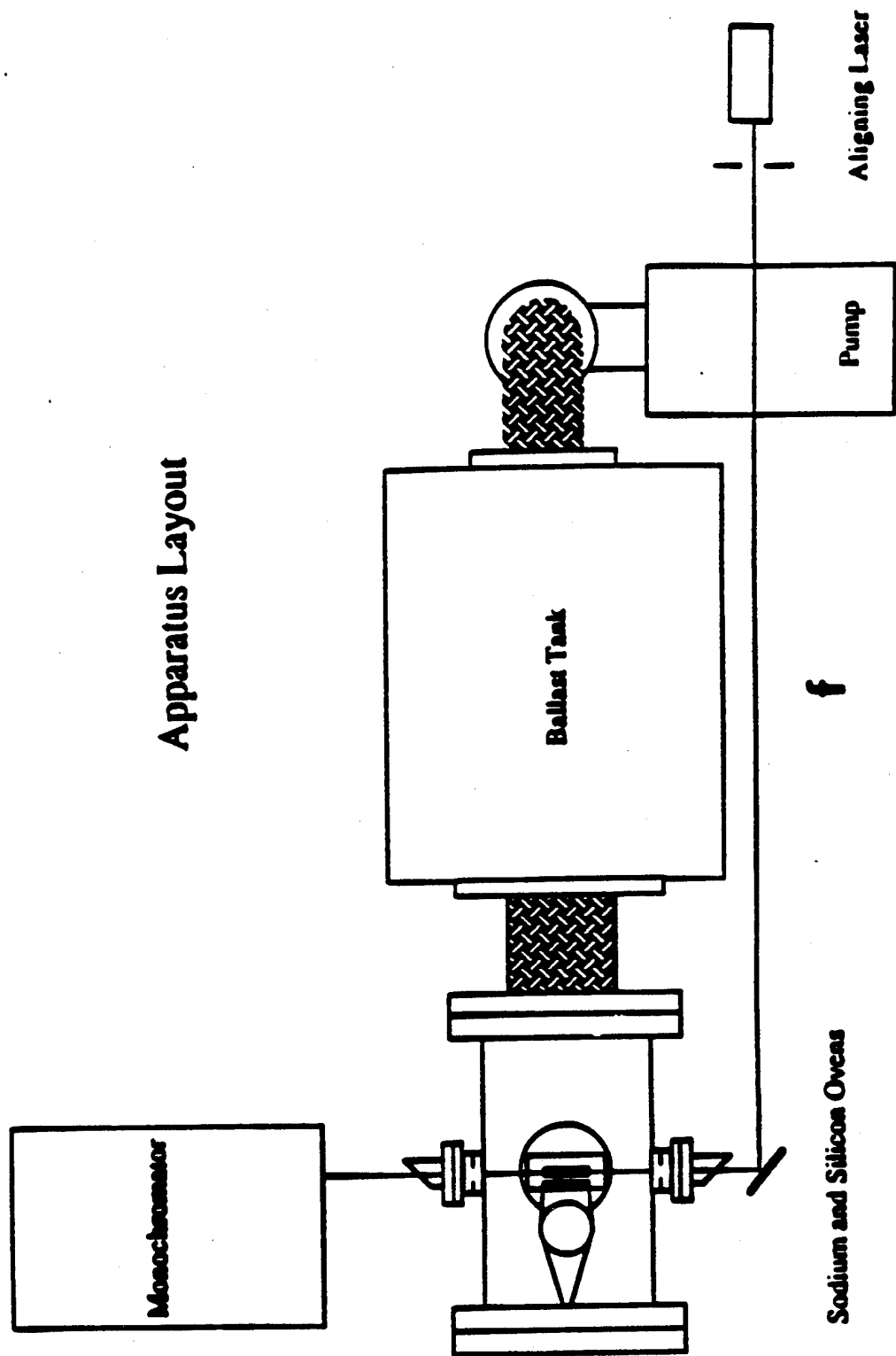


Figure 14

subsonic flow, by a high concentration of sodium or potassium atoms. The entrained (argon, helium, nitrogen) silicon and sodium flows can also be moved in-situ relative to each other and hence with respect to the reaction - energy transfer - amplification zone to optimize conditions for formation of the gain medium.

The entrainment flow device depicted in Figure 14 can be surrounded by a variety of optical trains to measure gain and lasing in the Si-SiO-Na system. These are discussed in detail in Appendices III and V. The three sodium atom transitions at  $\lambda \approx 569$  nm ( $\alpha \sim 0.1-0.15/\text{cm}$ ),  $\lambda \approx 616$  nm ( $\alpha \sim 0.03-0.05/\text{cm}$ ), and  $\lambda \approx 819$  nm ( $\alpha \sim 0.02-0.03$ ) demonstrate continuous gain, although optimal gain on each line is monitored under slightly different mixing conditions in the amplification zone (App. III). Gain has been measured (Appendices III, V) at all three wavelengths using the ingenious design of Roll and Mentel.<sup>44</sup> We compare the (paraxial) single vs. double pass amplified spontaneous emission emanating from the 5 cm amplification zone of Fig. 14. Further, at 569 nm, two additional gain measurements have been performed (Detailed - Appendix III), one deducing the amplification of the  $4d^2D - 3p^2P$  transition from a sodium discharge lamp and a second employing a scanning single-mode ring dye laser. Preliminary measurements at 616 nm using the sodium discharge lamp also demonstrate a continuous gain condition.

### "Full Cavity Measurements"

Full cavity measurements (detailed in Appendices III, V) have also been made on the sodium system. The results of these measurements at 569 nm for a 0.2% output coupled stable cavity configuration are shown in Figure 15. We find that the ratio of the output for full cavity operation to that obtained with a blocked high reflector easily exceeds  $10^3$ . Compare also the signal level observed with the blocked high reflector and that monitored with a completely blocked detector. The corresponding ratio obtained operating the full cavity below threshold using the 0.2% output coupled cavity was slightly greater than 1.8 for the Na D-line. These results clearly indicate continuous laser oscillation in the sodium system.

The value slightly greater than 1.8 for the Na D-line should be compared to a maximum of 1.2 for a much more lossy 4.5+% output coupled device ( $g_1 g_2 \sim 0.56$ ). In fact, a maximum (full cavity/blocked reflector) ratio of order

Figure 15: Full cavity output created with  $\sim 0.2\%$  output coupling for the continuous Si-SiO(Si-N<sub>2</sub>O)-Na amplifier at  $\lambda = 569$  nm. These measurements were taken in continuous flow with the cavity configuration depicted in Fig. 3(b). The full cavity output is compared to that obtained with both a blocked high reflector , and with the entire cavity isolated from the signal detection system. The ratio of the output obtained for the full cavity to that obtained with a blocked high reflector exceeds  $10^3/1$ .

# Resonant Cavity

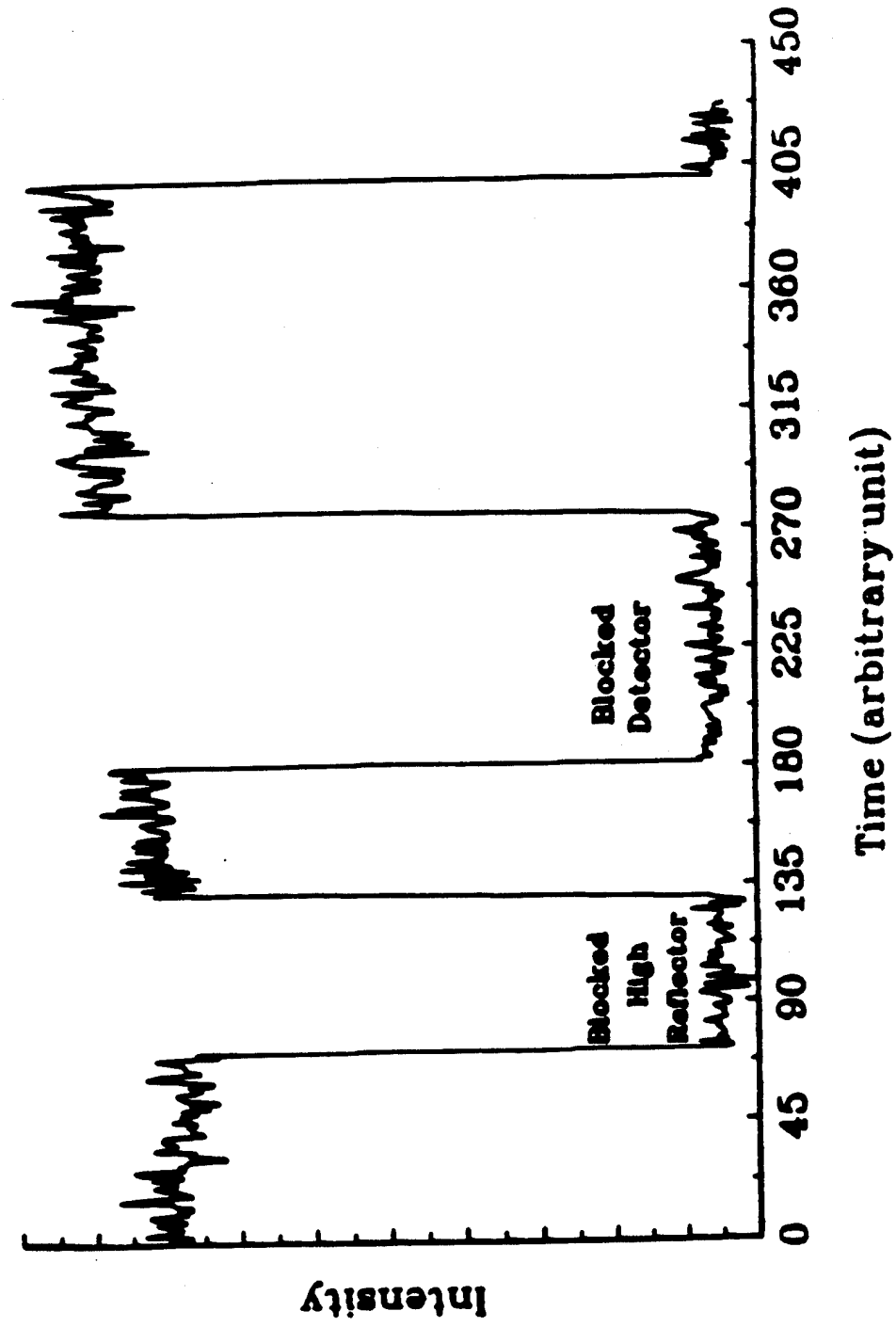


Figure 15

1.9-1.95 is typical for all those wavelengths considered ( $\lambda \approx 569, 616$ , Na D-line) when conditions in the reaction-amplification zone are such that no gain is monitored. We have also observed intermediate behavior associated with the establishment of moderate but not optimal gain conditions.

## **Improvement of the Energy Transfer Based Configuration - Ultimate Goals**

### **A. Concentric Reactant Mixing**

While the outlined configurations have been used to demonstrate lasing action in the visible region, this should be substantially enhanced with several improvements in the manner in which the lasing medium is created and the laser output is extracted from the cavity. The mixing zone depicted in Figure 14 is greatly stabilized by the moderate sized ( $\sim 15$  cubic feet) ballast separating the 150 cfm pump and reaction chamber. While this insures that the  $90^\circ$  intersection of the SiO and sodium atom flows can be used to establish a continuous lasing action, the  $90^\circ$  reactant intersection is by no means optimal. It remains to increase both the rate limiting silicon and sodium atom concentrations in the reaction zone while maintaining atomization. A logical way to approach this problem involves the conversion of the intersecting flow configuration of Figure 14 to a concentric interaction configuration. We are currently testing and modifying the two designs depicted in Figure 16 (see also Appendices III and V) as a means of attaining higher reactant - amplifying medium concentrations. These two designs attempt to create a more efficient mixing of those constituents forming the amplifying medium. In both designs, the sodium source is now placed directly above the silicon source, however, the designs differ in the sequence in which they introduce the reactants. One design (Fig. 16(a)) first creates the SiO metastables through the Si-N<sub>2</sub>O reaction and subsequently interacts the entrained metastables with an entrained Na flow. In a slightly modified design (Fig. 16(b)) we attempt to premix concentric entrained flows of silicon and sodium, oxidizing the mixture with N<sub>2</sub>O. The two designs both result in a substantial enhancement of reactant concentration and mixing as evidenced by the significant  $\sim 100$  fold increase in light emission from the reaction zone as monitored through a side-angle viewing port. However, they also produce a significant increase in particulate matter and gas phase condensibles for which the current pumping system does not appear to be well suited. These

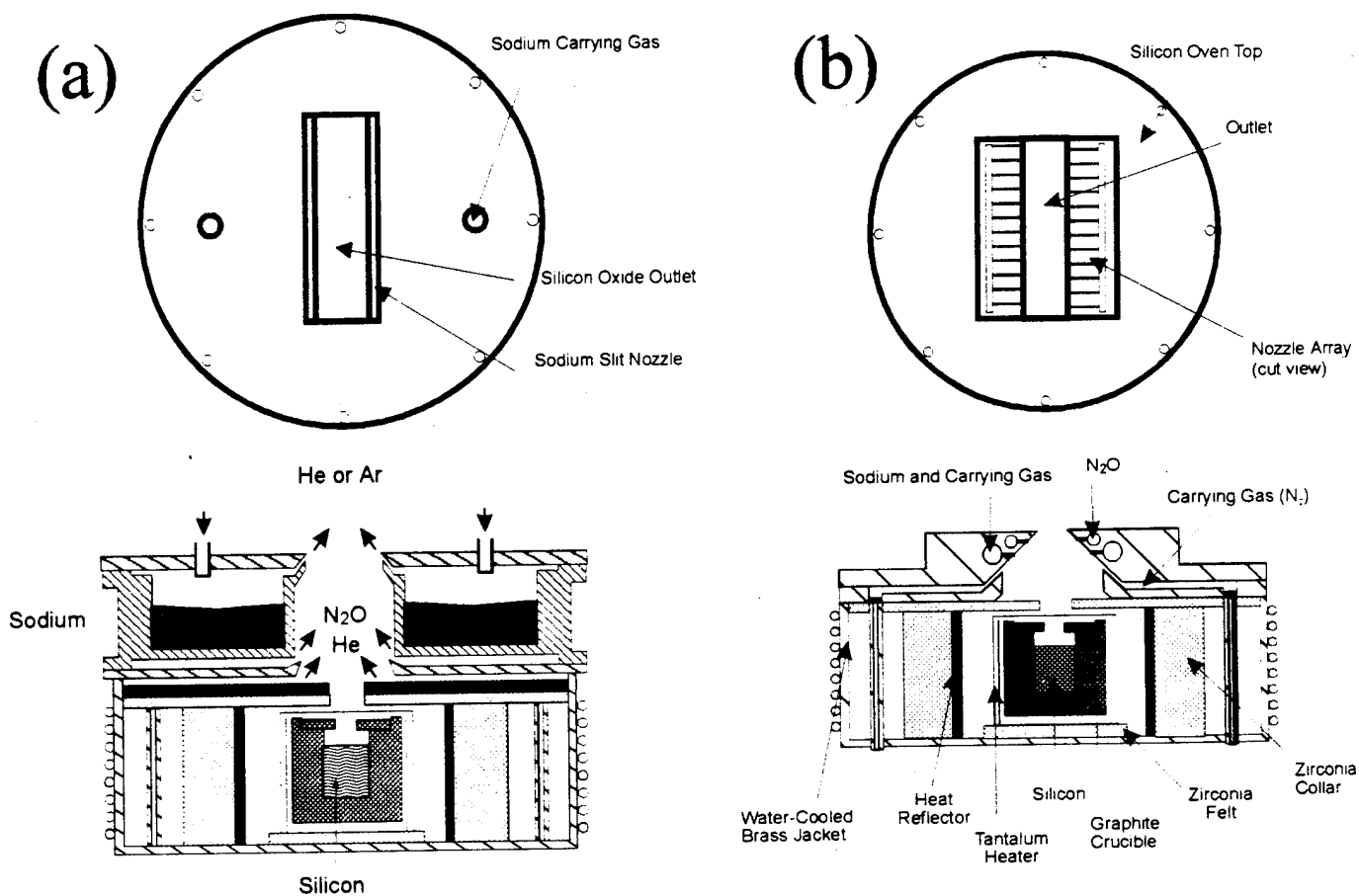


Figure 16(a): Concentric configuration for energy transfer pumping. The sodium oven is placed above the silicon oven. The oxidant N<sub>2</sub>O is introduced into the silicon flow to form SiO\* which then interacts with sodium vapor. The energy transfer zone is approximately 1" above the silicon oven.

Figure 16(b): Concentric configuration for energy transfer pumping with a sodium and N<sub>2</sub>O injector nozzle array placed above the silicon oven. In this configuration the sodium and silicon are mixed before the oxidant is introduced to initiate the energy transfer process.

### Sodium Atomic Emission SiO-Na Energy Transfer

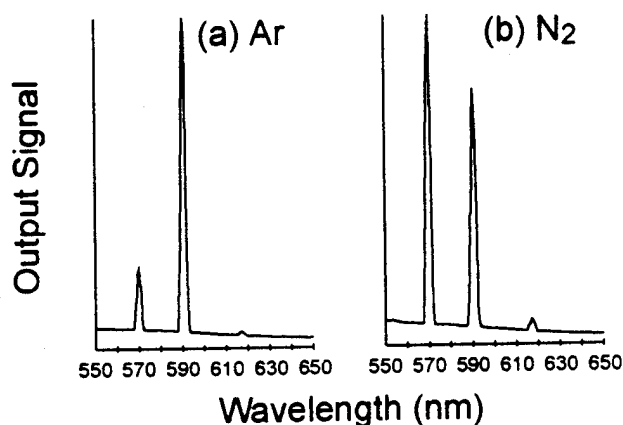


Figure 17: Energy transfer pumping spectra obtained for (a) Ar and (b) N<sub>2</sub> entrainment. The observed Na 4d<sup>2</sup>D - 3p<sup>2</sup>P emission feature (~ 569 nm) is seen to increase precipitously in intensity relative to the Na 3p<sup>2</sup>P - 3s<sup>2</sup>S D-line (~ 590 nm) with change of entrainment gas from Ar to N<sub>2</sub>.

condensibles have the attendant affect of degrading cavity windows, substantially increasing loss elements in the optical train. With some modification of the pumping system, the realignment of entrainment flows, the modification of entrainment gases to best suit the chemistry of the system, and the adjustment of window protecting flows, these problems should be greatly alleviated.

## B. Considering Self Absorption and Self Quenching

The increase of reactant concentrations may lead to a leveling off and eventual loss of the gain condition if self-absorption on the Na D-line transitions becomes a dominant factor or SiO triplet self-quenching begins to play a deleterious role. Evidence is obtained for some self-absorption at the highest sodium concentrations when the alkali atom production dominates the concomitant SiO metastable production. With our sodium atom source operated, in the absence of interacting silicon or N<sub>2</sub>O, at the temperature which we have employed to produce the highest flux densities in the amplification zone, we have measured the attenuation of the Na D-line emission from a sodium discharge lamp. We find an attenuation which is much less than 50%. In combination with the cross section for self absorption,  $4 \times 10^{-14} \text{ cm}^2$ , as measured by Ermin et al.,<sup>45</sup> this suggests a sodium atom concentration close to that estimated for the system (Appendices III and V). Of course, in the presence of the N<sub>2</sub>O and silicon reactants, the attenuation due to self absorption, while evidenced, is considerably diminished ( $\sim 5 - 10\%$ ).

Although concern with the possible deleterious effect which a pumping of the Na D-line might have on transitions terminating in the 3p<sup>2</sup>P level is somewhat alleviated in the present system by the sodium discharge experiments of Tribilov and Shukhtin,<sup>46</sup> and the 0.01 second duration laser pulse for the Na 4s<sup>2</sup>S - 3p<sup>2</sup>P infrared transition observed by Mishakov and Tkachenko<sup>47</sup> as quasicontinuous lasing, it must eventually limit the size of the laser systems. However, this might be forestalled to great degree if we take advantage of the efficient quenching of Na 3p<sup>2</sup>P atoms which Tanarro et al.<sup>48</sup> have demonstrated for N<sub>2</sub> and CO. In fact, as demonstrated in Figure 17, if we replace the Si-SiO and Na entraining argon or helium gases with N<sub>2</sub>, we observe a pronounced effect on the energy transfer spectrum taken for an intermediate sodium flux.

### C. Nitrogen vs. Argon Entrainment

While the 569 nm feature is dominated by the Na D-line emission when argon is used as an entrainment gas, its intensity can be made to exceed that of the D-line when  $N_2$  is used. This result, obtained and repeated for successive scans taken during the same experimental run, suggests the possibility for a considerable enhancement of the 569 nm output. This improvement might well result from the quenching of  $Na\ 3p^2P$ , however, it might also result from an increased inhibition of the  $Na + N_2O \rightarrow NaO + N_2$  reaction as the equilibrium is forced toward reactants.<sup>49</sup>

### D. Output Coupling

The experiments conducted thusfar have made use of two distinct output coupling configurations. As well as improving reactant concentrations the optimum output coupling for the current cavity remains to be evaluated. We have constructed a modification which will allow removal of the cavity windows that represent significant loss elements. With these improvements and further collaboration in both cavity and output coupling design with Professor Lee Sentman and his group at the University of Illinois,<sup>50</sup> the output from our full cavity configuration should be substantially enhanced.

### System Modeling

Recently, Smith et al.<sup>51</sup> carried out a laser chemistry modeling effort on the SiO-Na system. Starting with the initial concentrations of the reactants Na, Si, and  $N_2O$  which are achievable in the present system these authors have used a model which includes the 10 possible processes

1.  $Si+N_2O \rightarrow SiO^*+N_2$  - metastable excited state formation.
2.  $Si+N_2O \rightarrow SiO+N_2$  - ground state formation - power depleting.
3.  $SiO^*+Na \rightarrow SiO+Na^* (4d^2D)$  - upper state amplifying transition.
4.  $SiO^*+Na \rightarrow SiO+Na^* (3p^2P)$  - terminal level amplifying transition.
5.  $SiO^*+SiO^* \rightarrow SiO+SiO$  - self quenching of SiO metastables.
6.  $Na^* (4d^2D) \rightarrow Na^* (3p^2P) + h\nu (569\text{ nm})$  - spontaneous emission.
7.  $Na^* (4d^2D) + h\nu (569\text{ nm}) \rightarrow Na^* (3p^2P) + 2h\nu (569\text{ nm})$  stimulated emission.
8.  $Na^* (3p^2P) + h\nu (569\text{ nm}) \rightarrow Na^* (4d^2D)$  - optical pumping.

9.  $\text{Na}^* (3p^2P) \rightarrow \text{Na}^* (3s^2S) + h\nu (569 \text{ nm})$  - spontaneous emission.
10.  $h\nu (569 \text{ nm}) \rightarrow h\nu (569 \text{ nm})$  outcoupling fraction for 569 nm photons (laser cavity 5 cm in length - mirror reflectivities 99.99 and 99.80%.

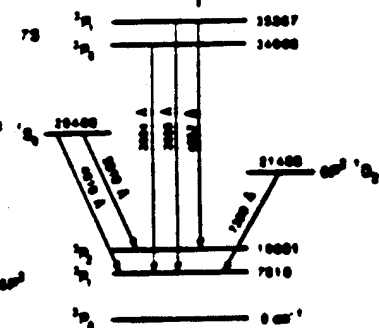
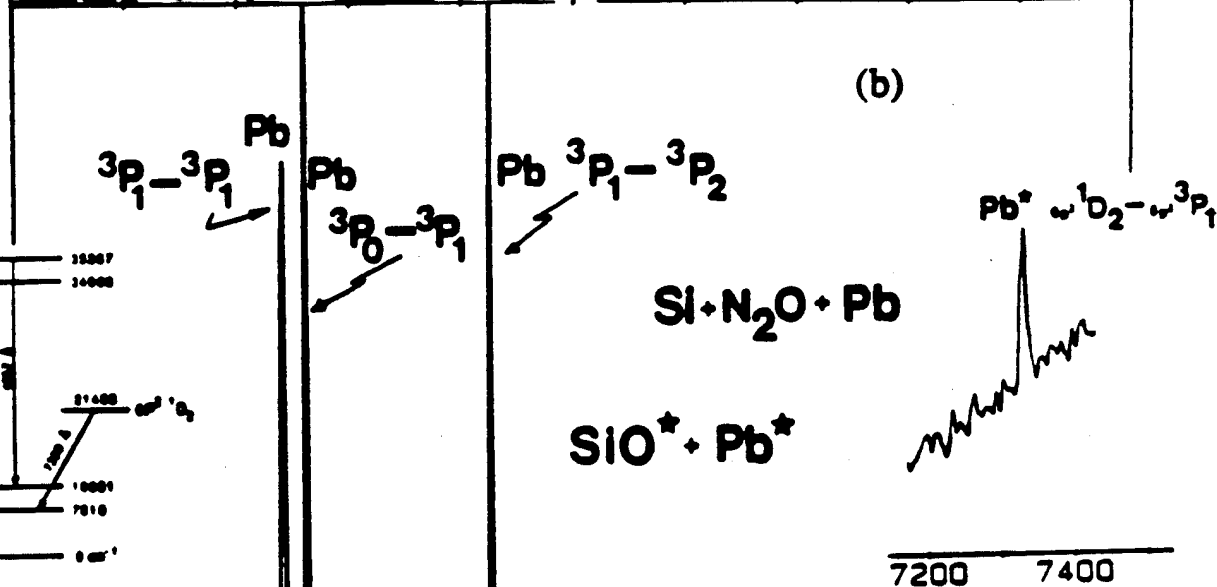
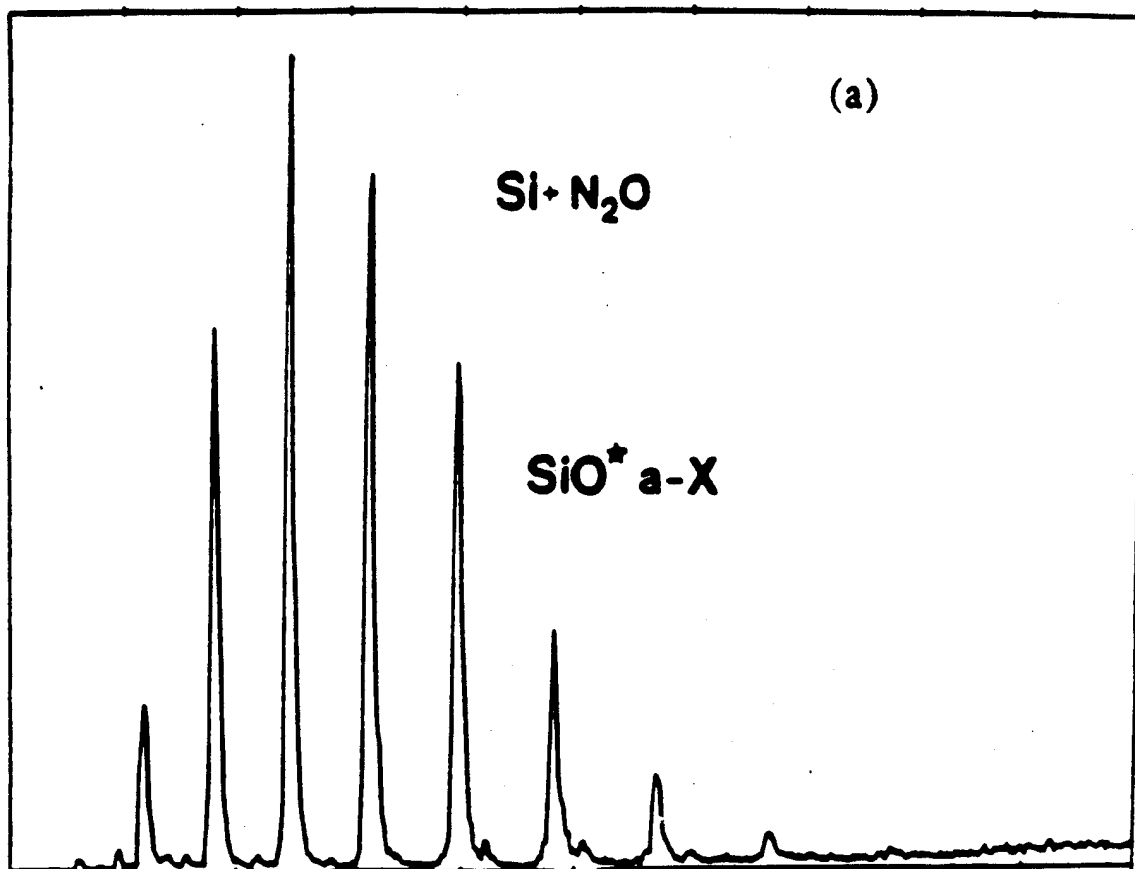
Using known kinetic rates, variable initial concentrations, reasonable and variable rates for those processes which have not been directly measured, and assuming a closed reaction in which the reactants are not replenished, Smith et al.<sup>51</sup> have deduced temporal profiles for the Na concentration, 569 nm photon concentration, energy density, and power density. They conclude that order of magnitude increases in the initial concentration of Si or  $\text{N}_2\text{O}$  have a profound effect on the system (power density increase) whereas significant changes in the Na concentration have relatively little effect. This signals the rate limiting nature of the silicon concentration and the importance of the branching into the metastable triplet states. It is also to be noted that a significant increase in power density may be muted by  $\text{SiO}^*$  self quenching, the rate of which certainly must be established for these systems. For the diversity of initial reactant concentrations and rates used in their model, Smith et al.<sup>51</sup> predict output power densities peaking between 100 (strong  $\text{SiO}^*$  self quenching) and 7000 mW/cc. These results are quite encouraging.

#### **Extension of Near Resonant Intermolecular Energy Transfer Concept to Additional Energy Transfer Pumped Atomic Receptors**

While we have emphasized the results obtained thusfar for the sodium system based on an  $\text{SiO}$  metastable pump, it is also feasible to use  $\text{GeO}$  metastables. In fact, we have obtained evidence that the energy transfer pumping of the sodium analog potassium based amplifiers associated with the  $5d^2D - 4p^2P$  ( $\lambda = 581, 583 \text{ nm}$ ),  $4d^2D - 4p^2P$  ( $\lambda = 694, 697 \text{ nm}$ ), and  $6s^2S - 4p^2P$  ( $\lambda = 691, 694 \text{ nm}$ ) potassium atom transitions might best be accomplished with pumping by  $\text{GeO}$  metastables.

We have also successfully energy transfer pumped potential amplifying transitions in lead (Pb), copper (Cu), and tin (Sn) receptor atoms. Two of these systems are particularly intriguing. Figure 18 demonstrates the results we have obtained when interacting  $\text{SiO}$  metastables ( $\text{Si-N}_2\text{O}$ ) with lead receptor atoms (see also Tables III and IV - Appendix V). Observed Pb transitions are indicated to the right of the figure. First, we notice that self absorption

Figure 18: Comparison of lead - SiO ( $A^3\Sigma^+, b^3\Pi$ ) near resonant energy transfer spectra. Metastable SiO molecules were created in the reaction  $\text{Si} + \text{N}_2\text{O} \rightarrow \text{SiO}^* + \text{N}_2$ . (a) The spectrum corresponds to a portion of the SiO metastable emission spectrum before lead atoms are brought into the reaction zone. (b) Spectrum recorded with high Pb flux ( $\sim$  torr vapor pressure) showing the manifestation of energy transfer pumping to produce electronically excited  $^3\text{P}^0$ ,  $^1\text{S}_0$  and  $^1\text{D}_2$  levels of the lead atom. (c) Energy levels for the lead atom with observed transitions as indicated in (b).



Pb atom energy levels and the observed transitions.

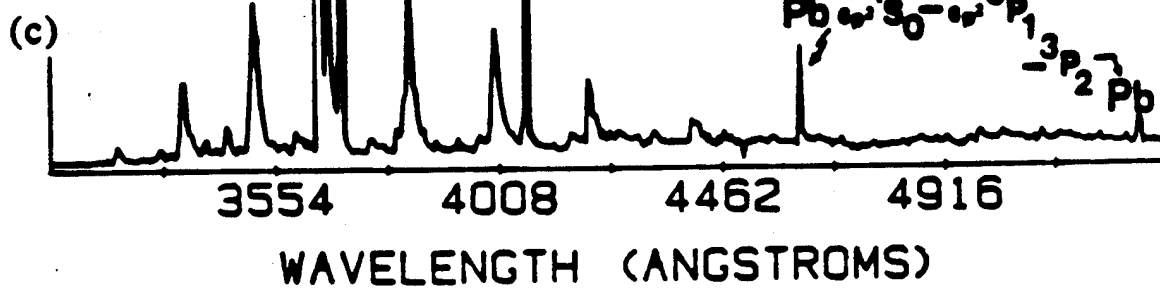


Figure 18

involving ground state Pb atoms is so dominant that no emission to the  $X^3P_0$  ground state is observed. Second, we find significant pumping of both the  $^1S_0$  and  $^1D_2$  levels. The corresponding transitions from the  $^1S_0$  level terminate in the lowest  $X^3P_2$  (531.2 nm) and  $X^3P_1$  (462 nm) levels. It is thought that collisional quenching and relaxation of the  $^1S_0$  level will be minimal relative to that of the  $X^3P$  manifold.<sup>52</sup> This may lead to potential inversions and amplification at  $\lambda = 462, 531$  nm.<sup>53</sup> The well known lead laser transition at  $\lambda = 723$  nm<sup>46</sup> with an A value  $10^6 \text{ sec}^{-1}$  terminates on the  $^1D_2$  level.

Surprisingly, we find no evidence for this transition which emanates from the upper  $^3P^0$  level (Fig. 18). We do find evidence for the  $^3P_1^0 - X^3P_1$  and  $^3P_1^0 - X^3P_2$  transitions and for the  $^1D_2 - ^3P_1$  transition at 733 nm.<sup>54</sup> This suggests that the  $^3P_1 - ^1D_2$  transition may be self-absorbed due to a significant  $^1D_2$  population. If we have observed the manifestation of a substantial  $^1D_2$  population, does this result from direct energy transfer pumping or is the  $^1D_2$  state populated by the 723 nm transition at times considerably shorter than the time scale for the present observations? This must be assessed in future experiments. The results obtained for the energy transfer pumping of lead atoms certainly suggest the possibility of additional amplifier systems. It is particularly encouraging that some of these may represent four level systems which obviate the self absorption bottleneck that may plague the Si-SiO-Na system at high Na concentration.

The near resonant energy transfer pumping of copper vapor is of interest not only because of the close analogy which it bears to the sodium and potassium systems but also, as Figure 19 indicates, because it is possible to energy transfer pump the copper vapor laser transitions<sup>55</sup> (see also Table IV - Appendix V) using metastable SiO (Si-SiO-Cu system). However, it is also of interest that the results demonstrated in Figure 19 were obtained using an approach which represents a significant extrapolation from the configuration in which a "premixed" Tl/Ge mixture has been used to obtain pulsed amplification on the Tl  $^2S_{1/2} - ^2P_{3/2}$  transition.<sup>43</sup> Here, Si and Cu were premixed and co-vaporized from a single crucible. The resulting mixture was then oxidized to yield the observed energy transfer pumping spectrum depicted in Figure 19. (It is worth noting that  $N_2O$ , used as the oxidant, produces a dark reaction with copper vapor.)

The results presented in Figures 18 and 19 clearly demonstrate that there are intriguing variations on the sodium based system. In fact the level

Figure 19: Copper - SiO ( $a^3\Sigma^+, b^3\Pi$ ) near resonant energy transfer spectra generated from a "premixed" Si-Cu mixture subsequently oxidized with N<sub>2</sub>O. (a) Spectrum showing a portion of the SiO metastable emission, the Cu  $2P_{3/2} - ^2D_{5/2}$  blue green emission line (copper vapor laser) and the Cu  $2P_{3/2,1/2} - ^2D_{3/2}$  yellow-orange emission features. (b) Energy levels for the copper atom.

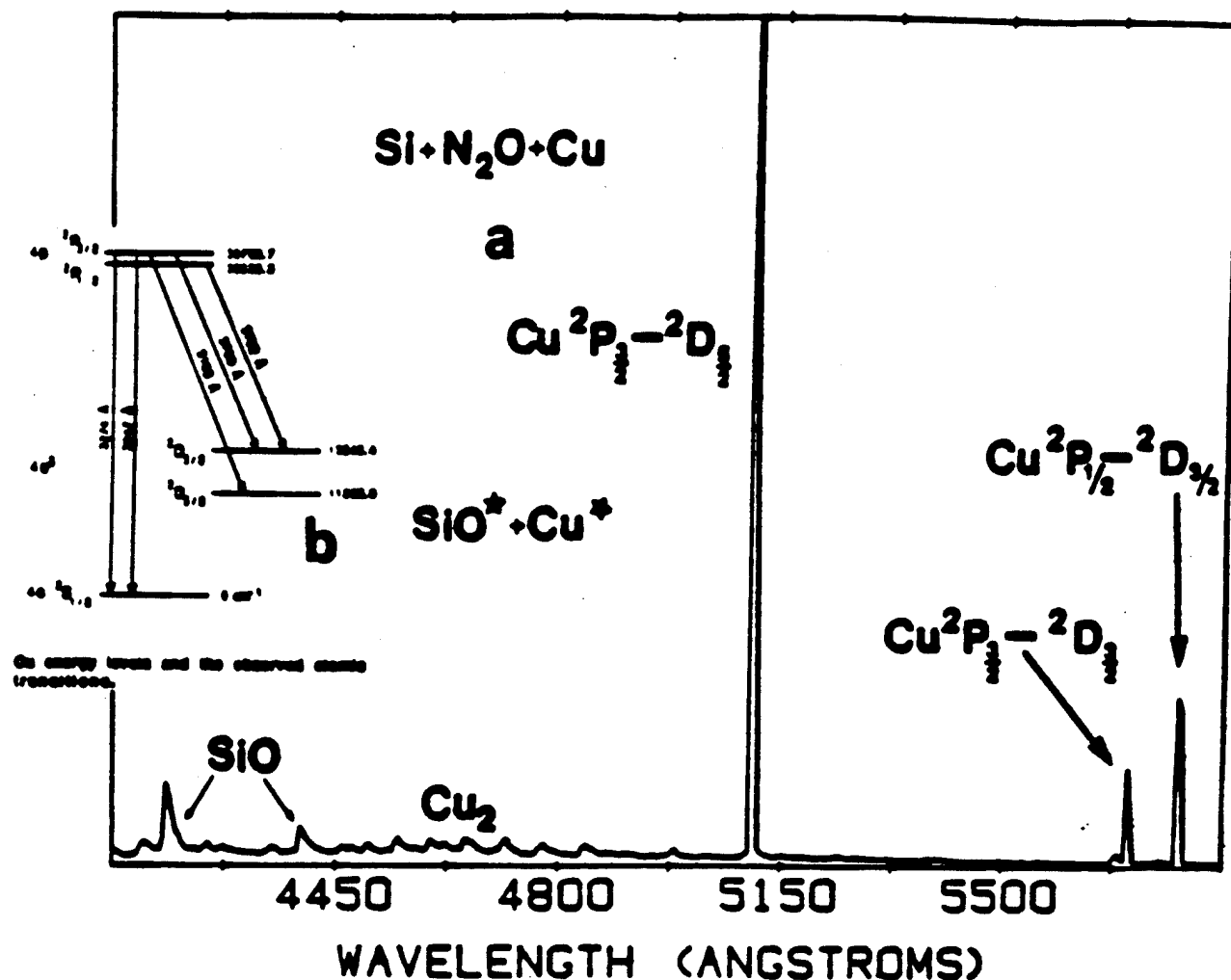
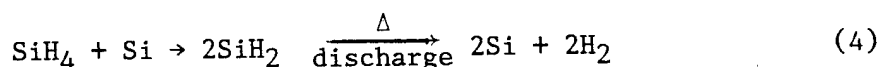


Figure 19 Copper - SiO ( $a^3\Pi^+$ ,  $b^3\Pi$ ) near resonant energy transfer spectra generated from a "premixed" Si-Cu mixture subsequently oxidized with  $N_2O$ . (a) Spectrum showing a portion of the SiO metastable emission, the  $Cu^2P_{3/2}-^2D_{3/2}$  blue green emission line (copper vapor laser) and the  $Cu^2P_{3/2, 1/2}-^2D_{3/2}$  yellow-orange emission features. (b) Energy levels for the copper atom with observed transitions as indicated in (a). See text for discussion.

structure depicted suggest that the three level excitation scheme may offer a considerable range of radiative configurations (lifetimes) which can be accessed in near resonant pumping.

### Improving the Si Atom and SiO Metastable Source Configurations

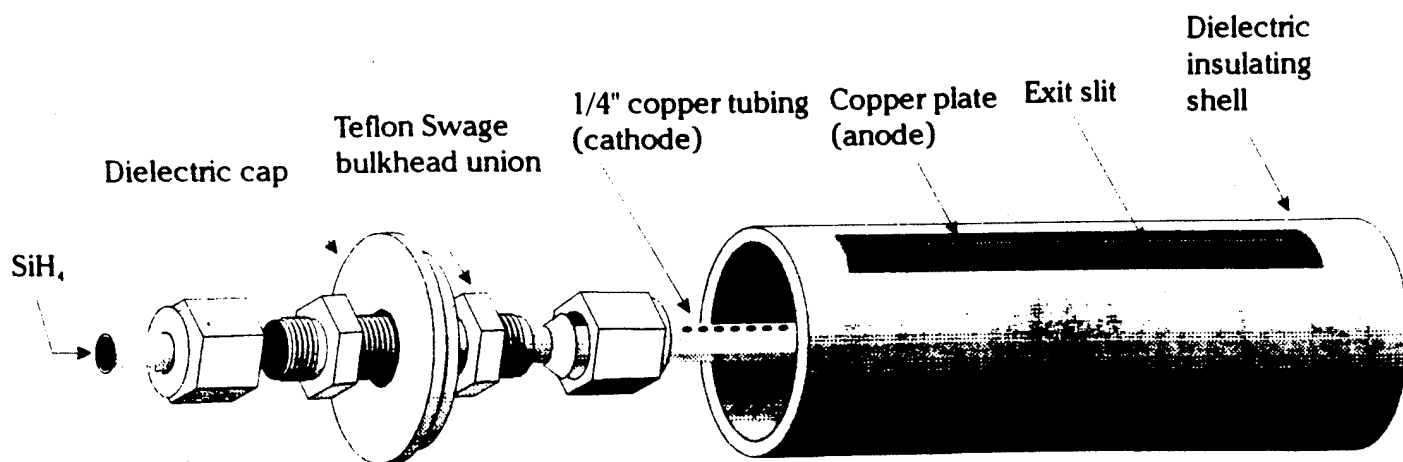
In order to obviate the need for a high temperature source technology to generate the silicon atoms which are subsequently oxidized to form metastable SiO, we have been concerned with the conversion of gaseous silane (SiH<sub>4</sub>) in high yield to atomic silicon. The development of a successful device for the generation of silicon atoms and SiO<sub>x</sub> species in large yield might also prove useful to the microelectronics industry. The sources which we have constructed and tested can be categorized into four groups involving thermolysis, low temperature thermolysis + subsequent discharge through the products of thermal decomposition, low and elevated temperature thermolysis followed by photolysis, and a hybrid approach which involves the thermolysis of silane over bulk silicon viz.



at temperatures considerably below those required to vaporize bulk silicon. Note that the process (4) is attractive because it yields two silicon atoms.

Figure 20 depicts an initial silane discharge configuration where SiH<sub>4</sub> passing into a nozzle arrayed copper tube (representing the cathode) then passes, inside a dielectric insulating shell, to a copper screen covered (anode) exit slit. This configuration, inserted into the previously developed SiO source configuration, replacing the high temperature Si oven (side view Figure 20(b)), has been used in preliminary experiments to pump the B-X transition of molecular bromine. The preliminary results outlined in Figure 21 suggest that well established optically pumped Br<sub>2</sub> (BrCl and IF) lasers with ideal excited state radiative lifetimes (B-X transition) might be accessible to an efficient (~ 3.4 eV energy) SiO metastable energy transfer pump quite analogous to that observed for A state nitrogen and the halogens.

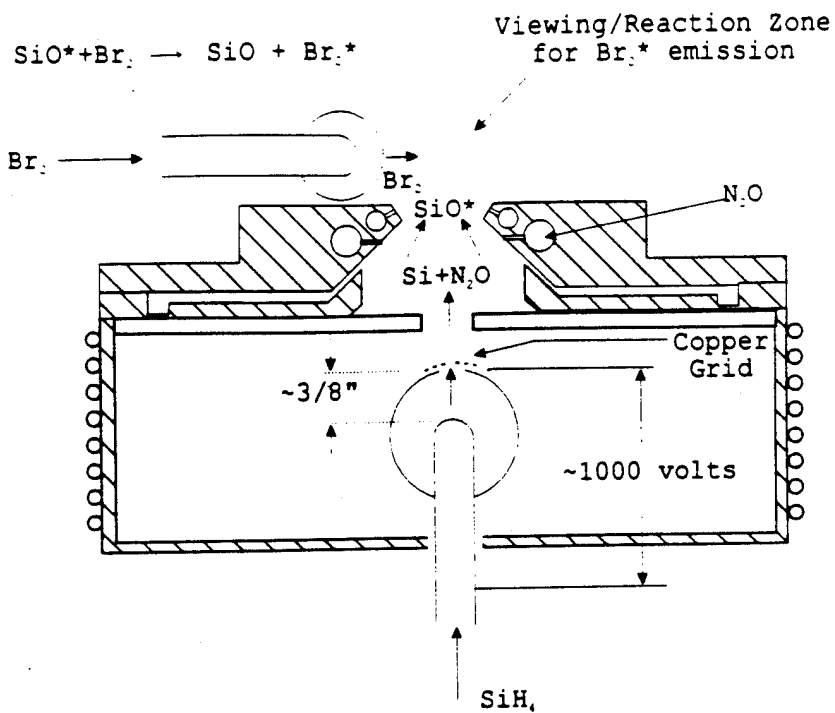
The thermal decomposition of silane is thought to be initiated through the reaction



#### DISCHARGE CONFIGURATION

Figure 20(a)

# Side View



## $\text{SiH}_4 - \text{N}_2\text{O} - \text{Br}_2$ Mixing Configuration

Figure 20(b)

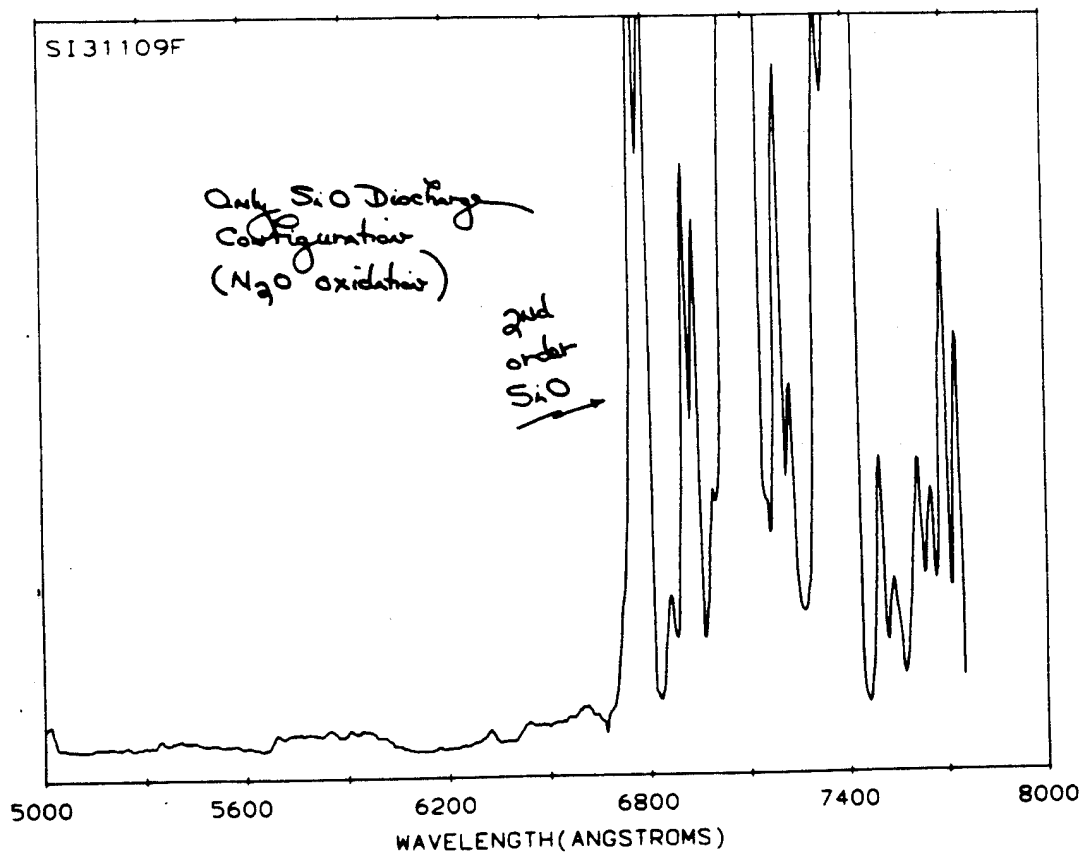


Figure 21(a)

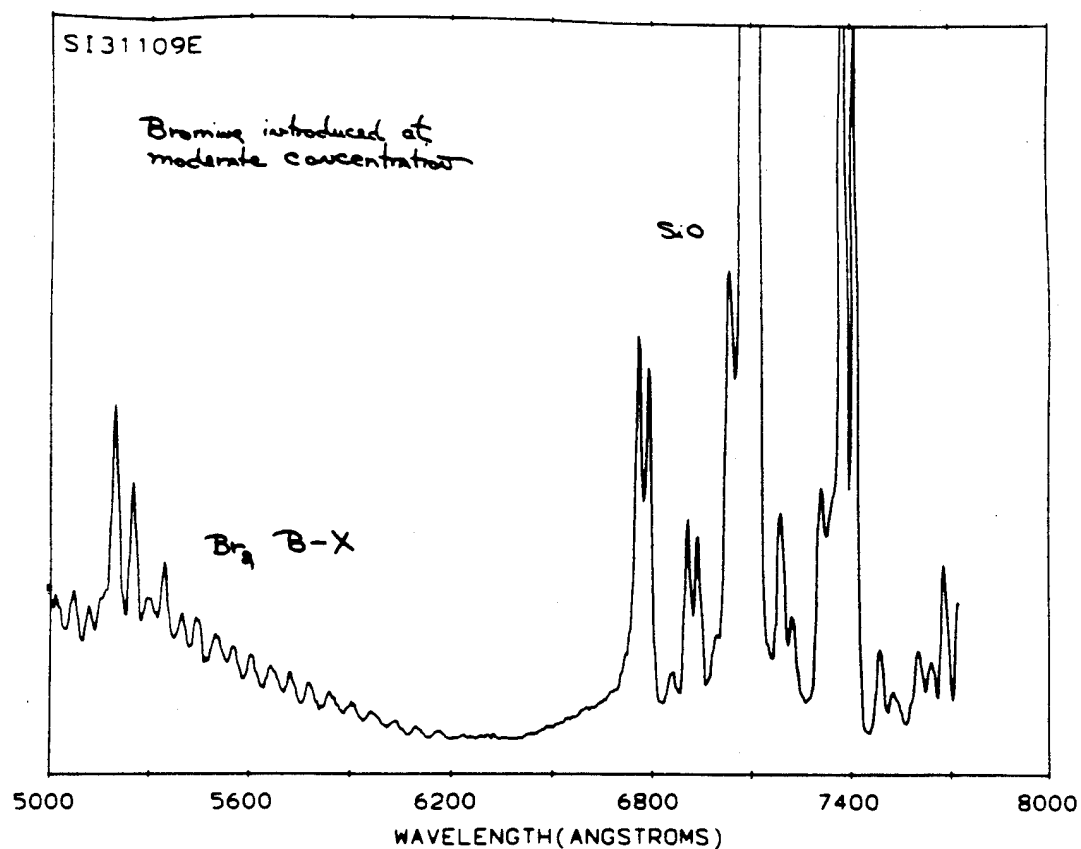


Figure 21 (b)

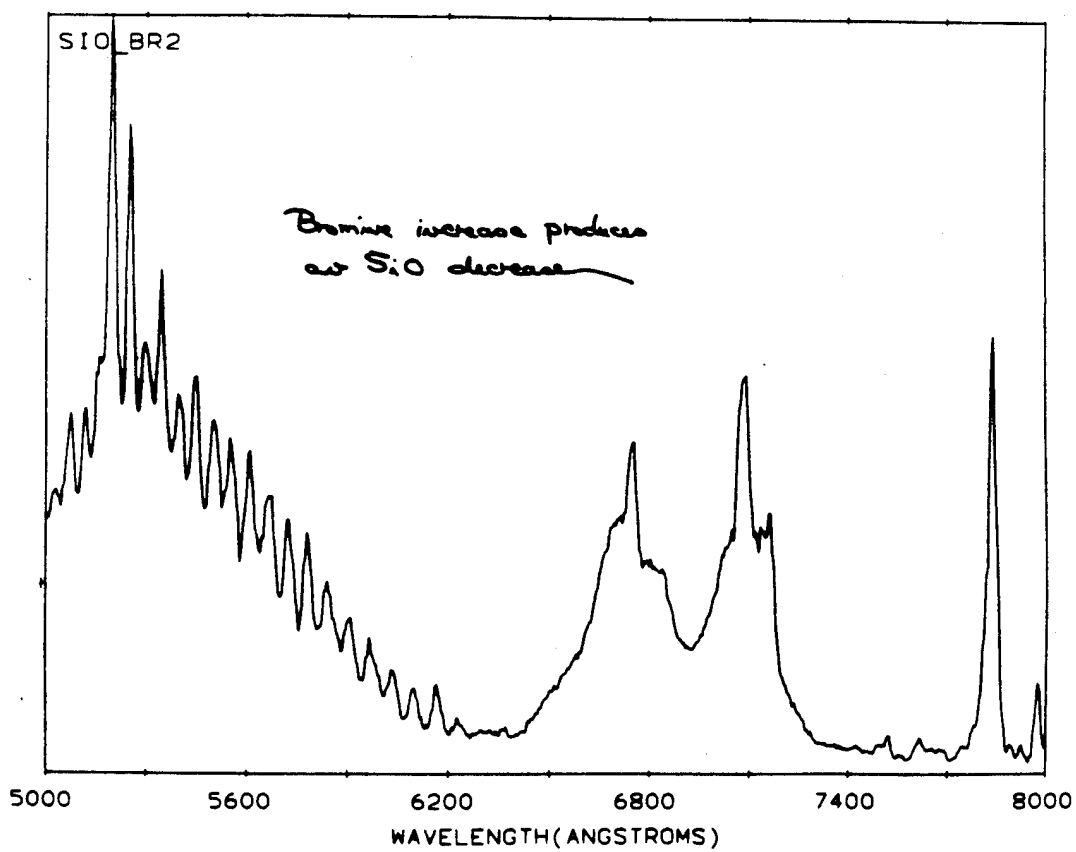
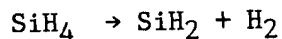


Figure 21 (c)



where further decomposition of the silylene ( $\text{SiH}_2$ ) radical may progress to form atomic silicon and molecular hydrogen. This latter reaction must compete with the reaction of silylene and silane (see Appendix XV) to produce higher silanes which can ultimately result in gas phase nucleation without careful control. The reactivity of silylene and silane has been suggested as an explanation for the low concentrations of  $\text{SiH}_2$  in electric discharges through silane where it ( $\text{SiH}_2$ ) is predicted to be an important intermediate of the discharged silane decomposition.<sup>57</sup>

The considerations outlined suggest that for the pyrolysis of silane or a combination of pyrolysis and discharge through the thermolizing products to proceed completely to silicon and hydrogen, it should be accomplished in an inert diluent to prevent side reactions. In an attempt to measure the unimolecular decay rate for silylene, Votintser et al.<sup>58</sup> employed dilutions ranging from 0.0004 - 0.001% of silane in argon in order to study the decomposition in a shock tube environment. These considerations must also be employed when developing a thermolysis based source for the production of metastable  $\text{SiO}$ . We have successfully used dilutions producing a 0.05% concentration of silane in argon (Appendix XV).

Figures 22, 23, and 24 indicate several early pyrolysis configurations which have been tested in the High Temperature Laboratory. Here we attempted to pyrolyze the silane directly using either a carbon (Fig. 22), nickel (Fig. 23), or tantalum wrapped ceramic (mullite) tube (Fig. 24), again placed within the modified confines of our previously developed  $\text{SiO}$  source configuration. We find significant conversion to silicon with all three designs, their limitation resulting primarily from the blockage of inlet and exit ports due to silicon condensation. This clearly signals the need for diluent gas entrainment - flow techniques as a means of limiting condensation of the silicon atoms at temperatures far below the melting point of silicon. These modifications are now successfully testing in our laboratory. We are also considering further modifications in conjunction with the reconstruction of the discharge configuration outlined in Figure 20.

Figure 25 outlines a hybrid discharge-pyrolysis source which incorporates the designs of Figures 20 and 23. Here we attempted to pyrolyze the silane in a nickel tube furnace which also acted as the cathode for a discharge

clamped oven configuration for pyrolysis of silane

(Carbon oven held by a set of current carrying clamps.)

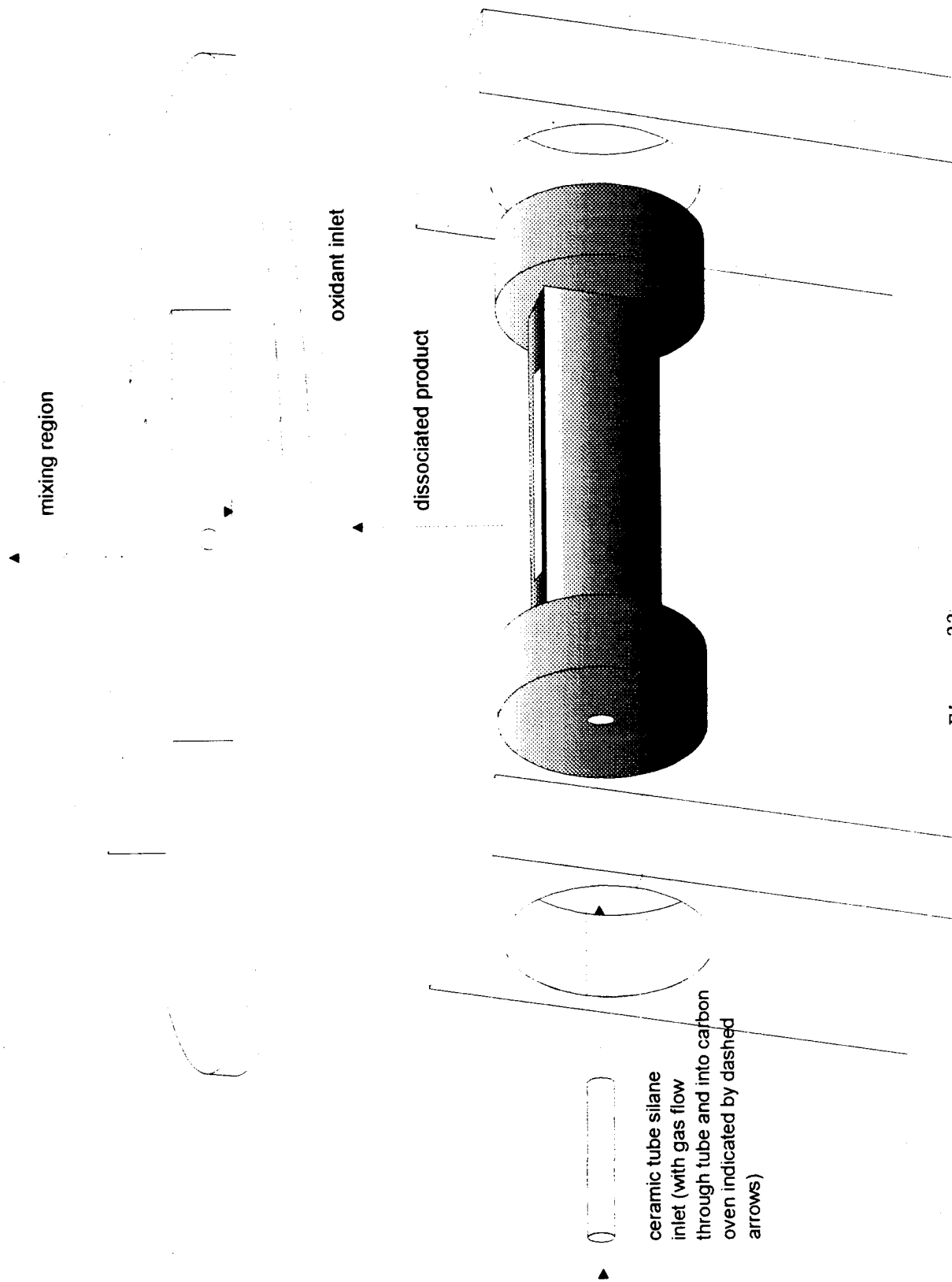


Figure 22

## heated nickel tube configuration

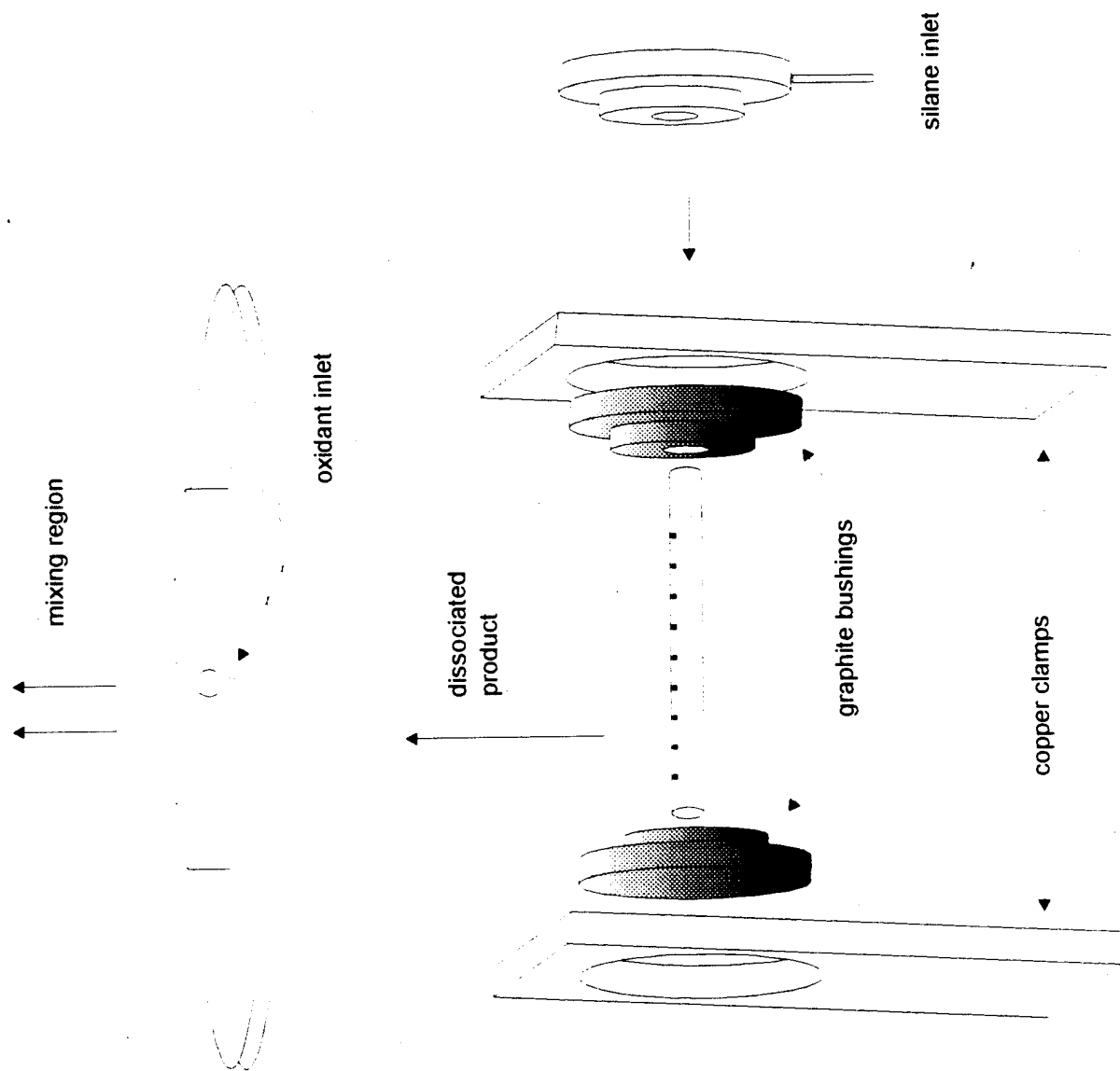


Figure 23

# heated mullite tube arrangement

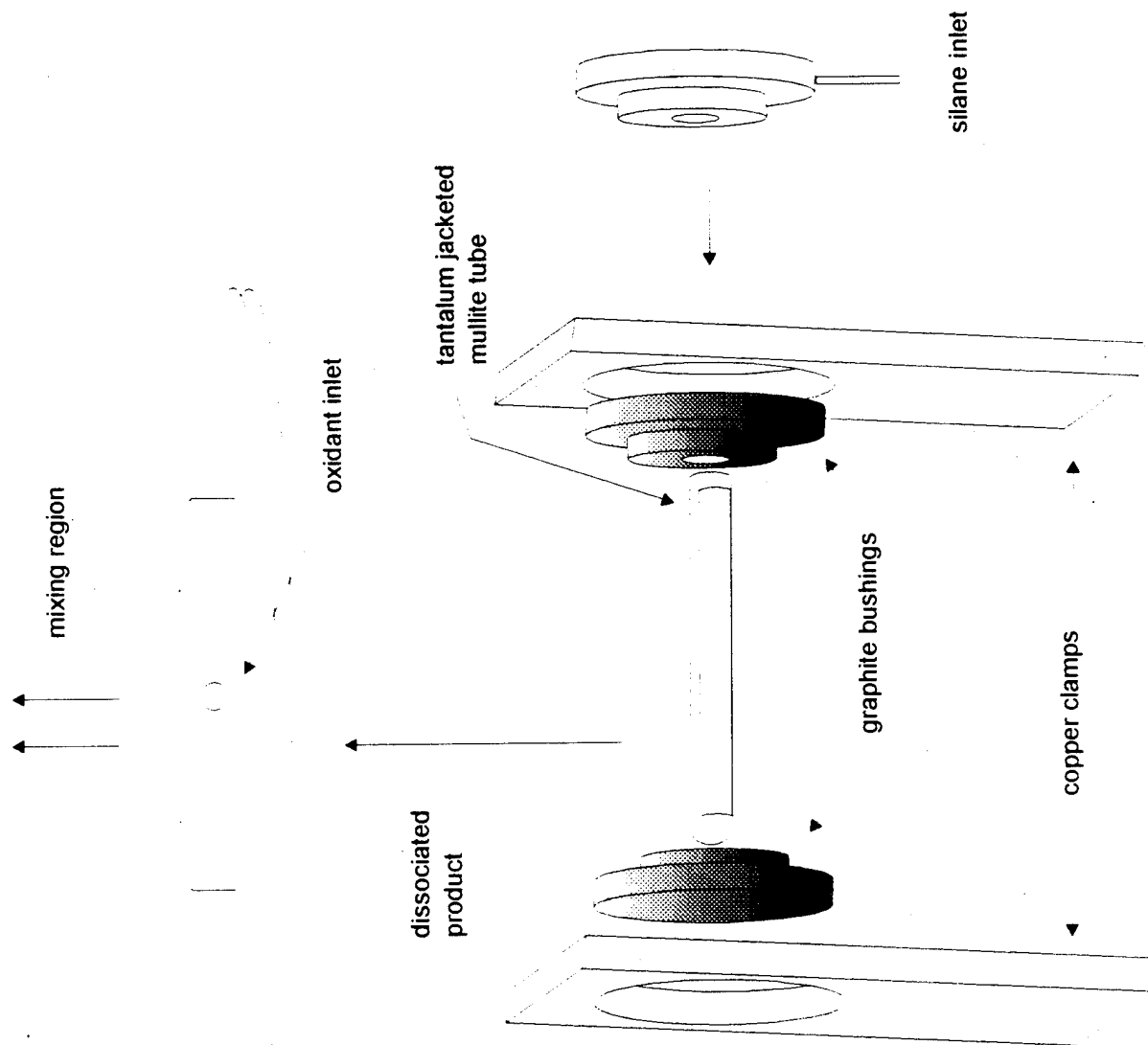


Figure 24

# hybrid discharge / pyrolysis arrangement

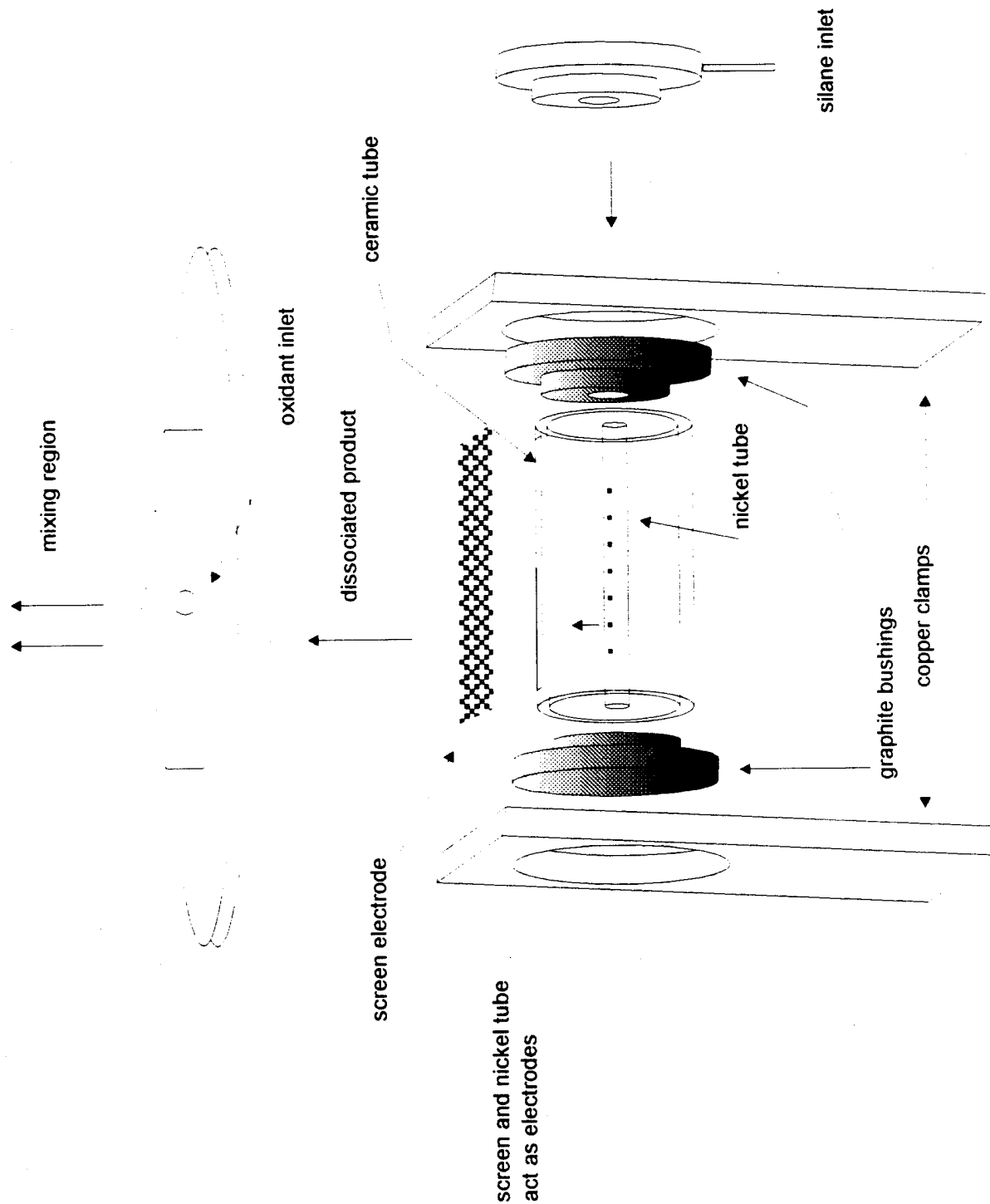
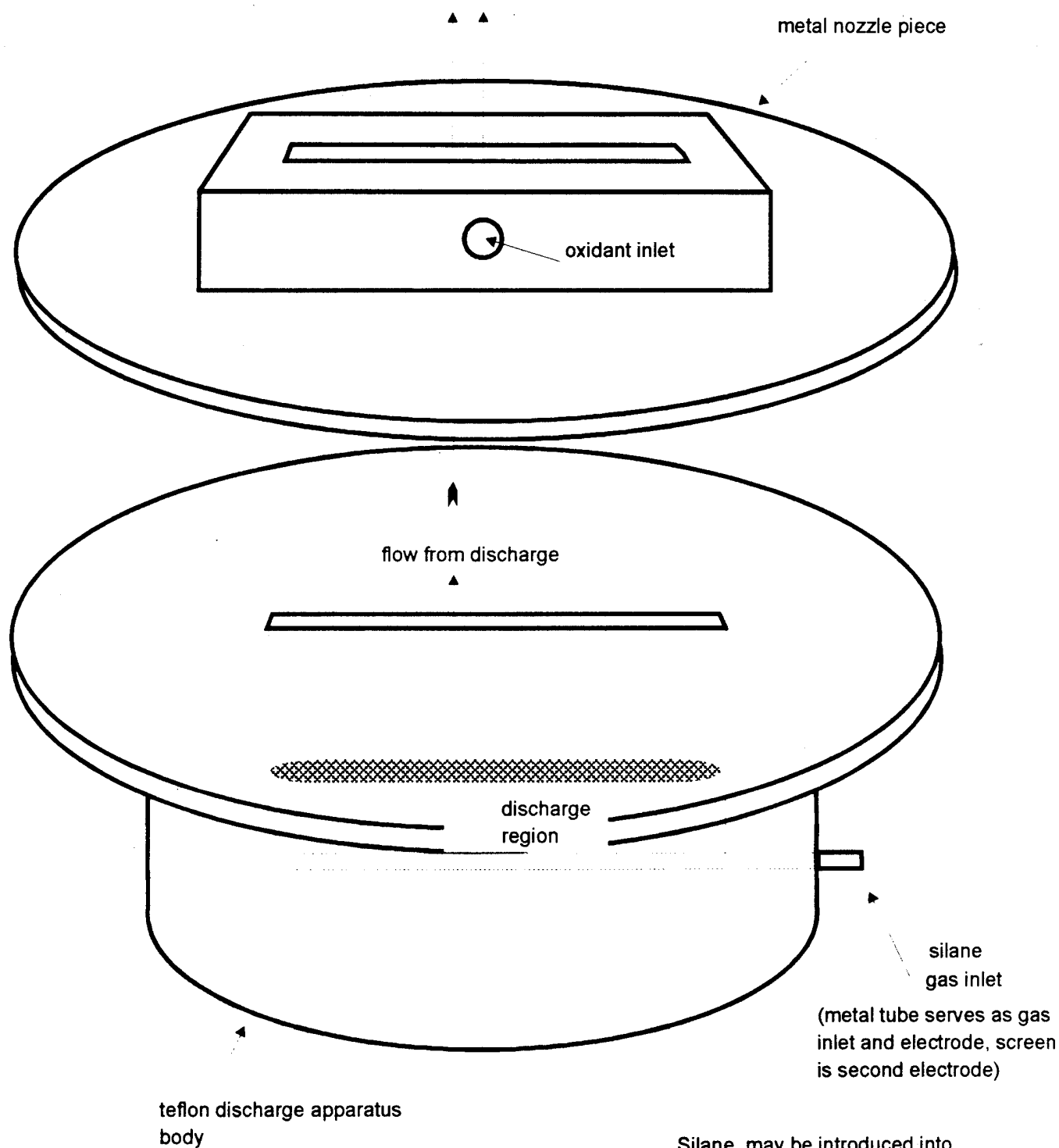


Figure 25



Silane may be introduced into discharge through the bottom inlet. Oxidant is injected through the top inlet.

Alternate: both reactants premixed and passed through the discharge.

Schematic Diagram of Discharge Apparatus

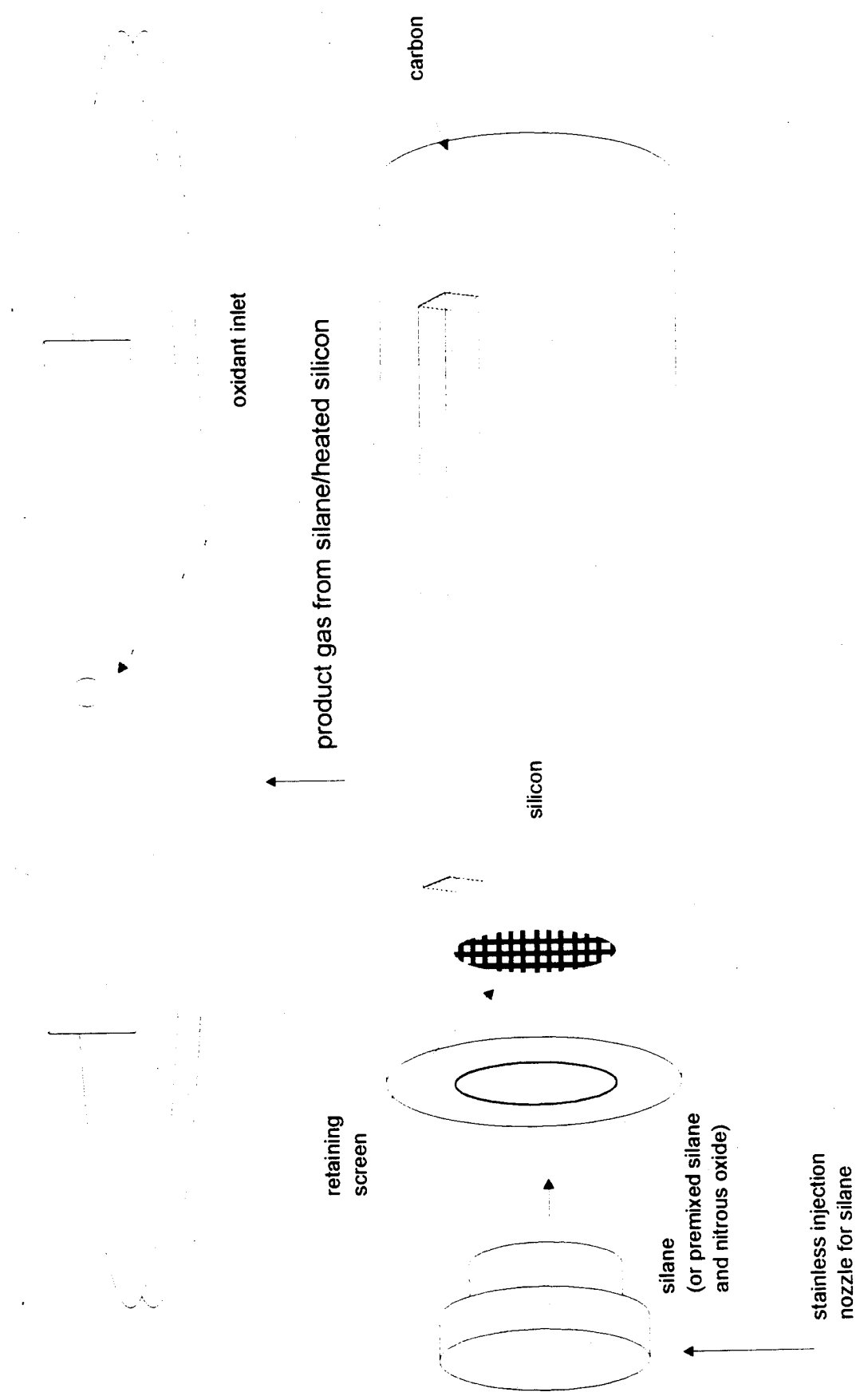
configuration. With some modification to include diluent flow in a more open configuration, this silicon source design appears promising.

The design depicted in Figure 26 represents a discharge device in which we attempted to better confine the gas flow by enclosing the silane inlet/electrode assembly in a teflon housing. With a proper balance of diluent gas, this configuration might eventually prove successful for a discharge based configuration, however, it will require modifications to avoid atomic silicon condensation in the discharge channel.

Figure 27 depicts a configuration in which we have attempted to engineer (as in Equation (4)) the conversion of a silane-silicon interaction to produce two silylene radicals and subsequently two silicon atoms. Here silane was made to flow over silicon contained and heated in a carbon tube furnace. This approach, with a proper balance of diluent also appears promising. In the absence of diluent, the efficient conversion of the silane to silicon and its subsequent condensation soon produces a blockage of oven components. If this problem can be remedied, the configuration of Fig. 27 appears to represent an excellent SiO metastable source configuration.

Figures 28 and 29 (see also Appendix XV) depict tubular pyrolizer configurations which we have now used successfully in the High Temperature Laboratory (Appendix XV) to produce intense SiO metastable flames. Figure 28 depicts a single pyrolizer whereas Figure 29 depicts the tandem assembly which, mounted in a ceramic base, can be used to produce an extended path length SiO metastable flame. The pyrolizers are constructed from alumina or zirconia tubing ( $\sim 6\text{mm}$  I.D., 10 cm in length) and employ a tantalum heating wire wrap sealed by high temperature cement and surrounded by a tantalum heat shield. Silane in an argon diluent ( $\sim 1\text{-}5\%$   $\text{SiH}_4$ ) produces a significant silicon flux which, when reacted with  $\text{N}_2\text{O}$  produces the intense SiO metastable flame depicted in Figure 30. Here calculations demonstrate (Appendix XV) that the ratio of  $\text{b}^3\Pi$  metastables to all other excited state species formed in the system exceeds 2200/1. This now very successful configuration is discussed in detail in Appendix XV.

Figures 31(a) and (b) represent an assembled and expanded view of the sintered glass reaction channel which we are using to attempt to overcome the silicon condensation problem. Here, the silane/diluent mixture passes through a sintered glass inner channel, the walls of which are permeable to an entraining argon, helium, or nitrogen gas flow (so as to prevent condensation

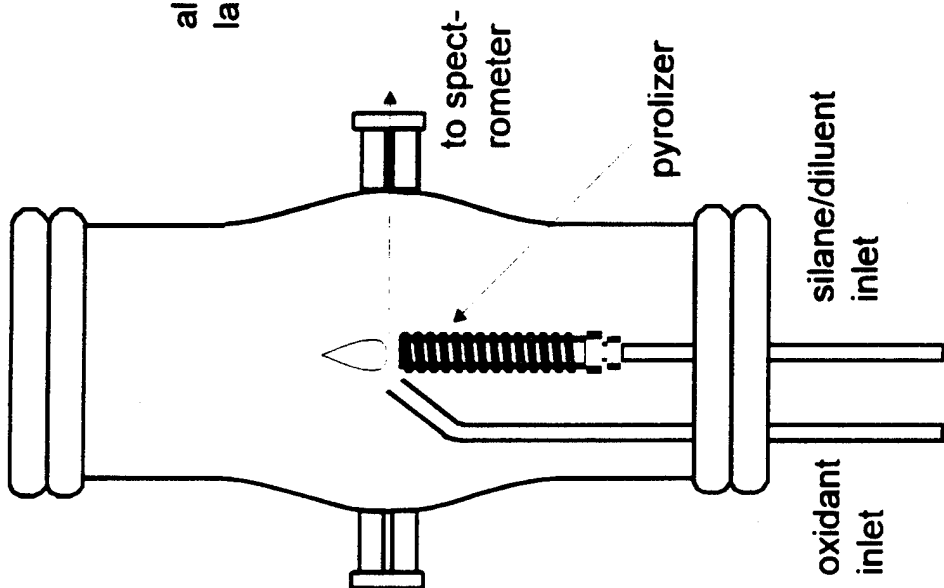
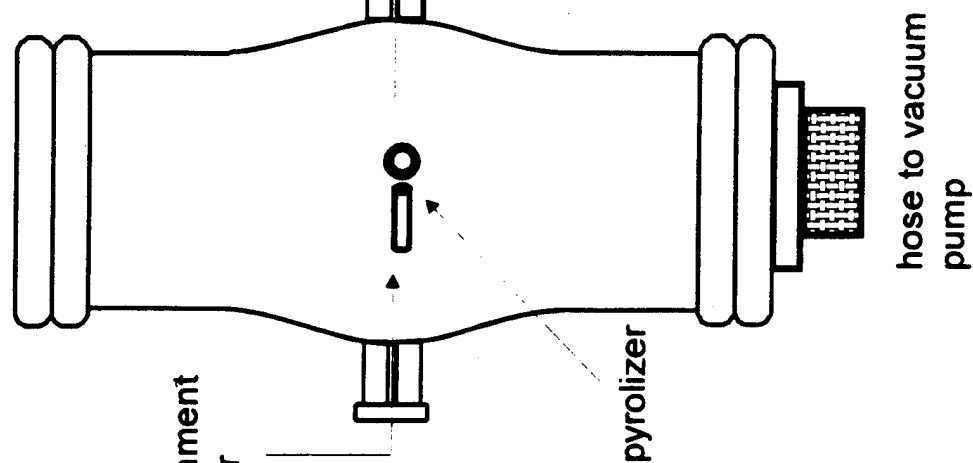


carbon piece heated directly with electric current or through a heated tantalum jacket

Figure 27

top view

side view



(b)

(a)

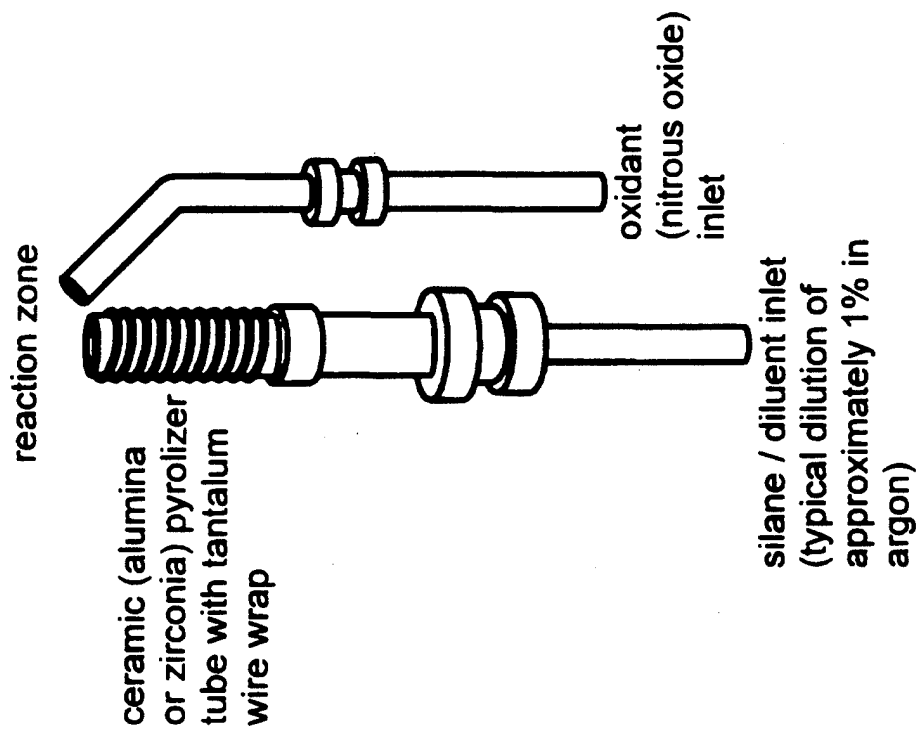


Figure 28

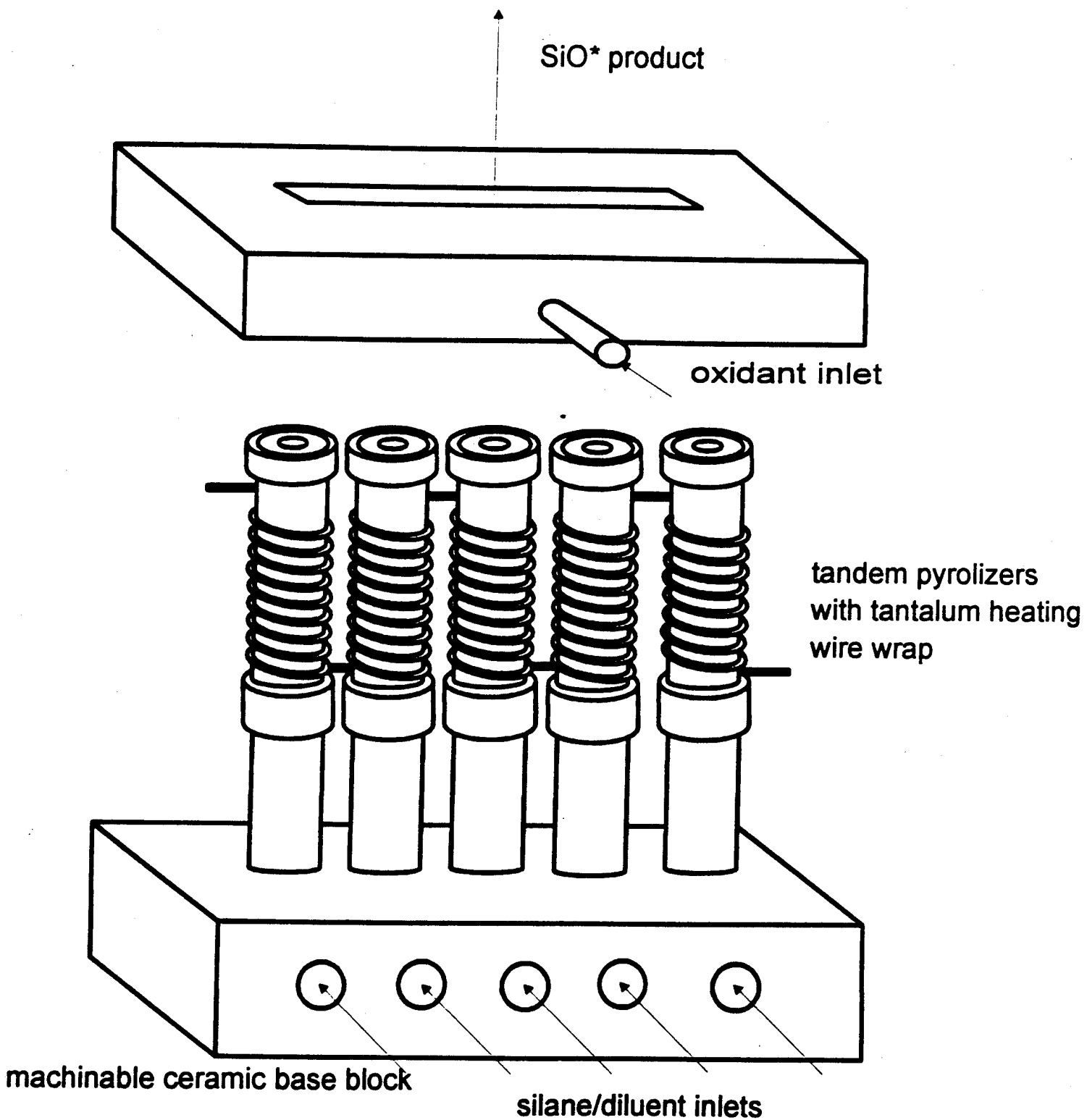


Figure 29

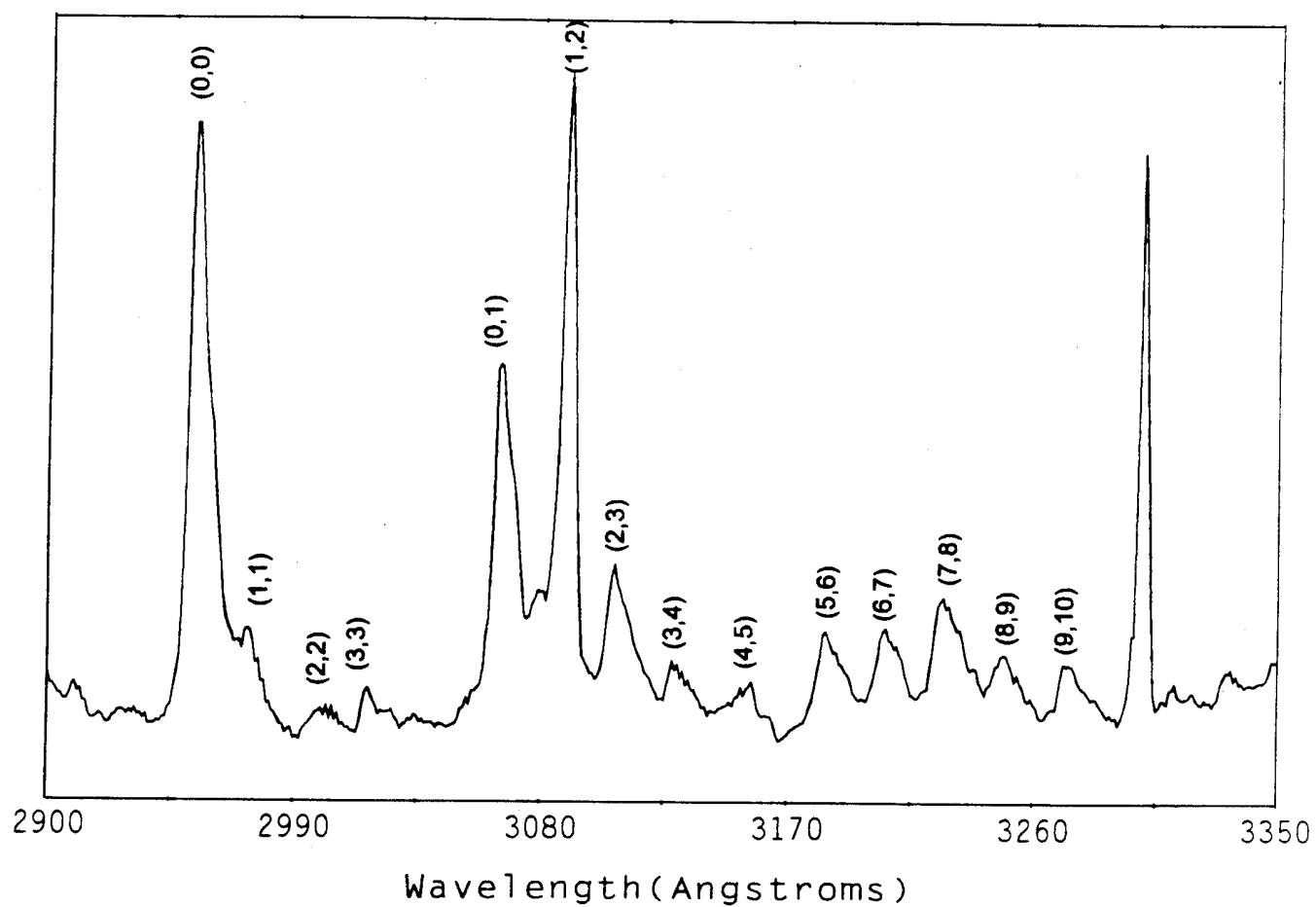
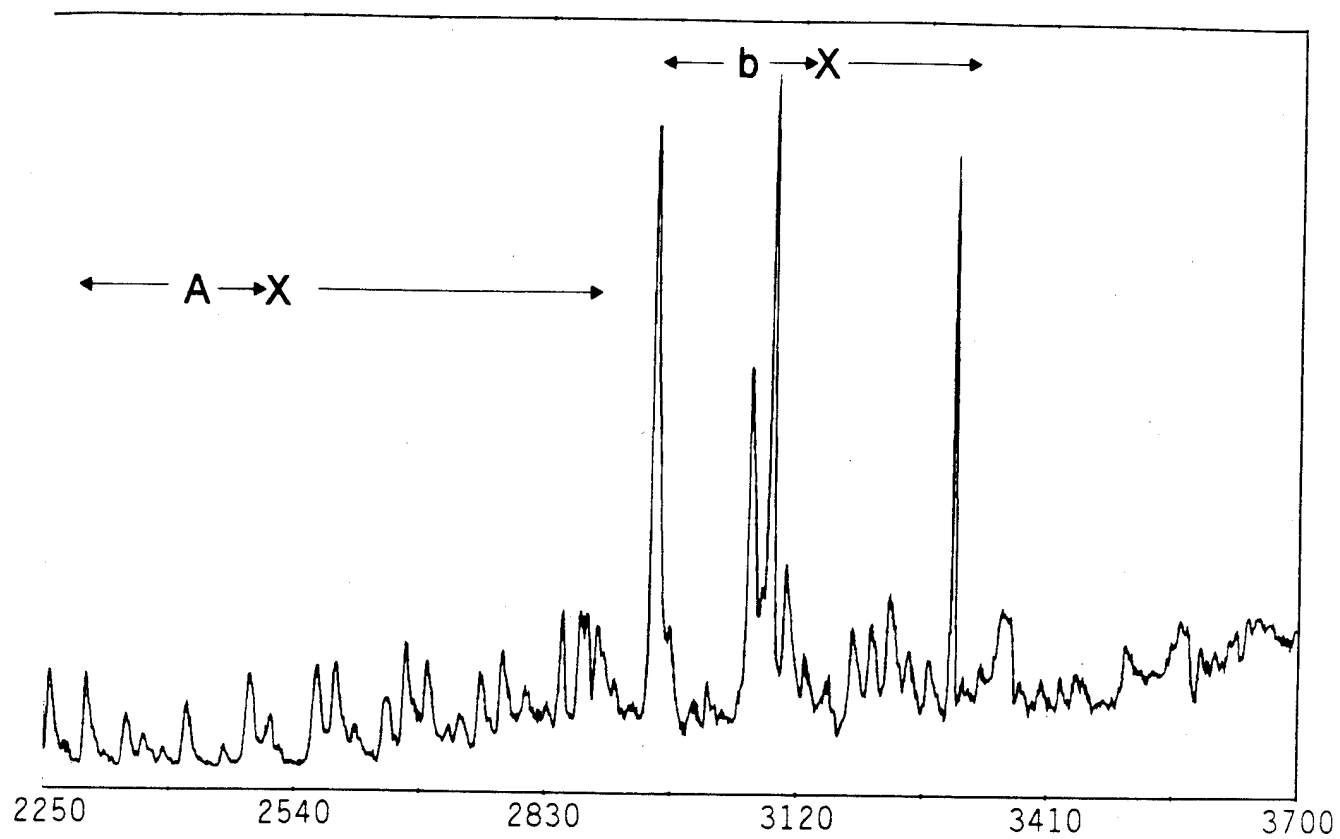
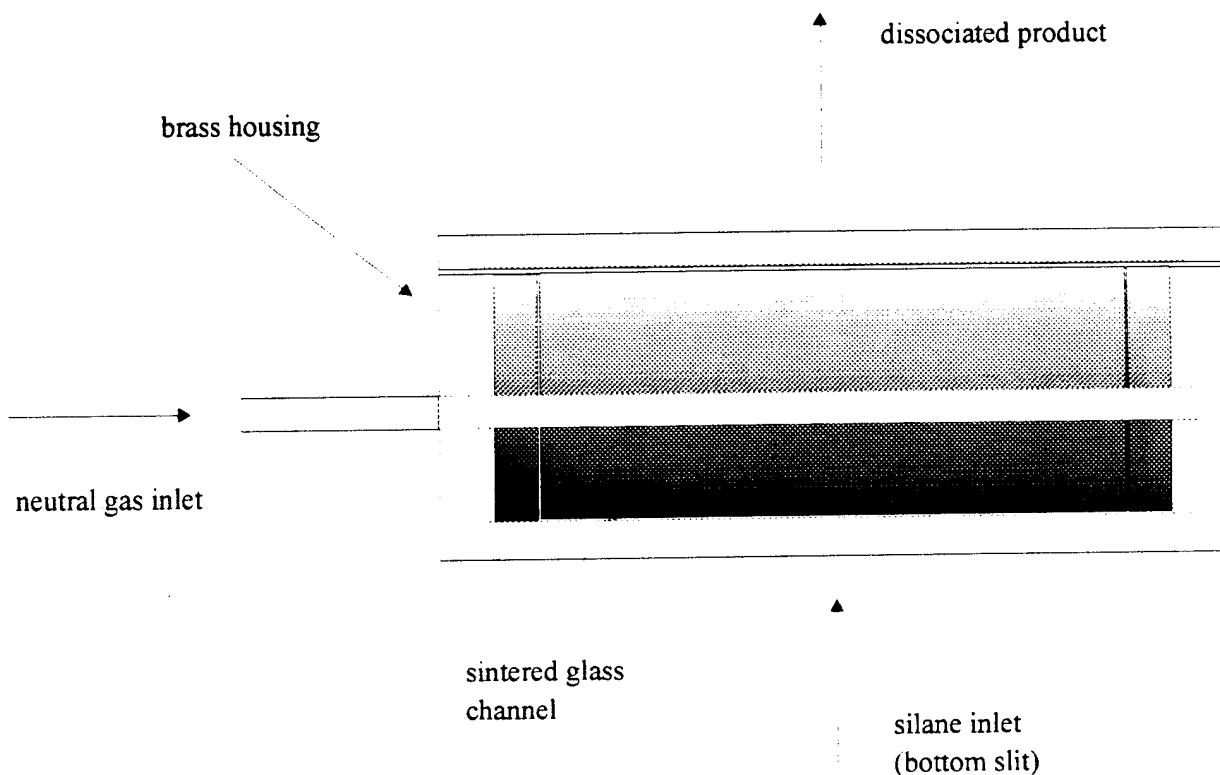


Figure 30

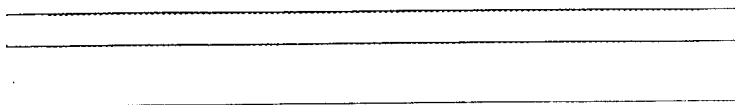


Exploded view of sintered glass channel and housing assembly. The glass assembly is sealed to a shelf in the housing and the lower face of the top plate with high temperature cement. The space between the glass channel and the housing is pressurized with a neutral gas introduced through holes in two inlet tubes (one tube is visible in this side view). The housing is heated with a Thermocoax wrap. Silane is introduced through the bottom slit in the housing, the dissociated species exit through the top slit.

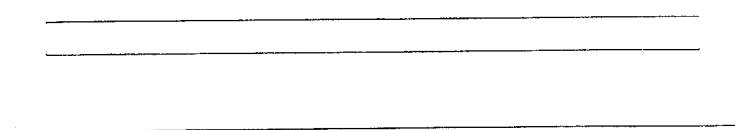
Length of brass housing is approximately 75 mm, height is 30 mm (including top plate) and width is 30 mm.

Figure 31 (a)

side view

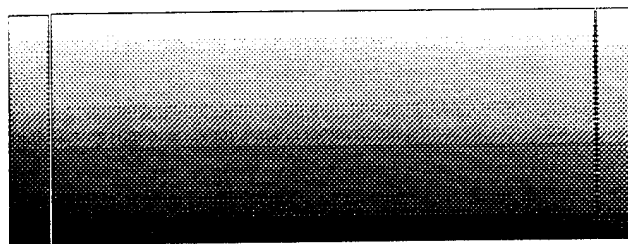


top view

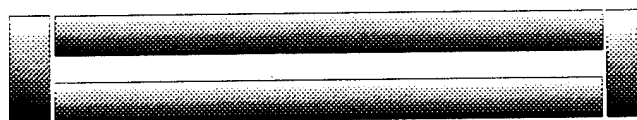


top plate (brass)

side view

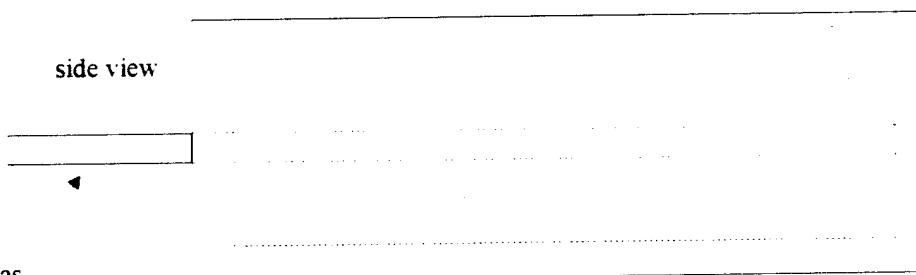


top view

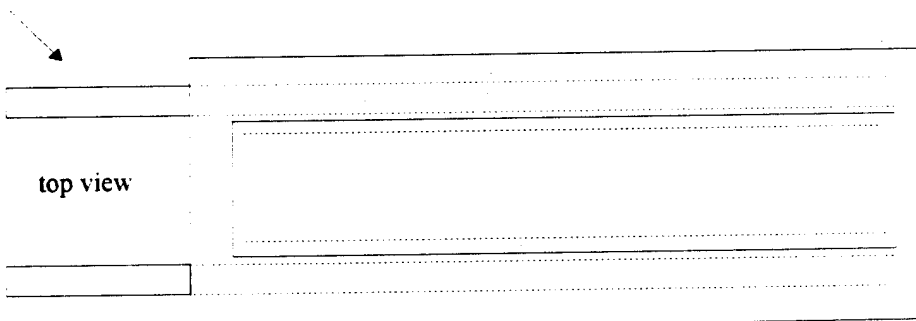


sintered glass channel

side view



neutral gas  
inlets



top view

main housing (brass)

sintered glass channel and housing

Figure 31(b)

on the inner channel walls). This device has now been used to produce a weak SiO flame may possibly be developed further in the High Temperature Laboratory.

With improvements in the arsenal of sources we have outlined, we are confident that we will be able to obtain substantial SiO metastable concentrations in excess of  $10^{14}/\text{cc}$  using a thermolysis and/or a hybrid thermolysis - discharge (photolysis) source operating at a temperature considerably below the silicon metalloid melting point.

## References

1. R. D. Levine and R. B. Bernstein, Molecular Reaction Dynamics, Oxford University Press, New York, 1974.
2. E. J. Mansky, W. Furr, and J. L. Gole, work in progress.
3. For example see Short Wavelength Chemical Laser Workshop, Charleston, S. C., Nov. 14-15, 1984.
4. C. R. Jones and K. D. Ware, SPIE Proceedings 380, 160 (1983). K. D. Ware and C. R. Jones, SPIE Proceedings 380, 322 (1983). S. Byron, et al. "Laser Pumping Sources", Philco Research Labs. Publication No. U-2771, July 1974. E. P. Chicklis et al., "Low-Cost Laser", Sanders Associates, Inc., Independent Research and Development Task NCG, August 1977.
5. D. M. Lindsay and J. L. Gole, J. Chem. Phys. 66, 3886 (1977).
6. M. J. Sayers and J. L. Gole, J. Chem. Phys. 67, 5442 (1977).
7. J. L. Gole and R. N. Zare, J. Chem. Phys. 57, 5331 (1972).
8. J. L. Gole and S. A. Pace, J. Chem. Phys. 73, 836 (1980).
9. W. H. Flygare, Acc. Chem. Res. 1, 121 (1968).
10. A. W. Hanner and J. L. Gole, J. Chem. Phys. 73, 5025 (1980). J. L. Gole and S. A. Pace, J. Phys. Chem. 85, 2651 (1981). J. L. Gole, B. Ohlsson, A. W. Hanner, and E. J. Greene, unpublished.
11. K. McAdam, private communication. See also A. B. F. Duncan, Rydberg Series in Atoms and Molecules, Academic Press, New York, 1971.
12. J. L. Gole, "Probing Ultrafast Energy Transfer Among the Excited States of Small High Temperature Molecules", in "Gas-Phase Chemiluminescence and Chemiionization", (Elsevier Science Publishers - A. Fontijn, editor) pg. 253.
13. We refer to processes which proceed at extremely high rates and appear to be virtually temperature independent.
14. W. H. Crumley, J. L. Gole, and D. A. Dixon, J. Chem. Phys. 76, 6439 (1982). S. H. Cobb, J. R. Woodward, and J. L. Gole, Chem. Phys. Lett. 143, 205 (1988). S. H. Cobb, J. R. Woodward, and J. L. Gole, Chem. Phys. Lett. 157, 197 (1989). S. H. Cobb, J. R. Woodward and J. L. Gole, "Continuous Chemical Laser Amplifiers in the Visible Region", Proceedings of the Fourth International Laser Science Conference, A.I.P. Conf. Proc. No. 191, Optical Science and Engineering Series 10, pg. 68.
15. J. L. Gole, J. R. Woodward, S. H. Cobb, K. K. Shen, and J. R. Doughty, SPIE Proceedings Volume 1397, Eighth International Symposium on Gas Flow and Chemical Lasers (1990), pg. 125 (and references therein).

16. "Chemically Driven Pulsed and Continuous Visible Laser Amplifiers and Oscillators", with K. K. Shen, H. Wang, and D. Grantier, Invited Talk, Proceedings of the 23rd AIAA Plasma-Dynamics and Laser Science Conference, Nashville, Tennessee, AIAA 92-2994 (1992).
17. B. Wellegehausen, in "Metal Bonding and Interactions in High Temperature Systems with Emphasis on Alkali Metals", A. C. S. Symposium Series 179, edited by J. L. Gole and W. C. Stwalley (Am. Chem. Soc., Washington, D. C.) p. 462. B. Wellegehausen, J. of Quantum Electronics 15, 1108 (1979).
18. See for example, R. S. Berry and C. W. Reimann, J. Chem. Phys. 38, 1540 (1963), R. S. Berry, J. Chem. Phys. 27, 1288 (1957), W. S. Struve, J. R. Krenos, D. L. McFadden, and D. R. Herschbach, J. Chem. Phys. 62, 404 (1975). R. C. Oldenberg, J. L. Gole, and R. N. Zare, J. Chem. Phys. 60, 4032 (1974).
19. Given  $\text{Na}_2$  and  $\text{Na}_3$  ionization potentials of 4.87 and 3.97 eV (A. Hermann, E. Schumacher, and L. Woste, J. Chem. Phys. 68, 2327 (1978) and an electron affinity of 3.363 eV for atomic bromine, we determine a very substantial electron jump cross section  $\sigma = \pi (14.38/3.97-3.36) = 1746 \text{ \AA}^2 (1.75 \times 10^{-13} \text{ cm}^2)$  for the  $\text{Na}_3 - \text{Br}$  reaction and  $\sigma = \pi (14.38/(4.87-3.36)) = 285 \text{ \AA}^2 (2.85 \times 10^{-14} \text{ cm}^2)$  for the  $\text{Na}_2 - \text{Br}$  reaction.
20. E. J. Mansky and J. L. Gole, work in progress.
21. J. L. Gole, G. J. Green, S. A. Pace and D. R. Preuss, J. Chem. Phys. 76, 2247 (1982), and references therein.
22. For example, M. M. Kappes, R. W. Kunz, and E. Schumacher, Chem. Phys. Lett. 91, 413 (1982).
23. We intend to facilitate the formation of  $\text{Na}_2$  in the B, C, and C' excited states in an electronically inverted configuration. To do this, Na molecules must be present and react with halogen atoms. Here, it is important to note that the oscillator strengths for any of the larger sodium polymers ( $\text{Na}$ ,  $n > 3$ ) are sufficiently small verses Na so that they do not interfere with the sodium dimer pump amplification cycle.
24. "Self-Flushing Optical Window to Prevent Collection of Condensates", W. H. Crumley and J. L. Gole, Rev. Sci. Instruments 57, 1692 (1986).
25. U. Gaubatz, H. Bissantz, U. Hefter, I. Colomb de Daunant, K. Bergmann, and P. L. Jones, J. Opt. Soc. Am. 6, 1386 (1989).
26. I. Littler, S. Balle, and K. Bergmann, "Molecular Beam Raman Laser with a 250 nW Threshold Pump Power", Opt. Comm. 77, 390-394, July (1990).
27. D. L. Rousseau and P. F. Williams, J. Chem. Phys. 64, 3519 (1976).
28. See, for example, J. Tang and A. C. Albrecht, "Raman Spectroscopy", edit by H. A. Szymanski (Plenum, New York, 1970), 2, pp. 33-68; A. C. Albrecht, J. Chem. Phys. 34, 1476 (1961).

29. "Chemically Enhanced Raman Scattering", with D. R. Grantier, J. Chem. Phys., to be submitted.
30. R. Balfour and A. E. Douglas, Can. Jour. Phys. 48, 901 (1970); K. Li and W. C. Stwalley, J. Chem. Phys. 59, 4423 (1973).
31. F. Reuse, S. N. Kanna, V. de Coulon, and J. Buttet, Phys. Rev. B 41, 11743 (1990).
32. "On the BiF Bond Dissociation Energy and Evaluation of the BiF Red Emission Band Systems", T. C. Devore, R. Kahlscheuer, L. Brock, and J. L. Gole, Chemical Physics 155, 423 (1991).
33. "Electronically Excited Charge Transfer Complex Formation in Magnesium Molecule - Halogen Atom Reactions Electronic Spectroscopy of  $Mg_xF$ ", T. C. Devore, R. Kahlscheuer, D. A. Dixon, H. Wang, C. B. Winstead, and J. L. Gole, in preparation.
34. D. Grantier and J. L. Gole, "The Expansion of Small Molecule Configuration Space: Highly Efficient Long Range Stabilization and Energy Transfer Involving Electronically Excited States", High Temp. Science, in press. J. L. Gole, "Highly Efficient Collisional Stabilization and the Symmetry Constrained Dynamics of High Temperature Complex Formation", J. Chem. Phys., in press. J. L. Gole, H. Wang, J. S. Joiner, and D. E. Dawson, "Confirmation of Long-Range Collision Complex Stabilization Through the Controlled Relaxation of High Internal Excitation", J. Chem. Phys., in press.
35. (a) F. Engleke, Chem. Phys. 44, 213 (1979).  
 (b) W. J. Rosano and J. M. Parson, J. Chem. Phys. 84, 6250 (1986).  
 (c) J. M. Parson, J. Phys. Chem. 90, 1811 (1986).  
 (d) M. Menzinger, Adv. Chem. Phys. 42, 1 (1980). M. Menzinger, "The  $M+X_2$  Reactions: A Case Study", in "Gas Phase Chemiluminescence and Chemiionization", A. Fontijn, editor, Elsevier Science Publishers, Amsterdam, 1985, pp. 25-66.  
 (e) M. Menzinger, "Chemiluminescence and Chemi-ionization: Metal-Halogen Reactions as Paradigms of Diabatic Reaction Dynamics", Acta Physica Polonica, A73, 85 (1988).
36. D. J. Wren and Michael Menzinger, Chem. Phys. Lett. 27, 572 (1974), were the first to suggest the possibility of a collisional stabilization process in the microtorr region. However, based in some part on a misconception concerning the lifetimes of the dihalide transitions contributing to the continuum emissions (see Ref. 35(a)) and their concern with the predictions of an RRKM model, they (see (Ref. 35(b),(c),(d))) concluded that the dihalides were formed via a double harpoon mechanism involving first the formation of a highly vibrationally excited metal monohalide which subsequently reacted in a second electron jump process to form the excited state of the dihalide. It is this two step process, thought to be the correct mechanism for excited state dihalide emission<sup>35</sup> which has now been disproven in favor of collisional stabilization.

37. See for example, J. R. Woodward, S. H. Cobb, K. K. Shen, and J. L. Gole, IEEE J. Quant. Elec. 26, 1574 (1990) - invited paper. K. K. Shen, H. Wang, and J. L. Gole, IEEE J. Quant. Elec. 29, 2346 (1993) and references therein.
38. J. R. Woodward, S. H. Cobb, and J. L. Gole, "Superfluorescent Chemically Driven Visible Laser Transitions Using Fast Near Resonant Energy Transfer", Proceedings of the Fourth International Laser Science Conference, AIP Conf. Proc. No. 191, Optical Science and Engineering Series 10, pg. 63.
39. G. J. Green and J. L. Gole, Chemical Physics 100, 133 (1985).
40. R. W. Woodward, J. S. Hayden, and J. L. Gole, Chemical Physics 100, 133 (1985).
41. See reference 37 and S. H. Cobb, Ph.D. Thesis, Georgia Institute of Technology, 1988.
42. For the Na  $4d^2D$  level, S. A. Kandela, Appl. Optics 23, 2151 (1984).
43. A. Gallagher and A. Lurio, Phys. Rev. 136, A87 (1964).
44. G. Roll and J. Mentel, J. Phys. D. Appl. Phys. 22, 483-487 (1989).
45. A. V. Eremin, I. M. Naboko, and S. A. Palopexhentsev, Opt. Spectrosc. (USSR) 60, 567 (1986).
46. A. S. Tribilov and A. M. Shukhtin, Opt. Spectrosc. 21, 69 (1966). See also, K. Krokkel, M. Hube, W. Luhs and B. Wellegehausen, Appl. Phys. B37, 137-140 (1985).
47. (a) V. G. Mishakov and T. L. Tkachenko, Opt. Spectrosc. (USSR) 64(3), 293 (1988). (b) V. V. Kuchinskii, V. G. Mishakov, A. S. Tibilov, and A. M. Shukhtin, Opt. Spectrosc. 39, 1043 (1975) [Opt. Spectrosc. (USSR) 39, 598 (1975)]. (c) A. A. Kudryavsev, V. N. Skrevob, and T. L. Tkachenko, Opt. Spectrosc. 58, 694 (1985) [Opt. Spectrosc. (USSR) 58, 420 (1985)]. (d) V. G. Mishakov, A. S. Tibilov, and A. M. Shukhtin, Opt. Spectrosc. 31, 324 (1971) [Opt. Spectrosc. (USSR) 31, 176 (1971)]. (e) N. N. Bezuglov and A. B. Tsyganov, Opt. Spectrosc. 59, 195 (1985) [Opt. Spectrosc. (USSR) 59, 115 (1985)].
48. I. Tanarro, F. Arqueros, and J. Campos, J. Chem. Phys. 77, 1826 (1982).
49. J. W. Ager III, C. L. Talcott, and C. J. Howard, J. Chem. Phys. 85, 5584 (1986). J. R. Woodward, J. S. Hayden, and J. L. Gole, Chemical Physics 134, 395 (1989).
50. A collaborative effort is being established with Professor Lee Sentman of the Department of Aerospace Engineering at the University of Illinois. Professor Sentman is one of the world experts on the fluid dynamics and design of HF chemical lasers.

51. Chemical Laser Experiments and Analysis, Directed Energy Devices Technology Support Delivery Order No. 0015 prepared by W. Smith, S. Taylor, J. Dansereau, J. Long, and W. Warren for U. S. Army Missile Command, Directed Energy Directorate, Redstone Arsenal, Alabama 35898.
52. J. Dering, SARA Incorporated, private communication.
53. G. R. Fowles and W. T. Silvast, Appl. Phys. Lett. 6, 236 (1965).
54. A. A. Isaev and G. G. Petrash, JETP Lett. 10, 119-121 (1969).
55. Ovazio Svelto, "Principles of Lasers", 3rd Edition, pp. 302, Plenum Press, New York (1989).
56. B. S. Meyerson and J. M. Jasinski, J. Appl. Phys. 61, (2) (1987).
57. J. M. Jasinski and Jock O. Chu, J. Chem. Phys. 81, 1678 (1988).
58. V. N. Votintsev, I. S. Zaslonko, V. S. Mikheev, and V. N. Smirnov, Kinetics and Catalysis 27, no. 4, pt. 2, 843 (1986).
59. "A New and Simple Pyrolysis Source for the Controlled Formation of SiO Metastables", with J. Stephens, Jour. Applied Physics, submitted.

## Publications:

- J. L. Gole, "The Unique Complexation and Oxidation of Metal-Based Clusters", in Advances in Metal and Semiconductor Clusters, Vol. 1, Spectroscopy and Dynamics, ed. M. A. Duncan, JAI Press (1993), pg. 159-209.
- K. K. Shen, He Wang, and J. L. Gole, "Evidence for Continuous Visible Chemical Lasing from the FAST Near Resonant Energy Transfer Pumping of Atomic Sodium", JQE **29**, 2346 (1993).
- He Wang and J. L. Gole, "A Chemiluminescent and Laser Induced Fluorescent Probe of a New Low-Lying A' 1 State of Gaseous AgF", J. Mol. Spectros. **161**, 28 (1993).
- He Wang and J. L. Gole, "Laser Induced Fluorescence Study and Radiative Lifetimes of the Low-Lying Electronic States of Gaseous AgF", J. Chem. Phys. **98**, 9311 (1993).
- T. C. Devore and J. L. Gole, "Fluorine Hot Atom Oxidation of Bismuth Vapor: A comment on the Evaluation of the BiF Bond Energy", Chemical Physics **174**, 409 (1993).
- D. Grantier, H. Wang, C. B. Winstead, and J. L. Gole, "Chemically Driven Continuous Visible Laser Amplifiers and Oscillators Based on Metal Molecule - Halogen Atom Reactions", Proceedings of the 24th AIAA Plasma-Dynamics and Laser Science Conference, Orlando, Florida, AIAA 93-3207.
- J. L. Gole, K. K. Shen, H. Wang, C. B. Winstead, and J. Stephens, "Chemically Driven Visible Laser Amplifiers and Oscillators Based on Fast Electronic Energy Transfer", Proceedings of the 24th AIAA Plasmadynamics and Laser Science Conference, Orlando, Florida, AIAA 93-3209.
- "Raman Pumping in the Absence of an External Light Source", with D. Grantier, J. Phys. Chem. Letters **98**, 7427 (1994).
- "The Expansion of Small Molecule Configuration Space: Highly Efficient Long Range Stabilization and Energy Transfer Involving Electronically Excited States", with D. R. Grantier, High Temp. Science, in press.
- "Chemically Induced Processes Evidencing Raman Gain", with D. R. Grantier and P. M. Medley, Proceedings of the Tenth International Symposium on Gas Flow and Chemical Lasers, Friedrichshafen, Germany, 1994, SPIE, Volume 2502, Pg. 505.
- "Highly Efficient Collisional Stabilization and the Symmetry Constrained Dynamics of High Temperature Complex Formation", J. Chem. Phys., in press.
- "Confirmation of Long-Range Collisional Complex Stabilization Through the Controlled Relaxation of High Internal Excitation", with H. Wang, J. S. Joiner, and D. E. Dawson, J. Chem. Phys., in press.
- "Energetics, Molecular Electronic Structure, and Spectroscopy of Forming Group IIA Dihalide Complexes", with T. C. Devore, in preparation.

"Electronically Excited Charge Transfer Complex Formation in Magnesium Molecule - Halogen Atom Reactions Electronic Spectroscopy of  $Mg_xF$ ", with T. C. Devore, R. Kahlscheuer, D. A. Dixon, H. Wang, and C. B. Winstead, in preparation.

C. B. Winstead, S. J. Paukstis, and J. L. Gole, "What is the Ionization Potential of Silicon Dimer", Chem. Phys. Letts. 23, 81 (1995).

"Chemically Enhanced Raman Scattering", with D. R. Grantier, J. Chem. Phys., to be submitted.

"Spectroscopy of the  $H\ 3\Sigma_u^-$  Electronic State of  $Si_2$  Using a Combined Laser Vaporization-REMPI-Oven Based LIF Study", with C. B. Winstead and S. J. Paukstis, Jour. of Molecular Spectroscopy, in press.

K. K. Shen, "The Creation and Characterization of Chemically Created Atomic Population Inversions for the Development of a Visible Chemical Laser", Ph.D. Thesis, Georgia Institute of Technology, August, 1993.

"A New and Simple Pyrolysis Source for the Controlled Formation of  $SiO$  Metastables", with J. Stephens, Jour. Applied Physics, submitted.

C. B. Winstead, "The Dynamics of Small Metal and Semiconductor Clusters", Ph.D. Thesis, Georgia Institute of Technology, May, 1995.

### **Invited Talks on Army Sponsored Research**

Atlanta Area Chemical Physics Seminar (1993) - Invited Talk - "Symmetry Constrained Dynamics of Group IIA Dihalide Formation".

AFOSR Conference on High Energy Density Materials (1993) - "Geometrical Isomerization and Light Metalloid Molecule Oxidation as a Means of Producing High Impulse Propellants".

24th AIAA Plasma Dynamics and Laser Science Conference, Orlando, Florida (1993) - Requested Talk - "Chemically Driven Visible Laser Amplifiers and Oscillators Based on Fast Electronic Energy Transfer".

24th AIAA Plasma Dynamics and Laser Science Conference, Orlando, Florida (1993) - Requested Talk - "Chemically Driven Visible Laser Amplifiers and Oscillators Based on Metal Molecule - Halogen Atom Reactions".

John L. Margrave Research Symposium, Rice University, Houston, Texas (1994) - "Chemically Enhanced Raman Scattering".

Gordon Research Conference on Advanced High Temperature Materials, Meridan, N. H. (1994) - "Raman Pumping in the Absence of an External Light Source".

Tenth International Symposium on Gas Flow and Chemical Lasers, Friedrichshafen, Germany (1994), "Chemically Driven Continuous Visible Laser Amplifiers and Oscillators Based on Metal Molecule-Halogen Atom Reactions".

## Scientific Personnel Supported by this Project (Degrees Awarded)

James L. Gole (Principal Investigator).

K. K. Shen (Pulsed and continuous energy transfer systems, cavity construction, laser amplifier and oscillator based on energy transfer from SiO to Na). Ph.D., August 1993.

D. Grantier (Cavity construction for Na<sub>3</sub>-X amplifier system, development of Na<sub>3</sub>-F chemiluminescent probe studies, assessment of Na<sub>2</sub> violet system).

James Stephens (SiO-Na energy transfer system, Development of silane (SiH<sub>4</sub>) based Si and SiO metastable sources).

Douglas Berlin (SiO-Na energy transfer system - gas flow calibration, Flowtube development).

He Wang, Postdoctoral (partial-assistance in cavity construction and modification, development of high resolution laser gain experiments and laser probes of chemical laser reaction products, extrapolation of Na<sub>3</sub>-X reaction schemes, extrapolation of SiO-Na energy transfer schemes to SiO-Pb, SiO-Cu, and SiO-Sn systems).

C. B. Winstead (partial assistance in experiments and cavity construction measurements on Si<sub>x</sub> molecules) - Ph.D. May, 1995.

T. C. Devore (analysis of Mg<sub>x</sub>-F, Bi<sub>x</sub>-F, F<sub>2</sub>, reactive systems).

D. A. Dixon (quantum chemistry on Mg<sub>x</sub>-F reactive system).

E. J. Mansky (formulation of theories to explain selectivity in Na<sub>3</sub>-X reactions).

Alan Kauppi, J. Steven Joiner, Douglas Dawson, and Peter Medley (undergraduate assistants to K. K. Shen, He Wang, and D. Grantier).

## APPENDIX I

"The Unique Complexation and Oxidation of Metal-Based Clusters", J. L. Gole in Advances in Metal and Semiconductor Clusters, Vol. 1, Spectroscopy and Dynamics, ed. M. A. Duncan, JAI Press, pg. 159-209.

# THE UNIQUE COMPLEXATION AND OXIDATION OF METAL-BASED CLUSTERS

James L. Gole

---

I. Introduction . . . . .	160
II. Quantum Level Probes of the Metal Clustered Oxides and Halides . . . . .	163
A. A Versatile Source Configuration for the Study of Small Cluster Oxidation . . . . .	163
B. Cluster Oxidation Studies—A Complementary Research Effort . . . . .	166
C. Comparative Energetics of Metal Cluster Oxidation Reactions . . . . .	167
D. Optical Signatures of Metal Cluster Oxidation—Their Significance . . . . .	170
E. Silver Cluster Oxidation . . . . .	170
F. Copper Cluster Oxidation . . . . .	175
G. Boron Cluster Oxidation . . . . .	179
H. Transition Metal Cluster Oxidation . . . . .	181
I. Trends and Future Extensions . . . . .	182
III. Continuous Visible Chemical Laser Amplifier from a Metal Cluster Oxidation Reaction . . . . .	184

---

**Advances in Metal and Semiconductor Clusters**  
**Volume 1, pages 159–209**  
**Copyright © 1993 by JAI Press Inc.**  
**All rights of reproduction in any form reserved**  
**ISBN: 1-55938-171-X**

IV. Electric Field Enhanced Laser-Induced Plasma Spectroscopy . . . . .	192
A. Nature of the EFELIPS Experiment . . . . .	192
B. Positive and Negative Ion Selection . . . . .	195
C. The Silicon Trimer Emission Spectrum . . . . .	196
D. Aluminum Based Ion-Molecule Complexes . . . . .	199
Acknowledgments . . . . .	205
References and Notes . . . . .	205

## I. INTRODUCTION

Because they not only represent bridging regions of molecular bonding and electronic structure but also display distinct intermolecular interactions and reactivity, clusters, and metal and metalloid clusters in particular, are now attracting the attention of physicists, chemical physicists, and chemists alike.<sup>1,2</sup> These intermediate states of matter warrant investigation because the analysis of their properties impacts strongly on our understanding of (1) the nucleation of atoms into small metal or metalloid particles, (2) the development of features that form the character of the bulk semiconductor or metallic phase,<sup>3</sup> and (3) the basis for reactive interaction with this bulk phase.

Most heterogeneous chemical conversion processes require intimate interaction with the surface of a condensed phase. The widespread applicability of these processes in a variety of practical applications encompassing metal combustion, chemical vapor deposition, plasma etching, and general industrial catalysis has fueled a significant theoretical and experimental research effort to understand the intimate interactions associated with surface participation and reactivity. An increasingly popular and potentially enlightening component of this effort now involves the modeling of a small group of interacting atoms (cluster) on the surface. Within this framework the detailed study of small clusters and their oxidation to produce metal clustered oxides can provide needed insights relevant to the incorporation of local interactions into modeling at much larger scales.

With a dual emphasis on their unique nature, as well as the potential for both theoretical and experimental extrapolation to larger scales appropriate for describing bulk properties, several elegant technologies are emerging, often in combination, to study clusters and their compounds. These efforts have as their objective a fingerprinting of electronic structure, molecular bonding, and a unique and varied cluster chemical reactivity.<sup>1-3</sup> Despite many impressive approaches, the internal mode structure and dynamics associated not only with the metal clusters themselves<sup>4</sup> but also with the products of their kinetically controlled oxidation have been largely neglected. The limited information that is available<sup>5-7</sup> demonstrates that metal clusters undergo a unique and, in many instances, totally unexpected reactive branching.<sup>8</sup> The study of this reactive branching is fundamental to the development of rules required to extrapolate from simple  $A + BC$  reactions. Furthermore, the analysis of the quantum level structure of product metal cluster oxides and halides

formed in highly exothermic oxidation processes provides detailed and fundamental information on molecular structure and bonding.<sup>5-8</sup> In correlation with molecular dynamics simulations and quantum chemistry these data can serve as a touchstone for the development of a reasonable framework to describe (1) highly exothermic combustion processes or (2) local cooperative atomic phenomena and mobilities, the fingerprint of which can be useful in modeling the interface at metal cluster oxide surfaces where, for example, catalytic behavior is most likely influenced.

In effect, studies of gas-phase metal cluster oxidation afford the opportunity to characterize the intermediate region bordered on the one side by the gas-phase oxidation of metallic atoms and dimers and on the other by the surface oxidation of the bulk metallic phase. It has been suggested that these studies may provide information useful for the assessment of short and long range factors affecting surface oxidation.<sup>9</sup> It is also relevant that most catalysts are in an oxidized form. When modeling a catalytic metal oxide surface, we are concerned with how various few atom metal clustered oxide configurations can be formed, the approximate potentials describing the particle interaction, and the manner in which the interacting constituents can be altered. A valuable component of this information can be obtained from the study of metal cluster oxidation. In addition, fundamental information obtained on the highly ionic metal clustered oxides serves to complement characterizations of positively and negatively charged metal cluster ions whose properties may mimic charge localization on a metallic surface.<sup>1,3</sup>

We have been concerned with the study of the oxidation dynamics that a number of metal (and metalloid) clusters undergo as they form a distinct class of metal atom grouped cluster oxides<sup>5</sup> and halides<sup>6</sup> under kinetically, as opposed to thermodynamically, controlled conditions. An effort has begun to characterize the internal mode structure of the product metal clustered oxides and halides. In developing these studies, we have analyzed the first vibrationally resolved optical signatures for several "asymmetric" metal cluster oxides.<sup>5</sup> We have also demonstrated the first visible chemical laser amplifier from a metal cluster oxidation process.<sup>7</sup> These studies graphically demonstrate the dramatic and unexpected oxidation behavior characteristic of small metal cluster reactions and point to the potential for developing new insights on the nature of chemical reactivity.

The products of metal cluster oxidation may be studied using a combination of chemiluminescent (product formation in excited electronic states for highly exothermic oxidation) and laser fluorescent techniques. In these applications one must realize that observations of the internal mode structure, associated especially with the *polyatomic products* of metal cluster oxidation, may be plagued by the rapid depletion of excited state populations due to nonradiative processes. These processes can dominate and deplete the product states either before the emission of a monitoring photon (chemiluminescence) can occur or before an appropriate laser spectroscopic probe can be made operative.<sup>10</sup> To overcome this difficulty, we

require the development of intense metal cluster sources which offer a viable means to compensate for the dominant quenching of the optical signatures associated with the polyatomic emitters of interest.

Quantum level probes of the products of metal cluster oxidation are being developed with a current emphasis on two distinct source configurations. In one configuration a stream of metal clusters formed through the "supersonic expansion" of the metallic element of interest is made to intersect a selected oxidant (modified beam-gas configuration), the products of reaction being studied using a combination of chemiluminescent and laser fluorescent techniques. This configuration has been used to study the sodium trimer-halogen atom reactions.<sup>7</sup>

Of possibly more significance is the development of a second more versatile source configuration that lies intermediate to a low pressure molecular beam and high pressure flow device.<sup>11</sup> Clusters are formed from a high metal flux source and further agglomerated by an entraining argon or helium flow at room to liquid nitrogen temperature. Using this source, we have successfully obtained the first quantal information on the energy levels and optical signatures of several metal cluster oxides and selected halides ( $M_nO$ ,  $M_nX$ ). Our focus in these studies is to be distinguished from recent very exciting investigations in which small to intermediate size clusters have been generated in flow systems,<sup>12</sup> reacting with reagents in either merged continuous or pulsed flow streams under high pressure (~ 300–500 torr) conditions. The products of reactivity in these merged flows have been measured mass spectrometrically extracting important kinetic information; however, the technique is not yet oriented to a direct measure of structural or dynamic properties.

In the first part of our discussion, we will summarize (1) the experimental techniques for generating large concentrations of small metal clusters in a highly exothermic oxidizing environment and (2) a portion of the information that we have garnered thus far on the quantum levels of metal cluster oxide and fluoride compounds,  $M_xO_y$  and  $M_xF_y$ . These studies not only outline the potential use of chemiluminescence as a means of characterizing metal cluster oxide quantum levels, but also they suggest future laser-induced fluorescent probes of the metal cluster oxides.

In the second part of our discussion, we will focus on the use of supersonic expansion sources for cluster generation and the highly efficient alkali trimer-halogen atom reactions that have now been demonstrated to form the gain medium for the first continuous visible chemical laser amplifier.<sup>7</sup> Finally, we will outline the new technique of Electric Field Enhanced Laser-Induced Plasma Spectroscopy (EFELIPS) as a relatively simple and general approach to the mapping of electronic states and internal mode structure in small metal clusters, their ions, and small metal and metalloid based ion-molecule complexes.

## II. QUANTUM LEVEL PROBES OF THE METAL CLUSTERED OXIDES AND HALIDES

### A. A Versatile Source Configuration for the Study of Small Cluster Oxidation

To study the optical signatures and internal mode structure of metal cluster oxides and halides and the dynamics of metal cluster oxidation, we are developing a combination of both chemiluminescent and laser fluorescent probes across a wide pressure range. A major emphasis and the ultimate goal of these experiments will be to generate laser-induced fluorescent spectra of the metal cluster oxides (with potential extension to the halides) in order to assess the geometries and evaluate the molecular electronic structure of these metal atom clustered oxides.

A versatile entrainment device has been constructed and used primarily to develop chemiluminescent probes of the products of metal cluster oxidation. To carry out these studies we extrapolate on experience gained in the study of chemiluminescent metal atom oxidation reactions.<sup>13</sup> We focus on the development of "high flux" continuous metal flow sources, which we use to create large concentrations of small metal clusters. We create an intermediate environment to that of a low "source" pressure effusive device, where primarily atoms, a small percentage of diatomics, and, in some cases, small percentages of polyatomics are created,<sup>14</sup> and those conditions that prevail subsequent to the highly efficient agglomeration of a metallic plasma. The later condition is characteristic of laser vaporization—supersonic expansion at high backing gas pressures. Laser vaporization, when operated in the pulsed supersonic expansion mode, produces a wide diversity of much larger clusters (vs. effusive source) although at relatively small ( $\geq 10^7/\text{cm}^3$ ) effective concentration.<sup>15</sup>

We operate a metal source at temperatures or through containment designs that produce a Knudsen number much less than one and create the seed for the initial phases of a cluster forming environment. The high metal flux, which within itself can lead to agglomeration to form clusters, is further agglomerated to small clusters by an entraining argon or helium flow at room to liquid nitrogen temperature.

The heart of the agglomeration-entrainment device depicted schematically in Figure 1a consists of a large capacity furnace assembly. Here, using a tungsten basket heater (R. D. Mathis), a metal is heated in a particularly designed crucible, selected for the metal or metalloid whose oxidation is under study, to a temperature producing a vapor pressure between one and three orders of magnitude greater than that employed for effusive operation. The basket heater is wrapped in zirconia cloth (Zircar, Florida, N. Y.) and surrounded concentrically by (1) a tantalum heat shield and (2) a cylindrical heavy-walled zirconia tube (Zircar). Both the top and bottom of the basket heater zone are heavily insulated with zirconia cloth. This extra insulation allows the ready operation of the tungsten basket heater at temperatures consistently at the upper limits of its performance specifications.

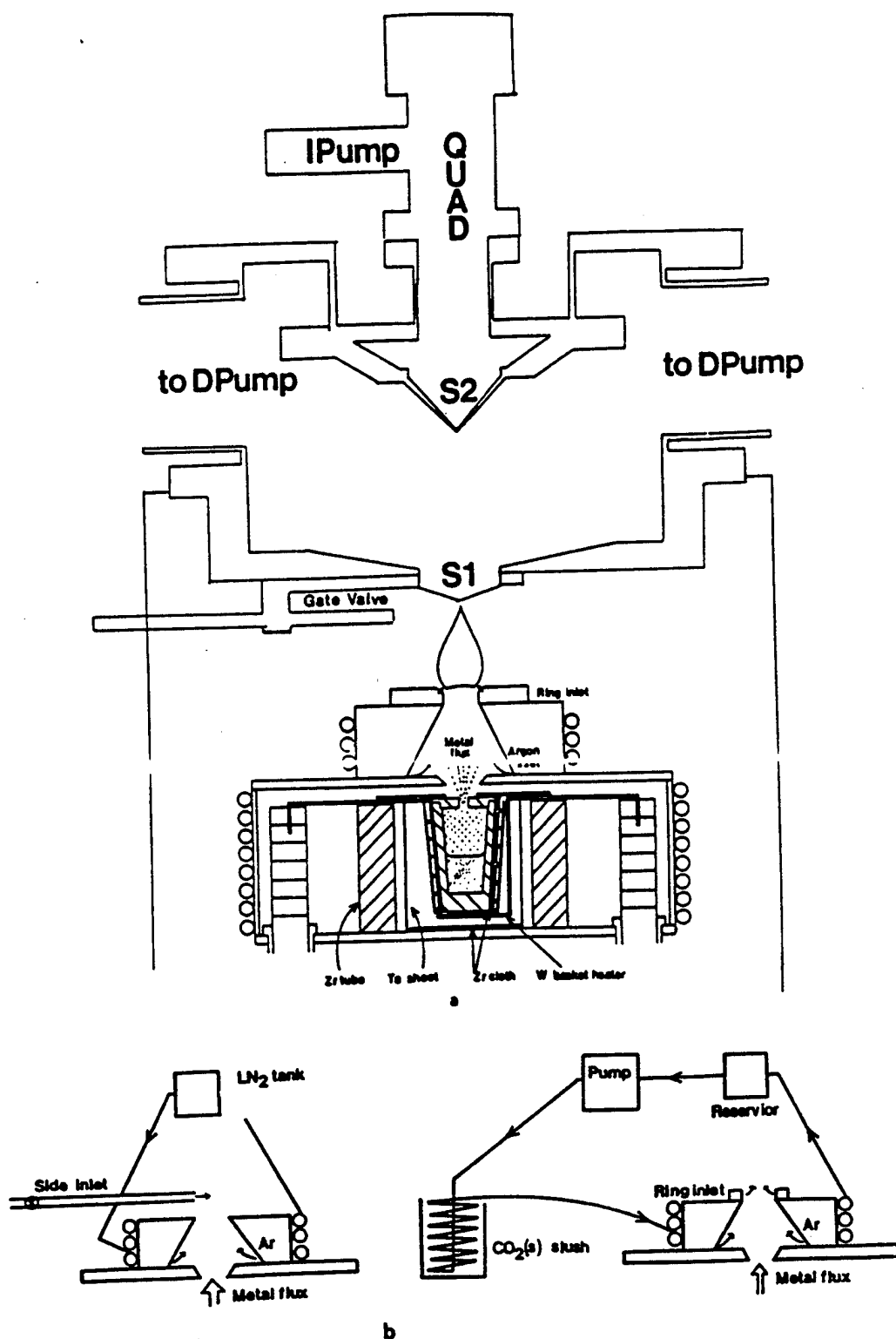


**Figure 1.** a, Schematic of metal entrainment-agglomeration-oxidation device showing tungsten basket heater, insulation, entrainment region, and oxidation region. Above the flame-oxidation region is a small quadrupole based mass spectrometer system. b, Outline of entraining gas cooling system.

The metal flux issuing from the lower crucible chamber is entrained in a rare gas (He or Ar; Airco 99.998%) flow ranging in pressure from 100 to 3000 millitorr, dependent upon the metal under study and the optimization of the chemiluminescent oxidation processes of interest. The agglomeration of the metal to form small clusters occurs both as a result of the high metal flux and as the metal flow is cooled by the variable temperature entrainment gas. To vary the temperature of the entrainment gas the entire upper assembly depicted in the figure, with which the gas is in intimate contact, is maintained at a desired temperature. This is accomplished with the systems depicted in Figure 1b. For cooling to temperatures approaching 196 K, methanol is continuously pumped through all cooling lines after passing through a dry ice slush bath. To obtain lower temperatures, liquid nitrogen is allowed to flow at varying rates through these cooling lines. The choice or degree of cooling is dictated by several parameters associated with the particular metal or metalloid clusters whose oxidation is under study.

At a suitable point above the flow, an oxidant intersects the entrained clusters, entering either from a concentric ring injector inlet as depicted in Figure 1a or from a nozzle perpendicular to the flow and elevated above the cooled upper region of the oven assembly (Figure 1b). Typical oxidant pressures range from 10 to 100 millitorr. For metatheses that are sufficiently exothermic, a chemiluminescent flame may be formed.

In the studies that we will outline, concentrations of metal, carrier gas, and oxidant are adjusted in a controlled manner to maximize or minimize the intensities of the emitters of interest over the spectral region 230–800 nm. The "multiple collision" flames vary in shape with a base diameter of 12 mm and a height ranging from 1 to 5 cm. They are adjusted primarily by varying four parameters: (1) metal flux, (2) entrainment gas cooling, (3) pumping speed, and (4) oxidant configuration and concentration. On the basis of previous studies,<sup>13</sup> the final internal rotational temperatures of the clusters before reaction will be considerably lower than the oven source from which the metal flow exits ( $\sim T_{\text{Rot}} \leq 200$  K for cold entrainment). When readily characterized for diatomic emitters,<sup>13</sup> the rotational temperatures for room temperature entrained reaction products are found to vary from 500 to 900 K. This range provides a reasonable estimate for the rotational temperature of the polyatomic products of the metal cluster oxidation reactions considered.

For processes that are chemiluminescent at low pressures, where excited states are populated due strictly to a well-defined reaction exoergicity and photons are emitted from the reaction products before subsequent collisions, extremely complex spectra may result; the controlled extension of these studies to the multiple collision regime can provide useful spectral simplification primarily as a result of differences in rotational, vibrational, and electronic relaxation rates. In addition to the merits of spectral simplification, multiple collision scans serve two primary purposes: (1) They allow the study of relaxation and quenching phenomena, and (2) they allow the study of rapid energy transfer among the excited states of high temperature molecules. Extensions from single to multiple collision conditions

**Table 1.** Parameters Associated with the Generation of Metal Cluster Flows

<i>Metal(Purity, Source)</i>	<i>Source Temperature (Vapor Pressures)</i>	<i>Effusive Operation</i>
Ag(99.99, Cerac)	1400–1700 K ( $10^{-1}$ –5 Torr)	$\leq 1400$ K ( $10^{-1}$ Torr)
Cu(99.9, Fisher)	1650–1960 K ( $10^{-1}$ –2 Torr)	$\leq 1650$ K ( $10^{-1}$ Torr)
B(99.7, Alfa)	2520–2800 K ( $10^{-1}$ –1 Torr)	$\leq 2520$ K ( $10^{-1}$ Torr)
Mn(99.95, Fisher)	1350–1600 K ( $10^{-1}$ –5 Torr)	$\leq 1300$ K ( $<10^{-1}$ Torr)

must be made under conditions such that only relaxation and rapid energy transfer characterize the spectra. We maintain a well-defined energy conservation. With the exception of complex light emitting processes, which are readily ascribed to a combination of the dynamics of product formation and rapid energy transfer, a reaction that is dark under single collision conditions remains dark under multiple collision conditions as energy is conserved. This is an important touchstone for the experiments.

Here, we focus primarily on highly exothermic copper, silver, and boron cluster oxidations, touching also on transition metal reactions that produce the metal cluster oxides and halides. For the present studies, the oven source parameters summarized in Table 1 correspond to a gas-phase metal flux between  $3 \times 10^{16}$  and  $5 \times 10^{18}$  particles/cm<sup>2</sup>-sec at the source crucible orifice, the concentrations at the upper limit being well in excess of that generated from an effusive source. The oxidants NO<sub>2</sub> and O<sub>3</sub><sup>16</sup> have been used in the majority of these studies. The spectra depicted in Figures 1–10 were taken with a 1-m Czerny–Turner scanning spectrometer/photomultiplier detector combination. The photomultiplier signals were channeled to a picoammeter whose output signal (partially damped) was fed to a computer-based data acquisition system or directly to a stripchart recorder.

### B. Cluster Oxidation Studies—A Complementary Research Effort

Several variants of the source configuration outlined in the previous section have been used to generate a substantial and usable continuous flux of metal clusters. The optical signatures of the reaction products associated with the oxidation of small boron (B<sub>x</sub> + NO<sub>2</sub>, N<sub>2</sub>O),<sup>5a-c</sup> copper (Cu<sub>x</sub> + O<sub>3</sub>, Cl<sub>2</sub>, Cl),<sup>5a,17,18</sup> silver (Ag<sub>x</sub> + O<sub>3</sub>, Cl<sub>2</sub>)<sup>5a,d,18</sup> manganese (Mn<sub>x</sub> + O<sub>3</sub>),<sup>5b,e</sup> and chromium (Cr<sub>x</sub> + O<sub>3</sub>, F<sub>2</sub>)<sup>6,19</sup> clusters have been studied. We have obtained the first quantal information on the energy levels and optical signatures of several asymmetric metal clustered oxides, M<sub>n</sub>O<sub>y</sub> ( $n \geq 2$ ) and preliminary data on the copper and chromium cluster chlorides and fluorides. These systems were chosen for study with a view toward contributing to the modeling of chemically important environments. Thus, the interest in these

systems ranges from the potential importance of the boron cluster oxides in boron particulate combustion systems,<sup>20</sup> to the potential importance of the copper cluster oxidation products toward the action of the copper oxides in superconducting materials.<sup>21</sup> This work has led to three general observations concerning cluster reactions:

1. Cluster oxidations, through a multicentered reaction capability, often yield product molecules in higher energy states than do the corresponding atomic reactions.
2. The products of metal cluster reactions encompass metal rich molecules. In many cases, metal-metal bonds are present and behave with an unusual fluxionality in these product molecules.
3. Kinetics rather than thermodynamics most often controls the nature of the initially formed products of metal cluster oxidation.

### C. Comparative Energetics of Metal Cluster Oxidation Reactions

Reactions between metal atoms and oxidants have long been used to produce metal oxides and halides for spectroscopic and kinetic investigation.<sup>22</sup> The energy released in these reactions of the form:



is given by:

$$\Delta E_{RXN} = D_0^0(MX) - D_0^0(X-Y) + \Delta E_{INT} \quad (2)$$

where  $D_0^0(A)$  is the bond dissociation energy of A and  $\Delta E_{INT}$  is the contribution from reactant internal and translational energy. For a typical oxidant ( $O_3$ ,  $N_2O$ ,  $F_2$ ) reacting with a transition metal atom, the process 1 gives a maximum exothermicity between approximately 2 and 4 eV.<sup>10</sup> The reaction exothermicity for the process:



is  $1.76 \pm 0.05$  eV. This process is energetic enough to populate the  $v' = 2$  level of the  $CuO \delta^2\Sigma^+$  state, and the data obtained for copper atom and cluster oxidation depicted in Figure 2 demonstrates that the available energy for the atomic oxidation process is in excellent agreement with the chemiluminescent spectrum observed for reaction 3 under near single collision conditions.

There is, however, growing evidence that the multicentered oxidation of metal dimers (or larger clusters) can result in a significantly more energetic process that populates considerably higher lying electronic states of those product molecules formed in reaction. Four center dimer reactions of the form:



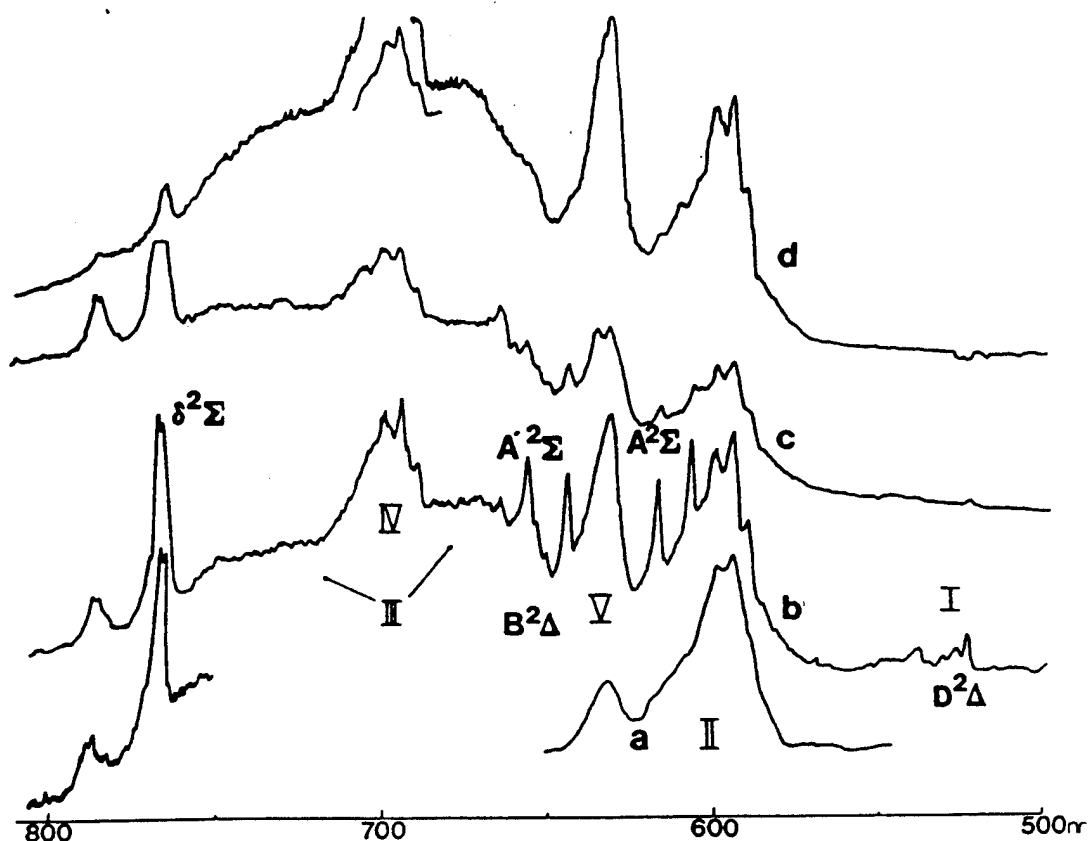


**Figure 2.** Chemiluminescent spectra observed for the oxidation of small copper clusters taken with an EMI 9808 phototube at a resolution of 12 Å. **a**, Single collision chemiluminescent spectrum taken with  $T_{\text{beam}}(\text{Cu}) \approx 1700\text{K}$ ; **b**, multiple collision chemiluminescent spectrum taken at an entrainment gas pressure of 600 mTorr obtained with room temperature water cooling; **c**, chemiluminescent spectrum obtained under multiple collision conditions ( $P_T \sim 600$  mTorr) using dry ice/methanol cooling; and **d**, chemiluminescent spectrum obtained under multiple collision conditions ( $P_T \sim 600$  mTorr) using liquid nitrogen cooling. Systems II, III, IV, and V are attributed to  $\text{Cu}_x\text{O}$  species.

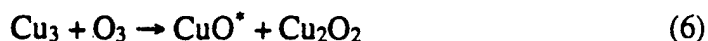
with

$$\Delta E_{\text{RXN}} \approx D_0^\circ(\text{MX}) + D_0^\circ(\text{MY}) - D_0^\circ(\text{M}_2) - D_0^\circ(\text{XY}) + \Delta E_{\text{INT}} \quad (5)$$

can release 1–2 eV more energy than the corresponding atomic reactions.

If this energy for multicentered reaction is largely collected in one of the product molecules, then a considerable enhancement of excited electronic states can be obtained. As indicated in Figure 2, the oxidation of copper clusters with ozone under multiple collision conditions produces emission, which originates from the  $\text{D}^2\Delta$ ,  $\text{C}^2\Pi$ ,  $\text{A}^2\Sigma$ ,  $\text{B}^2\Delta$  and  $\text{A}'^2\Sigma$  states of  $\text{CuO}$ . The population of these states requires up to 1 eV more energy than is available from the copper atom reaction. This increased

exothermicity could be provided by the reaction of vibrationally hot copper dimer or, equally likely with moderate to high metal agglomeration, by the reaction of ground-state copper trimer via the process:



The increased exothermicity inherent in multicentered metal cluster oxidation reactions provides an opportunity to produce and explore previously unobserved higher lying states in several metal oxide or halide product molecules. For example, the reaction between chromium atoms and dimers and molecular fluorine has recently been used to study three previously unknown electronic states of CrF.<sup>6</sup> Prior to this investigation, only the  $A^6\Sigma - X^6\Sigma$  transition of CrF had been analyzed.<sup>23</sup> The metal atom fluorination reaction:



has a reaction exothermicity close to 3 eV and produces two additional product CrF band systems. Vibrational analysis indicates that both terminate in the ground state. The reaction of chromium dimers with molecular fluorine viz.:



nearly doubles the reaction exothermicity. This increase in reaction exothermicity allows the population of an additional higher lying electronic state of CrF. The molecular constants determined for each of the newly observed states of CrF are summarized in Table 2.

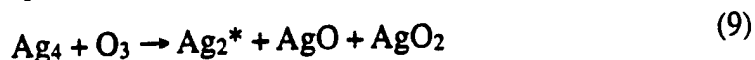
The oxidation of a highly agglomerated silver flow with ozone under multiple collision conditions produces emission from the  $A^2\Pi$  (400–420 nm) and the  $B^2\Pi$  (320–370 nm) states of AgO.<sup>2,5,6</sup> Neither the reaction of silver atoms nor the reaction of silver dimers can be expected to populate these AgO product states; the emission must result from the oxidation of Ag<sub>3</sub> or larger silver clusters.

At higher silver fluxes, the AgO emission is quenched and the spectrum is

**Table 2.** Molecular Constants Determined for CrF Formed in the Chemiluminescent Reactions of Chromium Atoms and Dimers with Molecular Fluorine

State	$T_e$	$\omega_e$	$\omega_e x_e$
$X^6\Sigma$	0	662.3(23)	3.4(9)
$A^6\Sigma$	9957.6	577.0(13)	0.6(4)
$B^6\Sigma$	16893(10)	605.2(20)	1.8(20)
$C^6\Pi$	-20600	-580(10)	—
$D^6\Sigma$	31705(15)	692(6)	1.8(20)

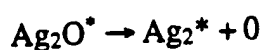
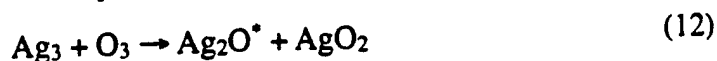
characterized by a combination of  $\text{Ag}_x\text{O}$  ( $x \geq 2$ ) and  $\text{Ag}_2$  band systems. The reactions or energy transfer producing the  $\text{Ag}_2$  emission have not been clearly established. However, multicentered processes such as:



represent the most likely candidate reactive encounters. The energy transfer:



and the reaction - dissociation sequence:



are also possible sources of the dimer excited electronic state.

#### D. Optical Signatures of Metal Cluster Oxidation—Their Significance

The oxidation of small metal clusters also produces novel metal rich molecules. Experimental conditions that generate emission spectra for these molecules have been established for the reaction systems  $\text{B}_x + \text{NO}_2$ ,<sup>5a-c</sup>  $\text{Mn}_x + \text{O}_3$ ,<sup>5a-c</sup>  $\text{Cu}_x + \text{O}_3$ ,<sup>5a,17</sup>  $\text{Cr}_x + \text{F}_2$ , and  $\text{Ag}_x + \text{O}_3$ .<sup>5a,d</sup> An analysis of the product emission spectra has provided the first quantal information on the energy levels and optical signatures for these metal atom clustered oxides and halides.

#### E. Silver Cluster Oxidation

The chemistry of silver derives its technological importance from its use in photography<sup>24</sup> and catalytic processes.<sup>25</sup> The epoxidation of ethene is catalyzed by supported silver whereas the dehydrogenation of methanol is catalyzed by bulk silver. In both systems, the silver catalyst must be in the form of a silver clustered oxide as are most metal catalysts. Studies that characterize the metal clustered oxides can be used to provide valuable insights into molecular structure, bonding, and atomic mobility in the  $\text{Ag}_x\text{O}$  constituencies as an aid to their modeling in the bulk configuration. A contribution to this modeling effort can be gained from the study of  $\text{Ag}_2\text{O}$  and from the extension of these  $\text{Ag}_2\text{O}$  studies to the higher metal clustered oxides  $\text{Ag}_x\text{O}$  ( $x \geq 3$ ). A further extension to the corresponding  $\text{Ag}_x\text{S}$  sulfides is also possible. These compounds are believed to play an important role, through sulfide-halide interactions, in film emulsions.<sup>26</sup>

In order to study the oxidation of small silver clusters using the apparatus depicted in Figure 1, silver metal is heated in a specially designed graphite crucible

to temperatures between 1400 and 1700 K. The high silver flux emanating from the crucible is entrained in a flow of rare gas (He, Ar) at room temperature. Agglomeration in the system occurs both as a result of (1) the high metal flux and (2) the cooling of the silver vapor by the room temperature entrainment gas. At a suitable point above the furnace assembly, ozone was introduced into the flow to produce a chemiluminescent flame corresponding, in large part, to an optical signature for the silver clustered oxides.

The  $\text{Ag}_x + \text{O}_3$  reaction produces a product molecule emitter whose spectrum extends from 506 to 680 nm (Figure 3) and which has tentatively been assigned to  $\text{Ag}_2\text{O}$ . The chemiluminescent spectrum between 500 and 700 nm contains two distinct emission band regions, which have been assigned as the A-X and B-X band systems of  $\text{Ag}_2\text{O}$ . The A-X transition that onsets at  $\sim 630$  nm is well fit by the expression:

$$\nu(\text{cm}^{-1}) = 15670 - 165 \nu_2'' + 0.4 (\nu_2'')^2 \quad (13)$$

The B-X transition that originates at 506 nm is well fit by the expression:

$$\begin{aligned} \nu(\nu_1'', \nu_2'', \nu_3'') = & 19766 - 442\nu_1'' - 165\nu_2'' - 256\nu_3'' \\ & + 6(\nu_1'')^2 + 6\nu_1''\nu_3'' + 25\nu_1''\nu_2'' \end{aligned} \quad (14)$$

Three vibrational frequencies ( $442 \text{ cm}^{-1}$ ,  $165 \text{ cm}^{-1}$ , and  $256 \text{ cm}^{-1}$ ) established for the molecular emitter suggest that it contains a Ag-Ag bond. The  $440 \text{ cm}^{-1}$  frequency is readily assigned to the Ag-O stretch. Because the geometry of the molecular emitter has not been established experimentally, there is uncertainty in the assignment of the two low frequency modes. Either the  $165 \text{ cm}^{-1}$  or the  $256 \text{ cm}^{-1}$  frequency might reasonably be assigned as a silver-silver stretch. The spectral features that onset at  $\sim 630$  nm display only a single vibrational frequency separation whereas the shorter wavelength band system displays all three frequencies. This behavior would suggest that both a substantial bond angle and bond length change accompany the transition associated with the higher energy band system. In contrast, the lone  $\sim 165 \text{ cm}^{-1}$  separation associated with the 630 nm system is indicative of a change in bond angle or bond length but not both, the later being unlikely because it should signal the observation of two stretch frequencies. For this reason the  $165 \text{ cm}^{-1}$  frequency is assigned to the bending mode of the  $\text{Ag}_2\text{O}$  molecule.

The assignment of the A-X and B-X band systems is consistent with the emission characteristics of a number of similar polyatomic systems.<sup>27</sup> The frequency expression for the B-X system displays large anharmonicity terms ( $25\nu_1''\nu_2''$ ). This is consistent with the rather floppy nature of metal clusters<sup>28</sup> and their compounds. The observed frequencies are consistent with a nonlinear Ag-Ag-O structure, with emission from the asymmetric cluster oxides characterizing these kinetically controlled oxidation experiments in contrast to the thermodynamically more stable symmetric species.

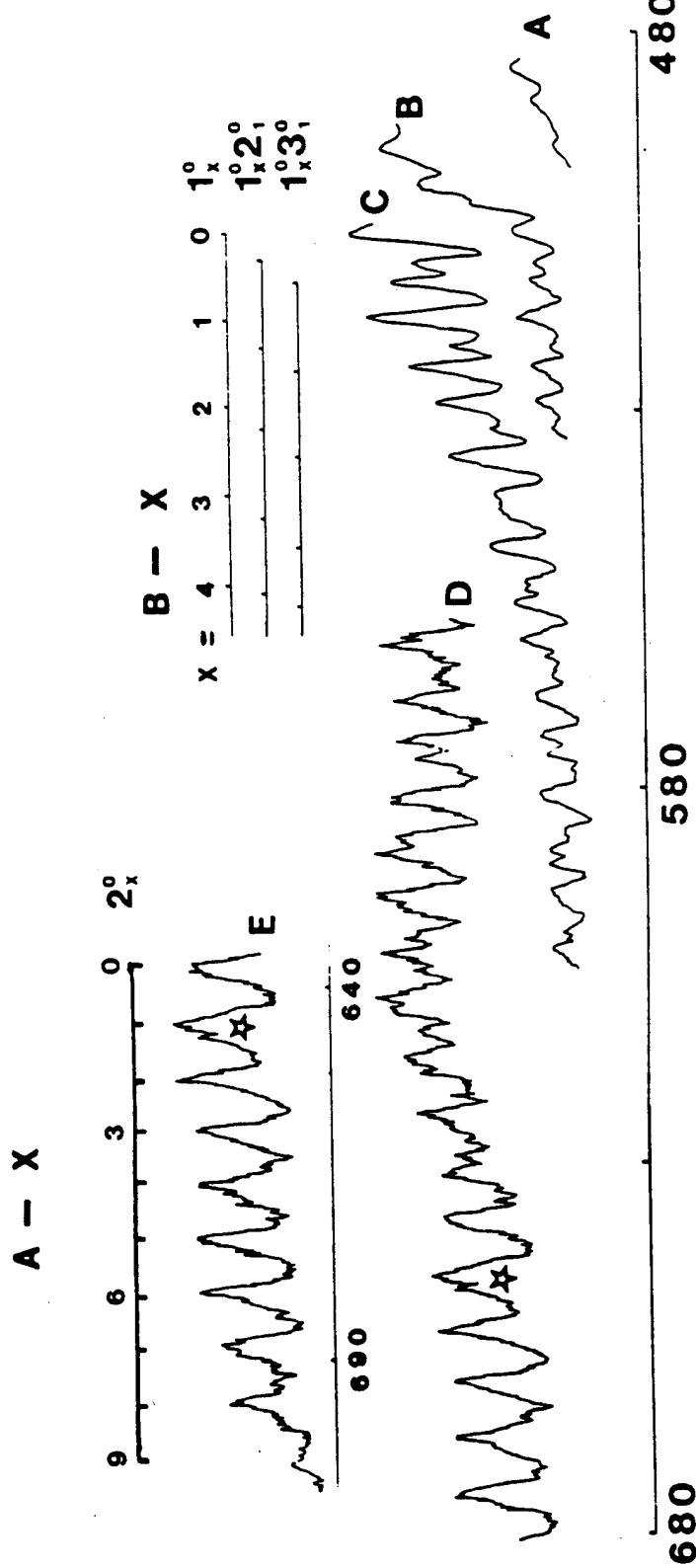
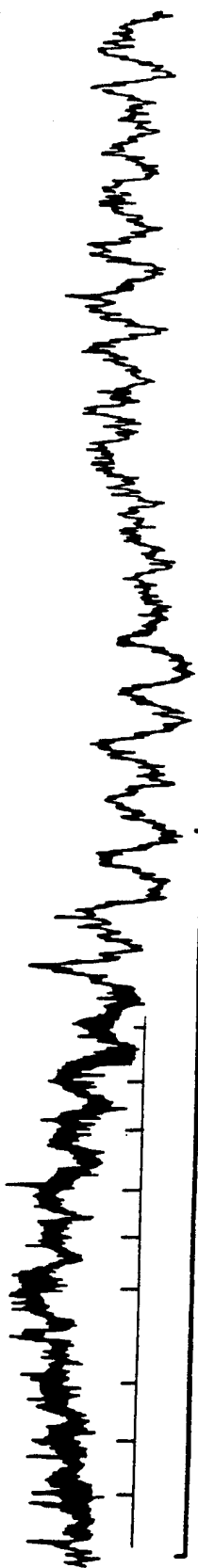


**Figure 3.** Chemiluminescent spectrum for the reaction of small silver clusters entrained in argon at a total pressure of 400 mTorr. The spectrum was taken with an EMI 9808 phototube at a resolution of 8 Å. Reaction is with ozone. Scan A depicts the long-wavelength end of the ~440 nm system. Scan B depicts the relative intensities of the tail of the 440-nm system and the 500-nm system tentatively correlated with Ag<sub>2</sub>O. Scan C depicts the 500-nm band system transition region. The assignments for the first 12 bands are noted. This system displays the Ag-O stretching, Ag-Ag stretching, and AgAgO bending frequencies [ $\nu_1 = 442$  (denoted 1 in the figure),  $\nu_2 = 165 \text{ cm}^{-1}$  (denoted 2 in the figure), and  $\nu_3 = 256$  ( $\nu_{\text{Ag-Ag}}$  - denoted 3 in the figure)]. Scan D depicts the continuation of the 500-nm system, which becomes more complex with emission to higher vibrational quantum levels and is dominated by combination bands. This system blends into the 630-nm system (E) correlated also with Ag<sub>2</sub>O. Scan E depicts the 630-nm band system (correlated with Ag<sub>2</sub>O), which may extend to shorter wavelength blending with the 500-nm system. This system is associated with a long progression in the Ag<sub>2</sub>O bending mode ( $\sim 165 \text{ cm}^{-1}$  - denoted 2 in the figure). See text for discussion.

$\text{Ag}_x\text{O}$

(b)



(a)

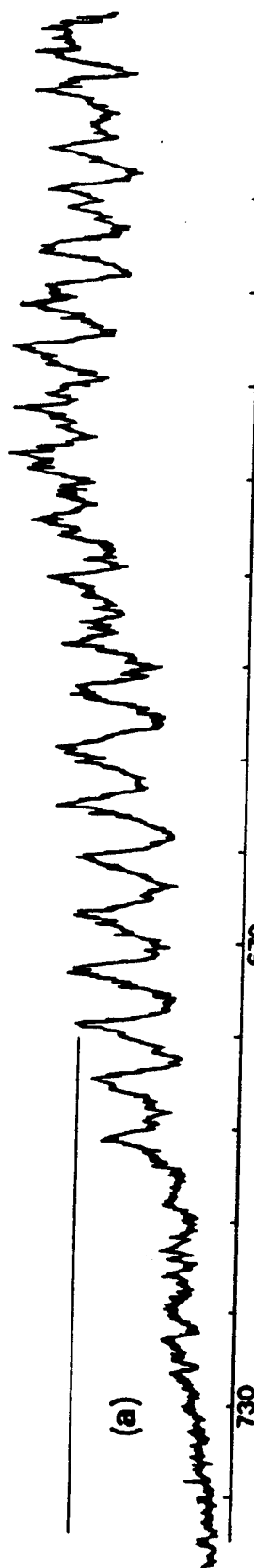


**Figure 4.** Chemiluminescent spectra for the reaction of small silver clusters entrained in dry ice cooled argon at a total pressure of 400 mTorr. The spectrum was taken with an EMI 9808 phototube at a resolution of 7 Å. Reaction is with ozone. Observed spectral emission in the region 550–730 nm is believed to correlate with the metal cluster oxides  $\text{Ag}_x\text{O}_y$  ( $x \approx 2$ ). The upper spectrum is obtained at considerably higher silver flux and appears to demonstrate the onset of a new band system (boldfaced) at  $\lambda \approx 660$  nm. See text for discussion.

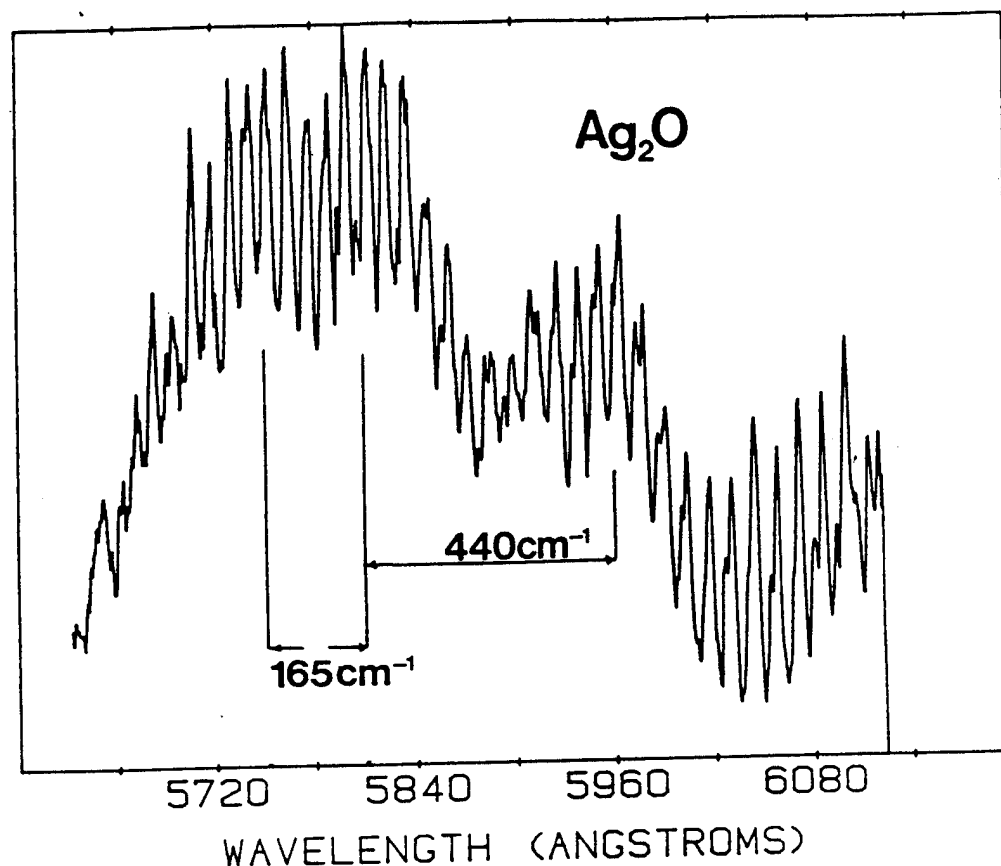


**Figure 5.**  $\text{Ag}_x\text{O}$  laser-induced fluorescence excitation spectrum generated with an argon ion pumped Rhodamine 6G dye laser of linewidth  $\approx 0.5\text{cm}^{-1}$  FWHM. The emission is detected with an RCA 4840 red sensitive phototube. Transitions in the region of the tentatively identified  $\text{Ag}_2\text{O}$  A-X and B-X band systems,  $\Delta\lambda = 562\text{--}612$  nm, have been laser induced. The dark  $\text{Ag}_x + \text{N}_2\text{O}$  reaction forms the ground-state metal cluster oxide. The LIF spectra consist of a  $\Delta\nu = 40\text{ cm}^{-1}$  sequence structure superimposed on short progressions that display the  $440$  and  $165\text{cm}^{-1}$  frequency separations characteristic of the spectra considered in Figure 3.

In some preliminary experiments the mass spectrometric sampling system indicated in Figure 1 has also been employed to aid spectral assignment. At even higher silver fluxes or under conditions in which the entraining helium and argon are cooled so as to approach dry ice (196 K) or liquid nitrogen (77 K) temperature further spectral features emerge at  $\lambda > 680$  nm (Figure 4). We have now tentatively observed at least two further systems thought to be associated with the higher silver clustered oxides  $\text{Ag}_x\text{O}$  ( $x \geq 2$ ), which are the subject of further study in our laboratory.<sup>29</sup>

Attempts are being made to employ laser-induced fluorescence to excite and characterize those transitions associated with the silver cluster oxides. An argon ion laser-pumped Rhodamine 6G dye laser has been used to induce transitions in

the region of the  $\text{Ag}_2\text{O}$  A-X and B-X band systems,  $\lambda = 562\text{--}612\text{ nm}$ , generating the LIF spectrum depicted in Figure 5. The dark  $\text{Ag}_x + \text{N}_2\text{O}$  oxidation reaction is employed to form the ground-state metal cluster oxide in an environment where neither reactant is excited by the scanning dye laser. We have successfully excited an LIF spectrum consisting of a  $\nabla v \approx 40\text{ cm}^{-1}$  sequence structure superimposed on short progressions displaying the  $440$  and  $165\text{ cm}^{-1}$  frequency separations characteristic of the chemiluminescent emission associated with the A-X and B-X band systems described previously. Further studies will require improvement in the LIF experiments in order to scan the  $\text{Ag}_2\text{O}$  (or higher  $\text{Ag}_x\text{O}$  clusters) spectrum at sufficiently high resolution to facilitate the spectral analysis which will allow the evaluation of the Ag-Ag-O ground state geometry. Furthermore, it will be necessary to improve our mass spectrometric sampling of the system.

### F. Copper Cluster Oxidation

The copper cluster oxides formed in oxidation reactions also represent important chemical entities. Of keenest recent interest may be their relevance to the assessment of the role the copper oxide lattice plays in high  $T_c$  superconductors where one is concerned with the movement of the copper and oxygen atoms as dictated by the  $\text{Cu}_x\text{O}$  potential.

Under a variety of experimental conditions, the first emission spectra for both the asymmetric copper clustered oxides (apparatus of Figure 1) and the symmetric  $\text{CuOCu}$  molecule have now been successfully generated.<sup>17</sup> A selection of the data obtained for these copper oxides is indicated in Figures 6, 7, and 8 where emission spectra for both symmetric and asymmetric  $\text{Cu}_2\text{O}$  as well as the higher order  $\text{Cu}_x\text{O}$  ( $x > 2$ ) complexes are displayed.

Significant differences between the electronic spectra and energy levels for the  $\text{CuCuO}$  and  $\text{CuOCu}$  molecules are evidenced not only by the distinctly different location of emission features but also by the appearance and extent of these features. The spectral features for the  $\text{CuCuO}$  molecule at  $\sim 600\text{ nm}$  appear to result from a short progression in a  $132\text{ cm}^{-1}$  bending mode whereas the observed structured emission spectra tentatively associated with the  $\text{CuOCu } ^1\text{B}_2 - ^1\text{A}_1$  transition appear to be dominated by moderate progressions in the ground and excited state symmetric stretching modes. The spectral features recorded for  $\text{CuOCu}$  bear a strong correlation with recent quantum chemical calculations by Bauschlicher, Langhoff, and Siegbahn<sup>30</sup> (Table 3). These authors have estimated bond lengths, bond angles, transition moments, and electronic state locations for the ground and several excited electronic states of the  $\text{CuOCu}$  molecule. These calculations are currently undergoing further refinement especially in correlation with the data derived from the emission spectra depicted in Figures 7 and 8. The relative intensities of the  $\text{CuOCu } ^1\text{A}_1$  and  $^1\text{B}_2$  transitions depicted in Figure 7 are in very good agreement with the calculated relative transition moments. Furthermore the change in bond angle and bond length predicted for the  $^1\text{A}_1 - ^1\text{A}_1$  transition

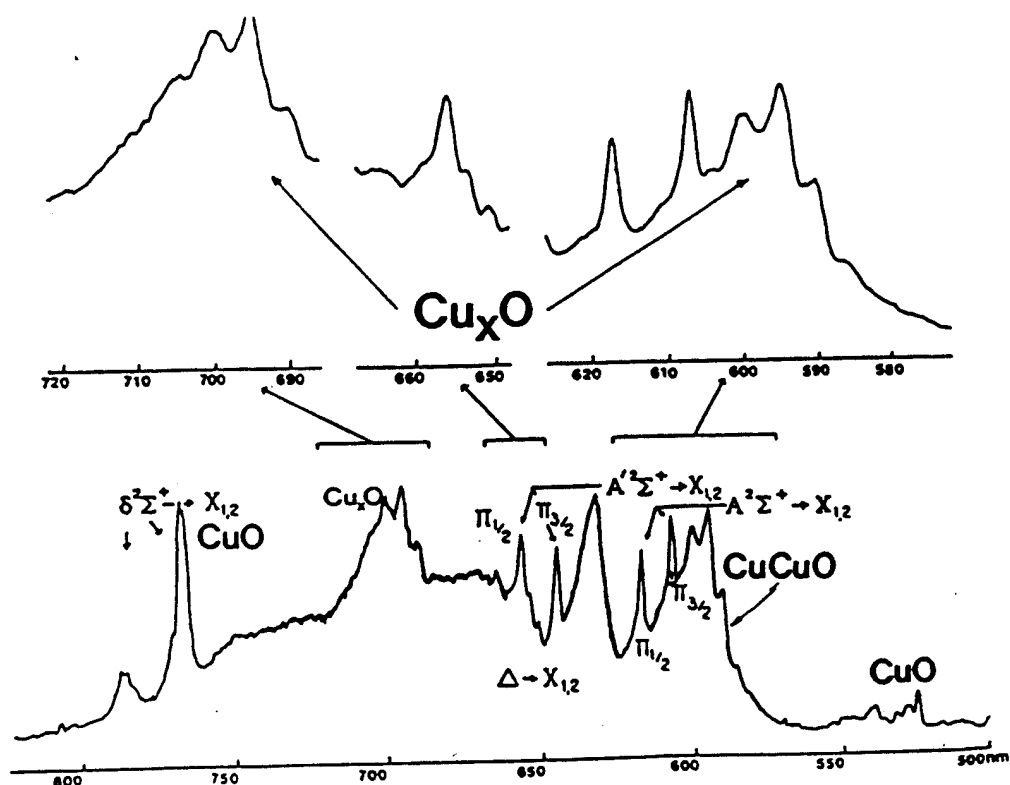


**Figure 6.** Chemiluminescent spectrum resulting from the multiple collision ( $P_{\text{Tot}} \sim 600$  mTorr) oxidation of small copper molecules and clusters. Clusters are formed in a moderate copper agglomeration mode (Knudsen number  $< 1$ ) and oxidized with ozone. The emission spectrum, taken with an EMI 9808 phototube at a resolution of  $8 \text{ \AA}$ , is dominated by  $\text{CuO}$  and  $\text{Cu}_x\text{O}$  ( $x \geq 2$ ) emission features where the polyatomic emitters correspond to the copper clustered oxides. (See also ref. 5a.)

**Table 3.** Calculated Properties of Ground and Excited States of Symmetrical  $\text{Cu}_2\text{O}$

State $T_e$ (approx.) ( $\text{cm}^{-1}$ )	$r(\text{Cu-O})$ (Angstroms)	Bond Angle (Degrees)
$^1\text{A}_1$ (Ground) 0	1.793	105.7
$^1\text{B}_1$ (0.3) <sup>a</sup> 14221	1.964	81.4
$^1\text{A}_1$ (1.6) <sup>a</sup> 17181	1.921	180.0
$^1\text{B}_2$ (1.0) <sup>a</sup> 20336	1.956	77.3
$^1\text{A}_2$ (0.1) <sup>a</sup> 22133	1.942	123.3

<sup>a</sup>Transition moment in atomic units.

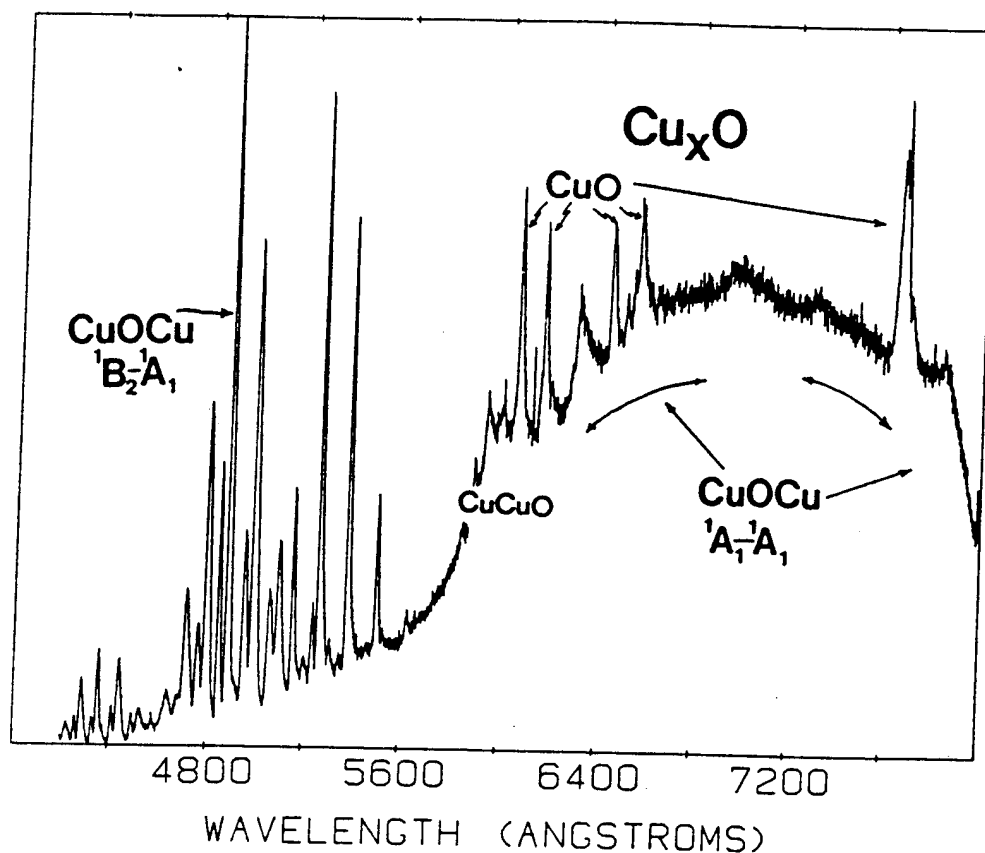


**Figure 7.** Chemiluminescent spectrum taken under multiple collision conditions in a non-effusive agglomeration mode dominated by emission from the symmetric  $\text{CuOCu}$  molecule but also showing emission corresponding to  $\text{CuO}$  and to the asymmetric  $\text{CuCuO}$  molecule. The spectrum was taken with an EMI 9808 phototube at a resolution of 5 Å.

( $\Delta\theta$  - a substantial  $75^\circ$ ) is commensurate with a long virtually unresolved progression dominated by the  $\text{CuOCu}$  bending mode much like that characterizing a similar transition in the water molecule at the fringes of the vacuum ultraviolet region.<sup>27</sup> For the  $^1B_2 - ^1A_1$  transition, the experimental data indicate a ground-state symmetric stretch frequency of  $\sim 640 \text{ cm}^{-1}$  ( $\nu_1'' = 640 \pm 10 \text{ cm}^{-1}$ ) and an excited state symmetric stretch normal mode frequency of  $409 \pm 10 \text{ cm}^{-1}$ .

The spectroscopy of the copper cluster oxides is now the focus of considerable further study. This effort includes laser-induced fluorescence at moderate and higher resolution to facilitate the evaluation of further vibrational mode structure and the determination of both the  $\text{CuCuO}$  and  $\text{CuOCu}$  ground-state geometries.

Using the constraints on the minimum reaction exothermicity necessary to facilitate a chemiluminescent reactive process and the limited mass spectrometric data obtained with the configuration depicted in Figure 1, one can suggest the

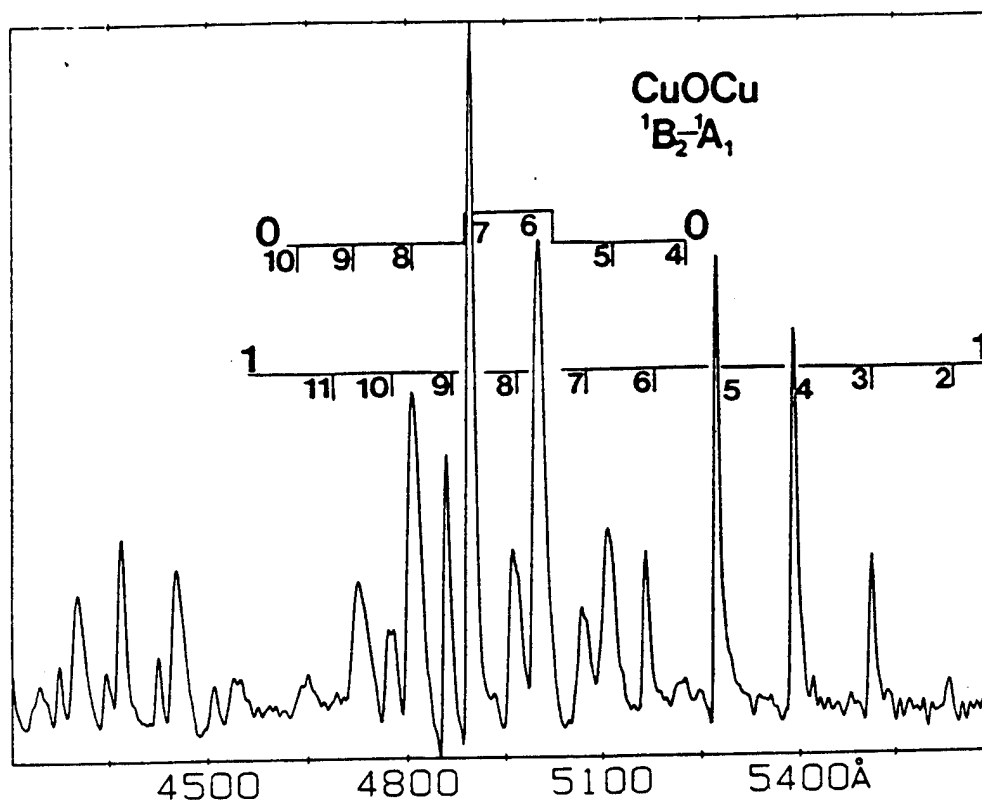
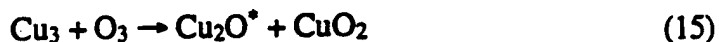


**Figure 8.** Closeup of chemiluminescent emission corresponding to the  ${}^1B_2 - {}^1A_1$  band system of CuOCu taken with an EMI 9808 phototube at a resolution of 5 Å. See also Figure 7 and text for discussion.

following most likely mechanisms for formation of the copper oxide emitters that give rise to the spectra depicted in Figures 6, 7, and 8. In the moderate to high agglomeration mode associated with the apparatus depicted in Figure 1, the  $\text{CuCuO}^*$  isomer whose emission is located near 600 nm is most likely formed via the reaction:



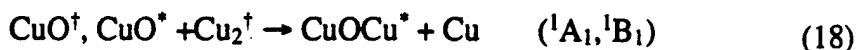
whereas lower-lying states may be formed through reaction of the dimer:



Here, the asterisks indicate electronic excitation. The higher-lying states of CuOCu may be formed via the reactions of vibrationally excited or possibly electronically excited CuO:



where the dagger indicates vibrational excitation. In the moderate agglomeration mode the CuOCu states may be formed through the process:



The experimental evidence that supports these tentative mechanisms will await further confirmation.

Studies of the copper cluster oxides are now providing the impetus for the quantum chemical generation of potential functions for the ground and excited states of the isomers of these molecules. Potential functions now generated for CuOCu and CuCuO indicate that although these molecules are quite bent, they are also characterized by very flat potentials in the bending mode. It appears that there is a high probability for interconversion of these two isomers. The generated potential functions are gauged by their fit of experimental vibrational frequencies generated in our initial experimental studies. This effort may well be relevant to the assessment of the role that the copper oxide lattice plays in high  $T_c$  superconductors.<sup>32</sup> Here the movement of the copper and oxygen atoms as dictated by the  $\text{Cu}_x\text{O}$  potential function, especially the vibrational modes associated with the out-of-plane bending of these species, may play a role in the high  $T_c$  mechanism.

### G. Boron Cluster Oxidation

Boron combustion can provide more than twice the volumetric energy density of conventional hydrocarbons. Although the emphasis in boron combustion and fuel research has been largely on boron particle ignition,<sup>33</sup> it is also recognized that as much as half of the potential energy content of boron fuels can be released in gas-phase oxidation processes, which might be exemplified by the conversion of  $\text{BO}(\text{g})$  to  $\text{B}_2\text{O}_3(\text{g})$ .<sup>33</sup> With a focus on homogeneous combustion chemistry, elegant studies have been in progress to assess the specific details of the gas-phase oxidation of  $\text{BO}(\text{g})$  to  $\text{B}_2\text{O}_3(\text{g})$ . Here, the key BO oxidation step in dry atmospheres is thought to be the rate limiting oxidation  $\text{BO}(\text{g}) + \text{O}_2(\text{g}) \rightarrow \text{BO}_2(\text{g}) + \text{O}(\text{g})$ , followed by the subsequent reaction of  $\text{BO}_2$  with additional BO molecules, the two-step process producing  $\text{B}_2\text{O}_3(\text{g})$ . If  $\text{BO}(\text{g})$  is a major constituent in dry atmospheres, it is likely that this molecule strongly influences the homogeneous combustion chemistry associated with the boron oxidation.<sup>34</sup> However, it is not certain that gaseous BO is the prime gas-phase constituent liberated in the ignition of boron particulates, and several important gas-phase compounds released as boron combusts might be neither gas-phase  $\text{BO}(\text{g})$  nor solid boron but rather intermediate species. It has been suggested that one of these species might be  $\text{B}_2\text{O}$ . If so, it is feasible that the process  $\text{B}_2\text{O}(\text{g}) + \text{O}_2(\text{g})$  can compete with the two-step mechanism indicated earlier for  $\text{B}_2\text{O}_3(\text{g})$  formation. It is up to the modern kineticist to assess this possibility; however, he can only be in a position to make this

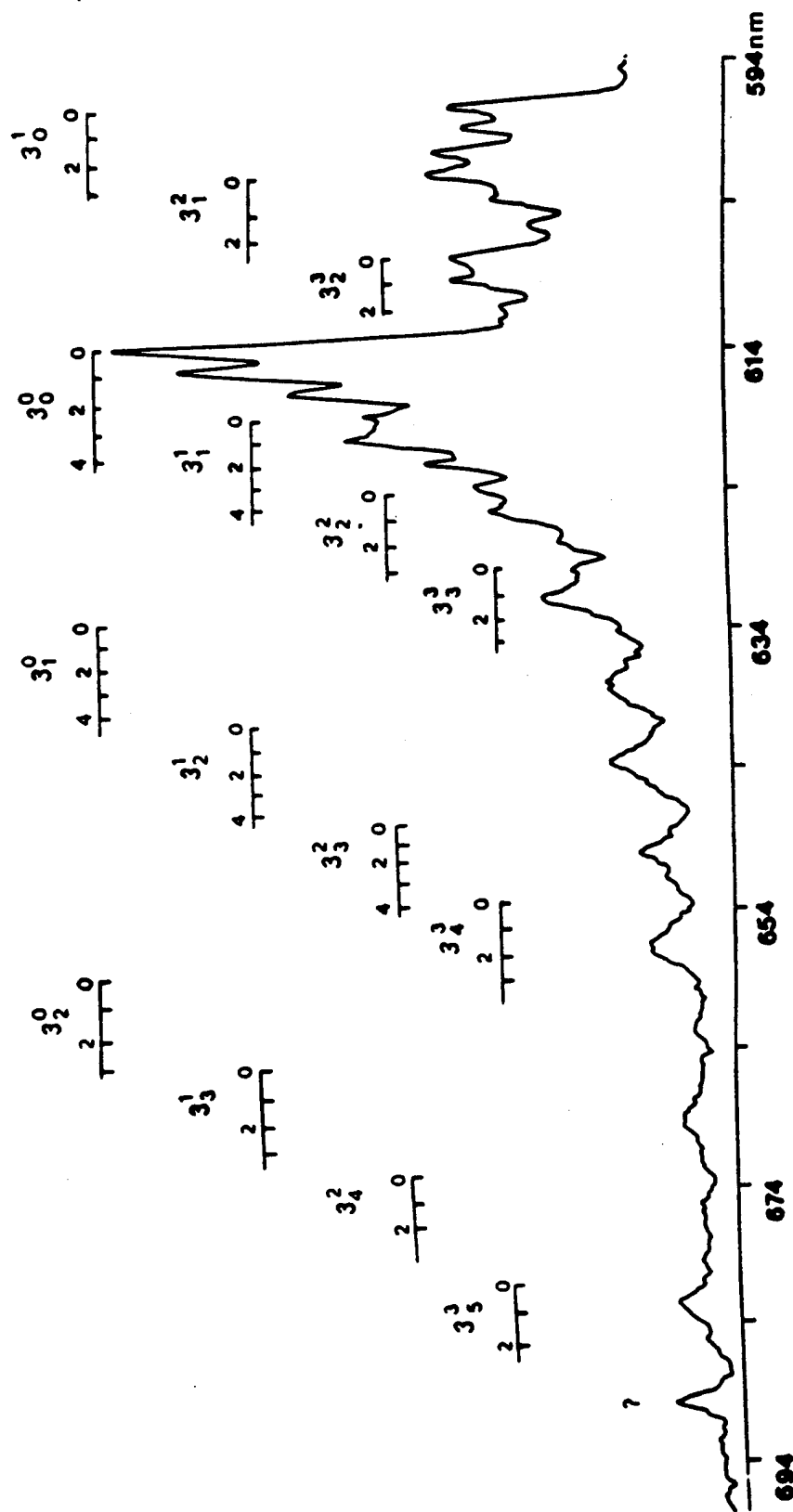


**Figure 9.** The observed visible emission spectrum of BBO taken with an EMI 9808 phototube at a resolution of 5 Å. Progressions in the B-B stretch (here called  $v_3$ ) are marked in the figure as  $3_3^0$ . The observed spectrum is characterized by a strong  $\Delta v = 0$ ,  $\Delta v = 40 \text{ cm}^{-1}$  B-B stretch and a weaker  $\Delta v = +1$  sequence ( $\Delta v = 40 \text{ cm}^{-1}$ ),  $440 \text{ cm}^{-1}$  to higher energy. A second sequence with  $\Delta v \sim 142 \text{ cm}^{-1}$  is also observed. Combining the  $440\text{-cm}^{-1}$  upper-state frequency with the  $142\text{-cm}^{-1}$  sequence structure implies a lower-state frequency of  $\sim 582 \text{ cm}^{-1}$  for the B-B stretch, consistent with ab initio calculations.

**Table 4.** Comparison of Observed and Calculated Vibrational Frequencies for the Isomers of B<sub>2</sub>O

Observed Frequencies	B-O-B (Calc)	B-B-O (Calc)
1970 (?)	1510 <sup>a</sup> /1430 <sup>b</sup>	1935 <sup>a</sup> /1856 <sup>b</sup>
—	771—	2821—
-582	1005/926	581/579

<sup>a</sup>Scaled values from Gina, H.; Jones, Li; Shillady, D., private communication.

<sup>b</sup>Scaled values from Zyubina, T. S.; Charkin, O. P.; Zyubin, A. S.; Zakzhevskii, A. S. *Zh. Neorg. Khim* 1982, 27, 558.

assessment with information on the manifold of electronic states characterizing the boron oxide molecules of multiple boron atom constituency.

When a moderate flux of boron vapor entrained in argon is cooled to dry ice temperatures and reacted with NO<sub>2</sub>, the new boron based electronic transition depicted in Figure 9 is observed.<sup>5a-c</sup> A comparison of the vibrational frequencies obtained from the analysis of this spectrum to the vibrational frequencies calculated for B<sub>2</sub>O and B<sub>2</sub>O<sub>2</sub> using SCF-CI calculations (Table 4)<sup>35-37</sup> demonstrates that this molecule is BBO, and not the thermodynamically more stable BOB isomer. This result is significant for two reasons. First, the products of the reaction (at least B<sub>2</sub>O) are kinetically controlled. Through their study, one begins to probe the dynamics of boron agglomerate reactions. Second, the product contains a metalloid-metalloid bond. This result, in concert with the data already considered for the copper and silver systems, suggests that metal cluster reactions may provide a way to study the thermodynamically less stable, but kinetically important, isomers, which are not easily produced using currently established laboratory techniques. The results obtained in the boron system are especially significant for they demonstrate that the molecular electronic structure of the asymmetric and symmetric boron cluster oxides (BBO vs. BOB) and their manifold of electronic states are quite different for even these "simplest" of cluster oxide isomers. This behavior is not readily discerned from simple molecular structure concepts.

## H. Transition Metal Cluster Oxidation

Our studies of the copper and silver cluster oxides as they pertain to the modeling of bulk systems can be extended to additional transition metal species. When proceeding with this extension, one should be cognizant that, with the exception of the coinage metals where reliable pseudopotential models are available, a focus in these efforts should be on the first row transition elements where theory is most

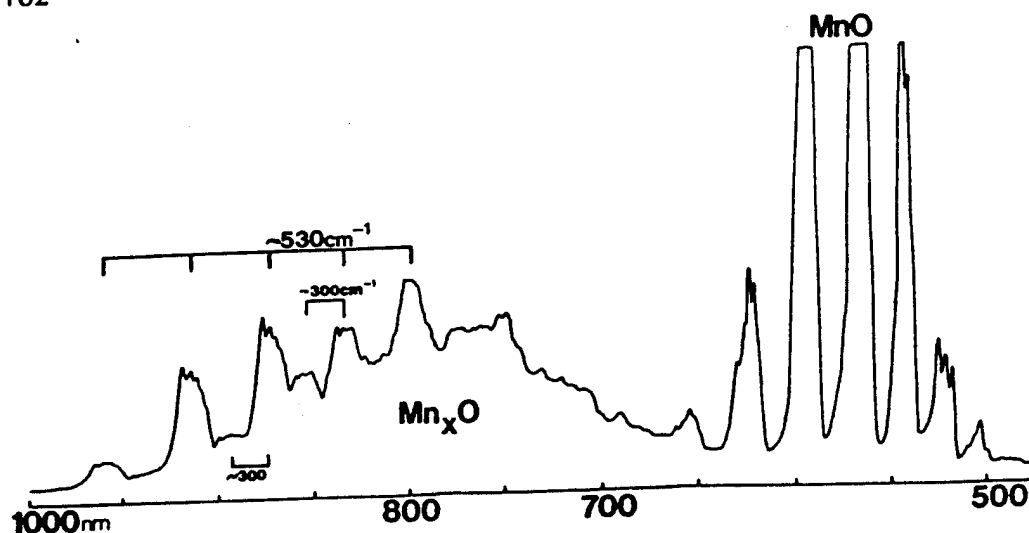


**Figure 10.** The chemiluminescent spectrum observed for the multiple collision (liquid nitrogen cooled argon) entrainment ( $P_{\text{Total}} \sim 1250$  mTorr) and oxidation of  $Mn_x$  clusters with ozone to produce an  $Mn_xO$  emission system where  $x$  is likely 2. The spectrum was taken with an EMI 9808 phototube at a resolution of 3 Å. The chemiluminescence from the  $MnO$  band system results from the oxidation of manganese atoms.

likely to succeed. Thus, the initial parallel extensions of efforts on the coinage metal clustered oxides have focused on the  $Mn_2O^{5b-e}$  molecule and very recently on the generation of preliminary data for  $Cr_2F$ .<sup>6</sup>

The oxidation of manganese clusters by  $O_3$  also produces a molecular emitter that contains a metal-metal bond (Figure 10). A vibrational analysis of this spectrum clearly shows ground-state vibrational frequencies of  $534\text{ cm}^{-1}$  and  $306\text{ cm}^{-1}$ . The  $306\text{ cm}^{-1}$  frequency is consistent with a frequency estimated for  $Mn_2^+$ . Because the  $534\text{ cm}^{-1}$  frequency is similar to the metal-oxygen stretch associated with the alkali metal oxides,<sup>38</sup> the molecular emitter is assigned as  $Mn_2O$  bonded as  $(Mn_2)^+O^-$ . Although the geometry of this molecule has not been firmly established, the presence of the Mn-Mn bond seems certain.

### I. Trends and Future Extensions

The characteristics associated with the metal cluster oxidation reactions summarized in this outline lead us to four general observations:

1. The oxidations of metal clusters, which can proceed by multicentered roots, can be more energetic than the corresponding reactions of metal atoms. This trend holds well for reactions of atoms, dimers, and trimers, but it is expected to level off considerably as one considers the reactions of larger clusters. An extension of this work to larger clusters will be needed before more specific rules can be formulated.

2. The energy of a cluster reaction may often be channeled into only one of the reaction products. The emission from electronically excited molecules produced in this manner can be used to obtain previously inaccessible optical signatures for the excited and ground states of these molecules. Thus these studies serve to better define the molecular electronic structure of the product molecules.

3. The products of the oxidation of larger clusters contain cluster agglomerate bonds. As the cluster reacts, it usually fragments. However, as the reacting clusters become larger, their reaction should facilitate the formation of a greater metal agglomeration in the oxidized metal products. The studies thus far have not established if there is a direct relationship between the relative size of the clusters that undergo reaction and the constituency of the oxidized cluster products; they require extension to larger clusters to determine whether the observed trends will continue. However, the initial observations suggest that larger cluster oxide species can be made and explored using combined chemiluminescent and LIF techniques. In most cases the products of these cluster oxidations contain metal-metal bonds. Thus, there exists a distinct possibility that the internal mode structure associated with the reactions of cluster molecules and their products may aid in the modeling of metallic surface behavior.

It may be possible to generate species, the fingerprints of which are relevant to the detailed microscopic description of those properties that can contribute to the catalytic behavior of an oxidized metal surface or, in a future study of silicon cluster halogenation, to the nature and quality of a surface etch [ $\text{Si}_n + \text{X} (\text{X}=\text{Cl}, \text{Cl}_2, \text{F}, \text{F}_2)$ ]. As an ultimate goal, we wish to develop a detailed description of the intimate environment associated with the metal cluster-oxygen or metal cluster-halogen interaction, (1) determining how small clusters of metal atoms interact with the oxygen or halogen atom and (2) considering the dynamic behavior that these clustered atoms may exhibit as they move about the oxygen or halogen atom. Using a combination of chemiluminescent and laser fluorescent probes of the asymmetric metal clustered oxides, it should be possible to establish structures and determine, through bond angle and vibrational frequency determinations, the manner in which these small metal clusters interact with an oxygen atom when they are formed in a unique kinetically controlled environment. It is precisely this information that can provide the productive tension between experiment and theory required for the development of systematically constructed and meaningful model systems describing the nature of ligand-metal surface interactions.

4. Reaction kinetics is a primary determinant of the products that are formed in these systems. The characterization of the products contributes information useful to the exploration of the mechanisms of cluster oxidation. Together with recent elegant mass spectrometric kinetic investigations of cluster reactions<sup>12</sup> and recent advances in theory, this information provides a useful format for the understanding of reaction pathways and the energetics of cluster reactions.

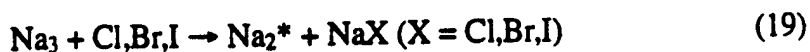
The characterization of the metal cluster oxides and halides complements the study of positively or negatively charged clusters now underway in several labora-

tories.<sup>39</sup> Evidence has been obtained for metal cluster grouped oxide configurations in which the metal cluster grouping is positively polarized or the cluster is strongly ionic with the equivalent of at least a complete positive charge distributed among the clustered metal atoms. Models of metal/support interactions in catalytic environments have long considered the importance of the net transfer of charge between the metal and its porous support material. This charge shift is thought to influence catalytic behavior by inducing a change in the electron richness of the metal. The combination of ion and cluster oxide studies may therefore cast some light on the validity and specifics of these models.

### III. CONTINUOUS VISIBLE CHEMICAL LASER AMPLIFIER FROM A METAL CLUSTER OXIDATION REACTION

Previously, we have used the supersonic expansion of pure sodium or potassium vapor to study the photodissociation of the alkali trimers  $\text{Na}_3$ <sup>40</sup> and  $\text{K}_3$ .<sup>41</sup> These studies were facilitated because the alkali metals are particularly amenable to the application of LIF techniques, with transition probabilities among alkali metal atom or dimer electronic states being among the largest recorded.<sup>42</sup> Therefore, with a desire to initiate efforts focused on the study of metal cluster oxidation, it seemed appropriate to study what were felt to be the simplest metal cluster oxidation reactions also producing reaction products with well defined and characterized electronic transitions. In retrospect, the study of alkali dimer and trimer-halogen atom reactive encounters has demonstrated several surprises.

The high cross section, highly exothermic  $\text{Na}_3\text{-X}$  (Cl, Br, I) reactions form  $\text{Na}_2^*$  in several of the sodium dimer excited electronic states<sup>43</sup> indicated schematically in Figure 11. The energetics of the reactive processes of interest are indicated in the figure. The  $\text{Na}_3\text{-Cl}$  and  $\text{Na}_3\text{-Br}$  reactions are sufficiently exothermic to readily populate the A  $^1\Sigma_u^+$ , B  $^1\Pi_u$ , C' ( $2^1\Sigma_g^+ - X^1\Sigma_g^+$ ) and C  $^1\Pi_u$  states of sodium dimer. The available energy results from the formation of a moderately strong sodium halide bond and the rupture of a weak sodium trimer bond. The  $\text{Na}_3\text{-I}$  reaction is much less exothermic; however, the contribution of the  $\text{Na}_3$  kinetic energy in concert with the reaction of halogen atoms, generated from a 1500 K source, in the high energy tail of their kinetic energy distribution allows the population of a few vibrational levels in the  $\text{Na}_2$  C  $^1\Pi_u$  state and several levels of the double minimum C' state. The optical signatures for the processes:



encompass emission from a limited number of  $\text{Na}_2$  band systems including the A, B, C, and C' states. Surprisingly, the observed emission is characterized by sharp well-defined emission regions<sup>43</sup> (Figures 12 and 13) superimposed on a much weaker but perceptible  $\text{Na}_2^*$  dominated background. As Figure 13 demonstrates, through comparison with the best fit calculated sodium dimer B-X spectrum, these

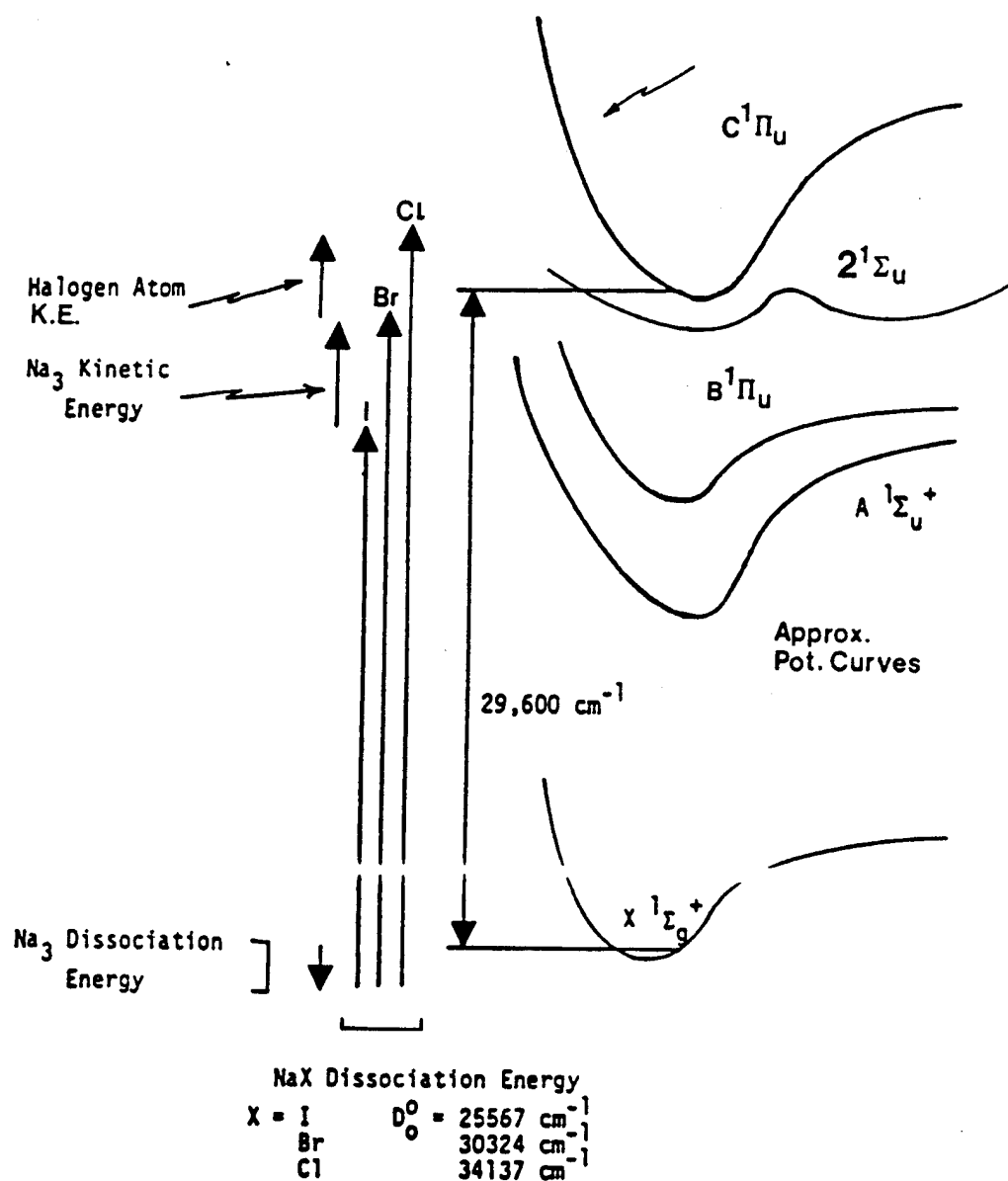


**Figure 11.** Energetics associated with the formation of  $\text{Na}_2$  produced by the  $\text{Na}_3 - \text{X}$  (Cl, Br, I) chemiluminescent reaction. Potential curves are drawn approximately.

sharp emission features are not readily explained by invoking a purely fluorescent process involving sodium dimer.<sup>43</sup>

The sharp nature of several of the B-X, C-X, and C'-X  $\text{Na}_2$  emission features (Figure 12), their near exponential growth with  $\text{Na}_3$  concentration relative to the background  $\text{Na}_2$  fluorescence, and their correlation in certain regions to the emission characteristic of optically pumped  $\text{Na}_2$  laser systems<sup>44</sup> [ex: 528.2 nm ( $\nu'$ ,  $\nu''$ ) = (6,14)B-X] suggested that stimulated emission associated with certain of the  $\text{Na}_2$  emission products might have been observed. Laser gain measurements have been carried out to assess this possibility.

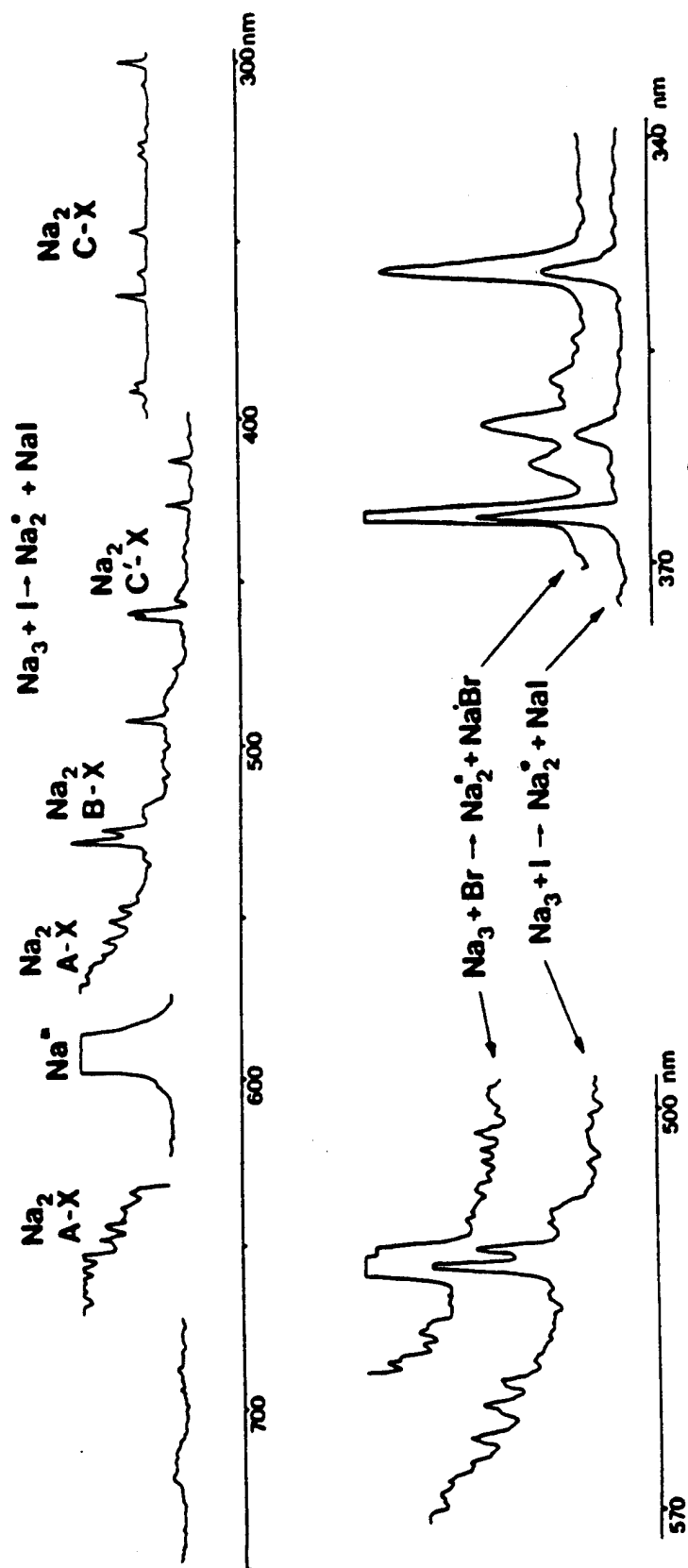


**Figure 12.** Chemiluminescent emission from the  $\text{Na}_3 + \text{Br}$  and  $\text{Na}_3 + \text{I}$  reactions forming excited states of  $\text{Na}_2$ , whose optical signature dominates the observed emission, and the sodium halide. Sharp emission features superimposed on a broad background are apparent including those at  $\sim 527$ ,  $\sim 492$ ,  $\sim 460.5$ ,  $\sim 436$ , and  $\sim 426$  nm. Spectral resolution is  $\sim 0.6$  nm. See text for discussion.

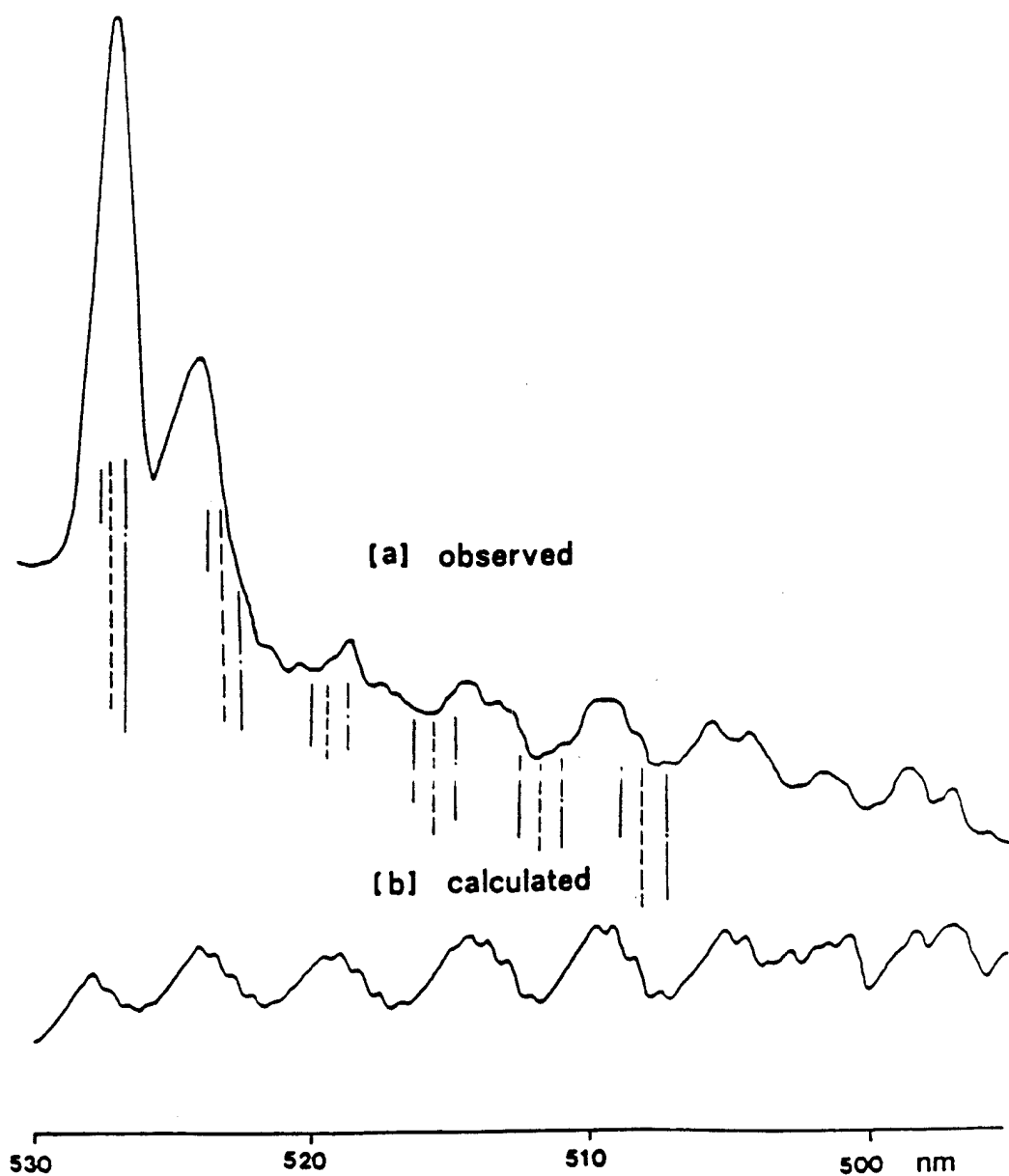
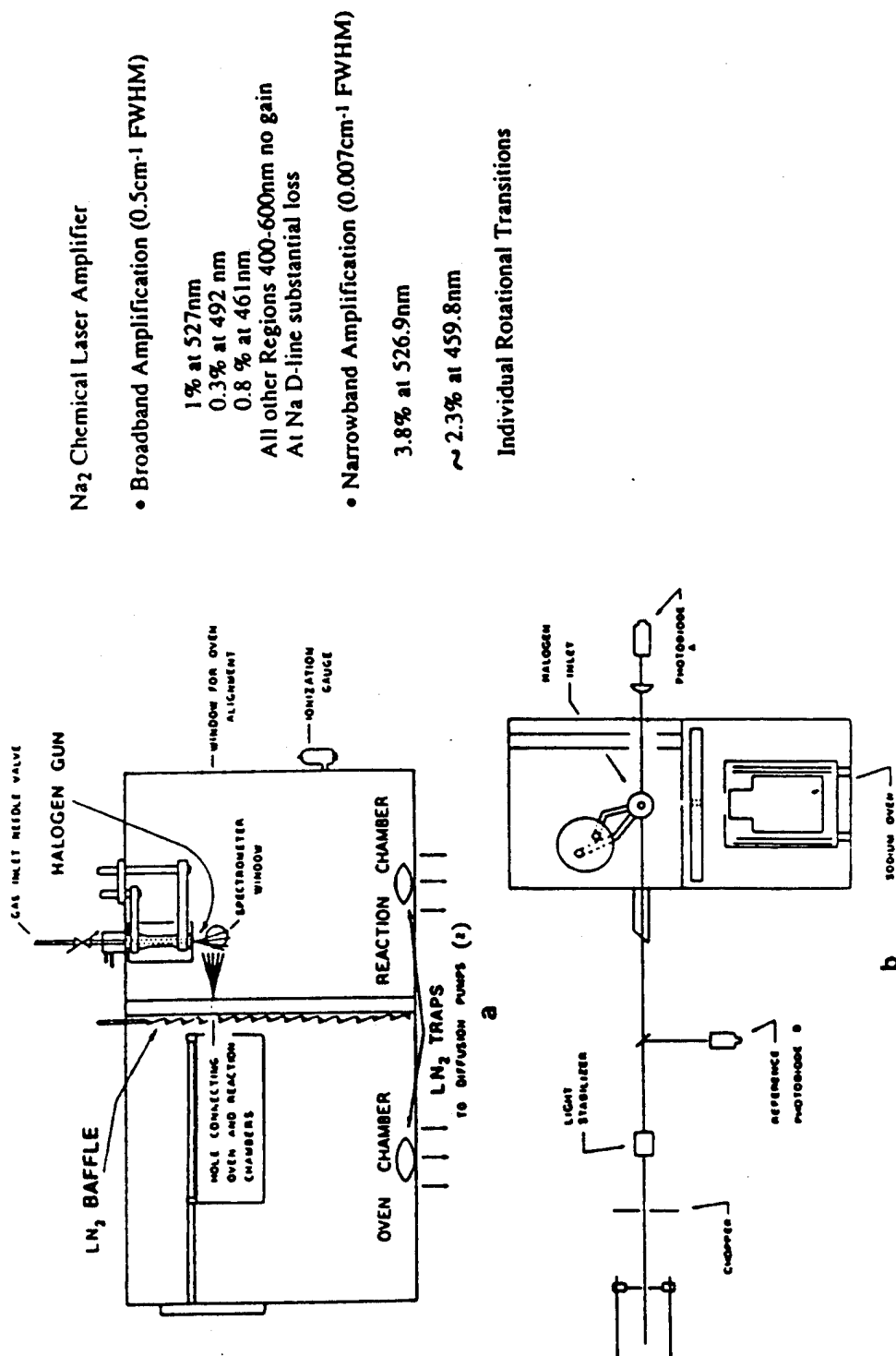


**Figure 13.** Comparison of (a) observed and (b) calculated emission spectra for the  $\text{Na}_2$  B-X emission system. The experimental spectrum corresponds to the chemiluminescence from the  $\text{Na}_3$ -Br reaction. The calculated spectrum, which was obtained for a rotational temperature,  $T_{\text{Rot}} \sim 1000$  K, represents an estimate of effective rotational temperatures for  $\text{Na}_2$  product formation under near single collision conditions and therefore not at equilibrium. Relative vibrational populations input for  $\text{Na}_2$  B-X,  $v' = 0-6$  were in the ratio 1.00:1.17:1.33:1.50:1.58:1.67:1.54. The locations of contributions from vibrational levels  $v' = 6$  (—),  $v' = 5$  (---), and  $v' = 4$  (- · -) of the  $\text{Na}_2$  B state in transition to vibrational levels  $v'' = 14-9$ ,  $v'' = 13-8$ , and  $v'' = 12-7$  of the  $\text{Na}_2$  ground state are indicated.



### $\text{Na}_2$ Chemical Laser Amplifier

- Broadband Amplification (0.5cm<sup>-1</sup> FWHM)

1% at 527nm

0.3% at 492 nm

0.8 % at 461nm

All other Regions 400-600nm no gain

At Na D-line substantial loss

- Narrowband Amplification (0.007cm<sup>-1</sup> FWHM)

3.8% at 526.9nm

~ 2.3% at 459.8nm

### Individual Rotational Transitions

**Figure 14.** Schematic of (a) apparatus for the study of the chemiluminescent  $\text{Na}_3$  - X reactions and (b) the arrangement of the experimental configuration for measuring gain from the  $\text{Na}_3$  - X metatheses. See text for discussion of configurations.

To carry out these studies, a unique source configuration (Figure 14a) has been developed that allows the supersonic expansion of pure sodium vapor to create a  $\text{Na}_3$  concentration not previously attained in a reaction-amplification zone. In these studies, 100+ grams of pure sodium was expanded from a double oven source mounted in the oven chamber depicted in Figure 14a. The supersonic flow passes through an adjustable orifice in an  $\text{LN}_2$  cooled baffle and bulkhead and into the reaction chamber depicted in the figure. Here the supersonically expanding  $\text{Na}_x$  beam is met by an intersecting flow of halogen atoms. In order to operate above threshold, the expenditure of sodium is carried out on a very short time frame ( $\sim 1200$  vs.  $3600\text{--}10,000$  seconds for a typical chemiluminescent experiment—Figure 12) to produce well in excess of  $10^{13}/\text{cc}$  trimer molecules in the reaction zone.<sup>45</sup> The concentration produced is between 10 and 500 times the maximum concentration for the fluorescence experiments ( $[\text{Na}_3] \sim 3 \times 10^{12}/\text{cc}$ ) depicted in Figures 12 and 13. These estimates are based on (1) an increased flux from the oven, (2) an increased beam directionality, and (3) an increased percentage of trimer in the beam.<sup>43</sup> In all of the experiments halogen atoms were produced by transiting halogen molecules through a needle valve assembly (halogen gun in Figure 14) into a high temperature carbon furnace.<sup>45</sup> The atoms, produced with  $>95\%$  efficiency, exit the furnace through several  $0.015\text{--}0.020\text{-mm}$  orifices into the reaction zone, initiating the trimer-halogen atom chemical reaction. The halogen flow is adjusted to optimize gain.

Using argon ion pumped dye lasers to study the  $\text{Na}_3 + \text{Br}$  reaction (Figure 14b) the entire wavelength region from  $420$  to  $600\text{ nm}$  (Figure 12) has been scanned at  $0.5\text{ cm}^{-1}$  resolution (FWHM).<sup>1</sup> The regions around  $527\text{ nm}$  (Figure 13) have been scanned at  $0.007\text{ cm}^{-1}$  resolution using a ring dye laser.<sup>43</sup> Laser gain, and hence amplification, is only found in certain select wavelength regions. Several of the sharper and more pronounced emission features apparent in the spectra depicted in Figure 12 correspond to a stimulated emission process and to the establishment of a population inversion. Ring dye laser studies demonstrate that the strong feature at  $527\text{ nm}$  (Figure 13) corresponds to stimulated emission from between four and seven unresolved rotational levels. Further studies will allow the assignment of the monitored gain to specific P, Q, and R branch transitions involving rotational levels  $J' = 35 \pm 5$  in the  $\text{B}^1\Pi_u$  state.

A schematic of the laser gain configuration is shown in Figure 14b. Here a dye laser beam was split into two branches, one branch being directed to a reference photodiode (B) and the other delivered and passing through the alkali-halogen atom reaction zone. The laser beam enters the  $\text{Na}_3 - \text{Br}$  reaction (vacuum) chamber oriented so as to be perpendicular to both the flow of halogen atoms and the supersonic sodium vapor beam. The focused intensity of the broadband source was  $\sim 0.05\text{ W}/\text{cm}^2$ . After passing through the reaction zone, the beam exits the reaction chamber and is collected and focused onto a second photodiode (A). A lock-in amplifier (EG&G/PAR model 124A) operated in the A-B mode provides the ability to detect changes in laser beam intensity occurring only in branch A as the laser

beam passes through the alkali-halogen reaction zone. The output from the lock-in is fed to a DSP Technology 2001 digital transient recorder equipped with a model 4100 signal averaging module. The averaged output from the recorder can be passed to an IBM PC-XT where the data are monitored and stored. These averaged outputs are used in determining percentage laser gain. An increase in A-B detector output corresponding to the introduction of the halogen atoms into the system, followed by an associated loss of output when the halogen flow is terminated, can be attributed to amplification and a gain condition. Within the individual dye laser regions considered, a scan of the dye laser as a function of wavelength produces no increase in output laser power in the absence of halogen atoms and sufficient sodium trimer molecules.

Optical gain through stimulated emission has been measured at  $0.5\text{ cm}^{-1}$  resolution in the regions 527 nm (1% gain), 492 nm (0.3% gain) and 460.5 nm (0.8% gain), correlating precisely with the reactive process and the relative intensities of those features observed while monitoring the light emitted from the  $\text{Na}_3\text{-Br}$  and  $\text{Na}_3\text{-I}$  reactions (Figures 12 and 13). High resolution ring dye laser scans in the 527-nm region indicate that the gain for the system is close to 3.8% for an individual rovibronic transition with approximately four to seven transitions showing gain. At 459.8 nm, a gain of 2.3% has been measured for an individual rotational level. These results demonstrate the continuous amplifying medium for a visible chemical laser in at least three wavelength regions.<sup>43</sup> Furthermore, a loss of the gain condition is readily detected as the trimer concentration decreases due to sample exhaustion or a source temperature decrease. The gain observed in these systems is thus strongly dependent on both the  $\text{Na}_3$  and halogen atom concentration. As the probe laser power is changed, the photodiode signal (A-B) is found to vary linearly with laser power, indicating that the measurements are taken in the small signal gain regime.

To further verify that these gain observations were not artifacts that could be observed at any wavelength including those corresponding to an intense spectral feature, the gain experiment was repeated at several wavelengths including the sodium D-line wavelength at 588.9 nm. No gain was observed at any other wavelength in the 420–600-nm region, and at the Na D-line wavelength the A-B signal was seen to decrease significantly, indicating considerable scattering or absorption of the probe laser photons.<sup>2</sup> It should also be noted that at those wavelengths exhibiting the largest gain, the output of detector A, as measured by a digital voltmeter with no averaging, readily increased with the introduction of halogen atoms into the reaction zone.

Because of the low  $\text{Na}_3$  ionization potential and the high halogen electron affinities,<sup>46</sup> the  $\text{Na}_3$ -halogen atom reactions are expected to proceed via an electron jump mechanism with extremely high cross sections,<sup>47</sup> producing substantial  $\text{Na}_2$  excited state populations. The created population inversions monitored thusfar are thought to be sustained by (1) the large number of free halogen atoms reacting with the  $\text{Na}_2$  molecules in those ground-state levels on which the transitions emanating from the  $\text{Na}_2$  excited states terminate, removing the population in these levels, and

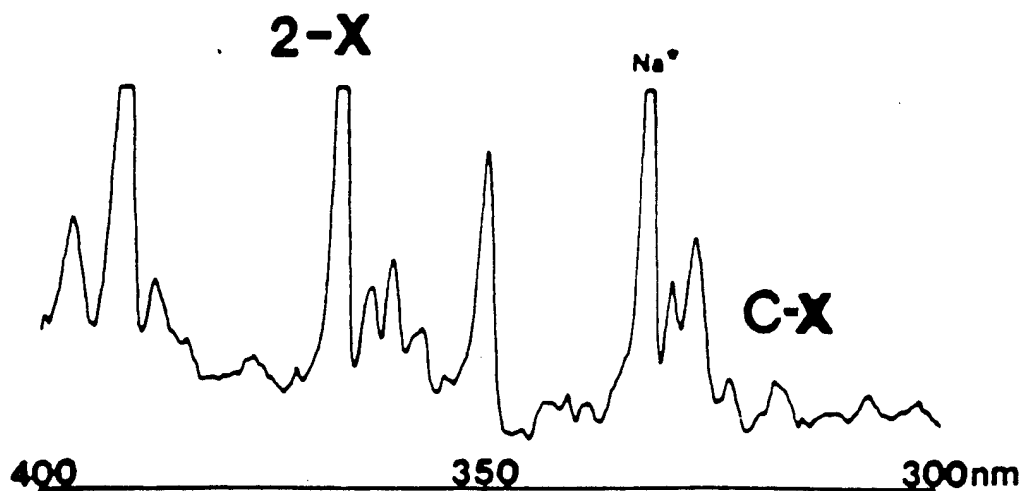


**Figure 15.** Chemiluminescence from the reaction  $\text{Na}_3 + \text{Br} \rightarrow \text{Na}_2^* + \text{NaBr}$ . The spectrum is dominated by the  $\text{Na}_2 \text{ C } ^1\Pi_u - \text{X } ^1\Sigma_g^+$  and  $2 \text{ } ^1\Sigma_u - \text{X } ^1\Sigma_g^+$  emission features. See text for discussion.

(2) collisional relaxation of ground-state sodium molecules. The cross section for reaction of vibrationally excited ground-state  $\text{Na}_2$  is expected to be substantial relative to that corresponding to collision-induced vibrational deactivation of the  $\text{Na}_2$  manifold. Extremely efficient reactions thus greatly aid the rapid depletion of the lower state levels in this system allowing one to sustain a continuous population inversion.

Our major efforts thusfar have focused on the  $\text{Na}_2 \text{ B-X}$  spectral region and the potential development of a laser oscillator at wavelengths in the vicinity of 527 and 460 nm. We are also concerned with the extension of these studies further into the ultraviolet primarily to assess potential amplification involving states of considerably longer radiative lifetime. The  $\text{Na}_2$  395-, 365-, and 350-nm emission regions depicted in Figure 15 represent a portion of the optical signature for the  $\text{Na}_3\text{-Br}$  reaction. They are of interest for they correspond again to sharp emission features, on a broad and weak background, whose appearance cannot be readily explained in terms of a purely fluorescent process. They are tentatively associated, at least in part, with the very recently described double minimum excited electronic state<sup>42</sup> indicated in Figure 11 ( $2 \text{ } ^1\Sigma_u^+ - \text{X } ^1\Sigma_g^+$ ). The radiative lifetimes associated with this double minimum state are complex and longer ( $>40$  ns) than those associated with the  $\text{Na}_2 \text{ B-X}$  region. These longer lifetimes enhance the potential for energy storage in a laser cavity. This, in turn, suggests that the laser gain studies in the visible should be extended to this spectral region to determine the feasibility of using these transitions as the source of laser amplifiers extending far into the ultraviolet. Furthermore, it will be appropriate to extend these studies to the other alkali metals, taking advantage of the possibility of forming laser amplifiers extending both to considerably shorter and longer wavelengths.

#### IV. ELECTRIC FIELD ENHANCED LASER-INDUCED PLASMA SPECTROSCOPY

Electric field enhanced laser induced plasma spectroscopy (EFELIPS) is being developed as a relatively simple and general approach to a mapping of electronic states and internal mode structure in small metal clusters, metal cluster compounds, metal based complexes, and their ions.

We make use of a variant of the laser vaporization source first developed and used to investigate the internal mode structure of metal molecules by Bondybey,<sup>48</sup> Smalley<sup>49</sup> and co-workers and now employed in a number of laboratories. Here, we form neutral clusters and positive and negative cluster ions, in concentrations that may exceed  $10^7/\text{cc}$ , through pulsed laser vaporization from a solid target followed by  $\text{LN}_2$  entrainment or correlated with pulsed supersonic expansion. In the present study, the species of interest are formed in supersonic expansion, neutral and ionic emission features being distinguished with a sorting procedure based on electric field deflection and enhancement.

We have been concerned with the application of the EFELIPS technique to study the formation and bonding in ion-molecule complexes probed through the study of laser-induced plasma generated excited state emissions and with the generation of emission spectra for neutral carbon, silicon, copper, and aluminum dimers and trimers. Laser-induced silicon plasmas have been used to generate emission spectra for silicon dimer and, in concert with supersonic expansion, to obtain cooled gas-phase emission spectra<sup>50</sup> correlating not only with absorption bands previously observed in rare gas matrices by Weltner and McLeod<sup>51</sup> and attributed to silicon trimer but also with recent negative ion photoelectron spectra for the trimer obtained by Kitsopoulos et al.<sup>52</sup> Transitions have been observed from the upper state of the gas-phase analogue of the Weltner-McLeod matrix bands to both the  $\text{Si}_3$  ground and low-lying A states partially mapped by Kitsopoulos et al. We have also generated<sup>53</sup> the first electronic emission spectra for aluminum based ion-molecule complexes,  $\text{Al}^+\text{CO}$  and  $\text{Al}^+\text{H}_2$ , with which are associated vibrational progressions attributed to the  $\text{Al}^+$ -molecule stretch or cluster bending mode. The observed emissions, which involve singlet ( $\text{Al}^+$ )-singlet ( $\text{CO}, \text{H}_2$ ) interactions, are ascribed to complexes formed in orbiting collisions with  $\text{Al}^+$  excited states. The spectra correlate closely with atomic transitions among these states extending throughout the visible and ultraviolet regions. Some evidence also has been obtained for  $\text{Al}^+-\text{N}_2$  complexation, and for short-lived complex formation resulting from select excited state  $\text{Al}^{++}$  interactions with  $\text{N}_2$ .

##### A. Nature of the EFELIPS Experiment

A schematic of the EFELIPS experimental configuration is shown in Figure 16. A superheated plasma is produced by focusing the fundamental ( $1.06\mu$ ) or second harmonic ( $0.532\mu$ ) output of a Nd:YAG laser onto a rotating-translating metal or

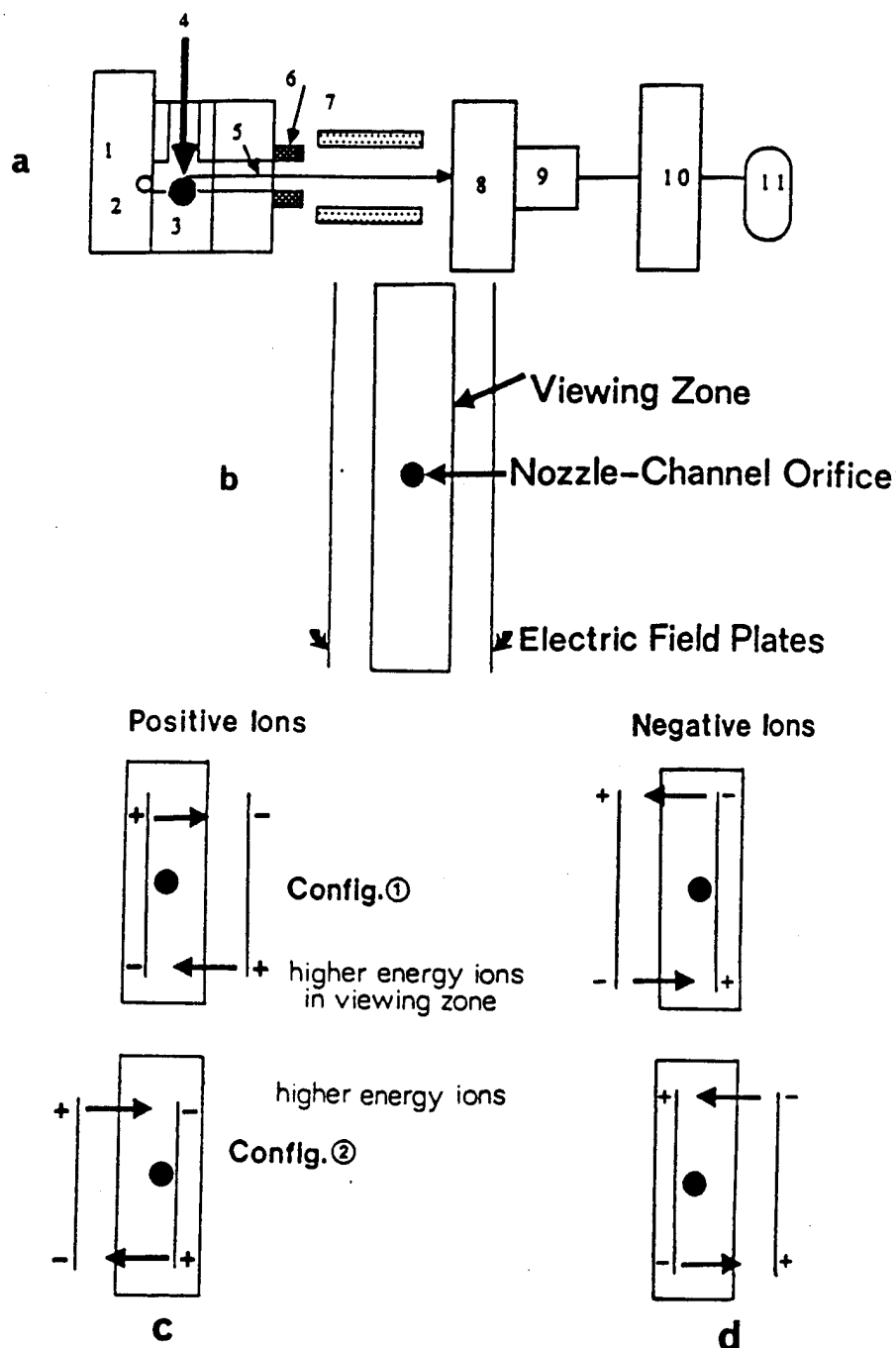


**Figure 16.** **a**, Schematic diagram (top view) of EFELIPS experimental configuration. The overall configuration consists of (1) a gas pulse valve, (2) the supersonic expansion nozzle beam backing pressure gas source, (3) a target rod, (4) a Nd-YAG vaporization laser beam, (5) an expansion channel, (6) an electron deflecting magnet, (7) electrodes for electric deflection and electron impact excitation, (8) a Jarrell-Ash 1/3-meter monochromator, (9) a diode array, (10) a multichannel analyzer, and (11) a computer or standard X-Y recorder. **b**, Symmetrically oriented electric field plates; **c**, asymmetric electric field plate orientations to identify the emission from positive ions; **d**, asymmetric electric field plate orientations to identify the emission from negative ions. See text for discussion.

metalloid rod. This plasma is entrained in a high pressure 150–200-microsecond pulse of helium or argon, which may be seeded with an entraining, reacting, or complexing gas (40–80 psi total backing pressure), emanating from a pulsed nozzle. This flow is supersonically expanded down a “short” channel to free flow. The timing sequence of the experiment is adjusted to place the much shorter time duration laser-created plasma pulse at a central position in time relative to the entraining pulsed gas flow. During this process, the emission from the plasma region and the initial reaches of the channel are focused onto the entrance slit of a monochromator on whose exit port is mounted an optical multichannel analyzer. The plasma emission is viewed directly down the expansion channel at right angles to the vaporizing Nd:YAG laser. The emission from a number of laser shots impinging on a diode array is averaged with the appropriate background corrections.

In the configuration depicted in Figure 16, we sample directly down the expansion channel, probing all processes that occur in the plasma region and channel with no time or temperature discrimination.<sup>50,53</sup> We have also examined the emission in a direction perpendicular to the channel direction and immediately upstream of the expansion in the free flow regime. The radiative lifetime selectivity inherent to the latter sampling mode and the spectral superposition inherent to the direct viewing configuration are considered in detail elsewhere.<sup>50,53</sup> The results now obtained indicate that larger clusters, which are formed in the later stages of channel expansion, absorb relatively little of the emitting radiation from diatomic and small polyatomic clusters formed in the initial stages of expansion or in the plasma. However, the emitters contributing to the final averaged spectrum can correspond to atoms or molecules at more than one “effective” temperature.

The plasma emission can be electric field enhanced using two 10-cm diameter circular electrodes (mounted in a plane perpendicular to the input laser), following the nozzle expansion channel and free flow region, and thus intermediate to the channel and monochromator. A dc potential voltage across the electrodes, producing a field parallel or antiparallel to the laser propagation direction, creates a means of distinguishing neutral and ionic species and enhancing the base plasma emission.

The considered enhancement results in some part from a combination of electron impact ionization or Penning ionization employing metastable states of helium or argon. The cross sections for electron impact and Penning ionization at thermal energies ( $\sim 10^{-16}$  cm<sup>2</sup>)<sup>54</sup> vastly exceed those for heavy ion bombardment ( $< 10^{-20}$  cm<sup>2</sup>)<sup>55</sup> in our system.<sup>50,53</sup> It is difficult to discern whether electron impact or Penning ionization plays a more important role toward the creation of an enhanced ionic emission in these systems.<sup>53</sup> The cross section for electron impact ionization may exceed that for Penning ionization; however, the concentration of helium or argon in these experiments is in excess of  $10^4$  times that of the plasma generated constituents.

Both metastable helium and argon emissions are observed presumably due to the electron impact excitation of helium and argon atoms. If the emitting positive ions are formed via energy transfer from these metastables, it is likely that they result

from a dissociative ionization process involving larger metal cluster groupings.<sup>53,56</sup> When a 3000-gauss magnet is operated at the initial reaches of the free flow region, directly following the channel orifice, the resulting  $M_x^+$  ion signals appear to decrease. This behavior is attributed to the scattering of the plasma electrons due to the magnetic field and their subsequent loss to the viewed electric field region. Whether the decrease in ion signal results directly from a decrease in effective exciting electrons or a decrease in the production of argon or helium metastables, which subsequently collisionally excite the ions, will be assessed in future experiments.

A combination of neutral, positively, and negatively charged atoms, clusters, and electrons are produced in the laser-induced plasma and expansion channel obeying the requirement that the entire constituency is electro-neutral. The neutral and ionic product distribution in the emerging supersonically expanding beam is spatially quite symmetric. Thus if the electric field plates are placed symmetrically about the nozzle-channel orifice (Figure 16b), a field polarity switch has only a small effect on the observed emission at a given field strength. This is because the ion distribution produced in the expansion is deflected in an almost totally symmetric fashion. However, if the electric field plates are positioned asymmetrically relative to the channel orifice (Figures 16c, 16d) the combination of field-induced effects can be used to distinguish positive and negative ion emission on the basis of electric field deflection.<sup>50,53</sup>

### B. Positive and Negative Ion Selection

The identification of positive or negative ions takes advantage of the spatial selectivity inherent to the combination of (1) the spectrometer-detector viewing zone, which is symmetric with respect to the nozzle + expansion channel orifice, and (2) the placement of the deflecting electric field plates. The configurations are indicated schematically in Figures 16c and 16d where the electric field plates are placed asymmetrically relative to the nozzle-expansion channel. In selecting and determining whether emission has been observed from a positive or negative ion, the emission is monitored as a function of electric field strength. Consider the behavior for positive ions indicated in Figure 16c as determined for four distinct field configurations resulting from the combination of two polarities and two asymmetric plate configurations. For the plate configuration positioned asymmetrically to the right, positive ions are deflected into or out of the viewing zone as a function of the plate polarities indicated. In configuration 1 the left (-) right (+) polarity enhances a positive ion signal relative to the symmetrically placed plate configuration (Figure 16b) as positive ions are swept into the viewing zone. This behavior is reversed if the electric field plates are placed as in configuration 2. Those combinations that enhance the positive ion concentration in the viewing zone impart more energy to the positive ion as it is accelerated in the electric field. The arguments presented in relation to Figure 16c are reversed for negative ion enhancement (Figure 16d).<sup>53</sup>

### C. The Silicon Trimer Emission Spectrum

The first vibrationally resolved electronic emission spectra for the silicon and germanium trimer molecules have been obtained using the LIPS technique. In the silicon system, transitions have been observed from an upper state, the analogue of that correlated with silicon trimer in matrix absorption, to both the ground (X) and low-lying A state (0.45 eV). The observed emission from the two band systems is tentatively associated with a dominance of short progressions in upper ( $\sim 310 \pm 20 \text{ cm}^{-1}$ ) and lower state ( $\sim 370 \pm 20 \text{ cm}^{-1}$  for X state and  $\sim 475 \pm 20 \text{ cm}^{-1}$  for A state) symmetric stretch frequencies or symmetric stretch-bend combination tones. Furthermore, we discern some indication of upper and lower state bending frequencies.

The spectra associated with silicon trimer are exemplified by the data on the E-X band system depicted in Figures 17 and 18. The two spectra depicted in Figure 17 indicate an increased cooling of the trimer E-X band system (excited E state trimers) in the supersonic expansion process. These bands can be correlated in a Deslandres-like scheme (Figure 18) with what appears to be short progressions in an  $\sim 310 \text{ cm}^{-1}$  upper state and  $\sim 370 \text{ cm}^{-1}$  lower state frequency, the former being in excellent agreement with the observations of Weltner and McLeod<sup>51</sup> ( $\omega' \sim 310 \text{ cm}^{-1}$ ) and the latter with the negative ion photoelectron measurements of Kitsopoulos et al.<sup>52</sup> ( $\omega'' \sim 360 \pm 40 \text{ cm}^{-1}$ ). Although some evidence for structure associated with ground and excited state bending modes is obtained, the spectra appear to be dominated by progressions that are best ascribed to the symmetric stretching mode or to combination tones involving the symmetric stretch and bending modes. The electronic origin of the observed gas-phase  $\text{Si}_3$  spectrum correlates well with the previously observed matrix spectrum.<sup>51</sup> This is not surprising for  $\text{Si}_3$  is a covalent molecule and therefore matrix interactions and the subsequent matrix shift are not expected to be substantial.

The EFELIPS experiment is ideally suited to the silicon trimer system as it is to the carbon, germanium, tin, and lead systems. This follows because the bond energies of the metalloid-metalloid or metal-metal bonds in the trimers exceed those for the dimers. Both in the carbon and silicon systems, the emission spectra observed for the trimers would indicate that a comparable excited state dimer and trimer concentration is formed in the plasma. One observes extensive emission spectra for both  $\text{C}_2$  and  $\text{C}_3$  viewed in direct observation of a laser vaporized carbon plasma. The ease with which the LIPS technique can be applied to the study of the emission spectra for Group IVA element polyatomics might be contrasted to the coinage metals where the bond energy of copper<sup>57</sup> and silver<sup>57</sup> trimer is greatly exceeded by that of the dimer<sup>58,59</sup> and where predissociation and photodissociation may dominate the spectra of excited electronic states. Here the observed dimer emission spectra are more readily observed<sup>60</sup> than are those of the much more weakly bound trimer emitters.

The  $\text{Si}_3$  ground state frequency ( $370 \pm 20 \text{ cm}^{-1}$ ) dominating the EFELIPS experiment and the negative ion photoelectron study of Kitsopoulos et al. ( $360 \pm$

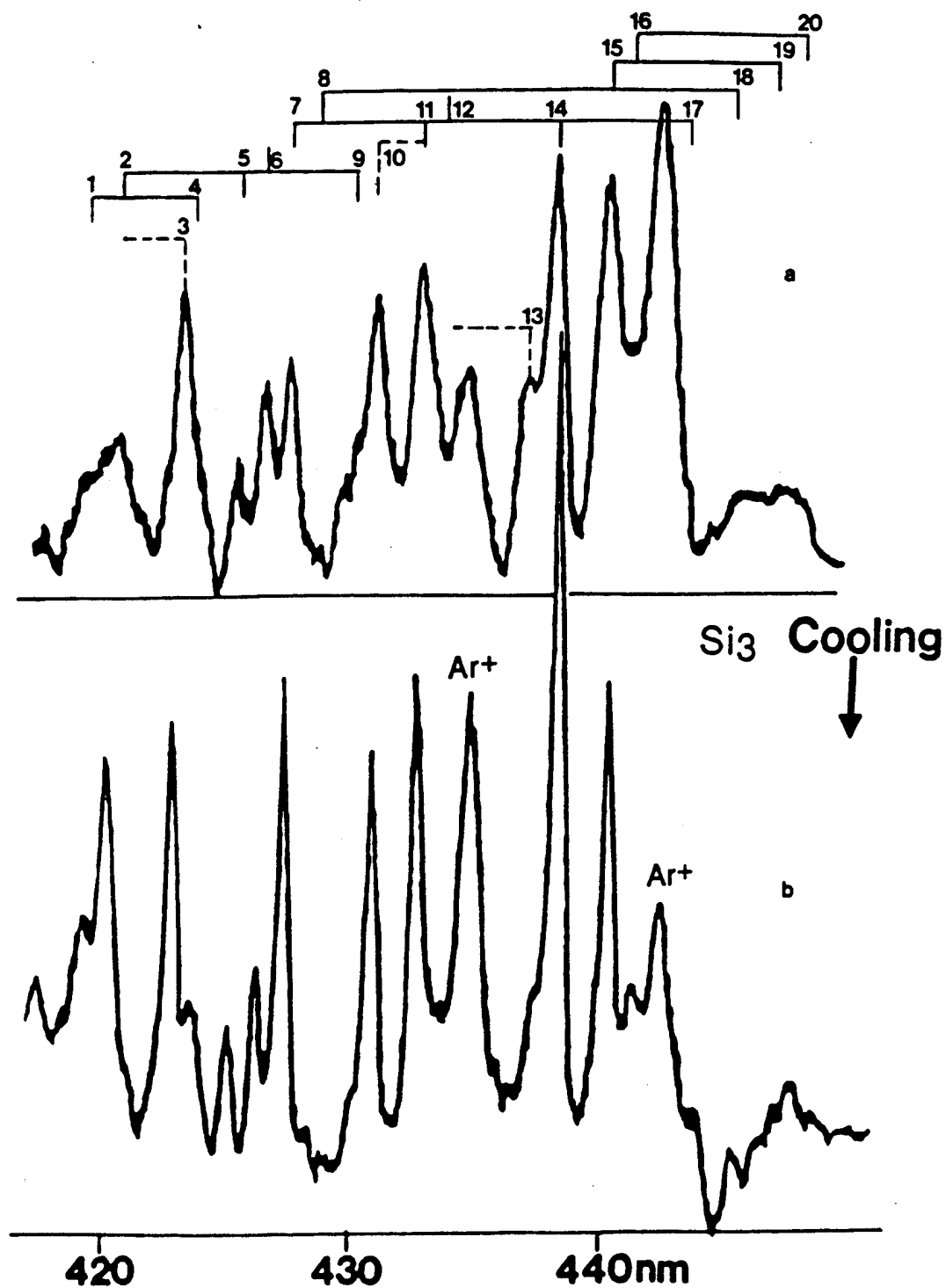


**Figure 17.** Laser-induced plasma emission spectrum for the "E"-X band system of silicon trimer. The spectrum in (b) was obtained at higher argon backing pressure ( $P_{\text{Total}} \approx 65$  psi) than was the spectrum in (a) ( $P_{\text{Total}} \approx 40$  psi) and is characterized by a colder rotational temperature attained in the supersonic expansion process. The features are arranged in a Deslandres-like scheme in Figure 18. See text for discussion.

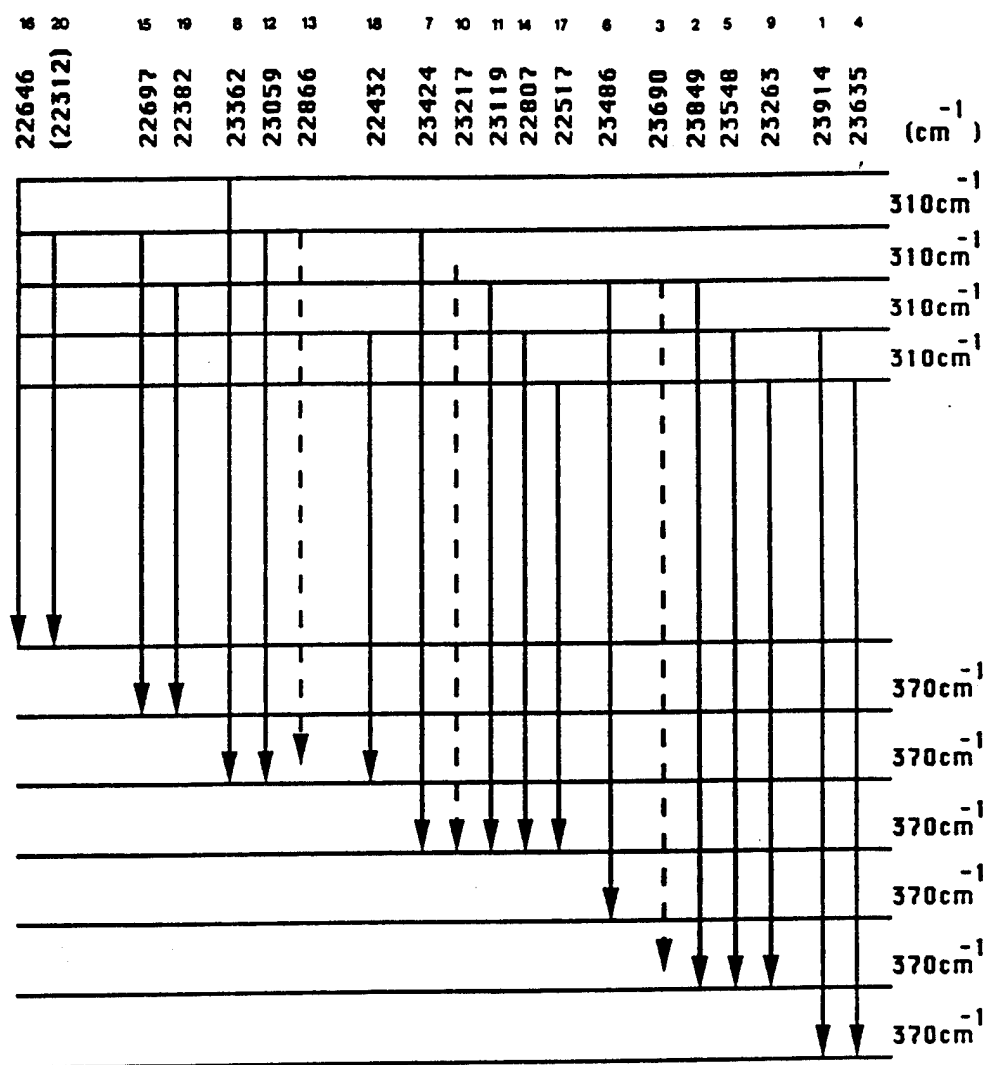


**Figure 18.** Deslandres-like scheme for the "E"-X band system of the silicon trimer. The features are correlated primarily (solid lines) with transitions in symmetric stretch or symmetric stretch-bend combination frequencies of the upper ("E") and ground (X) states of the trimer. Additional features (dashed lines) are shifted by frequency separations thought to correspond to ground or excited state bending modes. The E label for the state is tentative and based on a correlation with the data in refs. 51 and 52. See text for discussion.

$40\text{ cm}^{-1}$ ) are distinct from the calculated symmetric stretch frequency range, between  $574^{61}$  and  $582\text{ cm}^{-1}$ <sup>62</sup> for the totally symmetric mode of the  $\text{Si}_3\text{}^1\text{A}_1$  ground state. The disagreement with the  $574\text{ cm}^{-1}$  symmetric stretch frequency determined by Grev and Schaefer<sup>61</sup> or the  $582\text{ cm}^{-1}$  value determined by Raghavachari<sup>62</sup> may not be surprising because calculations at the Hartree-Fock level do not have sufficient flexibility to properly describe bond stretching. However, the magnitude of the disagreement is surprising. More recent calculations suggest that the symmetric stretch frequency for the "X"  $^1\text{A}_1$  state may be as low as  $550\text{ cm}^{-1}$ ,<sup>63</sup> however, this value is still much higher than the frequency separations which are observed experimentally. This may suggest more complex shortcomings in the theoretical description of the trimer ground state. Alternatively, both the photoelectron and LIPS experiments may probe regions of the ground-state potentials corresponding to geometries distinct from those associated with the minima of the potentials describing the bending or symmetric stretching mode. It may also be significant that the difference in frequency ( $\nu_1 - \nu_2$ ) for the symmetric stretch and bending mode ( $\nu_2 \sim 150\text{--}180\text{ cm}^{-1}$ ) corresponds well with the  $370\text{ cm}^{-1}$  separations observed in the LIPS and photoelectron studies, suggesting that one might ascribe the experimental frequency separations to combination tones.<sup>50</sup> However, a second and possibly more likely explanation<sup>63</sup> is that the observed transitions may be associated with a degenerate  $e'$  vibration associated with the lowest  $\text{D}_{3h}\text{}^3\text{A}_2'$  state of the trimer. The spectral transitions observed in emission may terminate in this lowest energy triplet state. It will be important for quantum chemists to describe these states and to evaluate their vibrational modes as well as their coupling to the highest level of description so as to aid the definitive assignment of the observed photoelectron, gas phase emission, and matrix isolation spectra.

#### D. Aluminum Based Ion-Molecule Complexes

Ion-molecule complexes are well known and have been formed and studied previously in a wide variety of experiments with a basis in mass spectroscopy and molecular beam techniques.<sup>64-76</sup> Although a number of synthetic approaches to ion-molecule formation have been described, spectroscopic and photochemical studies of ion-molecule complexes are limited. Brucat and co-workers<sup>64-66</sup> have obtained vibrationally resolved electronic spectra for transition metal-rare gas and transition metal- $\text{H}_2\text{O}$  complexes. More recently, Duncan and co-workers<sup>77,78</sup> have studied  $\text{Mg}^+\text{CO}_2$  and  $\text{Mg}^+\text{H}_2\text{O}(\text{D}_2\text{O})$  complexes. We have now used the EFELIPS technique to form electronically excited metal based ion-molecule complexes whose vibrationally resolved electronic emission is monitored through direct observation of a cooling and supersonically expanding laser-induced plasma.<sup>53</sup>

Exemplary of this study are electronically excited ion-molecule complexes of aluminum whose emission spectra extending across the visible and uv regions are depicted in Figures 19 and 20 for the range  $430\text{--}470$  and  $550\text{--}590\text{ nm}$ . Emission spectra associated with  $\text{Al}^+\text{CO}(\text{Al}^+\text{OC})$  and  $\text{Al}^+\text{H}_2$  complexation show clear vibra-

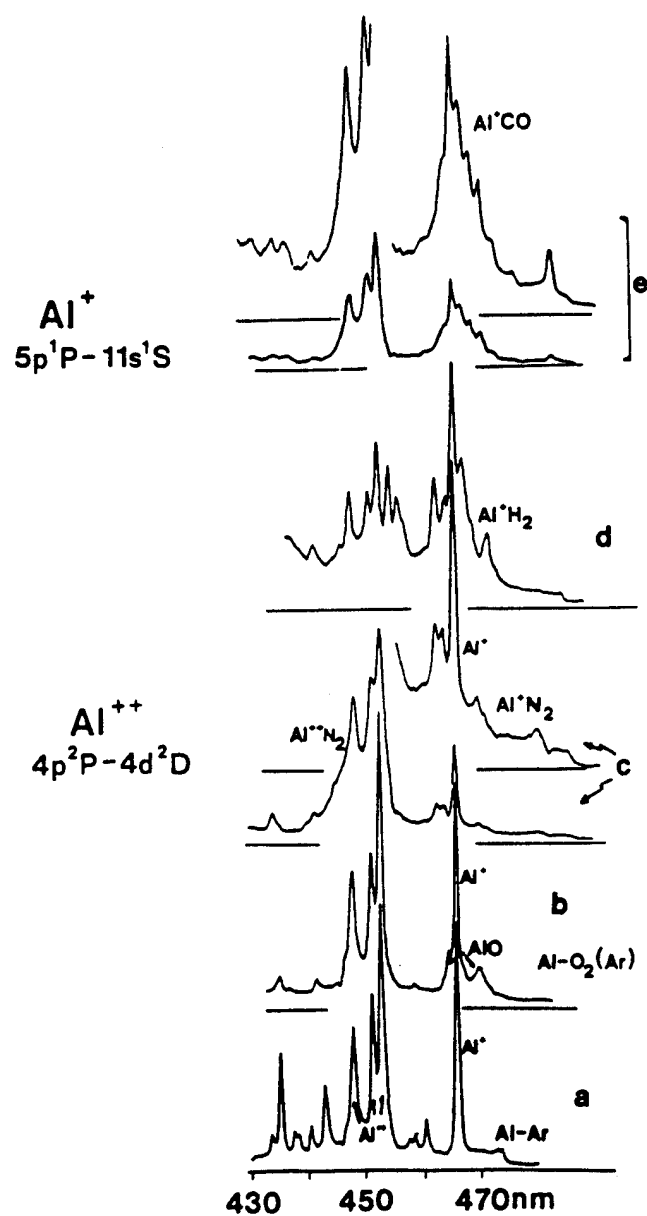


**Figure 19.** Laser-induced plasma emission spectra for aluminum based ion-molecule interactions. Spectra for the Al-O<sub>2</sub> seeded (40%)–argon, Al-N<sub>2</sub> (50%)–Ar, Al-H<sub>2</sub> seeded (30%)–Ar, and Al-CO (50%)–Ar are compared to those for the expansion of an aluminum plasma in pure argon. Evidence is obtained for complex formation as evidenced by vibrational structure accompanying the indicated Al<sup>+</sup> transitions in the CO, H<sub>2</sub>, and possibly N<sub>2</sub> systems and broadening in the N<sub>2</sub> system. See text for discussion.

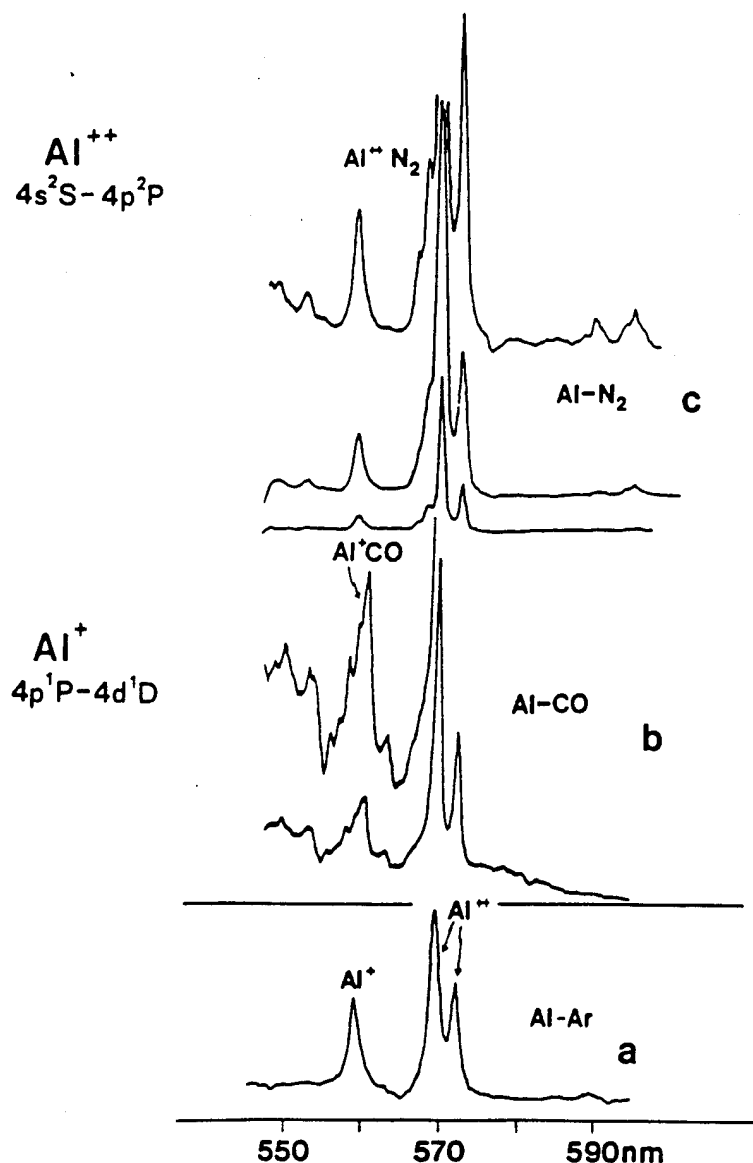


**Figure 20.** Laser-induced plasma emission spectra for aluminum based ion-molecule interactions. Spectra for the Al-N<sub>2</sub> (50%)-Ar and Al-CO (50%)-Ar systems are compared to those for the expansion of an aluminum plasma in pure argon. Evidence for vibrational structure attributed to Al<sup>+</sup>CO ion molecule complex formation associated with the Al<sup>+</sup> 4p <sup>1</sup>P - 4d <sup>1</sup>D transition and Al<sup>2+</sup>N<sub>2</sub> ion molecule complex formation associated with the Al<sup>2+</sup> 4s <sup>2</sup>S - 4p <sup>2</sup>P transition is depicted. See text for discussion.

tional structure associated with the Al<sup>+</sup>-molecule stretch or triatomic bending mode and can be correlated closely with transitions among several excited states of the Al<sup>+</sup> ion.<sup>53</sup>

In Figure 19, we compare emission spectra in the 430–470-nm range obtained for seeded Al-O<sub>2</sub> (Ar), Al-N<sub>2</sub> (Ar), Al-H<sub>2</sub> (Ar), and Al-CO (Ar) expansions with the corresponding emission associated with the Al-Ar system where we monitor only that emission from an argon entrained laser-induced aluminum plasma. The alumi-

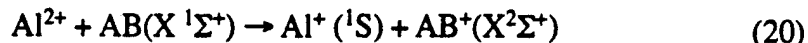
num-argon system shows no clear signs of complexation, the laser-induced plasma emission in this region being dominated by the  $\text{Al}^+ 5p\ ^1P - 11s\ ^1S$  and  $\text{Al}^{2+} 4p\ ^2P - 4d\ ^2D$  transitions.<sup>77</sup> In an aluminum- $\text{O}_2$  seeded (40%)–argon expansion, no evidence is obtained for complexation although weak emission corresponding to the  $\text{AlO}$ ,  $B^2\Sigma^+ - X^2\Sigma^+$ ,  $\Delta v = +1$  and  $+2$  sequences signals the formation of a chemical bond via the reaction of ground or excited state aluminum atoms and  $\text{O}_2$  to form ground or electronically excited  $\text{AlO}$  molecules. The observed features are likely produced by the direct formation and excitation of ground-state  $\text{AlO}$  molecules in the plasma or through direct chemiluminescent from electronically excited  $\text{AlO}$ .

The aluminum- $\text{N}_2$  (50%)–Ar system demonstrates a clear broadening of the  $\text{Al}^{2+}$  based emission features (vs. pure argon) in the 430–470-nm region whereas the aluminum-CO (50%)–Ar system demonstrates clear vibrational structure that must be associated with the formation of an  $\text{Al}^+\text{CO}$  complex. This is further emphasized in the 550–590-nm region (Figure 20) where, again in comparison with the  $\text{Al}^+ 4p\ ^1P - 4d\ ^1D$  and  $\text{Al}^{2+} 4s\ ^2S - 4p\ ^2P$  plasma emission<sup>77</sup> associated with a pure argon expansion, we observe evidence for complexation as manifest in clear vibrational structure for  $\text{Al}^+\text{CO}$  and  $\text{Al}^{2+}\text{N}_2$  excited state complexes.<sup>50</sup> These results are indicative of the broadening and vibrational structure associated with several  $\text{Al}^+$  and select  $\text{Al}^{2+}$  emission features extending across the visible and ultraviolet regions.<sup>53,77</sup> We emphasize the dichotomy in comparing the  $\text{N}_2$  and CO systems as the clear broadening and vibrational structure correlated with several  $\text{Al}^+$  emission features in the CO system is considerably muted in the  $\text{N}_2$  system. Meager evidence is obtained for  $\text{Al}^+ \text{N}_2$  complexation associated with the  $\text{Al}^+ 11s\ ^1S$  excited state. In contrast, the  $\text{Al}^{2+}$  emission features display clear and surprising broadening as well as vibrational structure that is virtually muted in the CO system (weak  $\text{Al}^{2+}\text{CO}$  complex emission). In view of the coulombic explosion<sup>78</sup> that is expected to dominate the behavior of multiply charged complexes resulting in rapid dissociation, the observed emission merits further discussion.

The observation of  $\text{Al}^{2+}$  emission features certainly demonstrates the substantial energy available to the constituency of a laser generated plasma. The observation of satellite features associated with certain of these  $\text{Al}^{2+}$  emission features that appear attributable to an  $\text{Al}^{2+}\text{-N}_2$  interaction may seem surprising in view of the lack of evidence for these complexes in experiments based in mass spectroscopy<sup>21</sup> and the anticipated coulombic explosion that accompanies multiply charged ions.<sup>79</sup> We suggest that these observations may be associated with the short time scale for ion emission verses that for mass spectrometric sampling.

The data that we have collected for the 430–470 and 550–590-nm regions may also signal the importance of the charge transfer process. In the  $\text{N}_2$  system, we observe evidence for vibrational structure with  $\Delta v \sim 40\text{ cm}^{-1}$  associated with the  $\text{Al}^{2+} 4s\ ^2S - 4p\ ^2P$  transition<sup>77</sup> (Figure 20). It is reasonable to associate this structure with the  $\text{Al}^{2+}\text{-N}_2$  interaction. Although we observe significant broadening, there is little evidence of vibrational structure associated with the  $\text{Al}^{2+} 4p\ ^2P - 4d\ ^2D$

transition.<sup>30</sup> The  $\text{Al}^{2+} 4p\ ^2P$  state lies at  $\sim 17.80$  eV whereas the  $4s\ ^2S$  and  $4d\ ^2D$  states lie at 15.64 eV and 20.55 eV respectively. The charge transfer processes:



to form ground state  $\text{Al}^+$  and  $\text{AB}^+$  are all highly exothermic, with the  $\text{N}_2$ ,  $\text{CO}$ , and  $\text{H}_2$  ionization potentials being 15.58, 14.01, and 15.43 eV respectively.<sup>79</sup> If, however, the charge transfer process forms  $\text{Al}^+$  atoms in high Rydberg states, the energy liberated in ion formation can be considerably less. Similarly, the formation of the excited states of the  $\text{CO}^+$  or  $\text{N}_2^+$  ions again lowers the excess energy available for dissociation via the charge transfer process, although this route does not appear to be readily available if  $\text{AB}^+ = \text{H}_2^+$  with its plethora of low-lying repulsive excited states.

The charge transfer process to produce ground state  $\text{N}_2^+$  is  $\sim 1.57$  eV less exothermic than that producing ground state  $\text{CO}^+$ . If we are given a sufficient branching into high Rydberg states of  $\text{Al}^+$ , the excess energy available if  $\text{AB} = \text{N}_2$  can be quite small. Furthermore, there exists the possibility for forming electronically excited  $\text{N}_2^+$  and  $\text{CO}^+$  products for which the tandem singly charged ion formation process can be made virtually thermoneutral in the sense that little or no excess energy is available or an activation barrier to product formation must be surmounted. Thus, it would not be surprising to find some component of the  $\text{Al}^{2+}$ -ions and  $\text{N}_2$  or  $\text{CO}$  molecules that does not complete the charge transfer process and instead interacts to form  $\text{Al}^{2+}\text{AB}$  excited state complexes. If the process of  $\text{Al}^{2+}$  based excited state complex formation and subsequent emission competes effectively with charge transfer complex formation and subsequent dissociation via coulombic explosion, these initial observations are consistent.

Finally, in Figure 19, we also observe evidence for  $\text{Al}^+ \text{-H}_2$  complexation in the aluminum- $\text{H}_2$  seeded (30%)-argon system. This behavior is also indicative of several  $\text{Al}^+$  emission features extending across the visible and ultraviolet. The broadening and vibrational structure observed in the range of studies with  $\text{CO}$ ,  $\text{H}_2$ , and  $\text{N}_2$  appears to be associated with the strongest  $\text{Al}^+$  emission features and thus the  $\text{Al}^+$  transitions with the shortest radiative lifetime. All complex emissions involve singlet ( $\text{Al}^+$ )-singlet ( $\text{CO}, \text{H}_2$ ) interactions as the resulting singly charged electronically excited molecular ion complexes are likely formed in orbiting collisions of  $\text{Al}^+$  with  $\text{CO}$  and  $\text{H}_2$ . The  $40\text{--}120\text{ cm}^{-1}$  vibrational level separations observed experimentally are consistent with quantum chemical calculations on the ground electronic  $^1\Sigma$  states of  $\text{Al}^+\text{CO}$ ,  $\text{Al}^+\text{OC}$ , and  $\text{Al}^+\text{H}_2$  (Table 5).

The combination of results suggests that the manifestation of complex formation and subsequent emission in these systems can be correlated. The radiative lifetimes associated with the excited state emissions observed must be sufficiently short so as to allow a reasonable and readily monitored emission rate on the time scale of vibration in the complex. The most clearly developed complex structure is associ-

**Table 5.** Calculated Frequencies and Infrared Intensities for Select Al<sup>+</sup> Ion-Molecule Complexes<sup>a</sup>

Molecule	$\nu$ (cm <sup>-1</sup> )	<i>I</i> (km/mol)
AlCO <sup>+</sup> <sup>b</sup>	2487 (2417) <sup>c</sup>	101
	134	0.4 pi (bend)
	85	51
AlOC <sup>+</sup> <sup>b</sup>	2341 (2417) <sup>c</sup>	319
	85	18
	85	4 pi
AlN <sub>2</sub> <sup>+</sup> <sup>b</sup>	2735	13
	101	1.6 pi
	41	41
AlH <sub>2</sub> <sup>+</sup> <sup>b</sup>	4510 (4582) <sup>c</sup>	24
	356	6 assym. stretch
	117	15 bend-stretch of Al <sup>+</sup> from H <sub>2</sub>

<sup>a</sup>Al<sup>+</sup> ground state 1s<sup>2</sup>2s<sup>2</sup>2p<sup>6</sup>3s<sup>2</sup>1S.<sup>b</sup>Al<sup>+</sup>CO, Al<sup>+</sup>OC, and Al<sup>+</sup>N<sub>2</sub> linear ground state. Al<sup>+</sup>H<sub>2</sub> has a C<sub>2v</sub> bent ground state.<sup>c</sup>Calculated frequencies for unperturbed diatomic molecules CO, N<sub>2</sub> and H<sub>2</sub>.

ated with the most intense Al<sup>+</sup> emission features.<sup>77</sup> These features are correlated with the shortest lived Al<sup>+</sup> excited states. Several additional weak Al<sup>+</sup> singlet-singlet transitions have been monitored with only a marginal indication of complex structure. These results suggest a strong correlation between the ability to observe the evidence of complex formation and the radiative lifetime associated with the Al<sup>+</sup> transitions of interest. The correlation suggests (1) the manifestation of short-lived complex formation and (2) that the radiative lifetime of the Al<sup>+</sup>-based excited state complex must be sufficiently short so that this emission rate competes favorably with the time scale for complex dissociation. If the dissociation of the excited state complex is sufficiently slow, it may be possible for excited state emission to compete effectively.

The suggested trends will need to be assessed more definitively in future experiments not only with aluminum but also with several additional closed shell or singlet state metal ions. The competition between emission and dissociation rate may also account in part for the observation of Al<sup>2+</sup>N<sub>2</sub> complex features despite coulombic explosion<sup>78</sup> as vibrational structure is also associated with the strongest Al<sup>2+</sup> transitions.<sup>77</sup>

Attempts to observe emission features associated with complex formation and correlating with open shell Al<sup>+</sup> triplet-triplet transitions, as manifest by satellite structure in the vicinity of the corresponding Al<sup>+</sup> transition features, have been unsuccessful. Triplet unpaired excited electronic states may contribute to limited

chemical bond formation more readily than do their singlet counterparts. In contrast to complex formation, chemical bond formation is expected to produce excited state emissions shifted considerably from those atomic features with which they correlate in the dissociation limit. These suggestions, of course, await further confirmation in the laboratory.

## ACKNOWLEDGMENTS

We thank the National Science Foundation, the ACS-PRF, the Eastman Kodak Company, the Georgia Tech Foundation through a grant from Mrs. Betty Peterman Gole, and the Army Research Office and the Air Force Office of Scientific Research. This work would not have been possible without the capable assistance of J. R. Woodward, S. H. Cobb, K. X. He, M. McQuaid, K. K. Shen, C. B. Winstead, T. R. Burkholder, and D. Grantier and collaboration with T. C. Devore, D. A. Dixon, S. Langhoff, and C. W. Bauschlicher.

## REFERENCES AND NOTES

1. *The Physics and Chemistry of Small Clusters*; Jena, P.; Rao, B. K.; Khanna, S. N., Eds.; NATO ASI Series, Series B: Physics, Volume 158; Plenum Press: New York and London, 1986.
2. Bauer, S. H. private communication. See also, Kung, R. T. V.; Bauer, S. H. In *8th International Shock Tube Symposium*; Stollery, J. L., Ed.; Chapman and Hall: London, 1971. Keifer, J.; Lutz, B. *J. Chem. Phys.* **1966**, *44*, 658. Stever, H. G. *Condensation Phenomena in High Speed Flows*. Princeton Series on High Speed Aerodynamics and Jet Propulsion. Vol. III, Sect. F.
3. a. *Metal Clusters*; Moskovits, M., Ed.; Wiley-Interscience, John Wiley and Sons: New York, 1986. b. *Metal Bonding and Interactions in High Temperature Systems*; Gole, J. L.; Stwalley, W. C., Eds.; ACS Symp. Ser. Vol. 179, 1982. c. *Diatomic Metals and Metallic Clusters*; Symp. Faraday Soc. **14**, 1980. d. Morse, M. *Chem. Reviews* **1986**, *86*, 1049.
4. Na<sub>3</sub>: a. Herrmann, A.; Hofmann, M.; Leutwyler, S.; Schumacher, E.; Woste, L. *Chem. Phys. Lett.* **1979**, *62*, 216. b. Gole, J. L.; Green, G.; J. Pace, S. A.; Preuss, D. R. *J. Chem. Phys.* **1982**, *76*, 2247. c. Delacretaz, G.; Grant, E. R.; Whetten, R. L.; Woste, L.; Zwanziger, J. W. *Phys. Rev. Lett.* **1986**, *56*, 2598. Cu<sub>3</sub>: d. Morse, M. D.; Hopkins, J. B.; Langridge-Smith, P. R. V.; Smalley, R. E. *J. Chem. Phys.* **1983**, *79*, 5316. e. Crumley, W. H.; Hayden, J. S.; Gole, J. L. *J. Chem. Phys.* **1986**, *84*, 5250. f. Rohlfing, E. A.; Valentini, J. J. *Chem. Phys. Lett.* **1986**, *126*, 113. Ag<sub>3</sub>: g. Cheng, P. Y.; Duncan, M. A. *Chem. Phys. Lett.* **1988**, *152*, 341. Al<sub>3</sub>: h. Fu, Z.; Lemire, G. W.; Hamrick, Y. M.; Taylor, S.; Shui, J.-C.; Morse, M. D. *J. Chem. Phys.* **1988**, *88*, 3524. Ni<sub>3</sub>: i. Ervin, K. M.; Ho, J.; Lineberger, W. C. *J. Chem. Phys.* **1988**, *89*, 4514. j. Woodward, R. W.; Cobb, S. H.; Gole, J. L. *J. Phys. Chem.* **1988**, *92*, 1404. Cu<sub>x</sub><sup>+</sup>: Jarrold, M. F.; Creegan, K. M. *Chem. Phys. Lett.* **1990**, *166*, 116. C<sub>x</sub>: l. Bernath, P. F.; Kinkle, K. H.; Keady, J. *J. Science* **1989**, *244*, 562. m. Heath, J.; Cooksy, A. L.; Gruebele, M. H. W.; Schumuttermaer, C. A.; Saykally, R. J. *Science* **1989**, *244*, 564. n. Moazzen-Ahmadi, N.; McKellar, A. R. W.; Amano, T.; *J. Chem. Phys.* **1989**, *91*, 2140. Si<sub>x</sub>: o. Kitsopoulos, T. N.; Chick, C. J.; Weaver, A.; Neumark, D. M. *J. Chem. Phys.* **1990**, *93*, 6108. p. Winstead, C. B.; X. He, K.; Hammond, T.; L. Gole, J. *Chemical Physics Letters* **1991**, *181*, 222.
5. a. Woodward, R. W.; Le, P. N.; Temmen, M.; Gole, J. L. *J. Phys. Chem.* **1987**, *91*, 2637. b. Gole, J. L. *Quantum Level Probes of Small Metal Clusters and Their Oxidations*, American Institute of Physics Conference Proceedings, No. 160, Advances in Laser Science II - Optical Science and Engineering Series 8, pg. 439. c. Devore, T. C.; Woodward, R. W.; Gole, J. L. *J. Phys. Chem.*

- 1988, 92, 6919. d. Woodward, R. W.; Le, P. N.; Devore, T. C.; Dixon, D. A.; Gole, J. L. *J. Phys. Chem.* 1990, 94, 756. e. Devore, T. C.; Woodward, J. R.; Gole, J. L. *J. Phys. Chem.* 1989, 93, 4920. f. McQuaid, M. J.; Gole, J. L. *Stability and Oxidation of Metal Based CO and CO<sub>2</sub> Complexes*; Proceedings of the Fourth International Laser Science Conference, A.I.P. Conf. Proc. No. 191, Optical Science and Engineering Series 10, pg. 687.
6. Devore, T. C.; McQuaid, M.; Gole, J. L. *High Temp. Science* 1990, 29, 1.
7. Cobb, S. H.; Woodward, J. R.; Gole, J. L. *Chem. Phys. Lett.* 1988, 143, 205; 1989, 156, 197.
8. Devore, T. C.; Gole, J. L. *Oxidation of Small Metal Clusters*; Proceedings of the Sixth International Conference on High Temperature Materials, High Temperature Science, 1989, 27, 49.
9. Taylor, T. N.; Campbell, C. T.; Rogers, Jr., J. W.; Ellis, W. P.; White, J. M. *Surface Science* 1983, 134, 529.
10. See for example references and discussion in a. Gole, J. L. The gas phase characterization of the molecular electronic structure of small metal clusters and cluster oxidation. In: *Metal Clusters*; Moskovits, M., John Wiley and Sons. b. Morse, M. D.; Hopkins, J. B.; Langridge-Smith, P. R.; Smalley, R. E. *J. Chem. Phys.* 1983, 79, 5216.
11. Note that this present approach bears some resemblance to the liquid nitrogen entrainment-induced agglomeration of metal clusters used by Stein and co-workers and Solliard. These authors formed much larger aggregates, which they studied using electron diffraction techniques. See for example: a. de Boer, B. G.; Stein, G. D. *Surf. Sci.* 1981, 106, 84. b. Solliard, C. Ph.D. Thesis, Ecole Polytechnique Federal de Lausanne, Switzerland, 1983. c. See also *Surf. Sci.* 1981, 106, 58; *J. de Phys.*, 1977, C2, 167.
12. a. Riley, S. J.; Parks, E. K.; Pobo, L. G.; Wexler, S. *Ber. Bunsenges. Phys. Chem.* 1984, 88, 287. b. Richtsmeier, S. C.; Parks, E. K.; Liu, K.; Pobo, L. G.; Riley, S. J. *J. Chem. Phys.* 1985, 82, 3659. c. Parks, E. K.; Liu, K.; Richtsmeier, S. C.; Pobo, L. G.; Riley, S. J. *J. Chem. Phys.* 1985, 82, 5470. d. Liu, K.; Parks, E. K.; Richtsmeier, S. C.; Pobo, L. G.; Riley, S. J. *J. Chem. Phys.* 1985, 83, 2882. e. Whetten, R. L.; Cox, D. M.; Trevor, D. J.; Kaldor, A. *Phys. Rev. Lett.* 1985, 54, 1494. f. Whetten, R. L.; Cox, D. M.; Trevor, D. J.; Kaldor, A. *J. Phys. Chem.* 1985, 89, 566. g. Trevor, D. J.; Whetten, R. L.; Cox, D. M.; Kaldor, A. *J. Am. Chem. Soc.* 1985, 107, 528. h. Cox, D. M.; Trevor, D. J.; Whetten, R. L.; Rohlfing, E. A.; Kaldor, A. *Phys. Rev. B*, in press. i. Geusic, M. E.; Morse, M. D.; Smalley, R. E. *J. Chem. Phys.* 1985, 82, 590. j. Geusic, M. E.; Morse, M. D.; O'Brien, S. C.; Smalley, R. E. *Rev. Sci. Instr.* 1985, 56, 2123. k. Morse, M. D.; Geusic, M. E.; Heath, J. R.; Smalley, R. E. *J. Chem. Phys.* 1985, 83, 2293.
13. See for example, a. Preuss, D. R.; Gole, J. L. *J. Chem. Phys.* 1977, 66, 2994; (b) Gole, J. L.; Preuss, D. R. *J. Chem. Phys.* 1977, 66, 3000. c. Dubois, L. H.; Gole, J. L. *J. Chem. Phys.* 1977, 66, 779. d. Lindsay, D. M.; Gole, J. L. *J. Chem. Phys.* 1977, 66, 3886. e. Gole, J. L.; Pace, S. A. *J. Chem. Phys.* 1980, 73, 836. f. Chalek, C. L.; Gole, J. L. *J. Chem. Phys.* 1976, 65, 2845. g. Gole, J. L.; Pace, S. A. *J. Phys. Chem.* 1981, 65, 2651. h. Gole, J. L. *Ann. Rev. Phys. Chem.* 1976, 27, 525.
14. a. Gole, J. L.; Stwalley, W. C. Characterization of Alkali Metal Aggregation from Dimer to Bulk. In: *Advances in Atomic and Molecular Physics*. b. Hilpert, K.; Gingerich, K. A. *Ber. Bunsenges. Phys. Chem.* 1980, 84, 739. c. Gingerich, K. A.; Cocke, D. L.; Finkbeiner, H. C.; Chang, C. A. *Chem. Phys. Lett.* 1973, 18, 102. d. Gingerich, K. A.; Cocke, D. L.; Choudary, U. V. *Inorg. Chem. Acta* 1975, 14, 147. e. Neubert, A.; Ihle, H. R.; Gingerich, K. A. presented at 6th Int. Conf. Thermodynamics, Merseburg D.D.R., Aug. 26-29, 1980. f. Kingcade, J. E.; Dufner, D. C.; Gupta, S. K.; Gingerich, K. A. *High Temp. Sci.* 1978, 10, 213. g. Gingerich, K. A.; Cocke, D. L.; Miller, F. J. *J. Chem. Phys.* 1976, 64, 4027. h. Kingcade, Jr., J. E.; Choudary, U. V.; Gingerich, K. A. *Inorg. Chem.* 1979, 18, 3094. i. Drowart, J.; DeMaria, G. *J. Chem. Phys.* 1959, 30, 308. j. Kant, A.; Strauss, B. *J. Chem. Phys.* 1966, 45, 822.
15. Liu, K.; Riley, S. private communication.
16. Lindsay, D. M.; Gole, J. L. *J. Chem. Phys.* 1977, 66, 3886.
17. a. Devore, T. C.; Bauschlicher, Jr., C. W.; Langhoff, S. R.; Siegbahn, Per E. M.; Sulkes, M.; Gole,

- J. L. Formation, Electronic Spectra, and Electronic Structure of the Low-Lying Singlet States of Symmetrical  $\text{Cu}_2\text{O}$ , to be submitted for publication. (b) Devore, T. C.; Bauschlicher, Jr., C. W.; Burkeholder, T.; Gole, J. L. A Comparative Study of the Oxidation of Atomic Copper and Higher Copper Clusters Under Single and Multiple Collision Conditions; Electronic Structure of the Asymmetric Copper Clustered Oxides,  $\text{Cu}_x\text{O}$ , to be submitted for publication.
18. Shen, K. K.; Winstead, C.; Brock, L.; Dulaney, K.; Devore, T.; Gole, J. L. work in progress.
  19. Devore, T. C.; Gole, J. L. *Chemical Physics* **1989**, *133*, 95.
  20. Gole, J. L. Kinetically Controlled Oxidations Forming Unique Metal Clustered Oxides and Halides; ACS-PRF #21252-AC6-C.
  21. Dixon, D. A. private communication.
  22. For example see: a. *Proceedings of the Symposium on High Temperature Metal Halide Chemistry*; Hildenbrand, D. L.; Cubicciotti, D. D., Eds.; The Electrochemical Society, Princeton, 1978. b. Cheung, A. S.-C.; Zymnicki, W.; Merer, A. J. *J. Molec. Spectrosc.* **1984**, *104*, 315. c. *Gas Phase Chemiluminescence and Chemiionization*; Fontijn, A., Ed.; Elsevier Science Publishers, 1985.
  23. Dubov, V. M.; Shenyaskaya, E. A. *Opt. Spectrosc. (USSR)* **1987**, *62*, 195.
  24. a. *The Physics of Latent Image Formation in the Silver Halides*; Baldereschi, A.; Czaja, W.; Tosatti, E.; Tosi, M., Eds.; World Scientific, Singapore, 1984. b. *The Theory of the Photographic Process*; James, T. H., Ed.; MacMillan: New York, 1977.
  25. *Ethylene and Industrial Derivatives*; Miller, S. A.; Benn, Ernest, Eds.; MacMillan: New York, 1977.
  26. Marchetti, A.; Deaton, J. private communication.
  27. See Herzberg, G. *Spectra of Polyatomic Molecules*; Van Nostrand Reinhold: New York, 1977.
  28. Morse, M. *Chem. Phys. Lett.* **1987**, *133*, 8.
  29. Shen, K. K.; Gole, J. L.; work in progress.
  30. Privately communicated and used by permission.
  31. Bauschlicher, C. W.; private communication.
  32. Dixon, D. A. private communication.
  33. a. Macek, A. *Combustion Science and Technology* **1969**, *1*, 181. b. King, M. K. *Modelling of Single Particle Boron Combustion*; 19th JANAF Combustion Meeting, CPIA-PUB-366, V.2, 1982. c. Glassman, I.; Williams, F. A.; Antaki, P. A *Physical and Chemical Interpretation of Boron Particle Combustion Meeting*, CPIA-PUB-366, V.1, 1982. d. King, M. K. "Boron Ignition and Combustion in Air-Augmented Rocket Afterburners," *Comb. Sci. Tech.* **1972**, *5*, 155. e. King, M. K. "Boron Particle Ignition in Hot Gas Streams," *Comb. Sci. Tech.* **1974**, *8*, 255. f. Mohen, G.; Williams, F. A. "Ignition and Combustion of Boron in  $\text{O}_2$ /Inert Atmospheres," *AIAA J.* **1972**, *10*, 776. g. Macek, A. "Combustion of Boron Particles at Atmospheric Pressure," *Comb. Sci. Tech.* **1969**, *1*, 181. h. Macek, A.; Semple, J. McK. "Combustion of Boron Particles at Elevated Pressure," *Thirteenth Symposium (International) on Combustion*, The Combustion Institute, Pittsburgh, p. 859, 1970. i. Macek, A. "Combustion of Boron Particles: Experiment and Theory," *Fourteenth Symposium (International) on Combustion*, The Combustion Institute, Pittsburgh, p. 1401, 1972. j. Macek, A.; Semple, J. A. *Combustion and Combustion Characteristics of Condensed Exhaust from Boron-Containing Fuel-Rich Rocket Motors*, 9th JANAF Combustion Meeting, CPIA-PUB-231, V.1 (1972). k. King, M. K. *J. Spacecraft* **1982**, *19*, 294.
  34. Oldenborg, R. C.; Baughcum, S. L. private communication.
  35. DeKock, R. L.; Barbachyn, M. R. *J. Inorg. Nucl. Chem.* **1981**, *43*, 2645.
  36. Zyubine, T. S.; Charkin, O. P.; Zyubin, A. S.; Zakzhevokii, A. S. *Zh. Neorg. Khim* **1982**, *27*, 558.
  37. Gina, H.; Jones, L.; Shillady, D. private communication.
  38. a. Woodward, J. R.; Hayden, J. S.; Gole, J. L. *Chemical Physics* **1989**, *134*, 395 and references therein. b. Shen, K. K.; Qi, X.; Gole, J. L. Formation of the Low-Lying  $\text{C}^2\Pi$  State of the Alkali Monoxides from  $\text{M}^2\text{P}$  Excited Alkali Metal Atom Reactions, submitted to *Chemical Physics*.
  39. a. Smalley, R. E. private communication. b. Zheng, L.-S.; Karner, C. M.; Brucat, P. J.; Yang, S. H.; Pettiette, C. L.; Craycraft, M. J.; Smalley, R. E. *J. Chem. Phys.* **1986**, *85*, 1681. c. Brucat, P.

- J.; Pettiette, C. L.; Yang, S.; Zhenc, L.-S.; Craycraft, M. J.; Smalley, R. E. *J. Chem. Phys.* **1986**, *85*, 4747. d. Brucat, P. J.; Zheng, L.-S.; Pettiette, C. L.; Yang, S.; Smalley, R. E. *J. Chem. Phys.* **1986**, *84*, 3078; e. Leopold, D. G.; Ho, J.; Lineberger, W. C. *J. Chem. Phys.* **1987**, *86*, 1715. f. Anderson, T.; Lykke, K. R.; Neumark, D. M.; Lineberger, W. C. *J. Chem. Phys.* **1987**, *86*, 1858. g. Leopold, D. G.; Lineberger, W. C. **1986**, *85*, 51. h. Neumark, D. M.; private communication.
40. Green, G. J.; Pace, S. A.; Preuss, D. R.; Gole, J. L. *J. Chem. Phys.* **1982**, *76*, 2247.
41. Hayden, J. S.; Woodward, J. R.; Gole, J. L. *J. Chem. Phys.* **1986**, *90*, 1799.
42. Stwalley, W. C. private communication.
43. a. Crumley, W. H.; Gole, J. L.; Dixon, D. A. *J. Chem. Phys.* **1982**, *76*, 6439. b. Cobb, S. H.; Woodward, J. R.; Gole, J. L. *Chem. Phys. Lett.* **1988**, *143*, 205. c. Cobb, S. H.; Woodward, J. R.; Gole, J. L. *Chem. Phys. Lett.* **1989**, *157*, 197. d. Cobb, S. H.; Woodward, J. R.; Gole, J. L. *Continuous Chemical Laser Amplifiers in the Visible Region*; Proceedings of the Fourth International Laser Science Conference, A.I.P. Conf. Proc. No. 191, Optical Science and Engineering Series 10, pg. 68.
44. a. Wellegehausen, B. *I.E.E.E. of Quant. Elect.* **1979**, *15*, 1108. b. Jones, P. L.; Gaubatz, U.; Hefter, U.; Bergmann, K. *Appl. Phys. Lett.* **1983**, *42*, 222. c. Wellegehausen, B. In: *Metal Bonding and Interactions in High Temperature Systems with Emphasis on Alkali Metals*; A. C. S. Symposium Series 179, Gole, J. L.; Stwalley, W. C., Eds.; Am. Chem. Soc.: Washington, D. C., p. 462.
45. a. Crumley, W. H. Ph.D. Thesis, Georgia Institute of Technology, 1985. b. Cobb, S. H. Ph.D. Thesis, Georgia Institute of Technology, 1988.
46. See for example, a. Berry, R. S.; Reimann, C. W. *J. Chem. Phys.* **1963**, *38*, 1540. b. Berry, R. S. *J. Chem. Phys.* **1957**, *27*, 1288. c. Struve, W. S.; Krenos, J. R.; McFadden, D. L.; Herschbach, D. R. *J. Chem. Phys.* **1975**, *62*, 404. d. Oldenborg, R. C.; Gole, J. L.; Zare, R. N. *J. Chem. Phys.* **1974**, *60*, 4032.
47. Given Na<sub>2</sub> and Na<sub>3</sub> ionization potentials of 4.87 and 3.97 eV (Hermann, A.; Schumacher, E.; Woste, L. *J. Chem. Phys.* **1978**, *68*, 2327.) and an electron affinity of 3.3363 eV for atomic bromine, we determined a very substantial electron jump cross section  $\sigma = \pi (14.38/3.97-3.36) = 1746 \text{ \AA}^2 (1.75 \times 10^{-13} \text{ cm}^2)$  for the Na<sub>3</sub> - Br reaction and  $\sigma = \pi(14.38/4.87-3.36) = 285 \text{ \AA}^2 (2.85 \times 10^{-14} \text{ cm}^2)$  for the Na<sub>2</sub> - Br reaction.
48. a. Bondybey, V. E.; English, J. H. *J. Chem. Phys.* **1981**, *74*, 6978. b. Bondybey, V. E.; English, J. H. *J. Chem. Phys.* **1982**, *76*, 2165. c. Bondybey, V. E.; Schwartz, G. P.; English, J. H. *J. Chem. Phys.* **1983**, *78*, 11. d. Bondybey, V. E. *J. Chem. Phys.* **1982**, *77*, 3771. e. Bondybey, V. E.; English, J. H. *Chem. Phys. Lett.* **1983**, *94*, 443. f. Gole, J. L.; English, J. H.; Bondybey, V. E. *J. Phys. Chem.* **1982**, *86*, 2560.
49. Geusic, M. E.; Morse, M. D.; O'Brien, S. C.; Smalley, R. E. *Rev. Sci. Instr.* **1985**, *56*, 2123.
50. Winstead, C. B.; He, K. X.; Hammond, T.; Gole, J. L. *Chem. Phys. Lett.* **1991**, *181*, 222.
51. Weltner, W.; McLeod, D. *J. Chem. Phys.* **1964**, *41*, 235.
52. Kitsopoulos, T. N.; Chick, C. J.; Weaver, A.; Neumark, D. M. *J. Chem. Phys.* **1990**, *93*, 6108.
53. He, K. X.; Hammond, T.; Winstead, C. B.; Gole, J. L.; Dixon, D. A. *J. Chem. Phys.* **1991**, *95*, 7183.
54. See for example, McDaniel, E. W. *Collision Phenomena in Ionized Gases*; Wiley and Sons: New York, 1964. Duncan, M. A.; Flannery, M. R.; McDaniel, E. W. private discussions.
55. Thomas, E. W. *Excitation in Heavy Particle Collisions*; Wiley Interscience, 1972.
56. Duncan, M. A.; private communication.
57. Hilbert, K.; Gingerich, K. A. *Ber Bunsenges Phys. Chem.* **1980**, *84*, 739. Bond energy for Ag-Ag<sub>2</sub> or Cu-Cu<sub>2</sub> bond from atomization energy minus diatomic bond energy.
58. Gingerich, K. A. *J. Cryst. Growth* **1971**, *9*, 31 - Data for Ag<sub>2</sub>.
59. Hilbert, K. *Ber Bunsenges Phys. Chem.* **1979**, *83*, 161 - Data for Cu<sub>2</sub>.
60. He, K. X.; Winstead, C. B.; Diestler, M.; Georges, N.; Hammond, T.; Gole, J. L.; unpublished.
61. Grev, R. S.; Schaefer, H. F. *Chem. Phys. Lett.* **1985**, *119*, 111.
62. Raghavachari, K. *J. Chem. Phys.* **1985**, *83*, 3520. *J. Chem. Phys.* **1986**, *84*, 5672.

63. Dixon, D. A.; Gole, J. L. *Chem. Phys. Lett.* **1992**, *188*, 560.
64. Schriver, K. E.; Hahn, M. Y.; Persson, J. L.; LaVilla, M. E.; Whetten, R. L. *J. Phys. Chem.* **1989**, *93*, 2869.
65. a. Lessen, D.; Brucat, P. J. *Chem. Phys. Lett.* **1988**, *149*, 10; (b) *ibid.* 573. (c) Lessen, D.; Brucat, P. J. *Chem. Phys. Lett.* **1988**, *152*, 473.
66. Lessen, D.; Brucat, P. J. *J. Chem. Phys.* **1989**, *90*, 6296.
67. Callender, C. L.; Mitchell, S. A.; Hacket, P. A. *J. Chem. Phys.* **1989**, *90*, 2535; *ibid.* 5252.
68. a. Castleman, A. W.; Holland, P. M.; Lindsay, D. M.; Peterson, K. I. *J. Am. Chem. Soc.* **1978**, *100*, 6039; b. Castleman, A. W. *Chem. Phys. Lett.* **1978**, *53*, 560. c. Holland, P. W.; Castleman, A. W. *J. Chem. Phys.* **1982**, *76*, 4195; (d) Glein, K. L.; Guo, B. C.; Kessee, R. G.; Castleman, A. W. *J. Phys. Chem.* **1989**, *93*, 6805.
69. Shaw, M. H.; Farrar, J. M. *J. Phys. Chem.* **1989**, *93*, 4386.
70. Magnera, T. F.; David, D. E.; Michl, J. *J. Am. Chem. Soc.* **1989**, *111*, 4100.
71. Marinelli, P. J.; Squires, P. R. *J. Am. Chem. Soc.* **1989**, *111*, 4101.
72. Bouchard, F.; Hepburn, J. W.; McMahon, T. B. *J. Am. Chem. Soc.* **1989**, *111*, 8934.
73. El-Shall, M. S.; Schriver, K. E.; Whetten, R. L.; Mautner, M. J. *J. Phys. Chem.* **1989**, *111*, 8934.
74. a. Hettich, R. L.; Freiser, B. S. *J. Am. Chem. Soc.* **1987**, *109*, 3543; b. Freiser, B. S. *Chemtracts-Anal. and Phys. Chem.* **1989**, *1*, 65. c. Lech, L. M. Ph.D. Thesis, Purdue University, 1988.
75. Gantefor, G.; Siekmann, H. R.; Lutz, H. O.; Meiwes-Broer, K. H. *Chem. Phys. Lett.* **1990**, *165*, 293.
76. a. Bauschlicher, C. W.; Partridge, H.; Langhoff, S. R. *J. Chem. Phys.* **1989**, *91*, 4733; (b) Rosi, M.; Bauschlicher, C. W. *J. Chem. Phys.* **1989**, *90*, 7264.
77. Willey, K. F.; Yeh, C. S.; Robbins, D. L.; Duncan, M. A. *Chem. Phys. Lett.* **1992**, *192*, 179.
78. Yeh, C. S.; Willey, K. F.; Robbins, D. L.; Pilgrim, J. S.; Duncan, M. A. *Chem. Phys. Lett.* **1992**, *196*, 233.
79. Striganov, A. R.; Sventitskii, N. S. *Tables of Spectral Lines of Neutral and Ionized Atoms*; IFI, Plenum: New York, 1968.
80. See for example, a. Saunders, W. A.; Fedrigo, S. *Chem. Phys. Lett.* **1989**, *156*, 14. b. Sattler, K.; Muehlbach, J.; Echt, O.; Pfau, P.; Recknagel, E. *Phys. Rev. Letts.* **1981**, *47*, 160. c. Pfau, P.; Sattler, K.; Plaum, R.; Recknagel, E. *Phys. Letts. A* **1984**, *104*, 262; d. Hoareau, A.; Melinon, P.; Cabaud, B.; Rayne, D.; Tribollet, B.; Broyer, M. *Chem. Phys. Letts.* **1988**, *143*, 602. e. Tomanek, D.; Mukherjee, S.; Bennemann, K. H. *Phys. Rev. B* **1983**, *28*, 665. f. Durant, G.; Daudy, J. P.; Malrieu, J. P. *J. Phys. (Paris)* **1986**, *47*, 1335. g. Liu, F.; Press, M. R.; Khanna, S. N.; Jena, P. *Phys. Rev. Letts.* **1987**, *59*, 2562. h. Khanna, S. N.; Reuse, F.; Buttet, J. *Phys. Rev. Letts.* **1988**, *61*, 535 and references therein.
81. See for example, McDaniel, E. W. *Atomic Collisions: Electron and Photon Projectiles*; John Wiley and Sons: New York, 1989.

## APPENDIX II

"Flourine Hot Atom Oxidation of Bismuth Vapor: A Comment on the Evaluation of the BiF bond Energy", T. C. Devore, and J. L. Gole, Chemical Physics 174, 409 (1993).

## Fluorine hot atom oxidation of bismuth vapor. A comment on the evaluation of the BiF bond energy

T.C. Devore

*Department of Chemistry, James Madison University, Harrisonburg, VA 22807, USA*

and

J.L. Gole

*School of Physics and High Temperature Laboratory, Georgia Institute of Technology, Atlanta, GA 30332, USA*

Received 25 February 1993

The energetics of the chemiluminescent reaction between bismuth dimers and fluorine atoms (T.C. Devore et al., *Chem. Phys.* 155 (1991) 423; 156 (1991) 156) has been evaluated to better refine a determination of the bismuth fluoride dissociation energy. By directly examining the spectrum of the  $\text{SF}_6$  discharge used to generate the F atoms to establish the significant energy imparted to these dissociation products and by exploring F atom chemiluminescent reactions with known energetics, the F atom beam is established to have contributed a maximum of 0.8–0.9 eV to the chemiluminescent process. Based upon the observed population of the  $v' = 4$  level of the  $\text{BiF } A0^+$  state resulting from the  $\text{Bi}_2 + \text{F}$  reaction, a BiF bond energy of  $3.9 \pm 0.2$  eV is established. This value is slightly higher than a very recent evaluation of the BiF bond energy (Yoo et al., *Chem. Phys.* 166 (1992) 215) but disagrees with previous determinations in the literature. Many of the previous evaluations of the group 15 halide dissociation energies have been based on Birge–Spencer extrapolations. The data now available for BiF permits an evaluation of the nature of these extrapolations for this molecule. The limitations of these extrapolations and possible corrections for these shortcomings are presented.

### 1. Introduction

Although the stabilities and molecular electronic structure of the group 15 halides,  $\text{PX-BiX}$  have been rather sparsely characterized (table 1) [1–18], considerable recent interest has been focused on the BiF molecule [19]. This interest has been based, in part, on the desire to energy transfer pump the  $\text{BiF } A0^+$  (II) state in order to form a visible chemical laser operating on the  $A-X (0^+)$  transition at wavelengths close to 450 nm. We have recently [16,17] been concerned with an evaluation of the BiF red emission systems which emanate from two excited electronic states located at energies and internuclear distances in close proximity ( $< 2000 \text{ cm}^{-1}$ ) to the  $\text{BiF } A0^+$  (II) state. This density of states, specific to the BiF molecule and representing some considerable deviation from the trends characterizing the lighter group

15 halides (fluorides), strongly influences the apparent level structure of the  $\text{BiF } A$  state.

In response to the intriguing suggestion by Ross et al. [15] that the BiF bond energy was close to 5 eV, exceeding by 2 eV previous estimates in the literature, we obtained an estimate of the BiF bond dissociation energy through a comparative evaluation of the chemiluminescent  $\text{Bi}_x (\text{Bi}, \text{Bi}_2) + \text{F}_2$  and  $\text{Bi}_2 + \text{F}$  reactive encounters. Based on an evaluation of the reaction energetics for the  $\text{Bi}_2 + \text{F}$  reaction *uncorrected* for (1) vibrational excitation in  $\text{Bi}_2$  and (2) the translational energy of those F atoms reacting with the bismuth dimer, we estimated that the upper limit for the bond energy of BiF could exceed 4.5 eV but indicated that the energetics needed to be refined before an accurate upper limit could be determined [16]. In this communication, we summarize the results of our studies to refine [17] this initially estimated value, taking into account the significant

Table 1  
Evaluated dissociation energies for group 15 halides PX-BiX

Element	Dissociation energy for MX (X = F, Cl, Br, I) in electron volts <sup>a)</sup>			
	F	Cl	Br	I
F	4.5 ± 1 <sup>b)</sup> [1], 4.55 ± 0.4 [2]	—	—	—
As	4.2 <sup>c)</sup> [3]	—	—	—
Sb	4.5 ± 1 <sup>d)</sup> [6]	3.7 ± 0.5 <sup>b)</sup> [5]	3.2 ± 0.6 <sup>b,e)</sup> [4]	2.5 ± 1 <sup>b,e)</sup> [7]
Bi	2.65 ± 0.3 <sup>e)</sup> [11-13] <sup>b)</sup> , > 4 <sup>f)</sup> 3.14 [21], 3.76 ± 0.13 [18]	3.13 ± 0.1 <sup>b)</sup> [9,10]	2.74 ± 0.01 <sup>b,e)</sup> [7.8]	

<sup>a)</sup> References in parentheses.

<sup>b)</sup> Linear Birge-Sponer extrapolation.

<sup>c)</sup> Theoretical calculation.

<sup>d)</sup> Linear Birge-Sponer extrapolations give values ranging from 4.2 to 5.7 – suggested by ref. [14].

<sup>e)</sup> Suggested by ref. [14].

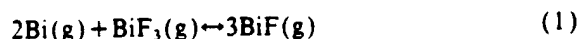
<sup>f)</sup> Refs. [15-17].

<sup>g)</sup> Mass spectrometry.

translational energy associated with fluorine atoms produced from an SF<sub>6</sub> discharge, discuss the implications of this refinement correlated with other recent studies of the BiF bond energy [15,18] and consider the recently proposed parameterizations of Yoo et al. [18], to evaluate the BiF bond dissociation energy.

## 2. The BiF bond dissociation energy

Recently Yoo et al. [18] have used photoion yield curves and a second and third law treatment based on the ion intensities for the reaction



to establish the dissociation energy of BiF as 3.76 ± 0.13 eV. This value is nearly 1 eV larger than the previously accepted values for the dissociation energy, 2.65 eV estimated from spectroscopic data by Gaydon [14], 3.0 eV determined using an empirical ionic model by Rai and Singh [20], and less than 3.14 eV determined by Jones and Mclean [21] from a possible predissociation of the A0<sup>+</sup> state; however, it is over 1 eV lower than the value of nearly 5 eV determined by Ross et al. [15] from a long extrapolation of vibrational level separations based on a Leroy-Bernstein [22] plot using the ground state molecular constants.

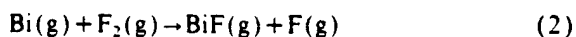
In investigating the spectroscopy and dynamics of the chemiluminescent reactions between bismuth va-

por (Bi, Bi<sub>2</sub>) and fluorine atoms and molecules, we [16,17] have focused some considerable attention on the intense chemiluminescent emission from the Bi<sub>2</sub>+F reaction. In our initial study [16] we suggested, in agreement with Ross et al. [15], that the upper limit for the BiF dissociation energy could be greater than 4.5 eV [16]. However, it was also stated that a more careful assessment of the internal energy of the reactants, particularly the translational energy of the F atom beam in the Bi<sub>2</sub>+F atom reaction, would be needed before a more precise value for the upper limit of the dissociation energy could be determined.

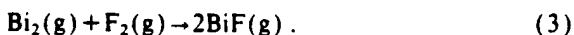
We have now further refined these experiments through an assessment of the F atom beam produced in the SF<sub>6</sub> discharge employed to study the Bi<sub>2</sub>+F reaction. It is clear that the F atoms are produced with a significant translational energy and that the translational energy is involved in the reaction since the F atom based chemiluminescent signature in the vicinity of the oxidant source displays a substantial directionality relative to that characterizing the bismuth vapor/F<sub>2</sub> interaction. Based upon a comparison of the reaction energetics for several known systems, we suggested an upper bound value of 4.2 ± 0.2 eV for the BiF bond energy based on an F atom translational energy in excess of 0.5 eV [17]. This F atom energy has now been more stringently parameterized to energies of order 0.8–0.9 eV. With this correction, assuming differences in the translational energy of the other reactants and products are negligible, the ther-

mochemical cycle [16,17]<sup>21</sup> involving Bi<sub>2</sub> and hot F atoms suggests a BiF bond energy of order  $3.9 \pm 0.2$  eV, slightly higher than that given by Yoo et al. [18]. The uncertainty is based upon estimates of the uncertainty in the F atom energy and will allow for possible vibrational excitation in the Bi<sub>2</sub>.

The determination of Yoo et al. [18] and our refinement of the dissociation energy provide insight into the chemiluminescent signature observed for the interaction of bismuth vapor and F<sub>2</sub> [16,17]. This reactive system produces strong emission from the low-lying vibrational levels of the A0<sup>+</sup> state and weak emission from the B0<sup>+</sup> state and high vibrational levels of the A0<sup>+</sup> state [16]. If the reaction



contributed to the observed strong chemiluminescence, this would require that the BiF bond energy exceed 4.45 eV [16,17]. Since the dissociation energy of BiF is close to 4 eV, the reaction (2) can produce only vibrationally excited ground state BiF. The Bi<sub>2</sub> present as a substantial constituent of the bismuth flux must react to produce BiF excited electronic states via the four center reaction [16,24]

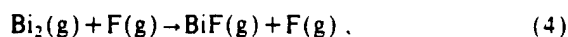


Since the  $\nu=6$  level of the B0<sup>+</sup> state and high vibrational levels of the A0<sup>+</sup> (II) state ( $\nu' > 20$  was identified with certainty in ref. [16] and Ross et al. [15] reported  $\nu'=26$  under similar experimental conditions) are populated, at least 3.7 eV of excess energy can be deposited into the product molecules formed via reaction (3). If we ignore the possible internal energy in the reactants and use 3.76 eV as the dissociation energy of BiF, reaction (3) can generate approximately 3.9 eV in one of the BiF products. Thus, up to  $\approx 95\%$  of the available reaction exothermicity can be deposited into one of the two product BiF molecules during the reaction! This large percentage of the reaction energy, pooled into only one of the product species, suggests that it may be possible to use chemiluminescent dimer reactions to provide reasonable estimates for bond energies. Further investigation will be needed to (1) determine if this conclusion will hold in general and (2) assess the

conditions under which this limit is reached. If this is a general result, the energetics of chemiluminescent cluster reactions could provide insight into cluster binding energies as well as product dissociation energies.

### 3. The Bi<sub>2</sub>-F reaction

The chemiluminescence from the reaction



where the F atoms are produced via a discharge through SF<sub>6</sub> has now been more thoroughly investigated [16,17]. The  $\nu'=4$  level of the BiF A0<sup>+</sup> state is populated by the reaction but emission from the B0<sup>+</sup> state and high vibrational levels of the A0<sup>+</sup> state are not readily observed. Approximately 3 eV of excess energy is required to produce the observed emission. Since reaction (3) is exothermic by less than 2 eV, Yoo et al. [18] questioned whether the Bi<sub>2</sub>+F reaction was studied [16] by Devore et al. and suggested that F<sub>2</sub> production in the discharge provided the necessary reactant to produce the observed emission in the bismuth vapor/SF<sub>6</sub> discharge system. This possibility was carefully considered [16]. There is no evidence to support the assumption that F<sub>2</sub> is present in the discharge system. The spectrum of the SF<sub>6</sub> discharge was examined [17] to determine if F<sub>2</sub> molecules were produced. A dispersed spectrum of the directly viewed discharge through pure SF<sub>6</sub> reveals (fig. 1) considerable F atom emission, some HF emission, and an as yet unidentified sulfur-based emitter (possibly SF<sub>5</sub>); however, the orange F<sub>2</sub> recombination emission bands [25], which are readily detected, were not observed. Further, if we examine the discharge tube configuration in a direction perpendicular to the reactant exit port, we monitor no emission. The generated potential reactants are relaxed to their ground states (or very low-lying excited states) before exiting the discharge source [17]. While it is possible that the SF<sub>6</sub> cylinder may have contained some F<sub>2</sub>, this does not seem likely. Finally, we observe [16] that there are several significant differences in the BiF spectra observed for the F<sub>2</sub> based reactive system and the F atom-Bi<sub>2</sub> reaction (3) which have been detailed previously [16,17]. Consequently, clear evidence against an F<sub>2</sub> contaminant

<sup>21</sup> Using  $D_0^0(\text{BiF}) \geq D_0^0(\text{Bi}_2) + E_{\text{internal}}(\text{BiF}) - E_{\text{internal}}(\text{Bi}_2) - E_{\text{Trans}}(\text{F})$ . For  $D_0^0(\text{Bi}_2)$ , see ref. [23].

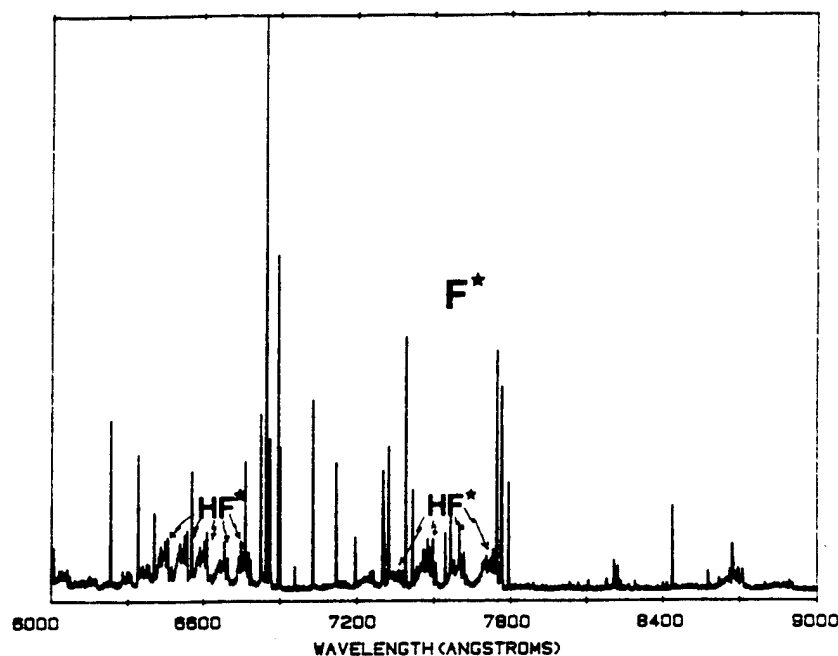


Fig. 1. Emission spectrum observed in the region  $\lambda > 600$  nm after passing a high voltage discharge through  $\text{SF}_6$ . The spectrum was obtained by aligning the discharge with a spectrometer monitoring the emission. The sharp line-like features correspond to fluorine atom transitions. The open structure band-like features correspond to HF overtone transitions. Spectral resolution is 0.1 nm.

is obtained. Further, it is clear from the F atom emission associated with the  $\text{SF}_6$  discharge, that considerable energy has been provided to the F atoms. We observe the reaction of hot F atoms with bismuth vapor.

#### 4. The Birge-Sponer extrapolation - bonding parameterization

Yoo et al. [18] have attempted to evaluate the accuracy of the Birge-Sponer extrapolation in determining the dissociation energy of BiF. Contrary to the image left by their discussion, we [16] did not explore this concept previously. The statement made in the introduction of ref. [16] is based on the discussion given by Gaydon [14] and later reiterated by Atkins [26], meant to note that the Birge-Sponer extrapolation can yield an upper bound to the bond energy. Nevertheless, the evaluation of the Birge-Sponer extrapolation for the group 15 halides is a noble undertaking since the dissociation energies for these molecules are not well established and are derived, at

least in part, from these extrapolations [17]. Yoo et al. [18] performed a linear least-squares extrapolation of the last 10 ground state vibrational levels ( $v'' = 26.5$  to 36.5) reported by Ross et al. [15] to estimate a value for  $D_0(\text{BiF})$  of 4.17 eV. This determined bond energy is notably larger than the experimental value of 3.76 eV which they found for the dissociation energy. The extrapolation, using only the last 10 observed levels is, of course, arbitrary and their motivation for choosing these levels for the extrapolation is not clear. As shown in table 2, a different value for the dissociation energy is obtained depending upon the number and location of the levels used in the extrapolation. Interestingly, if all 36 ground state energy levels reported by Ross et al. [15] are used for a linear least-squares treatment,  $D_0$  is estimated to be 3.83 eV, a value which is within experimental error of the experimentally determined dissociation energy. However, as demonstrated in the Birge-Sponer plot of fig. 2, the vibrational energies are clearly non-linear. Both the lower and the higher vibrational levels lie above the least-square line suggesting that a linear extrapolation will underestimate

Table 2

Apparent values determined for the dissociation energy of BiF by linear Birge-Sponer extrapolation using a subset of the ground state energy levels determined by Ross et al. [15]

Levels used	$D_0$ (eV)
0-5	3.38
0-10	3.45
0-15	3.55
0-20	3.62
0-25	3.69
0-30	3.75
0-36	3.83
5-36	3.85
10-36	3.89
16-36	3.99
21-36	4.06
26-36	4.17
31-36	4.30

the dissociation energy determined on the basis of evaluating the area under the  $\Delta G_{v+1/2}$  versus  $v$  curve. If only the first five energy levels are used, a typical experimental limitation, the value determined on the basis of linear extrapolation, 3.38 eV, is roughly 10% low. At least for BiF, extrapolations for the first few levels underestimate the dissociation energy while

extrapolations from the upper levels, for which the second-order anharmonicity correction term is beginning to become important, overestimate the dissociation energy. If this trend would hold in general it may be possible to establish upper and lower limits for the dissociation energy using this approach.

Yoo et al. [18] suggest that the dissociation energies obtained from linear Birge-Sponer plots can be modified to give excellent estimates for the dissociation energy by using the corrections for ionicity suggested by Hildenbrand [27,28]. In this case, they predict dissociation energies for the group 15 halides in excellent agreement with the experimental values using a linear Birge-Sponer extrapolated dissociation energy based upon only the first few observed ground state energy levels. While this might be a very encouraging result, *it is discomfoting to note that as more levels are added, the agreement between the experimental value and the predicted value becomes worse.* A better strategy here might be to use the well known relationship between the harmonic vibrational frequency and the first anharmonicity constant [29,30] for the Morse potential

$$D_e \approx \omega_e^2 / 4\omega_e x_e$$

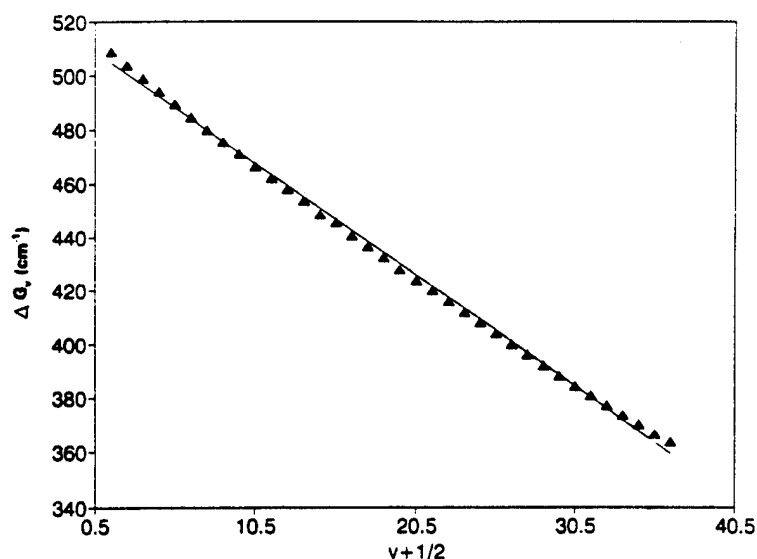


Fig. 2. Comparison of observed vibrational spacings for the  $v'' = 0.5-36.5$  levels of the ground  $X0^+$  state of BiF with a linear least-squares Birge-Sponer extrapolation using the entire manifold of known ground state energy levels. The deviation of the observed data from linearity can readily be seen. See text for discussion.

to estimate the uncorrected dissociation energy in the Hildenbrand equations. These corrections would then be independent of the number of levels used and the corrections could be related to modifications in the potential well due to ionicity. Investigations into the reliability of this approach are in progress.

It should be possible to accurately determine the dissociation energy from extended spectroscopic data such as that available for BiF. The data of Ross et al. [15] can be fit to a power series to evaluate the spectroscopic constants. These constants can then be used to calculate all of the vibrational spacings below the dissociation limit. The dissociation energy was evaluated by summing over all vibrational spacings [30].

$$D_0 = \sum_v \Delta G_{v+1/2}$$

with

$$\Delta G_{v+1/2} = \omega_e - 2\omega_e x_e(v+1) + \omega_e y_e(3v^2 + 6v + \frac{13}{4})$$

Although very good data exist for ground state levels up to  $v=36$ , the constants derived from non-linear analysis do not give  $\Delta G_{v+1/2}$  values that converge to zero for fits up to sixth order. Since higher-order fits are not experimentally justified, further evaluation has been limited to a second-order analysis. The constants derived for a second-order fit are given in table 3. Vibrational spacings calculated using these constants reach a minimum near  $v=120$ . If a small third-order correction term is added to make  $\Delta G_{v+1/2}=0$  at  $v=120$ , the dissociation energy calculated for BiF by summing over the vibrational energies is 3.8 eV; a value agreement to within experimental error of the measured value. Although there is some uncertainty in the parameterization, it is likely that this procedure will provide good estimates for the vibrational energy if enough vibrational levels are known so as to

Table 3  
Molecular constants determined by fitting the energy levels of Ross et al. [15] to the equation  $v=a+bv+cv^2+dv^3$ , where  $a=\omega_e-2\omega_e x_e+\frac{13}{4}\omega_e y_e+\dots$ ,  $b=-2\omega_e x_e+6\omega_e y_e+\dots$ ,  $c=3\omega_e y_e+\dots$

Constant	Value determined	Lit. Value
$\omega_e$	513.33	512.81 cm <sup>-1</sup>
$\omega_e x_e$	2.424	2.35 cm <sup>-1</sup>
$\omega_e y_e$	$6.248 \times 10^{-1}$	- cm <sup>-1</sup>
$d$	$1 \times 10^{-4}$	- cm <sup>-1</sup>
$D_0$	3.8	3.76 eV

provide a reasonable estimate for the anharmonicity constants.

### Acknowledgement

We thank David Grantier and Jeffrey Kispert for helpful assistance with the additional experiments outlined here and acknowledge data taken from the work of John Bray on the Cu<sub>x</sub>+F system, Lauri Brock, Dawn Jordan, and Kenneth Dulaney on the Mn<sub>x</sub>+F system, C.B. Winstead and H. Wang on the Mg<sub>x</sub>+F system, and He Wang on the Ag<sub>x</sub>+F system. TCD would like to thank the NSF-RUI program (CHE8900938) for partial support of this research. JLG acknowledges helpful communications with R. Bacis, B. Koffend, Michael Heaven, E. Dorko, T. Cool and E.H. Fink, who provided his results prior to publication. JLG also acknowledges the Air Force Office of Scientific Research-Army Research Office and the Strategic Defence Initiative for partial support of this research.

### References

- [1] A.E. Douglas and M. Frackowiak, Can. J. Phys. 40 (1962) 832.
- [2] L.V. Gurvich et al., Thermodynamic properties of individual substances, Vols. 1, 2 (USSR Academy of Sciences, Moscow, 1962) [in Russian].
- [3] P.A. O'Hare, R. Batana and A.C. Wahl, J. Chem. Phys. 59 (1973) 6495.
- [4] N.L. Singh and M.N. Avasthi, Indian J. Pure Appl. Phys. 1 (1963) 197.
- [5] W. Jevons, Proc. Phys. Soc. 48 (1936) 563.
- [6] H.G. Howell and G.D. Rochester, Proc. Phys. Soc. 51 (1939) 329.
- [7] T.A.P. Rao and P.T. Rao, Indian J. Phys. 36 (1962) 85.
- [8] F. Morgan, Proc. Soc. 49 (1936) 41.
- [9] S. Sankaranarayanan, M.M. Patel and P.S. Narayan, Proc. Indian Acad. Sci. 56 (1962) 171.
- [10] D. Cubicciotti, J. Phys. Chem. 64 (1960) 791.
- [11] P. Venkateswarlu and B.N. Khanna, Proc. Indian Acad. Sci. A51 (1960) 14.
- [12] K.C. Joshi, Proc. Phys. Soc. 78 (1961) 610.
- [13] S. Sankaranarayanan, P.S. Narayanan and M.M. Patel, Proc. Indian Acad. Sci. 59 (1964) 378.
- [14] R.B. Singh and D.K. Rai, Can. J. Phys. 43 (1965) 829.
- [15] A.G. Gaydon, Dissociation energies and spectra of diatomic molecules, 3rd Ed. (Chapman and Hall, London, 1968).

- [15] A.J. Ross, R. Bacis, J. D'Incan, C. Effutin, B. Koffend, A. Topouzkhanian and J. Verges, *Chem. Phys. Letters* 166 (1990) 539.
- [16] T.C. Devore, L. Brock, R. Kahlscheuer, K. Dulaney and J.L. Gole, *Chem. Phys.* 155 (1991) 432.
- [17] J.L. Gole, in: *Gas phase metal reactions*, ed. A. Fontijn (North-Holland, Amsterdam, 1992) pp. 578-604.
- [18] R.K. Yoo, B. Ruscic and J. Berkowitz, *Chem. Phys.* 166 (1992) 215.
- [19] J.M. Herbelin and R.A. Klingberg, *Intern. J. Chem. Kinetics* 16 (1984) 849;  
R.F. Heidner III, H. Helvajian, J.S. Holloway and J.B. Koffend, *J. Chem. Phys.* 84 (1986) 2137;  
D.J. Benard and B.K. Winker, *J. Appl. Phys.* 69 (1991) 2805.
- [20] B. Rai and J. Singh, *Spectry. Letters* 4 (1971) 129.
- [21] W.E. Jones and T.D. McLean, *J. Mol. Spectry.* 83 (1980) 317.
- [22] R.J. Leroy, in: *Molecular spectroscopy*, Vol. 1, eds. R.F. Barrow, D.A. Long and D.J. Millen (Chemical Society, London, 1973) p. 113; *J. Chem. Phys.* 73 (1980) 6003.
- [23] F. Kohl, O.M. Uy and K.D. Carlson, *J. Chem. Phys.* 47 (1967) 2667;  
D. Rouner, A. Drowart and J. Drowart, *Trans. Faraday Soc.* 63 (1967) 2906.
- [24] J.M. Parson, B.S. Cheong, R.P. Kampf and M.D. Oberlander, Effects of electronic excitation and dimerization of metals on product state distributions, in: *Gas phase metal reactions*, ed. A. Fontijn (North-Holland, Amsterdam, 1992).
- [25] H.G. Gale and G.S. Monk, *Astrophys. J.* 69 (1929) 77;  
T.L. Porter, *J. Chem. Phys.* 48 (1968) 2071.
- [26] P.W. Atkins, *Physical chemistry*, 4th Ed. (Freeman, San Francisco, 1990) p. 487.
- [27] D.L. Hildenbrand, *Advances in high temperature chemistry*, Vol. 1 (Academic Press, New York, 1967) p. 193.
- [28] D.L. Hildenbrand and E. Murad, *J. Chem. Phys.* 51 (1969) 807.
- [29] G. Herzberg, *Molecular spectra and molecular structure*, Vol. 1, *Spectra of diatomic molecules* (Van Nostrand, Princeton, 1950) p. 439.
- [30] J.M. Hollas, *Modern spectroscopy* (Wiley, New York, 1987) p. 119.

### APPENDIX III

"Evidence for Continuous Visible Chemical Lasing from the Fast Near Resonant Energy Transfer Pumping of Atomic Sodium", K. K. Shen, H. Wang, and J. L. Gole, JQE 29 , 2346 (1993).

# Evidence for Continuous Visible Chemical Lasing from the Fast Near Resonant Energy Transfer Pumping of Atomic Sodium

K. K. Shen, H. Wang, and J. L. Gole

**Abstract**—Energy transfer from selectively formed metastable states of SiO is used to pump sodium atom laser amplifiers at  $\lambda \approx 569$  nm ( $4d^2D-3p^2P$ ),  $\lambda \approx 616$  nm ( $5s^2S-3p^2P$ ), and  $\lambda \approx 819$  nm ( $3d^2D-3p^2P$ ). The  $a^3\Sigma^+$  and  $b^3\Pi$  states of SiO are generated in high yield from the  $\text{Si} + \text{N}_2\text{O} \rightarrow \text{SiO} + \text{N}_2$  reaction. The energy stored in the triplet states is transferred in a highly efficient collisional process to pump sodium atoms to their lowest excited  $3d^2D$ ,  $4d^2D$ , and  $5s^2S$  states. Adopting a sequence in which high concentrations of silicon and sodium atoms are mixed and oxidized, we monitor a *continuous* amplification (gain condition) which suggests the creation of a population inversion among the receptor sodium atom energy levels and forms the basis for full cavity oscillation on the Na  $4d^2D-3p^2P$  transition at 569 nm. The generic concept employed to create amplification and oscillation in this system should also be applicable to the efficient energy transfer pumping of potential amplifying transitions in potassium (K), lead (Pb), copper (Cu—analogue of Cu vapor laser), and tin (Sn) receptor atoms.

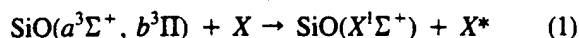
## I. INTRODUCTION

THE development of visible chemical lasers has continued to represent an elusive and challenging scientific problem for the past quarter century [1]. In addressing this challenge, [2]–[6] we have recently been concerned with the development of two generic approaches, utilizing the inherently large cross sections which characterize certain electronic energy transfer processes [7] to create population inversions on electronic transitions. We rely on a limited group of selective, fast, and direct “electron jump” chemical reactions [2] or on highly efficient intramolecular or intermolecular energy transfer processes [3]–[6] involving electronically excited states. Here, we address the creation of an electronically inverted atomic configuration through highly efficient intermolecular energy transfer from electronically excited metastable storage states to atomic receptors with a high propensity for lasing action. We present evidence for the electronic-to-electronic (E–E) energy transfer pumping of

sodium atom based amplifiers corresponding to the Na  $4d^2D-3p^2P$ ,  $5s^2S-3p^2P$ , and  $3d^2D-3p^2P$  transitions at  $\sim 569$ ,  $\sim 616$ , and  $\sim 819$  nm and the concomitant full cavity oscillation on the  $4d^2D-3p^2P$  transition at  $\lambda \approx 569$  nm.

In order to pump the Na atom levels ( $3d^2D$ ,  $4d^2D$ ,  $5s^2S$ ) of interest in this study, we first must form sufficient quantities of the metastable SiO  $a^3\Sigma^+$  and  $b^3\Pi$  states as the products of the primary spin conserving  $\text{Si}-\text{N}_2\text{O}^8$  and  $\text{Si}-\text{NO}_2^9$  reactions. One might envision the SiO “ $a^3\Sigma^+$ ” and “ $b^3\Pi$ ” metastable states (lifetimes estimated to be between  $10^{-1}$  and  $10^{-3}$  s) as a combined metastable triplet state reservoir which is, at best, weakly coupled to the ground electronic  $X^1\Sigma^+$  state of the metal oxide. As a result of their long radiative lifetime, these reservoir states can be maintained and subsequently made to transfer their energy to pump selected atomic transitions. To first order, such a pumping process for the atomic receptor will be most efficient if a near resonant energy exchange from the metastable metal oxide reservoir is feasible.

We make use of the efficient intermolecular energy transfer process



where  $X^*$  represents the electronically excited atomic species from which we wish to obtain lasing action and the SiO  $a^3\Sigma^+$  and  $b^3\Pi$  states are formed under multiple collision conditions in a focused argon or helium entrainment flow such that the nascent product distribution of the  $\text{Si}-\text{N}_2\text{O}^8$  or  $\text{Si}-\text{NO}_2^9$  reactions is rotationally thermalized and vibrationally relaxed [3, Fig. 4] to the lowest levels of the triplet state manifold. The success of this outlined scheme depends on the rates for the reactions forming the SiO or GeO metastables [10], [11] and the rate of the  $MO^*$  ( $M = \text{Si}, \text{Ge}$ )– $X$  intermolecular energy transfer, which, we anticipate, will be influenced by the nature of near resonances between the  $MO^*$  and  $X^*$  energy levels.

The outlined energy transfer process is found experimentally to be quite efficient for sodium (as well as potassium) atoms. To an even greater degree than that inherent to the previously studied chemically pumped Tl-based [3]–[6] amplifier–oscillator system [3, Tables I and II] at  $\lambda \approx 535$  nm, there exist near resonant matchups ( $\Delta E \approx 100 \text{ cm}^{-1}$ ) to receptor atom levels of interest in

Manuscript received January 4, 1993. This work was supported by the Georgia Tech Foundation through a grant from Mrs. Betty Peterman Gole, the Army Research Office through the Short Term Innovative Research Program, the Air Force Office of Scientific Research, and the Army Research Office and AFOSR/SDIO.

This paper is dedicated to the memory of Dr. Les Karlovitz, whose enthusiasm for life and the pursuit of academic excellence as the Dean of the College of Science and Liberal Studies will always be revered.

The authors are with the School of Physics, Georgia Institute of Technology, Atlanta, GA 30332.

IEEE Log Number 9210255.

TABLE I  
NEAR RESONANCES OF  $\text{SiO}^*$  ( $a^3\Sigma^+$ ,  $b^3\Pi-X^1\Sigma^+$ ) AND SELECT Na AND K  
ATOMIC TRANSITIONS IN ENERGY TRANSFER LASER PUMPING<sup>a</sup>

Atom	Upper Atomic Level	$\text{SiO}(v', v'')$			
		$a - X$		$b - X$	
		Trans.	$\Delta E(\text{cm}^{-1})^b$	Trans.	$\Delta E(\text{cm}^{-1})^b$
Na	$4d^2D_{5/2,3/2}$	—	—	(1,0) (2,1) (3,2)	294 45 -209
Na	$5s^2S_{1/2}$	(0,0)	200	(2,2) (3,3)	177 67
Na	$3d^2D_{5/2,3/2}$	(1,4)	180	(0,4)	-184
Na	$6s^2S_{1/2}$	(4,0)	155	(4,1)	137
Na	$4s^2S_{1/2}$	No near resonances			
K	$4d^2D_{5/2,3/2}$	(0,5)	-25	(2,7)	60
K	$5d^2D_{5/2,3/2}$	(0,3)	-420	(0,3)	20
K	$6s^2S_{1/2}$	(0,5)	-70	—	—
K	$6d^2D_{5/2,3/2}$	—	—	(0,2) (4,5) (3,4)	-286 40 264
K	$7s^2S_{1/2}$	—	—	(0,3)	-69

<sup>a</sup>Listed potential resonances for potassium are meant to be indicative but not exhaustive.

<sup>b</sup>—Molecular level energy—Atom level energy. Positive quantities denote exothermic energy transfer.

atomic sodium (and potassium) for both SiO and GeO metastables. We are concerned with the energy transfer pumping of levels which are not accessed through strong electric dipole transitions from the ground state of the alkali atom. Applying these criteria, we summarize the nature of relevant near resonances for the lowest vibrational levels of the  $a^3\Sigma^+$  and  $b^3\Pi$  states in Tables I and II. For the SiO–Na system, Table I suggests that the sodium  $4d^2D$  level might be the most easily pumped followed closely by the  $5s^2S$  level. The  $3d^2D$  and  $6s^2S$  levels appear somewhat less promising, with the potential resonances involving the  $3d^2D$  level and the lowest  $b^3\Pi$  vibrational levels being more favorable.

Collisions with SiO or GeO metastables [3] are used to energy transfer pump from the  $3s^2S$  Na ground state ( $4s^2S$  in K) to the  $4d^2D$  and  $5s^2S$  levels ( $5d^2D$  and  $6s^2S$  in K), forming the basis for amplification on the  $4d^2D-3p^2P$  ( $\lambda \approx 569$  nm) and  $5s^2S-3p^2P$  ( $\lambda \approx 616$  nm) transitions. In the sodium system (Fig. 1(a)), the  $3p^2P$  terminal laser level is the short-lived upper level of the Na D-line. The  $3p^2P-3s^2S$  transition is characterized by a high oscillator strength. This facilitates rapid loss of the terminal laser level to create ground state sodium atoms which, as Figs. 1(a) and (b) demonstrate, are again amenable to near resonant energy transfer pumping.

While the  $5s^2S$  and  $4d^2D$  levels are not readily accessed in an optically pumped transition, Fig. 1(b) demonstrates that, using SiO metastables formed in the Si–N<sub>2</sub>O reaction, we have successfully energy transfer pumped Na atoms to the  $^2S$  and  $^2D$  levels where they subsequently emit radiation at  $\lambda \approx 616$  nm and 569 nm as they undergo transition to the  $3p^2P$  levels. The energy transfer process which pumps these sodium atom levels appears at least as efficient as that observed for the T1 system [3—Figs. 4,

TABLE II  
NEAR RESONANCES OF  $\text{GeO}^*$  ( $a^3\Sigma^+$ ,  $b^3\Pi-X^1\Sigma^+$ ) AND SELECT Na AND K  
ATOMIC TRANSITIONS IN ENERGY TRANSFER LASER PUMPING<sup>a</sup>

Atom	Upper Atomic Level	$\text{GeO}(v', v'')$			
		$a - X$		$b - X$	
		Trans.	$\Delta E(\text{cm}^{-1})^b$	Trans.	$\Delta E(\text{cm}^{-1})^b$
Na	$3d^2D_{5/2,3/2}$	(2,0) (3,0) (0,2)	-367 250 130	(0,3)	-73
Na	$4s^2S_{1/2}$	—	—	(6,0)	-180
Na	$6s^2S_{1/2}$	—	—	(2,0)	245
Na	$5s^2S_{1/2}$	—	—	(3,0) (4,0)	-401 293
K	$4d^2D_{5/2,3/2}$	(0,0) (1,1)	160 -195	—	—
K	$5d^2D_{5/2,3/2}$	(4,0)	-149	(0,2)	-123
K	$6s^2S_{1/2}$	(0,0)	110	—	—
K	$6d^2D_{5/2,3/2}$	—	—	(2,2)	-185
K	$7s^2S_{1/2}$	(4,0)	-240	(0,2)	-110

<sup>a</sup>Listed potential resonances are meant to be indicative but not exhaustive.

<sup>b</sup>—Molecular level energy—Atom level energy. Positive quantities denote exothermic energy transfer.

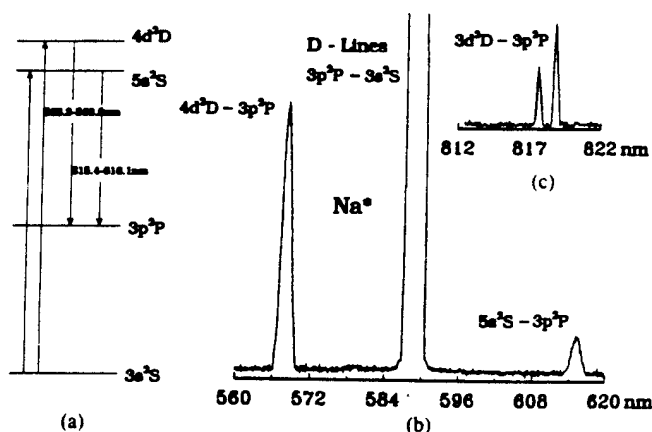


Fig. 1. (a) Na atom energy level scheme and pumping cycles to produce  $4d^2D$  and  $5s^2S$  excited states. (b) Typical energy transfer pumping spectrum for Na  $4d^2D-3p^2P$  and  $5s^2S-3p^2P$  transitions and  $3p^2P-3s^2S$  sodium D-line emission. The D-line emission results both from direct energy transfer pumping from ground state NaO and from subsequent fluorescence following emission to the  $3p^2P$  level. (c) Energy transfer pumping spectrum corresponding to Na  $3d^2D-3p^2P$  transition.

5]. The observed Na atom transitions, originating at the  $4d^2D$  and  $5s^2S$  levels, are characterized by moderate oscillator strengths. The accessed Na cycle, with its 50 ( $4d^2D-3p^2P$ ) [13] to  $\sim 100$  ( $5s^2S-3p^2P$ ) [14] nanosecond upper state radiative lifetimes (vs.  $T_1^2S_{1/2}$  at  $\sim 7$  ns [15]), and short-lived terminal laser level, would appear ideally suited to obtain high duty cycle laser amplifiers and oscillators. In fact, we find that these transitions demonstrate continuous gain. Further, as indicated in Fig. 1(c), we have obtained evidence for the energy transfer pump of the Na  $3d^2D$  level with which is associated an atomic emission at  $\lambda \approx 819$  nm ascribed to the Na  $3d^2D-3p^2P$  transition. We consider a range of measurements on the Si–SiO–Na system used to demonstrate continuous gain on the  $4d^2D-3p^2P$ ,  $5s^2S-3p^2P$ , and  $3d^2D-3p^2P$  transi-

tions at  $\lambda \approx 569$ ,  $\lambda \approx 616$ , and  $\lambda \approx 819$  nm, respectively, and present evidence for continuous oscillation at  $\lambda \approx 569$  nm. Appropriate spontaneous emission rates, degeneracy factors, and energy increments for the transitions of interest are summarized in Table III.

## II. EXPERIMENTAL

### A. "Creation of Reaction—Energy Transfer—Amplification Zone"

The reaction—energy transfer—amplification zone depicted in several views in Fig. 2 has been constructed to provide a versatile, moderate path length, amplification device. The apparatus is configured such that the Si(Ge)—SiO(GeO) source moves vertically and the Na(K) source moves horizontally relative to the amplification zone. The silicon source construction which provides an enveloping, focusing, and oxidizing sheath about the vaporizing silicon metalloid flux, is designed to concentrate the SiO metastable concentration in the vicinity of the amplification zone [3], [6]. With the silicon source temperature monitored by optical pyrometry, we estimate the Si atom concentration in the amplification zone as a minimum of  $10^{14}$ /cc for all studies involving gain measurement. The  $N_2O$  oxidant concentration exceeds  $5 \times 10^{14}$ /cc and the SiO metastable concentration exceeds  $10^{13}$ /cc based on a quantum yield exceeding 10% [16] for the spin conserving  $Si(^3P) + N_2O(^1\Sigma^+) \rightarrow SiO(a^3\Sigma^+, b^3\Pi) + N_2(^1\Sigma_g^+)$  reaction [3], [6], [8]. The Si—SiO flow configuration was operated with the silicon source temperature ranging between 1600 and 1800°C with the majority of the gain measurements conducted at the highest temperatures. The helium or argon entraining flow rate ranged between 300 and 450 mL/min, and the  $N_2O$  flow rate ranged between 1 and 5 mL/min. The conditions which we outline are adjusted to produce maximum gain in a given experiment and provide the longest path length SiO metastable flame yet realized.

The entrained Si—SiO flow is intersected at 90°, in subsonic flow, by a flux of sodium atoms which, based upon the Na source temperature and the measured rate of expenditure of sodium from the source, exceeds  $10^{18}$ /cm<sup>2</sup>-s in the reaction zone, corresponding to a density of order  $10^{13}$ /cc. The concentration of Na atoms is controlled experimentally, through the appropriate choice of oven source temperature and entrainment flow, to provide maximum gain under the conditions of a given experiment. To provide the necessary flux, the temperatures of the Na source oven range between 400 and 500°C for the reservoir and 480–550°C for the entrainment flow channel (Fig. 2); typical helium or argon entrainment flow through the sodium source ranges between 30 and 90 mL/min. The entrained Si and Na flows can also be moved *in situ* relative to each other and with respect to the reaction—energy transfer—amplification zone to optimize conditions for formation of the gain medium. Typically, the silicon source is maintained in a preset stationary position while the sodium slit source is moved to a

position elevated so as to provide maximal interaction of the intersecting flows at the focus of the enveloped SiO metastable flame. The separation of the two sources is usually of the order 2 cm. It should be emphasized that the chemiluminescent emission from the Si/ $N_2O$  "flame" is negligible in the 510–630 nm region where gain measurements (see also Fig. 5 following) on the  $Na\ 4d^2D-3p^2P$  ( $\lambda \approx 569$  nm) and  $5s^2S-3p^2P$  ( $\lambda \approx 616$  nm) emission features are performed.

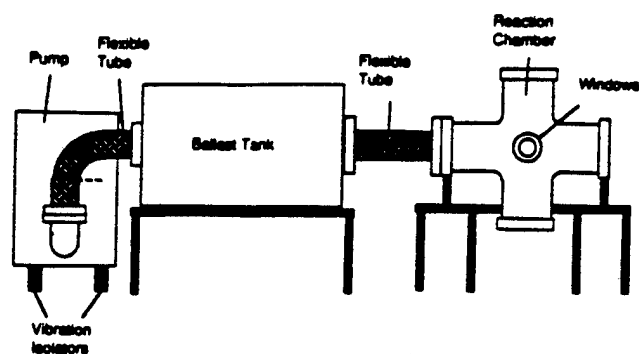
The mixing zone of Fig. 2 is greatly stabilized by the moderate sized (15 cubic feet) ballast separating the 150 cfm pump from the reaction chamber which it evacuates. Typical measured background pressures range between 10 and 30 mtorr whereas operating pressures, as measured by a thermocouple gauge well separated from the reaction zone, range between 500 and 1200 mtorr. Because there is a substantial pressure gradient between the reaction zone and the position of the monitoring thermocouple, the recorded pressures are at least 50% lower than the true pressure in the amplification region. In order to protect the cavity windows from the condensation of silicon oxide or sodium, "self-flushing" optical windows [17] were operated with a protective helium flow.

Using the described configuration, we have created an amplification zone from which we can monitor gain, as a function of slightly varying experimental conditions, on the  $Na\ 4d^2D-3p^2P$  ( $\lambda \approx 569$  nm),  $5s^2S-3p^2P$  ( $\lambda \approx 616$  nm) and  $3d^2D-3p^2P$  ( $\lambda \approx 819$  nm) transitions.

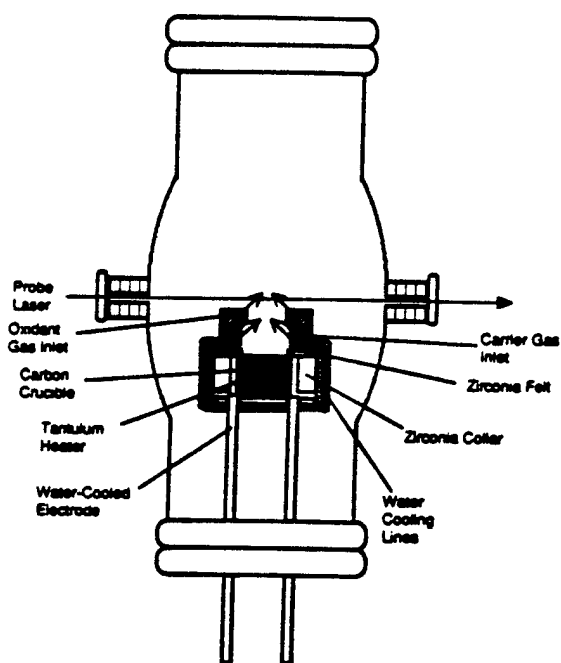
### B. Measurement of Optical Gain (Amplification)

1) *Roll-Mental Configuration*: Gain measurements have been carried out on the Si—SiO—Na system using three different experimental configurations. The simplest of these measurements was performed using the optical train depicted in Fig. 3(a). This device parallels the ingenious design of Roll and Mental [18] to study amplified spontaneous emission in HeSe lasers.  $L$  denotes the length of the gain medium created upon interaction of the SiO and the Na flows. The amplification zone, under vacuum, is surrounded (Fig. 3(a)) by two AR-coated windows (CVI PW2037C) or two Brewster angle windows (CVI W-B25SS) connected outside the self-flushing optical window denoted in the previous section.

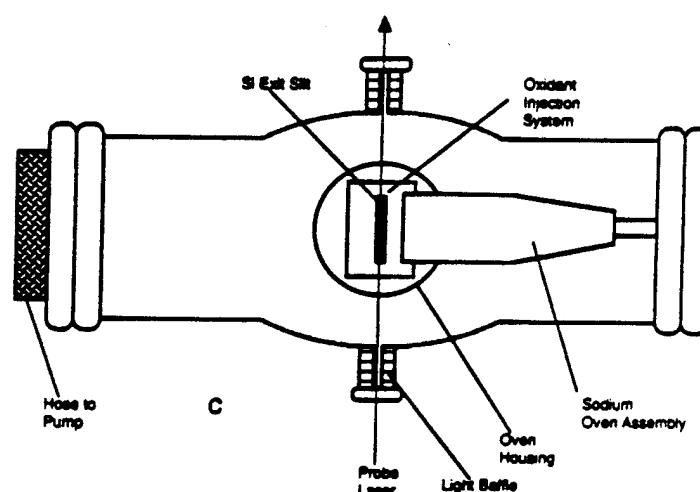
Several flat mirror high reflectors were employed with the Roll-Mental optical train, ranging in reflectivity from 96 to 99.9% and varying in surface coating and substrate. All of these high reflectors yielded closely comparable results, similar to those in Fig. 5, when employed for gain measurements. The output from the surrounding gain medium was sent through a Fourier aperture (pinhole) and into a monochromator using lenses 1 and 2. The monochromator allowed separation of individual emission features. Coarse alignment for both the gain configuration depicted in Fig. 3(a) and the full cavity (oscillator) configuration depicted in Fig. 3(b) was accomplished with a HeNe laser positioned as in Fig. 3(c) ~ 15 feet from the gain and full cavity configurations. After alignment, the



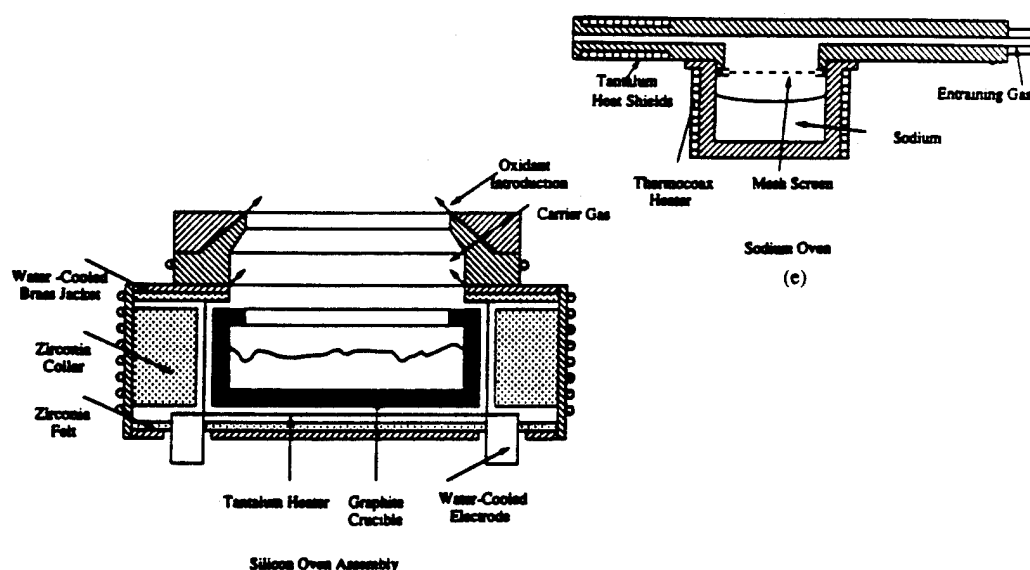
(a)



(b)



(c)



(d)

(e)

Fig. 2. (a) Schematic of reaction chamber and windows defining optical train, ballast tank to moderate pumping fluctuations, and pumping configuration, for extended path length Si-SiO (Si-N<sub>2</sub>O)-Na reaction amplification zone. (b), (c) Side and overhead views of reaction chamber showing positioning of Si oven source, relative locations of Si and Na oven sources, oxidant injection system, and relative positions of these devices with respect to the optical train. (d), (e) Closeup view of silicon and sodium oven assemblies.

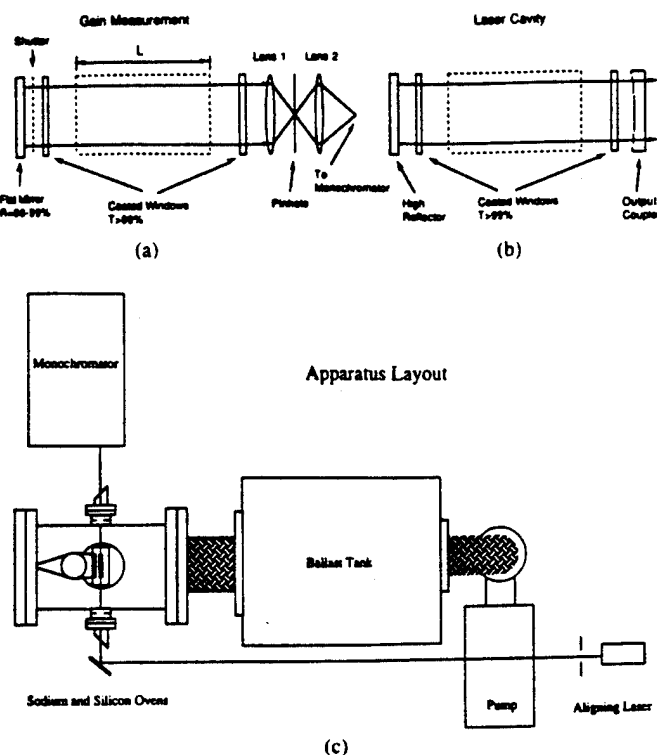


Fig. 3. (a) Gain measurement configuration after Roll and Mentel [18]. The region marked  $L$  in the figure corresponds to the reaction-amplification zone. (b) Laser cavity configuration to characterize potential oscillation in the Si-SiO-Na system at 569 nm. (c) Schematic overview of reaction chamber-amplification zone, ballast, and pump for extended path length Si-SiO(Si-N<sub>2</sub>O)-Na gain medium. The figure indicates the coarse alignment path ( $\sim 15$  ft) for the HeNe laser and its correlation with the optical train surrounding the reaction zone and terminating at the monochromator. See also Fig. 2.

HeNe laser is no longer an integral part of the system. In other words, the configurations (Fig. 3) operate without light sources external to the reaction-amplification zone. Thus these configurations are to be distinguished from the sodium lamp and ring dye laser based gain measurements depicted in Fig. 4.

2) *Sodium Discharge Lamp*: Using a sodium discharge lamp and the configuration depicted in Fig. 4(a), we have measured gain on the Na  $4d^2D-3p^2P$  transition at 569 nm. The enhancement of the Na  $4d^2D-3p^2P$  emission line (or other sodium transitions) is evaluated by isolating the transition of interest with a 10-nm bandpass filter. The lamp light output brought into the amplification zone is evaluated, and, if necessary, made comparable to the chemiluminescent intensity using neutral density filters positioned between the bandpass filter and lens at the beginning of the optical train.

A phase sensitive detection mode was used. The output intensity of the sodium discharge lamp was modulated at a frequency of 700 Hz. A beam splitter directs a portion of the lamp output signal to a photomultiplier providing the reference signal B. The remaining light is collimated, sent through the gain medium (amplification zone), and detected, after being dispersed by the monochromator. The output photomultiplier attached to the exit slit of the monochromator provides the signal for channel A. This

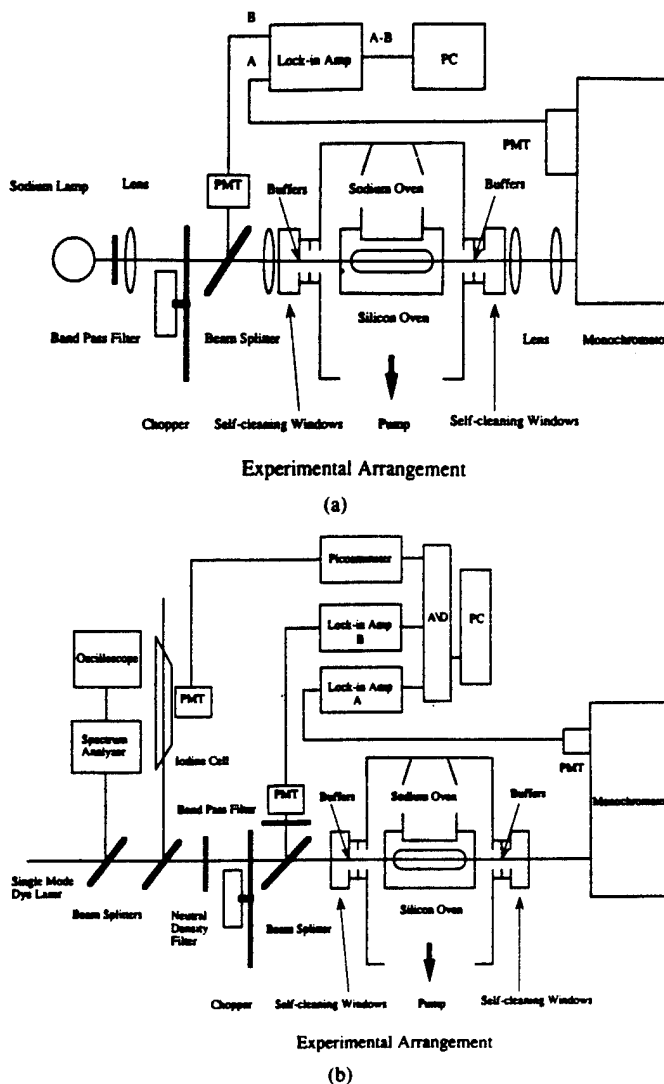


Fig. 4. (a) Schematic of Na-lamp based gain measurement configuration. The cross sectional area of the sodium lamp output, input to the reaction-amplification zone, greatly exceeds that of the gain medium. See text for discussion. (b) Schematic of ring dye laser based gain measurement configuration. The dye laser is operated single mode and scans the frequency range of the  $\lambda = 569$  nm Na  $4d^2D-3p^2P$  transition with calibration versus  $I_2$ . See text for discussion.

form of detection serves two purposes in this experiment. First, it allows selective monitoring of the chemiluminescent intensity during the period of the experiment, and second, it acts as a band pass filter peaked at the laser transition of interest, when the gain measurement is made. The A-B signal difference is sent to the lockin amplifier as the gain.

Before the detection of gain in the amplification zone, it is necessary to calibrate the A-B channel by evaluating the chemiluminescent signal. After optimizing the amplification zone conditions so as to maximize a continuous chemiluminescent signal, the oxidant (N<sub>2</sub>O) flow is cut off and the A-B lockin signal is balanced to a null value, corresponding to the complete absence of a chemiluminescent flame. For a typical run, as the N<sub>2</sub>O flow is turned on and off producing chemiluminescence, we record the train of peaks depicted in Fig. 6, corresponding to a con-

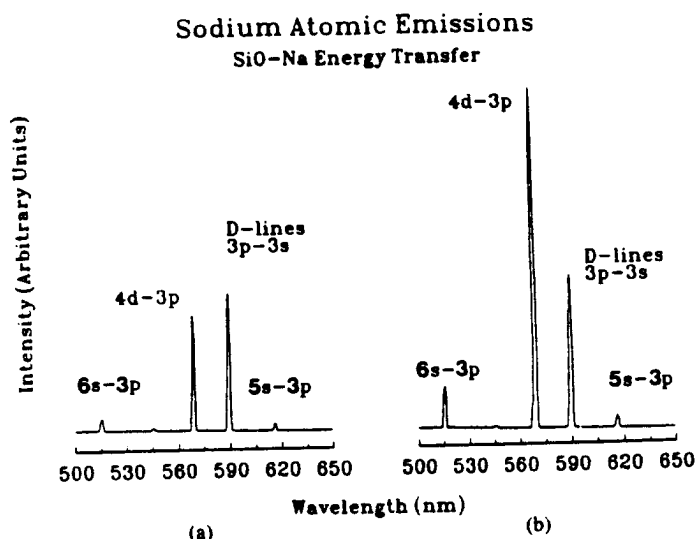


Fig. 5. (a) Single-pass continuous amplified spontaneous emission (ASE) intensity ( $I_1$ ) measured using a Spex 1 meter spectrometer and RCA 4840 phototube and the gain configuration depicted in Fig. 3(a) for the Si-SiO-Na system. Spectral resolution is 1 nm. Because the figure is uncorrected for photo-tube response, decreasing from 510 to 630 nm, or grating blaze (500 nm), the emission associated with the  $6s^2S-3p^2P$  transition appears more intense than that associated with the  $5s^2S-3p^2P$  transition. (b) Double pass continuous amplified spontaneous emission (ASE) intensity ( $I_2$ ) measured using the gain configuration depicted in Fig. 3(a) for the Si-SiO-Na system. The Na D-line intensity is comparable to that in Fig. 5(a). The ratio of the  $I_2/I_1$  intensity for the 569-nm Na emission feature is 2.6/1 for this individual study and can approach 3.8/1 under optimal conditions for the system. Spectral resolution is  $\sim 1$  nm (see (a)).

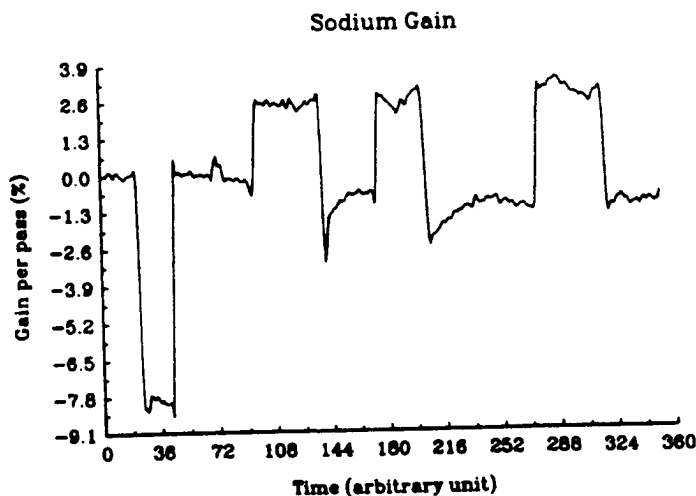


Fig. 6. Plot of gain per pass at  $\lambda = 569$  nm corresponding to the Na  $4d^2D-3p^2P$  transition. The negative peak corresponds to an 8% loss in the signal channel due to the insertion of a glass filter. The positive peaks (gain) correspond to the introduction of the oxidant  $N_2O$  into the reaction-energy transfer-amplification zone outlined in Figs. 2 and 4(a). See text for discussion.

tinuous gain condition during the period in which oxidant is supplied to the amplification zone.<sup>1</sup>

**3) Scanning High Resolution Ring Dye Laser:** We have also used a cw single mode ring dye laser (Spectra Physics 380A) to perform laser gain measurements in a

<sup>1</sup>We have also verified that the channel A signal will *not* increase as strong unchopped light is sent through the amplification zone-reaction chamber.

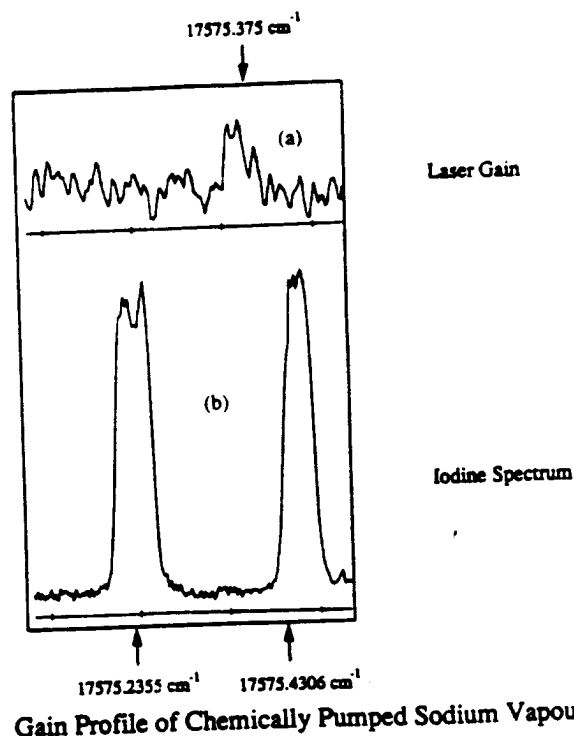


Fig. 7. (a) Continuous single-mode ring dye laser scan in the region of the  $\lambda = 569$  nm Na  $4d^2D-3p^2P$  transitions indicating a  $\sim 1.5\%$  gain at the frequency corresponding to the  $4d^2D_{5/2}-3p^2P_{3/2}$  transition (Table III). This represents a lower bound to the gain. (b)  $I_2$  calibration spectrum. See text for discussion.

frequency scanning (laser with calibration vs. iodine) mode (Fig. 4(b)). The dye laser pumped by a Spectra Physics Model 171  $Ar^+$  laser, was made to lase continuously without mode hopping over the time scale of a frequency scan in the region about 569 nm (using a mixture of R590 and R560 Rhodamine dyes). The behavior of the single mode ring dye laser output was continuously monitored using a Spectra Physics Model 450-03 spectrum analyzer. The absolute frequency was first crudely calibrated using a monochromator at 0.1 Å resolution and then monitored by comparison to a simultaneously generated high resolution  $I_2$  spectrum. In order to insure stable ring dye laser operation, the argon laser was operated at a power of 6–7 W. The dye laser output was maintained at  $\sim 200$  mW to prevent mode hopping.

Experiments were again carried out in an AC mode. After splitting a portion of the dye laser output to the spectrum analyzer and an  $I_2$  cell, the remaining portion was brought over a 30-ft path to the cavity configuration where, before passing through the amplification zone to the monochromator, the power level was further reduced, using neutral density filters, to a level comparable to the chemiluminescent intensity (still maintaining a reasonable S/N). To further reduce the noise level, the chopper (Fig. 4(b)) used in these experiments was operated at 700 Hz. In addition, two lockin amplifiers (Stanford Research, SR-510) were used to insure a proper phase lock for both the reference and signal channels. Using this experimental configuration, we generate and calibrate the laser gain spectrum depicted in Fig. 7. Here, the high res-

TABLE III  
SPONTANEOUS EMISSION RATES, DEGENERACY FACTORS, AND ENERGY INCREMENTS FOR Na  $4d^2D-3p^2P$ ,  $5s^2S-3p^2P$ , AND  $3d^2D-3p^2P$  TRANSITIONS<sup>a</sup>

Transition	Energy (cm <sup>-1</sup> )	A Value (10 <sup>7</sup> sec <sup>-1</sup> )	$g_u$	$g_l$
$4d^2D_{5/2}-3p^2P_{3/2}$	17575.375	1.2	6	4
$4d^2D_{3/2}-3p^2P_{3/2}$	17575.41	0.21	4	4
$4d^2D_{3/2}-3p^2P_{1/2}$	17592.606	1.03	4	2
$5s^2S_{1/2}-3p^2P_{3/2}$	16227.317	0.52	2	4
$5s^2S_{1/2}-3p^2P_{1/2}$	16244.513	0.26	2	2
$3d^2D_{5/2}-3p^2P_{3/2}$	12199.476	5.4	6	4
$3d^2D_{3/2}-3p^2P_{3/2}$	12199.525	0.90	4	4
$3d^2D_{3/2}-3p^2P_{1/2}$	12216.721	4.53	4	2

<sup>a</sup>Data from *Handbook of Chemistry and Physics*, 64th Ed.

<sup>b</sup>Degeneracy of upper level.

<sup>c</sup>Degeneracy of lower level.

olution laser gain scan indicates gain at 17575.375 cm<sup>-1</sup> corresponding to the  $4d^2D_{5/2}-3p^2P_{3/2}$  transition (Table III).<sup>2</sup>

4) *Full Cavity Measurements*: Full cavity measurements were carried out using the optical train depicted in Fig. 3(b). In effect, we replace the Roll-Mentel gain configuration with a full laser cavity operated with either AR coated or Brewster angle windows surrounding the amplification zone. No external light sources are used in these experiments. We have, thus far, adopted two stable cavity configurations, both employing a 99.9% high reflector, one with 4.5% output coupling and a second with 0.2% output coupling. In the first configuration, we surround the ~5 cm medium with a cavity, 44 cm in length and operated with  $g_1g_2 \sim 0.56$ . With this cavity, we achieve results which, to first order, demonstrate the potential for cavity oscillation. If we replace the 4.5% output coupler, which represents a substantial cavity loss element, with a 0.2% output coupler and operate under near optimum reactive flow conditions with  $g_1g_2 \sim 0.82$ , we obtain the results depicted in Fig. 8.

### III. RESULTS AND DISCUSSION

#### A. Gain Measurements

A readily reproducible result obtained using the Roll-Mentel configuration (Fig. 3(a)) for continuous gain measurements is depicted in Fig. 5. The gain coefficient can be calculated from the data in Fig. 5 and the relationship

$$\alpha = \ln((I_2 - I_1)/I_1RT^2)/L. \quad (2)$$

Here,  $L$  is the effective gain medium length (medium is not necessarily uniform),  $R$  is the mirror reflectivity, and  $T$  is the transmission of the amplification zone vacuum chamber window in front of the mirror (Fig. 3(a)).  $I_1$  is the measured (spectrometer) light intensity from the gain medium with the shutter placed in front of the high reflector in Fig. 3(a). Light of intensity,  $I_1$ , which impinges

<sup>2</sup>Based upon the data given in Table III, the Na  $4d^2D_{5/2}-3p^2P_{3/2}$  transition should represent the most favorable to achieve gain and oscillation. The  $4d^2D_{5/2}$  level emits dominantly to  $3p^2P_{3/2}$  whereas the  $4d^2D_{3/2}$  level depletes its population to both the  $3p^2P_{1/2}$  and  $3p^2P_{3/2}$  levels. Consideration of collisional relaxation among the  $3p^2P$  levels would also suggest that the collisionally depleted  $3p^2P_{3/2}$  level is favored as the lower laser level.

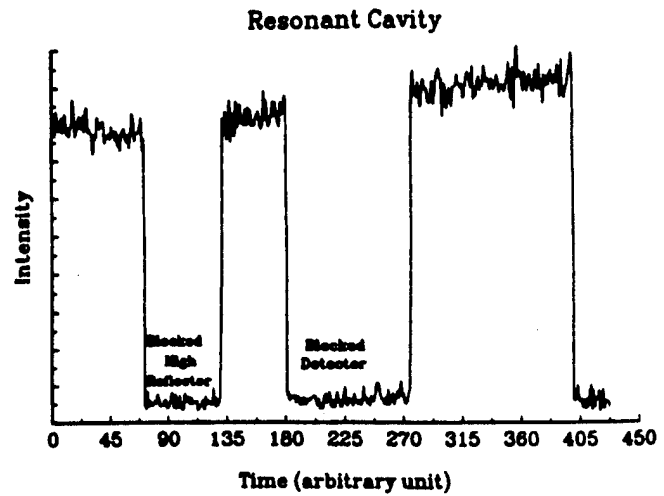


Fig. 8. Full cavity output created with ~0.2% output coupling for the continuous Si-SiO(Si-N<sub>2</sub>O)-Na amplifier at  $\lambda = 569$  nm. These measurements were taken in continuous flow with the cavity configuration depicted in Fig. 4(b). The full cavity output is compared to that obtained with both a blocked high reflector and with the entire cavity isolated from the signal detection system. The ratio of the output obtained for the full cavity to that obtained with a blocked high reflector exceeds  $10^3/1$ .

on the detector after passing through some portion of the gain medium is associated with a single pass ASE intensity. With the high reflector open to and aligned with the gain medium, we measure light of intensity,  $I_2$ , which is contributed to by (1) light passing directly through the gain medium to the detector ( $I_1$ ) and (2) light reflected back through the amplification zone from the high reflector. We refer to  $I_2$  as the double pass ASE intensity. Thus, in Eq. (2), we compare the intensity difference ( $I_2 - I_1$ ) to  $I_1$  correcting for the reflectivity and transmissivity.

The stark change in the relative intensities of the 569 nm Na  $4d^2D-3p^2P$  and Na D-line emissions for the single and double pass ASE output is quite evident in Fig. 5. The two spectra shown in Fig. 5 are taken under conditions optimized to the pumping of the  $4d^2D$  level such that the 569 nm transition shows noticeable positive gain. The ratio of the double to single pass intensity for the 569 nm feature depicted is 2.6/1. This corresponds to a gain coefficient,  $\alpha \sim 0.11/\text{cm}$  (Eq. (2)). Because of the relatively long time interval needed to scan a spectrum, the gain determined on the basis of successive scans, as depicted in Fig. 5, is by no means an optimal value. More reliable gains are determined when only one transition is monitored and the shutter in front of the total reflector is quickly closed. Under optimal operating conditions, using a 1" diameter 99.9% high reflector, we have achieved amplification such that the ratio of light output when the rear high reflector is accessed to that when the rear high reflector is blocked ranges from 3.4 to 3.8 ( $\alpha \sim 0.16-0.23/\text{cm}$ ). This is a ratio which demonstrates clear gain. It should be compared with the measured ratio for a purely fluorescent feature (Na D-line and higher lying excited state Na transitions) which is usually between 1.1 and 1.2 for the Na D-line, and corresponds to 1.6 for the  $5s^2S-3p^2P$  transition whose emission is depicted in Fig. 5. The theoretical maximum value for the ratio associated with

pure fluorescence, based on a lossless single reflection, is 2. When the experimental conditions are not favorable for formation of the gain medium, we find significant losses for the reflected light ( $\alpha$  negative in (2)) employing the same methods we have used to demonstrate the gain in Fig. 5.

The Na atom transitions at  $\lambda \approx 569$  nm ( $\alpha \sim 0.1$ – $0.15$ ),  $\lambda \approx 616$  nm ( $\alpha \sim 0.03$ – $0.05$ /cm), and  $\lambda \approx 819$  nm ( $\alpha \sim 0.02$ – $0.03$ /cm) have all been shown to demonstrate gain. The  $\alpha$  values given in parentheses are meant to represent typical values determined from (2) using  $L = 5$  cm.

Using the Na discharge lamp based optical configuration (Fig. 4(a)), we record the train of peaks depicted in Fig. 6. These peaks correlate precisely with the introduction of the oxidant  $N_2O$  into the reaction–energy transfer–amplification zone to produce a continuous gain condition. The percent gain indicated by these peak signals is calibrated using a glass filter inserted into the signal channel so as to produce a known loss peak ( $\sim 8\%$  in Fig. 6). Under the experimental conditions associated with Fig. 6, the typical gain is close to 3.6%. Calibrated gains through the amplification zone in excess of 5% can be achieved. Preliminary measurements at 616 nm indicate gains on the order of  $1.2 \rightarrow 1.5\%$ .

Our measured gains using the lamp based optical configuration are believed to represent lower bounds to the true values due to the significant radial extent (cross sectional area) of the lamp output which intersects a much smaller mixing zone and gain medium. When the 569-nm light exiting the gain medium is focused onto the entrance slit of the monochromator, the measured gain is diluted by the mismatch in cross sectional area as not only the gain zone but also regions of negligible gain and even absorption (pumping of  $3p^2P$  level) are monitored.

The signal we record upon scanning a ring dye laser through the region encompassing 569 nm is depicted in Fig. 7. The signal corresponds to a gain in excess of 1.5% for the  $4d^2D_{5/2}$ – $3p^2P_{3/2}$  transition. This percent laser gain again represents a lower bound determination of the single pass amplification for (1) the bandwidth of the ring dye laser (effective linewidth  $\sim 40$  MHz) is considerably smaller than the width of the 569 nm Na  $4d^2D$ – $3p^2P$  stimulated emission gain profile ( $\sim 2$  GHz) [19] and (2) the precise overlap of the sharply defined laser output beam and the amplification zone is certainly unlikely. Because of the inherently narrow bandwidth of the ring dye laser, we select a narrow velocity group within the gain profile velocity distribution. This excludes the remainder of atoms throughout the profile. In order to compare the gain levels measured in this experiment with those for the Roll–Mentel and lamp configurations, we must integrate over the gain profile taking into account the bandwidth of the probe laser. This correction will, of course, lead to the evaluation of a higher single-pass gain.

Taken as a whole, the importance of the three distinct gain measurements, is that they clearly demonstrate the formation of an energy transfer pumped sodium atom laser

amplifier. The magnitude of the gain is probably best represented by the results obtained with the Roll–Mentel configuration. However, these determined gain values correspond to that of a single pass configuration. The effective threshold gain in an oscillating full cavity, influenced both by the increased rate of loss of the population inversion due to the stimulated emission process and by the nature of reactant mixing and energy transfer in the amplification zone, will be notably smaller.

### B. Full Cavity Measurements—The Indication of Oscillation

We have obtained results with 4.5% and 0.2% output coupled cavities which suggest the onset of full cavity amplification and oscillation.

In the first set of experiments, using a 4.5+ % output coupler and 99.9% high reflector we compare the output for the full cavity versus that with the high reflector blocked. Upon tuning the output coupler and high reflector, after adjusting the mixing Si,  $N_2O$ , and Na flows, we achieve conditions, at low to moderate sodium flux (conc. estimated to be  $\sim 10^{12}$ /cc in the reaction zone), such that the ratio of the full cavity output to single pass amplification is between 20 and 25/1 in a steady state mode. Walking the cavity mirrors (angle tuning) destroys the amplification. Upon realignment, similar increases in intensity at the steady state value are again observed. We emphasize that these results are sharply dependent on the angle tuning of the cavity. By comparison, if we monitor the reaction–amplification zone configuration of Fig. 2 when only a fluorescent medium associated with the  $4d^2D$ – $3p^2P$  Na transition is formed, as evidenced by gain measurements at 569 nm and at the Na  $D$ -line, or when we are below threshold despite some stimulated emission in the cavity, we find a typical steady state enhancement between 1.2 and 1.4.

The 4.5% output coupler provides a substantial loss element in the cavity. If we replace this output coupler with a 0.2% output coupler and operate the system under near optimum reactive flow conditions in a stable cavity configuration with  $g_1g_2 \sim 0.82$ , we find that the ratio of the output for full cavity operation to that obtained with a blocked high reflector (Fig. 8) exceeds  $10^3$ . Compare also the signal level observed with the blocked high reflector and that monitored with a completely blocked detector. *This result clearly indicates continuous full cavity laser oscillation in the SiO–sodium system.*

If we operate the 0.2% output coupled cavity below threshold, monitoring a purely fluorescent process, the ratio of full cavity to single pass output (blocked high reflector) is found to be slightly greater than 1.8 for the Na  $D$ -line ( $3p^2P$ – $3s^2S$ ). This value should be compared to a maximum of 1.2 for the much more lossy 4.5+ % output coupled device. In fact, a maximum (full cavity/blocked reflector) ratio of order 1.9–1.95 is typical for all those wavelengths considered ( $\lambda = 569, 616, \text{Na } D\text{-line}$ ) when conditions in the reaction–amplification zone are such that

no gain is monitored. We have also observed intermediate behavior associated with the establishment of moderate but not optimal gain conditions.<sup>3</sup> Finally, we find that the ratio of the output power for the 4.5% output coupled configuration to that for the 0.2% output coupled configuration is only 1.9/1. When compared to the output coupling ratio of 22.5, this result clearly supports the presence of a stimulated emission process. *These findings in concert with the observed  $10^3$  enhancement monitored under near optimum reactive flow conditions signal the characteristic operation of a full oscillating cavity.*

The current results are exciting not only because they demonstrate lasing action in the visible region but also because they can be substantially enhanced with several improvements in the manner in which the lasing medium is created and the laser output is extracted from the cavity. It remains to increase both the rate limiting silicon and sodium atom concentrations in the reaction zone while maintaining atomization. This increase may lead to a leveling off and eventual loss of the gain condition if self-absorption on the Na *D*-line transitions becomes a dominant factor or SiO triplet self-quenching begins to play a deleterious role. Evidence is obtained for some self-absorption at high sodium concentration when the alkali atom production dominates the concomitant SiO metastable production.

With our sodium atom source operated, in the absence of interacting silicon or  $N_2O$ , at the temperatures which we have employed to produce the highest flux densities in the amplification zone, we have measured the attenuation of the Na *D*-line emission from the sodium discharge lamp. We find an attenuation which is less than 50%. In combination with the cross section for self-absorption,  $4 \times 10^{-14} \text{ cm}^2$ , as measured by Ermin *et al.*, [20] this suggests a sodium atom concentration close to that estimated previously. Of course, in the presence of  $N_2O$  and silicon reactants, the attenuation due to self absorption, while evidenced, is considerably diminished ( $\sim 5$ –10%). Although concern with the possible deleterious effect which a pumping of the Na *D*-line might have on transitions terminating in the  $3p^2P$  level is somewhat alleviated, in the present system, by the sodium discharge experiment of Tribilov and Shukhtin [21], and the 0.01-s duration laser pulse for the Na  $4s^2S$ – $3p^2P$  infrared transition observed by Mishakov and Tkachenko [22] as quasicontinuous lasing, it must eventually limit the size of the laser system.

The  $90^\circ$  intersection of the SiO metastable and Na atom flows can be used to clearly establish a continuous lasing action; however this is by no means the ideal mixing configuration. With the installation of a concentrically based SiO–Na interaction–energy transfer mixing configuration, we can anticipate a further improvement in the cavity output.

The experiments conducted thus far have made use of only two distinct output coupling configurations. As well as improving reactant concentrations, the optimum output

coupling for the current cavity remains to be evaluated [23]. Finally, we are constructing a modification which will allow removal of the cavity windows that represent significant loss elements. With these improvements, the output from our full cavity configuration should be substantially enhanced.

#### IV. CONCLUSION AND EXTENSION

We have demonstrated continuous lasing action in the visible region using the near resonant energy transfer pumping of an atomic receptor with a high propensity to lasing action. Not only can the present cavity configuration be enhanced but also the generic nature of the concept is demonstrable.

While our emphasis has been on the sodium system and the results presented involve a metastable SiO pump, it is also feasible to use GeO metastables for energy transfer pumping (Table II). In fact, we have obtained evidence that the energy transfer pumping of the sodium analog potassium based amplifiers associated with the  $5d^2D$ – $4p^2P$  ( $\lambda \approx 581, 583 \text{ nm}$ ),  $4d^2D$ – $4p^2P$  ( $\lambda \approx 694, 697 \text{ nm}$ ), and  $6s^2S$ – $4p^2P$  ( $\lambda \approx 691, 694 \text{ nm}$ ) potassium atom transitions might best be accomplished by GeO metastables. Finally, we have also extended the concept to the successful energy transfer pumping of potential amplifying transitions in lead (Pb), copper (Cu), and tin (Sn) receptor atoms. These systems will be the subject of future study in our laboratory.

#### ACKNOWLEDGMENT

It is a pleasure to acknowledge most helpful discussions with Drs. R. Jones, Bill Watt, T. Cool, Stan Patterson, Rolf Gross, Sherwin Amimoto, John Dering, Glen Peram, and E. Dorko concerning this study.

#### REFERENCES

- [1] J. I. Steinfeld, Ed., *Electronic Transition Lasers I*. Cambridge, MA: MIT Press, 1976; L. E. Wilson, S. N. Suchard, and J. I. Steinfeld, Eds., *Electronic Transition Lasers II*. Cambridge, Massachusetts: MIT Press, 1977; Short Wavelength Chemical Laser Workshop, Charleston, SC, November 1984 and SAIC Inc., Atlanta, GA, 1989; H. Hohla and K. L. Kompa, "The photo-chemical iodine laser," in *Handbook of Chemical Lasers*, R. W. Gross and J. F. Bott, Eds. New York: Wiley, 1976, p. 667.
- [2] W. H. Crumley, J. L. Gole, and D. A. Dixon, *J. Chem. Phys.*, vol. 76, p. 6439, 1982; S. H. Cobb, J. R. Woodward, and J. L. Gole, *Chem. Phys. Lett.*, vol. 143, p. 205, 1988; S. H. Cobb, J. R. Woodward, and J. L. Gole, *Chem. Phys. Lett.*, vol. 157, p. 197, 1989; S. H. Cobb, J. R. Woodward, and J. L. Gole, "Continuous chemical laser amplifiers in the visible region," *Proceedings of the Fourth International Laser Science Conference*, A.I.P. Conf. Proc. No. 191, Optical Science and Engineering Series 10, p. 68.
- [3] J. R. Woodward, S. H. Cobb, K. K. Shen, and J. L. Gole, "A chemically driven visible laser transition using fast near resonant energy transfer," in *IEEE J. Quantum Electron.*, vol. 26, 1574, 1990; J. R. Woodward, S. H. Cobb, and J. L. Gole, "Superfluorescent chemically driven visible laser transitions using fast near resonant energy transfer," *Proceedings of the Fourth International Laser Science Conference*, A.I.P. Conf. Proc. No. 191, Optical Science and Engineering Series 10, p. 63.
- [4] J. L. Gole, J. R. Woodward, S. H. Cobb, K. K. Shen, and J. R. Doughty, *SPIE Proceedings Volume 1397, Eighth International Symposium on Gas Flow and Chemical Lasers*, 1990, p. 125.

<sup>3</sup>Ratios ranging from 40/1 to 100/1 have been routinely measured.

- [5] J. L. Gole, K. K. Shen, C. B. Winstead, and D. Grantier, "An approach to visible chemical laser development using fast near resonant energy transfer," *Journal de Physique IV, Colloque C7, supplement au Journal de Physique III*, vol. 1, Dec. 1991, p. 609.
- [6] "Chemically driven pulsed and continuous visible laser amplifiers and oscillators," by J. L. Gole, K. K. Shen, H. Wang, and D. Grantier. Invited Talk. *Proceedings of the 23rd AIAA Plasma-Dynamics and Laser Science Conference*, Nashville, TN, AIAA 92-2994.
- [7] R. D. Levine and R. B. Bernstein, *Molecular Reaction Dynamics*. New York: Oxford University Press, 1974.
- [8] G. J. Green and J. L. Gole, *Chemical Physics*, vol. 100, p. 133, 1985.
- [9] R. W. Woodward, J. S. Hayden, and J. L. Gole, *Chemical Physics*, vol. 100, p. 153, 1985.
- [10] P. M. Szwarc, S. J. Davis, and T. M. Niemczyk, *Chem. Phys. Lett.*, vol. 55, p. 274, 1978.
- [11] S. H. Cobb, M. McQuaid, and J. L. Gole, unpublished, see also refs. 3-6. D. Husain and P. E. Norris, *J. C. S. Faraday, II*, 93, 106, 335 (1978) and D. Husain and P. E. Norris, *Chemical Physics Letters*, vol. 51, p. 206, 1977.
- [12] A. Gaupp, P. Kuske, and H. J. Andra, "Accurate lifetime measurements of the lowest  $^2P_{1/2}$  states in neutral lithium and sodium," *Phys. Rev. A*, vol. 26, pp. 3351-3359, 1982.
- [13] S. A. Kandel, *Appl. Optics*, vol. 23, p. 2151, 1984.
- [14] X. He, B. Li, A. Chen, and C. Zhang, *J. Phys. B, At. Molec. and Opt. Phys.*, vol. 23, p. 661, 1990.
- [15] For thallium see A. Gallagher and A. Lurio, *Phys. Rev.*, vol. 136, p. A87, 1964.
- [16] S. H. Cobb, R. Woodward, K. K. Shen, C. B. Winstead, J. M. Stephens, and J. L. Gole, work in progress.
- [17] W. H. Crumley, and J. L. Gole, "Self-flushing optical window to prevent collection of condensates," *Rev. Sci. Instruments*, vol. 57, p. 1692, 1986.
- [18] G. Roll and J. Mentel, *J. Phys. D, Appl. Phys.*, vol. 22, pp. 483-487, 1989.
- [19] J. L. Gole and K. K. Shen, unpublished calculation.
- [20] A. V. Eremin, I. M. Naboko, and S. A. Palopezhentsev, *Opt. Spectrosc. (USSR)*, vol. 60, p. 567, 1986.
- [21] A. S. Tibilov and A. M. Shukhtin, *Opt. Spectrosc.*, vol. 21, p. 69, 1966. See also, K. Krok, M. Hube, W. Luhs and B. Wellegehausen, *Appl. Phys. B37*, pp. 137-140, 1985.
- [22] (a) V. G. Mishakov and T. L. Tkachenko, *Opt. Spectrosc. (USSR)*, vol. 64(3), p. 293, 1988. (b) V. V. Kuchinskii, V. G. Mishakov, A. S. Tibilov, and A. M. Shukhtin, *Opt. Spektrosk.*, vol. 39, p. 1043, 1975 [*Opt. Spectrosc. (USSR)*, vol. 39, p. 598, 1975]. (c) A. A. Kudryavsev, V. N. Skrebov, and T. L. Tkachenko, *Opt. Spektrosk.*, vol. 58, p. 694, 1985 [*Opt. Spectrosc. (USSR)*, vol. 58, p. 420, 1985]. (d) V. G. Mishakov, A. S. Tibilov, and A. M. Shukhtin, *Opt. Spektrosk.*, vol. 31, p. 324, 1971 [*Opt. Spectrosc. (USSR)*, vol. 31, p. 176, 1971]. (e) N. N. Bezuglov and A. B. Tsyganov, *Opt. Spektrosk.*, vol. 59, p. 195, 1985 [*Opt. Spectrosc. (USSR)*, vol. 59, p. 115, 1985].
- [23] A. E. Siegman, *Lasers*. Mill Valley, CA: University Science Books, 1987.

**Kangkang Shen** was born in Hangzhou, China, on October 28, 1958. He received the B.S. degree in optical engineering from Zhejiang University, Hangzhou, China, in 1982. He received the M.Sc. degree in physics from San Diego State University, CA, in 1987 and transferred to the Georgia Institute of Technology, Atlanta, where he was a graduate student in the High Temperature Laboratory pursuing laser-induced fluorescence studies of metal cluster oxidation and visible chemical laser development. He received his Ph.D. degree in physics in July 1993, and is currently employed by GCH Systems Inc., CA.

From 1982 to 1985 he was employed as an engineer in the Spectroscopy Division of the Central Laboratory of Zhejiang University.

**He Wang** was born in Beijing, China, on December 17, 1955. He received the B.S. degree in optical engineering from Zhejiang University, Hangzhou, China, in 1982. He received the M.S. degree in optics (laser physics) from the Shanghai Institute of Optics and Fine Mechanics, Shanghai, China, in 1984. He received his Ph.D. degree in physics from the University of Iowa, Ames, in 1991. He was a postdoctoral fellow in the High Temperature Laboratory of the Georgia Institute of Technology, where he pursued laser-induced fluorescence studies of metal cluster oxidation and visible chemical laser development. He is currently a research scientist in the Department of Physics of the University of Connecticut, Storrs.

**James L. Gole** was born in Chicago, IL, on September 17, 1945. He received the B.S. degree in chemistry from the University of California, Santa Barbara, where he was an NSF undergraduate research fellow, in 1967. He received the Ph.D. degree from Rice University, Houston, TX, in 1971, where he was a Phillips Petroleum Research Fellow. He was an NSF postdoctoral fellow at Columbia University, NY, from 1971 to 1973.

He joined the Department of Chemistry, Massachusetts Institute of Technology, Cambridge, in 1973, and in 1977 moved to the School of Chemistry of the Georgia Institute of Technology, Atlanta, where he became a professor of Chemistry in 1981. In 1983, he joined the School of Physics, GIT, where he is currently a professor of Physics.

He is interested in the molecular electronic structure of high-temperature molecules, chemiluminescence techniques as applied to the study of molecular dynamics and to the determination of molecular parameters, laser-induced fluorescence, high-temperature vacuum ultraviolet spectroscopy, and quantum chemistry. His current fields of interest include high-temperature chemical physics, laser spectroscopy of small metal clusters and metal cluster oxides, chemiluminescence phenomena as applied to the study of reaction dynamics and the nature of metal cluster oxide and halide formation, ultrafast intra- and intermolecular energy transfer, chemical lasers, and quantum chemistry. He has filed 6 patents and has published about 140 papers.

Dr. Gole has been chairman of the ILS Conference, the APS Laser Science Topical Groups Conference on Laser Science, Chairman of Lasers in Chemistry and Biology of the Quantum Electronics and Laser Science Conference, and a member of the editorial board of High Temperature Science. In 1989 he received the Sustained Research Award of the Sigma Xi Research Society and in 1990 was named GIT Outstanding Faculty Research Author. He is a member of Sigma Xi, Phi Lambda Upsilon, AAAS, APS, and ACS.

#### APPENDIX IV

"Chemically Driven Continuous Visible Laser Amplifiers and Oscillators Based on Metal Molecule - Halogen Atom Reactions", D. Grantier, H. Wang, C. B. Winstead, and J. L. Gole, Proceedings of the 24th AIAA Plasma-dynamics and Laser Science Conference, Orlando, Florida, AIAA 93-3207 (1993).



**AIAA 93-3207**

**Chemically Driven Continuous  
Visible Laser Amplifiers and  
Oscillators Based on Metal  
Molecule - Halogen Atom  
Reactions**

D. Grantier, H. Wang, C. B. Winstead, and J. Gole  
School of Physics, Georgia Institute of Technology  
Atlanta, GA 30332

**AIAA 24th  
Plasmadynamics & Lasers Conference  
July 6-9, 1993 / Orlando, FL**

CHEMICALLY DRIVEN CONTINUOUS VISIBLE LASER AMPLIFIERS AND OSCILLATORS  
BASED ON METAL MOLECULE - HALOGEN ATOM REACTIONS

D. Grantier, H. Wang, C. B. Winstead and J. Gole  
School of Physics  
Georgia Institute of Technology  
Atlanta, GA 30332

ABSTRACT

Using the highly efficient and selective formation of sodium dimer excited states from the sodium trimer-halogen atom  $\text{Na}_3\text{-X(F,Cl,Br,I)}$  reactions and extrapolated analog systems, we seek to develop visible and ultraviolet lasers based on the successful production of visible chemical laser amplifiers. The  $\text{Na}_3\text{-X(Cl,Br,I)}$  reactions have been shown to create a continuous electronic population inversion based on the chemical pumping of sodium dimer ( $\text{Na}_2$ ). Optical gain through stimulated emission has been demonstrated in the regions close to 527, 492, and 460 nm. These observations are in close analog to optically pumped alkali dimer lasers. A model which invokes the vibrational and rotational selectivity inherent to a dissociative ionic recombination process ( $\text{Na}_3^+ + \text{X}^- \rightarrow \text{Na}_2 + \text{NaX}$ ), correlated with the coupling between select sodium dimer excited states, provides a semiquantitative explanation of the observed trends. An analysis of the system suggests that the monitored gain (max of 3.8% at  $\approx 527$  nm corres. to  $\alpha \approx 8 \times 10^{-3}/\text{cm}$  for an individual rovibronic level) can be enhanced considerably with a more versatile source configuration. The considered amplifiers are therefore being optimized with a focus to increasing amplifier gain length and amplifying medium concentration. A device has been constructed to allow the ready movement of extended length alkali trimer and halogen atom slit sources relative to each other so as to create interacting alkali and halogen atom sheaths. The controlled intersection of these sheaths can form an extended reaction - amplification zone. This extended gain zone is required to facilitate the conversion of the created amplifiers to visible chemical laser oscillators. We report results obtained with this up-scaled device, where the alkali metal is expanded in both pure and seeded supersonic expansion. We report progress in extending the  $\text{Na}_3 - \text{X}$  amplifier concept to the study of the  $\text{Na}_3 - \text{F}$  and  $\text{Li}_3 - \text{X}$  alkali trimer-halogen atom based reactions, the potential excimer forming  $\text{M}_3$  ( $\text{M}=\text{Mg,Ca,Sr,Ba, and Mn}$ ) -  $\text{X(F,Cl)} \rightarrow \text{M}_2^* + \text{MX}$  reactions, and the correlated formation of Group IIA dihalide excited states from  $\text{M} + \text{X}_2$  reactive encounters.

INTRODUCTION

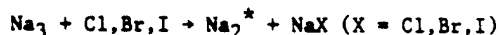
"A Highly Efficient and Selective Electron-Jump-Harpoon Process"

The collision dynamics of processes proceeding on electronically excited surfaces is fundamental to the attainment of population inversions based on electronic transitions in the visible spectral region.<sup>1-3</sup> A particular subgroup of these electronic energy transfer processes involves metal atoms or molecules of low ionization potential.

These species react very efficiently with atoms or molecules of significant electron affinity via what is termed the electron jump-harpoon process. It is this process, specifically involving the reaction of metal trimers and forming the product metal dimer and metal halide, that may represent one of the few direct chemical routes to produce electronically inverted products. The alkali trimer molecule,  $\text{Na}_3$ , readily provides an electron to harpoon a hungry halogen atom, X, producing a switch from the interaction of two neutral species to that of two ions ( $\text{Na}_3^+ + \text{X}^-$ ). The convergence, crossing, and interaction of the two potentials describing the neutral (covalent) and ionic (coulombic) constituencies allows an effective switch of the reactants (curve crossing). For  $\text{Na}_3$ , with its low ionization potential, the curve crossing occurs at very long range ( $> 10\text{\AA}$ ) leading to a high cross section for product  $\text{Na}_2$  formation. Based upon the experimental results obtained thus far in our laboratory, the sodium trimer reactions show not only vibrational but also rotational selectivity as they create electronic population inversions in the product  $\text{Na}_2$ . Theoretical considerations would suggest that these trimer reactions and their analogs represent key processes to yield electronically inverted products in direct chemical reaction.<sup>1,2</sup>

Continuous Chemical Laser Amplifiers in the Visible Region Based on Highly Efficient and Selective Chemical Reaction

The  $\text{Na}_3 - \text{X}$  reactions form an unusual class of reactive encounters. The optical signatures for the processes



encompass emission from a limited group of low-lying  $\text{Na}_2$  excited states.<sup>4</sup> The observed dimer emission is characterized by sharply defined emission regions<sup>4</sup> (Fig. 1) superimposed on a much weaker  $\text{Na}_2$  background fluorescence. The sharp emission features cannot be explained by invoking a purely fluorescent process, and resemble in their behavior characteristics similar to those of optically pumped  $\text{Na}_2$  laser systems.<sup>4,5,6</sup> In the visible spectral region, these features grow at a near exponential rate with increasing  $\text{Na}_3$  concentration, relative to the  $\text{Na}_2$  background spectrum, suggesting the possibility that stimulated emission might be associated with certain of the emitting  $\text{Na}_2$  reaction products. Laser gain measurements carried out to assess this possibility throughout the visible region reveal optical gain through stimulated emission and the creation of population inversions on these select  $\text{Na}_2$  electronic transitions.

Measurements at  $0.5 \text{ cm}^{-1}$  resolution suggest amplification in regions close to 527 nm (1% gain).

492 nm (0.3% gain) and 460.5 nm (0.8% gain), correlating precisely with the reactive process and the relative intensities of those features observed while monitoring the light emitted from the  $\text{Na}_3$ -Br reaction (Fig. 1). High resolution ring dye laser scans in the 527 nm region indicate that the gain for the system is a minimum of 3.8% for the dominant rovibronic transition in this region with approximately four to seven individual rotational transitions showing gain. At 459.8 nm, we also have measured a 2.3% gain for an individual rotational transition. These results demonstrate the continuous amplifying medium for a visible chemical laser in at least three wavelength regions.<sup>4,5</sup> At no other scanned wavelengths do we find any indication of gain as we monitor the entire wavelength region from 420 to 600 nm. We have generally observed slight losses of the laser photon flux resulting primarily from scattering, and, to a much smaller extent, absorption upon transmission through the  $\text{Na}_3$  - Br reaction zone. In the region of the sodium D-line, we monitor a substantial absorption and loss as a function of the trimer-halogen atom reaction.<sup>4,5</sup>

As we have suggested in our initial comments, the  $\text{Na}_3$ -halogen atom reactions are thought to proceed via an electron jump mechanism with extremely high cross sections,<sup>7</sup> producing substantial  $\text{Na}_2$  excited state populations. The question of why the  $\text{Na}_3$ -X reactions appear to demonstrate vibrational and rotational selectivity in certain wavelength regions may be explained by invoking a model for the dissociative ionic recombination,  $\text{Na}_3^+ + \text{X}^- \rightarrow \text{Na}_2 + \text{NaX}$ , and the curve crossings which influence the distribution of product molecules for this process.<sup>2</sup> Such a model, coupled with an analysis of the electronic coupling between select sodium dimer excited states,<sup>2</sup> appears to provide a semiquantitative explanation of the observed population inversions.

Once created, the monitored population inversions are thought to be maintained in a continuously amplifying system (1) by the large number of free halogen atoms reacting with the  $\text{Na}_2$  molecules in those ground state levels on which the transitions emanating from the  $\text{Na}_2$  excited states terminate and (2) by collisional relaxation of the ground state sodium dimer molecules. The cross section for reaction of vibrationally excited ground state  $\text{Na}_2$  is expected to be quite substantial relative to the cross section for collision induced vibrational deactivation of the  $\text{Na}_2$  manifold. Extremely efficient reactions are thought to greatly assist the depletion of the lower state levels in this system allowing one to sustain a continuous population inversion. Our major efforts thusfar have focused on the  $\text{Na}_2$  B-X spectral region and the potential development of laser oscillators at wavelengths in the vicinity of 527 and 460 nm. In order to approach these studies, we have been developing the means to create a considerably longer path length amplification region.

#### Development of an Extended Path Length $\text{Na}_3$ - X (Cl, Br, I) Reaction - Amplification Zone

It is necessary to improve the magnitude of the amplification determined previously for the sodium dimer amplifiers at  $\sim 527$ ,  $\sim 492$ , and

$\sim 460$  nm. In these previous experiments we have obtained a substantial  $\text{Na}_3$  concentration ( $\geq 10^{13}/\text{cc}$ ) in a limited reaction-amplification zone.<sup>4,5</sup> In order to demonstrate continuous chemical laser oscillation, however, it is desirable to create this enhanced sodium trimer - halogen atom reaction zone over an extended amplification zone path length. The overall apparatus design depicted in Figures 2 and 3 is meant to accommodate high intersecting reactant flows from both sodium trimer and (dual rotatable) halogen atom sources in order to produce a considerably enhanced concentration of  $\text{Na}_2$  amplifiers over an extended path length. This system attempts to increase the  $\text{Na}_3$  reaction - amplification zone concentration by repositioning the trimer and halogen atom sources relative to each other<sup>4,5</sup> and facilitating the halogenation process much closer to the alkali source nozzle itself, in a gas dynamic configuration. We incorporate the facility for the in-situ adjustment of the alkali and halogen source positions.

In order to increase the reaction zone and gain length, we are testing a continuous flow slit source technology to create at least a 5 cm long amplification zone. Here, a small circular "pinhole" nozzle used in previous experiments<sup>4,5</sup> is now replaced by a slit approximately 100  $\mu$  in width by 2 1/2" in length. Two slit configurations have been employed to accomplish this goal. The design used initially, depicted in Figure 3(a), of 0.003" width, was fabricated from 316 stainless steel using an EDM (electric discharge machining) process. These slits were not sufficiently resistive to the corrosive effects of the system reactants (primarily sodium) and quickly widened to 0.020" ( $\sim 2$  runs). An improved slit nozzle constructed from molybdenum (Fig. 3(b)) has proven considerably more resistant, widening from 0.003 to 0.006" after six experimental runs.

In order to produce a more efficient cooling in the alkali expansion it is desirable to operate with narrower slits which exhibit a minimal interaction with the expanding alkali vapor. Figures 3(c)-(e), in combination, outline a more successful design. As depicted in Figs. 3(c) and 3(d), the nozzle consists of two pieces. Two sheets of 0.005" tantalum are prepared and mounted on the back portion of the nozzle (Fig. 3(d)) as they are positioned to form the slit. The front of the nozzle, with a mildly diverging section, fits over the back portion of the device, tightly sandwiching the tantalum sheets and thus forming the actual slit (Fig. 3(e)). These tantalum sheets can be positioned under a Vickers microscope to produce a slit less than 0.003" in width. These widths are precisely adjusted and determined using single slit diffraction techniques.

The overall alkali source design pictured in Fig. 2(a) in side and partial frontal view corresponds to a full seeded configuration where helium or argon can be passed through the rear gas source assembly, flowing over molten sodium. The mixture is subsequently expanded through the frontal nozzle slit configuration. In a pure sodium supersonic expansion, the  $\text{Na}_3$  constituency is dominated by a much larger atom and cold dimer concentration.<sup>8</sup> The expanded dimer will not interfere at the  $\text{Na}_2$  amplifier wavelengths

characteristic of the  $\text{Na}_3$ -halogen atom reaction systems, however, it is desirable to minimize the atom and dimer while increasing the trimer concentration. The trimer concentration can be altered and improved by seeding the expansion with helium, argon, or other noble gas atoms. In fact several researchers<sup>9</sup> have demonstrated that the atom and dimer concentrations can be decreased considerably relative to the much larger sodium polymers. We do not wish to operate at these extreme expansion conditions but, rather, seek a middle ground which will allow enhanced formation of the trimer over that of the pure expansion concentration.<sup>10</sup> This condition can be realized through the appropriate adjustment of parameters which can be manipulated in the expansion including (1) the rear oven stagnation pressure (argon + sodium), (2) the frontal nozzle temperature, and (3) the ratio of the supersonic expansion source pressure to the overall expansion chamber pressure.

In the overall experimental design depicted in Figure 2(b), the sodium slit source is positioned relative to the dual halogen slit sources located above and below the reaction zone. The halogen slit sources are designed to optimize the interaction of the alkali expansion products with the created halogen atoms. The optical cavity is colinear with the geometric intersection of the planar halogen and alkali flows as indicated in Figure 2 and is terminated on each end by self-cleaning optical windows (as indicated in Figure 2(c)). The entire sodium oven and cooling jacket assembly can be translated in the forward and backward directions relative to the halogen slit sources for optimal control of the positioning of the reaction zone relative to the laser cavity. In summary, the reaction zone cavity configuration is designed to allow for (1) short transit of the reactants  $\text{Na}_3$  and  $\text{X} = \text{Cl}, \text{Br}, \text{I}$  to the reaction - amplification zone, (2) flexible movement of these sources with respect to each other and with respect to the flow patterns created in the system and (3) minimal interaction of these reactants with laser cavity windows. To insure this minimal interaction, the self-cleaning optical windows noted previously<sup>11</sup> are used. The reaction zone is evacuated through a 35 cubic foot ballast tank followed by a 1250 CFM Stokes - Roots-Blower combination.

The oven and nozzle chambers are currently heated differentially and resistively using Thermocoax wire (Amperex, inconel sheath, 0.079" diameter). The wrapped heating elements are powered by two independent Variac transformer power supplies capable of delivering 25 amps at 180 volts (a.c.). For the halogen dissociation furnaces (Fig. 2(d)), desired temperatures are achieved through the resistive heating (250+ amps, ~ 50 volts (a.c.)) of a hollowed high density carbon cylinder. The central channel of each cylinder is accessed to the reaction zone region through a single slit ~ 0.006" wide by two inches in length running midway down the cylinder. Typically, these halogen dissociation furnaces are operated at temperatures between 1700K and 1900K as determined by optical pyrometry. At these temperatures, those halogen molecules entering the radiator should be greater than 95% dissociated. The halogen, if it is liquid bromine (or iodine) is held in a glass bulk separated from the inlet to the reaction zone

by a teflon stopcock. In the case of iodine, this bulb is heated to attain the necessary flow rates which are finely controlled using a Whitey SS-22RS4 needle valve.

In a typical "seeded" argon experiment, both the rear stagnation oven and frontal nozzle are brought slowly to a temperature of ~ 450K during which time hydrogen is evolved from the sample. A small positive pressure argon purge is maintained during the entire heating cycle to prevent backstreaming of the sodium vapor into the seed gas line. With the hydrogen evolution complete, the oven can be brought rapidly to the operating temperature of a given experiment. A major aspect of our efforts has involved the continued improvement of this cycle in order to generate the initial experimental studies described in the following section. Simultaneously, the halogen furnaces are heated at a moderate rate. Since the electrodes supplying current to the halogen furnaces are water cooled (Fig. 2(b)), their temperature is increased slowly to prevent them from cracking.

#### Overview of Initial Experimental Results

As the operating temperature of the sodium supersonic expansion source is reached, bromine molecules are passed into and dissociated in the halogen furnaces and subsequently fed to the reaction zone. This process produces a bright yellow-green cylindrical region formed between the two halogen outlets. By varying the flow of bromine through the needle valve, we induce a change in the relative intensity and spatial extent of the emission. If the system is operated at a relatively low bromine flux, the observed chemiluminescence loses much of the characteristic yellow brightness associated with the sodium D-line emission and bears a dominantly green appearance. This is apparent for both pure and seeded expansions. As the spectrum of Figure 4 demonstrates for a pure expansion, the monitored spectral features are dominated by  $\text{Na}_2$  B-X and A-X emission features accompanied by a weak Na D-line emission. As the bromine flux is increased, the observed emission takes on a strong yellow green appearance, due most likely to a significant increase in Na D-line emission. This is exemplified in Figure 5.<sup>12</sup>

In the configuration outlined in Figure 2, the halogen sources are separated by approximately 6.4 cm. The expanding sodium vapor is introduced from its source configuration at a distance from the reaction-viewing-zone which can be varied in-situ from ~ 12.7 to 3.8 cm. Thusfar, we have found that a variation over these distances has little effect on the content of the observed spectral chemiluminescence and only serves to increase or decrease the intensity of the light emission as the halogen source/alkali source distance is varied. Currently, we have chosen to operate with the alkali expansion source positioned between 5 and 3.8 cm from the halogen sources.

The halogen atom sources, while not yet rotatable in-situ can be configured to intersect the plane of the alkali expansion slit source at varying angles by adjusting their orientation prior to a given experiment. These adjustments in the

orientation of the reactant flows ( $\sim \pm 15^\circ$  relative to the vertical for the halogen source - while maintaining the reaction - viewing zone orientation) do produce a change in the spectral content of the observed emission features. For example, when the horizontal component of the velocity vector of the halogen atom flow is directed parallel to the alkali flow, we observe a very weak broad spectral emission at 436.5 nm (Fig. 6(a)) correlating closely with what has been identified as a triplet-triplet bound-free transition in  $\text{Na}_2$ .<sup>13</sup> When the halogen sources are configured perpendicular to the alkali flow or are even slightly rotated from the parallel to an angle  $10^\circ$  antiparallel (Fig. 6(b)) to the alkali flow, a notable enhancement of the 436.5 nm feature is observed. As the halogen flow rate is increased, the 436.5 nm feature is further enhanced<sup>14,15</sup> (Fig. 6(c)).

In our initial successful operation of the  $\text{Na}_x$  - X system, we were concerned with the evaluation of pure sodium supersonic expansions and the optimization of expansion conditions so as to demonstrate the formation of a cooled sodium dimer ( $\text{Na}_2$ ) constituency. This process, of course, represents the first step in our attempt to build up the trimer ( $\text{Na}_3$ ) concentration to the level desired to create an extended path length sodium dimer amplification zone.

With the alkali source nozzle and halogen sources positioned within 3.8 cm of each other, the alkali system operated under conditions which should produce significant concentrations of cooled  $\text{Na}_2$ , the halogen slit sources oriented at  $75^\circ$  relative to the sodium flow in a direction away from the alkali nozzle a moderate bromine flux, we observe the emission associated with  $\text{Na}_x$ -Br reactions depicted in Fig. 5. This signature, observed along the path of the optical train in Fig. 2, consists of a dominant Na D-line and considerably weaker  $\text{Na}_2$  B-X emission feature. Also associated with the D-line are several features which initially were thought to result from the selective excitation of  $\text{Na}_2$  A  $^1\Sigma_u^+$  vibrational levels. This observed structure if it corresponds to A-X emission must be associated with the lowest vibrational levels of the  $\text{Na}_2$  X  $^1\Sigma_g^+$  ground state. The emission does not correlate with the strongest A-X transitions (Frank-Condon factors) which can be readily excited through laser induced pumping from the ground electronic state.<sup>8</sup> In order to account for selectively produced  $\text{Na}_2$  fluorescence features in the region of the D-line, we attempted to fit the spectrum to a linear combination of several vibrational progressions involving the  $v' \geq 21$  levels of the A state (ex:  $\text{Na}_2$  A  $^1\Sigma_u^+$ ,  $v' = 21 \rightarrow \text{Na}_2$ ,  $^1\Sigma_g^+$ ,  $v'' = 1-6$ ) or to a very selective emission from one of the  $v' = 21, 24, 27, 30$  levels of the A state. Further, the sharp nature of the observed emission features suggests that they might be associated with the energy transfer pumping of cooled  $\text{Na}_2$ . The experimental conditions are such that a significant alkali dimer concentration which can react quite efficiently with Br atoms to produce ground state  $\text{NaBr}$  is present in the expansion ( $T_{\text{oven}} = 875$  K,  $T_{\text{nozzle}} = 935$  K,  $P_{\text{rxn. zone}} = 10^{-1}$  Torr) but a substantial alkali trimer concentration may not yet be generated. This suggests that the signature might result from the energy transfer pumping of cold  $\text{Na}_2$  by vibrationally excited  $\text{NaBr}$ ,

to produce an A-X emission spectrum much sharper than that characterizing the  $\text{Na}_3$  - Br reaction.<sup>4,5</sup> All attempts to fit the spectrum to  $\text{Na}_2$  A-X fluorescence, consistent with the constraints we have outlined, have not been successful.

We must conclude that the features depicted in Fig. 5 do not correspond to emission from the  $\text{Na}_2$  A state. An alternate assignment for these surprising features can be garnered from a comparison with the optical signatures associated with "seeded" sodium expansions and with the emission spectra generated in a pure sodium expansion at low bromine flux (Fig. 4) where the Na D-line is (1) considerably weaker than the  $\text{Na}_2$  A-X and B-X fluorescence features and (2) devoid of any satellite structure. This result, obtained in pure expansion, signals the correlation of an associated intense D-line emission with the manifestation of satellite structure. Further, we note that the spectrum in Fig. 5 appears to demonstrate a synergism between the features appearing to the red and those appearing to the blue of the D-line.

Equally revealing information is obtained from "seeded" expansion studies at moderate bromine concentrations. Figures 7(a) and 7(b) depict higher resolution scans of the region around the D-line. The dual spectra in Figure 7(b) demonstrate that each of the satellite features has associated with it a doublet character. The doublet structure might be attributed to P and R branches in a resonance fluorescence series<sup>16</sup> resulting from the absorption of Na D-line photons. Indeed such a doublet structure induced by a Cd resonance lamp was reported by Brown in a classic resonance fluorescence study.<sup>17</sup> Yet it appears difficult to find previous reports of such a resonance fluorescence excitation due to Na D-line optical pumping. Indeed, the Frank-Condon factors for such resonance excitations at the wavelengths of the Na D-line are not conducive to this process. We also note that the relative intensities of the doublet structures associated with the satellite features follow the relative intensities of the two D-line components ( $16973.4 \text{ cm}^{-1}$  ( $^2P_{3/2} - ^2S_{1/2}$  @ 589 nm),  $16956.2$  ( $^2P_{1/2} - ^2S_{1/2}$  @ 589.6 nm). This may be fortuitous,<sup>16</sup> however, it also suggests an alternate explanation.

The satellite features in the vicinity of the Na D-line might correspond to Raman scattering. If the observed features result from Raman scattering due to the Na D-line and we assign the long and short wavelength features as corresponding to Stokes and anti-Stokes scattering components, their relative intensities should consistently predict a reasonable temperature for the  $\text{Na}_2$  molecules experiencing the Raman effect. The relative intensities of these Stokes and anti-Stokes features and thus the ratios  $I_{s2}/I_{a2}$ ,  $I_{s3}/I_{a3}$ , and  $I_{s4}/I_{a4}$  (the s-1 and a-1 bands are significantly overlapped by the D-line) should be directly proportional to  $e^{\Delta E/kT}$  where  $\Delta E$  is the appropriate energy increment in vibrational energy. These ratios are in excellent agreement (Table I) and suggest a sodium dimer temperature close to 200K. This temperature is quite consistent with the expected heating of the cold  $\text{Na}_2$  produced from our slit expansion source.

Thus the evidence obtained in our overall

analysis of the data presented in Figures 5 and 7 would suggest that the features in the region of the Na D-line are best attributed to Raman scattering from an intense Na atomic emission source. This result, the attainment of a Raman spectrum on the time scale inherent to these experiments suggests an excited state Na atom concentration sufficient to produce effects normally associated with (1) resonant Raman or (2) non-resonant laser Raman experiments. These excited state concentrations portend of the unique chemical physics which will be associated with these systems.

Our previous discussion has emphasized the surprising optical effects which we have already found to characterize the  $\text{Na}_x$  - Br reactive system at high concentration. The data in Figure 8 were obtained with  $T_{\text{oven}} = 825 \text{ K}$ ,  $T_{\text{nozzle}} = 875 \text{ K}$ ,  $P_{\text{rxn.zone}} = 1.5 \times 10^{-1} \text{ Torr}$ . If, in a fast ramping of the "seeded" sodium system after hydrogen evolution, we establish operating conditions close to  $T_{\text{oven}} = 880 \text{ K}$ ,  $T_{\text{nozzle}} = 925 \text{ K}$ ,  $P_{\text{rxn.zone}} = 1.5 \times 10^{-1} \text{ Torr}$ , a further stage in the attainment of the  $\text{Na}_3$  - X reaction amplification configuration is obtained. The spectra in Figs. 8(a) and 8(b) obtained at this higher temperature correspond also to the introduction of a moderate bromine flux. Not only do we maintain the Na D-line excited Raman signal but we also obtain evidence for the significant excitation of the higher lying excited states of the sodium atom. These spectra bear a phenomenal similarity to the sodium fluorescence spectra, induced by Allegrini et al.<sup>18</sup>, and depicted in Figure 9. However, Allegrini et al.<sup>18</sup> produced their spectrum with a cw dye laser tuned to the  $3s^2S_{1/2} - 3p^2P_{3/2}$  D-line transition. Their spectrum (a) is obtained at a temperature of 653 K ( $P_{\text{Na}} = 0.195 \text{ mm/Hg}$ ) and a laser pump energy of  $1 \text{ W/cm}^2$  whereas the amplified blue green  $\text{Na}_2$  B-X emission (b) is obtained at a temperature of 673 K ( $0.344 \text{ mm/Hg}$ ) and a laser pump power of  $2 \text{ W/cm}^2$ . The atomic emissions from higher lying Na atomic states in both studies are believed to result from energy pooling processes involving the Na D-line viz.



The similarity of the spectra which we generate from a purely chemical process (with the exception of the Raman scattering) and the fluorescent data generated by Allegrini et al. with their significant laser pump powers is quite astounding and consistent with our suggestion of a Raman signal generated from the production of high  $\text{Na } 3p^2P$  excited atomic concentrations and the subsequent light scattering of an intense D-line photon flux by sodium dimers. These correlations further suggest that we are well on the way to generating the necessary concentrations to produce substantial emission from  $\text{Na}_3$  - X reactive encounters. It now remains for us to continually improve the expansion conditions so as to increase the sodium trimer concentration. This will be accomplished both in a pure Na vapor expansion and with the mixed sodium-argon or sodium-helium expansion described above.

#### Extension of the $\text{Na}_3$ - X(Cl,Br,I) Amplifier Concept

Although the experimental configuration which

we have used to demonstrate amplification from the  $\text{Na}_3$ -Br reaction is not optimal for producing a chemical laser oscillator, it can readily be used to assess the possibility of forming chemical laser amplifiers from the reactions of lithium trimer with halogen atoms and to evaluate the extension of the oxidation process to fluorine atoms. The later experiments, specifically studies of the  $\text{Na}_3$ -F reactive encounters are now underway. We have also constructed a molybdenum based double oven lithium supersonic expansion source which can be used to test the viability of lithium trimer-halogen atom reactions as a means of producing lithium dimer chemical laser amplifiers.

The  $\text{Na}_2$  amplifiers which we have characterized in the visible region operate on bound-bound transitions. It is not difficult to envision an extrapolation on the  $\text{Na}_3$ -X reaction concept which involves the readily ionizable alkaline earth metal trimers and the formation of excited state dimers which can undergo bound-free excimer transitions. With this focus, we are attempting to generate the  $\text{M}_2$  excimer analogs of the  $\text{Na}_2$  laser amplifiers discussed previously. The ground electronic state of  $\text{Mg}_2$  is very weakly bound.<sup>19</sup> However, detailed calculations suggest the  $\text{Mg}_2$  - Mg bond strength may be on the order of 0.6 eV,<sup>20</sup> quite comparable to that of  $\text{Na}_3$ . We are now forming magnesium molecules, specifically  $\text{Mg}_2$  and  $\text{Mg}_3$ , and observing the excited state products of their oxidation with F and Cl atoms. A halogen atom discharge source which we have developed to study the  $\text{Bi}_2 + \text{F}$  reaction<sup>21,22</sup> is being used to investigate the  $\text{Mg}_2$ -F,  $\text{Mg}_3$ -F,  $\text{Mg}_2$ -Cl, and  $\text{Mg}_3$ -Cl reactions. To date, we have not observed strong  $\text{Mg}_2$  emission from the  $\text{Mg}_3$  - F, Cl reactions, however, surprisingly, preliminary results on this system signal the formation of excited state  $\text{Mg}_x\text{F}$  (Figure 10) and  $\text{Mg}_x\text{Cl}$  charge transfer complexes where x is most likely two. Although we have not yet demonstrated the potential for forming an  $\text{Mg}_2$  based excimer amplifier laser system, the creation of a long-lived  $\text{Mg}_x\text{F}$  complex suggests that, with some modification, this may be feasible. Further it should also be possible to extend these studies to the reactions of the heavier alkaline earths  $\text{Ca}_x$  -  $\text{Ba}_x$ . A similar situation must also prevade if we consider the reaction of readily ionized manganese trimer molecules with fluorine or chlorine atoms. Again the manganese dimer molecule is very weakly bound in its ground electronic state. The dissociation energy ( $D_0$ ) of dimanganese has been estimated by a variety of methods to be between 0.02 and 0.15 eV.<sup>23</sup> The force constant calculated for the manganese trimer bond,  $0.38 \text{ m-dyne/\AA}$ <sup>24</sup> is four times larger than that of diatomic manganese suggesting that  $\text{Mn}_3$  is also much more tightly bound than  $\text{Mn}_2$ , but more weakly bound than  $\text{Na}_3$ . These characteristics, in conjunction with a respectable  $\text{MnF}$  bond energy (4.35 eV.<sup>25</sup>) suggest that the  $\text{Mn}_3 + \text{F} \rightarrow \text{Mn}_2 + \text{MnF}$  reactive encounter may represent a feasible source of excimer emission.

Finally, we should note the correlation which these suggested extrapolations have with the complementary study of the Group IIA metal-halogen molecule reactions as they lead to the formation of the Group IIA dihalide. As a complement to the study of the alkaline earth molecule reactions which we outline, we have used a combination of single and multiple collision chemiluminescent

studies and laser induced fluorescence spectroscopy<sup>26</sup> to (1) demonstrate the highly efficient collisional stabilization of electronically excited Group IIA dihalide collision complexes formed in direct  $M + X_2 \rightarrow MX_2$  reactive encounters, (2) delineate the first direct evidence for symmetry constraints associated with dihalide formation in the  $M + X_2$  insertion process, (3) obtain the first discrete emission spectra for these dihalide complexes, and (4) demonstrate that the dihalide formation via the collisionally stabilized  $M + X_2$  reactive association may well involve a dominant branching into electronically excited states of the dihalide complex suggesting the possibility of an electronic population inversion.

The demonstrated collisional stabilization is not readily explained within the RRKM framework suggesting that new models will be necessary to explain the efficient interaction of electronically excited states as well as highly vibrationally excited ground states. The data from this study now begins to provide important information on the efficient stabilization of excited state intermediate complexes, defining a much broader range of interaction than has typically been associated with collisional stabilization phenomena. The demonstrated interaction range of these dihalides and the enhanced interaction of high temperature molecules in general has direct implication for the understanding of molecular formation and energy transfer in the high stress environments which include not only those created in a chemical laser system or combustor but also in a high impulse propulsion system.

#### Acknowledgement

It is a pleasure to acknowledge most helpful discussions with Drs. R. Jones, Bill Watt, T. Cool, Stan Patterson, Rolf Gross, Sherwin Amimoto, John Dering, Glen Perram, and E. Dorko concerning this study. The support of the Georgia Tech Foundation through a grant from Mrs. Betty Peterman Gole, the Army Research Office through the Short Term Innovative Research Program, the Air Force Office of Scientific Research and Army Research Office and AFOSR/SDIO is greatly appreciated.

#### References

1. R. D. Levine and R. B. Bernstein, *Molecular Reaction Dynamics and Chemical Reactivity*, Oxford University Press, New York, 1987.
2. E. J. Mansky and J. L. Gole, work in progress.
3. Short Wavelength Chemical Laser Workshop, Charleston, S.C., Nov. 14-15, 1984.
4. W. H. Crumley, J. L. Gole, and D. A. Dixon, *J. Chem. Phys.* **76**, 6439 (1982). S. H. Cobb, J. R. Woodward, and J. L. Gole, *Chem. Phys. Lett.* **143**, 205 (1988). S. H. Cobb, J. R. Woodward, and J. L. Gole, *Chem. Phys. Lett.* **157**, 197 (1989). S. H. Cobb, J. R. Woodward, and J. L. Gole, *Proceedings of the Fourth International Laser Science Conference, A.I.P. Conf. Proc. No. 191, Optical Science and Engineering Series 10*, pg. 68.
5. J. L. Gole, K. K. Shen, H. Wang, and D. Grantier, "Chemically Driven Pulsed and Continuous Visible Laser Amplifiers and Oscillators", *Proceedings of the 23rd AIAA Plasma-Dynamics and Laser Science Conference*, Nashville, Tennessee, AIAA 92-2994 (1992).
6. B. Wellegehausen, in "Metal Bonding and Interaction in High Temperature Systems with Emphasis on Alkali Metals", A. C. S. Symposium Series 179, edited by J. L. Gole and W. C. Stwalley (Am. Chem. Soc., Washington, D. C.) p. 462, B. Wellegehausen, *J. of Quantum Electronics* **15**, 1108 (1979).
7. See for example, R. S. Berry and C. W. Reimann, *J. Chem. Phys.* **38**, 1540 (1963), R. S. Berry, *J. Chem. Phys.* **27**, 1288 (1957), W. S. Struve, J. R. Krenos, D. L. McFadden, and D. R. Herschbach, *J. Chem. Phys.* **62**, 404 (1975). R. C. Oldenberg, J. L. Gole and R. N. Zare, *J. Chem. Phys.* **60**, 4032 (1974). Given  $Na_2$  and  $Na_3$  ionization potentials of 4.87 and 3.97 eV (A. Hermann, E. Schumacher, and L. Woste, *J. Chem. Phys.* **68**, 2327 (1978) and an electron affinity of 3.363 eV for atomic bromine, we determine a very substantial electron jump cross section  $\sigma = \pi (14.38 / (4.87 - 3.36))^2 = 285 \text{ \AA}^2 (2.85 \times 10^{-14} \text{ cm}^2)$  for the  $Na_2 - Br$  reaction.
8. J. L. Gole, G. J. Green, S. A. Pace and D. R. Prauss, *J. Chem. Phys.* **76**, 2247 (1982), and references therein.
9. For example, M. M. Kappes, R. W. Kunz, and E. Schumacher, *Chem. Phys. Lett.* **91**, 413 (1982).
10. We wish to facilitate the formation of  $Na_2$  in the B, C, and C' excited states in an electronically inverted configuration. To do this,  $Na_3$  molecules must be present and react with halogen atoms. Here, it is important to note that the oscillator strengths for any of the larger sodium polymers ( $Na_n$ ,  $n \geq 3$ ) are sufficiently small versus  $Na_2$  so that they do not interfere with the sodium dimer pump amplification cycle.
11. "Self-Flushing Optical Window to Prevent Collection of Condensates", W. H. Crumley, and J. L. Gole, *Rev. Sci. Instruments* **57**, 1692 (1986).
12. K. K. Shen, H. Wang, D. Grantier, and J. L. Gole, "Visible Chemical Lasers from Alkali Based Electronic Inversions", *Proceedings of SPIE OE\* LASE '93 Conference*, January 16-23, 1993, Los Angeles, CA, in press.
13. J. T. Bahns and W. C. Stwalley, *Applied Physics Letters* **44**, 826 (1984).
14. G. Pichler, J. T. Bahns, K. M. Sando, W. C. Stwalley, D. D. Konowalow, L. Li, R. W. Field, and W. Muller, *Chem. Phys. Letters* **129**, 425 (1986).
15. A. Kopystynska and L. Moi, *Physics Reports* **92**, 135 (1982).
16. With a P-R branch separation given by  $4B_v''$  ( $J+1/2$ ) =  $R(J-1) - P(J+1)$  and  $Na_2$  ground state constants  $B_0 = 0.154707$ ,  $\alpha_0 = 0.000874 \text{ cm}^{-1}$  we find  $B_v''=0 = 0.15427$  and for a frequency separation of order 15-20  $\text{cm}^{-1}$  and  $4B_v''=0 = 0.61708 \text{ cm}^{-1}$  the implied ground state J value lies between 24 and 32. For  $v''$  increasing, these J values increase. From the relationship  $J_{\text{max}} = 0.59 [T(^{\circ}\text{K})/B_v]^{1/2}$ ,  $Na_2$   $1^2_{g^+}$ ,  $v''=0$  at room temperature (300K) has a  $J_{\text{max}}$  of 26. At 200 $^{\circ}\text{K}$ ,  $J_{\text{max}} = 21$ . Thus it is not possible at this time to unequivocally rule out the possible assignment of the doublet

structure to the peaking of P and R branches in a  $1\epsilon_u^+ - 1\epsilon_g^+$  transition. See G. Herzberg, Spectra of Diatomic Molecules, Van Nostrand and Company, 1966.

17. W. G. Brown, Z. Physik 82, 768 (1933).
18. M. Allegrini, G. Alzetta, A. Kopystynska, L. Moi, and G. Orriolis, Opt. Commun. 22, 329 (1977).
19. R. Balfour and A. E. Douglas, Can. Jour. Phys. 48, 901 (1970); K. Li and W. C. Stwalley, J. Chem. Phys. 59, 4423 (1973).
20. F. Reuse, S. N. Khanna, V. de Coulon, and J. Buttet, Phys. Rev. B 41, 11743 (1990).
21. T. C. Devore, R. Kahlscheuer, L. Brock, and J. L. Gole, "On the BiF Bond Dissociation Energy and Evaluation of the BiF Red Emission Band Systems", Chemical Physics 155, 423 (1991).
22. T. C. Devore and J. L. Gole, "Fluorine Hot Atom Oxidation of Bismuth Vapor: A Comment on the Evaluation of the BiF Bond Energy", submitted to Chemical Physics, in press.
23. A. T. L. Haslett, M. Moskovits, and A. L. Weitzmann, J. Molec. Spectrosc. 135, 259 (1989).
24. K. D. Bier, T. L. Haslett, A. D. Kirkwood, and M. Moskovits, J. Chem. Phys. 89, 6 (1989).
25. M. Kent, T. Ehlert, and J. L. Margrave, JACS 86, 5090 (1964).
26. H. Wang, J. Towson, and J. L. Gole, "The Chemistry of Group IIA Dihalide Formation from Alkaline Earth Atom-Halogen Interactions", in preparation.

Table 1

i	$I_{s_i}$ $I_{a_i}$	T (K)
1	2.1	390
2	4.1	205
3	4.6	188
4	4.4	195

Table 1: Ratio of relative intensities of stokes ( $I_{s_i}$ ) vs. antistokes ( $I_{a_i}$ ) features shown with corresponding calculated vibrational temperatures corresponding to those features seen in figures 5 and 7.  $I_{s_i}$  denotes the  $i^{\text{th}}$  stokes feature from the Na D line.  $I_{a_i}$  denotes the antistokes feature. The ratio,  $I_{s_i}/I_{a_i}$  may not accurately represent the actual vibrational temperature of the Raman (dimer) scatterer due to partial overlap of the feature with the Na D line. See text for discussion.

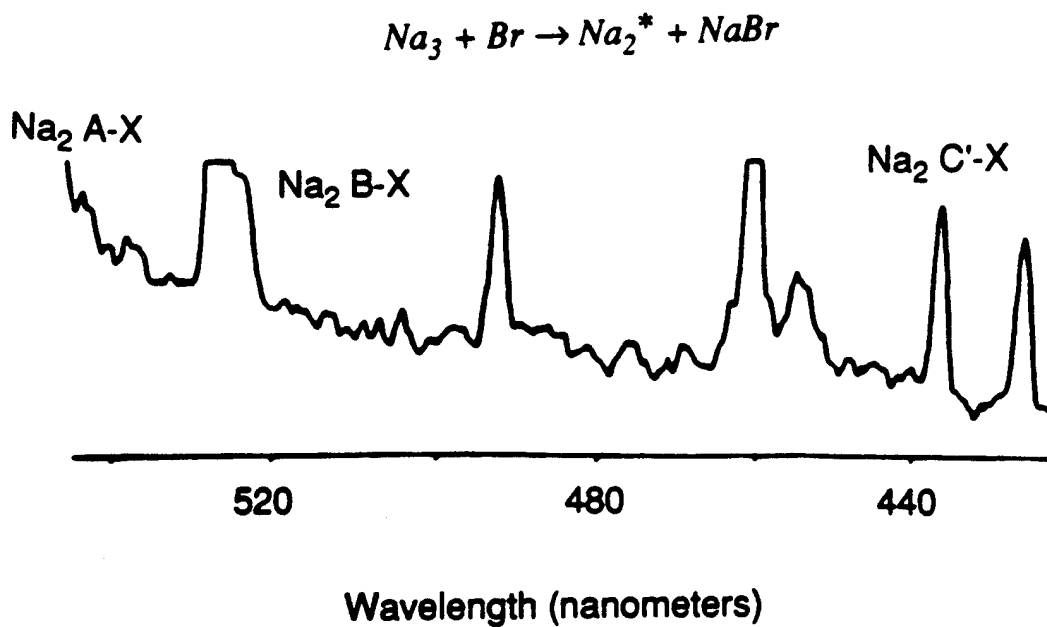
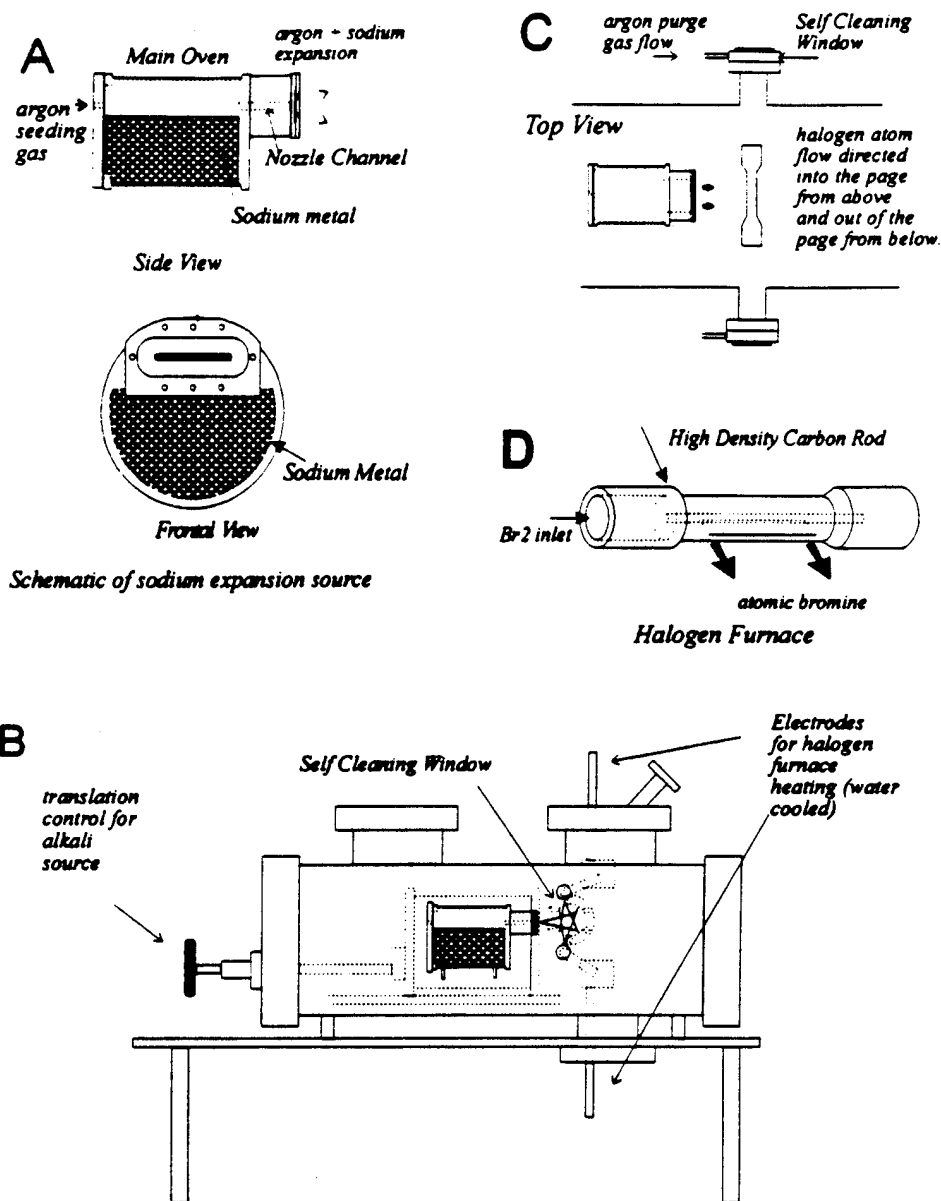


Figure 1: Chemiluminescent emission resulting from the reaction  $\text{Na}_3 + \text{Br} \rightarrow \text{Na}_2 + \text{NaBr}$ . The spectra display sharp fluorescence features in the visible at ~527, ~492, ~460.5 nm superimposed on a broader Na<sub>2</sub> background emission.

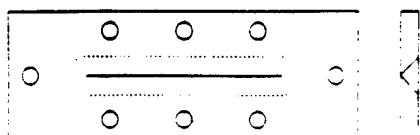


**Figure 2(a):** Schematic of the alkali metal planar supersonic expansion source. This device allows for the sodium vapor to be cooled in a "pure" expansion (without carrier gas) or in a "seeded" flow, in which argon or helium is used to maintain a high backing pressure and hence produce a colder expansion.

**Figure 2(b):** Experimental overview of reaction chamber. The orientation of the alkali expansion source depicted in Fig. 2(a) is shown relative to the positions of the halogen atom sources. The alkali oven system is constructed so as to allow for its in-situ translation during the experiment

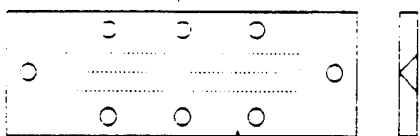
**Figure 2(c):** Overview of experimental reaction chamber configuration from above. The spatial coincidence of the reaction zone and the optical train is demonstrated.

**Figure 2(d):** Schematic of halogen atom planar flow source. See text for discussion.



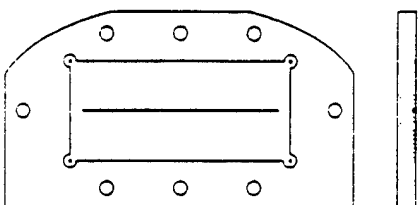
**A**

*Stainless steel expansion slit*



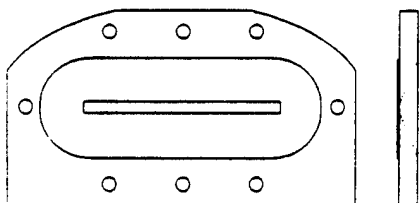
**B**

*Molybdenum expansion slit*



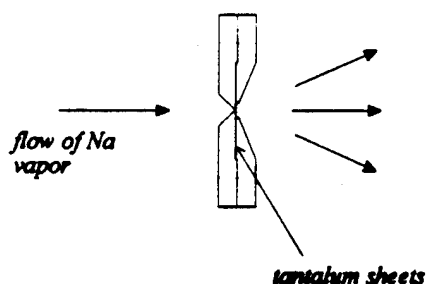
**C**

*Rear plate of a  
dual-plate nozzle  
configuration.*



**D**

*Front plate of  
a dual-plate nozzle  
configuration*



**E**

*Schematic showing fit of  
front and rear plates forming  
the tantalum slit*

**Figure 3(a):** Stainless steel nozzle of 0.003" width constructed using an EDM technique and tested in preliminary stages of the experiment.

**Figure 3(b):** Molybdenum slit nozzle following an identical design to the slit depicted in Fig. 3(a). This slit proved considerably more resistive to alkali erosion.

**Figure 3(c):** Rear plate of a dual-plate nozzle configuration (stainless steel).

**Figure 3(d):** Front plate of a dual-plate nozzle configuration (stainless steel).

**Figure 3(e):** Schematic depiction of the nozzle assembly from the front and back plates depicted in Figures 3(c) and 3(d). The two plates sandwich two parallel sheets of 0.005" tantalum which comprise a 0.003" expansion slit. See text for discussion.

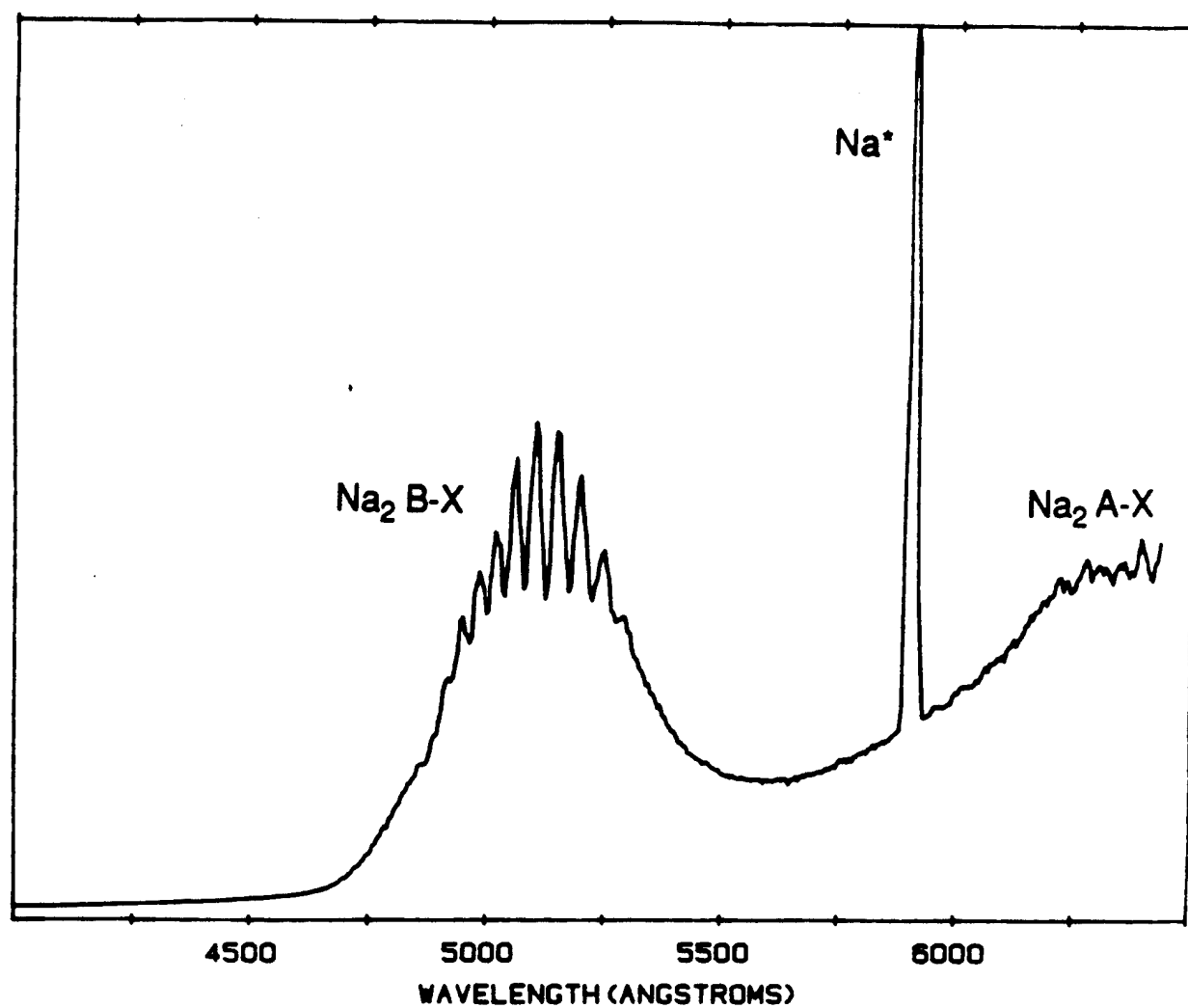


Figure 4: Na<sub>2</sub> B-X and A-X chemiluminescent emission spectrum recorded at low bromine flux under pure sodium expansion conditions.

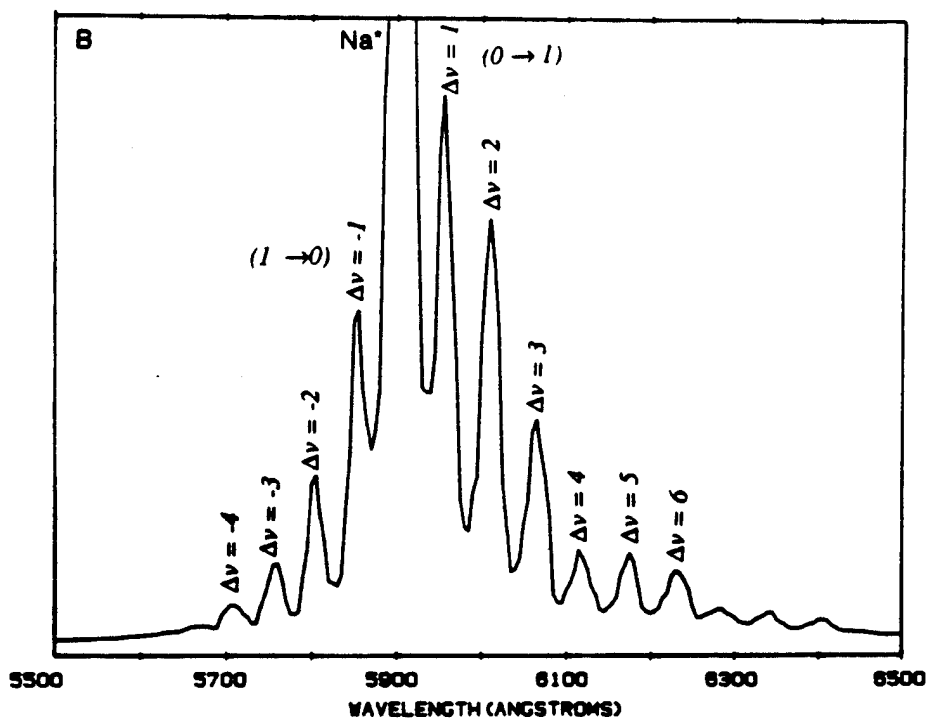
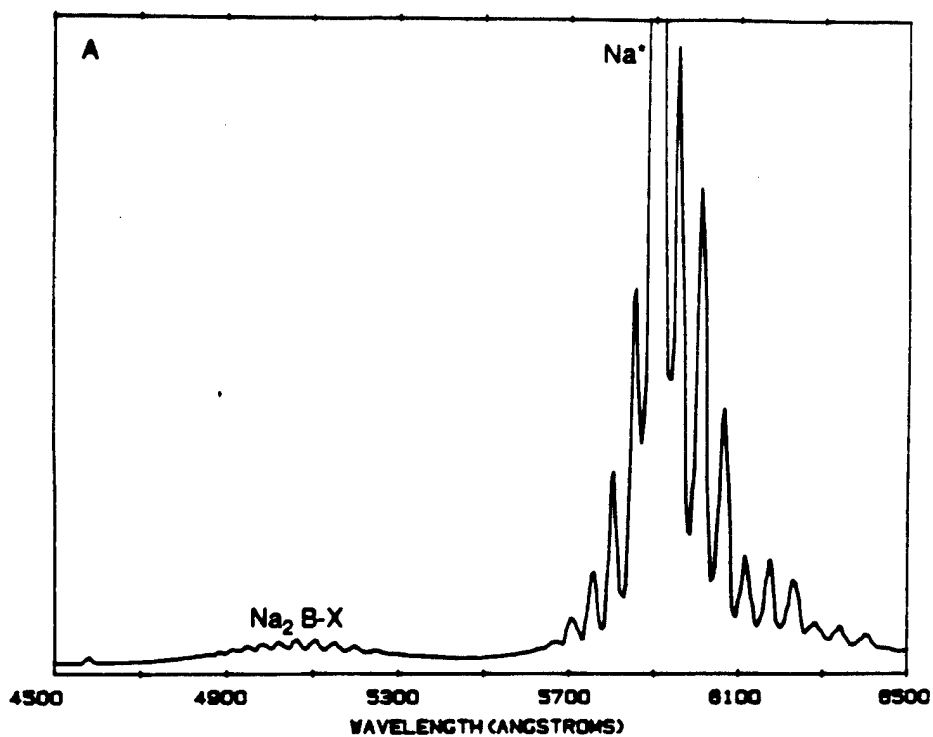


Figure 3:  $\text{Na}_2^*$  chemiluminescent emission from  $\text{Na}_2$ -Br reactive encounters. The system was operated at moderate bromine flux using a pure sodium expansion. See text for discussion.

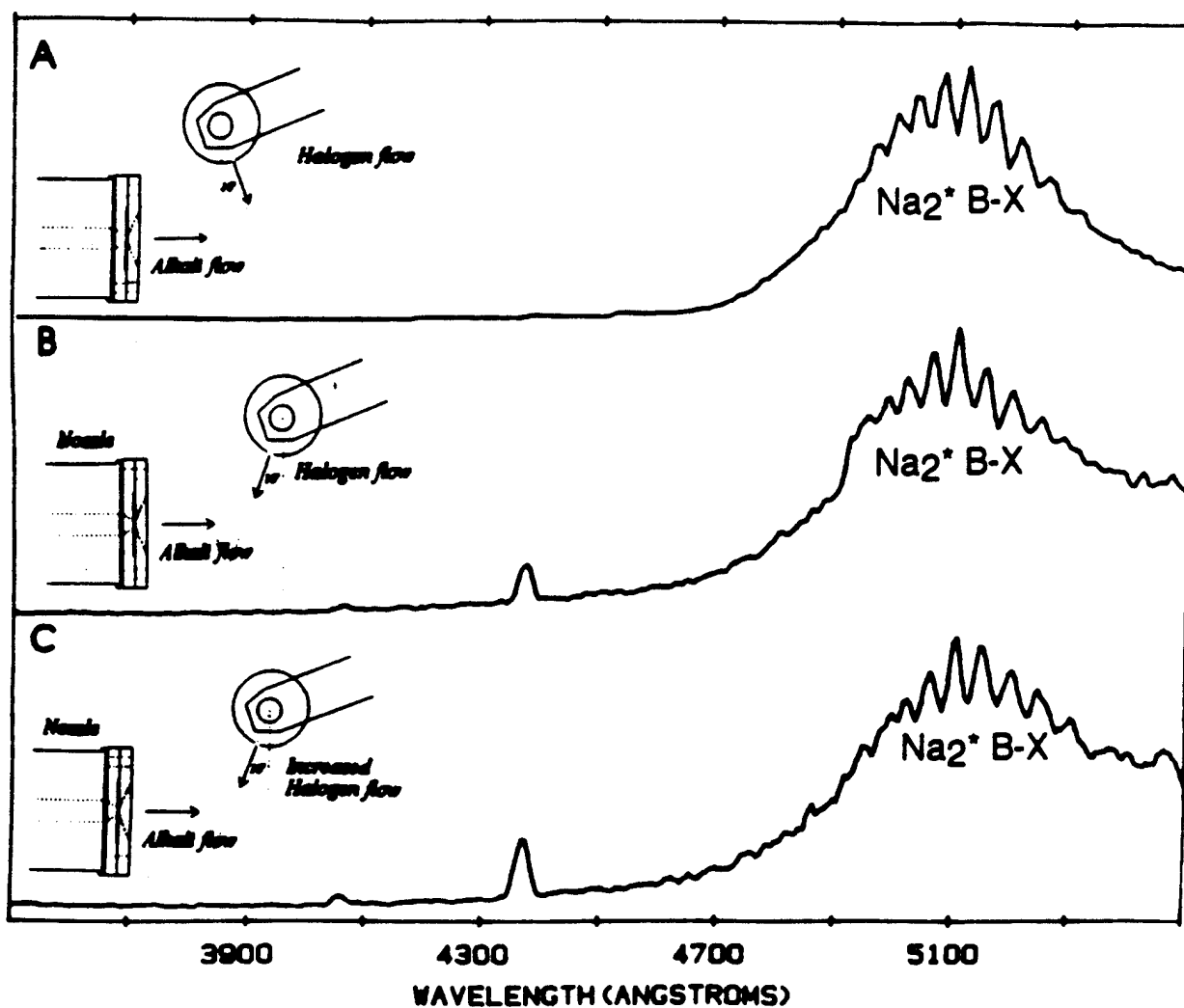


Figure 6: Demonstration of the effect of halogen flow relative to the alkali flow. (a) The halogen flow is oriented to flow with a vector flow component parallel to the alkali expansion. (b) The halogen flow is oriented so as to oppose the supersonic expansion. (c) Same as (b) with increased flow. See text for discussion.

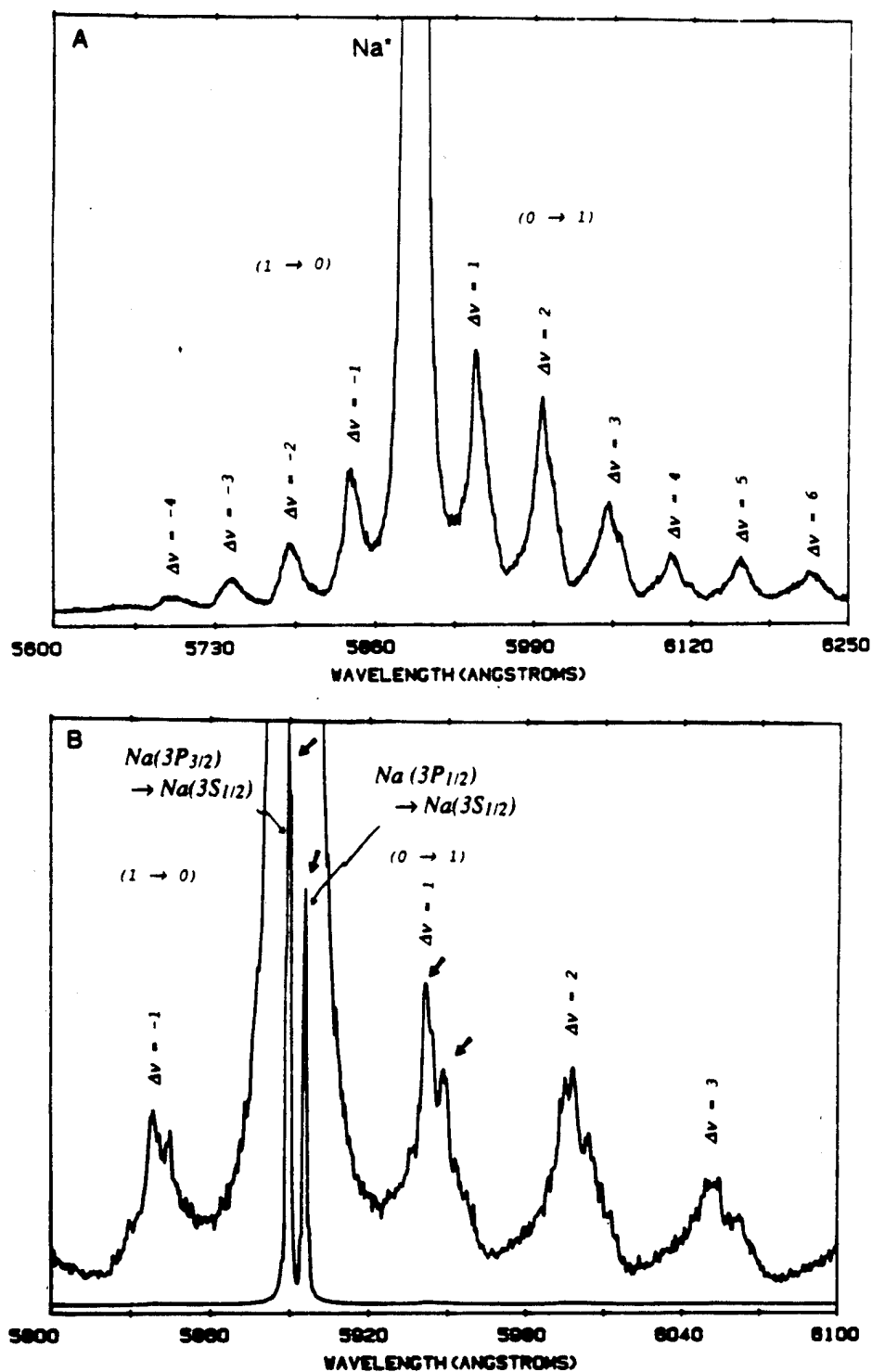


Figure 7: High resolution scans of  $\text{Na}^+$  induced Raman spectra showing transitions associated with the labeled lower state levels. (a) 0.1 nm resolution scan. (b) 0.05 nm resolution scan. Note the correlation of the relative intensities of the peaks corresponding to the doublets of each side band with the relative intensities of the  $\text{Na}(3P_{3/2}) \rightarrow \text{Na}(3S_{1/2})$  and the  $\text{Na}(3P_{1/2}) \rightarrow \text{Na}(3S_{1/2})$  emission features (indicated by arrows).

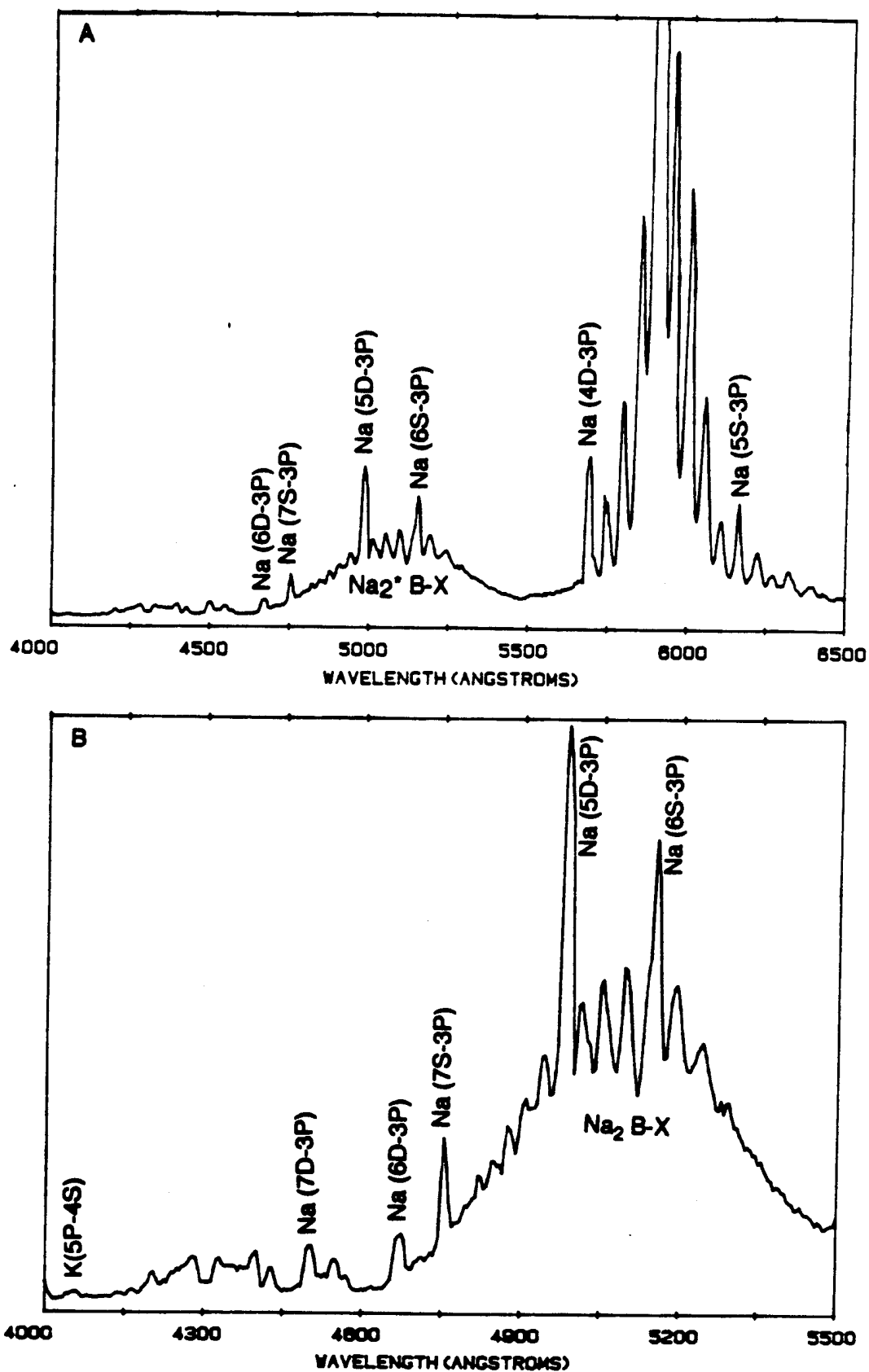


Figure 8: Chemiluminescence spectrum obtained at high bromine and sodium flux demonstrating the pumping of higher excited states of the sodium atom, most likely through energy pooling, (a) in the wavelength region 400-650 nm, and (b) 400-550 nm. Note that figure (b) represents a magnification of figure (a).  $T_{\text{oven}} = 880\text{K}$ .  $T_{\text{nozzle}} = 925\text{K}$ .

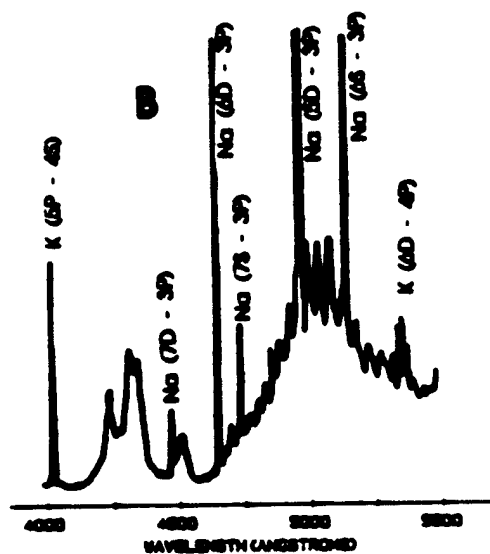
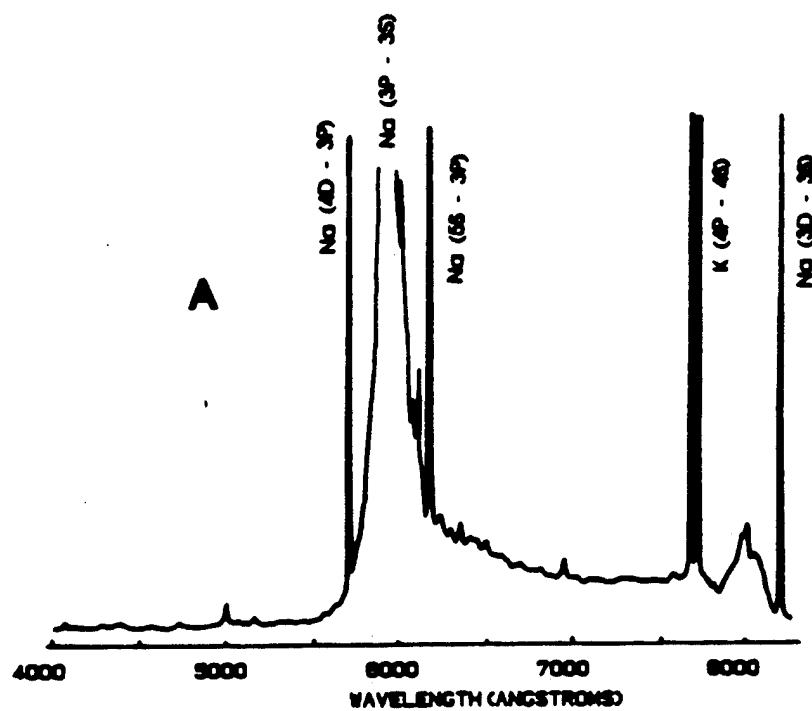


Figure 9: Laser induced sodium fluorescence spectra obtained by Allegrini et al.<sup>18</sup> See text for discussion.

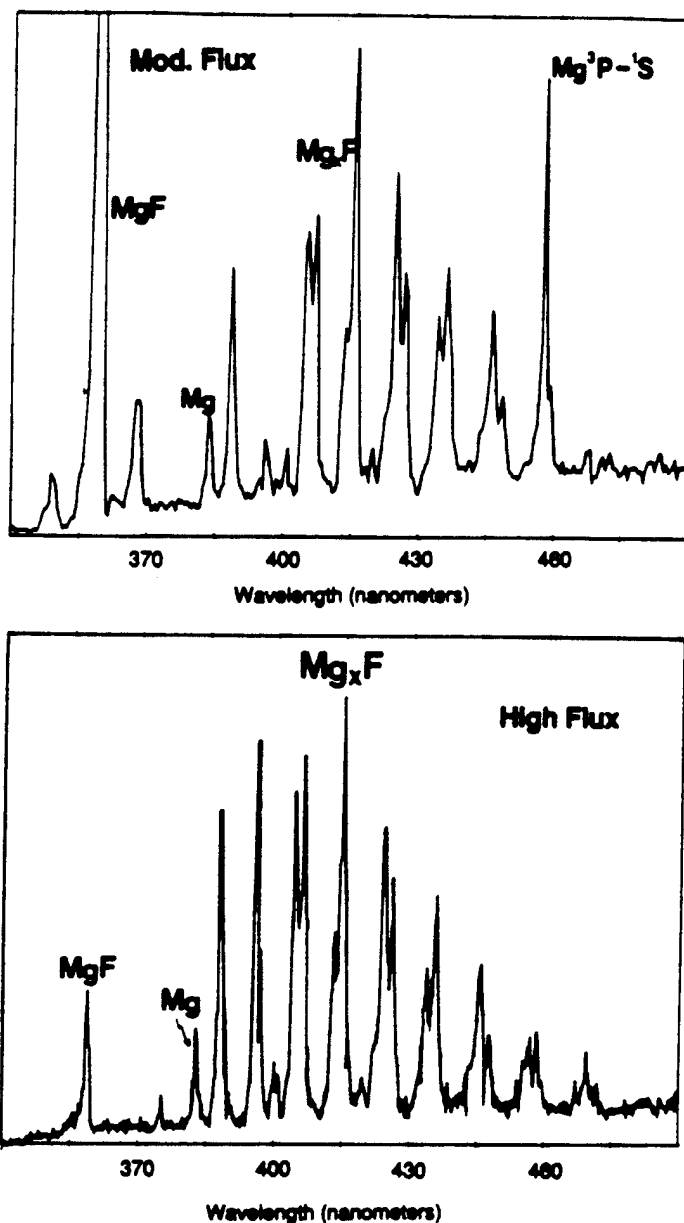


Figure 10: Chemiluminescent spectra resulting from the reaction of small magnesium molecules ( $Mg_2$ ,  $Mg_3$ ), formed in a high metal mole fraction agglomeration flow of dry ice cooled helium, with fluorine atoms. The observed spectra correspond to  $MgF$  ( $A^2\Pi - X^2\Sigma^+$ ),  $Mg\ 3p - 1s$ ,  $3s - 3p$ , and  $3d - 3p$  atomic, and  $Mg_xF$  emission features, which vary in intensity with increasing mole fraction of magnesium. The progression of bands associated with the  $Mg_xF$  emitter (charge transfer complex), where  $x$  is likely 2, appears to correspond to a progression in the  $MgF$  stretch on which is superimposed features associated with an  $Mg_2^+$  moiety. Preliminary studies indicate that  $MgF\ A^2\Pi$  and  $Mg\ 3p$  are formed from the  $Mg_2 + F$  reaction,  $Mg\ 3d$  and  $Mg\ 3s$  are formed from an energy pooling process involving  $Mg\ 3p$  and  $MgF\ A^2\Pi$  and the  $Mg_xF$  charge transfer emission results from the  $Mg_3-F$  reaction. The spectra are taken with an RCA 1P28 phototube at 1 nm resolution.

## APPENDIX V

"Chemically Driven Visible Laser Amplifiers and Oscillators Based on Fast Electronic Energy Transfer", K. K. Shen, H. Wang, C. B. Winstead, and J. L. Gole, Proceedings of the 24th AIAA Plasmadynamics and Laser Science Conference, Orlando, Florida, AIAA 93-3209 (1993).



**AIAA 93-3209**

**Chemically Driven Visible Laser  
Amplifiers and Oscillators Based  
on Fast Electronic Energy Transfer**

**J.L. Gole, K. K. Shen, H. Wang, C. B. Winstead and J.  
Stephens**

**School of Physics, Georgia Institute of Technology  
Atlanta, GA. 30332**

**AIAA 24th  
Plasmadynamics & Lasers Conference  
July 6-9, 1993 / Orlando, FL**

**For permission to copy or republish, contact the American Institute of Aeronautics and Astronautics  
370 L'Enfant Promenade, S.W., Washington, D.C. 20024**

CHEMICALLY DRIVEN VISIBLE LASER AMPLIFIERS AND OSCILLATORS  
BASED ON FAST INTERMOLECULAR ELECTRONIC ENERGY TRANSFER

J. L. Gole, K. K. Shen, H. Wang, C. B. Winstead and J. Stephens  
School of Physics  
Georgia Institute of Technology  
Atlanta, GA 30332

ABSTRACT

Efficient near-resonant intermolecular energy transfer from selectively formed metastable states of SiO and GeO ( $a^3\Sigma^+, b^3\Pi$ ) has been used to form continuous sodium and potassium atom based laser amplifiers at 569 nm (Na), 616 nm (Na), 819 nm (Na), and 581 nm (K). Adopting a variety of pumping sequences in which substantial concentrations of the energy storing metastables are brought into intimate contact with the appropriate atomic receptor, either as a premixed metalloid (Si, Ge)-receptor atom (Na, K) combination is oxidized or through intersection of the metastable pump-receptor atom flows, we have energy transfer pumped  $X\ ^2S_{1/2}$  Na atoms (SiO) to their excited  $4d^2D$  and  $5s^2S$  states and  $2S_{1/2}$  K atoms (GeO) to their  $5d^2D$  state. We observe a system temporal behavior, signaling the creation of a population inversion, and corresponding to a gain condition on the Na  $4d^2D - 3p^2P$  ( $\alpha$  gain coeff.)  $\geq 0.1/\text{cm}$  transition at 569 nm, the Na  $5s^2S - 3p^2P$  ( $\alpha > 0.03/\text{cm}$ ) transition at 616 nm, and the K  $5d^2D - 4p^2P$  ( $\alpha > 0.08/\text{cm}$ ) transition at 581 nm. The gain condition, established for the sodium system using three independent (Roll-Mentel ratio method, sodium lamp line-selected gain measurement, high resolution ring dye laser gain measurement) monitoring techniques, forms the basis for full cavity oscillation on the Na  $4d^2D - 3p^2P$  and  $5s^2S - 3p^2P$  transitions at 569 and 616 nm. At 569 nm, with 0.2% output coupling from a full cavity configuration surrounding a 5 cm reaction - energy transfer - amplification zone formed by the 90° intersection of entrained metastable SiO and Na atom flows, we have achieved an optimum continuous light output exceeding  $10^3$  times that observed with a blocked (single pass) high reflector. This observation of the manifestation of oscillation is consistent with recent modeling studies. Improvements in reactant mixing and active medium concentration through implementation of a concentric flow configuration, the optimization of output coupling, and the operation of the full cavity optical train in windowless configuration, all of which promise a considerable improvement in cavity output, are summarized. Within a generic framework, the first order approach to the creation of amplifiers and oscillators in the alkali based systems might also be extrapolated to exploit the efficient near resonant energy transfer pumping of potential amplifying transitions in lead (Pb), copper (Cu-analog of Cu vapor laser), and tin (Sn) receptor atoms.

Approach to Energy Transfer Pumping

The approach which we outline to develop the first visible chemical laser amplifiers and oscillators<sup>1-5</sup> has relied on a two step procedure wherein chemical energy is produced and stored in a

first step and then transferred in a collision induced process to an appropriate lasing medium in a second step. Following this scheme, we can attempt to produce inversions using (1) "ultrafast" intramolecular energy transfer among the excited electronic states of small diatomic molecules<sup>6-9</sup> or (2) intermolecular transfer from electronically excited metastable storage states to readily lasing atomic receptors. The nature of the amplifying medium dictates the required temporal separation of the two steps of interest.

In developing visible chemical lasers from energy transfer related processes, it is important to note that electronically and highly vibrationally excited molecules, with their inherently diffuse electron density and large amplitude vibrational motions simply interact more efficiently than do ground state molecules in their lowest vibrational-rotational levels. We have determined that several diatomic metal monoxides display collision induced electronic-to-electronic ( $E-E$ )<sup>7-10</sup> and vibrational-to-electronic ( $V-E$ )<sup>11</sup> intramolecular energy transfers which proceed at rates comparable to or far in excess of gas kinetic. Transfers from metastable to shorter lived excited states may proceed at rates which approach 500 times gas kinetic (cross sections well in excess of  $4000\ \text{\AA}^2$ ). It appears that even the low-lying electronic states of several high temperature molecules (the products of metal oxidation) interact with a collision partner which induces energy transfer with a much larger impact parameter than previously anticipated. In a sense we are dealing with "pseudo-macromolecules" which display many of the characteristics inherent to Rydberg states<sup>12</sup> with their large transfer and relaxation cross sections. In several cases the rates for the observed transfers may be comparable to the radiative lifetimes associated with the usually shorter lived and potentially useful upper levels in which the intramolecular transfer terminates.<sup>13</sup> Rates of this magnitude, properly employed, can be competitive with optical pumping!

At some point, there is little distinction between fast intramolecular energy transfer processes, correlating with electronic state couplings and the periods of molecular vibrations (rotations), and intermolecular energy transfer, governed by the duration of collisions with electronically excited states.<sup>14</sup> It is therefore reasonable to expect certain near resonant intermolecular energy transfers to proceed with extremely high cross sections. We consider that an electronically excited molecule, with its diffuse electron density, has a much larger interaction range as it influences reaction and collision partners. The increased interaction rates which several experiments now suggest are certainly encouraging for the development of visible chemical lasers from energy transfer processes.

Relatively simple metal or metalloid oxidation reactions, which involve a branching to long-lived metastable states in a high quantum yield process, while rare, show the promise of creating an energy storage medium to pump atomic transitions with an established high propensity for lasing action.<sup>1</sup> To accommodate this desired pump sequence, we have developed techniques to form copious quantities of the metastable SiO and GeO  $a^3\Sigma^+$  and  $b^3\Pi$  states as the products of the primarily spin conserving Si-N<sub>2</sub>O,<sup>15</sup> Si-NO<sub>2</sub>,<sup>16</sup> Ge-N<sub>2</sub>O, and Ge-O<sub>3</sub> reactions. These long-lived triplet states act as an energy reservoir for fast near resonant intermolecular energy transfer to efficiently pump atomic transitions including select transitions in sodium,<sup>2-5</sup> potassium,<sup>2-5</sup> thallium,<sup>1,2</sup> gallium,<sup>1,2</sup> lead,<sup>3,4</sup> copper,<sup>3,4</sup> and tin.<sup>3,4</sup> Here, we focus primarily on the electronic-to-electronic (E-E) energy transfer pumping of sodium atom based amplifiers corresponding to the Na  $4d^2D - 3p^2P$ ,  $5s^2S - 3p^2P$ , and  $3d^2D - 3p^2P$  transitions at  $\sim 569$ ,  $\sim 616$ , and  $\sim 819$  nm and the concomitant full cavity oscillation on the  $4d^2D - 3p^2P$  transition at  $\lambda \approx 569$  nm. We also consider the implications of the results obtained with sodium as they apply to the future development of potassium, lead, copper, and tin atom based systems.

In order to pump the  $3d^2D$ ,  $4d^2D$ , and  $5s^2S$  levels of atomic sodium,<sup>2-4</sup> we make use of the efficient intermolecular energy transfer process



where  $X^*$  represents the electronically excited atomic species from which we wish to obtain lasing action and the SiO  $a^3\Sigma^+$  and  $b^3\Pi$  states are formed under multiple collision conditions in a focused argon or helium entrainment flow such that the nascent product distribution of the Si-N<sub>2</sub>O<sup>15</sup> or Si-NO<sub>2</sub><sup>16</sup> reactions is rotationally thermalized and vibrationally relaxed (Ref. 1, Figure 4) to the lowest levels of the triplet state manifold. The success of this outlined scheme depends on the rates for the reactions forming the SiO or GeO metastables<sup>17,18</sup> and the rate of the  $\text{MO}^* (\text{M}=\text{Si, Ge}) - X$  intermolecular energy transfer, which, we anticipate, will be influenced by the nature of near resonances between the  $\text{MO}^*$  and  $X^*$  energy levels.

The outlined energy transfer process is found experimentally to be quite efficient for sodium (as well as potassium) atoms. To an even greater degree than that inherent to the previously studied chemically pumped Tl based<sup>1,2</sup> amplifier-oscillator system (Tables I and II of Ref. 1) at  $\lambda \approx 535$  nm, there exist near resonant matchups ( $\Delta E \approx 100 \text{ cm}^{-1}$ ) to receptor atom levels of interest in atomic sodium (and potassium) for both SiO and GeO metastables. We are concerned with the energy transfer pumping of levels which are not accessed through strong electric dipole transitions from the ground state of the alkali atom. Applying these criteria, we summarize the nature of relevant near resonances for the lowest vibrational levels of the  $a^3\Sigma^+$  and  $b^3\Pi$  states of SiO and GeO and the Na and K atomic transitions in Tables I and II. For the SiO - Na system, Table I suggests that the sodium  $4d^2D$  level might be most easily pumped followed closely by the  $5s^2S$  level. The  $3d^2D$  and  $6s^2S$  levels appear somewhat less promising, with the potential reson-

ances involving the  $3d^2D$  level and the lower  $b^3\Pi$  vibrational levels being more favorable. A similar analysis for the potassium (Tables I and II) and lead (Tables III and IV) atom transitions suggests that, at least to first order, both systems are comparable if not more favorable than sodium. In fact, Table V suggests the possibility for an efficient energy transfer pumping of the upper  $4p^2P$  levels of the copper vapor laser and Table VI enumerates a select group of tin atom receptors. All of these systems show promise for the development of energy transfer based amplifiers and while the primary focus of our discussion will be the SiO-Na system, the devices which we are developing to create, enhance, and characterize this amplifying medium are designed for ready conversion to similar studies of potassium, lead, copper, and tin energy transfer pumping.

### Evidence for Efficient Energy Transfer Pumping

Collisions with SiO or GeO metastables have been used to energy transfer pump from the  $3s^2S$  Na ground state to the Na  $3d^2D$ ,  $4d^2D$  and  $5s^2S$  levels forming the basis for amplification on transitions from these levels to the  $3p^2P$  terminal laser level (Fig. 1(a)), the short-lived upper level of the Na D-line.<sup>19</sup> Because the  $3p^2P - 3s^2S$  transition is characterized by a high oscillator strength, it facilitates rapid loss<sup>2-5</sup> of the terminal laser level, especially in a D-line quenching environment, creating ground state Na atoms which are again amenable to near resonant energy transfer pumping.

The  $3d^2D$ ,  $4d^2D$ , and  $5s^2S$  levels are not readily accessed via optical pumping<sup>20</sup> from the ground  $3s^2S$  state of the sodium atom, however, as Figs. 1(b) and 1(c) demonstrate, using SiO metastables formed in the Si-N<sub>2</sub>O reaction, we have successfully energy transfer pumped Na atoms to the  $4s^2S$  and  $2D$  levels where, for the  $3d^2D$ ,  $5s^2S$ , and  $4d^2D$  levels, they subsequently emit radiation at  $\approx 819$ ,  $616$ , and  $569 \text{ nm}$ <sup>21</sup> as they undergo transition to the  $3p^2P$  levels. The observed Na atom transitions, originating at the  $4d^2D$  and  $5s^2S$  levels, are characterized by moderate oscillator strengths. The accessed Na cycle, with its 50 ( $4d^2D - 3p^2P$ )<sup>22</sup> to  $\sim 100$  ( $5s^2S - 3p^2P$ )<sup>23</sup> nanosecond upper state radiative lifetimes (vs. Tl  $2S_{1/2}$  at 7nsec.<sup>1,24</sup>) and short-lived terminal laser level, would appear ideally suited to obtain high duty cycle laser amplifiers and oscillators. In fact, we find that these transitions demonstrate continuous gain. In following sections, we outline a range of measurements on the Si-SiO-Na system which can be readily extrapolated to the potassium, lead, copper, and tin systems and which have been used to demonstrate continuous gain on the  $4d^2D - 4p^2P$ ,  $5s^2S - 3p^2P$ , and  $3d^2D - 3p^2P$  transitions at  $\lambda \approx 569$ ,  $\lambda \approx 616$ , and  $\lambda \approx 819 \text{ nm}$  respectively, and obtain evidence for continuous oscillation at  $\lambda \approx 569 \text{ nm}$ .

As figures 2, 3, and 4 suggest the efficient energy transfer pumping manifest in the SiO-sodium system is also clearly apparent for potassium (Fig. 2), lead (Fig. 3), and copper (Fig. 4) receptors. As in the sodium based spectrum of Fig. 1,<sup>2-4</sup> the K D-line transitions ( $K 4p^2P - 4s^2S$ ) at  $\lambda \approx 767-770 \text{ nm}$  dominates emission from the  $6s^2S$ ,  $7s^2S$ ,  $4d^2D$ ,  $5d^2D$ , and  $6d^2D$  levels, all of which feed the short-lived

4p<sup>2</sup>P upper level of the K D-line. Preliminary experiments using an SiO pump suggest gain on the 6s<sup>2</sup>S - 4p<sup>2</sup>P, 7s<sup>2</sup>S - 4p<sup>2</sup>P, 5d<sup>2</sup>D - 4p<sup>2</sup>P, and 6d<sup>2</sup>D - 4p<sup>2</sup>P transitions with an estimated gain coefficient  $\alpha \sim 0.08$  for the 5d<sup>2</sup>D - 4p<sup>2</sup>P amplifier at  $\lambda \sim 581$  nm. While we have emphasized the use of an SiO pump for the sodium system, Table II demonstrates that several potential potassium based amplifiers might best be created using GeO metastables.<sup>3-5</sup>

Figure 3 demonstrates the results we have obtained when using SiO metastables (Si-N<sub>2</sub>O) to pump lead receptor atoms. Observed Pb transitions are indicated to the right of the figure. We notice that self-absorption involving ground state X <sup>3</sup>P<sub>0</sub> lead atoms is so dominant that no emission to the ground state is observed. This self absorption is even more pronounced than that observed for the Tl system. We find significant pumping of both the <sup>1</sup>S<sub>0</sub> and <sup>1</sup>D<sub>2</sub> levels, as Table III suggests and Table IV indicates, might be considerably improved with a GeO metastable pump. The transitions from the <sup>1</sup>S<sub>0</sub> level terminate in the lowest X <sup>3</sup>P<sub>2</sub> (531.2 nm) and X <sup>3</sup>P<sub>1</sub> (462 nm) levels. If collisional quenching and relaxation of the <sup>1</sup>S<sub>0</sub> level are minimal relative to that of the X <sup>3</sup>P manifold (<sup>3</sup>P<sub>2</sub>, <sup>3</sup>P<sub>1</sub>) it may be possible to create population inversions on the <sup>1</sup>S<sub>0</sub> - <sup>3</sup>P<sub>2</sub> and <sup>1</sup>S<sub>0</sub> - <sup>3</sup>P<sub>1</sub> transitions and produce amplification at 531.2 and 462 nm. The well known lead laser transition at  $\lambda = 723$  nm<sup>25</sup> corresponding to a <sup>3</sup>P<sub>1</sub> - <sup>1</sup>D<sub>2</sub> transition (Fig. 3) has an A value close to 10<sup>6</sup> sec<sup>-1</sup> yet we find no evidence for this transition. We do, however, find evidence for both the <sup>3</sup>P<sub>1</sub> - X <sup>3</sup>P<sub>1</sub> and <sup>3</sup>P<sub>1</sub> - X <sup>3</sup>P<sub>2</sub> transitions and for the <sup>1</sup>D<sub>2</sub> - <sup>3</sup>P<sub>1</sub> transition at 733 nm.<sup>26</sup> These results suggest that the <sup>3</sup>P<sub>1</sub> - <sup>1</sup>D<sub>2</sub> transition may be self absorbed due to a significant <sup>1</sup>D<sub>2</sub> population which also facilitates the observation of the 733 nm transition. It will be important to assess whether the manifestation of a significant <sup>1</sup>D<sub>2</sub> population results from direct energy transfer pumping or whether the <sup>1</sup>D<sub>2</sub> state is populated by the 723 nm laser transition on a time scale considerably shorter than that for the observation of energy transfer.<sup>1</sup> The results obtained for the energy transfer pumping of lead atoms certainly suggest the possibility of creating additional amplifiers. It is particularly encouraging that some of the associated transitions may operate within four level systems thus obviating the self-absorption bottleneck that may plague the Si-SiO-Na system at high sodium concentration.

Figure 4 demonstrates results obtained for the Si-SiO-Cu system obtained using an approach representing a significant extrapolation from the mixing configuration which we have outlined previously and consider in following sections. Here Si and Cu were premixed at room temperature and co-vaporized from a single crucible. The mixture was then oxidized to yield the energy transfer pumping spectrum in Figure 4.

With the examples given in Figures 1-4 (Tables I - VI), it should be apparent that a variety of energy transfer pumping configurations might be invoked to produce amplification across the visible region.

## GAIN MEASUREMENTS FOR SiO-Na - NATURE OF THE REACTION-ENERGY TRANSFER-AMPLIFICATION ZONE FOR SODIUM BASED EXPERIMENTS

### Gain Measurement

Gain measurements have been carried out on the amplification region created in the sodium system using three different experimental configurations. The simplest of these measurements employs the optical train depicted in Fig. 5(a) most recently surrounding a  $\sim 5$  cm energy transfer - amplification zone<sup>2-4</sup> created using the mixing configuration depicted in Fig. 6. The optical train parallels the ingenious design of Roll and Mentel,<sup>4,27</sup> used to measure amplified spontaneous emission (ASE).<sup>2-4,27</sup> The gain coefficient  $\alpha$ , can be calculated from

$$\alpha = \ln ((I_2 - I_1) / I_1 R T^2) / L \quad (2)$$

Here, L is the effective gain medium length (the medium is not necessarily uniform), R is the mirror reflectivity, and T is the transmission of the amplification zone vacuum chamber window in front of the mirror (Fig. 5(a)).  $I_1$  is the measured "single pass" (spectrometer) light intensity from the gain medium with the shutter placed in front of the high reflector. With the high reflector open to and aligned with the gain medium, we measure light of intensity,  $I_2$ , which is contributed to by (1) light passing directly through the gain medium to the detector ( $I_1$ ) and (2) light reflected back through the amplification zone from the high reflector. We refer to  $I_2$  as the double pass ASE intensity. Thus, in Equation (2), we compare the intensity difference ( $I_2 - I_1$ ) to  $I_1$  correcting for the reflectivity and transmissivity.

A considerable change in the relative intensities of the 569 nm Na 4d<sup>2</sup>D - 3p<sup>2</sup>P and Na D-line emissions for the single and double pass ASE output is quite evident in Figure 7. The ratio of the double to single pass intensity for the 569 nm feature depicted in the Figure is 2.6/1, corresponding to a gain coefficient,  $\alpha \sim 0.11/\text{cm}$  (Eq. 2), which is by no means the optimal value that has been achieved with the current configuration. Under optimal operating conditions, using a 1" diameter 99.9% high reflector, we have achieved amplification such that the ratio of light output when the rear high reflector is accessed to that when the rear high reflector is blocked ranges from 3.4 to 3.8 ( $\alpha \sim 0.16$ -0.23/cm). This is a ratio which demonstrates clear gain. It should be compared with the measured ratio for a purely fluorescent feature (Na D-line and higher lying excited state Na transitions) which is usually between 1.1 and 1.2 for the Na D-line, and corresponds to 1.6 for the 5s<sup>2</sup>S - 5p<sup>2</sup>P transition whose emission is also depicted in Figure 7. The theoretical maximum value for the ratio associated with pure fluorescence based on a lossless single reflection is 2. When the experimental conditions are not favorable for formation of the gain medium, we measure significant losses for the reflected light ( $\alpha$  negative in Eq. (2)) employing the same methods we have used to demonstrate the gain in Figure 7. The Na atom transitions at  $\lambda = 569$  nm ( $\alpha \sim 0.1$ -0.15),  $\lambda = 616$  nm ( $\alpha \sim 0.03$ -0.05/cm), and  $\lambda = 819$  nm ( $\alpha \sim 0.02$ -0.03/cm) have all been shown to demonstrate gain. The  $\alpha$  values given in

parentheses are meant to represent typical values determined from Eq. 2 using  $L \approx 5$  cm.

In a second series of more complex gain measurements we have determined gain on the emission lines from a sodium discharge lamp. Using a configuration described in more detail elsewhere,<sup>3,4</sup> we have measured the enhancement of the Na  $4d^2D - 3p^2P$  emission line (or other sodium transitions) which can be evaluated by singling out the transition of interest with a 10 nm bandpass filter. Under working experimental conditions, using the selected 569 nm output from the lamp, we have measured a calibrated gain close to 3.6%. Calibrated gains associated with the amplification zone which are in excess of 5% have been achieved in a few cases. Preliminary measurements at 616 nm indicate a lower gain, on the order of  $1.2 \rightarrow 1.5\%$ . These measured gains using the lamp based optical configuration are believed to represent lower bounds to the true values due to the significant radial extent (cross sectional area) of the lamp output which intersects a much smaller mixing zone and gain medium. When the 569 nm light exiting the gain medium is focused onto the entrance slit of the monochromator, the measured gain is diluted by the mismatch in cross sectional area as not only the gain zone but also regions of negligible gain and even absorption (pumping of  $3p^2P$  level) are monitored.

We have also used the output from a high resolution ring dye laser to carry out laser gain measurements in a frequency scanning mode (laser calibrated with iodine).<sup>2,4</sup> Upon scanning the ring dye laser through the region encompassing the 569 nm feature, we record a gain in excess of 1.5% for the Na  $4d^2D_{5/2} - 3p^2P_{3/2}$  transition.<sup>5,28</sup> This percent laser gain also represents a lower bound determination<sup>3,4</sup> of the single pass amplification. This results because (1) the bandwidth of the ring dye laser (effective linewidth  $\sim 40$  MHz) is considerably smaller than the width of the 569 nm Na  $4d^2D - 3p^2P$  stimulated emission gain profile ( $\sim 2$  GHz) and (2) the precise overlap of the sharply defined laser output beam and the amplification zone is tenuous.<sup>3,4</sup>

These three distinct gain measurements clearly demonstrate the formation of an energy transfer pumped sodium atom laser amplifier. The magnitude of the gain is probably best represented by the results obtained with the Roll-Mentel configuration. However, it is important to note that these determined gain values correspond to a single-pass through the amplification zone. The effective gain in an oscillating full cavity, influenced both by the increased rate of loss of the population inversion due to the stimulated emission process and by the nature of reactant mixing and energy transfer in the amplification zone, will be notably smaller.

#### Amplification Zone

The flow configuration depicted in Fig. 6 produces the longest path length SiO metastable flame ( $\sim 5$  + cm) thusfar obtained. This entrainment flow configuration was designed to create large concentrations of SiO (GeO) metastables intersected at  $\sim 90^\circ$  in subsonic flow, by a high concentration of sodium atoms. The choice of

entrainment gas for the vast majority of the initial experiments has been helium or argon for both the silicon and sodium flows, however, these gases have been replaced by  $N_2$  and soon will be at least partially converted to a mixture of  $N_2$  and CO in an attempt to carefully modify the chemistry of the amplification zone. The configuration of Fig. 6 has also been designed so that the entrained silicon and sodium flows can be moved in-situ relative to each other and hence with respect to the reaction - energy transfer - amplification zone to optimize conditions for formation of the gain medium. In developing the crossed interaction zone to its full extent, we have been concerned with the optimization of reactant mixing considering the rate limiting effect of the silicon concentration, the importance of virtually complete sodium atomization, and the confinement of the reactants and receptors to the cavity axis region. With the silicon source temperature monitored by optical pyrometry, we estimate the Si atom concentration in the amplification zone as a minimum of  $10^{14}/cc$  for all studies involving gain measurement. The  $N_2O$  oxidant concentration exceeds  $5 \times 10^{14}/cc$  and the SiO metastable concentration exceeds  $10^{13}/cc$ .<sup>4</sup> Based upon the Na source temperature, the measured rate of expenditure of sodium from the source exceeds  $10^{18}/cm^2\text{-sec}$  in the reaction zone, which corresponds to a density of order  $10^{13}/cc$ .<sup>4</sup> The reactant and entrainment flows must also be controlled so as to protect the cavity windows from the condensation of metastable silicon or germanium oxide and/or sodium. This latter requirement is met (Fig. 6), in part, using "self cleaning" optical windows<sup>49</sup> with a protective helium (not argon) flow. The "rate limiting" silicon concentration signals a focus on the modification of the oven source configuration depicted in Figure 6 so as to continually improve the silicon atom flux as well as the flow conditions whereby this reactant is transferred to the reaction-energy transfer-amplification zone.

The mixing zone of Fig. 6 is greatly stabilized by the moderate sized ( $\sim 15$  cubic feet) ballast separating the 150 cfm pump and reaction chamber. The  $90^\circ$  intersection of the SiO (GeO) and Na atom flows, once stabilized, can be used to clearly establish a continuous lasing action, however, this is, by no means, the ideal mixing configuration. We have now constructed and are attempting to test and optimize devices which allow the concentric mixing of Si, Na, and  $N_2O$  flows so as to replace the  $90^\circ$  intersection of the entrained SiO and Na flows.

#### Full Cavity Measurements - The Indication of Oscillation

Using the  $90^\circ$  intersecting flow configuration we replace the gain measurement system with a full mirror laser cavity in which the output coupling (1" diameter mirror) corresponds to 0.2%. We employ the same 1" diameter, 99.9% reflector as used in the gain evaluation studies, and operate the system under near optimum reactive flow conditions in a stable cavity configuration with  $g_1 g_2 \sim 0.82$ . We find that the ratio of the output for full cavity operation to that obtained with a blocked high reflector (Figure 8) exceeds  $10^3$ . Compare this also to the signal level observed (Fig. 8) with the blocked high reflector and that

monitored with a completely blocked detector. This result clearly indicates continuous full cavity laser oscillation in the SiO-sodium system.

If we operate the 0.2% output coupled cavity below threshold, monitoring a dominantly fluorescent process, the ratio of full cavity to single pass output (blocked high reflector) is found to be slightly greater than 1.8 for the Na D-line ( $3p^2P - 3s^2S$ ). This value should be compared to a maximum of 1.2 for a much more lossy 4.5% output coupled device ( $g_1 g_2 \approx 0.56$ ). In fact, a maximum (full cavity/blocked reflector) ratio of order 1.9-1.95 is typical for all those wavelengths considered ( $\lambda \approx 569, 616, \text{Na D-line}$ ) when conditions in the reaction-amplification zone are such that no gain is monitored. We have also observed intermediate behavior associated with the establishment of moderate but not optimal gain conditions.

#### Improvement of the Energy Transfer Based Configuration - Ultimate Goals

The current results are exciting not only because they demonstrate lasing action in the visible region but also because they should be substantially enhanced with several improvements in the manner in which the lasing medium is created and the laser output is extracted from the cavity. It remains to increase both the rate limiting silicon and sodium atom concentrations in the reaction zone while maintaining atomization. A logical way to approach this problem involves the conversion of the intersecting flow configuration of Figure 6 to a concentric interaction configuration. We are currently testing and modifying the two designs depicted in Figs. 9(a) and (b) as a means of attaining higher reactant - amplifying medium concentrations. These two designs attempt to create a more efficient mixing of those constituents forming the amplifying medium. In both designs, the sodium source is now placed directly above the silicon source, however, the designs differ in the sequence in which they introduce the reactants. The design of Figure 9(a) first creates the SiO metastables through the Si-N<sub>2</sub>O reaction and subsequently interacts the entrained metastables with an entrained Na flow. In the slightly modified design of Fig. 9(b) we attempt to premix concentric entrained flows of silicon and sodium, oxidizing the mixture with N<sub>2</sub>O. The two designs depicted in Figure 9 both result in a substantial enhancement of reactant concentration and mixing as evidenced especially for the configuration of Fig. 9(b) by the significant 100 fold increase in light emission from the reaction zone as monitored through a side-angle viewing port (Fig. 6). However, they also produce a significant increase in particulate matter and gas phase condensibles for which the current pumping system does not appear to be well suited. These condensibles have the attendant affect of degrading cavity windows, substantially increasing loss elements in the optical train. With some modification of the pumping system, the realignment of entrainment flows, the modification of entrainment gases to best suit the chemistry of the system, and the adjustment of window protecting flows, these problems should be greatly alleviated.

The increase of reactant concentrations may lead to a leveling off and eventual loss of the gain condition if self-absorption on the Na D-line transitions becomes a dominant factor or SiO triplet self-quenching begins to play a deleterious role. Evidence is obtained for some self-absorption at the highest sodium concentrations when the alkali atom production dominates the concomitant SiO metastable production. With our sodium atom source operated, in the absence of interacting silicon or N<sub>2</sub>O, at the temperatures which we have employed to produce the highest flux densities in the amplification zone, we have measured the attenuation of the Na D-line emission from a sodium discharge lamp. We find an attenuation which is much less than 50%. In combination with the cross section for self absorption,  $4 \times 10^{-14} \text{ cm}^2$ , as measured by Ermin et al.,<sup>30</sup> this suggests a sodium atom concentration close to that estimated previously. Of course, in the presence of N<sub>2</sub>O and silicon reactants, the attenuation due to self absorption, while evidenced, is considerably diminished ( $\sim 5 - 10\%$ ).

Although concern with the possible deleterious effect which a pumping of the Na D-line might have on transitions terminating in the  $3p^2P$  level is somewhat alleviated in the present system by the sodium discharge experiments of Tribilov and Shukhtin,<sup>31</sup> and the 0.01 second duration laser pulse for the Na  $4s^2S - 3p^2P$  infrared transition observed by Mishakov and Tkachenko<sup>32</sup> as quasicontinuous lasing, it must eventually limit the size of the laser systems. However, this might be forestalled to great degree if we take advantage of the efficient quenching of Na  $3p^2P$  atoms which Tanarro et al.<sup>33</sup> have demonstrated for N<sub>2</sub> and CO. In fact, if we replace the Si-SiO and Na entraining argon or helium gases<sup>3,4</sup> with N<sub>2</sub>, we observe a pronounced effect on the energy transfer spectrum (Fig. 10) taken for an intermediate sodium flux. While the 569 nm feature is dominated by the Na D-line emission when argon is used as an entrainment gas, its intensity can be made to exceed that of the D-line when N<sub>2</sub> is used. This result, obtained and repeated for successive scans taken during the same experimental run, suggests the possibility for a considerable enhancement of the 569 nm output. This improvement might well result from the quenching of Na  $3p^2P$ , however, it might also result from an increased inhibition of the Na + N<sub>2</sub>O  $\rightarrow$  NaO + N<sub>2</sub> reaction as the equilibrium is forced toward reactants.<sup>34</sup>

There is reason to believe that the extension of this chemistry will provide further improvements in the system. It is desirable that we insure the efficient oxidation of silicon atoms by N<sub>2</sub>O, however the subsequent reaction of N<sub>2</sub>O, whether in excess or scattered by the flow, with those Na atoms to which we wish to transfer energy is clearly undesirable. This can be prevented in large part if these N<sub>2</sub>O molecules are allowed to react with CO. To enhance this possibility, and with an eye to improving the quenching results depicted in Figure 10, we will soon operate our system with the simultaneous CO entrainment of sodium and the N<sub>2</sub> entrainment of silicon.

The experiments conducted thusfar have made use of only two distinct output coupling configurations. As well as improving reactant

concentrations, the optimum output coupling for the current cavity remains to be evaluated. Finally, we have constructed a modification which will allow removal of the cavity windows that represent significant loss elements. With these improvements, the output from our full cavity configuration should be substantially enhanced.

### System Modeling

Recently, Smith et al.<sup>35</sup> have begun a laser chemistry modeling effort on the SiO-Na system. Starting with the initial concentrations of the reactants Na, Si, and N<sub>2</sub>O which are achievable in the present system these authors have used a model which includes the 10 possible processes

1.  $\text{Si} + \text{N}_2\text{O} \rightarrow \text{SiO}^* + \text{N}_2$  - metastable excited state formation.
2.  $\text{Si} + \text{N}_2\text{O} \rightarrow \text{SiO} + \text{N}_2$  - ground state formation - power depleting.
3.  $\text{SiO}^* + \text{Na} \rightarrow \text{SiO} + \text{Na}^* (4d^2D)$  - upper state amplifying transition.
4.  $\text{SiO}^* + \text{Na} \rightarrow \text{SiO} + \text{Na}^* (3p^2P)$  - terminal level amplifying transition.
5.  $\text{SiO}^* + \text{SiO} \rightarrow \text{SiO} + \text{SiO}$  - self quenching of SiO metastables.
6.  $\text{Na}^* (4d^2D) \rightarrow \text{Na}^* (3p^2P) + h\nu (569 \text{ nm})$  - spontaneous emission.
7.  $\text{Na}^* (4d^2D) + h\nu (569 \text{ nm}) \rightarrow \text{Na}^* (3p^2P) + 2h\nu (569 \text{ nm})$  stimulated emission.
8.  $\text{Na}^* (3p^2P) + h\nu (569 \text{ nm}) \rightarrow \text{Na}^* (4d^2D)$  - optical pumping.
9.  $\text{Na}^* (3p^2P) \rightarrow \text{Na} (3s^2S) + h\nu (589 \text{ nm})$  - spontaneous emission.
10.  $h\nu (569 \text{ nm}) \rightarrow h\nu (569 \text{ nm})$  outcoupling fraction for 569 nm photons (laser cavity 5 cm in length - mirror reflectivities 99.99 and 99.80%).

Using known kinetic rates, variable initial concentrations, reasonable and variable rates for those processes which have not been directly measured, and assuming a closed reaction in which the reactants are not replenished, Smith et al.<sup>35</sup> have deduced temporal profiles for the Na concentration, 569 nm photon concentration, energy density, and power density. They conclude that order of magnitude increases in the initial concentration of Si or N<sub>2</sub>O have a profound effect on the system (power density increase) whereas significant changes in the Na concentration have relatively little effect. This signals the rate limiting nature of the silicon concentration and the importance of the branching into the metastable triplet states. It is also to be noted that a significant increase in power density may be muted by SiO<sup>\*</sup> self quenching, the rate of which certainly must be established for these systems. For the diversity of initial reactant concentrations and rates used in their model, Smith et al.<sup>35</sup> predict output power densities peaking between 100 (strong SiO<sup>\*</sup> self quenching) and 7000 mW/cc. These results, which will soon be supplemented by a more detailed modeling effort, are quite encouraging.

### Acknowledgement

It is a pleasure to acknowledge most helpful discussions with Drs. R. Jones, Bill Watt, T. Cool, Stan Patterson, Rolf Gross, Sherwin Amimoto, John

Dering, Glen Perram, and E. Dorko concerning this study. The support of the Georgia Tech Foundation through a grant from Mrs. Betty Peterman Gole, the Army Research Office through the Short Term Innovative Research Program, the Air Force Office of Scientific Research and Army Research Office and AFOSR/SDIO is greatly appreciated.

### REFERENCES

1. J. R. Woodward, S. H. Cobb, K. K. Shen, and J. L. Gole, IEEE Jour. of Quant. Elect. JOE **26**, 1574 (1990). J. R. Woodward, S. H. Cobb, and J. L. Gole, Proceedings of the Fourth International Laser Science Conference, A.I.P. Conf. Proc. No. 191, Optical Science and Engineering Series 10, pg. 63.
2. J. L. Gole, J. R. Woodward, S. H. Cobb, K. K. Shen, and J. R. Doughty, SPIE Proceedings Volume 1397, Eighth International Symposium on Gas Flow and Chemical Lasers (1990), pg. 125 (and references therein). J. L. Gole, K. K. Shen, C. B. Winstead, and D. Grantier, Journal de Physique IV, Colloque C7, supplement au Journal de Physique III, Vol. 1, December 1991, pg. 609.
3. J. L. Gole, K. K. Shen, H. Wang, and D. Grantier, "Chemically Driven Pulsed and Continuous Visible Laser Amplifiers and Oscillators", Proceedings of the 23 AIAA Plasma-Dynamics and Laser Science Conference, Nashville, Tennessee, AIAA 92-2994 (1992).
4. K. K. Shen, H. Wang, and J. L. Gole, "Evidence for Continuous Visible Chemical Lasing from the Fast Near Resonant Pumping of Atomic Sodium", IEEE Journal of Quantum Electronics, in press.
5. K. K. Shen, H. Wang, D. Grantier, and J. L. Gole, "Visible Chemical Lasers From Alkali Based Electronic Inversions" Proceedings of SPIE OE LASE '93 Conference, January 16-23, 1993, Los Angeles, California, in press.
6. D. M. Lindsay and J. L. Gole, J. Chem. Phys. **66**, 3886 (1977).
7. M. J. Sayers and J. L. Gole, J. Chem. Phys. **67**, 5442 (1977).
8. J. L. Gole and R. N. Zare, J. Chem. Phys. **57**, 5331 (1972).
9. J. L. Gole and S. A. Pace, J. Chem. Phys. **73**, 836 (1980).
10. W. H. Flygare, Acc. Chem. Res. **1**, 121 (1968).
11. A. W. Hanner and J. L. Gole, J. Chem. Phys. **73**, 5025 (1980). J. L. Gole and S. A. Pace, J. Phys. Chem. **85**, 2651 (1981). J. L. Gole, B. Ohlsson, A. W. Hanner, and E. J. Greene, unpublished.
12. K. McAdam, private communication. See also A. B. F. Duncan, Rydberg Series in Atoms and Molecules, Academic Press, New York, 1971.
13. J. L. Gole, "Probing Ultrafast Energy Transfer Among the Excited States of Small High Temperature Molecules", in "Gas-Phase Chemiluminescence and Chemionization", (Elsevier Science Publishers - A. Fontijn, editor) pg. 253.
14. R. D. Levine and R. B. Bernstein, Molecular Reaction Dynamics, Oxford University Press, New York, 1974. E. J. Mansky, W. Furr, and J. L. Gole, work in progress.
15. G. J. Green and J. L. Gole, Chemical Physics **100**, 133 (1985).
16. R. W. Woodward, J. S. Hayden, and J. L. Gole,

- Chemical Physics 100, 153 (1985).
17. P. M. Swearingen, S. J. Davis, and T. M. Niemczyk, Chem. Phys. Lett. 55, 274 (1978).
  18. S. H. Cobb, M. McQuaid, and J. L. Gole, unpublished, see also references 3-6. D. Husain and P. E. Norris, J. C. S. Faraday, II, 93, 106, 335 (1978) and D. Husain and P. E. Norris, Chemical Physics Letters 51, 206 (1977).
  19. A. Gaupp, P. Kuske, and H. J. Andra, "Accurate Lifetime Measurements of the Lowest  $2P_{1/2}$  States in Neutral Lithium and Sodium", Physical Review A, Vol. 26, pp. 3351-3359 (1982).
  20. Elementary Atomic Structure, by G. K. Woodgate, Clarendon Press, Oxford, 1980.
  21. C. E. Moore, "Atomic Energy Levels", N. B. S. Circular 467, Volumes I, II, and III. See also, R. W. F. Gross and J. F. Bott, Handbook of Chemical Lasers, Wiley and Sons, New York, 1976.
  22. For the Na  $4d^2D$  level, S. A. Kandela, Appl. Optics 23, 2151 (1984).
  23. For the Na  $5s^4S$  level, X. He, B. Li, A. Chen, and C. Zhang, J. Phys. B., At. Molec. and Opt. Phys. 23, 661 (1990).
  24. A. Gallagher and A. Lurio, Phys. Rev. 136, A87 (1964).
  25. G. R. Fowles and W. T. Silvest, Appl. Phys. Lett. 6, 236 (1965).
  26. A. A. Isaev and G. G. Petrash, JETP Lett. 10, 119-21 (1969).
  27. G. Roll and J. Mentel, J. Phys. D. Appl. Phys. 22, 483-487 (1989).
  28. The Na  $4d^2D_{5/2} - 3p^2P_{3/2}$  transition should represent the most favorable to achieve gain and oscillation. The  $4d^2D_{5/2}$  level emits dominantly to  $3p^2P_{3/2}$  whereas the  $4d^2D_{3/2}$  level depletes its population to both the  $3p^2P_{1/2}$  and  $3p^2P_{3/2}$  levels. Consideration of collisional relaxation among the  $3p^2P$  levels would also suggest that the collisionally depleted  $3p^2P_{3/2}$  level is favored as the lower laser level.
  29. "Self-Flushing Optical Window to Prevent Collection of Condensates", W. H. Crumley, and J. L. Gole, Rev. Sci. Instruments 57, 1692 (1986).
  30. A. V. Eremin, I. M. Naboko, and S. A. Palopezhentsev, Opt. Spectrosc. (USSR) 60, 567 (1986).
  31. A. S. Tribilov and A. M. Shukhtin, Opt. Spectrosc. 21, 69 (1966). See also, K. Krokkel, M. Hubs, W. Luhs and B. Wellegehausen, Appl. Phys. B37, 137-140 (1985).
  32. (a) V. G. Mishakov and T. L. Tkachenko, Opt. Spectrosc. (USSR) 64(3), 293 (1988). (b) V. V. Kuchinskii, V. G. Mishakov, A. S. Tibilov, and A. M. Shukhtin, Opt. Spektrosk. 39, 1043 (1975) [Opt. Spectrosc. (USSR) 39, 598 (1975)]. (c) A. A. Kudryavsev, V. N. Skrebov, and T. L. Tkachenko, Opt. Spectrosc. 58, 694 (1985) [Opt. Spectrosc. (USSR) 58, 420 (1985)]. (d) V. G. Mishakov, A. S. Tibilov, and A. M. Shukhtin, Opt. Spektrosk. 31, 324 (1971) [Opt. Spectrosc. (USSR) 31, 176 (1971)]. (e) N. N. Bezuglov and A. B. Tsyganov, Opt. Spektrosk. 59, 195 (1985) [Opt. Spectrosc. (USSR) 59, 115 (1985)].
  33. I. Tanarro, F. Arqueros, and J. Campos, J. Chem. Phys. 77, 1826 (1982).
  34. J. W. Ager III, C. L. Talcott, and C. J. Howard, J. Chem. Phys. 85, 5584 (1986). J. R. Woodward, J. S. Hayden, and J. L. Gole, Chemical Physics 134, 395 (1989).
  35. Chemical Laser Experiments and Analysis, Directed Energy Devices Technology Support Delivery Order No. 0015 prepared by W. Smith, S. Taylor, J. Dansereau, J. Long, and W. Warren for U. S. Army Missile Command, Directed Energy Directorate, Redstone Arsenal, Alabama 35898.

Table I

Near Resonances of  $\text{SiO}^*$  ( $a^3\Sigma^+$ ,  $b^3\pi-X^1\Sigma^+$ ) and Select Na and K Atomic Transitions in Energy Transfer Laser Pumping<sup>a</sup>

Atom	Upper Atomic Level	$\text{SiO}(v', v'')$			
		a-X Trans. $\Delta E(\text{cm}^{-1})^b$		b-X Trans. $\Delta E(\text{cm}^{-1})^b$	
Na	$4d^2D_{5/2,3/2}$	--	--	(1,0) (2,1) (3,2)	294 45 -209
Na	$5s^2S_{1/2}$	(0,0)	200	(2,2) (3,3)	177 67
Na	$3d^2D_{5/2,3/2}$	(1,4)	180	(0,4)	-184
Na	$6s^2S_{1/2}$	(4,0)	155	(4,1)	137
Na	$4s^2S_{1/2}$	No near resonances			
K	$4d^2D_{5/2,3/2}$	(0,5)	-25	(2,7)	60
K	$5d^2D_{5/2,3/2}$	(0,3)	-420	(0,3)	20
K	$6s^2S_{1/2}$	(0,5)	-70	--	--
K	$6d^2D_{5/2,3/2}$	--	--	(0,2) (4,5) (3,4)	-286 40 264
K	$7s^2S_{1/2}$	--	--	(0,3)	-69

a. Listed potential resonances are meant to be indicative but not exhaustive.

b.  $\Delta E$  Molecular level energy - Atom level energy. Positive quantities denote exothermic energy transfer.

Table II

Near Resonances of  $\text{GeO}^*$  ( $a^3\Sigma^+$ ,  $b^3\pi-X^1\Sigma^+$ ) and Select Na and K Atomic Transitions in Energy Transfer Laser Pumping<sup>a</sup>

Atom	Upper Atomic Level	$\text{GeO}(v', v'')$			
		a-X Trans. $\Delta E(\text{cm}^{-1})^b$		b-X Trans. $\Delta E(\text{cm}^{-1})^b$	
Na	$3d^2D_{5/2,3/2}$	(2,0) (3,0)	-367 250	(0,3)	-73
Na	$4s^2S_{1/2}$	(0,2)	130	--	--
Na	$6s^2S_{1/2}$	--	--	(6,0)	-180
Na	$5s^2S_{1/2}$	--	--	(2,0)	245
Na	$4d^2D_{5/2,3/2}$	--	--	(3,0) (4,0)	-401 293
K	$4d^2D_{5/2,3/2}$	(0,0) (1,1)	160 -195	--	--
K	$5d^2D_{5/2,3/2}$	(4,0)	-149	(0,2)	-123
K	$6s^2S_{1/2}$	(0,0)	110	--	--
K	$6d^2D_{5/2,3/2}$	--	--	(2,2)	-185
K	$7s^2S_{1/2}$	(4,0)	-240	(0,2)	-110

a. Listed potential resonances are meant to be indicative but not exhaustive.

b.  $\Delta E$  Molecular level energy - Atom level energy. Positive quantities denote exothermic energy transfer.

Table III

Near Resonances of  $\text{SiO}^*$  ( $a^3\Sigma^+, b^3\Pi-X^1\Sigma^+$ ) and Select Pb Atomic Transitions in Energy Transfer Laser Pumping.

Atom	Upper Atomic Level	$\text{SiO}(v', v'')$			
		a-X Trans. $\Delta E(\text{cm}^{-1})^a$		b-X Trans. $\Delta E(\text{cm}^{-1})^a$	
Pb	$6p^2 \ ^1D$	(0,10)	192	---	---
Pb	$6p^2 \ ^1S$	(0,3)	282	---	---
		(1,4)	-42		
		(2,5)	-436		
Pb	$6p7s \ ^3P_0$	(2,0)	24	(1,0)	-117
				(2,1)	366
Pb	$6p7s \ ^3P_1$	(3,0)	474	(2,0)	529
				(3,1)	269
				(4,2)	6
				(5,3)	-260

a.  $\sim$  Molecular level energy - Atomic level energy. Positive quantities denote exothermic energy transfer.

Table IV

Near Resonances of  $\text{GeO}^*$  ( $a^3\Sigma^+, b^3\Pi-X^1\Sigma^+$ ) and Select Pb Atomic Transitions in Energy Transfer Laser Pumping.

Atom	Upper Atomic Level	$\text{GeO}(v', v'')$			
		a-X Trans. $\Delta E(\text{cm}^{-1})^a$		b-X Trans. $\Delta E(\text{cm}^{-1})^a$	
Pb	$6p^2 \ ^1D$	(0,6)	366	---	---
		(1,7)	69		
		(2,8)	-225		
Pb	$6p^2 \ ^1S$	(3,0)	-43	(2,4)	122
				(3,5)	-117
Pb	$6p7s \ ^3P_0$	---	---	(4,0)	-120
				(5,1)	415
Pb	$6p7s \ ^3P_1$	---	---	(5,0)	235
				(6,1)	-70

a.  $\sim$  Molecular level energy - Atomic level energy. Positive quantities denote exothermic energy transfer.

Table V

Near Resonances of  $\text{SiO}^*$ ,  $\text{GeO}^*$  ( $a^3\Sigma^+$ ,  $b^3\Pi \rightarrow X^1\Sigma^+$ ) and Select Cu Atomic Transitions in Energy Transfer Laser Pumping

Atom	MO*	Upper Atomic Level	MO*(v',v'')			
			a-X Trans.	E(cm <sup>-1</sup> ) <sup>a</sup>	b-X Trans.	E(cm <sup>-1</sup> ) <sup>a</sup>
Cu	GeO	$4p^2P_{3/2}$	--	--	(0,1)	247
					(1,2)	3
					(2,3)	-233
Cu	GeO	$4p^2P_{1/2}$	--	--	(1,2)	251
					(2,3)	15
					(3,4)	-243
Cu	SiO	$4p^2P_{3/2}$	(0,2)	171	(2,4)	198
					(3,5)	-15
					(4,6)	-229
Cu	SiO	$4p^2P_{1/2}$	--	--	(2,4)	446
					(3,5)	233
					(4,6)	19
					(5,7)	-202

a. Molecular level energy - Atom level energy. Positive quantities denote exothermic energy transfer.

Table VI

Near Resonances of  $\text{SiO}^*$ ,  $\text{GeO}^*$  ( $a^3\Sigma^+$ ,  $b^3\Pi \rightarrow X^1\Sigma^+$ ) and Select Sn Atomic Transitions in Energy Transfer Laser Pumping.

Atom	MO*	Upper Atomic Level	MO*(v',v'')			
			a-X Trans.	$\Delta E(\text{cm}^{-1})^a$	b-X Trans.	$\Delta E(\text{cm}^{-1})^a$
Sn	SiO	$6s5p\ ^3P_0$	(2,0)	343	(1,0)	202
					(2,1)	-47
					(3,2)	295
Sn	GeO	$6s5p\ ^3P_0$	---	---	(4,0)	199
					(5,1)	-96
Sn	SiO	$6s5p\ ^3P_1$	(2,0)	70	(1,0)	-71
					(2,1)	320
Sn	GeO	$6s5p\ ^3P_1$	---	---	(4,0)	-74
					(5,1)	369

No near resonances of  $\text{SiO}$ ,  $\text{GeO}$  metastables with  $\text{Sn } ^1D_2$  @ 8613.0 and  $\text{Sn } ^1S_0$  @ 17162.6  $\text{cm}^{-1}$

a.  $\Delta$  Molecular level energy - Atomic level energy. Positive quantities denote exothermic energy transfer.

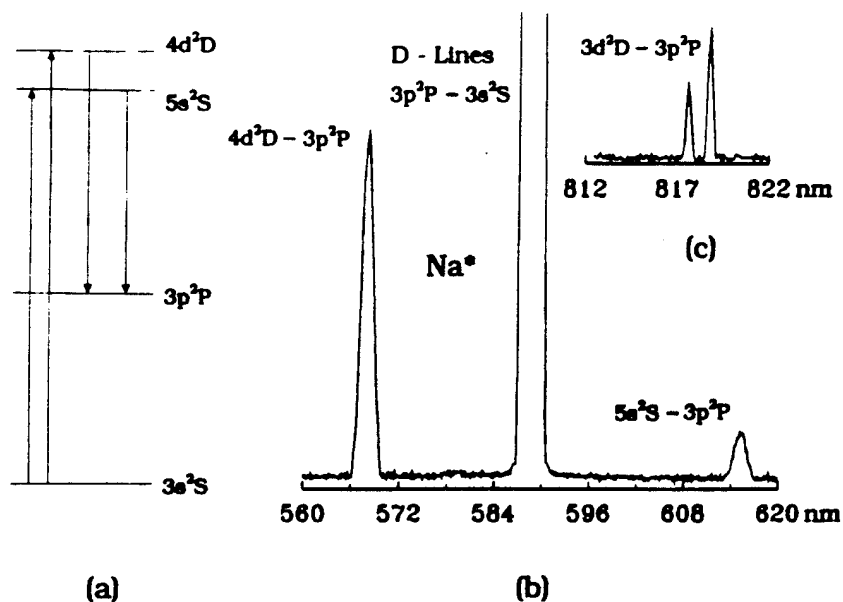


Figure 1(a): Na atom energy level scheme and pumping cycles to produce  $4d^2D$  and  $5s^2S$  excited states.  
 Figure 1(b): Typical energy transfer pumping spectrum for Na  $4d^2D - 3p^2P$  and  $5s^2S - 3p^2P$  transitions and  $3p^2P - 3s^2S$  sodium D-line emission. The D-line emission results both from direct energy transfer pumping from ground state NaO and from subsequent fluorescence following emission to the  $3p^2P$  level.  
 Figure 1(c): Energy transfer pumping spectrum corresponding to Na  $3d^2D - 3p^2P$  transition.

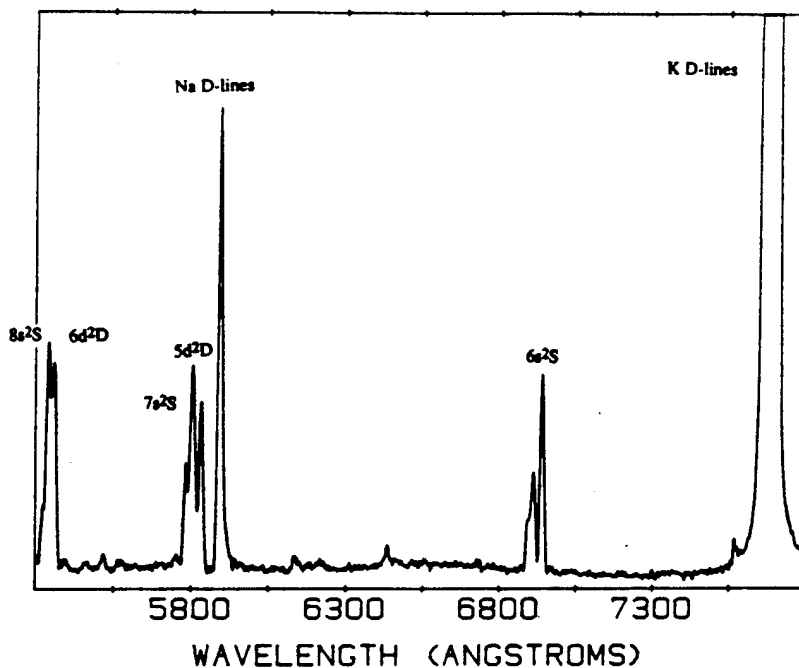


Figure 2: Potassium - SiO ( $a^3\Sigma^+$ ,  $b^3\Pi$ ) near resonant energy transfer spectrum showing the potassium D lines, and atomic emissions corresponding to the  $6s-4p$ ,  $5d-4p$ ,  $7s-4p$ ,  $6d-4p$  and  $8s-4p$  transitions.

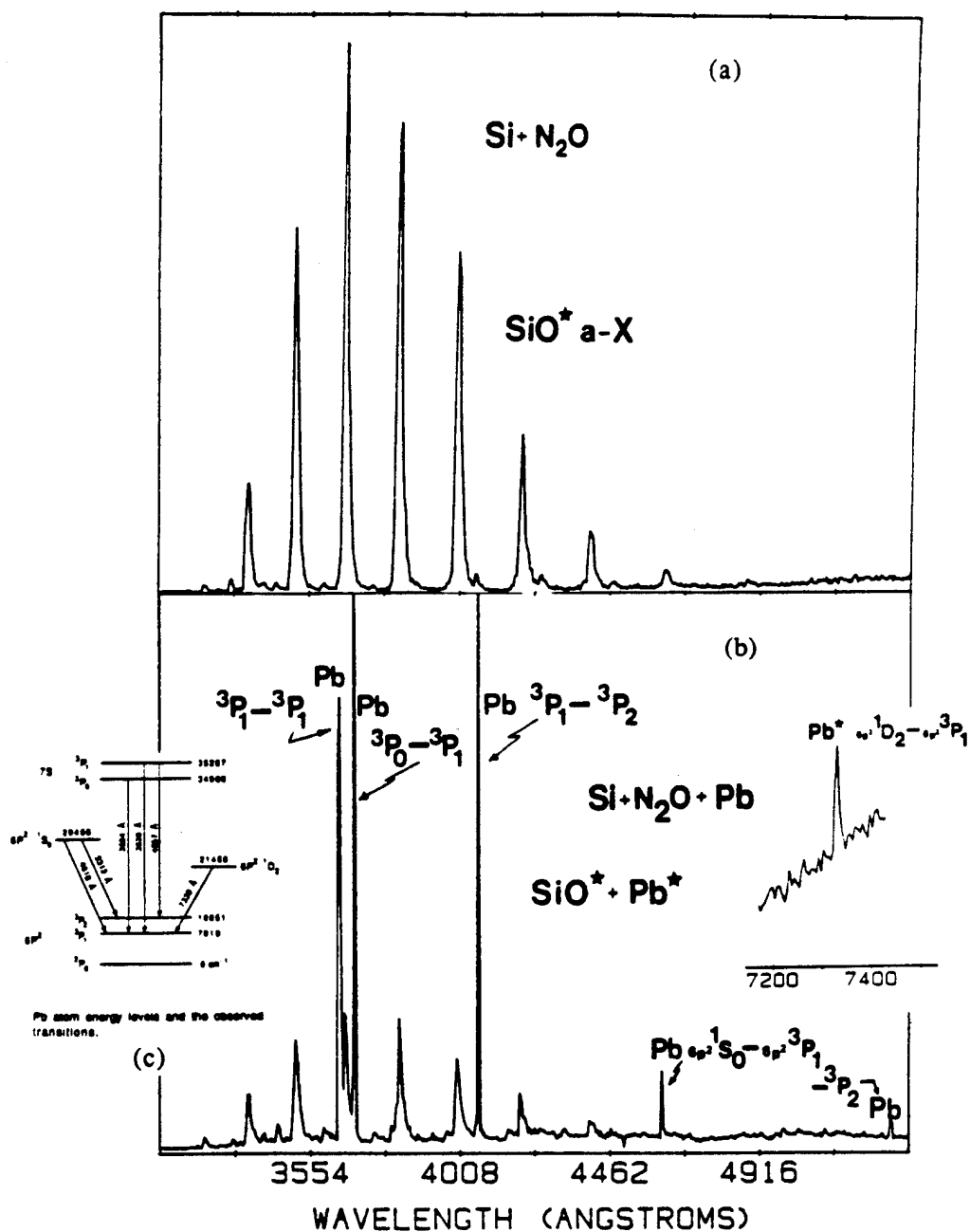


Figure 3: Comparison of lead -  $\text{SiO}$  ( $a^3\Sigma^+$ ,  $b^3\Pi$ ) near resonant energy transfer spectra. Metastable  $\text{SiO}$  molecules were created in the reaction  $\text{Si} + \text{N}_2\text{O} \rightarrow \text{SiO}^* + \text{N}_2$ . (a) The spectrum corresponds to a portion of the  $\text{SiO}$  metastable emission spectrum before lead atoms are brought into the reaction zone. (b) Spectrum recorded with high  $\text{Pb}$  Flux ( $\sim 1$  torr vapor pressure) showing the manifestation of energy transfer pumping to produce electronically excited  $^3\text{P}_0$ ,  $^3\text{P}_1$ ,  $^1\text{S}_0$ , and  $^1\text{D}_2$  levels of the lead atom. (c) Energy levels for the lead atom with observed transitions as indicated in (b). See text for discussion.

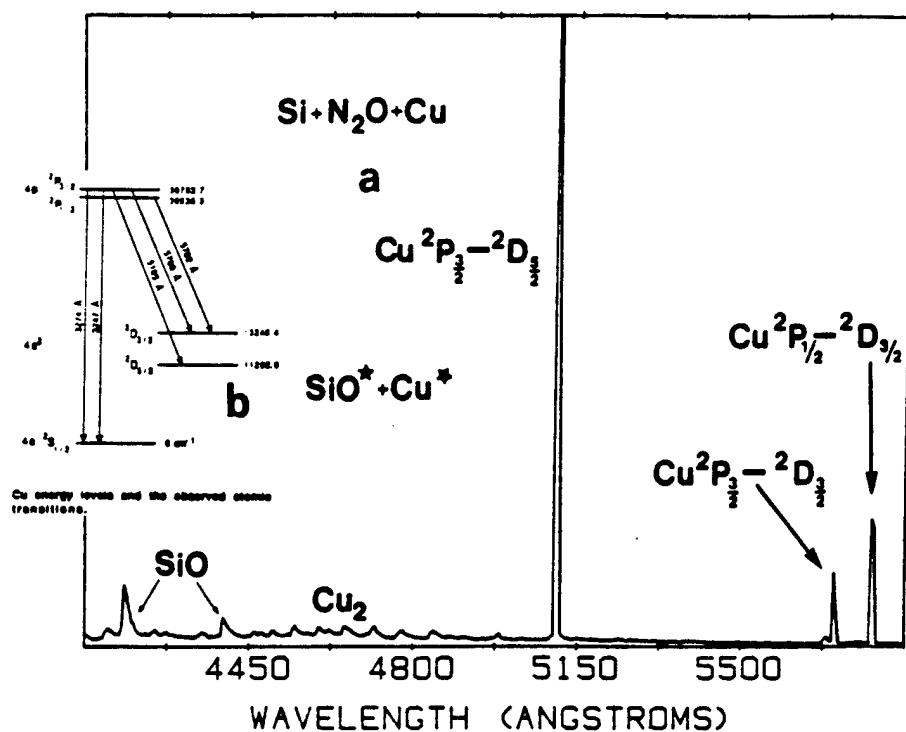


Figure 4: Copper - SiO ( $a^3\Sigma^+$ ,  $b^3\Pi$ ) near resonant energy transfer spectra generated from a "premixed" Si-Cu mixture subsequently oxidized with N<sub>2</sub>O. (a) Spectrum showing a portion of the SiO metastable emission, the  $\text{Cu}^{2+}P_{3/2} - ^2D_{5/2}$  blue green emission line (copper vapor laser) and the  $\text{Cu}^{2+}P_{3/2} - ^2D_{3/2}$  yellow-orange emission features. (b) Energy levels for the copper atom with observed transitions as indicated in (a). See text for discussion.

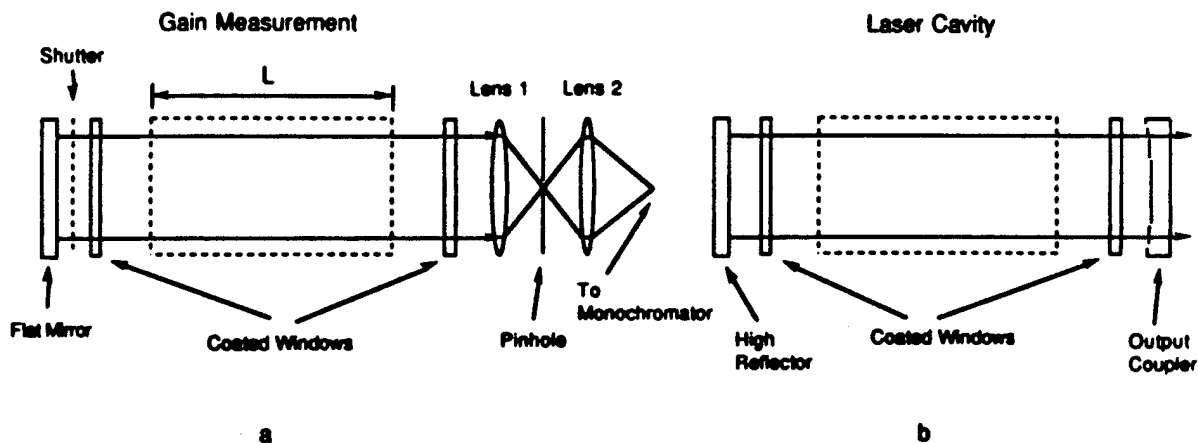


Figure 5(a): Gain measurement configuration after Roll and Mentel (ref. 27). The region marked L in the figure corresponds to the reaction - amplification zone.

Figure 5(b): Laser cavity configuration to characterize potential oscillation in the Si-SiO-Na system at 569 nm.

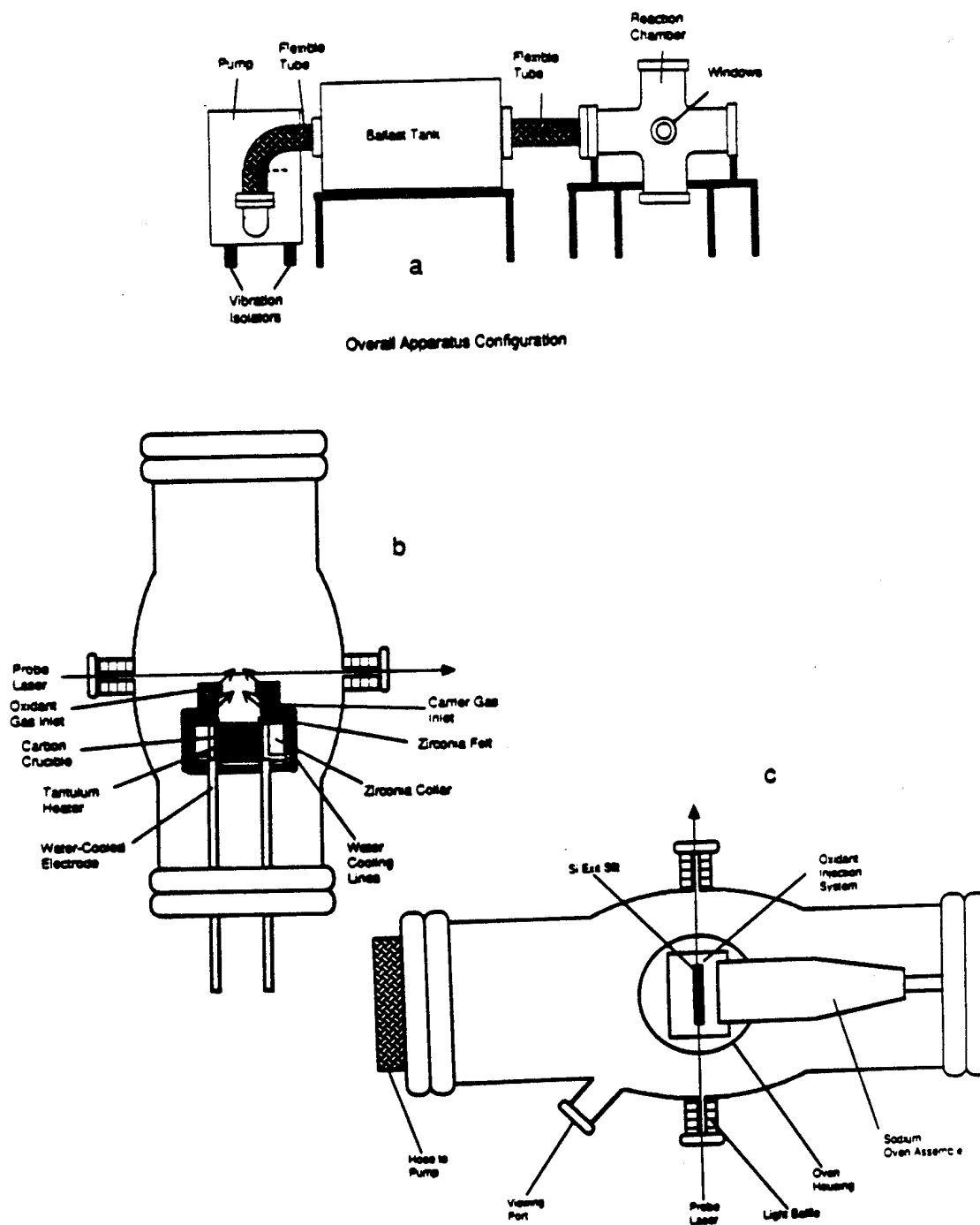


Figure 6: (a) Schematic of reaction chamber and windows defining optical train, ballast tank to moderate pumping fluctuations, and pumping configuration, for extended path length Si-SiO (Si-N<sub>2</sub>O)-Na reaction amplification zone. (b),(c) Side and overhead views of reaction chamber showing positioning of Si oven source, relative locations of Si and Na oven sources, oxidant injection system, and relative positions of these devices with respect to the optical train.

# Sodium Atomic Emissions SiO-Na Energy Transfer

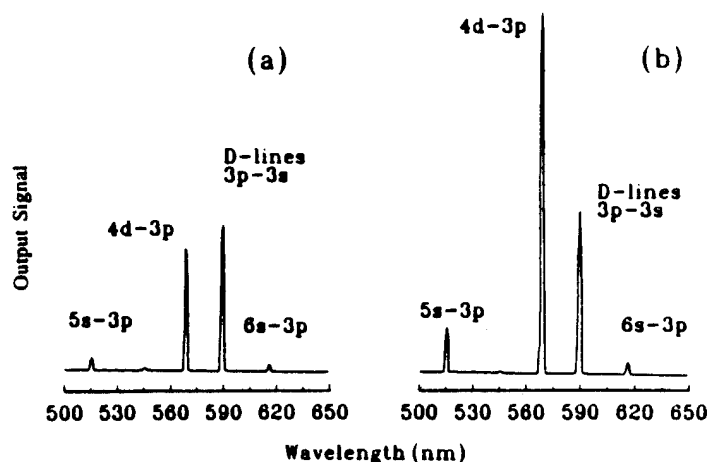


Figure 7(a): Single pass continuous amplified spontaneous emission (ASE) intensity ( $I_1$ ) measured using a Spex 1 meter spectrometer and RCA 4840 phototube and the gain configuration depicted in Figure 3(a) for the Si-SiO-Na system. Spectral resolution is 1 nm. Because the figure is uncorrected for photo-tube response, decreasing from 510 to 630 nm, or grating blaze (500 nm), the emission associated with the  $6s^2S - 3p^2P$  transition appears more intense than that associated with the  $5s^2S - 3p^2P$  transition.

Figure 7(b): Double pass continuous amplified spontaneous emission (ASE) intensity ( $I_2$ ) measured using the gain configuration depicted in Fig. 3(a) for the Si-SiO-Na system. The Na D-line intensity is comparable to that in Fig. 5(a). The ratio of the  $I_2/I_1$  intensity for the 569 nm Na emission feature is 2.6/1 for this individual study and can approach 3.8/1 under optimal conditions for the system. Spectral resolution is  $\sim 1$  nm (see (a)).

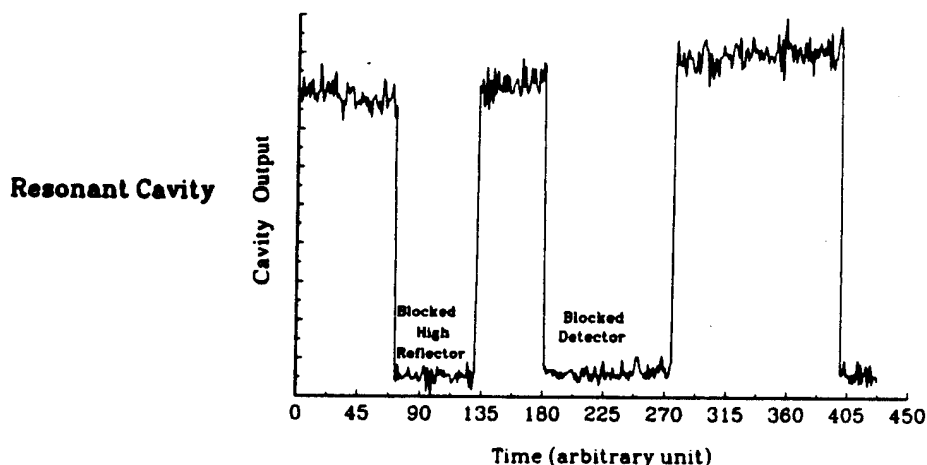


Figure 8: Full cavity output created with  $\sim 0.2\%$  output coupling for the continuous Si-SiO(Si-N<sub>2</sub>O)-Na amplifier at  $\lambda \approx 569$  nm. These measurements were taken in continuous flow with the cavity configuration depicted in Fig. 6(b). The full cavity output is compared to the obtained with both a blocked high reflector and with the entire cavity isolated from the signal detection system. The ratio of the output obtained for the full cavity to that obtained with a blocked high reflector exceeds  $10^3/1$ .

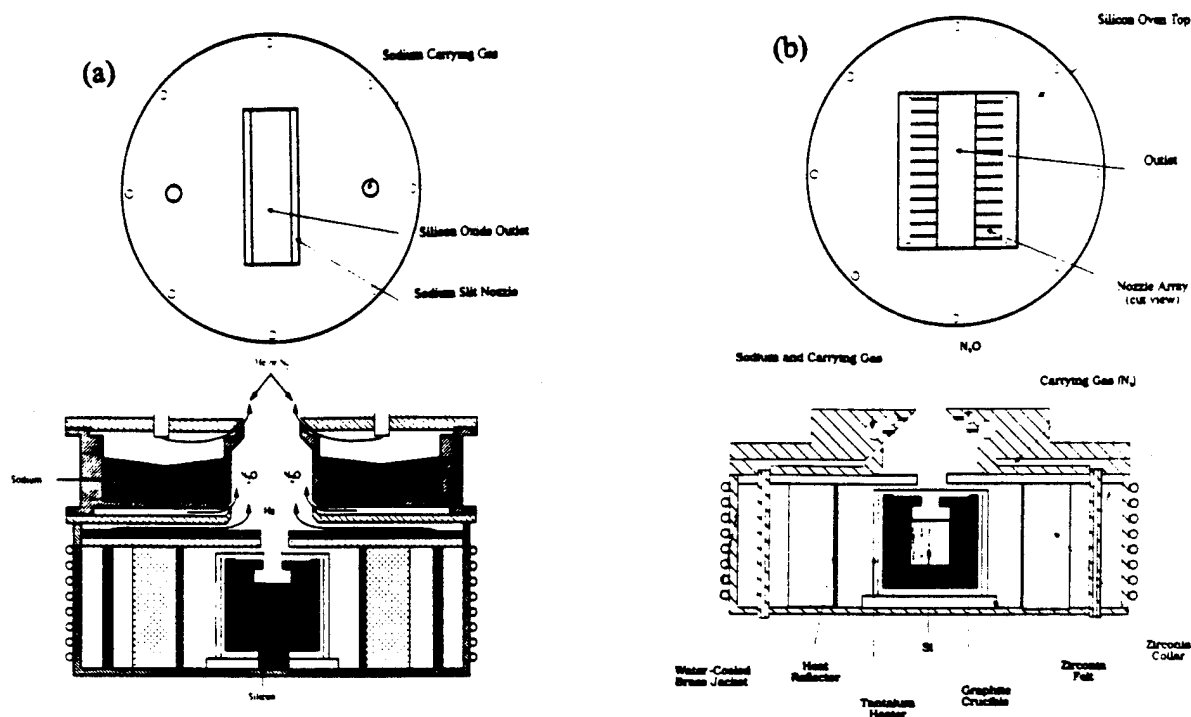


Figure 9(a): Concentric configuration for energy transfer pumping. The sodium oven is placed above the silicon oven. The oxidant  $N_2O$  is introduced into the silicon flow to form  $SiO^*$  which then interacts with sodium vapor. The energy transfer zone is approximately 1" above the silicon oven.

Figure 9(b): Concentric configuration for energy transfer pumping with a sodium and  $N_2O$  injector nozzle array placed above the silicon oven. In this configuration the sodium and silicon are mixed before the oxidant is introduced to initiate the energy transfer process.

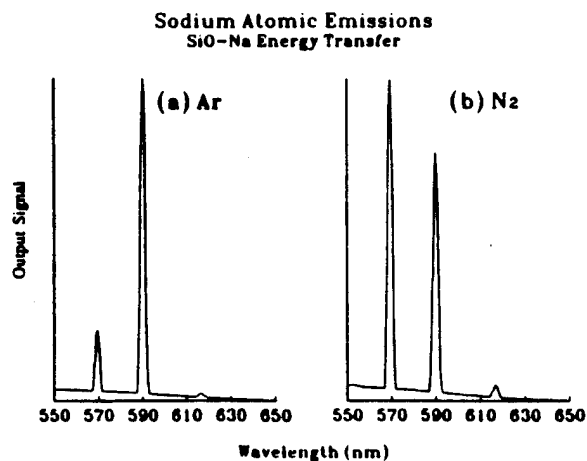


Figure 10: Energy transfer pumping spectra obtained for (a) Ar and (b)  $N_2$  entrainment. The observed Na  $4d^2D-3p^2P$  emission feature ( $\sim 569nm$ ) is seen to increase precipitously in intensity relative to the Na  $3p^2P-3s^2S$  D-line ( $\sim 589nm$ ) with change of entrainment gas from argon to  $N_2$ . See also Fig. 1.

## APPENDIX VI

"Laser Induced Fluorescence and Radiative Lifetimes of the Low-Lying Electronic States of Gaseous AgF", H. Wang, and J. L. Gole, J. Mol. Spectros. 161, 28 (1993).

# Laser induced fluorescence and radiative lifetimes of the low-lying electronic states of gaseous AgF

He Wang and James L. Gole

School of Physics, Georgia Institute of Technology, Atlanta, Georgia 30332

(Received 10 February 1993; accepted 12 March 1993)

At the fringes of the visible region, two low-lying  $1 (\Omega=1)$  electronic states  $A'\Omega 1$  and  $a\Omega 1$  of gaseous AgF located  $\sim 4300 \text{ cm}^{-1}$  below the previously known lowest excited  $A0^+$  state have been excited for the first time in a silver vapor-fluorine reaction system. The  $A'\Omega 1-X^1\Sigma^+$  and  $a\Omega 1-X^1\Sigma^+$  band systems (also observed in chemiluminescence) have been excited and studied using pulsed laser induced fluorescence spectroscopy. The band system associated with the  $A'\Omega 1-X^1\Sigma^+$  transition has been rotationally analyzed. The UV fluorescence of the  $A0^+$  and  $B0^+-X^1\Sigma^+$  transitions has also been excited. The radiative lifetimes of these four low-lying electronic states have been measured as  $7.1 \mu\text{s}$  ( $A'\Omega 1$ ),  $9.1 \mu\text{s}$  ( $a\Omega 1$ ),  $240 \text{ ns}$  ( $A0^+$ ), and  $21 \text{ ns}$  ( $B0^+$ ), respectively, revealing that the two  $\Omega=1$  states are of triplet character, while the two  $0^+$  states are of singlet character. The observed low-lying states of AgF appear to dissociate adiabatically to neutral atoms in contrast to the apparent dissociation of the low-lying electronic states in CuF to ion pairs. The observation of the low-lying  $1$  states of AgF also indicates the existence of similar stable  $1$  states for the remaining silver halides, all of which should absorb visible photons. Major molecular constants of the newly observed  $A'\Omega 1$  state of  $^{107}\text{AgF}$  are  $T_e=24\,950.71(10) \text{ cm}^{-1}$ ,  $\Delta G_{1/2}=506.74(8) \text{ cm}^{-1}$ ,  $B_e=0.281\,32(15) \text{ cm}^{-1}$ ,  $D_e=0.116(60) \times 10^{-6} \text{ cm}^{-1}$ , and  $r_e=1.927 \text{ \AA}$ .

## 1. INTRODUCTION

In contrast to atomic oxidation via  $A+BC$  reactive encounters, the internal mode structure and dynamics associated with the kinetically controlled highly exothermic oxidation of metal molecules is largely unaddressed. However, the limited information which is available demonstrates that these metal molecules can undergo a unique and sometimes unexpected reactive branching.<sup>1-3</sup> The study of this reactive branching can provide information useful for the development of extrapolations from simple  $A+BC$  reactions as well as detailed maps of the quantum level structure of product metal based oxides and halides formed in reaction.<sup>4-6</sup>

Recently, Devore *et al.*<sup>6</sup> have begun a study of the silver molecule ( $\text{Ag}_x$ ,  $x \geq 2$ )-ozone reactions, correlating the observed emission from these reactive encounters with  $\text{AgO}$ ,  $\text{Ag}_2$ , and  $\text{Ag}_x\text{O}$  ( $x \geq 2$ ) excited state product formation. Here, we report an experimental study of the silver vapor-fluorine reaction system. We have obtained the first evidence for two stable  $1 (\Omega=1)$  states of the gaseous silver monohalide AgF, which lie  $\sim 4300 \text{ cm}^{-1}$  below the previously known lowest excited  $A0^+$  state. The band systems associated with the  $A'\Omega 1-X^1\Sigma^+$  (Ref. 7),  $a\Omega 1-X^1\Sigma^+$ ,  $A0^+-X^1\Sigma^+$ , and  $B0^+-X^1\Sigma^+$  transitions have been studied using a combination of chemiluminescence and pulsed laser induced fluorescence spectroscopy following fluoride formation from the four center  $\text{Ag}_2\text{-F}_2$  reaction.

The silver halide molecules  $\text{AgX}$  ( $X=\text{F}, \text{Cl}, \text{Br}$ , and  $\text{I}$ ) are potentially important in the photographic process.<sup>8</sup> Their spectroscopic study has had a long albeit limited history.<sup>9-14</sup> The halide ground states are highly ionic with  $\text{AgCl}$  and  $\text{AgBr}$ , respectively, of 52% (Ref. 15) and 47%

(Ref. 16) ionic character and the AgF ground state dipole moment being  $6.22 \text{ D}$ .<sup>17</sup> The heavy halides follow primarily Hund's case (c) coupling. If we assume a covalent model, the ground state of AgF dissociates to  $\text{Ag } ^2S_{1/2} + \text{F } ^2P_{3/2}$  ground state atoms whose combination generates five molecular states  $0^+$ ,  $0^-$ ,  $1$ ,  $1$ , and  $2$ . At slightly higher energy, the  $\text{Ag } ^2S_{1/2} + \text{F } ^2P_{1/2}$  atoms can combine to yield  $0^+$ ,  $0^-$ , and  $1$  states. The ground state of AgF, identified with  $^1\Sigma^+$  symmetry, has been well studied by Barrow and Clements<sup>18,19</sup> using UV absorption and by Hoeft *et al.*<sup>17</sup> using microwave spectroscopy. The absorption spectrum of AgF reported by Barrow and Clements in Ref. 19 consists of a continuum transition at about  $303.0 \text{ nm}$  and two band systems originating from the  $A0^+$  ( $T_e=29\,220 \text{ cm}^{-1}$ ) and the  $B0^+$  ( $T_e=31\,663 \text{ cm}^{-1}$ ) states, with the former dissociating to the  $\text{Ag } ^2S_{1/2} + \text{F } ^2P_{1/2}$  atomic limit and the latter to the higher atomic dissociation products  $\text{Ag } ^2P_{1/2} + \text{F } ^2P_{3/2}$ . Predissociation has also been observed in high  $J$  rotational levels for both the  $A0^+$  and  $B0^+$  states. However, no transitions in the visible region or stable electronic states with  $\Omega=1$  symmetry have been reported previously for any of the silver halides.

Furthermore, striking differences have been found between the observed spectra of AgF (Refs. 18 and 19) and CuF (Ref. 20) even though Cu and Ag have similar electron configurations as a result of their positions in the periodic table. All five observed low-lying electronic states of CuF are located between  $14\,500$  and  $22\,800 \text{ cm}^{-1}$ , at much lower energy than the  $A0^+$  state of AgF. The lowest CuF electronic state identified is of  $^3\Sigma^+$  symmetry (with components  $\Omega=0^-$  and  $1$ ). The radiative lifetimes of the CuF states have been found experimentally to be fairly long, of the order of one to several microseconds<sup>21,22</sup> even for the reported singlet-singlet transitions. This behavior has been

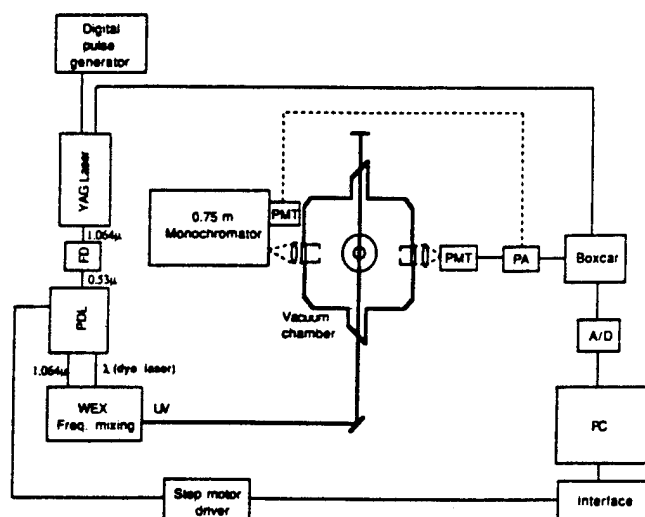


FIG. 1. Experimental setup for chemiluminescence and laser induced fluorescence spectroscopy.

explained with *ab initio* calculations<sup>23-25</sup> within a framework in which all observed bands of CuF are assigned to transitions between the excited  $\text{Cu}^+(3d^9 4s)F^-(2p^6)$  structure and the closed-shell  $\text{Cu}^+(3d^{10})F^-(2p^6)X^1\Sigma^+$  ground state ion pair. These transitions correspond to forbidden  $3d-4s$  electron transfers in the  $\text{Cu}^+$  atomic limit.

It seems apparent that the observation of additional low-lying electronic states in AgF and the measurement of the radiative lifetimes for several of the low-lying states of the AgF molecule can provide key information which can be used to better understand differences and correlations in both the spectral and electronic properties of CuF and AgF. These lifetime measurements are also important as they characterize predissociations. In obtaining the first evidence for two stable  $\Omega=1$  states of AgF, we have rotationally analyzed the  $A'\Omega 1-X^1\Sigma^+$  transition.<sup>7</sup> The radiative lifetimes of the four observed low-lying electronic states of AgF have also been measured. The spin characters and the dissociation limits of these low-lying states are discussed. The internal energy distribution of the reaction product AgF molecules and the possible reaction paths to produce excited and ground state AgF are also considered. Our spectroscopic analysis of the  $A'\Omega 1-X^1\Sigma^+$  transition is presented in detail elsewhere.<sup>7</sup>

## II. EXPERIMENT

AgF molecules were generated in reactive encounters under multiple collision conditions as a helium entrained silver flow was intersected by molecular fluorine. The overall experimental configuration is depicted schematically in Fig. 1. The entrainment flow device used in this study has been described in detail previously.<sup>2</sup> Briefly, silver metal was heated in a graphite crucible to temperatures in the range close to 1600 K. The silver flux emanating from the crucible was entrained in a flow of helium gas at a total pressure of 1 Torr. The fluorine gas was introduced into the entrained silver flow through a concentric ring inlet located  $\sim 1$  cm above the crucible. A chemiluminescence

flame was generated in the reaction zone which could be dispersed by a 0.75 m Spex 1702 monochromator, operated in first order with a 1200 groove/mm grating blazed at 500 nm, and positioned at right angles to the reactant flow signals being detected with an RCA 1P28 photomultiplier. The photomultiplier (PMT) signal was fed to a Keithley 417 autoscale picoammeter and recorded with a personal computer.

In order to carry out the laser-induced fluorescence (LIF) experiments, the second harmonic of a Quanta-ray Nd:YAG laser ( $0.53 \mu$ ) was used to pump a Spectra-Physics PDL-3 pulsed tunable dye laser system operated with DCM or LD698 dye. The output of the pulsed dye laser (with a linewidth of  $0.07 \text{ cm}^{-1}$  and a pulsewidth of 9 ns) was then either mixed with the fundamental output of the YAG laser or frequency doubled in a frequency mixer (Quanta-Ray WEX-1) to produce the UV (in the range 310–410 nm) coherent radiation which was introduced to the reaction chamber in a direction perpendicular to both the reactant flow and detector. The YAG laser was triggered by a digital pulse generator (SRS DG535) with a repetition rate of 15 Hz. The Q-switching signal of the YAG oscillator was used to trigger a boxcar integrator (SRS SR250) for better synchronization. The fluorescence induced by the UV laser pulse was collected with a RCA 1P28 photomultiplier (2.2 ns rise time) and, through a fast preamplifier (CLC 100 Video Amplifier, 500 MHz), sent to the gated integrator to record the spectrum as a function of the laser frequency. A fast digital oscilloscope (HP 54111D, 0.7 ns rise time) was used to real time monitor and record the fluorescence decay. The integration gate was set to a proper width in the range from 20 to 300 ns dictated by the nature of the monitored fluorescence decay with a delay timed such that the gate opens just after the short laser scattering pulse, thus reducing background noise. A personal computer drives the dye laser stepper motor, scanning the dye laser frequency and acquiring the averaged output data from the boxcar synchronously. In order to achieve a linear scan in wavelength when the dye laser frequency was mixed with the infrared, the scan step size of the dye laser was calculated in real time using the PC. The output frequency of the WEX-1 was calibrated using aluminum atom lines.<sup>7</sup>

## III. SPECTROSCOPY AND RADIATIVE LIFETIMES

An overview of the chemiluminescent emission from the silver vapor-fluorine molecule reaction is depicted in Fig. 2(a). The peak at 342 nm is readily identified as the  $(v',v'')=(0,0)$  band of the  $A'\Omega 1-X^1\Sigma^+$  transition of AgF. However, the spectrum is dominated by intense vibrationally resolved structure due to the  $A'\Omega 1-X^1\Sigma^+$  band system observed for the first time as a result of the silver molecule-molecular fluorine reaction. Figures 2(b) and 2(c) display two detailed views of the regions near 400 and 409 nm and reveal two of the weaker features associated with a second system which we label and correlate with an  $a\Omega 1-X^1\Sigma^+$  transition. As Fig. 3(a) demonstrates, both the  $A'\Omega 1-X^1\Sigma^+$  and  $a\Omega 1-X^1\Sigma^+$  band systems can be excited with the output from a pulsed dye laser scanning

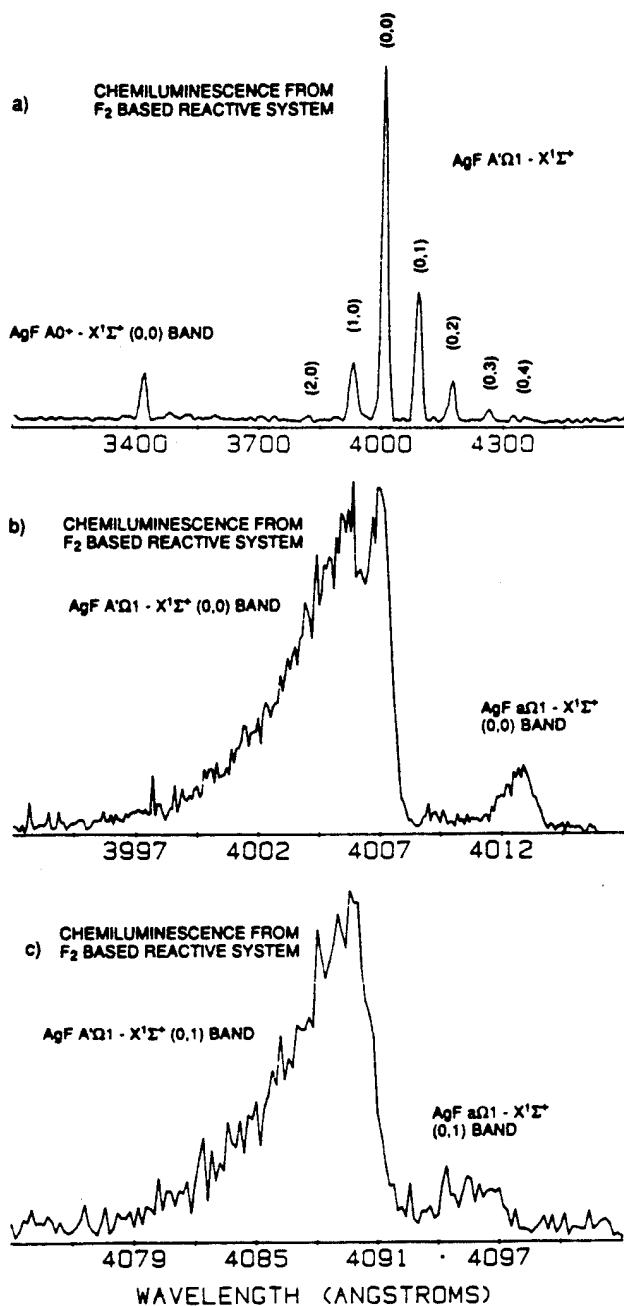


FIG. 2. (a) Overview chemiluminescence spectrum for the reaction  $\text{Ag}_2 + \text{F}_2 \rightarrow \text{AgF}^* + \text{AgF}$  at a resolution of 5 Å. (b) Chemiluminescence spectrum for the reaction  $\text{Ag}_2 + \text{F}_2 \rightarrow \text{AgF}^* + \text{AgF}$  in the region near 400 nm at a resolution of 0.1 Å. (c) Chemiluminescence spectrum for the reaction  $\text{Ag}_2 + \text{F}_2 \rightarrow \text{AgF}^* + \text{AgF}$  in the region near 409 nm at a resolution of 0.1 Å.

through the region about 400 nm. Figure 3(b) depicts a simulation for the (0,0) band of the  $A'-X$  system. Both the CL and LIF signals associated with the structure in Figs. 2 and 3 correlate with the Ag vapor concentration and fluorine gas pressure. These measured band separations agree well, within experimental error, with the known vibrational separations for the ground  $X^1\Sigma^+$  state of  $^{107}\text{AgF}$  given by Barrow and Clements.<sup>19</sup> Based on this comparison, one can tentatively attribute the observed structure to a transition of the AgF molecule originating from a newly

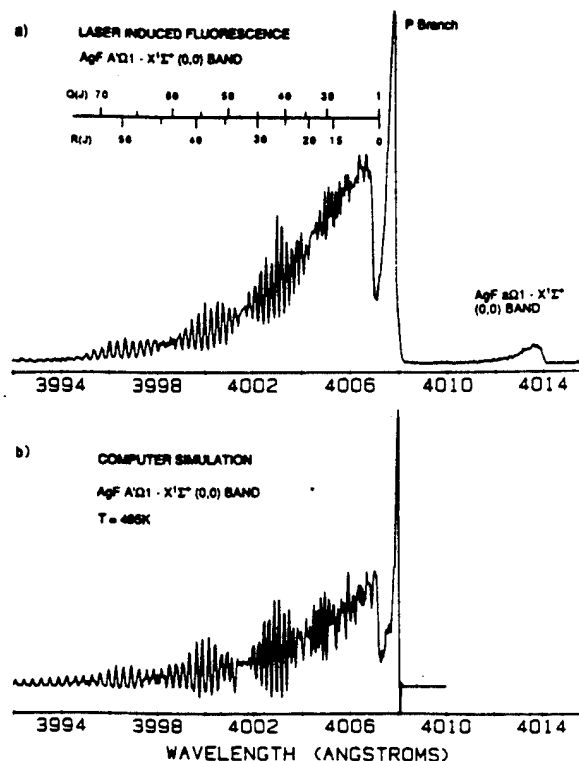


FIG. 3. (a) Pulsed laser induced fluorescence spectrum of the  $A'\Omega 1-X^1\Sigma^+$  (0,0) band of AgF. The intensity anomalies are due to the superpositions of the  $R$  branch and the  $Q$  branch peaks. (b) Computer simulation of the  $A'\Omega 1-X^1\Sigma^+$  (0,0) band of AgF.

observed  $A'$  electronic state. Using LIF, we identify this electronically excited state as an  $\Omega=1$  state. The vibrational assignment, as listed in Table I and shown in Fig. 2(a), can be readily obtained and further confirmed with dispersed laser induced fluorescence.

#### A. Rotational analysis of the $A'\Omega 1-X^1\Sigma^+$ band system

Figure 3(a) corresponds to the rotationally resolved LIF spectrum for the  $(v',v'')=(0,0)$  band of the  $A'\Omega 1-X^1\Sigma^+$  band system which we computer simulate in Fig. 3(b). These features are considered in more detail elsewhere.<sup>7</sup> The LIF spectrum corresponding to the  $(v',v'')$

TABLE I. Measured vibrational separations of the ground  $X^1\Sigma^+$  state of AgF observed by chemiluminescence and laser induced fluorescence. Also listed are the experimental data obtained by Barrow *et al.* in Ref. 19 (for  $^{107}\text{AgF}$ ).

$v$	$\Delta G$ (Ref. 19) ( $\text{cm}^{-1}$ )	$\Delta G$ (Observed by CL) ( $\text{cm}^{-1}$ )	$\Delta G$ (Observed by LIF) ( $\text{cm}^{-1}$ )
0	$508.26 \pm 0.04$	$509.6 \pm 6$	$508.14 \pm 0.1$
1	$503.08 \pm 0.04$	$500.7 \pm 6$	...
2	$497.89 \pm 0.04$	$491.6 \pm 6$	...
3	...	$485.5 \pm 6$	...
4			

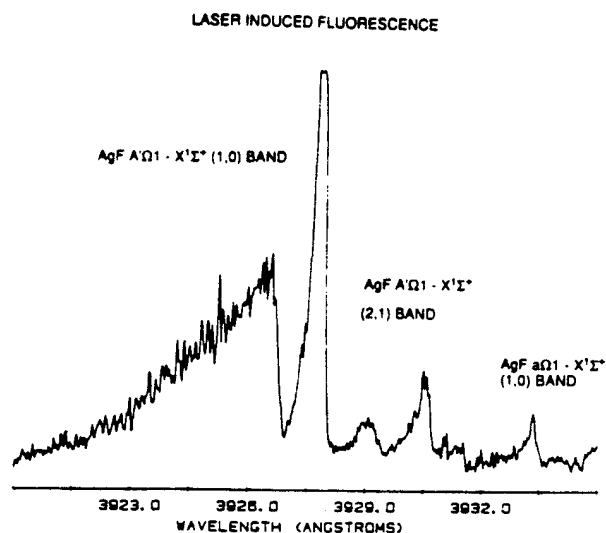


FIG. 4. Pulsed laser induced fluorescence spectrum of the  $A'\Omega 1-X'\Sigma^+(1,0)$  band of AgF.

$= (1,0)$  and  $(2,1)$  bands of the  $A'-X$  system have also been observed and are depicted in Figure 4. The two weak peaks at 401.39 [also observed in CL in Fig. 2(b)] and 393.33 nm in Figs. 3(a) and 4 cannot be assigned to the  $A'\Omega 1$  electronic state and are associated tentatively with a second  $\Omega=1$  state based on the atomic-molecular correlations which we consider shortly. The rotational spectra for the  $A'$  system show typical blue degraded rotational progressions with clear  $P$  heads to the red, indicating that the upper electronic state has a larger rotational constant  $B_e$  than does the ground  $X^1\Sigma^+$  state. Two rotational branches ( $R$  and  $Q$ ) have been identified from the blue degraded rotational structure labeled in Fig. 3.<sup>7</sup> Apparent intensity anomalies result from the superposition of the  $R$  and  $Q$  branches with the latter progressing slightly behind the former. This conclusion is based on the analysis of the simulation calculation depicted in Fig. 3(b). In analyzing the dispersed fluorescence induced by pumping at the  $P$  head of the  $(v',v'')=(0,0)$  band, we have confirmed the vibrational assignment for the dominant features of the chemiluminescent spectrum depicted in Fig. 2(a).<sup>7</sup>

The electronic assignment for the dominant  $A'-X$  system has been made by considering the rotational transition patterns. In Hund's case (c), transitions with  $\Delta\Omega=0$  and  $\Omega=\Omega'=0$  are similar to  $^1\Sigma-^1\Sigma$  transitions (with  $R$  and  $P$  branches), and transitions with  $\Delta\Omega=1$  and  $\Omega'=1$ ,  $\Omega''=0$  have the pattern of  $^1\Pi-^1\Sigma$  band systems (with  $R$ ,  $Q$ , and  $P$  branches).<sup>26</sup> Rotational assignments for well-resolved  $R$  and  $Q$  peaks (Fig. 3 and Ref. 7) of the  $A'-X$  system were easily determined using the following expressions and the previously known ground state rotational constants given in Ref. 19:

$$\nu_R = \nu_0 + (B'_v + B''_v)(J+1) + (B'_v - B''_v)(J+1)^2, \quad J > 0, \quad (1)$$

$$\nu_Q = \nu_0 + (B'_v + B''_v)J + (B'_v - B''_v)J^2, \quad J > 1, \quad (2)$$

$$\nu_P = \nu_0 - (B'_v + B''_v)J + (B'_v - B''_v)J^2, \quad J > 2, \quad (3)$$

TABLE II. Molecular constants of the  $A'\Omega 1$  state of  $^{107}\text{AgF}$ . The vibrational and rotational constants for  $^{109}\text{AgF}$  are calculated from the ones of  $^{107}\text{AgF}$  with the formulas given in the footnote. All numbers are in  $\text{cm}^{-1}$  except for  $r_e$ .<sup>a</sup>

	$^{107}\text{AgF}$	$^{109}\text{AgF}^b$
$T_e$	24 950.71(10)	24 950.71(10)
$\Delta G_{1/2}$	506.744(80)	506.041
$B_e$	0.281 32(15)	0.280 54
$\alpha_e$	$0.404 4(89) \times 10^{-2}$	$0.402 7 \times 10^{-2}$
$D_e$	$0.116(60) \times 10^{-6}$	$0.115 \times 10^{-6}$
$H_e$	$-0.403(83) \times 10^{-10}$	$-0.400 \times 10^{-10}$
$r_e$ (Å)	1.927	1.927

<sup>a</sup>The numbers in parentheses are  $1\sigma$  uncertainties.

<sup>b</sup>The following formulas are used:  $B'_e = \rho^2 B_e$ ,  $\alpha'_e = \rho^3 \alpha_e$ ,  $D'_e = \rho^4 D_e$ ,  $H'_e = \rho^5 H_e$ ,  $\omega'_e = \rho \omega_e$ ,  $\omega'_e X'_e = \rho^2 \omega_e X_e$ , and  $\rho^2 = \mu/\mu'$ , where  $\mu$  and  $\mu'$  are the reduced masses of the two isotopes. For  $^{107}\text{AgF}$  and  $^{109}\text{AgF}$ ,  $\rho = 1.001 39$ .

where  $\nu_R$ ,  $\nu_Q$ , and  $\nu_P$  are the peak positions of the  $R$ ,  $Q$ , and  $P$  branches, respectively.  $J$  is the lower state rotational quantum number and  $B'_v$  and  $B''_v$  are the rotational constants of the upper and the lower states. The centers of the deep valleys near the  $P$  heads in Figs. 3(a) and 4 are very good approximations to the band origins  $\nu_0$ . With the vibrational and rotational assignments and the ground state molecular constants of  $^{107}\text{AgF}$  given in Ref. 19, term values for the observed vibronic levels were calculated. A set of Dunham coefficients consistent with the assignment of an  $A'\Omega 1$  state were obtained and are listed in Table II. The constants in Table II can reproduce all well-resolved  $R$  and  $Q$  branch levels with a standard deviation of  $0.1 \text{ cm}^{-1}$ . We note that, under the present experimental resolution, no  $\Omega$ -type doubling has been observed for the  $A'\Omega 1-X^1\Sigma^+$  transition.

The vibrational and rotational constants of the isotope  $^{109}\text{AgF}$  listed in Table II were calculated from those of  $^{107}\text{AgF}$  using the well-known formula for isotope effect.<sup>27</sup> The isotope splittings of the  $A'\Omega 1-X^1\Sigma^+(0,0)$  band [also the  $A0^+$ ,  $B0^+-X^1\Sigma^+(0,0)$  bands as depicted in Fig. 5] are too small to be resolved for those rotational levels observed under the current experimental resolution.<sup>7</sup> Furthermore, in comparing Figs. 3(a) and 4, we find that the  $(v',v'')=(1,0)$  band of the  $A'\Omega 1-X^1\Sigma^+$  system is not as well resolved as the  $(v',v'')=(0,0)$  band due to the increasing isotope splittings for higher vibrational levels.

The rotational simulation for the  $A'\Omega 1-X^1\Sigma^+(0,0)$  band, depicted in Fig. 3(b), was carried out assuming a Boltzmann rotational distribution ( $T=495 \text{ K}$ ) for the ground state and the  $\Omega 1-^1\Sigma^+$  transition pattern (with  $R$ ,  $Q$ , and  $P$  branches). The determined rotational temperature  $T=495 \text{ K}$  may not be an accurate measure of the thermodynamic temperature since Hund's case (c) mixing effects have not been considered in the calculation. The molecular constants for  $^{107}\text{AgF}$  given in Table II were used with no isotope effect taken into account in the calculation. The agreement of the intensity patterns for the simulation and the LIF spectrum further confirms the electronic assignment to a newly observed  $A'\Omega 1$  state. From the molecular constants given in Table II, calculated Franck-

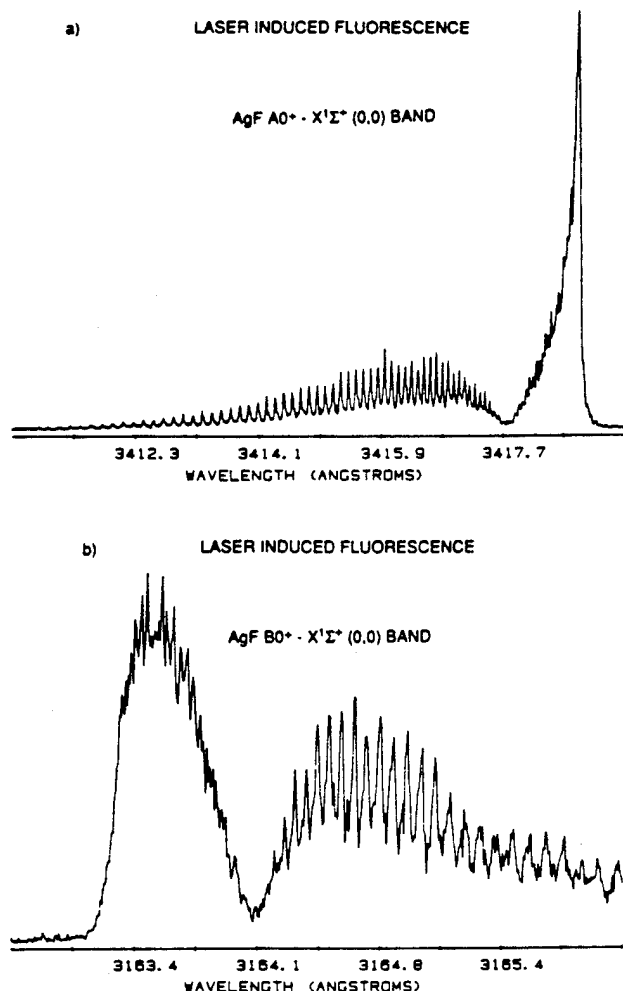


FIG. 5. Pulsed laser induced fluorescence spectra of (a) the  $A0^+-X'\Sigma^+(0,0)$  band, and (b) the  $B0^+-X'\Sigma^+(0,0)$  band of AgF.

Condon factors are found to be in excellent agreement with the CL intensity distribution.<sup>7</sup>

### B. The $A\Omega 1-X'\Sigma^+$ band system

The three weak peaks which are located at 409.5, 401.39, and 393.33 nm as depicted in Figs. 2(b), 2(c), 3(a), and 4, cannot be identified as vibrational bands of the  $A'\Omega 1-X'\Sigma^+$  system and are tentatively considered to originate from another electronic state. Since no rotational structure has been resolved for these features, the electronic symmetry of the emitting state is not clear. We can, however, make a suggested assignment based on correlations between the molecular states and their atomic limits (see the following). The three weak peaks, located 39, 38, and 36  $\text{cm}^{-1}$ , respectively, to the red of the  $P$  heads of the (0,1), (0,0), and (1,0) bands of the  $A'\Omega 1-X'\Sigma^+$  system, have a separation of 508 and 510  $\text{cm}^{-1}$ . The former agrees closely with  $\Delta\omega_{1/2}$  (508.26  $\text{cm}^{-1}$ ) of the ground  $X'\Sigma^+$  state of AgF, while the latter is similar to the  $\Delta\omega_{1/2}$  (506.7  $\text{cm}^{-1}$ ) of the  $A'\Omega 1$  state. It is also noted that the 409.5 nm peak is observed only in emission (chemiluminescence). The 401.39 nm peak is observed both in emission (CL) and LIF excitation, while the 393.33 nm peak is recorded

TABLE III. Molecular constants associated with (A) the  $A0^+-X'\Sigma^+(0,0)$  and (B) the  $B0^+-X'\Sigma^+(0,0)$  bands of  $^{107}\text{AgF}$ . The  $B_0$  and  $D_0$  values are for the upper states.

(A) $A0^+-X'\Sigma^+(0,0)$ band		
	This work	Ref. 19
$\nu_0$ ( $\text{cm}^{-1}$ )	29 250.20(1)	29 250.87
$B_0$ ( $\text{cm}^{-1}$ )	0.272 543(21)	0.272 68
$D_0$ ( $\text{cm}^{-1}$ )	$3.61(7) \times 10^{-7}$	$3.71 \times 10^{-7}$
(B) $B0^+-X'\Sigma^+(0,0)$ band		
$\nu_0$ ( $\text{cm}^{-1}$ )	31 594.77(2)	31 594.13
$B_0$ ( $\text{cm}^{-1}$ )	0.255 47(10)	0.255 486
$D_0$ ( $\text{cm}^{-1}$ )	$6.5(\pm 2.0) \times 10^{-7}$	$4.72 \times 10^{-7}$

only in LIF excitation. It appears, therefore, very likely that the peak at 401.39 nm corresponds to the (0,0) band of an  $a\Omega 1-X'\Sigma^+$  transition. An electronic state with a potential energy curve very similar to that of the  $A'\Omega 1$  state but located about 38  $\text{cm}^{-1}$  below the  $A'\Omega 1$  state is suggested. This  $a\Omega 1$  state also has, as we outline shortly, a radiative lifetime similar to the  $A'\Omega 1$  state.

### C. The $A0^+$ , $B0^+-X'\Sigma^+$ band systems

Laser induced fluorescence has also been observed for the AgF  $A0^+-X'\Sigma^+(0,0)$  and  $B0^+-X'\Sigma^+(0,0)$  bands in the UV region. Laser induced fluorescence spectra are depicted in Figs. 5(a) and 5(b), respectively. Both the  $A-X$  and  $B-X$  emission spectra show clear  $^1\Sigma^+-^1\Sigma^+$ -like features. The  $A-X$  (0,0) band is blue degraded, whereas the  $B-X$  (0,0) band is red degraded. The molecular constants determined for these two bands are tabulated in Table III and compared with those given in Ref. 19. The LIF intensity for these two systems is considerably stronger than that for the  $A'\Omega 1-X'\Sigma^+$  transition. Intense laser fluorescence could be observed for the  $A-X$  and  $B-X$  systems at oven temperatures just above the silver melting point (1234 K), while a considerably higher temperature (1600 K) was needed to observe both CL and LIF for the  $A'\Omega 1-X'\Sigma^+$  transition. The  $(v',v'')=(1,0)$  bands for both the  $A0^+-X'\Sigma^+$  and  $B0^+-X'\Sigma^+$  systems were not observed even with a sensitivity ten times higher than that necessary to record the (0,0) bands. This is partly due to unfavorable Franck-Condon factors and partly the result of the predissociation of these two states as considered in Ref. 19.

### D. Radiative lifetimes

Using a digital oscilloscope, we have recorded the exponential fluorescence decay with a laser pump frequency set at the intense  $P$  heads of the  $A'\Omega 1-X'\Sigma^+(0,0)$  and  $A0^+-X'\Sigma^+(0,0)$  bands and the  $R$  head of the  $B0^+-X'\Sigma^+(0,0)$  band. Typical fluorescence decay waveforms (an average of ten laser shots) for the  $A'\Omega 1-X'\Sigma^+(0,0)$ ,  $A0^+-X'\Sigma^+(0,0)$ , and  $B0^+-X'\Sigma^+(0,0)$  transitions are shown in Fig. 6. Table IV lists the measured radiative lifetimes for the four low-lying electronic states characterized in this study (together with several of their other properties). The fluorescence decay of the long-lived  $A'\Omega 1$  state has been found to be sensitive to the fluorine gas pressure.

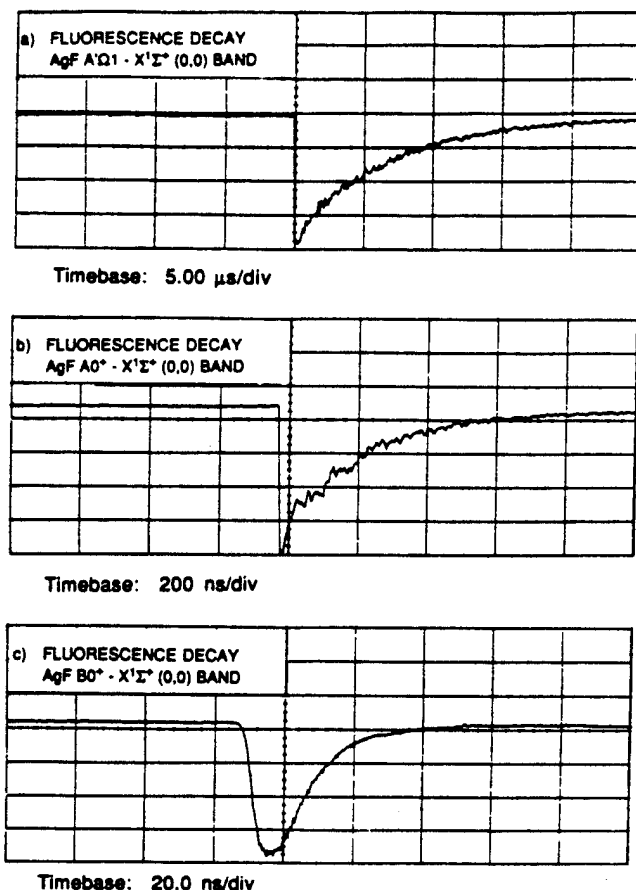


FIG. 6. Exponential fluorescence decay waveforms, each of which is an average of ten laser shots. The *P* or *R* heads of the following bands are excited: (a) the AgF  $A'\Omega_1-X'\Sigma^+$  (0,0) band (5  $\mu\text{s}/\text{division}$ ); (b) the AgF  $A0^+-X'\Sigma^+$  (0,0) band (200 ns/division); and (c) the  $B0^+-X'\Sigma^+$  (0,0) band (20 ns/division).

Under the optimal conditions for obtaining a LIF signal, fluorescence decays ranging from 12 to 4  $\mu\text{s}$  (with an averaged value of 7.1  $\mu\text{s}$ ) were recorded when the fluorine gas pressure was increased. No quenching effects have been observed with increasing He entrainment gas pressure and no pressure dependence is found to be associated with the shorter-lived  $A0^+-X'\Sigma^+$  and  $B0^+-X'\Sigma^+$  transitions. With real-time monitoring of the fluorescence decay while

scanning the laser frequency, we find no apparent rotational dependence for the radiative lifetimes. Finally, we should note that since the laser pulse used to induce the fluorescence has a pulse duration of 9 ns [full width at half-maximum (FWHM)], the build-up process for LIF, which is virtually identical to the laser pulse rise time, cannot be detected on the 5  $\mu\text{s}/\text{division}$  and 200 ns/division time scales of Figs. 6(a) and 6(b). However, the build-up process is well resolved in Fig. 6(c) taken on a comparable time scale of 20 ns/division.

#### IV. DISCUSSION

Under the conditions of the present experiment, the four center silver dimer-fluorine molecule reaction is considered to be the dominant process for the formation of both excited and ground state AgF molecules



$$\Delta E = 2D_0^0(\text{Ag-F}) - D_0^0(\text{Ag-Ag}) - D_0^0(\text{F-F}) = 4.04 \text{ eV}. \quad (5)$$

The process (4) results in chemiluminescent emission dominated by the  $A0^+-X'\Sigma^+$  and  $A'\Omega_1-X'\Sigma^+$  band systems [Figs. 2(a) and 2(b)]. The AgF  $A'\Omega_1-X'\Sigma^+$  emission system can also be excited employing the reaction of silver molecules  $\text{Ag}_x$  ( $x \geq 3$ ) and fluorine atoms,<sup>7</sup> a process which we consider elsewhere.<sup>7</sup>

The three major band systems observed in this study—the  $A'\Omega_1$ ,  $A0^+$ , and  $B0^+-X'\Sigma^+$  transitions—are Hund's case (c) allowed. However, as Table IV summarizes, they have clearly distinct and well-separated radiative lifetimes. We can divide the four low-lying electronic states into three classes, i.e., the long-lived  $A'\Omega_1$  (7.1  $\mu\text{s}$ ) and  $a\Omega_1$  (9.1  $\mu\text{s}$ ) states, the intermediate lifetime  $A0^+$  (240 ns) state and the short-lived  $B0^+$  (21 ns) state. We can attempt to understand this lifetime behavior by correlating these states to (1) the spin characters of their dominating Hund's case (a) components and (2) their dissociation limits.

The  $\Omega=1$  states have three components  $^3\Pi_1$ ,  $^3\Sigma_{(\Omega=1)}^+$ , and  $^1\Pi$ , while the  $0^+$  states correspond to a mix of two  $^3n_0$  and  $^1\Sigma^+$ . The long lifetime of the  $A'\Omega_1$  state apparently indicates that the triplet components [very likely the

TABLE IV. A summary of the major properties of the low-lying electronic states of gaseous AgF. The estimated dissociation energies are obtained from the thermochemical value  $D^0 = 29\,600 \pm 1400 \text{ cm}^{-1}$  for the AgF ground state (Ref. 28).

State	$T_e$ ( $\text{cm}^{-1}$ )	$r_e$ ( $\text{\AA}$ )	Spin character	Lifetime	Dissociation energy $D_e$ ( $\text{cm}^{-1}$ )	Atomic limits
$X'\Sigma^+$	0	1.983	Singlet	...	29 600	↓
$a\Omega_1$	(24 913) <sup>a</sup>	...	Triplet	$9.1 \pm 3.3 \mu\text{s}$	(4 687)	↓
$A'\Omega_1$	24 950.71 <sup>a</sup>	1.927	Triplet	$7.1 \pm 2.6 \mu\text{s}$	4 649	$\text{Ag } ^2S_{1/2} + \text{F } ^2P_{3/2}$
$A0^+$	29 220 <sup>b</sup>	$1.957(r_0)$	Singlet	$240 \pm 14 \text{ ns}$	784	$\text{Ag } ^2S_{1/2} + \text{F } ^2P_{1/2}$
$B0^+$	31 663 <sup>b</sup>	$2.022(r_0)$	Singlet	$21 \pm 1.2 \text{ ns}$	27 489	$\text{Ag } ^2P_{1/2} + \text{F } ^2P_{3/2}$
Repulsive ( $\Omega_1$ )	...	...	...	...	...	$\text{Ag } ^2S_{1/2} + \text{F } ^2P_{1/2}$

<sup>a</sup>This work.

<sup>b</sup>Data taken from Ref. 31.

$^3\Pi_1$  component by comparison with the lifetimes of the low-lying electronic states of CuF (Refs. 21, 22, and 25)] dominate this state. Thus, the transition probability for emission terminating in the ground  $X^1\Sigma^+$  state is (intensity) borrowed from the  $^1\Pi$  state. Similarly, a dominant triplet character is also likely for the  $a\Omega 1$  state with its long radiative lifetime (9.1  $\mu$ s) and weaker transition intensity. We suggest that this state is an  $\Omega=1$  state by process of elimination. Two of the remaining possible transitions  $0^-$  and  $\Omega 2-X^1\Sigma^+$  are strictly forbidden electric dipole transitions and should be possessed of even longer radiative lifetimes and hence a much weaker emission intensity. For CuF, these lifetimes range from several hundred microseconds to milliseconds, the emission being 1000 times weaker than the  $\Omega 1-X^1\Sigma^+$  system.<sup>21,22,25</sup> A remaining possibility, the assignment to a  $0^+$  state, is readily eliminated by considering atomic asymptotic limits.

Ground state silver and fluorine atoms  $\text{Ag } ^2S_{1/2} + \text{F } ^2P_{3/2}$  combine to generate one  $0^+$  ( $X^1\Sigma^+$ ), one  $0^-$ , two  $\Omega=1$ , and one  $\Omega=2$  molecular state, whereas the  $\text{Ag } ^2S_{1/2} + \text{F } ^2P_{1/2}$  combination, which lies 400  $\text{cm}^{-1}$  above the ground atomic state, yields one  $0^+$  ( $A0^+$ ), one  $0^-$ , and only one  $\Omega=1$  state. If the repulsive  $\Omega 1$  state assigned by Barrow and Clements<sup>19</sup> dissociates diabatically to the second atomic state as indicated in Fig. 2 of Ref. 19, the newly observed  $A'$  and  $a$  states can only dissociate to ground state atoms and must be the two  $\Omega=1$  states generated by this atomic combination (note that the next possible neutral atomic asymptote  $\text{Ag } ^2P_{1/2} + \text{F } ^2P_{3/2}$  is located approximately 30 000  $\text{cm}^{-1}$  above the ground atomic state and is thus too energetic to correlate with these two lowest-lying states). If the repulsive  $\Omega 1$  state correlates diabatically to the ground state atomic limit  $\text{Ag } ^2S_{1/2} + \text{F } ^2P_{3/2}$ , the  $A'\Omega 1$  state must diabatically dissociate to the second atomic limit  $\text{Ag } ^2S_{1/2} + \text{F } ^2P_{1/2}$  by crossing this repulsive potential. This possibility, which seems highly unlikely, would appear to be eliminated by the avoided crossing rule. The repulsive  $\Omega 1$  state and the  $A'\Omega 1$  state will adiabatically correlate to the same dissociation limits rather than undergo a curve crossing. Figure 7 illustrates correlation diagrams between the low-lying molecular states of silver fluoride and their corresponding atomic asymptotes, as proposed above and considered by other workers.<sup>19</sup> The values of  $D_e$  for AgF are based on the thermochemical value  $D^0 = 29\,600 \pm 1400 \text{ cm}^{-1}$ .<sup>28</sup> Note that the transitions  $A'\Omega 1$ ,  $a\Omega 1-X^1\Sigma^+$  also involve no change in angular momentum or electron configuration for the atoms, which must account, at least in part, for the long lifetimes of these two states.

The  $A0^+$  state has an intermediate lifetime of 240 ns, which, on the one hand, suggests possible singlet character ( $^1\Sigma^+$ ) upon comparison with the known transitions for CuF.<sup>21,22,25</sup> However, this lifetime is certainly longer than that associated with a typical allowed singlet-singlet transition for diatomic molecules [e.g., 12 ns for the  $A^1\Sigma_u^+ - X^1\Sigma_g^+$  system of  $\text{Na}_2$  (Refs. 29 and 30)]. The observed lifetime for the  $A0^+$  state might be explained by noting that the  $A0^+-X^1\Sigma^+$  system corresponds to a weak  $p-p$  ( $\Delta l = 0$ ) F atom transition as indicated in Fig. 7. Using a similar argument, the short lifetime of the  $B0^+$  state (21

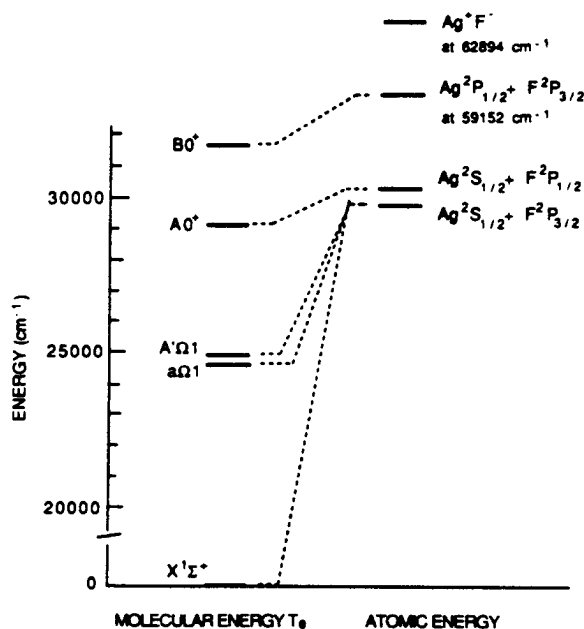


FIG. 7. Correlation diagram for the low-lying molecular states and the corresponding atomic asymptotic limits of the AgF system.

ns) can be readily understood from (1) its singlet character ( $^1\Sigma^+$ ) and (2) the strongly allowed  $p-s$  ( $\Delta l = 1$ ) transition in atomic Ag. In summary, Table IV lists the  $T_e$ 's and  $r_e$ 's, spin character, measured lifetimes, dissociation energies, and proposed dissociation limits for the four low-lying electronic states of AgF.

Although copper and silver fluoride are isoelectronic, the five observed low-lying states of CuF lie at considerably lower energies ( $\sim 14\,500$ – $22\,800 \text{ cm}^{-1}$ ) than even the newly observed  $A'\Omega 1$  and  $a\Omega 1$  states of AgF. Furthermore, the radiative lifetimes of the low-lying CuF states considerably exceed those of AgF. We suggest that these differences may be attributed to a significantly different molecular electronic structure for these isoelectronic diatomics.

Using *ab initio* calculations as a guide, Dufour *et al.*<sup>23</sup> have developed a consistent model to account for the observed behavior of the CuF excited states assigning them to a single structure  $\text{Cu}^+ (3d^9 4s) \text{F}^- (2p^6)$  with the manifold of observed emissions resulting from transitions between the states resulting from this structure and the closed shell,  $\text{Cu}^+ (3d^{10}) \text{F}^- (2p^6)$ ,  $X^1\Sigma^+$  ground state ion pair. The relatively long-lived CuF transitions are thought to correspond to electric dipole forbidden  $3d-4s$  electron transfers in the  $\text{Cu}^+$  atomic limit.

The situation in AgF is clearly different. This might be explained by considering the distinctly different energy level patterns for the copper and silver atoms and their ions as catalogued in Table V. We note that the lowest energy atomic transitions in silver (1) lie at considerably higher energy than those in atomic copper and (2) involve an allowed  $p-s$  electron transfer vs the Cu forbidden  $d-s$  transition. Furthermore, although the lowest energy excited states in  $\text{Cu}^+$  and  $\text{Ag}^+$  are both  $^3D$  and the lowest

TABLE V. The lowest electronic configurations and the corresponding energies of Cu and Ag atoms and  $\text{Cu}^+$  and  $\text{Ag}^+$  ions. All data are taken from Ref. 32.

Cu atom			Ag atom		
Electron configuration	$J$	Energy ( $\text{cm}^{-1}$ )	Electron configuration	$J$	Energy ( $\text{cm}^{-1}$ )
$3d^{10}4s^2S$	1/2	0.0	$4d^{10}5s^2S$	1/2	0.0
$3d^94s^2^2D$	5/2	11 202.565	$4d^95p^2P^0$	1/2	29 552.05
	3/2	13 245.423		3/2	30 472.71
$3d^{10}4p^2P^0$	1/2	30 535.302	$4d^95s^2^2D$	5/2	30 242.26
	3/2	30 783.686		3/2	34 714.16

$\text{Cu}^+$ ion			$\text{Ag}^+$ ion		
Electron configuration	$J$	Energy ( $\text{cm}^{-1}$ )	Electron configuration	$J$	Energy ( $\text{cm}^{-1}$ )
$3d^{10}1S$	0	0.0	$4d^{10}1S$	0	0.0
$3d^94s^3D$	3	21 928.60	$4d^95s^3D$	3	39 163.9
	2	22 847.03		2	40 741.0
	1	23 998.31		1	43 738.7

energy atomic emissions in both ions correspond to electric dipole forbidden  $d-s$  transitions, these states lie at significantly higher energy for the silver ion, making correlation with the low-lying molecular states of AgF tenuous in an ionic model.

The combination of data in Table V, in fact, favors a model correlated more closely with the neutral silver atomic limits which we have considered in our previous discussion. In order to construct the correlation diagram of Fig. 7, we take the AgF bond energy to be  $29\,600 \pm 1400 \text{ cm}^{-1}$ .<sup>28</sup> With this energy increment, we estimate  $D_e$  for the  $X^1\Sigma^+$  state as  $\sim 29\,600 \text{ cm}^{-1}$ , for the  $a\Omega 1$  state as  $\sim 4687 \text{ cm}^{-1}$ , and for the  $A'\Omega 1$  state as  $\sim 4649 \text{ cm}^{-1}$  as they dissociate to ground state silver and fluorine atoms. We estimate the  $A0^+$  state to be stable by only  $\sim 784 \text{ cm}^{-1}$  as it dissociates to  $\text{Ag } ^2S_{1/2} + \text{F } ^2P_{1/2}$  at  $30\,004 \text{ cm}^{-1}$ . The  $B0^+$  state whose short radiative lifetime signals its correlation with  $\text{Ag } ^2P_{1/2}$  is, of course, predissociated.

## V. CONCLUSION

We have observed the optical signatures for two low-lying  $\Omega=1$  states  $A'\Omega 1$  and  $a\Omega 1$  of AgF which dissociate to ground state atoms and lie about  $4300 \text{ cm}^{-1}$  below the previously known lowest excited  $A0^+$  state. The measured radiative lifetimes reveal that the two  $\Omega=1$  states are of triplet character, while the two  $0^+$  states  $A0^+$  and  $B0^+$  are singlet. It appears that all of the observed low-lying electronic states of AgF dissociate adiabatically to neutral atoms in contrast to the ion-pair dissociation attributed to the low-lying states of CuF. The observation of the two  $\Omega=1$  states suggests the probable existence of the similar stable low-lying electronic states for the remaining silver halides. The long-lived  $A'\Omega 1$  state is also important because of its suitability as an intermediate state for studies of high-lying electronic states and photoionization using multiple resonance laser excitation.

*Note added in proof.* On the electronic assignment of the low-lying  $a$  state, we emphasize that it is almost impossible, at this time, to make an unambiguous electronic assignment for the weak  $a$  state because of the lack of either well resolved rotational structure for the  $a-X^1\Sigma^+$  bands or *ab initio* calculations of the radiative lifetimes for the low-lying electronic states of AgF. We have contemplated that the  $A'\Omega 1$  and this  $a$  states might be the  $\Omega=1$  and  $\Omega=0^-$  components of a Hund's case (a)  $^3\Sigma^+$  state which correlates with the  $a^3\Sigma^+$  state observed in CuF.<sup>20</sup> However, we are troubled by the fact that (1) the  $A'-a$  separation in AgF ( $\sim 38 \text{ cm}^{-1}$ ) is so similar to the separation of the  $\Omega=1$  and  $0^-$  components in CuF ( $43.5 \text{ cm}^{-1}$ ),<sup>20</sup> and (2) that the radiative lifetime of the  $a$  state is virtually the same as that of the  $A'\Omega 1$  state. For those reasons, we tentatively suggest that this weak  $a$  state be an  $\Omega=1$  state by process of elimination as described in the paper and do not rule out the possibility that this state might be assigned to another possible electronic symmetry.

## ACKNOWLEDGMENTS

We are grateful to Professor R. F. Barrow for his valuable comments and suggestions on this work. H. Wang would like to thank Professor T. C. Devore for helpful discussions on the analysis of the spectrum and Mr. C. B. Winstead for his technical help in the pulsed laser system and the data acquisition system. This work was partially supported by the Army Research Office, the Eastman Kodak Company, and the Air Force Office of Scientific Research through the Strategic Defense Initiative.

- J. L. Gole, in *Advances in Metal and Semiconductor Clusters*, edited by M. A. Duncan (JAI, Greenwich, 1993), Vol. 1, p. 159.
- (a) R. W. Woodward, P. N. Le, M. Temmen, and J. L. Gole, *J. Phys. Chem.* **91**, 2537 (1987); (b) J. L. Gole, *AIP Conf. Proc.* **160**, 439 (1987); (c) T. C. Devore, R. W. Woodward, and J. L. Gole, *J. Phys. Chem.* **92**, 6919 (1988); (d) T. C. Devore, J. R. Woodward, and J. L. Gole, *ibid.* **93**, 4920 (1989); (e) M. J. McQuaid and J. L. Gole, *AIP Conf. Proc.* **191**, 687 (1988).
- T. C. Devore and J. L. Gole, *Proc. Sixth Int. Conf. High Temp. Mater., High Temp. Sci.* **27**, 49 (1989).
- (a) *Metal Clusters*, edited by M. Moskovits (Wiley-Interscience, New York, 1986); (b) *ACS Symp. Ser.* **179**, edited by J. L. Gole and W. C. Strwalley (1982); (c) M. Morse, *Chem. Rev.* **86**, 1049 (1986).
- (a) M. J. McQuaid, K. Morris, and J. L. Gole, *J. Am. Chem. Soc.* **110**, 5280 (1988); (b) J. L. Gole, *NATO ASI Ser.* **374**, 1025 (1992); (c) in *Gas Phase Metal Reactions*, edited by A. Fontijn (Elsevier, Amsterdam, 1992), pp. 573-604.
- T. C. Devore, J. R. Woodward, P. N. Le, J. L. Gole, and D. A. Dixon, *J. Phys. Chem.* **94**, 756 (1990).
- H. Wang and J. L. Gole, *J. Mol. Spectrosc.* (in press).
- (a) *The Physics of Latent Image Formation in the Silver Halides*, edited by A. Baldeschiesi, W. Czaja, E. Tosatti, and M. Tosi (World Scientific, Singapore, 1984); (b) *The Theory of the Photographic Process*, edited by T. H. James (MacMillan, New York, 1977); (c) A. Marchetti and J. Deaton (private communication).
- B. A. Brice, *Phys. Rev.* **35**, 960 (1930).
- B. A. Brice, *Phys. Rev.* **38**, 658 (1931).
- F. A. Jenkins and G. D. Rochester, *Phys. Rev.* **52**, 1141 (1937).
- R. S. Mulliken, *Phys. Rev.* **51**, 310 (1937).
- N. Metropolis, *Phys. Rev.* **55**, 636 (1939).
- N. Metropolis and H. Beutler, *Phys. Rev.* **55**, 1113 (1939).
- L. C. Krisher and W. G. Norris, *J. Chem. Phys.* **44**, 391 (1966); **44**, 974 (1966).
- E. Pearson and W. Gordy, *Phys. Rev.* **152**, 42 (1966).

- <sup>17</sup>J. Hoeft, F. J. Lovas, E. Tiemann, and T. Topping, *Z. Naturforsch. Teil A* **25**, 35 (1970).
- <sup>18</sup>R. M. Clements and R. F. Barrow, *Chem. Commun.* **1254**, 27 (1968).
- <sup>19</sup>R. F. Barrow and R. M. Clements, *Proc. R. Soc. London Ser. A* **322**, 243 (1971).
- <sup>20</sup>F. Ahmed, R. F. Barrow, A. H. Chojnicki, C. Dufour, and J. Schamps, *J. Phys. B* **15**, 3816 (1982).
- <sup>21</sup>R. E. Steele and H. P. Broida, *J. Chem. Phys.* **69**, 2300 (1978).
- <sup>22</sup>J. M. Delaval, Y. Lefebvre, H. Bocquet, P. Bernage, and P. Niay, *Chem. Phys.* **111**, 129 (1987).
- <sup>23</sup>C. Dufour, J. Schamps, and R. F. Barrow, *J. Phys. B* **15**, 3819 (1982).
- <sup>24</sup>J. M. Delaval and J. Schamps, *Chem. Phys.* **100**, 21 (1985).
- <sup>25</sup>J. Schamps, J. M. Delaval, and O. Faucher, *Chem. Phys.* **145**, 101 (1990).
- <sup>26</sup>G. Herzberg, *Molecular Spectra and Molecular Structure. I Spectra of Diatomic Molecules*, 2nd ed. (Krieger, Malabar, 1989).
- <sup>27</sup>J. L. Dunham, *Phys. Rev.* **41**, 721 (1932).
- <sup>28</sup>K. F. Zmbov and J. L. Margrave, *J. Phys. Chem.* **71**, 446 (1967).
- <sup>29</sup>T. W. Ducas, M. G. Littman, M. L. Zimmerman, and D. Kleppner, *J. Chem. Phys.* **65**, 842 (1976).
- <sup>30</sup>W. T. Zemke, K. K. Verma, T. Vu, and W. C. Stwalley, *J. Mol. Spectrosc.* **85**, 150 (1981).
- <sup>31</sup>K. P. Huber and G. Herzberg, *Molecular Spectra and Molecular Structure IV. Constants of Diatomic Molecules* (Van Nostrand-Reinhold, New York, 1979).
- <sup>32</sup>Charlotte E. Moore, *Atomic Energy Levels* (U.S. Government Printing Office, Washington, D.C., 1949), Vols. 2 and 3.

## APPENDIX VII

"A Chemiluminescent and Laser Induced Fluorescent Probe Of A New Low-Lying  $A'\Omega 1$  State of Gaseous  $\text{AgF}$ ", H. Wang and J. L. Gole, J. Mol. Spectros, 161, 28 (1993).

# A Chemiluminescent and Laser-Induced Fluorescent Probe of a New Low-Lying $A' \Omega = 1$ State of Gaseous AgF

HE WANG AND JAMES L. GOLE

*School of Physics, Georgia Institute of Technology, Atlanta, Georgia 30332*

A new  $A' 1 (\Omega = 1)$  state of AgF at the fringes of the visible region has been excited and analyzed. The chemiluminescence from this state, which is located  $\sim 4300 \text{ cm}^{-1}$  below the previously known lowest excited  $A 0^+$  state, is observed for the first time in a beam-gas reaction where silver molecules,  $\text{Ag}_x$ , are reacted with either atomic or molecular fluorine. Using pulsed laser-induced fluorescence, two vibrational bands  $(v', v'') = (0, 0)$  and  $(1, 0)$  have been rotationally resolved and electronic and rotational assignments have been obtained. Molecular constants which can reproduce the observed data with a standard deviation of  $0.1 \text{ cm}^{-1}$ , the RKR potential energy curve, and the Franck-Condon factors for the  $A' 1-X^1\Sigma^+$  transition have been determined. The internal energy distributions of the reaction product AgF molecules are studied by vibrational intensity analysis and rotational simulation calculations. The possible reaction paths to produce the excited  $A'$  state from either the four-center  $\text{Ag}_2 + \text{F}_2$  or  $\text{Ag}_x (x \geq 3) + \text{F}$  reactions and the formation of ground state AgF molecules are discussed through consideration of reactant-product correlations and energetics. The dissociation energy of the newly observed  $A' 1$  state is  $4649 \pm 1400 \text{ cm}^{-1}$ . The observation of this low-lying  $\Omega = 1$  state indicates the existence of similar stable  $\Omega = 1$  states for the remaining silver halides, all of which should readily absorb visible photons. Their existence, which may have implications for the detailed understanding of the photographic process, provides intermediate states for multiple-resonance laser excitation and multiphoton laser ionization. © 1993 Academic Press, Inc.

## INTRODUCTION

The study of the highly exothermic kinetically controlled oxidation of metal molecules not only provides a means to extrapolate and modify concepts which govern simple  $A + BC$  reactive encounters (1-3), but also, through a unique reactive branching, facilitates the formation of previously inaccessible reaction products. The analyzed quantum level structure of the product metal-based oxides and halides formed in highly exothermic oxidation processes can provide useful information on molecular structure and bonding (4-6) especially when detailed chemiluminescent (CL) studies can be used to pinpoint regions which will be accessible to a laser-induced fluorescent (LIF) probe.

In developing such studies, we have observed particularly intriguing groups of metal cluster oxidations. For example, the sodium trimer-halogen atom reactive interactions signal a surprising chemistry (7-9) as the high cross section  $\text{Na}_n (n = 2, 3) - X (\text{Cl}, \text{Br}, \text{I})$  encounters create a continuous electronic population inversion based on the chemical pumping of sodium dimer ( $\text{Na}_2$ ). While this unusual reactive behavior has potential for extension to other alkali trimers, we also realize that the Group IB dimers and trimers constitute direct analogs of the alkali systems, suggesting that additional insight might be gained through the study of the  $\text{Ag}_n - X$  oxidation reactions. Further, the oxidation behavior of small silver agglomerates is of significance in both the photographic process (10) and catalysis (11).

Recently, Devore *et al.* (6) have reported and analyzed the chemiluminescent emission from silver cluster-ozone reactions, correlating a portion of these emissions with  $\text{Ag}_x\text{O}$  ( $x \geq 2$ ) emitters. Here, we report an experimental study of the silver vapor-fluorine reaction system. We have obtained the first evidence for a stable  $\Omega = 1$  state of the gaseous silver monohalide AgF, which lies  $4300\text{ cm}^{-1}$  below the previously known lowest excited  $A\ 0^+$  state. The band system associated with the  $A' 1-X^1\Sigma^+$  transition has been studied using a combination of CL and LIF spectroscopy.

Spectroscopic studies of the silver monohalides,  $\text{AgX}$  ( $X = \text{F}, \text{Cl}, \text{Br}$ ), have a long, albeit limited, history (12-17). The halide ground states are highly ionic, with AgCl and AgBr respectively 52 (18) and 46% (19) ionic character, and the AgF ground state dipole moment determined to be 6.22 D (20). The heavy halides follow primarily Hund's case (c) coupling. The ground state of AgF dissociates to  $\text{Ag } ^2S_{1/2} + \text{F } ^2P_{3/2}$  ground state atoms whose combination generates five molecular states,  $0^+$ ,  $0^-$ , 1, 1, and 2. At slightly higher energy the  $\text{Ag } ^2S_{1/2} + \text{F } ^2P_{1/2}$  atoms can combine to yield  $0^+$ ,  $0^-$ , and 1 states. From the manifold of states resulting from these two atomic combinations, only the  $A\ 0^+ (^2S_{1/2} + ^2P_{1/2})$  and  $X^1\Sigma^+ (^2S_{1/2} + ^2P_{3/2})$  states had been identified before the current study. Joshi and Sharma (21) first reported the near UV absorption spectrum of the AgF  $B\ 0^+-X^1\Sigma^+$  system. They also reported the observation of some features due to the  $A\ 0^+-X^1\Sigma^+$  transition. Barrow and Clements (22, 23) carried out a rotational analysis of these two ultraviolet systems and Hoeft *et al.* studied the rotational spectrum of the AgF ground state using microwave absorption (20). Until the present study no visible absorption spectrum and no transition involving a stable  $\Omega = 1$  state has been reported for the silver halides.

#### EXPERIMENTAL DETAILS

Both chemiluminescence and pulsed laser-induced fluorescence were generated under multiple-collision conditions as a stream of silver entrained in helium was intersected by molecular or atomic fluorine. The overall experimental configuration is depicted schematically in Fig. 1. The entrainment flow device used in this study has been described previously (2). Briefly, silver metal was heated in a specially designed graphite crucible to temperatures in the range of 1600 K. The silver, emanating from the crucible, was entrained in a flow of helium gas at a total pressure of 1 Torr. For those experiments employing molecular fluorine, fluorine gas was introduced into the entrained silver flow through a concentric ring inlet located  $\sim 1\text{ cm}$  above the crucible. For those experiments which used atomic fluorine as an oxidant, fluorine atoms were formed by electric discharge through  $\text{SF}_6$  and used in a manner previously applied to studies of the  $\text{Bi}_2 + \text{F}$  (24) and  $\text{Mg}_x + \text{F}$  (25) reactive systems. Entrained fluorine atoms exited a directed-flow channel perpendicular to the direction of the entrained silver and about 1.5 cm above the silver source crucible. For both the fluorine atom and the fluorine molecule oxidation studies a chemiluminescent flame was generated in the reaction zone. However, this flame was considerably more intense for the fluorine molecule-based reactive encounters. The chemiluminescence from the reaction zone was observed at right angles to the reactant flows using a 0.75-m Spex 1702 monochromator operated in first order with a 1200 groove/mm grating blazed at 500 nm and an RCA 1P28 photomultiplier. The PMT signal was fed to a Keithley 417 autoscale picoammeter and recorded with a computer.

The pulsed LIF studies were performed employing only the fluorine molecule-based reactions. The second harmonic of a Quanta-ray Nd:YAG laser ( $0.53\ \mu$ ) was used to pump a Spectra Physics PDL-3 pulsed tunable dye laser system operated with DCM

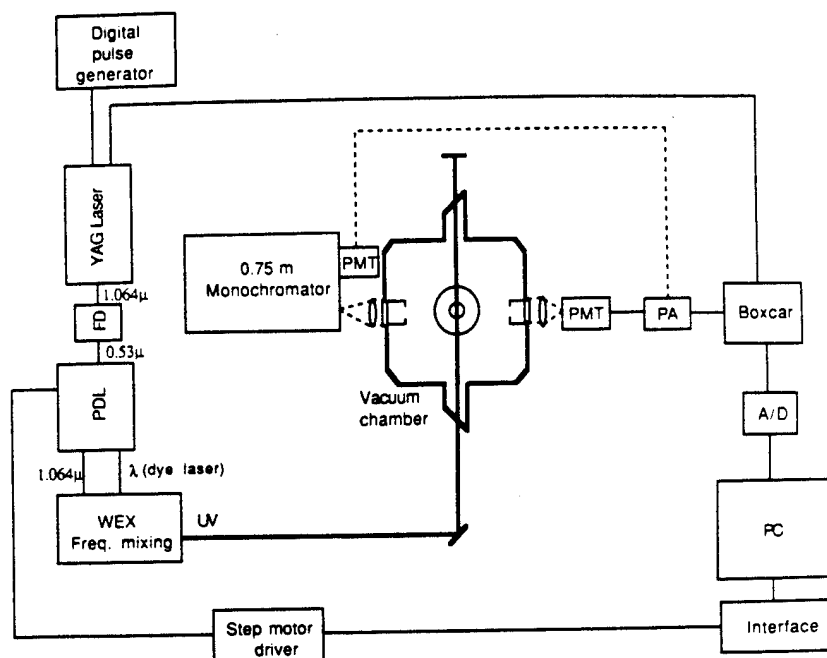


FIG. 1. Experimental setup for chemiluminescence and laser-induced fluorescence spectroscopy.

dye. The output of the pulsed dye laser (with a linewidth of  $0.07\text{ cm}^{-1}$  and a pulse width of 9 nsec) was then mixed with the fundamental output of the YAG laser in a frequency mixer (Quanta-Ray WEX-1) to produce the near-UV coherent radiation which was introduced to the reaction chamber in a direction perpendicular to the reactant flow. The YAG laser was triggered by a digital pulse generator (SRS DG535) with a repetition rate of 15 Hz. The Q-switching signal of the YAG oscillator was used to trigger a Boxcar integrator (SRS SR250) for better synchronization. The pulsed laser-induced fluorescence was collected with a 1P28 photomultiplier (2.2 nsec rise time) and sent to the gated integrator through a fast preamplifier (CLC 100 Video Amplifier, 500 MHz). The integration gate was set to a width of 300 nsec with a time delay such that the gate opens just after the short laser scattering pulse, thus reducing background noise. A computer drives the laser stepper motor, scans the dye laser, and acquires the averaged output data from the Boxcar synchronously. In order to achieve a linear scan in wavelength with the frequency mixer, the scan step size of the dye laser was calculated in real time using the PC. The output frequency of the WEX-1 was calibrated using aluminum atomic lines.

#### RESULTS AND ANALYSIS

Chemiluminescent spectra characterizing the entrained silver-fluorine atom and silver-fluorine molecule reactive encounters are depicted in Figs. 2a and 2b, respectively. The chemiluminescence from the fluorine atom-based system is considerably weaker than that obtained in the fluorine molecule reactive environment. It appears that the available energy corresponding to those processes which involve fluorine molecule reactions exceeds the energy available from the fluorine atom system. This sug-

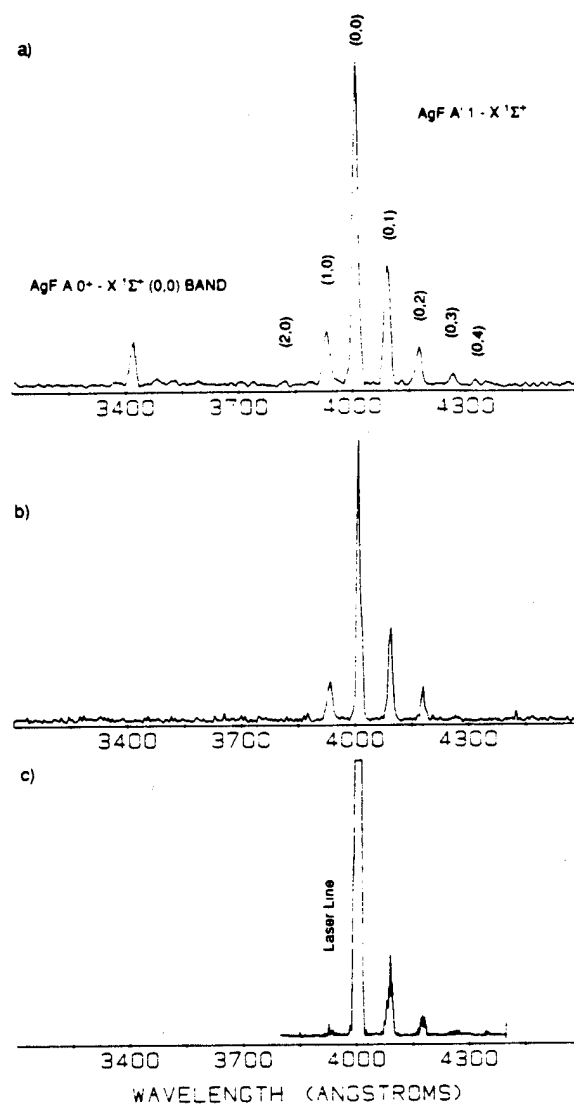


FIG. 2. (a) Chemiluminescence spectrum from the fluorine molecule-based reactive system at a resolution of 5 Å. (b) Chemiluminescence spectrum from the fluorine atom-based reactive system at a resolution of 5 Å. (c) The dispersed fluorescence induced by laser pumping at the  $P$  head of the  $A' 1-X' 1\Sigma^+ (0,0)$  band of AgF.

gests the possibility of multicentered fluorine molecule-silver molecule reaction dynamics which produces two metal fluoride molecules. The situation, which is also apparent in several metal molecule-based oxidative environments, certainly represents a departure from  $A + BC$  reaction dynamics (1-6). The peak at 342 nm, present only when fluorine molecules are used as reactants, is readily identified as the  $(v', v'') = (0,0)$  band of the  $A 0^+-X' 1\Sigma^+$  transition of AgF. However, the spectrum is dominated by an intense vibrationally resolved structure around 400 nm observed for the first time in these silver-fluorine-based reactive systems. The CL signals associated with

this newly observed structure correlate with both the silver vapor concentration and the fluorine gas pressure. Table I catalogs the peak separations from the strongest CL peak to longer wavelengths. These separations agree well, within experimental error, with the known vibrational separations for the ground  $X^1\Sigma^+$  state of  $^{107}\text{AgF}$  given by Barrow and Clements (23). Based on this comparison, we can tentatively attribute the observed structure to a transition of the AgF molecule originating from a newly observed electronic state. We use LIF to identify the newly monitored electronically excited state as an  $\Omega = 1$  state (LIF to the ground  $^1\Sigma^+$  state). The vibrational assignment, as listed in Table I (note also Fig. 2a), can also be readily obtained and further confirmed by dispersed laser-induced fluorescence as exemplified in Fig. 2c.

Figures 3a and 3b present representative rotationally resolved LIF spectra corresponding to the  $(v', v'') = (0, 0)$  and  $(1, 0)$  bands, respectively. The  $(v', v'') = (2, 1)$  band was also observed as depicted in Fig. 3b. Two detailed scans of the rotational structure of the  $(0, 0)$  band are shown in Figs. 4a and 4b. The rotational spectra show typical blue degraded rotational progressions with clear  $P$  heads to the red, indicating that the upper state has a larger rotational constant,  $B_e$ , than does the lower state. Two rotational branches ( $R$  and  $Q$ ) have been identified from the blue degraded rotational structure as labeled in Figs. 3 and 4. The apparent intensity anomalies are attributed to the superposition of the  $R$  branch and the  $Q$  branch. This argument is proved with a simulation calculation described below. The observed  $P$  head positions are listed in Table II. Figure 2c depicts the dispersed fluorescence induced by laser pumping at the  $P$  head of the  $(v', v'') = (0, 0)$  band. The apparent disappearance of the  $(v', v'') = (1, 0)$  band, which is otherwise clearly seen in the CL emission spectrum (Figs. 2a and 2b), confirms our vibrational assignment.

The electronic assignment has been made by considering the rotational transition patterns. In Hund's case (c), we have the electronic selection rule  $\Delta\Omega = 0, \pm 1$  since  $\Lambda$  and  $\Sigma$  are no longer good quantum numbers. Furthermore, case (c) coupling may be regarded as case (a) coupling with very large multiplet splittings, the band structures in case (c) being quite similar to those in case (a). That is, transitions with  $\Omega = 0$  and  $\Omega' = \Omega'' = 0$  are similar to  $^1\Sigma - ^1\Sigma$  transitions (with  $R$  and  $P$  branches), and transitions with  $\Omega = 1$  and  $\Omega' = 1, \Omega'' = 0$  are similar to  $^1\Pi - ^1\Sigma$  transitions (with  $R, Q$ , and  $P$  branches) (26). Based on the above arguments, our newly observed electronic state can be assigned as a  $\Omega = 1$  state without ambiguity. To match the previous nomenclature, we will call this newly observed state the  $A'1$  state.

TABLE I  
Vibrational Separations of the Ground  $X^1\Sigma^+$  State of AgF Observed by Chemiluminescence and Laser-Induced Fluorescence

$v$	$\Delta G_{\text{Ref. 23}}$ ( $\text{cm}^{-1}$ )	$\Delta G_{\text{Obs. by CL}}$ ( $\text{cm}^{-1}$ )	$\Delta G_{\text{Obs. by LIF}}$ ( $\text{cm}^{-1}$ )
0	508.26 $\pm$ 0.04	509.6 $\pm$ 6	508.14 $\pm$ 0.1
1	503.08 $\pm$ 0.04	500.7 $\pm$ 6	-
2	497.89 $\pm$ 0.04	491.6 $\pm$ 6	-
3	-	485.5 $\pm$ 6	-
4			

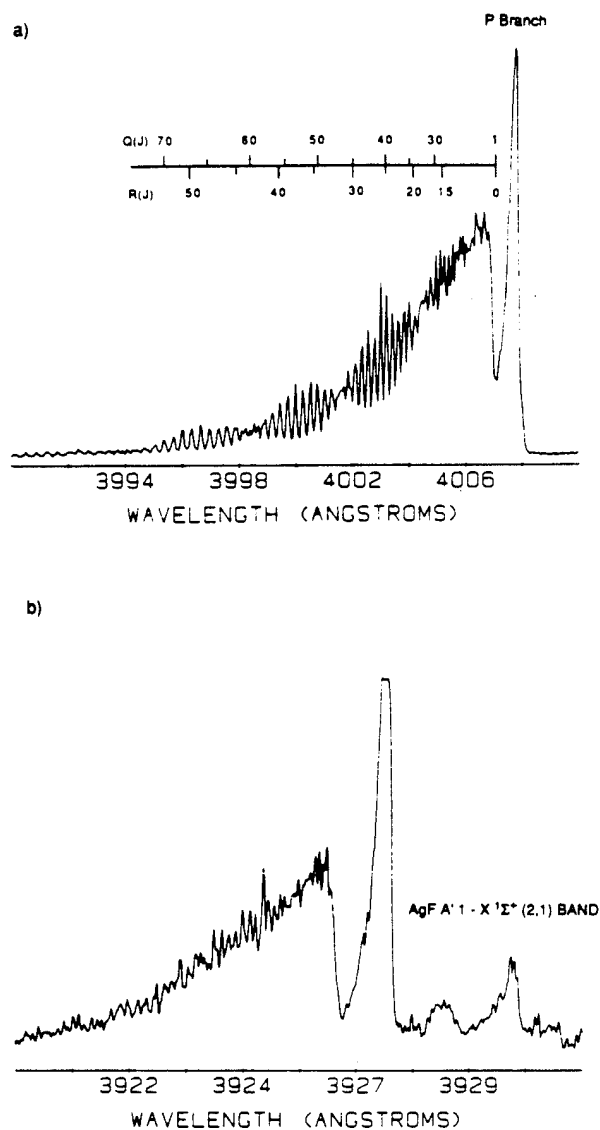


FIG. 3. Pulsed laser-induced fluorescence spectra of the  $A' 1-X' 1\Sigma^+$  system of AgF. (a)  $(v', v'') = (0, 0)$  band and (b)  $(v', v'') = (1, 0)$  band. The intensity anomalies are due to the superposition of the  $R$ -branch and the  $Q$ -branch peaks.

The rotational assignment for the  $R$ ,  $P$ , and  $Q$  branches was easily determined using the following equations and the previously known ground state rotational constants given in Ref. (23):

$$\nu_R = \nu_0 + (B'_v + B''_v)(J+1) + (B'_v - B''_v)(J+1)^2 \quad J \geq 0, \quad (1)$$

$$\nu_Q = \nu_0 + (B'_v - B''_v)J + (B'_v - B''_v)J^2 \quad J \geq 1, \quad (2)$$

$$\nu_P = \nu_0 - (B'_v + B''_v)J + (B'_v - B''_v)J^2 \quad J \geq 2, \quad (3)$$

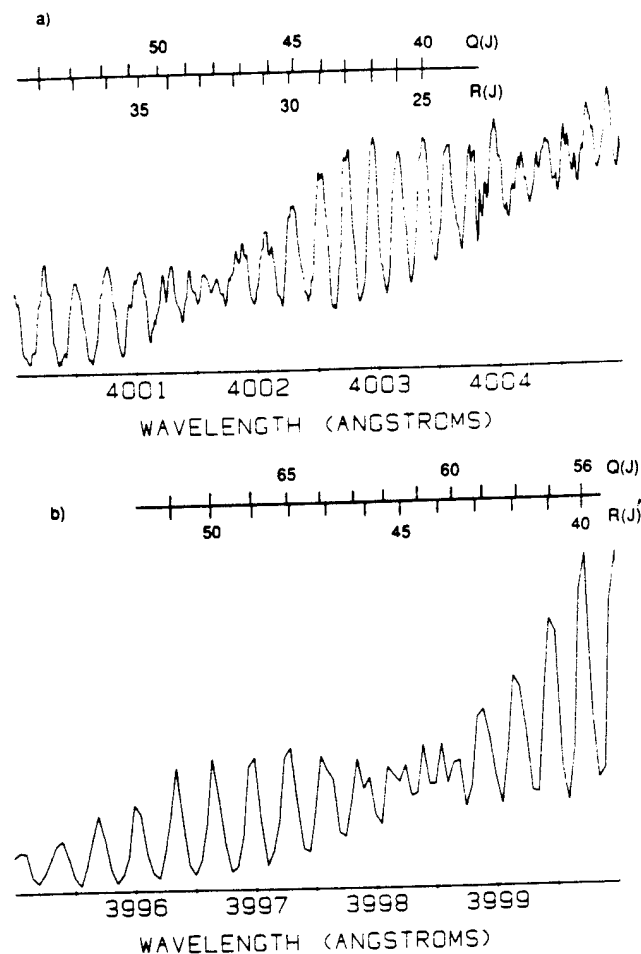


FIG. 4. Two detailed LIF scans (laser scan step size,  $0.01 \text{ cm}^{-1}$ ) for the  $R$  and  $Q$  branches of the  $(v', v'') = (0, 0)$  band of  $\text{AgF}$ .

where  $\nu_R$ ,  $\nu_Q$ , and  $\nu_P$  are the peak positions of the  $R$ ,  $Q$ , and  $P$  branches, respectively.  $J$  is the lower state rotational quantum number, and  $B'_v$  and  $B''_v$  are the rotational constants for the upper and the lower state. The centers of the deep valleys near the  $P$  heads in Figs. 3a and 3b are very good approximations of the band origins  $\nu_0$ . With the vibrational and rotational assignments and the ground state molecular constants of  $^{107}\text{AgF}$  given by Barrow and Clements (23), a total of 71 well resolved  $R$  and  $Q$  lines have been fit to the well-known Dunham formula (27)

$$T(v, J) = \sum Y_{jk}(v + 1/2)^j [J(J + 1) - 1]^k, \quad (4)$$

where  $T(v, J)$  are the vibronic energy levels and  $Y_{jk}$  are the Dunham coefficients. Tables III, IV, and V tabulate the observed and the calculated spectral lines and the differences between them for the  $R$  and  $Q$  branches of the  $(v', v'') = (0, 0)$  band and the  $R$  branch of the  $(v', v'') = (1, 0)$  band, respectively. Table VI gives the molecular constants for the newly observed  $A' 1$  state of  $^{107}\text{AgF}$  and  $^{109}\text{AgF}$ . The constants listed

TABLE II

*P* Bandhead Positions of the  $A'1-X'1\Sigma^+$  System Observed by Laser-Induced Fluorescence

$(v', v'')$	<i>P</i> Head $\lambda$ (Å)
(0,0)	4007.76
(0,1)	4090.90
(1,0)	3927.81
(2,1)	3930.82

TABLE III

Observed and Calculated *R*-Branch Vibronic Transitions for the  $(v', v'') = (0, 0)$  Band of the  $A'1-X'1\Sigma^+$  System of  $^{107}\text{AgF}$ 

Assignment <i>J</i>	<i>R</i> ( <i>J</i> ) ( $\text{cm}^{-1}$ )		$\Delta v$ ( $\text{cm}^{-1}$ ) Obs. - Cal.
	Observed	Calculated	
15	24960.234	24960.165	0.069
16	24961.168	24961.192	-0.024
17	24962.356	24962.249	0.107
18	24963.352	24963.335	0.017
23	24969.148	24969.210	-0.062
24	24970.522	24970.475	0.047
25	24971.772	24971.769	0.003
26	24973.080	24973.093	-0.013
27	24974.389	24974.447	-0.058
28	24975.699	24975.830	-0.131
30	24978.570	24978.687	-0.117
32	24981.502	24981.662	-0.160
33	24983.127	24983.195	-0.068
34	24984.813	24984.757	0.057
35	24986.500	24986.348	0.152
36	24988.121	24987.969	0.152
37	24989.744	24989.619	0.125
38	24991.367	24991.299	0.068
39	24992.930	24993.007	-0.077
41	24996.367	24996.511	-0.144
42	24998.242	24998.306	-0.064
44	25001.992	25001.981	0.011
45	25003.869	25003.860	0.009
46	25005.744	25005.766	-0.022
48	25009.813	25009.661	0.152
49	25011.688	25011.649	0.039
50	25013.879	25013.662	0.217
51	25015.756	25015.701	0.055
52	25017.949	25017.766	0.183
53	25019.826	25019.855	-0.029

TABLE IV

Observed and Calculated  $Q$ -Branch Vibronic Transitions for the  $(v', v'') = (0, 0)$  Band of the  $A' 1-X' 1\Sigma^+$  System of  $^{107}\text{AgF}$

Assignment $J$	$Q(J)$ ( $\text{cm}^{-1}$ )		$\Delta V$ ( $\text{cm}^{-1}$ ) Obs. - Cal.
	Observed	Calculated	
30	24961.418	24961.391	0.027
31	24962.356	24962.308	0.048
32	24963.352	24963.255	0.097
39	24970.522	24970.718	-0.196
40	24971.772	24971.903	-0.131
41	24973.080	24973.116	-0.036
42	24974.389	24974.359	0.030
43	24975.699	24975.631	0.068
44	24977.010	24976.931	0.079
47	24981.066	24981.001	0.065
48	24982.502	24982.413	0.089
49	24983.940	24983.853	0.087
50	24985.313	24985.319	-0.006
53	24989.744	24989.875	-0.131
54	24991.367	24991.445	-0.078
55	24992.930	24993.038	-0.108
56	24994.492	24994.656	-0.164
57	24996.367	24996.297	0.070
61	25002.932	25003.080	-0.148
62	25004.807	25004.827	-0.020
63	25006.369	25006.592	-0.223
64	25008.248	25008.375	-0.127
67	25013.879	25013.819	0.060
68	25015.756	25015.662	0.094

in Table VI can reproduce all well resolved experimental  $R$ - and  $Q$ -branch levels with a standard deviation of  $0.1 \text{ cm}^{-1}$ . We note that, under the present experimental resolution, no  $\Omega$ -type doubling has been observed for the  $A' 1-X' 1\Sigma^+$  transition.

The vibrational and rotational constants of the isotope  $^{109}\text{AgF}$  were calculated from those of  $^{107}\text{AgF}$  using the well-known formula for isotope effect (27). The isotope splittings of the  $R$  and  $Q$  branches for the  $(v', v'') = (0, 0)$  band have been estimated from the molecular constants given in Table VI (for the  $A' 1$  state) and in Ref. (23) (for the  $X' 1\Sigma^+$  ground state) and plotted as a function of  $J$  in Fig. 5. The electronic isotope shift has been ignored in first-order approximation. Apparently, for the rotational spectral lines which we have observed, the isotope splittings for the lowest vibrational band are too small to be resolved under our experimental conditions. This is due primarily to the similarity of the vibrational and rotational constants for the upper and the lower states. It is also obvious in comparing Figs. 3a and 3b that the  $(v', v'') = (1, 0)$  band is not as well resolved as the  $(v', v'') = (0, 0)$  band due to the increasing isotope splittings for higher excited state vibrational quantum levels.

A comparison between the CL spectrum, the LIF spectrum, and a computer simulation of the  $A' 1-X' 1\Sigma^+$ ,  $(v', v'') = (0, 0)$  band is shown in Fig. 6. The rotational simulation was carried out assuming a Boltzman rotational distribution ( $T = 495 \text{ K}$ )

TABLE V

Observed and Calculated  $R$ -Branch Vibronic Transitions for the  $(v', v'') = (1, 0)$  Band of the  $A'1-\bar{X}^1\Sigma^+$  System of  $^{107}\text{AgF}$

Assignment J	R(J) ( $\text{cm}^{-1}$ )		$\Delta V$ ( $\text{cm}^{-1}$ ) Obs. - Cal.
	Observed	Calculated	
14	25465.174	25464.945	0.229
15	25466.082	25465.813	0.269
16	25466.731	25466.702	0.029
17	25467.770	25467.613	0.157
18	25468.549	25468.546	0.003
19	25469.457	25469.500	-0.043
21	25471.402	25471.473	-0.071
22	25472.441	25472.492	-0.051
23	25473.350	25473.532	-0.182
28	25479.193	25479.060	0.133
29	25480.232	25480.231	0.001
30	25481.531	25481.423	0.108
31	25482.699	25482.637	0.062
32	25483.740	25483.873	-0.133
33	25484.908	25485.130	-0.222
34	25486.338	25486.409	-0.071
35	25487.768	25487.710	-0.058

for the ground state and the  $1-\bar{X}^1\Sigma^+$  transition pattern (with  $R$ ,  $Q$ , and  $P$  branches). The molecular constants for  $^{107}\text{AgF}$  given in Table VI were used and no isotope effect was taken into account in the calculation. The agreement of the intensity patterns for the simulation and the LIF spectrum further confirms our electronic assignment to

TABLE VI

Dunham Coefficients for the  $A'1$  State of  $^{107}\text{AgF}$

$Y_{jk}$	$^{107}\text{AgF}$	$^{109}\text{AgF}^*$
$T_e$	24950.71(10)	24950.71(10)
$Y_{10} (\Delta G_{1/2})$	506.744(80)	506.041
$Y_{01} (B_e)$	0.28132(15)	0.28054
$Y_{11} (-\alpha_e)$	$-0.4044(89) \times 10^{-2}$	$-0.4027 \times 10^{-2}$
$Y_{02} (-D_e)$	$-0.116(60) \times 10^{-6}$	$-0.115 \times 10^{-6}$
$Y_{03} (H_e)$	$-0.403(83) \times 10^{-10}$	$-0.400 \times 10^{-10}$
$R_e (\text{\AA})$	1.927	1.927

Note. All numbers are in  $\text{cm}^{-1}$  except for  $R_e$ . The numbers in parentheses are  $1\sigma$  uncertainties.

\* The following formulas are used:  $B_e' = \rho^2 B_e$ ,  $\alpha_e' = \rho^3 \alpha_e$ ,  $D_e' = \rho^4 D_e$ ,  $H_e' = \rho^6 H_e$ ,  $\omega_e' = \rho \omega_e$ ,  $\omega_e' x_e' = \rho^2 \omega_{exe}$ ,  $\rho^2 = \mu/\mu'$ , where  $\mu$  and  $\mu'$  are the reduced masses of the two isotopes. For  $^{107}\text{AgF}$  and  $^{109}\text{AgF}$   $\rho = 1.00139$ .

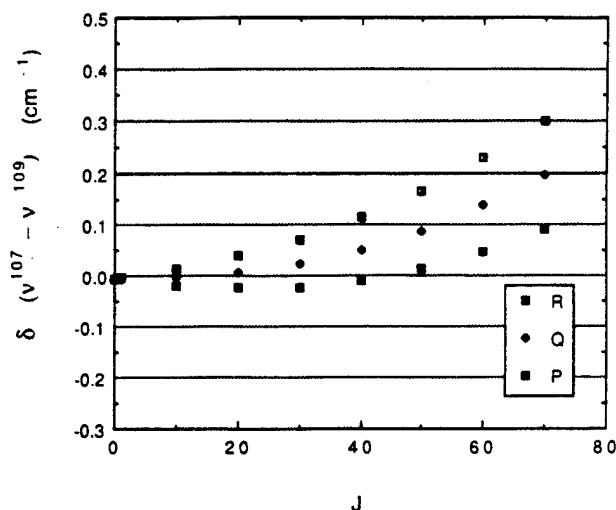
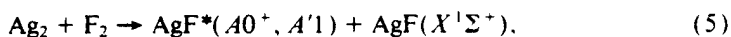


FIG. 5. Isotope splittings of the spectral lines of the  $A'1-X^1\Sigma^+(0,0)$  band of  $^{107}\text{AgF}$  and  $^{109}\text{AgF}$  calculated from the constants given in Table VI and Ref. (23).

the newly observed  $A'1$  state. From the Dunham coefficients given in Table VI, an RKR potential energy curve for the  $A'1$  state and hence the Franck-Condon factors for the  $A'1-X^1\Sigma^+$  system have been calculated. Table VII tabulates the RKR potential energy curve and Fig. 7 indicates the very good agreement between the calculated FCFs and the CL intensity distribution.

#### DISCUSSION

Since the silver atom-fluorine molecule reaction process  $\text{Ag} + \text{F}_2 \rightarrow \text{AgF} + \text{F}$  ( $\Delta E = 2.03$  eV) is not exothermic enough to excite the chemiluminescence that we observe in this study, the reactions of silver molecules must lead to the observed emission. For the  $\text{Ag}_x\text{-F}_2$  system, the four-center silver dimer-fluorine molecule reaction is considered to be the dominant process.



with an exothermicity of  $\Delta E = 2D_0^0(\text{Ag-F}) - D_0^0(\text{Ag-Ag}) - D_0^0(\text{F-F}) = 4.04$  eV (26, 28, 29), producing chemiluminescence corresponding to the  $A0^+ \rightarrow X^1\Sigma^+$ ,  $(v', v'') = (0, 0)$  band with a photon energy of  $\sim 3.62$  eV. The much weaker chemiluminescence from the  $\text{Ag}_x\text{-F}$  system, observed under considerably more stringent agglomeration conditions, must result from the reaction of a polyatomic silver molecule, the most likely candidate being silver trimer ( $\text{Ag}_3$ ) with its 0.99 eV bond dissociation energy (30). The silver trimer-fluorine atom reaction, with an exothermicity of  $\Delta E = D_0^0(\text{Ag-F}) - D_0^0(\text{Ag}_2\text{-Ag}) = 2.65$  eV is not sufficiently energetic to populate the  $A'1$  state based strictly on its reaction exothermicity. However, the hot F atom translational energy easily exceeds 0.5 eV (24), the extra energy needed to form the  $A'1$  state at 3.10 eV. Finally, it is worth noting that additional silver cluster reactions such as the multicentered

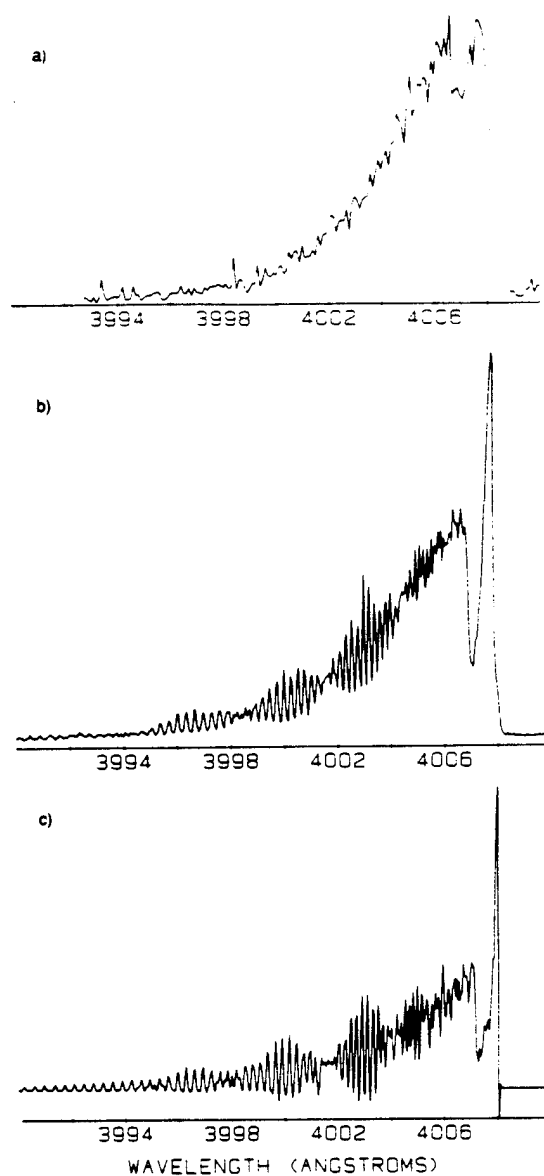
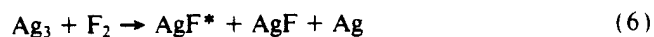


FIG. 6. Comparison between (a) chemiluminescence, (b) laser-induced fluorescence, and (c) computer simulation ( $T = 495$  K) of the  $A' 1-X' 1\Sigma^+ (0,0)$  band of AgF.



and



may also be considered as possible precursors to excited AgF products.

By comparing the blue degraded CL spectrum of the  $A' 1-X' 1\Sigma^+ (0,0)$  band given in Fig. 6a with the LIF spectrum in Fig. 6b, we observe that the excited state and the

TABLE VII

RKR Potential Energy Curve of the  $A' 1$  State of AgF Derived from the Molecular Constant of  $^{107}\text{AgF}$ 

$v$	$B_v (\text{cm}^{-1})$	$G_v (\text{cm}^{-1})$	$R_{v-} (\text{\AA})$	$R_{v+} (\text{\AA})$
0	0.27930	253.372	1.869	1.997
1	0.27525	760.115	1.833	2.056
$R_e = 1.927 \text{\AA}$				

ground state have similar rotational population distributions. This suggests that the product AgF molecules are nearly fully relaxed under our multiple-collision conditions. The rotational simulation shown in Fig. 6c corresponds to a rotational temperature of 495 K and  $J_{\text{MAX}} = 25$ . The determined rotational temperature,  $T = 495$  K, may not be an accurate measure of the thermodynamic temperature since Hund's case (c) mixing effects have not been considered in the calculation. The vibrational temperature is roughly estimated to be 415 K from the LIF intensity ratio of the  $(v', v'') = (1, 0)$  and  $(2, 1)$  bands shown in Fig. 3b and the calculated Franck-Condon factors.

As we have indicated in the Introduction, the lowest atomic limit of the AgF system ( $\text{Ag } ^2S_{1/2} + \text{F } ^2P_{3/2}$ ) generates two  $\Omega = 1$  molecular states, whereas the ( $\text{Ag } ^2S_{1/2} + \text{F } ^2P_{1/2}$ ) combination couples to produce only one  $\Omega = 1$  state. In Ref. (23), Barrow and Clements report the observation of a continuum transition centered at 303.0 nm as well as predissociation in the vibronic levels of the  $B 0^+$  state of AgF. They attribute the predissociation to the potential curve crossing of the  $B 0^+$  state by a repulsive  $\Omega = 1$  state, which seems to dissociate to the second atomic limit (Fig. 2 of Ref. (23)). Therefore the newly observed  $A' 1$  state reported in this paper can only dissociate to the ground atomic limit. Figure 8 outlines the correlation diagram for the  $X^1\Sigma^+$ ,  $A' 1$ ,  $A 0^+$ , and  $B 0^+$  molecular states and their corresponding atomic dissociation asymptotes. A value of the dissociation energy of the  $A' 1$  state,  $D_e$ , can be estimated

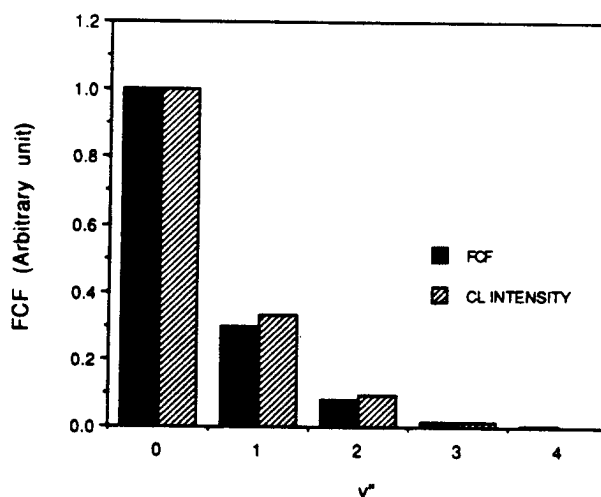


FIG. 7. Comparison between the calculated Franck-Condon factors and the CL intensity distribution for the  $A' 1 v' = 0 - X' 1 \Sigma^+ v'' = x$  transitions of AgF.

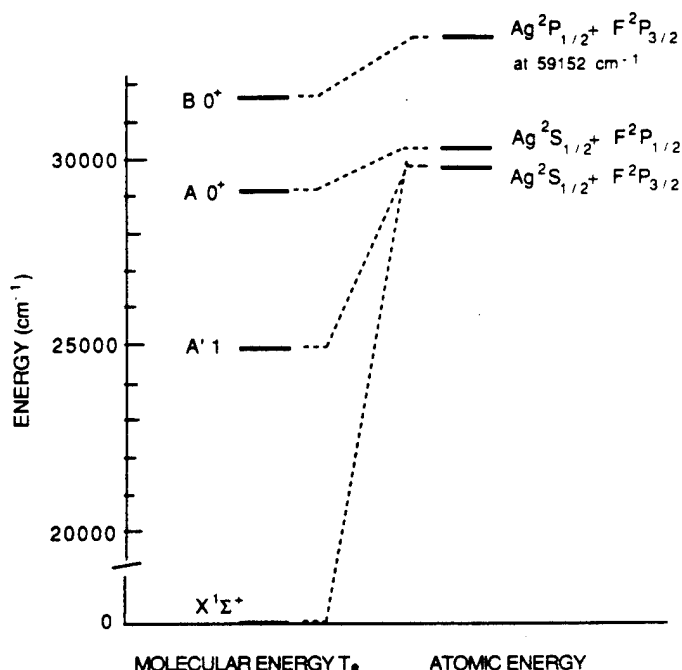


FIG. 8. Correlation diagram of the low-lying molecular states and the corresponding atomic asymptotic limits of the AgF system.

to be  $4649 \pm 1400 \text{ cm}^{-1}$  from the thermochemical value,  $D^0 = 29\,600 \pm 1400 \text{ cm}^{-1}$  (29) for the AgF ground state.

The observation of the  $A'1$  state of AgF indicates that there may exist similar stable  $\Omega = 1$  states for the remaining silver monohalides located a few thousand wavenumbers below the previously known lowest excited  $A 0^+$  states. Table VIII summarizes the observed  $T_e$  values for the low-lying electronic states of the silver monohalides. In addition to the ground state, the  $B 0^+$  state is the only excited state well studied for

TABLE VIII

Summary of the Observed  $T_e$  Values of the Low-Lying Electronic States of the Silver Monohalides

	AgF	AgCl	AgBr	AgI
$X^1\Sigma^+$	0	0	0	0
$A'1$	24950.71 <sup>a</sup>	-	(-23810 <sup>d</sup> )	-
$A 0^+$	29220 <sup>b</sup>	-	-	23906 <sup>c</sup>
$B 0^+$	31663 <sup>b</sup>	31602.65 <sup>b</sup>	31280.43 <sup>b</sup>	31194.06 <sup>b</sup>

<sup>a</sup> This work.

<sup>b</sup> Data taken from reference 28.

<sup>c</sup> Electronic symmetry is not clear.

<sup>d</sup> Transitions around 420nm mentioned by Metropolis and Beutler in reference 17. No electronic symmetry is assigned.

the remaining silver monohalide molecules with  $T_e$  values smoothly shifted to the red from AgF to AgI. No corresponding stable  $A\ 0^+$  states have been observed for AgCl and AgBr. It should be noted that the electronic symmetry of the  $A$  state of AgI listed in Table VIII is unclear (28). This state seems to more closely correlate with the  $A' 1$  state rather than the  $A\ 0^+$  state of AgF. With no electronic symmetry assigned, Metropolis and Beutler (17) also mention transitions around 420 nm ( $23\ 810\text{ cm}^{-1}$ ) for AgBr which we tentatively associate with the  $A' 1$  state in Table VIII. The experimental search for the similar  $A' 1$  states of AgCl, AgBr, and AgI is in progress in our laboratory.

#### CONCLUSION

The  $A\ 0^+$  state has been found not to be the lowest excited electronic state of the AgF molecule as previously indicated in Ref. (28). About  $4300\text{ cm}^{-1}$  below the  $A\ 0^+$  state, a stable  $A' 1$  state has been observed and rovibrationally analyzed for the first time using the combination of chemiluminescence and pulsed laser-induced fluorescence. The possible existence of similar stable  $\Omega = 1$  states for other silver monohalides is predicted. The observation of this  $A' 1$  state is also of importance for its possible role as an intermediate state in multiple-resonance laser spectroscopy and multiphoton laser ionization experiments.

#### ACKNOWLEDGMENTS

We are grateful to Professor R. F. Barrow for his valuable comments and suggestions on this work. H. Wang would like to thank Professor T. C. Devore for helpful discussions on the analysis of the spectrum and Mr. C. B. Winstead for his technical help in the pulsed laser system and the data acquisition system. This work was partially supported by the Army Research Office, the Eastman Kodak Company, and the Air Force Office of Scientific Research through the Strategic Defense Initiative.

RECEIVED: February 12, 1993

#### REFERENCES

1. J. L. GOLE, in "Advances in Metal and Semiconductor Clusters," Vol. I, "Spectroscopy and Dynamics" (M. A. Duncan, Ed.), pp. 159-209, Jai Press, Greenwich, CT, 1993.
2. (a) R. W. WOODWARD, P. N. LE, M. TEMMEN, AND J. L. GOLE, *J. Phys. Chem.* **91**, 2637-2645 (1987); (b) J. L. GOLE, *Opt. Sci. Eng. Ser.* **8**, 439; (c) T. C. DEVORE, R. W. WOODWARD, AND J. L. GOLE, *J. Phys. Chem.* **92**, 6919-6923 (1988); (d) T. C. DEVORE, J. R. WOODWARD, AND J. L. GOLE, *J. Phys. Chem.* **93**, 4920-4923 (1989); (e) M. J. MCQUAID AND J. L. GOLE, *Opt. Sci. Eng. Ser.* **10**, 687.
3. T. C. DEVORE AND J. L. GOLE, *High Temp. Sci.* **27**, 49-59 (1989).
4. (a) M. MOSKOVITS (Ed.), "Metal Clusters," Wiley-Interscience, New York, 1986; (b) J. L. GOLE AND W. C. STWALLEY, *ACS Symp. Ser.* **179** (1982); (c) J. L. GOLE AND W. C. STWALLEY, *Symp. Faraday Soc.* **14** (1980); (d) M. MORSE, *Chem. Rev.* **86**, 1049-1109 (1986).
5. (a) M. J. MCQUAID, K. MORRIS, AND J. L. GOLE, *J. Am. Chem. Soc.* **110**, 5280-5285 (1988); (b) J. L. GOLE in "Proceedings of the International Symposium on the Physics and Chemistry of Finite Systems: From Clusters to Crystals," NATO ASI Series C: Mathematical and Physical Sciences, Vol. 374, p. 1025, Kluwer Academic, Norwell, MA, 1992; (c) J. L. GOLE, in "Gas Phase Metal Reactions" (A. Fontijn, Ed.), pp. 573-604, Elsevier/North-Holland, Amsterdam/New York, 1992.
6. T. C. DEVORE, J. R. WOODWARD, P. N. LE, J. L. GOLE, AND D. A. DIXON, *J. Phys. Chem.* **94**, 756-760 (1990).
7. S. H. COBB, J. R. WOODWARD, AND J. L. GOLE, *Chem. Phys. Lett.* **143**, 205-213 (1988); **156**, 197-203 (1989).
8. (a) W. H. CRUMLEY, J. L. GOLE, AND D. A. DIXON, *J. Chem. Phys.* **76**, 6439-6441 (1982); (b) W. H. CRUMLEY, Ph.D. Thesis, Georgia Institute of Technology, 1985; (c) S. H. COBB, Ph.D. Thesis, Georgia Institute of Technology, 1988.

9. (a) K. K. SHEN, J. R. WOODWARD, S. H. COBB, J. R. DOUGHTY, AND J. L. GOLE, *SPIE Vol. 1397*, 125-135 (1991). (b) K. K. SHEN, H. WANG, D. GRANTIER, AND J. L. GOLE, in "Proceedings of the 23rd AIAA Plasma-Dynamics and Laser Science Conference," Nashville, TN, pp. 92-2994, 1992.
10. (a) A. BALDERESCHI, W. CZAJA, E. TOSATTI AND M. TOSI, (Eds.), "The Physics of Latent Image Formation in the Silver Halides," World Scientific, Singapore, 1984. (b) T. H. JAMES, Ed., "The Theory of the Photographic Process," MacMillan, New York, 1977. (c) A. MARCHETTI AND J. DEATON, private communication.
11. S. A. MILLER AND E. BENN (Eds.), "Ethylene and Industrial Derivatives," MacMillan, New York, 1977.
12. B. A. BRICE, *Phys. Rev.* **35**, 960-972 (1930).
13. B. A. BRICE, *Phys. Rev.* **38**, 658-669 (1931).
14. F. A. JENKINS AND G. D. ROCHESTER, *Phys. Rev.* **52**, 1141-1143 (1937).
15. R. S. MULLIKEN, *Phys. Rev.* **51**, 310-332 (1937).
16. N. METROPOLIS, *Phys. Rev.* **55**, 636-638 (1939).
17. N. METROPOLIS AND H. BEUTLER, *Phys. Rev.* **55**, 1113-1113 (1939).
18. L. C. KRISHER AND W. G. NORRIS, *J. Chem. Phys.* **44**, 391-394, 974 (1966).
19. E. PEARSON AND W. GORDY, *Phys. Rev.* **152**, 42-45 (1966).
20. J. HOEFT, F. J. LOVAS, E. TIEMANN, AND T. TORRING, *Z. Naturforsch., A* **25**, 35-39 (1970).
21. M. M. JOSHI AND D. SHARMA, *Indian J. Pure Appl. Phys.* **1**, 86 (1963).
22. R. M. CLEMENTS AND R. F. BARROW, *Chem. Comm. No. 1254*, 27-28 (1968).
23. R. F. BARROW AND R. M. CLEMENTS, *Proc. R. Soc. London A* **322**, 243-249 (1971).
24. T. C. DEVORE, L. BROCK, R. KAHLSCHEUER, K. DULANEY, AND J. L. GOLE, *Chem. Phys.* **155**, 423-433 (1991); T. C. DEVORE AND J. L. GOLE, submitted for publication.
25. T. C. DEVORE, R. KAHLSCHEUER, D. A. DIXON, AND J. L. GOLE, submitted for publication.
26. G. HERZBERG, "Molecular Spectra and Molecular Structure." Vol. I. "Spectra of Diatomic Molecules," Second ed., Robert E. Krieger, Malabar, 1989.
27. J. L. DUNHAM, *Phys. Rev.* **41**, 721-731 (1932).
28. K. P. HUBER AND G. HERZBERG, "Molecular Spectra and Molecular Structure IV: Constants of Diatomic Molecules," Van Nostrand-Reinhold, New York, 1979.
29. K. F. ZMBOV AND J. L. MARGRAVE, *J. Phys. Chem.* **71**, 446-448 (1967).
30. K. HILPERT AND K. A. GINGERICH, *Ber. Bunsenges. Phys. Chem.* **84**, 739-745 (1980).

## APPENDIX VIII

"Raman Pumping in the Absence of an External Light Source", D. Grantier, and J. L. Gole, J. Phys. Chem. Letters, 98, 7427 (1994).

## Raman Pumping in the Absence of an External Light Source

David R. Grantier and James L. Gole\*

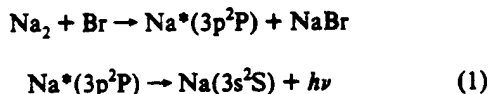
School of Physics, Georgia Institute of Technology, Atlanta, Georgia 30332

Received: April 4, 1994\*

The first observation of a chemically enhanced resonance Raman pumping process, observed in the absence of an external light source, is reported. In an extended path length reactive environment, sodium dimer molecules are Raman pumped by radiation from the Na D-line produced by the reaction of additional dimer molecules with bromine atoms. The observed Raman spectrum would appear to result from much more than a simple light scattering process.

### Introduction

Recently, we have been concerned with the reactions of small supersonically cooled sodium molecules with halogen atoms ( $\text{Na}_n + \text{X} \rightarrow \text{Na}^*_{n-1} + \text{NaX}$ ;  $\text{X} = \text{Cl}, \text{Br}, \text{I}, n = 2, 3$ ).<sup>1,2</sup> These reactions have been shown to demonstrate gain on transitions involving the electronically excited  $\text{Na}_2$  products of the  $\text{Na}_3 + \text{Br}$  reaction.<sup>3,4</sup> In an extension of these experiments, focused on the development of a long path length amplifying medium employing slit source based supersonic expansions, we have observed the first resonance Raman pumping generated in a purely chemical reactive environment. The observations made in the present study bear a close analogy to those of Wellegehausen,<sup>5,6</sup> Bergmann,<sup>7</sup> and co-workers in their analysis of optically pumped sodium dimer lasers operative on a stimulated Raman scattering process. Here, however, we observe a series of Raman-like Stokes and anti-Stokes features which (1) are associated with the lowest vibrational levels of  $\text{Na}_2$ , (2) correlate with a scattering process involving the Na D-line components ( $\text{Na } 3p^2P_{3/2,1/2} \rightarrow 3s^2S_{1/2}$ ) created in the chemical reaction sequence



(3) are not readily generated by light scattering due to an external laser light source, and (4) appear to be enhanced by the environment of the reaction zone itself. The D-line emission is scattered by cooled sodium dimers ( $\text{Na}_2$ ) formed, as a result of supersonic expansion, in the lowest vibrational levels of the  $\text{Na}_2$  ground electronic state. Multiple Stokes and anti-Stokes features assigned as resonance Raman progressions are well simulated on the basis of the resonance Raman theory outlined by Rousseau and Williams<sup>8</sup> and others.<sup>9</sup> The results of initial gain studies, in which amplification has been observed on many of the Stokes and anti-Stokes components of the Raman spectrum, are suggestive of a stimulated Raman scattering process similar to that associated with optically pumped alkali dimer lasers. However, the scattering line width  $\Gamma$  associated with the present process is determined to be close to  $4 \text{ cm}^{-1}$ . These results suggest an unusually fast resonance Raman scattering process which appears to be chemically enhanced.

### Experimental Section

The apparatus which we have used to generate high sodium fluxes in supersonic expansion from an extended slit source is described in detail elsewhere.<sup>10,11</sup> A dual oven (large capacity ( $\sim 350 \text{ g}$ ) stagnation chamber and frontal nozzle expansion channel) system has been designed to produce a supersonic flux

of alkali vapor through a slit nozzle approximately 0.003 in. wide by 2 in. in length. The slit is formed from two sheets of 0.005 in. tantalum prepared, mounted, and sandwiched between frontal and rear nozzle sections. The precise width of the created tantalum slit is adjusted to 0.003 in. under a Vickers microscope and verified for accuracy (across the length of the slit) using single slit diffraction techniques.

The rear stagnation chamber (850–900 K) and frontal nozzle expansion channel (900–950 K) are heated independently. Expansion from the slit source produces a near planar flux (slight divergence) at the reaction region consisting primarily of sodium atoms and internally cooled dimers.<sup>11</sup> In the reaction region, the sodium flux is intersected at variable angles from above and below by two diverging but nearly planar bromine atom flows emerging also from slits machined into graphite tube furnaces<sup>10,11</sup> operated at temperatures<sup>12</sup>  $T > 1700 \text{ K}$  necessary to ensure a greater than 95% conversion of bromine molecules to bromine atoms. At the significant reactant fluxes necessary to generate a strong Raman scattering signal, the absolute number density of bromine atoms in the reaction zone is conservatively estimated<sup>10</sup> at between  $10^{14}$  and  $10^{15} \text{ cm}^{-3}$  whereas the absolute number density of sodium dimers in the reaction zone may exceed  $10^{16} \text{ cm}^{-3}$ .

The optical signature of the long path length sodium molecule-bromine atom reaction zone is focused onto the entrance slit of a SPEX 1704 scanning monochromator coupled to an RCA 1P28 photomultiplier tube (PMT). The PMT is maintained at  $\sim 1000 \text{ V}$ , and the response current is sent through an IEEE interfaced autoranging picoammeter (Keithley) to an IBM compatible AT class microcomputer.

We have also attempted, unsuccessfully, to reproduce the Raman signal created following the reaction sequence (1) by resonantly pumping the supersonically expanded sodium dimers with external laser light. Intensity stabilized broad-band (multimode) laser light ( $\sim 1 \text{ W}$ ) from an argon ion laser (Spectra Physics, Model 171) at 4765 and 4880 Å and dye laser light ( $\sim 100 \text{ mW}$ ) at 5890 and 5896 Å (argon ion pumped R6G) was frequency chopped and passed through the reaction zone in an effort to generate a Raman scattering signal similar to that observed from the chemical reaction pumping. The frequency content of the emergent beam was again monitored with a monochromator-PMT combination. The PMT response, detected with a phase-sensitive amplifier, was digitized and stored in an IBM AT class microcomputer.

In addition to those experiments outlined, an optical configuration similar to the ingenious design of Roll and Mentel<sup>13</sup> was constructed about the extended  $\text{Na}_2$ -Br reaction zone and used to measure optical gain on several of the observed features depicted in Figure 1. These gain measurements are discussed in more detail elsewhere.<sup>10</sup>

\* Abstract published in *Advance ACS Abstracts*, July 15, 1994.

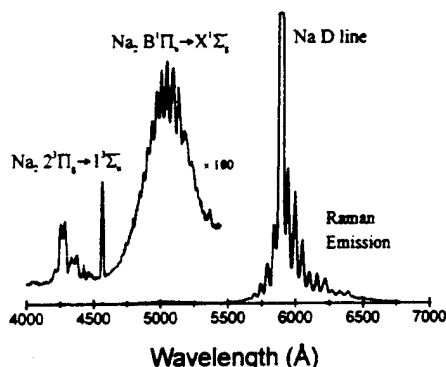


**Figure 1.** Survey spectrum of chemiluminescent emission and Raman scattering from various electronic states of diatomic sodium. The  $\text{Na}_2$   $2^3\Pi_u \rightarrow 1^3\Sigma_g^+$  transition corresponds to a triplet-triplet bound-free excimer-like emission process (resolution  $\sim 12$  Å,  $T_{\text{oven}} \sim 875$  K,  $T_{\text{nozzle}} \sim 935$  K).

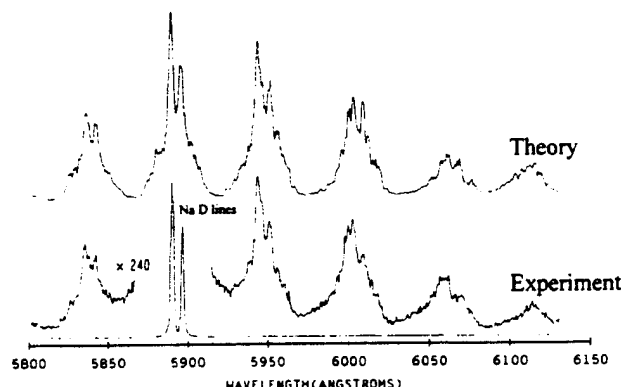


**Figure 2.** Raman-like spectrum taken at a resolution of  $\sim 1.5$  Å ( $T_{\text{oven}} \sim 875$  K,  $T_{\text{nozzle}} \sim 935$  K) depicting the two Na D-line components and the satellite Raman structure. The spin-orbit frequency difference of the two Na D-line components is reproduced in the scattered radiation. A simulated spectrum (calculated from eq 2) is presented for comparison ( $T_{\text{rot}} \sim 400$  K,  $\Gamma = 4$  cm $^{-1}$ ). See text for discussion.

## Results and Analysis

There are several near-resonant rovibronic transitions associated with the  $X^1\Sigma_g^+$  and the  $A^1\Sigma_u^+$  states of  $\text{Na}_2$ <sup>10</sup> and the atomic emission from the Na D-lines,  $\omega_{P1}$  and  $\omega_{P2}$  ( $2P_{3/2} \rightarrow 2S_{1/2}$  at 16 973.379 cm $^{-1}$  and  $2P_{1/2} \rightarrow 2S_{1/2}$  at 16 956.183 cm $^{-1}$ ).<sup>14</sup> We suggest that these near resonances are responsible, in large part, for the unusually intense optical signature depicted in Figure 1.

The spectrum in Figure 1 was taken at a resolution of  $\sim 12$  Å. The relative intensity of the strong sodium dimer  $B \rightarrow X$  chemiluminescence to the even stronger Raman-like emission features symmetrically surrounding the Na D-line is readily apparent. The frequency separation between adjacent Stokes (anti-Stokes) features corresponds closely to 155 cm $^{-1}$ , correlating with the separations between the lowest sodium dimer ground-state vibrational levels. Despite considerable effort, we have found that these features cannot be made to fit a resonance fluorescence series but can be readily assigned to Stokes and anti-Stokes bands associated with a resonance Raman progression.<sup>10</sup>

Additional evidence suggestive of a Raman process is presented in Figure 2. The spectrum depicted in Figure 2 was taken under equivalent reaction zone conditions to those of the spectrum depicted in Figure 1. The intermediate resolution,  $\sim 1.5$  Å, at which this spectrum was obtained is sufficient to clearly resolve the atomic sodium  $2P_{3/2} \rightarrow 2P_{1/2}$  component splitting ( $\sim 17.2$  cm $^{-1}$ ) while leaving individual rotational lines unresolved. The relative intensities of each of the sodium D-line components are clearly evident in the scattered Raman emission. Furthermore, the frequency separation of the atomic line component splitting is clearly reproduced (within the experimental resolution of the scan) for both the vibrational Stokes and anti-Stokes components of the scattering.

We have successfully modeled the group of features symmetrically surrounding the Na D-line with the resonant Raman intensity expression<sup>8-10</sup>

$$I_s(\nu_G, J_G; \nu_F, J_F) = \frac{32\pi^3 \omega_s^4 I_P}{9c^4 h^2} M(\xi_0)^4 e^{-BJ_G(J_G+1)hc/kT} N(\nu_G) \times \sum_{v_1, J_1} \left( 3S_{J_{G1}} S_{J_{F1}} \frac{|\langle v_F | v_1 \rangle \langle v_1 | v_G \rangle|^2}{(\omega_{G1} - \omega_{P1})^2 + \Gamma^2} + 2S_{J_{G1}} S_{J_{F1}} \frac{|\langle v_F | v_1 \rangle \langle v_1 | v_G \rangle|^2}{(\omega_{G1} - \omega_{P2})^2 + \Gamma^2} \right) \quad (2)$$

where  $I_s$  is the total intensity for a scattered Stokes or anti-Stokes line as a function of frequency,  $\omega$ , and pump intensity,  $I_P$ , and  $c$  is the speed of light. We consider transitions from an initial rovibrational ground electronic state of the  $\text{Na}_2$  molecule labeled G to some final rovibrational electronic ground state labeled F through an intermediate excited electronic state labeled I where  $\omega_{G1}$  and  $\omega_{IF}$  represent the rovibronic energy difference between the G and I and I and F levels, and  $\Gamma$  refers to the line width arising from all damping phenomena. The  $S_J$  terms correspond to the appropriate Hönl-London factors for the  $\text{Na}_2$   $A^1\Sigma_u^+ \rightarrow X^1\Sigma_g^+$  transition,<sup>10</sup>  $M(\xi_0)$  represents the electronic matrix element, expressed as a function of the normalized nuclear coordinate,  $\xi = R(\mu\omega/h)^{1/2}$ , and  $\langle v_F | v_1 \rangle$  and  $\langle v_1 | v_G \rangle$  represent Franck-Condon overlap integrals. We have included a thermalized ground-state rotational distribution and a ground-state weighting function  $N(\nu_G)$ , which represents the deviation from a Boltzmann distribution. We also allow pumping due to each component of the sodium D-line ( $\omega_{P1}(2P_{3/2})$  and  $\omega_{P2}(2P_{1/2})$ ) to contribute to the scattered emission intensity,  $I_s$ . Here, the  $2P_{3/2} \rightarrow 2P_{1/2}$  intensity weighting resulting from the reaction populated D-line components is 3:2, as determined from the experimental spectrum.

Numerical calculations<sup>10</sup> were carried out by allowing the near-resonant atomic sodium transitions,  $\omega_{P1}$  and  $\omega_{P2}$ , appropriately broadened, to pump the first 30 levels in the  $\text{Na}_2$   $X^1\Sigma_g^+$  state to the first 70 levels of the  $\text{Na}_2$   $A^1\Sigma_u^+$  state. Deexcitation from the upper electronic state was allowed to proceed to the first 30 levels of the ground state. Rotational levels  $J'', J' = 0-120$  were included with each vibrational level of both the excited electronic  $A^1\Sigma_u^+$  state and the ground electronic  $X^1\Sigma_g^+$  state of the sodium dimer scatterer. Each simulated spectrum produced in the modeling program was convolved with a Gaussian function to approximate the effects of a finite spectrometer slit width.<sup>10</sup>

The data in Figure 3 depict the fit to the vibrational structure surrounding the Na D-line under conditions of pure sodium expansion. All attempts to extract a vibrational temperature through comparison of the observed and calculated Raman spectra were unsuccessful. The low-resolution ( $\sim 12$  Å) vibrational Raman spectrum depicted in Figure 3 does not correspond to a thermalized vibrational distribution. The calculated spectrum in Figure 3, corresponding to a non-Boltzmann vibrational distribution, closely matches the experimental scan and also provides a consistent fit to higher resolution spectra. Although the rotational population distribution may also be non-Boltzmann, we find that with an effective rotational temperature of 400 K we are able to obtain a close agreement between the experimental and calculated spectrum depicted in Figure 4. This suggests that only slight modifications from a thermalized distribution will be necessary to exactly fit the rotational features. We need consider elsewhere that there are several possible sources for the deviation of the Raman scattering features, depicted in Figure 3, from a thermalized vibrational distribution.<sup>10</sup>

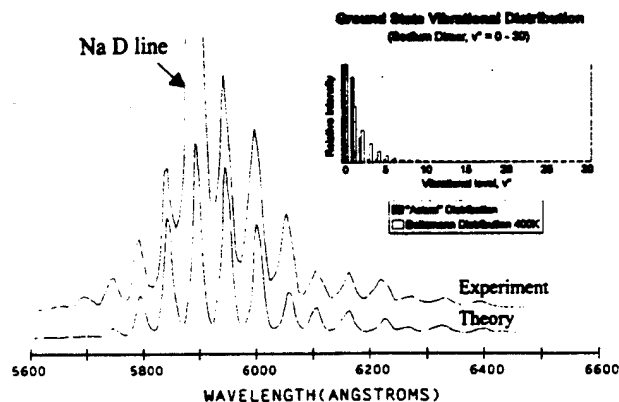


Figure 3. Comparison of experimental spectrum with computer-modeled distribution (resolution  $\sim 5$  Å,  $T_{\text{exc}} \sim 875$  K,  $T_{\text{exc}} \sim 935$  K). Optimum agreement between calculation and experiment was found for the slightly nonthermal distribution depicted in the upper right-hand corner of the figure. A Boltzmann distribution at 400 K is included for comparison. See text for discussion.

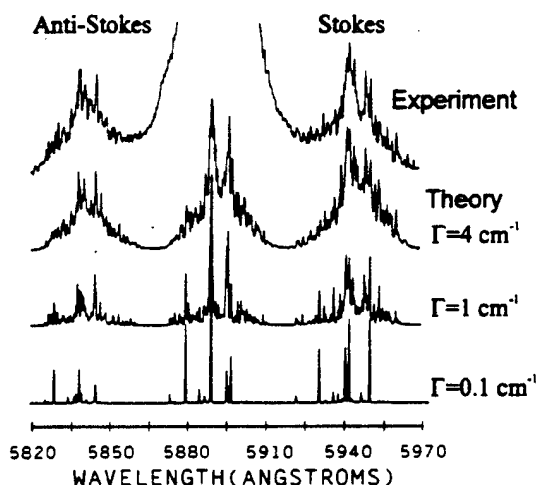


Figure 4. High-resolution spectrum ( $\sim 0.5$  Å) and simulated spectra for  $\Gamma = 0.1, 1$ , and  $4$   $\text{cm}^{-1}$  demonstrating the marked improvement in the fit to the experimental Raman-like features for increasing values of  $\Gamma$ . See text for discussion.

A still higher resolution scan ( $\sim 0.4$  Å) of the first Stokes and anti-Stokes features is depicted and computer simulated in Figure 4. The computer simulation is again based on the application of eq 2. In a surprising result, we find that a line width  $\Gamma \approx 4$   $\text{cm}^{-1}$  is required to provide optimum agreement between the simulated and experimental results with correlation coefficients exceeding 0.92 for the anti-Stokes and 0.89 for the Stokes features, respectively. A further confirmation of the required line width is also indicated in Figure 4 where we compare the experimental spectrum to  $\Gamma = 4$ ,  $1$ , and  $0.1$   $\text{cm}^{-1}$  simulations based on eq 2.

While there are improvements that can be made in the simulations depicted in Figure 4, it is unlikely that simple power broadening can be responsible for the large effective line width indicated by our spectral simulations. On the basis of the required power broadening for a two-level quantum system driven at resonance, we estimate that an electric field of  $\sim 1.3$  kV/cm and an absolute power density of  $\sim 0.215$  MW/cm<sup>2</sup> are necessary to produce the requisite spectral broadening of  $4$   $\text{cm}^{-1}$ .

The apparent  $\sim 4$   $\text{cm}^{-1}$  spectral broadening suggests the possibility of a scattering lifetime of order  $10^{-11}$  s, implying a process which is considerably more efficient than would be expected on the basis of resonance Raman pumping involving the  $\text{Na}_2$  A-X transition ( $\sim 10^{-8}$  s based on the radiative lifetime<sup>15</sup>). Several additional experiments involving the direct pumping of the sodium expansion in the absence of bromine atom reactant at the Na D-line frequencies (argon ion pumped R6G) and at 4765 and 4880 Å using a multimode argon ion laser failed to

reveal optical signatures corresponding to those depicted in Figures 1-4. In fact, while it was possible to excite laser-induced fluorescence corresponding to the  $\text{Na}_2$  A-X and B-X band systems analogous to that observed previously,<sup>16</sup> although at somewhat higher temperatures in the present experiments, no clear Raman features were generated. This result also suggests a more efficient process than that associated with resonance Raman pumping.

These results suggest that we have observed more than a "simple" Raman-like scattering process. We might consider a further long-range interaction of the electronically excited sodium  $3p^2P$  atoms with those  $\text{Na}_2$  molecules which are Raman pumped, an interaction of the  $\text{Na}_2$  molecules with the Br atoms that induces a time-varying enhancement of the dimer polarizability (hyperpolarizability) or (less likely) the presence of a large electric field created due to the reactive environment in the vicinity of the reaction zone. It would appear that this interaction or perturbation leads to a much more efficient Raman-like scattering process and appears to demonstrate a stimulated Raman gain condition.<sup>10</sup>

While further experiments will be necessary to clarify the mechanism for the scattering process, the long path length reaction zone employed in these experiments appears to have revealed the manifestation of a significant cooperative phenomena. The moderate Rydberg character of the Na  $3p^2P$  excited state, with its diffuse electron density, may, in fact, lend itself to a considerable long-range interaction inducing cooperative effects. The assessment of these cooperative effects awaits further study.

**Acknowledgment.** The authors gratefully acknowledge the helpful comments of Professors Ron Felton and Michael Heaven and Dr. Kangkang Shen. Helpful comments and technical assistance from Mr. C. B. Winstead is also greatly appreciated. The support of the Georgia Tech Foundation through a grant from Mrs. Betty Peterman Gole, the Army Research Office through the Short Term Innovative Research Program, the Air Force Office of Scientific Research, and the Army Research Office and AFOSR/SDIO is greatly appreciated.

## References and Notes

- (1) Crumley, W. H.; Gole, J. L.; Dixon, D. A. *J. Chem. Phys.* **1982**, *76*, 6439.
- (2) (a) Gole, J. L. The Unique Nature of Metal Cluster Oxidation. In *Physics and Chemistry of Finite Systems: From Clusters to Crystals*; Jena, P., Khanna, S. N., Rao, B. K., Eds.; NATO ASI Ser. Vol. II; 1992; p 1025. (b) Gole, J. L. Toward the Modeling of the Oxidation of Small Metal and Metalloid Molecules. In *Gas Phase Metal Reactions*; Fontijn, A., Ed.; North-Holland: Amsterdam, 1992; pp 578-604. (c) Gole, J. L. The Unique Complexation and Oxidation of Metal-Based Clusters. In *Advances in Metal and Semiconductor Clusters*; Duncan, M. A., Ed.; JAI Press: London, 1993; Vol. 1, pp 159-209.
- (3) Cobb, S. H.; Woodward, J. R.; Gole, J. L. *Chem. Phys. Lett.* **1989**, *156*, 197.
- (4) "Chemically Driven Pulsed and Continuous Visible Laser Amplifiers and Oscillators", with K. K. Shen, H. Wang, and D. Grantier; Invited Talk. Proceedings of the 23rd AIAA Plasma-Dynamics and Laser Science Conference, Nashville, Tennessee, AIAA 92-2994, 1992.
- (5) Wellegehausen, B. *IEEE J. Quantum Electron.* **1979**, *15*, 1108.
- (6) Wellegehausen, B. In *Metal Bonding and Interactions in High Temperature Systems with Emphasis on Alkali Metals*; ACS Symp. Ser. 179; Gole, J. L., Stwalley, W. C., Eds.; American Chemical Society: Washington, DC, p 462.
- (7) Gaubatz, U.; Bissantz, H.; Hefter, U.; Colomb de Daunant, I.; Bergmann, K.; Jones, P. L. *J. Opt. Soc. Am.* **1989**, *6*, 1386.
- (8) Rousseau, D. L.; Williams, P. F. *J. Chem. Phys.* **1976**, *64*, 3519.
- (9) See, for example: Tang, J.; Albrecht, A. C. In *Raman Spectroscopy*; Szymanski, H. A., Ed.; Plenum: New York, 1970; Vol 2, pp 33-68. Albrecht, A. C. *J. Chem. Phys.* **1961**, *34*, 1476.
- (10) Grantier, D. R.; Gole, J. L. Chemically Enhanced Raman Scattering, to be submitted for publication.
- (11) Grantier, D.; Wang, H.; Winstead, C. B.; Gole, J. L. Proceedings of the 24th AIAA Plasma Dynamics and Lasers Conference, Orlando, FL, AIAA 93-3207, 1993.
- (12) Cobb, S. Ph.D. Thesis, Georgia Institute of Technology, Atlanta, GA, 1988.
- (13) Roll, G.; Mentel, J. *J. Phys. D: Appl. Phys.* **1989**, *22*, 483.
- (14) Moore, C. E. *Atomic Energy Levels*; National Bureau of Standards: Washington, DC, 1949.
- (15) Zemke, W. T.; Verma, K. K.; Vu, T.; Stwalley, W. C. *J. Mol. Spectrosc.* **1981**, *85*, 150.
- (16) Gole, J. L.; Green, G. J.; Pace, S. A.; Preuss, D. R. *J. Chem. Phys.* **1982**, *76*, 2247.

## APPENDIX IX

"The Expansion of Small Molecule Configuration Space: Highly Efficient Long Range Stabilization and Energy Transfer Involving Electronically Excited States", D. R. Grantier, and J. L. Gole, High Temp. Science, in press.

## Abstract

Highly efficient long range interactions in high temperature reactive environments are exemplified with two studies. A combination of single and multiple collision chemiluminescent studies has been used to (1) demonstrate the highly efficient collisional stabilization of electronically excited Group IIA dihalide collision complexes formed in direct  $M + X_2 \rightarrow MX_2$  reactive encounters, (2) delineate the first direct evidence for symmetry constraints associated with dihalide formation in the  $M + X_2$  insertion process, and (3) obtain the first discrete emission spectra for these dihalide complexes. A demonstrated collisional stabilization not readily explained within the RRKM framework suggests that new models will be necessary to explain the efficient interaction of electronically excited states. Information provided on the efficient stabilization of excited state intermediate complexes defines a much broader range of interaction than has typically been associated with collisional stabilization phenomena. The importance of long range interactions is further demonstrated by the first observation of a chemically enhanced stimulated resonance Raman pumping process, observed in the absence of an external light source. In an extended path length reactive environment, sodium dimer molecules are Raman pumped by radiation from the Na D-line produced by the reaction of additional dimer molecules with bromine atoms. The observed Raman spectrum would appear to result from much more than a simple light scattering process. The demonstrated interaction ranges and the enhanced interaction of high temperature molecules in general have direct implication for the understanding of molecular formation and energy transfer in the high stress environments which include combustors and high impulse propulsion systems.

The Expansion of Small Molecule Configuration Space:  
Highly Efficient Long Range Stabilization and Energy Transfer Involving  
Electronically Excited States

James L. Gole and David R. Grantier

School of Physics  
Georgia Institute of Technology  
Atlanta, Georgia 30332

## INTRODUCTION

It is a pleasure to contribute this paper to the Margrave Symposium Volume of High Temperature Science. John Margrave has demonstrated an amazing versatility in the scientific problems with which he has been involved. In a very strong sense this is reflected in the diversity of students both graduate and undergraduate which have matriculated in his laboratory and whose interests and pursuits range from inorganic synthesis to fundamental problems in chemical physics. The symposium in his honor at Rice University on April 29, 1994 brought together many old friends and produced some very interesting tales.

This paper discusses topics which relate to the enhanced interactions characteristic of high temperature reactive environments. The storage and efficient conversion of the energy generated in (1) the products of highly exothermic reactive processes, (2) highly dense plasma-like reactive environments, and (3) the non-equilibrium laser based stimulated emission process can be influenced by similar although sometimes complex mechanisms. The realization of the potential conversion efficiency of these systems requires that we identify overriding factors associated not only with chemical reactivity but also with poorly understood energy transfer and stabilization processes.

Through a series of unique coupled experiments<sup>1-8</sup> spanning a seven decade pressure range from the near "single collision" pressure regime associated with the nascent products of chemical reaction to the moderate pressure diffusion flame environment, we observe the clear manifestation of long range energy transfer and stabilization. We suggest that the processes of interest may influence the dynamics of reactive interaction and energy pooling in combustion, propulsion, plasma, and laser environments, by utilizing the substantial configuration space encompassed by a diffuse excited state electron density. There have been few concerted efforts to assess and model these efficient pathways which we exemplify by outlining two ongoing studies involving (1) an evaluation of the extremely efficient radiative three body collisional stabilization of Group IIA atom (Ca, Sr, Ba)-halogen molecule reactive encounters leading to dihalide excited state formation and (2) the first chemically induced Raman pumping of a diatomic molecule in the absence of an external light source.

## SYMMETRY CONSTRAINED DYNAMICS OF GROUP IIA DIHALIDE FORMATION

The transformation from covalent to ionic bonding and its influence on molecular electronic structure and reaction dynamics has long been fundamental to our understanding of chemistry, attracting the interest of chemists and chemical physicists alike.<sup>9</sup> The reactions which form the Group IIA dihalides can be studied to provide insights for our understanding of these transformations and the nature of intermediate complex formation as strong ionic chemical bonds are formed. Through a series of selected preliminary experiments, we have obtained a wealth of evidence which casts new light on the dynamics of Group IIA dihalide formation via Group IIA metal-halogen molecule reactions. Further, we identify a symmetry constrained dynamics associated with the electron jump harpooning process and the formation of long-lived  $MX_2$  ionic complexes where M corresponds to the Group IIA metal (M=Ca,Sr,Ba) and X to a halogen atom (X=Cl,Br,I). These complexes, while forming via a direct  $M + X_2$  insertion reaction, are subject to a highly efficient collisional stabilization which may well exemplify the extended range of interaction (cross section) characteristic of many high temperature molecules.<sup>2-5</sup> The controlled collisional relaxation of the Group IIA dihalide excited states has now produced the first discrete spectroscopic data on the low-lying and ground states of these highly ionic high temperature molecules, greatly aiding mechanistic interpretation. The results which we outline suggest that the study of these systems will provide an abundance of both dynamic and spectroscopic information, providing an opportunity for the systematic study of chemical and structural properties as they influence both reactivity and molecular electronic structure and leading to detailed periodic correlations which are basic to chemistry.

The Group IIA dihalides have been studied extensively by Hildenbrand<sup>10</sup> who has used an astute combination of mass spectrometric data and a variety of structural estimates to evaluate the validity of ionic models. As Table I demonstrates, the IIA halides are unusual in that the strength of the second halogen bond is at least comparable to or considerably greater than that of the first. In other words, the atomization energy, especially of the heavier halogen dihalides, is at least twice the dissociation energy of the metal monohalide. This bonding characteristic suggests that the Group IIA-halogen molecule reactions might present ideal systems in which to study few body

complexation processes and hence the efficient collisional stabilization of intermediate complexes. Further, any spectroscopic data obtained on the dihalides, in combination with a firm thermochemical base, furnishes an important link to further refine the extent and validity of the ionic models which Hildenbrand<sup>10</sup> and others<sup>11</sup> have developed to aid our understanding of high temperature chemistry. Within the framework of modeling reactivity and structure, the Group IIA metal reactions offer a wide range of atomic size as well as change in ionization potential and electron affinity. Their diversity far exceeds that of the much simpler alkali metals, yet they are sufficiently simple so as to render detailed modeling both useful and definitive.

### A Clarification of Historical Perspective

The reactions of Group IIA metal atoms and halogen molecules have been studied under near single collision conditions in low pressure ( $10^{-6}$  -  $10^{-4}$  Torr) beam-gas or beam-beam environments by a number of researchers. The analysis of their experimental results has been both controversial and ever-evolving. As first observed by Jonah and Zare<sup>12</sup>, for the Ba + Cl<sub>2</sub> reaction (Fig. 1), the Group IIA metal (M=Ca,Sr,Ba)-halogen molecule ( $X_2 = Cl_2, Br_2, I_2$ ) reactions produce a broad structureless emission feature (see Figs. 1,2) spanning the near ultraviolet and visible regions. Jonah and Zare initially attributed this feature to a two-body ( $M + X_2$ ) radiative association viz.



first order in the Group IIA metal and halogen molecule. However, Wren and Menzinger<sup>13</sup> soon revealed a quadratic dependence of the light emission on oxidant pressure. This second order oxidant pressure dependence, dominating at pressures as low as  $3 \times 10^{-6}$  Torr, appeared to signal the presence of a three-body radiative recombination process.

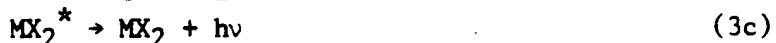


under conditions generally identified with the single collision pressure regime. Here the dagger signifies that the  $MX_2$  species is formed at energies above its dissociation limit, however, the partitioning of the available energy into internal excitation and product translational motion is not

specified.<sup>7</sup>

In invoking mechanism (2), Wren and Menzinger<sup>13</sup> thus suggested a very efficient collisional stabilization process operative in the micro-torr region, involving a collision complex of some considerable extent. The viability of an enhanced interactive range of electronically and/or highly vibrationally excited species is supported by recent studies of energy transfer collisions with the excited states of high temperature molecules.<sup>2-5</sup> However, Rosano and Parson<sup>14</sup> noted that (within an RRKM framework), in order for step (2b) to be significant, the quasibound  $MX_2$  would have to have an unusually long lifetime,  $\sim 10^{-5}$ s at  $10^{-5}$  Torr; if its lifetime is estimated to be on the order of a molecular vibration,  $\sim 10^{-13}$ s, the pressure would have to be on the order of an atmosphere. The results which we outline in following sections would suggest that these arguments, while soundly based, require modification as the reactions of interest are characterized by a much broader range of complex interaction.

In the absence of additional information, the considerations outlined above lead Menzinger,<sup>15</sup> Rosano and Parson,<sup>14</sup> and Engelke<sup>16</sup> to conclude that the third order dependence for  $MX_2^*$  formation must be due exclusively to two sequential harpooning processes



involving<sup>15</sup> highly vibrationally excited ground state  $MX(X^2\Sigma^+)$ . To support this mechanism these authors have noted the small amount of product recoil for step (3a))<sup>14</sup> and the "apparent" insensitivity of the  $MX_2^*$  emission to addition of a nonreactive buffer gas.<sup>15</sup> Further, in pointing out the established "known" validity of mechanism 2, Menzinger<sup>15</sup> has also argued that the low ionization potential for  $MX(X^2\Sigma^+)$  (slightly below that of the metal atom<sup>17</sup> and decreasing for vibrationally excited  $MX$ ) establishes that reaction (3(b)) corresponds to a more efficient electron jump process than reaction (3(a)).

Although the arguments of Rosano and Parson favoring mechanism (3), focused on the  $MX_2$  excited state radiative lifetime, can be compelling, they result, in large part, from a misconception<sup>16</sup> concerning the nature of the lowest energy dihalide excited electronic states. It is likely that at least the lowest-lying dihalide transition (A-X band system) does involve a long-

lived,  $\tau_{\text{rad}} \geq 10^{-5}$  sec, excited electronic state.<sup>7</sup> Therefore, provided that bound excited state levels are populated (which the extent of the emission continua in Figures 1 and 2 suggest and which multiple collision relaxation studies confirm), the collisional stabilization of a long-lived electronically excited dihalide emitter is possible. However, this is a requirement which becomes less stringent if the formed Group IIA dihalide complex is capable of interaction over a much longer range.<sup>7</sup>

### Periodicity of Group IIA Dihalide States

Klemperer et al.<sup>18</sup>, using the technique of electric quadrupole deflection of molecular beams, determined the grid of dihalide geometries outlined in Table II. This table demonstrates clear trends as linear geometries are favored by the light metal-heavy halogen combination whereas bent structures are favored by the heavy metal-light halogen combination. These geometric trends can be explained<sup>19-22</sup> on the basis of a modification of Walsh's correlation diagrams for  $AB_2$  type molecules to take into account the influence of normally unfilled d orbitals on the metal atom. The IIA-dihalides are predicted to be strictly linear if described using only s and p orbitals within the Walsh framework. The strongly ionic character of the Group IIA dihalides also leads to important modifications of the Walsh-type diagram.<sup>23</sup>

Figure 3 corresponds to a molecular orbital correlation diagram for  $BeF_2$ .<sup>23</sup> Here we plot valence orbital energy as a function of bond angle. The orbital occupation for the ground state of  $BeF_2$  is complete through the  $\pi_g$  orbital (16 valence electrons). It is clear that the sum of the valence orbital energies leads to the prediction of greatest stability for a bond angle of  $180^\circ$ .

The makeup of the valence molecular orbitals in  $BeF_2$  has been discussed<sup>23</sup> and comparisons of the  $BeF_2$  correlation diagram (Figure 3) with Walsh's valence molecular orbital diagram for  $CO_2$  have been made. For our purposes, it is important to note that the lowest energy excited states in  $BeF_2$  are predicted to result from transitions involving the highest occupied  $\pi_g(b_2)$  and  $\pi_g(a_2)$  molecular orbitals of the ground state to the lowest unoccupied  $\sigma_g(a_1)$  molecular orbital. This is in contrast to the case of  $CO_2$  where experiments have confirmed Walsh's prediction that the lowest energy transitions are from the  $\pi_g(b_2)$  and  $\pi_g(a_2)$  molecular orbitals to the  $\pi_u(a_1)$

molecular orbital. This predicted change in the ordering of the  $\pi_u(a_1)$  and  $\sigma_g(a_1)$  orbitals for  $\text{BeF}_2$  and  $\text{CO}_2$  suggests that the lowest energy transitions in  $\text{BeF}_2$  and, for that matter, several of the remaining Group IIA dihalides, should be quite weak in absorption since a  $(g \rightarrow g)$  transition is electric dipole forbidden for the linear molecule. In fact, the lowest energy HOMO-LUMO transition (analog of  $A^1\Pi_g - X^1\Sigma_g^+$  for the linear dihalide) has not been observed even in attempted studies of the absorption spectrum for the highly bent  $\text{BaF}_2$  molecule. Researchers have been lead to believe<sup>24</sup> that the absorption spectra for these inherently high temperature molecules cannot be obtained and studied; however, the experimental results which we discuss in the following sections demonstrate otherwise and fingerprint regions for studying this spectroscopy.

In emission, one might expect to observe reasonably intense transitions from a  $^1B_2$  state [electron configuration ...  $(1a_2)^2 (4b_2)(6a_1)$  for the highest three valence orbitals] as the spectrum is expected to involve long progressions in the bending mode of the upper and lower states. However, as can be noted in the pressure dependence of the multiple collision relaxed chemiluminescent emission,<sup>7</sup> these transitions will also feel the effect of the  $g \rightarrow g$  selection rule. Transitions from the  $^1A_2$  state [electron configuration ...  $(1a_2) (4b_2)^2(6a_1)$  for the highest three valence orbitals] would be expected to be very weak due to the electric dipole selection rules for a  $C_{2v}$  molecule. Transitions from the  $^3B_2$  states are "spin forbidden" and are therefore also expected to be weak. We anticipate the change in bond angle which accompanies these lowest energy transitions to be so pronounced that the observed emission spectrum can be expected to extend over several hundred angstroms. This is evidenced by an emission system tentatively ascribed to the  $^1B_2 - X^1A_1$  (A-X) transition (see Figures 4 and 5) observed under multiple collision conditions, and resulting from  $\text{Ca-Cl}_2$ ,  $\text{Ca-Br}_2$ ,  $\text{Sr-Cl}_2$  (Figs. 5,6), and  $\text{Sr-Br}_2$  (Figs. 4,6) reactive encounters. At elevated pressures, the A-X band system feature (Figs. 4,5) which extends from the fringes of the ultraviolet to considerably longer wavelength is efficiently quenched relative to the B-X band systems indicated in Figs. 4 and 6, as would be expected for a long-lived excited state.<sup>7</sup>

Transitions which involve excitation from the  $\pi_g$  to the  $\pi_u$  valence molecular orbital (Fig. 3) are expected to occur at higher energy. These electric dipole allowed transitions should be characterized by both a strong

absorption and emission spectrum, the latter of which has tentatively been identified for the Ca-Cl<sub>2</sub>, Ca-Br<sub>2</sub>, Sr-Cl<sub>2</sub> (Fig. 6), Sr-Br<sub>2</sub> (Figs. 4,6) and Sr-ICl (Fig. 6) (SrICl-transition is  $\pi$  to  $\pi$ ) systems at the fringes of the ultraviolet. The bond angle change accompanying this transition will not be as pronounced as that accompanying the lowest energy band system, however the change from  $\pi$ -nonbonding to  $\pi$ -antibonding character should result in a progression in the dihalide stretching frequency. Features ascribed to this mode have tentatively be associated with the observed emission spectra (see also Figures 6 and 7).

### Periodicity of Group IIA Dihalide Formation

#### "Near 'Single Collision' Studies and Symmetry Effects"

The Group IIA metal-halogen molecule reactions involve the interaction of metals with reasonably low ionization potentials<sup>25</sup> and halogen molecules of high electron affinity.<sup>26</sup> They are therefore expected to proceed via an electron jump process whereby the Group IIA atom throws out an electron to harpoon the halogen molecule, forming an  $M^+ X_2^-$  complex. The data presented in Figures 1 and 2 obtained under near single collision conditions<sup>1,7</sup> ( $10^{-4}$  -  $10^{-6}$  Torr) for the Ba-Cl<sub>2</sub>, Ba-Br<sub>2</sub>, and Ba-I<sub>2</sub> reactions, exemplifies the "continuum" emissions observed for the Ca, Sr, and Ba reactions with Cl<sub>2</sub>, Br<sub>2</sub>, and I<sub>2</sub>. The spectra are dominated by dihalide emission features extending from  $\sim 3000$  to  $6000 \text{ \AA}$ . The apparatus used to obtain these experimental results has been discussed elsewhere.<sup>1,7</sup> In contrast to the Ca, Sr, and Ba reactions with the chlorides, bromides, and iodides which yield a spectrum dominated by Group IIA dihalide emission, the reactions involving F<sub>2</sub> are strongly dominated by emission from the monofluorides. Only a weak emission continuum is observed ( $3500\text{--}5000 \text{ \AA}$ ) for the magnesium system and this emission is found to be quadratic in the fluorine molecule concentration. This clearly represents an important periodic trend in dihalide formation. In retrospect, the lack of a notable difluoride emission for the Mg, Ca, Sr, and Ba reactions casts suspicion on the double harpoon mechanism (3) since this reaction sequence easily supplies the energy necessary (see Table I) to access difluoride excited states. We suggest<sup>7</sup> that these characteristics may result, at least in part, because the fluorine molecule negative ions produced in the electron jump process dissociate much more rapidly than do the

corresponding  $\text{Cl}_2^-$ ,  $\text{Br}_2^-$ , or  $\text{I}_2^-$  ions. However, we must also note that, whereas  $D_0^0(\text{MF}_2) \approx 2D_0^0(\text{MF})$ , the atomization energies of the chlorides, bromides, and iodides well exceed twice the metal monohalide bond energy.

An important symmetry constraint is signaled by the intensity of the emission from the dihalides formed in the reactions of Ca, Sr, and Ba with the mixed halogen molecules IBr and ICl. This is illustrated in Figure 2 where we compare total scans for the  $\text{Ba} + \text{I}_2$ ,  $\text{Ba} + \text{IBr}$ , and  $\text{Ba} + \text{Br}_2$  reaction systems. These scans, which demonstrate a much weaker emission for heteronuclear halogen molecule reaction, were taken under the same resolution and with nearly identical halogen pressures and metal beam fluxes. Similar, if not more pronounced, results have been observed when comparing the tri-groupings  $\text{Ba} + \text{Cl}_2$ , ICl, and  $\text{I}_2$ . We will suggest that the dominant intensity for the  $\text{Cl}_2$ ,  $\text{Br}_2$ , and  $\text{I}_2$  reactions results because of the  $\text{C}_{2v}$  reaction path available to the homonuclear but not accessible to the heteronuclear halogen reactions. The availability of this  $\text{C}_{2v}$  reactive geometry (conical intersection) promotes excited state dihalide formation for  $\text{M} + \text{X}_2$  but not  $\text{M} + \text{XY}$  reactive encounters. These effects can certainly be manifest in the collisional stabilization mechanism (2) but not in the two step harpoon mechanism (3). While the difference in continuum intensity is quite pronounced for the barium reactions, this difference decreases for the strontium reactions and is almost muted for calcium. This behavior is consistent with the electron jump model and an increasing characteristic velocity at the curve crossing region associated with an  $\text{M} + \text{X}_2 \rightarrow \text{M}^+ + \text{X}_2^-$  "outer harpooning" process (see also following) which diminishes the coupling (cross section) for the interaction of the  $\text{M} + \text{X}_2$  and  $\text{M}^+ + \text{X}_2^-$  curves.

### "Multiple Collision Relaxation Studies"

The successful extension of the low pressure studies outlined above, in a controlled manner, using primarily helium buffer gas, provides the means to collisionally relax the dihalide continuum so as to reveal what appear to be three discrete band systems. This is a key step in the unraveling of the dynamics of these systems. Thusfar, we have successfully relaxed the continuous emission features associated with the  $\text{Ca}-\text{Cl}_2$ ,  $\text{Ca}-\text{Br}_2$ ,  $\text{Sr}-\text{Cl}_2$ ,  $\text{Sr}-\text{Br}_2$ ,  $\text{Sr}-\text{I}_2$ , and  $\text{Sr}-\text{ICl}$  reactive encounters. The overview spectrum depicted in Fig. 4 for the  $\text{Sr} + \text{Br}_2$  combination is exemplary. The lower energy system

(feature), which extends from the fringes of the ultraviolet through the visible, is dominated by a long progression in the  $\text{SrX}_2$  bending mode. This is clearly apparent in the  $\text{SrCl}_2$  emission spectrum depicted in Figure 5. The observed feature most likely corresponds to a  ${}^1\text{B}_2((1a_2)^2(4b_2)(6a_1)) \rightarrow X {}^1\text{A}_1((1a_2)^2(4b_2)^2)$  transition which correlates in linear configuration to the  ${}^1\Pi_g - {}^1\Sigma_g^+$  transition involving the  $\sigma_g$  and  $\pi_g$  molecular orbitals (Fig. 3). For all of the reactive combinations studied thusfar, we find that both Group IIA metal and halogen molecule collisions effectively quench this feature, a fact which is not surprising in view of the anticipated longer lifetime ( $\tau_{\text{radiative}}$ ) associated with the excited state emitter. We will want to improve our methods for exciting and observing this band system while expanding the grid of collision partners considered to barium based reactive encounters. This will require some considerable care as the increased density of states associated with the barium halides certainly can lead to a more efficient quenching process even with the decreasing radiative lifetime expected for the lowest-lying barium dihalide states ( $\tau_{\text{rad}}(\text{BaF}_2) < \tau_{\text{rad}}(\text{BaCl}_2) < \tau_{\text{R}}(\text{BaBr}_2) < \tau_{\text{R}}(\text{BaI}_2)$ ). It should be noted that the expected trends in the barium dihalide radiative lifetimes appear manifest in the pressure dependent behavior of the observed low pressure ( $10^{-4} - 10^{-6}$  torr) emission continua.<sup>7</sup>

The more clearly resolved higher energy band system depicted in Figure 4, and displayed in greater detail for the  $\text{Sr} + \text{Cl}_2$ ,  $\text{Sr} + \text{Br}_2$ , and  $\text{Sr} + \text{ICl}$  reactive encounters in Figure 6, would seem to correspond to one of the allowed  ${}^1\text{B}_2((1a_2)(4b_2)^2(2b_1))$  or  $(1a_2)^2(4b_2)(7a_1)) \rightarrow X {}^1\text{A}_1$  transitions which correlate in linear configuration to the allowed  ${}^1\Pi_u - {}^1\Sigma_g^+$  transition involving the  $\pi_u$  and  $\pi_g$  molecular orbitals (Fig. 3). This transition, which in absorption would involve primarily a change from Sr-X nonbonding to Sr-X antibonding character, should be dominated by progressions in the  $\text{SrX}_2$  or  $\text{SrXY}$  stretching modes. The frequency separations between the observed features are consistent with this suggestion.<sup>7</sup>

#### Support for a Collisionally Stabilized Dihalide Complex

The results we have obtained in our study of the  $\text{Sr-ICl}$  system (Fig. 6) and the mixed  $\text{Sr} - \text{Br}_2 + \text{Cl}_2$  system (Figure 7) are particularly significant for they demonstrate that the observed dihalide emission results, in large

part, from the collisional stabilization process (2). If the two step double harpooning mechanism (3) were to be operative, the combination of Sr-ICl and SrX-ICl reactive encounters should produce SrCl<sub>2</sub>, SrICl, and SrI<sub>2</sub> emission with the dichloride emission clearly dominating that for the mixed halide and SrI<sub>2</sub>. If the collisional stabilization mechanism is operative, the observed emission spectrum will correspond to the SrICl complex formed in a dynamically constrained (see following) electron jump process.

The reaction of strontium with Cl<sub>2</sub> + Br<sub>2</sub> mixtures of varying relative chlorine and bromine concentration should produce emission from SrCl<sub>2</sub>, SrBrCl, and SrBr<sub>2</sub> if the two step double harpooning mechanism (3) is operative. If the highly efficient collisional stabilization process (2) is operative, the observed spectra should consist of the sum of only SrCl<sub>2</sub> and SrBr<sub>2</sub> emissions varying with relative Cl<sub>2</sub> and Br<sub>2</sub> concentration.

A study of the Sr-ICl reaction, with its attendant symmetry based dynamic constraint, can be difficult for vibrationally excited SrCl molecules produced from the relaxation of emitting SrCl electronically excited products which can react with ICl in a sufficiently exothermic process to produce an SrCl<sub>2</sub> emission feature. In fact, under certain conditions, the observed spectral signature can be contaminated by SrCl<sub>2</sub> (A-X Fig. 5) formed via the reaction of a thermalized ground state SrCl product with ICl. It is also relevant that ultraviolet spectrum in Figure 6 corresponds to one of the "allowed" SrX<sub>2</sub> B<sup>1</sup>B<sub>2</sub> - X<sup>1</sup>A<sub>1</sub> transitions and therefore should display a minimal difference between the transition moments for the SrX<sub>2</sub> (X=Cl,Br) and corresponding SrXY (XY=ICl) emitters. We have observed a dominant emission corresponding to the SrICl complex both in the B-X region depicted in Fig. 6 and at higher energies corresponding to a C-X band system which can be populated by the more exothermic ICl reaction. The spectrum in Fig. 6 does show some Cl<sub>2</sub> contamination for the higher temperature conditions (higher Sr flux) under which the three spectra in the figure were obtained however, the dominance of the SrICl emission system is apparent. This dominance demonstrates the probable formation of SrICl in a collisionally stabilized direct reactive encounter.

The collage of spectra in Fig. 7 which are obtained for varying mixtures of Br<sub>2</sub> and Cl<sub>2</sub> correspond to sums of emission features resulting exclusively from the dichloride and dibromide with no evidence for the mixed halogen (SrBrCl) emitter. This is especially significant when we note that the sum of

both SrCl and SrBr emission features characterize the monohalide emissions for all of the chlorine - bromine mixtures (compare to Sr+Cl<sub>2</sub> (top) and Sr+Br<sub>2</sub> (bottom)) considered in Fig. 7.

These results, which demonstrate the utility of combining near single collision and multiple collision chemiluminescent studies, are fundamental to our assessment of the electron jump process leading to excited state dihalide formation. They strongly suggest the probability that the extremely efficient collisional stabilization mechanism (2) is the dominant means of forming the dihalide excited state. This conclusion is also further supported by the lack of a continuum emission associated with the fluorine based reactions which should also yield dihalide emission if the two step double harpooning mechanism (3) is operative.

The implication of these results is broader for it suggests that the extent of interaction of these high temperature molecular complexes, as they form, considerably exceeds that which we normally associate with collisional stabilization and energy transfer processes. High temperature molecules in electronically excited states or in high vibrational levels of their ground electronic states simply are capable of much longer range interactions. It is important that we understand the formation and interaction of these species for this must, in the final analysis, contribute strongly to the behavior of systems operating under extreme conditions. A neglect of these phenomena in models of combustion or propulsion systems renders these models unrealistic.

#### **A Symmetry Constrained Electron Jump Process**

As we have noted, the low Group IIA metal ionization potentials and the high halogen electron affinities suggest that the Group IIA-halogen molecule reactions proceed via an electron jump process wherein the metal atom, M, throws out an electron and harpoons the halogen molecule, X<sub>2</sub>, to initiate reaction. The relative intensities of the continuum emissions observed for homo- and heteronuclear halogen reactions can be understood within the model<sup>7</sup> using the correlations outlined in Table III and extrapolating on the simple, yet elegant, (Fig. 8) arguments of Menzinger<sup>15</sup> used to explain metal monohalide chemiluminescent emissions from the fluorine and chlorine molecule reactions.

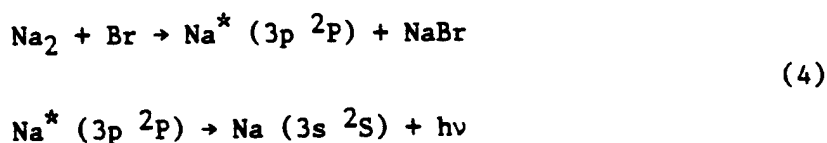
Reactions to produce the dihalide are thought to proceed<sup>7</sup> through an

electron jump "outer harpooning" process involving the interaction of the  $M + X_2$  ( $|1\rangle$  in Fig. 8) covalent and  $M^+ + X_2^-$  ( $|3\rangle$  in Fig. 8) ionic curves. For a  $C_s$  or  $C_{\infty v}$  collision geometry, this process involves the strong coupling of  $^1A'$  or  $^1\Sigma$  covalent and ionic potentials (Table III) of the same symmetry leading to an avoided crossing, harpooning, and formation of the ground state metal halide. However, if the collision geometry is of  $C_{2v}$  symmetry, the symmetry species of the covalent and ionic curves (Table III) are  $^1A_1$  and  $^1B_2$  respectively and the curves for the two states intersect. It is through this intersection and a range of approach angles within a cone of acceptance around the  $X_2$  bisector<sup>27</sup> that the system slips past the "outer harpooning" region corresponding to the  $|1\rangle|3\rangle$  crossing (Fig. 8) and gains access to the "inner harpooning" region. The crossing involving the ionic configuration  $|3\rangle$  and the doubly ionic configuration  $|5\rangle$  (Table III and Fig. 8) will be avoided as the  $|3\rangle|5\rangle$  interaction between these curves, of the same symmetry, is thought to be significant. Access to the "inner harpooning" region thus promotes an avoided crossing leading to the chemiluminescent channels.<sup>7,12</sup> The low statistical weight of the near  $C_{2v}$  collisions is partly responsible for the low chemiluminescent quantum yields in these systems. For the  $M+XY$  reactive encounters, which cannot access a  $C_{2v}$  collision trajectory, the outer harpooning process must always correspond to an avoided crossing which shields the channel for chemiluminescent product formation.<sup>28</sup> However, as the characteristic velocity at the ionic-covalent crossing region increases in traversing the Group IIA metals from Ba to Ca, the symmetry effect which is clearly apparent in Fig. 2 diminishes.

Although this model qualitatively explains the observed trends in dihalide emission intensity, further detailed calculations of the couplings at the avoided crossing regions will be needed to place these arguments on a more quantitative base. These calculations, which will also rely on the spectroscopic parameterization obtained from the dihalide spectra exemplified in Figures 5-7. The calculations are, of course, best accomplished following some initial effort to parameterize dihalide electronic and vibronic structure from our observations of the optical signatures associated with the dihalides (energy levels, radiative lifetimes, differential bond angle changes) all of which also serves an important purpose for the refinement of ionic models.

## CHEMICALLY INDUCED RAMAN PUMPING

In studying the reactions of small supersonically cooled sodium molecules ( $\text{Na}_n$ ,  $n=2,3$ )<sup>29,30</sup> with halogen atoms ( $X=\text{Cl}, \text{Br}, \text{I}$ ), we have recently demonstrated the existence of population inversions associated with the electronically excited  $\text{Na}_2$  products of the  $\text{Na}_3 + \text{Br}$  reaction. In an extension of these experiments to develop a long path length amplifying medium, we discern, for the first time, the Raman pumping of  $\text{Na}_2$  in the absence of an external light source. We observe a series of Raman-like Stokes and anti-Stokes features which (1) are associated with the lowest vibrational levels of  $\text{Na}_2$ , (2) correlate with a scattering process involving the Na D-line components ( $\text{Na } 3p^2P_{3/2,1/2} - 3s^2S_{1/2}$ ) created in the chemical reaction sequence



(3) are not readily generated by light scattering due to an external laser light source, and (4) appear to be enhanced by the environment of the reaction zone itself. The D-line emission is scattered by cooled sodium dimers ( $\text{Na}_2$ ) formed, as a result of supersonic expansion, in the lowest vibrational levels of the  $\text{Na}_2$  ground electronic state. Multiple Stokes and anti-Stokes features, assigned as resonance Raman progressions are well simulated on the basis of the resonance Raman effect.<sup>31,32</sup> However, the scattering linewidth,  $\Gamma$ , associated with the present process is determined to be close to  $4 \text{ cm}^{-1}$ . This result suggests an unusually fast resonance Raman scattering process which appears to be chemically enhanced.

### Outline of Extended Slit Source Sodium Expansion Configuration

We have generated high sodium atom and dimer fluxes using an extended slit source configuration which is described in detail elsewhere.<sup>8,33</sup> Using a dual oven configuration, we produce a supersonically expanded flux of alkali vapor through a tantalum slit nozzle 0.003" wide by two inches in length. With an independently heated stagnation chamber (850-900K) and frontal nozzle

expansion channel (900-950K), we produce a near planar flow of primarily sodium atoms and internally cooled sodium dimers.<sup>8,33</sup> This sodium flux is intersected at variable angles from above and below by two nearly planar but diverging bromine atom flows, emerging from slits machined into graphite tube furnaces, operated at temperatures in excess of 1700K to insure a 95+% conversion of bromine molecules to bromine atoms. At the significant reactant fluxes necessary to generate a strong Raman scattering signal, the absolute number density of bromine atoms in the reaction zone is conservatively estimated<sup>8</sup> at between  $10^{14}$  and  $10^{15}$  cm<sup>-3</sup> whereas the absolute number density of sodium dimers may exceed  $10^{16}$  cm<sup>-3</sup>.

The optical signature of the long path length sodium molecule-bromine atom reaction zone is focused onto the entrance slit of a SPEX 1704 scanning monochromator coupled to an RCA 1P28 photomultiplier tube (PMT). The PMT is maintained at ~1000 volts and the response current is sent through an IEEE interfaced autoranging picoammeter (Keithley) to an IBM compatible AT class microcomputer.

We have attempted to reproduce the Raman signal created following the reaction sequence (4) by resonantly pumping the sodium expansion with external laser light. Intensity stabilized broadband (multimode) laser light (~1 W) from an argon ion laser (Spectra Physics, model 171) at 4765 Å and 4880 Å and dye laser light (~100 mW) at 5890 Å and 5896 Å (argon ion pumped R6G) was frequency chopped and passed through the expansion zone in an unsuccessful effort to generate a Raman scattering signal similar to that observed from the chemical reaction pumping. The frequency content of the emergent beam was again monitored with a monochromator-PMT combination. The PMT response, detected with a phase sensitive amplifier, was digitized and stored in an IBM AT-class microcomputer.

### **Chemically Induced Resonance Raman Pumping**

There are several near-resonant rovibronic transitions associated with the  $X^1\Sigma_g^+$  and the  $A^1\Sigma_u^+$  states of Na<sub>2</sub><sup>8,33</sup> and the atomic emission from the Na D-lines,  $\omega_{P1}$  and  $\omega_{P2}$  ( $2P_{3/2} \rightarrow 2S_{1/2}$  @ 16973.379 cm<sup>-1</sup> and  $2P_{1/2} \rightarrow 2S_{1/2}$  @ 16956.183 cm<sup>-1</sup>) which may be responsible, in large part, for the unusually intense optical signature depicted in Figure 9. The spectrum in Figure 9 was taken at a resolution of ~12 Å. The relative intensity of the strong sodium

dimer  $B \rightarrow X$  chemiluminescence to the even stronger Raman-like emission features symmetrically surrounding the Na D-line is readily apparent. The frequency separation between adjacent Stokes (anti-Stokes) features corresponds closely to  $155 \text{ cm}^{-1}$ , correlating with the separations between the lowest sodium dimer ground state vibrational levels. We have found that these features cannot be made to fit a resonance fluorescence series but can be confidently assigned to Stokes and anti-Stokes bands associated with a resonance Raman progression.<sup>8,33</sup>

Evidence suggestive of a Raman process is also detailed in the spectrum of Figure 10 taken under equivalent reaction zone conditions. The intermediate resolution,  $\sim 1.5 \text{ \AA}$ , at which this spectrum was obtained is sufficient to clearly resolve the atomic sodium  $^2P_{3/2}$ - $^2P_{1/2}$  D-line splitting ( $\sim 17.2 \text{ cm}^{-1}$ ) and the relative intensities of each of the sodium D-line components are clearly evident in the scattered Raman emission. Furthermore, the frequency separation of these atomic line components is clearly reproduced (within the experimental resolution of the scan) in both the vibrational Stokes and anti-Stokes features of the scattering.

We have successfully modeled the group of features symmetrically surrounding the Na D-line with the resonant Raman intensity expression.<sup>8,31-33</sup>

$$I_S(v_G, J_G; v_F, J_F) = \frac{32\pi^3 \omega_s^4 I_P}{9c^4 h^2} M(\xi_0)^4 e^{-\frac{B_J(J_G+1)hc}{kT}} N(v_G) \quad (5)$$

$$\times \sum_{v_I, J_I} \left( 3S_{J_{sr}} S_{J_{ir}} \frac{|\langle v_F | v_I \rangle \langle v_I | v_G \rangle|^2}{(\omega_{GI} - \omega_{PI})^2 + \Gamma^2} + 2S_{J_{sr}} S_{J_{ir}} \frac{|\langle v_F | v_I \rangle \langle v_I | v_G \rangle|^2}{(\omega_{GI} - \omega_{PI})^2 + \Gamma^2} \right)$$

where  $I_s$  is the total intensity for a scattered Stokes or anti-Stokes line as a function of frequency,  $\omega$ , and pump intensity,  $I_p$ , and  $c$  is the speed of light. We consider transitions from an initial rovibrational ground electronic state of the  $\text{Na}_2$  molecule labeled G to some final rovibrational electronic ground state labeled F through an intermediate excited electronic state labeled I where  $\omega_{GI}$  and  $\omega_{IF}$  represent the rovibronic energy difference between the G and I and I and F levels and  $\Gamma$  refers to the linewidth arising from all damping phenomena. The  $S_j$  terms correspond to the appropriate Honl-London factors for the  $\text{Na}_2$   $A^1\Sigma_u^+ - X^1\Sigma_g^+$  transition,<sup>8,33</sup>  $M(\xi_0)$  represents the electronic matrix element, expressed as a function of the normalized nuclear coordinate,  $\xi = R(\mu\omega/h)^{1/2}$ , and  $\langle v_F | v_I \rangle$  and  $\langle v_I | v_G \rangle$  represent Franck-Condon overlap integrals. We have included a thermalized ground state rotational distribution and a ground state weighting function  $N(v_G)$ , which represents the deviation from a Boltzmann distribution. We also allow pumping due to each component of the sodium D line, ( $\omega_{p1}(^2P_{3/2})$  and  $\omega_{p2}(^2P_{1/2})$ ), to contribute to the scattered emission intensity,  $I_s$ . Here, the  $^2P_{3/2}:^2P_{1/2}$  intensity weighting resulting from the reaction populated D-line components is 3:2, as determined from the experimental spectrum.

Numerical calculations were carried out by allowing the near-resonant atomic sodium transitions,  $\omega_{p1}$  and  $\omega_{p2}$ , appropriately broadened, to pump the first thirty levels in the  $\text{Na}_2$   $X^1\Sigma_g^+$  state to the first seventy levels of the  $\text{Na}_2$   $A^1\Sigma_u^+$  state. De-excitation from the upper electronic state was allowed to proceed to the first thirty levels of the ground state. Rotational levels  $J'', J' = 0$  to 120 were included with each vibrational level of both the excited electronic  $A^1\Sigma_u^+$  state and the ground electronic  $X^1\Sigma_g^+$  state of the sodium dimer scatterer. Each simulated spectrum produced in the modelling program was also convolved with a gaussian function to approximate the effects of a finite spectrometer slit width.

The data in Figure 11 depicts the fit to the vibrational structure surrounding the Na D-line for reaction with a pure sodium expansion. This low resolution ( $\sim 12 \text{ \AA}$ ) vibrational Raman spectrum does not correspond to a thermalized vibrational distribution but rather to a non-Boltzmann vibrational distribution. The modeled spectrum closely matches the experimental scan and also provides a consistent fit to higher resolution spectra. Although the rotational population distribution may be non-Boltzmann, we find that, with an effective rotational temperature of 400K, we are able to obtain close

agreement between experiment and calculation. This suggests that only slight modifications from a thermalized distribution will be necessary to exactly fit the rotational features. There are several possible sources for the deviation of the Raman scattering features from a thermalized vibrational distribution.<sup>8,33</sup>

A higher resolution scan ( $\sim 0.4 \text{ \AA}$ ) of the first Stokes and anti-Stokes features is depicted and computer simulated in Figure 12, based again on the application of Equation (5). In a surprising result, we find that a linewidth,  $\Gamma \approx 4 \text{ cm}^{-1}$ , is required to provide optimum agreement between the simulated and experimental results with correlation coefficients exceeding 0.92 for the anti-Stokes and 0.89 for the Stokes features, respectively. A further confirmation of the required linewidth is also indicated in Figure 12 where we compare the experimental spectrum to  $\Gamma = 4, 1$ , and  $0.1 \text{ cm}^{-1}$  simulations based on Equation (5).

While there are improvements that can be made in the simulations depicted in Figure 12, it is unlikely that simple power broadening can be responsible for the large effective linewidth indicated by our spectral simulations. Based on the required power broadening for a two level quantum system driven at resonance, we estimate that an electric field of  $\sim 1.3 \text{ KV/cm}$  and an absolute power density of  $\sim 0.215 \text{ MW/cm}^2$  is necessary to produce the requisite spectral broadening of  $4 \text{ cm}^{-1}$ .

The apparent spectral broadening suggests the possibility of a scattering lifetime on the order of  $\sim 10^{-11}$  seconds, implying a process which is considerably more efficient than would be expected on the basis of resonance Raman pumping involving the  $\text{Na}_2 \text{ A-X}$  transition ( $\sim 10^{-8}$  seconds based on the radiative lifetime<sup>34</sup>). Several additional experiments involving the direct pumping of the sodium expansion in the absence of bromine atom reactant at the Na D-line frequencies (argon ion pumped R6G) and at  $4765 \text{ \AA}$  and  $4880 \text{ \AA}$  using a multimode argon ion laser, failed to reveal optical signatures corresponding to those depicted in Figures 9-12. In fact, while it was possible to excite laser induced fluorescence corresponding to the  $\text{Na}_2 \text{ A-X}$  and B-X band systems analogous to that observed previously,<sup>35</sup> although at somewhat higher temperatures in the present experiments, no clear Raman features were generated. This result also suggests a more efficient process than that associated with resonance Raman pumping.

These results suggest that we have observed more than a "simple" Raman-

like scattering process. We might consider a further long range interaction of the electronically excited sodium  $3p^2P$  atoms with those  $Na_2$  molecules which are Raman pumped, an interaction of the  $Na_2$  molecules with the Br atoms that induces a time varying enhancement of the dimer polarizability (hyperpolarizability), or (less likely) the presence of a large electric field created due to the reactive environment in the vicinity of the reaction zone. It would appear that this interaction or perturbation is long range and leads to a highly efficient Raman-like scattering process.

While further experiments will be necessary to clarify the mechanism for the scattering process, the long path length reaction zone employed in these experiments appears to have revealed the manifestation of significant long range cooperative phenomena. The moderate Rydberg character of the  $Na\ 3p^2P$  excited state, with its diffuse electron density, may, in fact, lend itself to a considerable long range interaction inducing cooperative effects. The assessment of these cooperative effects awaits further study.

#### Acknowledgement

The authors gratefully acknowledge the helpful comments of Professors Ron Felton and Michael Heaven, and Dr. Kangkang Shen. Helpful comments and technical assistance from Mr. C. B. Winstead are also greatly appreciated. The support of the Georgia Tech Foundation through a grant from Mrs. Betty Peterman Gole, the Army Research Office through the Short Term Innovative Research Program, the Air Force Office of Scientific Research and the Army Research Office and AFOSR/SDIO is greatly appreciated.

## References

1. See for example, L. H. Dubois and J. L. Gole, J. Chem. Phys. 66, 779 (1977), D. R. Preuss and J. L. Gole, J. Chem. Phys. 66, 880 (1977), 66, 2994 (1977); G. J. Green and J. L. Gole, Chem. Phys. 46, 67 (1980), 69, 357 (1982), 100, 133 (1985) and references therein. D. M. Lindsay, J. R. Lombardi, and J. L. Gole, Chem. Phys. 37, 333 (1979), S. B. Oblath and J. L. Gole, Combust. and Flame 37, 293 (1980), Joerg Pfeifer and J. L. Gole, J. Chem. Phys. 80, 565 (1984), D. F. Dever, B. Cardelino, and J. L. Gole, High. Temp. Sci. 18, 159 (1984), T. C. Devore, L. Brock, R. Kahlscheuer, and K. Dulaney, Chem. Phys. 155, 423 (1991). H. Wang and J. L. Gole, J. Chem. Phys. 98, 9311 (1993), J. Mol. Spectros. 161, 28 (1993). J. L. Gole, "The Unique Complexation and Oxidation of Metal-Based Clusters", in Advances in Metal and Semiconductor Clusters, Vol. 1, Spectroscopy and Dynamics, ed. M. A. Duncan, JAI Press (1993), pg. 159-209 and references therein. J. L. Gole, "Toward the Modeling of the Oxidation of Small Metal and Metalloid Molecules," in "Gas Phase Metal Reactions", edited by A. Fontijn, North Holland, Amsterdam (1992), pp. 578-604 and references therein.
2. J. L. Gole, "Probing Ultrafast Energy Transfer Among the Excited States of Small High Temperature Molecules", in "Gas Phase Chemiluminescence and Chemiionization", A. Fontijn (editor) - Elsevier Science Publishers, 1985, p. 253.
3. D. M. Lindsay and J. L. Gole, J. Chem. Phys. 66, 3886 (1977). M. J. Sayers and J. L. Gole, J. Chem. Phys. 67, 5442 (1977). J. L. Gole and S. A. Pace, J. Chem. Phys. 73, 836 (1980).
4. G. J. Green and J. L. Gole, Chemical Physics 100, 133 (1985). R. W. Woodward, J. S. Hayden, and J. L. Gole, Chemical Physics 100, 153 (1985).
5. A. W. Hanner and J. L. Gole, J. Chem. Phys. 73, 5025 (1980). J. L. Gole and S. A. Pace, J. Phys. Chem. 85, 2651 (1981). J. L. Gole, B. Ohlsson, A. W. Hanner, and E. J. Greene, unpublished.
6. J. R. Woodward, S. H. Cobb, K. K. Shen, and J. L. Gole, JQE 26, 1574 (1990) - invited paper. K. K. Shen, H. Wang, and J. L. Gole, JQE 29, 2346 (1993).
7. J. L. Gole, "The Symmetry Constrained Dynamics Associated with Group IIA Dihalide Complex Formation via  $M + X_2$  Reactions - Evidence Suggesting the Highly Efficient Collisional Stabilization of Dihalide Excited State Complexes", in preparation. T. C. Devore, J. L. Gole, and H. Wang, "Controlled Relaxation of Group IIA Dihalide Excited State Complexes - Resolution of Low Pressure Continuum Emissions to Discrete Structure and Confirmation of Dihalide Complex Formation via Highly Efficient R3BR", in preparation.
8. D. Grantier and J. L. Gole, "Chemically Enhanced Raman Scattering", in preparation.

9. Linus Pauling, The Nature of the Chemical Bond, Cornell University Press, Ithaca, New York, 1960. R. D. Levine and R. B. Bernstein, Molecular Reaction Dynamics and Chemical Reactivity, Oxford University Press, New York, 1987.
10. D. L. Hildenbrand, "Model Calculations of Thermochemical Properties of Gaseous Metal Halides", in Proceedings of the Symposium on High Temperature Metal Halide Chemistry, Vol. 78-1, The Electro-Chemical Society, pg. 248.
11. M. C. Drake and G. M. Rosenblatt, "Trends in Structure and Vibrational Frequencies of  $\text{MX}_2$  and  $\text{MX}_3$  High Temperature Halide Vapors", in Proceedings of the Symposium on High Temperature Metal Halide Chemistry, Vol. 78-1, The Electrochemical Society, pg. 234.
12. C. D. Jonah and R. N. Zare, Chem. Phys. Lett. 9, 65 (1971).
13. D. J. Wren and M. Menzinger, Chem. Phys. Lett. 18, 431 (1973), 20, 471 (1973), and 27, 572 (1974).
14. W. J. Rosano and J. M. Parson, J. Chem. Phys. 84, 6250 (1986).
15. M. Menzinger, Adv. Chem. Phys. 42, 1 (1980). M. Menzinger, "The  $\text{M}+\text{X}_2$  Reactions: A Case Study". In Gas Phase Chemiluminescence and Chemiionization; A. Fontijn, Editor; Elsevier Science Publishers: Amsterdam, 1985, pp. 25-66. M. Menzinger, "Chemiluminescent and Chemiionization Metal-Halogen Reactions as Paradigms of Diabatic Reaction Dynamics", Acta Physica Polonica A73, 85 (1988).
16. F. Engelke, Chem. Phys. 44, 213 (1979).
17. D. Wren, Ph.D. Thesis, U. of Toronto, 1978.
18. L. Wharton, R. A. Berg, and W. Klemperer, J. Chem. Phys. 39, 2023 (1966). A. Buchler, J. L. Stauffer, W. Klemperer, and L. Wharton, J. Chem. Phys. 39, 2299 (1963). A. Buchler, J. L. Stauffer, and W. Klemperer, J. Chem. Phys. 40, 3471 (1964); J. Am. Chem. Soc. 86, 4544 (1964).
19. Edward F. Hayes, J. Phys. Chem. 70, 3740 (1966).
20. D. R. Yarkony, W. J. Hunt, H. F. Schaefer, Molecular Physics 26, 941-952 (1973).
21. R. L. DeKock, M. A. Peterson, L. K. Timmer, E. J. Baerendo, and P. Vernooijs, Polyhedron 9, 1919 (1990).
22. James L. Gole, Albert K. Q. Siu, and Edward F. Hayes, J. Chem. Phys. 58, 857 (1973).
23. James L. Gole, J. Chem. Phys. 58, 869 (1973).
24. R. H. Hauge, private communication.

25. See for example, NBS Special Publication 505, Bibliography on Atomic Transition Probabilities (1914 through October 1977) and Supplement I (November 1977 through March 1980), U. S. Department of Commerce/National Bureau of Standards. C. E. Moore, "Atomic Energy Levels", (National Bureau of Standards, 1949).
26. See for example, R. S. Berry and C. W. Reimann, J. Chem. Phys. 38, 1540 (1963), R. S. Berry, J. Chem. Phys. 27, 1288 (1957), W. S. Struve, J. R. Krenos, D. L. McFadden, and D. R. Herschbach, J. Chem. Phys. 62, 404 (1975), R. C. Oldenberg, J. L. Gole and R. N. Zare, J. Chem. Phys. 60, 4032 (1974).
27. T. Carrington, Accts. Chem. Res. 7, 20 (1974).
28. Note that the radiative lifetimes associated with the lowest energy MX<sub>Y</sub> emission band systems ( $\sigma - \pi$  transitions) will be shorter than their MX<sub>2</sub> counterparts ( $\sigma g - \pi g$  transitions). Thus the MX<sub>Y</sub><sup>\*</sup> excited state production is considerably muted relative to that indicated in Fig. 2.
29. (a) J. L. Gole, "The Unique Nature of Metal Cluster Oxidation", J. L. Gole, in Physics and Chemistry of Finite Systems: From Clusters to Crystals, Volume II, Edited by P. Jena, S. N. Khanna, and B. K. Rao, NATO ASI Series, Vol. II, pg. 1025 (1992).  
 (b) J. L. Gole, "Toward the Modeling of the Oxidation of Small Metal and Metalloid Molecules", in "Gas Phase Metal Reactions", edited by A. Fontijn, North Holland, Amsterdam (1992) pp. 578-604.  
 (c) J. L. Gole, "The Unique Complexation and Oxidation of Metal-Based Clusters", in Advances in Metal and Semiconductor Clusters, Vol. 1, Spectroscopy and Dynamics, ed. M. A. Duncan, JAI Press (1993), pg. 159-209.
30. S. H. Cobb, J. R. Woodward, and J. L. Gole, Chem. Phys. Lett. 156, 197 (1989). "Chemically Driven Pulsed and Continuous Visible Laser Amplifiers and Oscillators", J. L. Gole, K. K. Shen, H. Wang, and D. Grantier, Invited Talk, Proceedings of the 23rd AIAA Plasma-Dynamics and Laser Science Conference, Nashville, Tennessee, AIAA 92-2994 (1992).
31. D. L. Rousseau and P. F. Williams, J. Chem. Phys. 64, 3519 (1976).
32. See, for example, J. Tang and A. C. Albrecht in "Raman Spectroscopy", edited by H. A. Szymanski (Plenum, New York, 1970), Vol. 2, pp. 33-68. A. C. Albrecht, J. Chem. Phys. 34, 1476 (1961).
33. D. Grantier, H. Wang, C. B. Winstead, and J. L. Gole, Proceedings of the 24th AIAA Plasma Dynamics and Lasers Conference, Orlando, Florida, AIAA 93-3207 (1993).
34. W. T. Zemke, K. K. Verma, T. Vu, and W. C. Stwalley, J. Mol. Spectrosc. 85, 150 (1981).
35. J. L. Gole, G. J. Green, S. A. Pace, and D. R. Preuss, J. Chem. Phys. 76, 2247 (1982).

TABLE I

## Geometry of Group IIA Dihalides

Metal	<u>Halide</u>			
	F	Cl	Br	I
Be	<sup>a</sup> <i>l</i>	<i>l</i>	<i>l</i>	<i>l</i>
Mg	<i>l</i>	<i>l</i>	<i>l</i>	<i>l</i>
Ca	<i>b</i>	<i>l</i>	<i>l</i>	<i>l</i>
Sr	<i>b</i>	<i>b</i>	<i>l</i>	<i>l</i>
Ba	<i>b</i>	<i>b</i>	<i>b</i>	<i>b</i>

<sup>a</sup>  
*l*, linear; *b*, bent

Table II

## Experimentally Determined Bond Energies of Group IIA Mono- and Dihalides

	$D_0^\circ$ kcal/mole <sup>a</sup>			
	<u>F</u>	<u>Cl</u>	<u>Br</u>	<u>I</u>
Hg	109	75	(58)	(45)
Ca	126 266(140°)	94 214(180°)	73 186(180°)	62 155(180°)
Sr	129 260(120°)	96 211(140°)	79 189(180°)	64 155(180°)
Ba	139 271(100°)	104 220(120°)	85 197(150°)	72 166(180°)

<sup>a</sup>For each entry, the upper value corresponds to the metal monohalide bond energy and the lower value corresponds to that for the metal dihalide.

Table III

States Arising from  $M + X_2$  Reactant Configurations

	$C_\infty$	$C_{2v}$	$C_{\infty v}$
$M(1s) + X_2(1\Sigma_g^+)$	$1A'$	$1A_1$	$1\Sigma$
$M^+(2s) + X_2^-(2\Sigma_u^+)$	$1,3A'$	$1,3B_2$	$1,3\Sigma$
$M^{+2}(1s) + X_2^{=}(1\Sigma_g^+)$	$1A'$	$1A_1$	$1\Sigma$

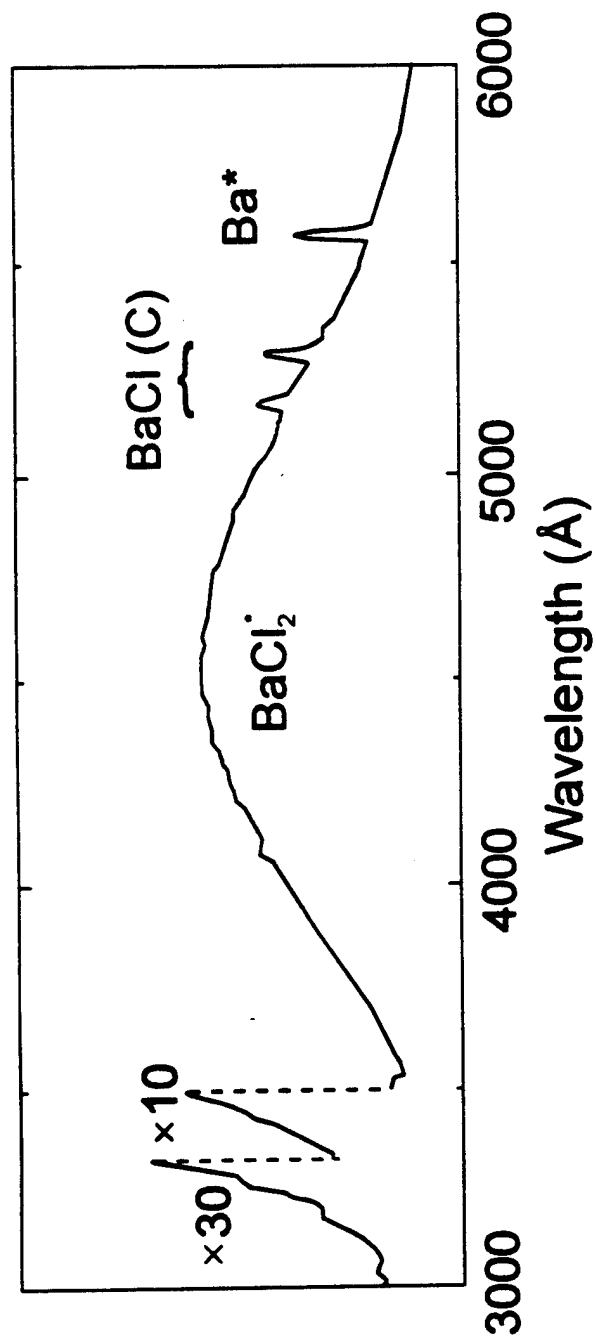


Figure 1

Chemiluminescent spectrum of the  $\text{Ba}(\text{'s}) + \text{Cl}_2$  reaction

# $\text{BaX}_2$ Chemiluminescent Spectra

$\text{Ba} + \text{Br}_2$  —————  
 $\text{Ba} + \text{IBr}$  - - - - -  
 $\text{Ba} + \text{I}_2$  - - - - -

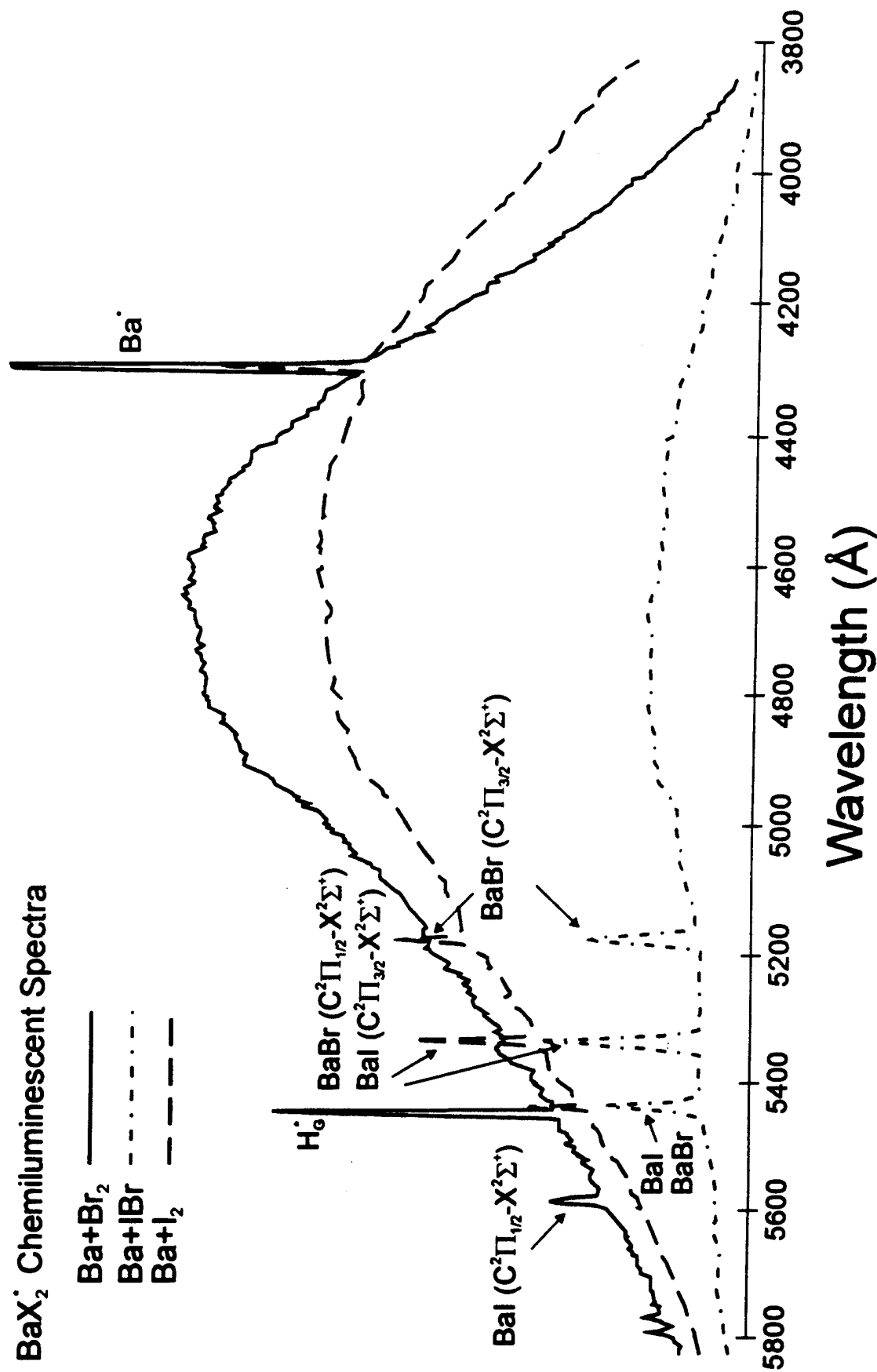


Figure 2

Chemiluminescent spectra for the  $\text{BaX}_2(\text{XY})$  product of the  $\text{Ba}(\text{'S}) + \text{I}_2$ ,  $\text{IBr}$ , and  $\text{Br}_2$  reactions and the  $\text{BaX}$  products of the  $\text{Ba}(\text{'D}) + \text{I}_2$ ,  $\text{IBr}$ , and  $\text{Br}_2$  reactions.

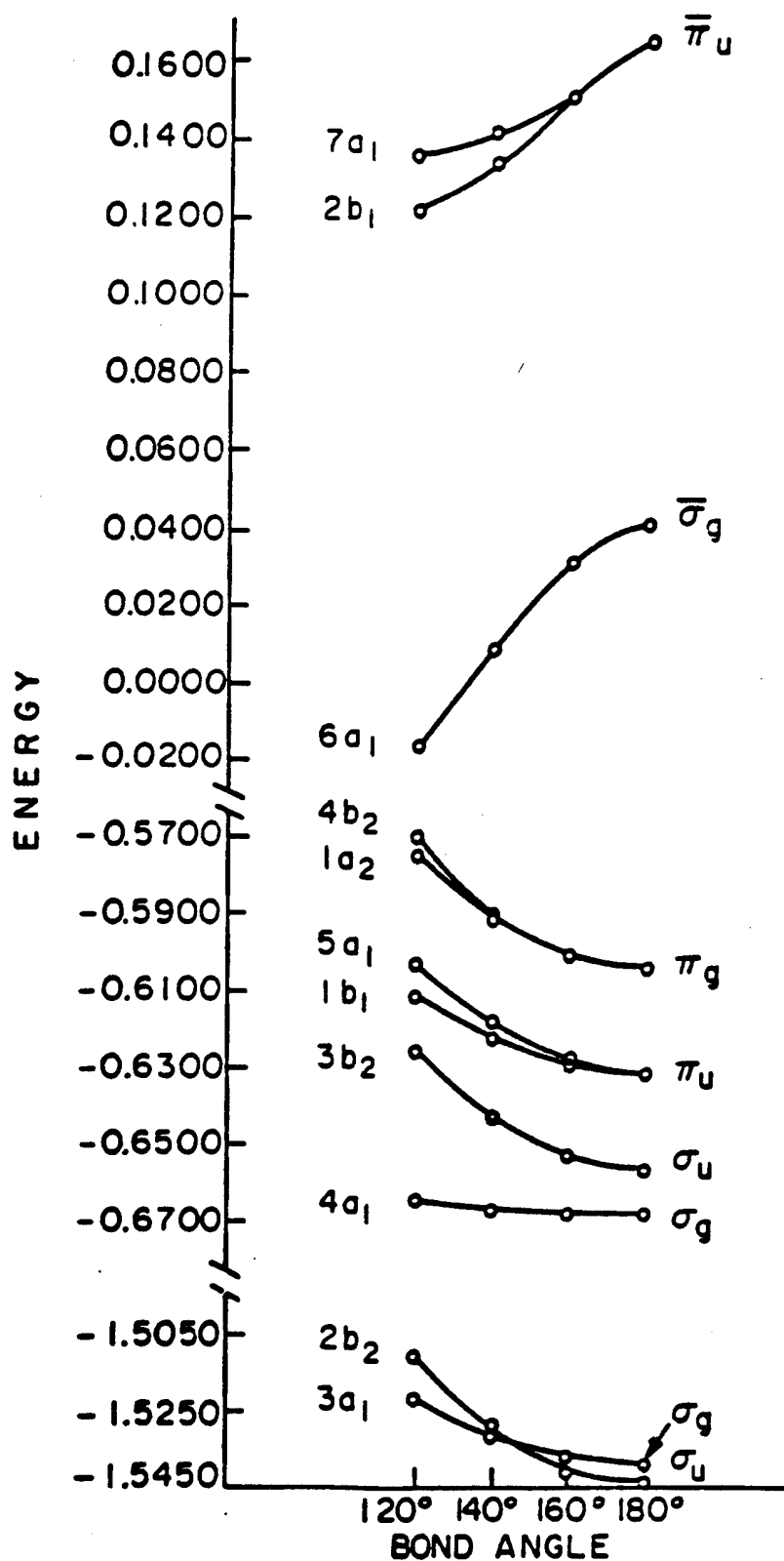


Figure 3: Correlation Diagram for BeF<sub>2</sub>

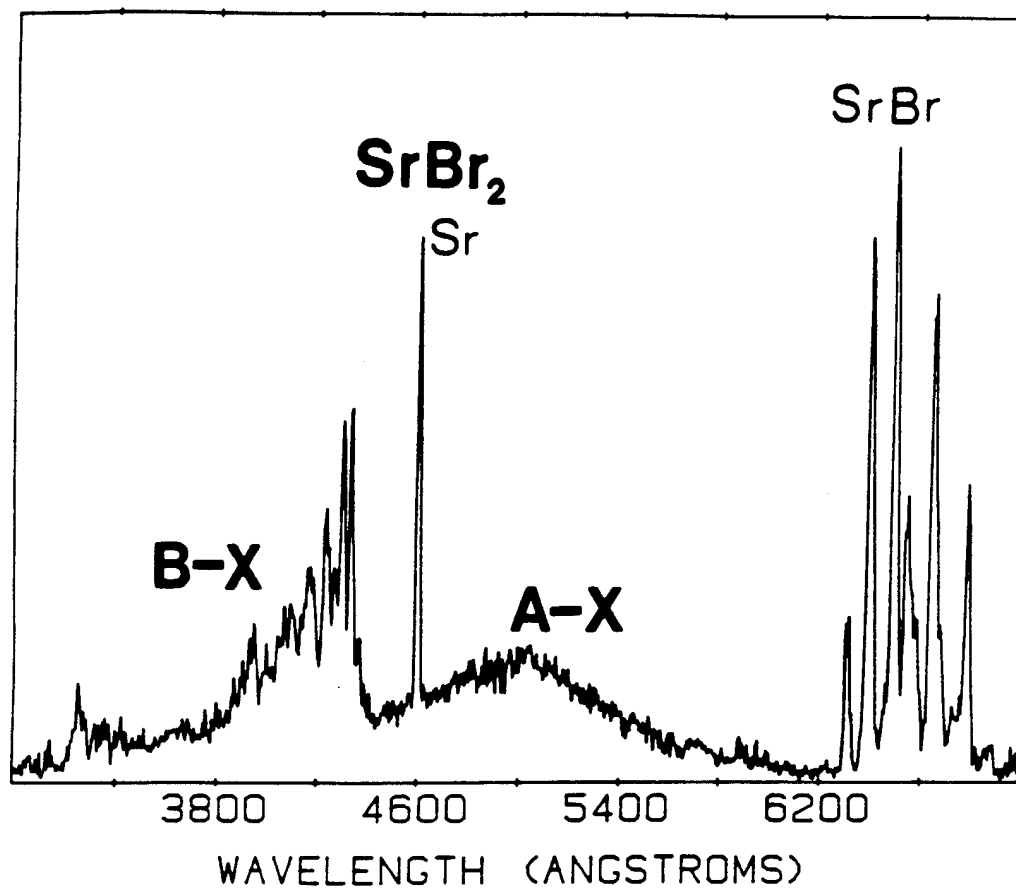
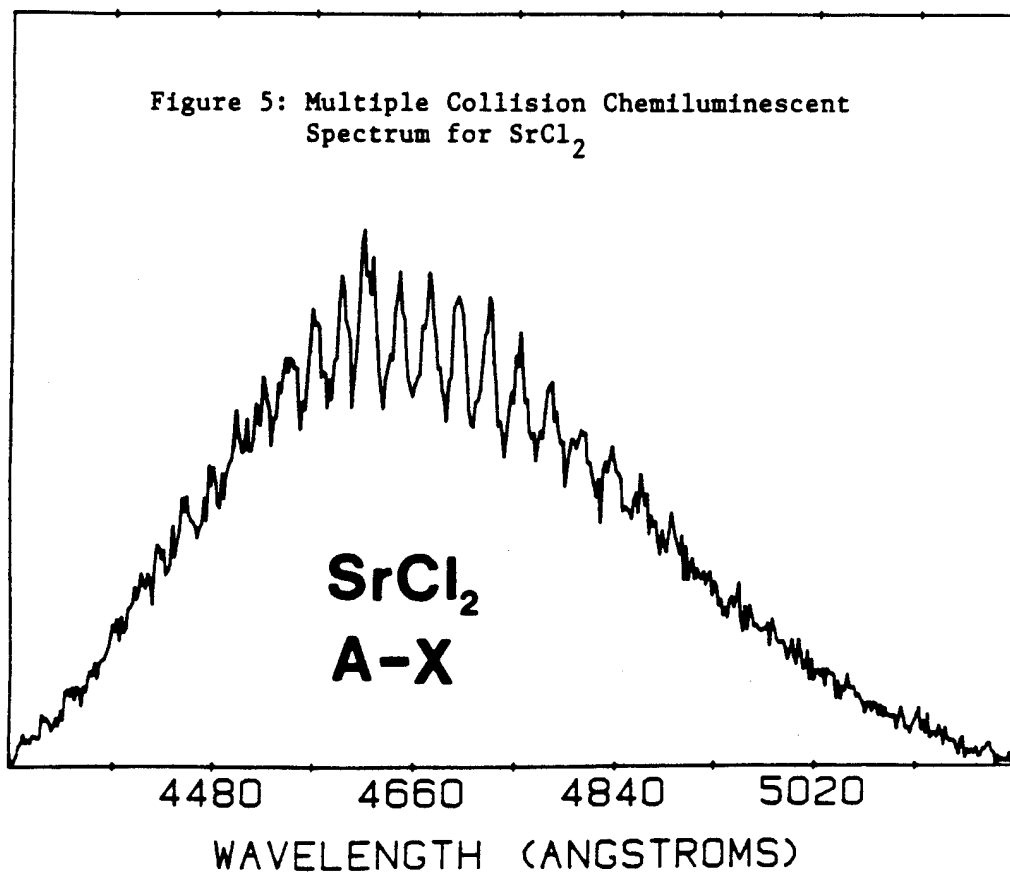


Figure 4: Multiple Collision SrBr<sub>2</sub> Chemiluminescent Spectrum



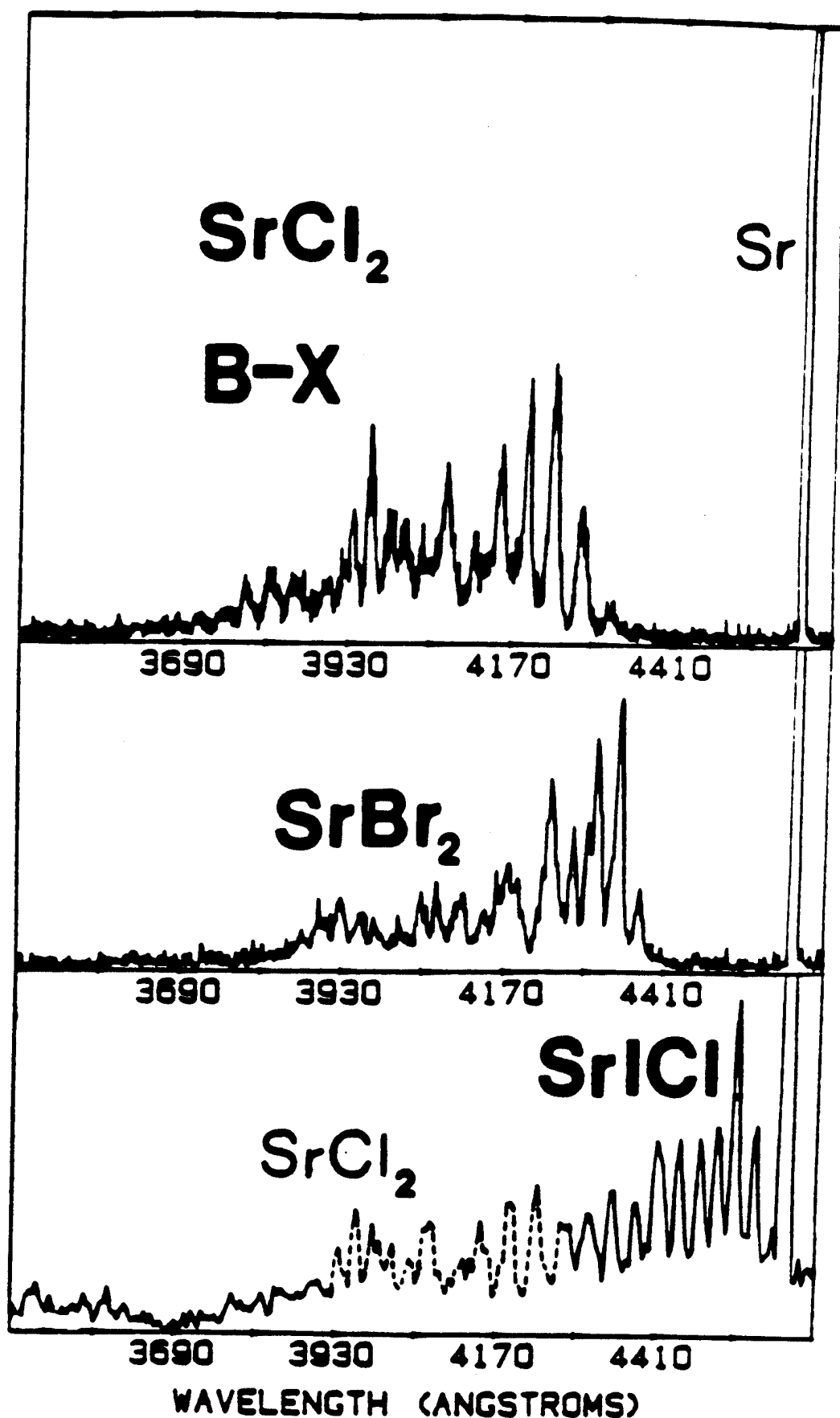


Figure 6: Multiple Collision Chemiluminescent Emission Spectra for  $\text{SrCl}_2$ ,  $\text{SrBr}_2$ , and  $\text{SrICl}$ . See text for discussion.

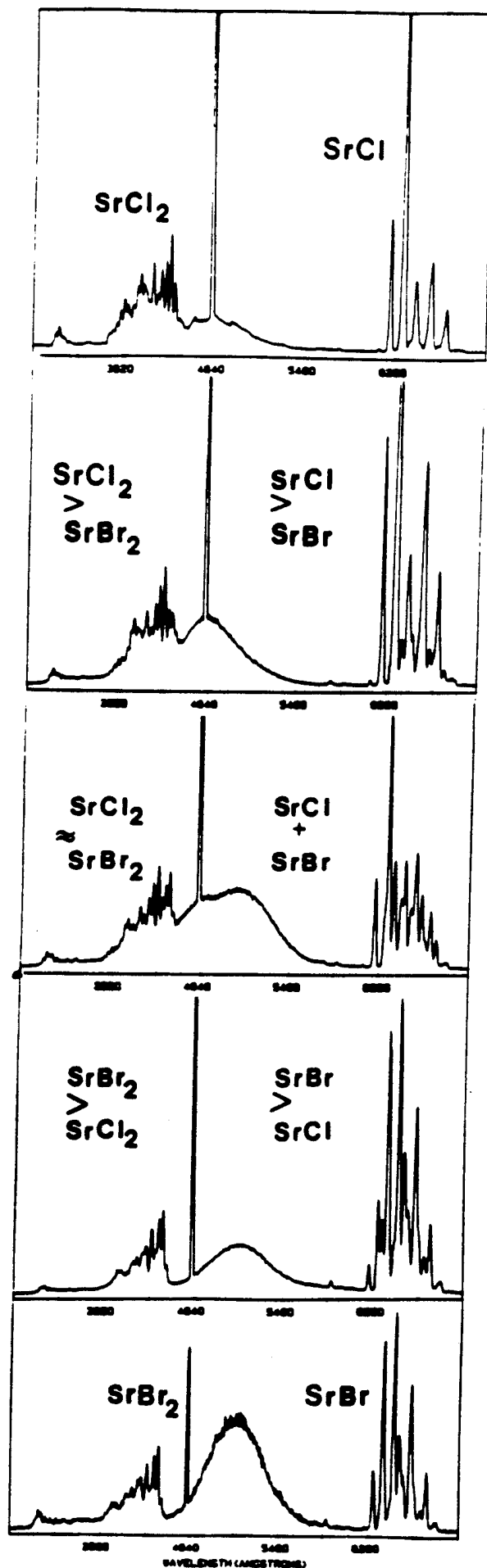


Figure 7: Multiple Collision Chemiluminescent Spectra for Reactive Mixtures of Sr Metal  $\text{Cl}_2$  and  $\text{Br}_2$ . See text for discussion.

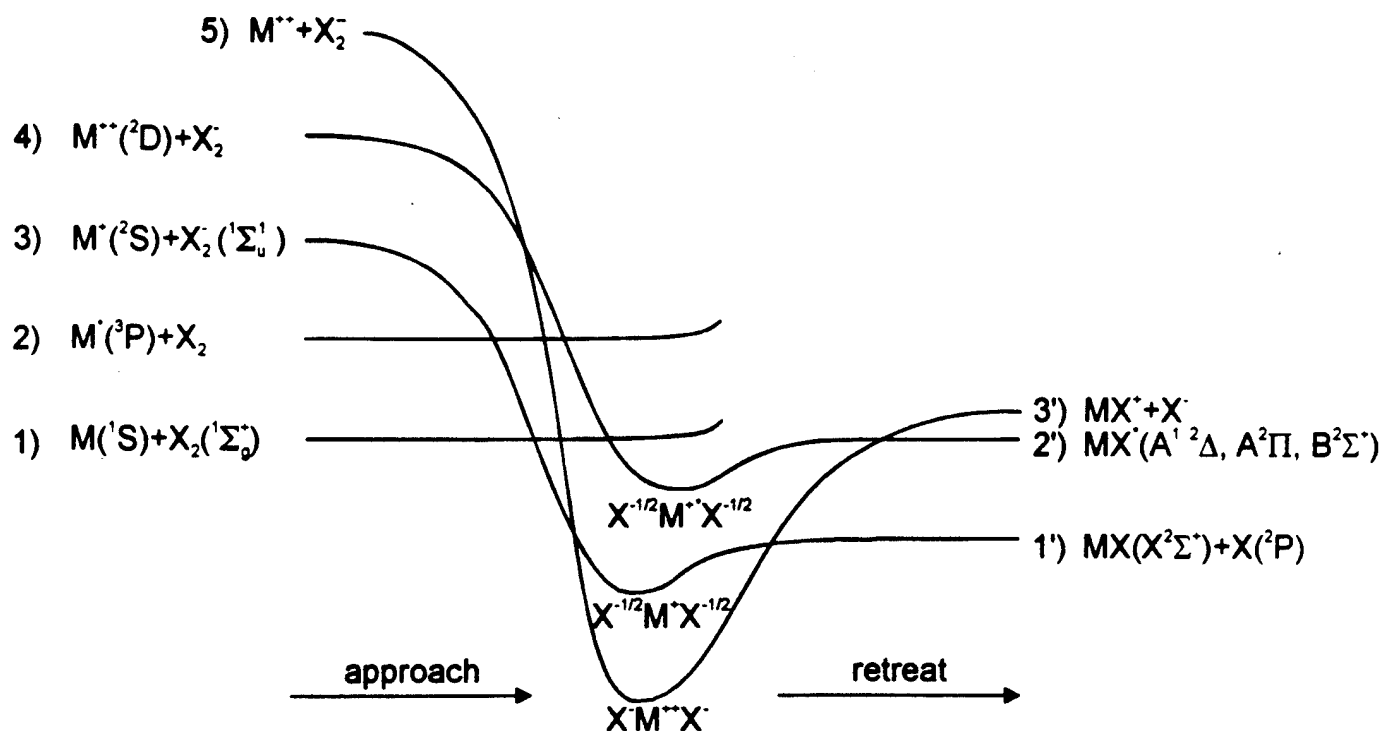


Figure 8

Correlation of electron configurations for Group IIA metal (M) - Halogen molecule ( $X_2$ ) reactive encounters.

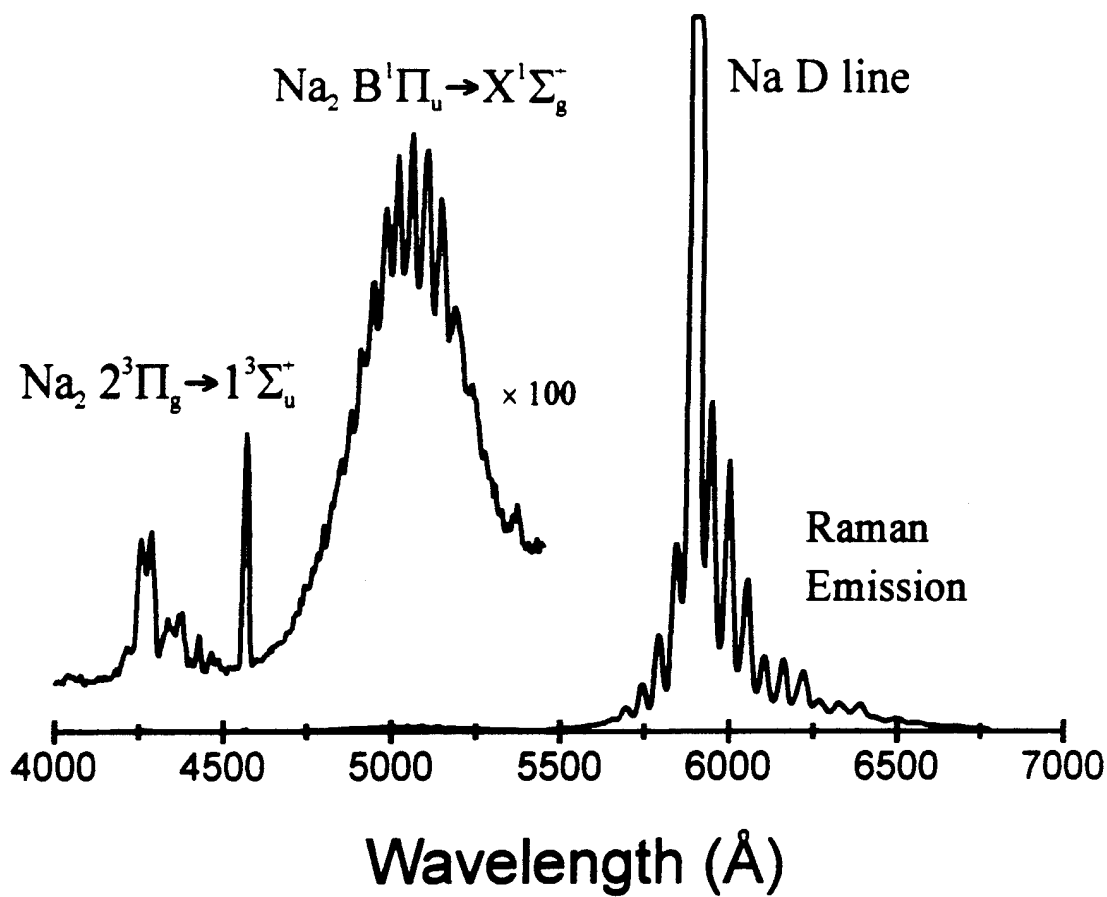


Figure 9

Survey spectrum of chemiluminescent emission and Raman scattering from various electronic states of diatomic sodium. The Na<sub>2</sub> 2<sup>3</sup>Π<sub>g</sub> → 1<sup>3</sup>Σ<sub>u</sub><sup>+</sup> transition corresponds to a triplet-triplet bound-free excimer like emission process. (Res. ~ 12 Å, T<sub>oven</sub> ~ 875K, T<sub>nozzle</sub> ~ 935K)

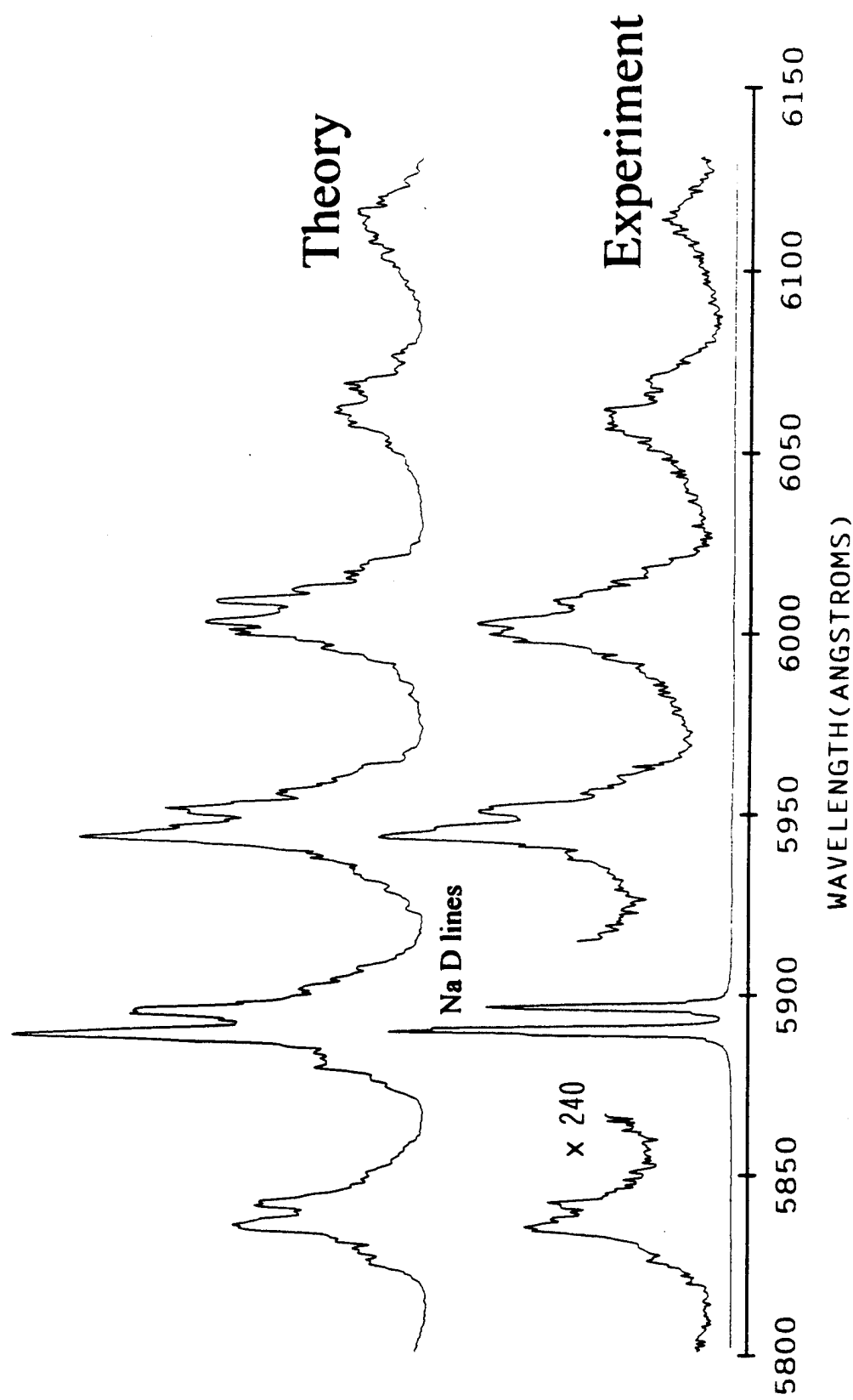


Figure 10

Raman-like spectrum taken at a resolution of  $\sim 1.5 \text{ \AA}$  ( $T_{\text{oven}} \sim 875\text{K}$ ,  $T_{\text{nozzle}} \sim 935\text{K}$ ) depicting the two Na D-line components and the satellite Raman structure. The spin-orbit frequency difference of the two Na D-line components is reproduced in the scattered radiation. A simulated spectrum is presented for comparison ( $T_{\text{rot}} \sim 400\text{K}$ ,  $\Gamma = 4 \text{ cm}^{-1}$ ). See text for discussion.

# Ground State Vibrational Distribution (Sodium Dimer, $v'' = 0 - 30$ )

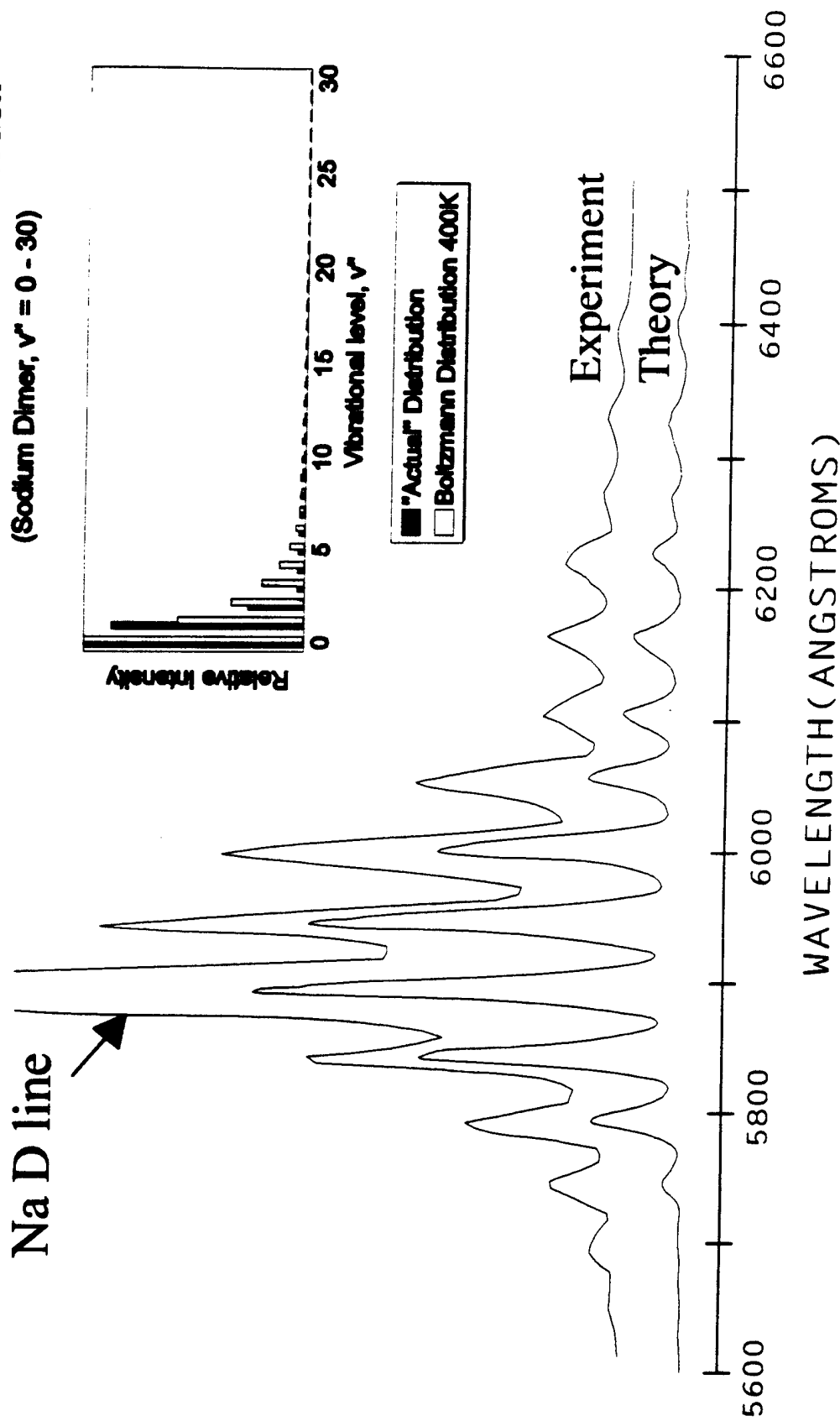


Figure 11

Comparison of experimental spectrum with computer modelled distribution (res.  $\sim 5 \text{ \AA}$ ,  $T_{\text{even}} \sim 875\text{K}$ ,  $T_{\text{nozzle}} \sim 935\text{K}$ ). Optimum agreement between calculation and experiment was found for the slightly nonthermal distribution depicted in the upper righthand corner of the figure. A Boltzmann distribution at 400K is included for comparison. See text for discussion.

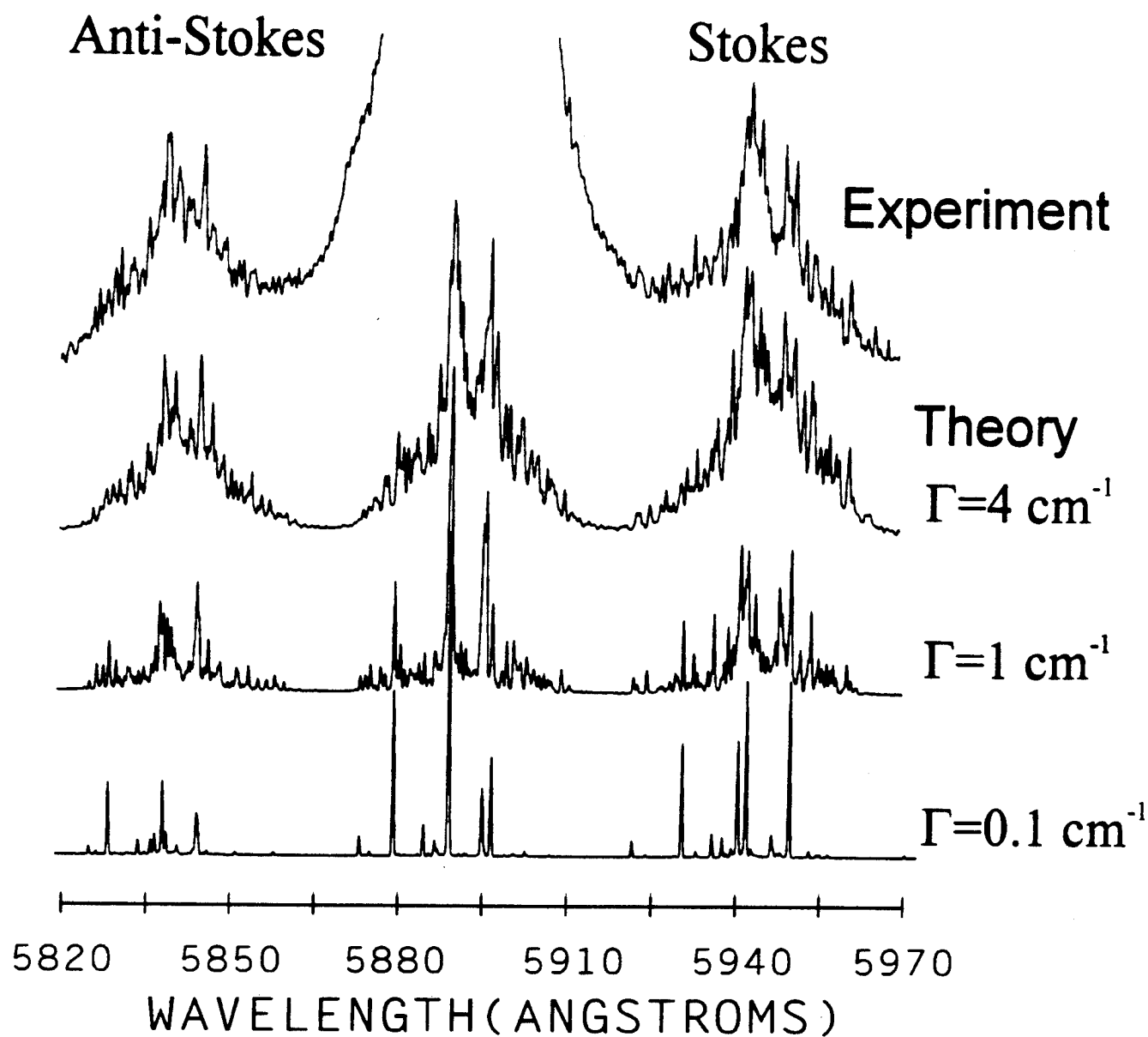


Figure 12

High resolution spectrum ( $\sim 0.5 \text{ \AA}$ ) and simulated spectra for  $\Gamma = 0.1$ , 1, and  $4 \text{ cm}^{-1}$  demonstrating the marked improvement in the fit to the experimental Raman-like features for increasing values of  $\Gamma$ . See text for discussion

## APPENDIX X

"Chemically Induced Processes Evidencing Raman Gain", D. R. Grantier, P. M. Medley, and J. L. Gole, Proceedings of the Tenth International Symposium on Gas Flow and Chemical Lasers, Friedrichshafen Germany, 1994 SPIE Volume 2502, pg. 505

# Chemically Induced Processes Evidencing Raman Gain

David R. Grantier,  
Peter M. Medley,  
and  
James L. Gole

Georgia Institute of Technology, School of Physics  
Atlanta, Georgia 30332

## **ABSTRACT**

The highly selective  $\text{Na}_2 + \text{X}$  (Cl, Br, I) reactions have been shown to create a continuous electronic population inversion based on the chemical pumping of  $\text{Na}_2$ . Optical gain through stimulated emission has been demonstrated in regions close to 527, 492, and 460 nm ( $\alpha = 8 \times 10^{-3} \text{ cm}^{-1}$  for an individual rotational level at  $\sim 527 \text{ nm}$ ). A device has been constructed with a focus to increasing amplifier gain length and amplifying medium concentration based on the controlled intersection of supersonically expanded sodium and halogen atom sheaths. The interaction forms an extended reaction-amplification zone centered on-axis in an optical cavity, thus facilitating the conversion of the observed amplifiers to chemical laser oscillators. Initial results with this upscaled device, where the sodium metal expanded in both pure and seeded supersonic expansion is intersected by a bromine atom flow, provide the first example of chemically enhanced Raman scattering (CHERS). Unique Raman signals are induced by and correlate with emission from the Na D-line components formed in the chemical reaction zone primarily as a result of the  $\text{Na}_2 + \text{Br} \rightarrow \text{Na}^* + \text{NaBr}$  reaction, cannot be readily generated by light scattering due to an external light source, and appear to be enhanced by the environment of the reaction zone itself. The Na D-line emitters interact with cooled sodium dimers in a resonance Raman scattering process, for which computer simulations suggest a scattering linewidth,  $\Gamma \sim 4 \text{ cm}^{-1}$ . These results suggest an unusually fast resonance Raman scattering process which appears to be chemically enhanced. The results of initial double pass gain measurements suggest that a stimulated Raman process, similar to that associated with optically pumped alkali dimer lasers, has been observed.

## APPENDIX XI

"Highly Efficient Collisional Stabilization and the Symmetry Constrained Dynamics of High Temperature Complex Formation", J. L. Gole J. Chem. Phys., 102, 7425 (1995).

# Highly efficient collisional stabilization and the symmetry constrained dynamics of high temperature complex formation

James L. Gole

School of Physics, Georgia Institute of Technology, Atlanta, Georgia 30332

(Received 26 July 1994; accepted 3 February 1995)

The highly efficient collisional stabilization of high temperature complexes of some considerable spatial extent is demonstrated. A series of near single collision and well defined multiple collision (following paper) chemiluminescent and laser induced fluorescent studies extending over six decades of pressure demonstrate the stabilization of electronically excited group IIA dihalide collision complexes via a radiative three body recombination process (R3BR) operative at microTorr pressures. Over the pressure range  $1 \times 10^{-6}$ – $5 \times 10^{-4}$  Torr, a comparative study of the emission from  $M$  ( $M = \text{Ca, Sr, Ba}$ )– $X_2$  ( $\text{Cl}_2, \text{Br}_2, \text{I}_2$ ) and  $M$ – $XY$  ( $\text{ICl, IBr}$ ) reactive encounters identifies a symmetry constrained dynamics associated with the formation of the dihalide product complexes. The onset of the monitored R3BR process at  $1 \times 10^{-6}$  Torr signals an extremely large stabilization cross section ( $\sigma_s > 3000 \text{ \AA}^2$ ) which may not be readily explained within the RRKM framework. Comparisons between the highly ionic dihalides and the isoelectronic  $\text{CO}_2$  molecule are noted as they affect excited state dynamics. The pressure dependence of the light emission from these complexes in the near single collision pressure range displays a striking correlation with the periodicity of dihalide molecular electronic structure and the resultant nature of the low-lying dihalide electronic transitions. The absence of a difluoride emission associated with the  $M(\text{Ca, Sr, Ba})\text{--F}_2$  reactive encounters signals an important periodic trend in these systems. A simple first order model within the electron jump framework is presented to explain the qualitative trends inherent to these reactions. © 1995 American Institute of Physics.

## INTRODUCTION

Collisions which lead to complex stabilization or rapid energy redistribution can play an important role in high temperature environments, including combustion and gasification streams,<sup>1–3</sup> as they influence energy storage and conversion. Further, they may play an important role in deposition processes whose inception is influenced by the formation of the gas phase constituency.<sup>3</sup> Here, we present evidence which suggests that a number of these interactions may be operative over a much broader region of configuration space than previously anticipated to the extent that a ready explanation of the present observations with existing models of recombination and energy transfer may be tenuous.

Typically, radiative association processes, which provide information on highly excited molecular states and dissociation limits,<sup>4</sup> have been studied at sufficiently high pressures so as to allow collisional stabilization of the associating species and, consequently, the time necessary for a spontaneous radiative event. As these collisional stabilization processes can lead to some loss of dynamical information, it has been the province of the molecular beamist to extend their study, performing experiments which isolate and evaluate contributions from two-body radiative recombination.<sup>5–10</sup> Thus, using crossed beams, Kasai *et al.*<sup>6</sup> observed a binary reaction of NO and O, Parson<sup>5</sup> obtained strong evidence for the  $\text{Cr--O}_2$  association process, and Yoshimura *et al.*<sup>7</sup> measured the  $\text{HNO A--X}$  emission from associating H and NO.

The experiments of Yoshimura *et al.*<sup>7</sup> are particularly intriguing with their emphasis on the study of a hydrogen based association as a means of monitoring discrete emission from a two-body association reaction. Their results, while

carefully obtained, seem surprising for they indicate excited state relaxation under beam conditions before the emission of a photon from the lowest vibrational levels of the HNO A state [at energies well below ( $\sim 3000 \text{ cm}^{-1}$ ) the HNO dissociation limit]. Further, the observations under beam conditions seem counter to a pronounced A state vibrational excitation at somewhat higher pressures. This behavior, which might be explained by highly efficient long range collisional events involving the forming HNO ground and low-lying A state, suggests that a much broader region of configuration space might be relevant to the description of several reactive environments. In fact, while the focus of the outlined molecular beam experiments has been to isolate the two-body association process, it is of equal if not greater importance that they signal the efficiency of multicenter stabilization processes that are operative at extremely low pressures and can strongly influence system behavior over large pressure ranges. It is with this focus that we have carried out a detailed study of the formation, collisional stabilization, and relaxation of a set of periodically correlated collision processes involving the formation and interaction of complexes of considerable spatial extent.<sup>2,11,12</sup>

The reactions of alkaline earth atoms with halogen molecules to form group IIA dihalides,  $\text{MX}_2^*$ , once thought to be bimolecular,<sup>8,9</sup> have been shown to be termolecular and second order in the halogen concentration at microTorr pressures. On the basis of several considerations,<sup>13–17</sup> it has been strongly suggested that the dihalide formation requires a two step mechanism involving a vibrationally excited ground state  $\text{MX}^\dagger$  intermediate, viz.,





This sequence involves two electron jump processes and produces the desired second order dependence on halogen concentration for the observed  $\text{MX}_2$  emission.

While sequence (1) is quite appealing and would seem to be in accord with well established theoretical models and a number of experimental observations,<sup>13-17</sup> an alternate mechanism, consistent with the halogen pressure dependence, centers on the collisional stabilization of a highly vibrationally excited  $\text{MX}_2^{*+}$  intermediate, viz.,



where the stabilization process, a radiative three-body recombination (R3BR), must overcome the propensity for a "rapid" dissociation of the highly excited  $\text{MX}_2^{*+}$  complex.

Through a series of near single collision<sup>18</sup> and well defined multiple collision<sup>19-21</sup> chemiluminescent and laser induced fluorescent studies extending over six decades of pressure, we demonstrate the highly efficient stabilization of electronically excited group IIA dihalide collision complexes

via the R3BR process (mechanism 2). We identify a symmetry constrained dynamics associated with the formation of these complexes, obtaining the first vibrationally resolved emission spectra for the dihalides. The onset of the monitored R3BR process at  $1 \times 10^{-6}$  Torr, as confirmed by the multiple collision studies detailed in the following discussion,<sup>2,3</sup> signals an extremely large stabilization cross section ( $\sigma_s > 3000 \text{ \AA}^2$ ) which may not be readily explained within the RRKM framework. This suggests that new models, adjusted to the interactions of electronically or highly vibrationally excited states, will be necessary to clarify these processes. The monitored complexations, which define a much broader range of interaction than has typically been associated with collisional stabilization phenomena, are best clarified by considering the periodicity inherent to a broad grid of group IIA metal,  $\text{M}(\text{Mg}, \text{Ca}, \text{Sr}, \text{Ba})$ -halogen molecule,  $\text{X}_2(\text{F}_2, \text{Cl}_2, \text{ClF}, \text{Br}_2, \text{ICl}, \text{IBr}, \text{I}_2)$  reactions.

In this first paper, we demonstrate the symmetry constrained dynamics inherent to group IIA metal-halogen molecule reactions as it signals the highly efficient concerted and collisionally stabilized formation of group IIA dihalide excited states. In the following paper, through the controlled extension and relaxation of the near single collision process under multiple collision conditions, we confirm the highly

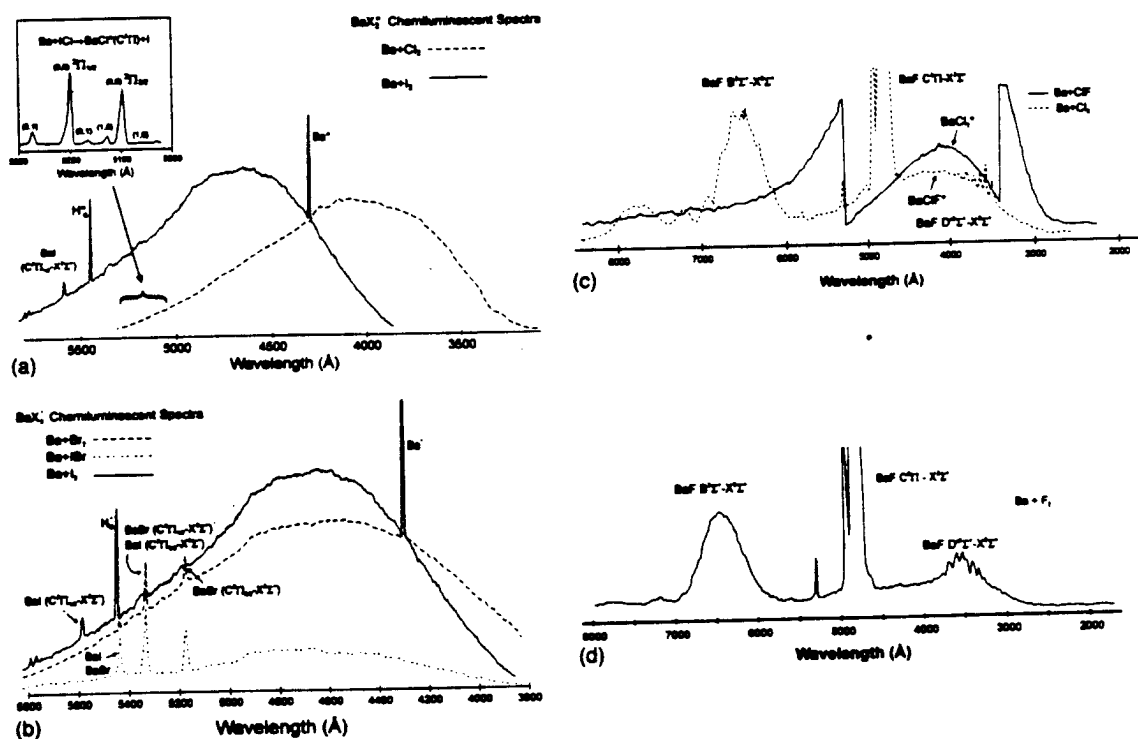


FIG. 1. Chemiluminescent spectra for (a) the  $\text{BaX}_2$  ( $\text{XY}$ ) products of the  $\text{Ba}(^1\text{S}) + \text{Cl}_2$ ,  $\text{ICl}$ ,  $\text{I}_2$  reactions at comparable Group IIA metal beam flux and comparable halogen pressures over the range  $5 \times 10^{-6}$ – $1 \times 10^{-4}$  Torr as measured by a capacitance manometer. On the scale of the figure, the emission from a  $\text{BaCl}$  complex is negligible and the optical signature of the  $\text{Ba} + \text{ICl}$  reaction consists almost exclusively of emission from the  $\text{BaCl } C^2\Pi - X^2\Sigma^+$  transition. (b) The  $\text{BaX}_2$  ( $\text{XY}$ ) products of the  $\text{Ba}(^1\text{S}) + \text{Br}_2$ ,  $\text{IBr}$ ,  $\text{I}_2$  reactions at comparable group IIA metal beam flux and halogen pressures over the range  $5 \times 10^{-6}$ – $1 \times 10^{-4}$  Torr as measured by capacitance manometer; the  $\text{BaX}$  products of the  $\text{Ba}(^3\text{D}) + \text{I}_2$ ,  $\text{IBr}$ , and  $\text{Br}_2$  reactions are also evident in the figure. (c) The  $\text{BaX}_2$  ( $\text{XY}$ ) products of the  $\text{Ba}(^1\text{S}) + \text{Cl}_2$ ,  $\text{ClF}$  reactions at comparable group IIA metal beam flux and halogen pressures over the range  $5 \times 10^{-6}$ – $1 \times 10^{-4}$  Torr as measured by capacitance manometer; the  $\text{BaF}^*$  emission features resulting from the  $\text{Ba}(^1\text{S}) + \text{ClF} \rightarrow \text{BaF}^* + \text{Cl}$  reaction are also indicated in the figure. (d) The  $\text{BaF}^*$  products of the  $\text{Ba} + \text{F}_2 \rightarrow \text{BaF}^* + \text{F}$  reaction over the pressure range  $5 \times 10^{-6}$ – $1 \times 10^{-4}$  Torr as measured by capacitance manometer. All spectra were taken at a resolution of 12 Å. See the text for discussion.

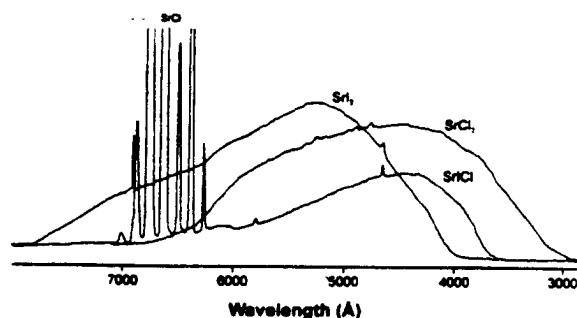


FIG. 2. Chemiluminescent spectra for (a) the  $\text{SrX}_2$  ( $XY$ ) products of the  $\text{Sr} (^1S) + \text{Cl}_2$ ,  $\text{ICl}$ ,  $\text{I}_2$  reactions at comparable group IIA metal beam flux and halogen pressures over the range  $1 \times 10^{-5}$ – $1 \times 10^{-4}$  Torr as measured by a capacitance manometer; observed  $\text{SrX}$  emission features are also identified in the figure. The relative intensity of the  $\text{SrIBr}$  continuum chemiluminescence from the  $\text{Sr} (^1S) + \text{IBr}$  reaction versus that for the  $\text{Sr} (^1S) + \text{I}_2$ ,  $\text{Br}_2$  reactions is similar to that for the  $\text{Sr} (^1S) + \text{ICl}$  reaction versus the  $\text{Sr} (^1S) + \text{I}_2$ ,  $\text{Cl}_2$  reactions. All spectra were taken at a resolution of 12 Å. See the text for discussion.

efficient R3BR mechanism as well as establishing discrete assignments for the near single collision emission continuum.

## EXPERIMENT

The apparatus used to study group IIA–halogen molecule reactions under near single collision conditions represents a variant of one that has been described previously.<sup>18</sup> Calcium, strontium, and barium metal were vaporized effusively from capped tantalum crucibles into a chamber whose background pressure was maintained at  $5 \times 10^{-7}$  Torr. The metals effuse from a hole  $\leq 1/8$  in. diameter, 1/2 in. from the top of the capped crucibles. The crucibles were surrounded by a 1 in. diameter tantalum radiator which acted as a resistive heating element to produce uniform crucible temperatures in the range between 1000 and 1200 K. Group IIA metallic beams, passing through holes in the heating radiator, tantalum heat shields concentrically surrounding the radiator, and a water-cooled copper jacket surrounding the entire grouping, entered a differentially pumped system. The beams then passed through an iris based adjustable orifice into a tenuous atmosphere of oxidant gas (reaction chamber) producing the chemiluminescent emissions recorded in Figs. 1–3. There have been relatively few measurements of the calcium, strontium, and barium vapor pressures. Based on these studies,<sup>22</sup> the vapor pressures in the crucibles ranged from  $10^{-2}$  to 1 Torr.

Fluorine (Air Products Specialty Gases >98% purity),  $\text{ClF}$  (K and K Laboratories 98%),  $\text{Cl}_2$  (Matheson >99.5%),  $\text{Br}_2$  (Matheson >99.9%, Fisher >99.95%),  $\text{ICl}$  (Kodak >99.9%, Alfa >99.8%),  $\text{IBr}$  (Alfa >99.8%), and  $\text{I}_2$  (Fisher >99.8%) were obtained commercially. The three oxidant gases  $\text{F}_2$ ,  $\text{ClF}$ , and  $\text{Cl}_2$  were allowed to bleed into the reaction chamber through a double micrometer needle valve assembly. In order to insure that the  $\text{ClF}$  was not contaminated, we purified the gas in two stages. The sample was placed in a glass ballast trap which was then placed in liquid nitrogen and evacuated in order to remove any possible fluorine con-

taminants. Subsequently, during the experimental run, the sample was placed in an *n*-amyl alcohol slush, thus insuring against  $\text{Cl}_2$  contamination.

For studies involving  $\text{Br}_2$ ,  $\text{IBr}$ , and  $\text{I}_2$ , the gas handling system was modified so that substances which are liquids or solids at room temperature could be introduced as gases into the reaction chamber. Small stainless steel or Pyrex containers were attached to the first micrometer needle valve and a succession of pumping–freezing cycles was used to remove volatile impurities. The vapor pressure of  $\text{Br}_2$  is sufficiently high to permit the production of a gas beam at room temperature. The same would appear to be true for  $\text{IBr}$ ; however, as with  $\text{I}_2$ , it was necessary to increase the vaporization rate by heating the sample slightly in order to obtain a sufficient vapor pressure.

For these single collision studies, the oxidant gases were mildly collimated but filled the entire reaction chamber at pressures ranging from  $1 \times 10^{-6}$  to  $5 \times 10^{-4}$  Torr. The permanent gases were first partially transferred to a ballast tank which provides gas pressure stability during the course of an experiment. Background pressures were monitored primarily with an ionization gauge (ETI) 25 cm from the reaction zone, however, the majority of the *in situ* reaction pressure measurements were made with a capacitance manometer (MKS Baration) 3 cm from the reaction zone. If both gauges were used to monitor gas pressure during an experimental run, the values measured using the capacitance manometer were between 15% and 25% higher than those measured by the ionization gauge, depending upon the gas in use. The pressure dependence plots presented in the following sections were obtained, using the capacitance manometer, by monitoring the light emission from the reaction zone. Corrections, which take into account slight pressure gradients across the chamber, have been made to these pressure dependence plots.

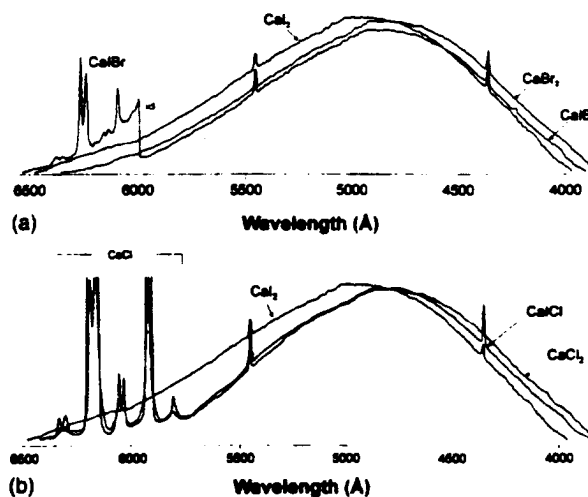


FIG. 3. Chemiluminescent spectra for (a) the  $\text{CaX}_2$  ( $XY$ ) products of the  $\text{Ca} (^1S) + \text{Cl}_2$ ,  $\text{ICl}$ ,  $\text{I}_2$  reactions at comparable group IIA metal beam flux and halogen pressures over the range  $3 \times 10^{-5}$ – $2 \times 10^{-4}$  Torr as measured by a capacitance manometer; observed  $\text{CaX}$  emission features are also identified in the figure. (b) The  $\text{CaX}_2$  ( $XY$ ) products of the  $\text{Ca} (^1S) + \text{Br}_2$ ,  $\text{IBr}$ ,  $\text{I}_2$  reactions at comparable group IIA metal beam flux and halogen pressures over the range  $4 \times 10^{-5}$ – $2 \times 10^{-4}$  Torr as measured by capacitance manometer. All spectra were taken at a resolution of 12 Å. See the text for discussion.

TABLE I. Experimentally determined bond energies of group IIA mono- and dihalides.

	$D_0^0$ kcal/mol <sup>a</sup>			
	F	Cl	Br	I
Mg	109	75	(58)	(45)
Ca	126	94	73	62
	266(140°)	214(180°)	186(180°)	155(180°)
Sr	129	96	79	64
	260(120°)	211(140°)	189(180°)	155(180°)
Ba	139	104	85	72
	271(100°)	220(120°)	197(150°)	166(180°)

<sup>a</sup>For each entry, the upper value corresponds to the metal monohalide bond energy and the lower value corresponds to that for the metal dihalide.

Metal source temperatures were measured with a Leeds and Northrup disappearing filament optical pyrometer focused on the back center of the crucible containing the metal of interest. The crucible was observed through a quartz window directly behind the oven and through a 5/16 in. diameter hole in the tantalum radiator. The pyrometer was calibrated during each run sequence by comparison with a calibrated tungsten 5% rhenium vs tungsten 25% rhenium thermocouple (Control Products Corp.). The thermocouple junction, was sheathed in BeO and tantalum and protected by a tungsten well. This assembly was placed vertically through the base of the oven, between the crucible and the tantalum radiator, and located in its closest possible proximity to the crucible orifice.

The chemiluminescence from the reactions of interest was monitored at right angles to the metal flow. Spectral emissions were dispersed with a 1 m Spex scanning monochromator operated in first order with a Bausch and Lomb 1200 groove/mm grating blazed at 5000 Å. Either RCA 1P28 or 4840 or a dry ice cooled EMI 9808 photomultiplier tube were used to detect the dispersed fluorescence and provide a signal for either a Keithley 417 fast picoammeter or a 417 autoranging picoammeter. The output signal from the picoammeters was then sent either to a Hewlett Packard chart recorder or to a personal computer for storage and subsequent analysis. All spectra were wavelength calibrated with a mercury arc lamp<sup>23</sup> or with respect to group IIA metal atomic emissions.<sup>23</sup>

## RESULTS AND DISCUSSION—PERIODICITY OF GROUP IIA DIHALIDE FORMATION

### Near "single collision" chemiluminescence and symmetry constrained product formation

As Table I demonstrates, the strength of the second group IIA metal-halogen bond is at least comparable to or considerably exceeds that of the first. In other words the atomization energy, especially of the heavier halogen dihalides, is at least twice the dissociation energy of the metal monohalide. This bonding characteristic suggests that the group IIA-halogen molecule reactions might represent good candidates to study few body complexation processes.

The low group IIA metal ionization potentials<sup>23</sup> and the high halogen electron affinities<sup>24</sup> signal that these reactions are expected to proceed via the electron jump process

whereby the group IIA metal throws out an electron and harpoons the halogen molecule forming an  $M^+X_2^-$  complex. The data presented in Figs. 1–3 summarizes the observed dihalide emission spectra generated for the reactions of Ca, Sr, and Ba with the homonuclear ( $Cl_2, Br_2, I_2$ ) and mixed ( $ClF, ICl, IBr$ ) halogens, under near single collision conditions (at pressures ranging from  $10^{-6}$ – $10^{-4}$  Torr). The emission from the mixed halogen reactions with strontium and barium is distinctly weaker than that from the homonuclear metatheses.

In contrast to the  $M=Ca, Sr, Ba-X_2$  ( $X=Cl, Br, I$ ) reactions which yield a strong dihalide emission, the reactions of molecular fluorine with these metals leads only to monofluoride emission. In fact, only a weak emission continuum in the range  $\sim 3500$ – $5500$  Å is observed for the magnesium system and this emission is found to be quadratic in the fluorine molecule concentration. This dichotomy represents an important periodic trend in the formation of the dihalides.

The lack of a notable difluoride emission for the Ca, Sr, and Ba reactions represents a serious challenge to the validity of the double harpoon mechanism (1). The data in Table I as well as periodic correlations with atomic dissociation products<sup>25</sup> suggest that the reaction sequence (1) easily supplies the energy necessary to access difluoride excited states. We suggest that the lack of a  $CaF_2$ ,  $SrF_2$ , or  $BaF_2$  emission results, at least in part, because the fluorine molecule negative ions produced in the electron jump process dissociate much more rapidly than do the corresponding  $Cl_2^-$ ,  $Br_2^-$ , or  $I_2^-$  ions.<sup>26</sup> This results not only from the considerably smaller bond energy of the fluorine molecule but also from the nature of the vertical electron attachment process which creates the fluorine negative ion high on the repulsive wall of its ground state potential.<sup>26</sup> In contrast, the process for the more tightly bound, heavier halogens, whose size better accommodates electron attachment, can lead to the formation of a considerably longer-lived negative ion. While it is difficult to create a long-lived  $M^+X_2^-$  complex in those reactions with molecular fluorine, complex formation may be accommodated for the heavier halogens. The observation of both BaF monohalide and BaClF dihalide continuum emission for the reaction of barium with a strongly bound ClF (59.2 kcal/mol)<sup>27</sup> molecule [Fig. 1(c)] and the corresponding lack of a difluoride emission resulting from the  $Ba+F_2$  reaction (Appendix) support the outlined suggestions. However, we must also note (Table I) that, whereas the  $(MF_2)$  atomization energies are near to  $2D_0^0(MF)$ , the atomization energies of the chlorides, bromides, and iodides well exceed twice the metal monohalide bond energy.

An important symmetry constraint is signaled by the intensity of the emission from the dihalides formed in the reactions of calcium, strontium, and barium with the mixed halogen molecules IBr and ICl. Figures 1(a) and 1(b) demonstrate a much weaker emission for the heteronuclear halogen molecule reactions with barium. The compared spectra were taken at the same resolution and with nearly identical halogen pressures and metal beam fluxes. We will suggest that the dominant intensity for the  $Cl_2$ ,  $Br_2$ , and  $I_2$  reactions results because of the  $C_{2v}$  reaction path available to the homonuclear (but not accessible to the heteronuclear) halo-

TABLE II. Geometry of group IIA dihalides.

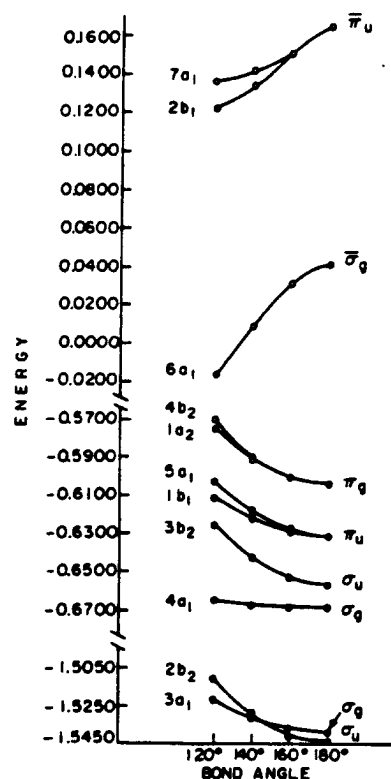
Metal	Halide			
	F	Cl	Br	I
Be	<i>l</i> <sup>a</sup>	<i>l</i>	<i>l</i>	<i>l</i>
Mg	<i>l</i>	<i>l</i>	<i>l</i>	<i>l</i>
Ca	<i>b</i>	<i>l</i>	<i>l</i>	<i>l</i>
Sr	<i>b</i>	<i>b</i>	<i>l</i>	<i>l</i>
Ba	<i>b</i>	<i>b</i>	<i>b</i>	<i>b</i>

<sup>a</sup>*l*, linear; *b*, bent.

gen reactions. The availability of this  $C_{2v}$  reactive geometry (conical intersection) promotes excited state dihalide formation for  $M+X_2$  but not  $M+XY$  reactive encounters. The observed symmetry effects can be manifest by the collisional stabilization mechanism (2) but are highly unlikely for the two step harpoon mechanism (1). While the difference in continuum intensity is quite pronounced for the barium reactions, this difference decreases for the strontium reactions (Fig. 2) and is almost muted for the calcium reactions (Fig. 3). This behavior is consistent with the electron jump model and an increasing reactant relative velocity for the calcium and strontium reactions at the curve crossing region associated with the  $M+X_2 \rightarrow M^+ + X_2^-$  harpooning process.

### A group IIA dihalide correlation diagram

The expected nature of the transitions responsible for the observed dihalide emission continua depicted in Figs. 1–3 can be summarized using the data in Tables II<sup>28</sup> and III and the molecular orbital correlation diagram depicted in Fig. 4.<sup>29</sup> We will discuss the contributing transition regions (Table III) in greater detail when considering the vibronically resolved dihalide emission spectra observed under multiple collision conditions.<sup>30</sup> For our present purposes, however, it is relevant that we consider the grid of ground state dihalide geometries determined by Klempner *et al.*<sup>28</sup> (electric quad-

FIG. 4. Bond angle variation valence correlation diagram for the highly ionic  $\text{BeF}_2$  molecule. Energy is in hartrees. See the text for discussion.

rupole deflection of molecular beams) and outlined in Table II. A clear trend from linear to bent character, which has been discussed by several authors,<sup>31–34</sup> is apparent as linear geometries are favored by the light metal–heavy halogen combinations whereas bent structures are favored by the heavy metal–light halogen combinations.

The strongly ionic character of the group IIA dihalides has important consequences as the  $\text{BeF}_2$  valence correlation

TABLE III. Group IIA dihalides—low-lying electronic states and electronic transitions in  $D_{\infty h}$  (absorption) or  $C_{2v}$  (emission) symmetry.

Electron configuration <sup>a</sup> (Absorption)	State designation (Absorption)	Electron configuration <sup>a</sup> (Emission)	State designation (Emission)	Comments <sup>b</sup>
$\dots(x,y,\pi_g)^4$ <sup>c</sup> linear	$\tilde{X}^1\Sigma_g^+$ ground state	$\dots(xa_2)^2(yb_2)^2$	$\tilde{X}^1A_1$ Ground state	
$\dots(x,y,\pi_g)^3(l\sigma_g)^c$ linear	${}^{1,3}\Pi_g$ $\tilde{A}-\tilde{X}$ region	$\dots(xa_2)^1(yb_2)^2(la_1)^1$ $\dots(xa_2)^2(yb_2)^1(la_1)^1$	${}^{1,3}A_2$ ${}^{1,3}B_2$ $\tilde{A}-\tilde{X}$ region <sup>e</sup>	$\tilde{A}-\tilde{X}$ region transitions <sup>b</sup> will produce large change in bond angle
$\dots(x,y,\pi_g)^3(m\pi_g)^c$ linear	${}^{1,3}\Sigma_u$ $\tilde{B}-\tilde{X}$ region ${}^{1,3}\Pi_u$ $\tilde{C}-\tilde{X}$ region	$\dots(xa_2)^1(yb_2)^2(mb_1)^1$ $\dots(xa_2)^2(yb_2)^1(mb_1)^1$	${}^{1,3}\tilde{B}_2$ ${}^{1,3}A_2$ $\tilde{B}-\tilde{X}$ region <sup>f</sup>	$\tilde{B}-\tilde{X}$ region transitions <sup>b</sup> will produce significant change in bond length
		$\dots(xa_2)^1(yb_2)^2(na_1)^1$ $\dots(xa_2)^2(yb_2)^1(na_1)^1$	${}^{1,3}A_2$ ${}^{1,3}B_2$ $\tilde{C}-\tilde{X}$ region <sup>g</sup>	$\tilde{C}-\tilde{X}$ region transitions <sup>b</sup> will produce significant change in bond length

<sup>a</sup>Highest occupied orbitals (x,y) and lowest promotion orbitals (l,m,n).<sup>b</sup> $B_2-X^1A_1$  transition is electric dipole allowed,  $A_2-X^1A_1$  transition is vibronically allowed through coupling with the ground or excited state asymmetric stretch of  $b_2$  symmetry. The corresponding triplet–singlet transitions will be weaker.<sup>c</sup>For  $\text{MX}_2$  ( $\text{SrCl}_2$ ,...) we have  $(x,y,\pi)^4$ ,  $(x,y,\pi)^3(l\sigma)$ , and  $(x,y,\pi)^3(m\pi)$ .<sup>d</sup>For  $\text{MX}_2$  ( $\text{SrCl}_2$ ,...) we have (for example)  $(xa'')(ya')^2(la')^1$ ,  ${}^{1,3}A''$ ;  $(xa'')^2(ya')(la')$ ,  ${}^{1,3}A'$  in the  $A-X$  region.<sup>e</sup>For the  $A-X$  region see Figs. 1 and 2 in Ref. 3.<sup>f</sup>For the  $B-X$  region see Figs. 3–5 in Ref. 3.<sup>g</sup>For the  $C-X$  region see Fig. 6 in Ref. 3.

diagram of Fig. 4 demonstrates. Here, the orbital occupation for the ground state of  $\text{BeF}_2$  is complete through the  $\pi_g$  orbital and the greater stability of the sum of valence orbital energies at  $180^\circ$  predicts a linear ground state geometry. This correlation diagram, while oriented to the energetics of the  $\text{BeF}_2$  valence orbitals as a function of bond angle,<sup>29</sup> carries the essence of the bonding trends in these highly ionic  $AB_2$  type molecules. Even with a modification of this diagram to encompass changes associated with the transition from light metal-heavy halogen linear configurations to heavy metal-light halogen bent configurations, the important considerations relate to the nature and ordering of the  $\pi_g$  HOMO and  $\sigma_g$  and  $\pi_u$  LUMO orbitals of the linear configuration. In contrast to  $\text{CO}_2$  where the lowest lying LUMO is of  $\pi_u$  symmetry, the highly ionic character of the  $\text{BeF}_2$  molecule facilitates a switch such that the  $\sigma_g$  LUMO lies lowest. The corresponding lowest energy transitions, which are electric dipole forbidden for the linear dihalides in absorption, should also be quite weak for the heavier bent dihalides because of their very low bending mode frequencies and floppy nature.<sup>35</sup> Transitions involving the  $\pi_g$  HOMO and  $\pi_u$  LUMO orbitals are electric dipole allowed, representing the analogs of the lowest energy allowed transitions in  $\text{CO}_2$ ; however, the specific nature of the orbital makeup in  $\text{BeF}_2$  suggests that the oscillator strength of these transitions will be smaller than that of  $\text{CO}_2$ .

In emission, the lowest energy "allowed" dihalide transitions should be from a highly bent  $^1B_2$  excited state and the  $\tilde{A}^1B_2-\tilde{X}^1A_1$  band system should be dominated by long progressions in the bending modes of the upper and (near linear) ground electronic states. However, even though the transition in the emission is allowed (governed by the  $C_{2v}$  selection rules), the lack of any absorption data, even for the highly bent  $\text{BaF}_2$  molecule, suggests a low transition probability resulting in a long-lived excited state emitter. The expected emission contributes to the observed continua in Figs. 1-3. The controlled relaxation of the emission continua reveals three band systems (see Ref. 30) and clearly separates the  $\tilde{A}-\tilde{X}$  emission system for the  $\text{Ca}-\text{Cl}_2$ ,  $\text{Ca}-\text{Br}_2$ ,  $\text{Sr}-\text{Cl}_2$ , and  $\text{Sr}-\text{Br}_2$ , reactive encounters. A ready pressure dependent quenching of the relaxed chemiluminescent spectrum for the  $\tilde{A}-\tilde{X}$  system would appear to manifest its low transition probability [the  $g-g$  selection rule in absorption (Table III)].

In this same spectral region, transitions from a  $^1A_2$  excited state would be expected to be weak due to the electric dipole selection rules for a  $C_{2v}$  molecule. However, the vibrationally coupled transition involving the asymmetric stretch ( $b_2$ ) mode is allowed. This might produce a band system of moderate strength characterized by an alternating intensity pattern with frequency intervals indicative of the asymmetric stretch. We find little evidence for this vibrationally allowed emission in the observed relaxed multiple collision spectra for the dihalides. Transitions involving the  $^3B_2$  state (corresponding to the spin unpaired electron configuration which is the analog of the  $^1B_2$  state) are "spin forbidden" and are therefore also expected to be weak.

We anticipate the change in bond angle which accompanies these lowest energy transitions to be so pronounced that

the observed emission spectrum can be expected to extend over several hundred angstroms. We summarize our conclusions on the lowest energy transitions for the dihalides in Table III.

At somewhat higher energies in emission (Table III) we expect to observe transitions from excited states which result from promotion to the  $b_1(\pi_u)$  and, at somewhat higher energies, the  $a_1(\pi_u)$  orbital. We associate the resulting electron configurations and transitions with the  $\tilde{B}$  and  $\tilde{C}$  state regions summarized in Table III, the electric dipole allowed transitions corresponding to  $\tilde{B}^1B_2-\tilde{X}^1A_1$  and  $\tilde{C}^1B_2-\tilde{X}^1A_1$ , respectively. The bond angle change accompanying these transitions is not as pronounced as that accompanying the lowest energy  $A-X$  band system, however a change from  $\pi$  non-bonding to  $\pi$  antibonding character should result in a spectrum dominated by progressions in the dihalide stretching frequency. Emission corresponding to the  $\tilde{B}-\tilde{X}$  system has been observed for  $\text{Ca}-\text{Cl}_2$ ,  $\text{Ca}-\text{Br}_2$ ,  $\text{Sr}-\text{Cl}_2$ ,  $\text{Sr}-\text{Br}_2$ , and  $\text{Sr}-\text{ICl}$  reactive encounters, whereas the  $\tilde{C}-\tilde{X}$  system is excited only as a result of the strontium reactions.<sup>30</sup>

#### Periodic trends in the pressure dependence of dihalide emission features: Collisional stabilization of dihalide excited states

The behavior of the chemiluminescent intensity as a function of oxidant pressure follows a dependence of the form  $p^\beta e^{-ap}$ , where  $\beta$  represents the order of the reaction relative to the constituents under study and  $e^{-ap}$  represents an attenuation factor proportional to the reaction cross section.<sup>36</sup> Reactions following first order bimolecular kinetics will display a linear increase in chemiluminescence intensity with increasing oxidant pressure until attenuation effects become significant. Faster than first order reactions will display a positive curvature since  $\beta$  is greater than one.<sup>37</sup> Both the collisional stabilization mechanism (2) and the two step double harpoon mechanism (1) should display a quadratic dependence in the oxidant pressure.

In Fig. 5 we present plots of chemiluminescent intensity verses oxidant pressure for the  $\text{Ba}+\text{Cl}_2$  and  $\text{Ba}+\text{ClF}$  reactions. The plot for the  $\text{Ba}+\text{Cl}_2$  reaction represents the compilation of two experimental runs at  $4500 \text{ \AA}$  (res=10  $\text{\AA}$ ), whereas the data for the  $\text{Ba}+\text{ClF}$  reaction were taken at  $4000 \text{ \AA}$ . These plots indicate a second order dependence on oxidant pressure. They can be compared with the number density vs light intensity plots of Wren and Menzinger<sup>10</sup> for the  $\text{Ba}-\text{F}_2$ ,  $\text{Cl}_2$ ,  $\text{Br}_2$ , and  $\text{I}_2$  reactions depicted in Fig. 6. While these authors interpret their data for the  $\text{Ba}+\text{Cl}_2$ ,  $\text{Br}_2$ , and  $\text{I}_2$  reactions as displaying a linear onset followed by a quadratic increase in light intensity as a function of pressure, we find no evidence for linearity at pressures as low as  $1 \times 10^{-6}$  Torr either for the  $\text{Ba}+\text{Cl}_2$  reaction or for the  $\text{Ba}+\text{I}_2$  reaction whose pressure dependence is depicted in Fig. 7. Further insight into the behavior of the emission continuum is gained from Table IV where we plot relative intensities as a function of pressure and wavelength for the  $\text{BaCl}_2^*$  continuum. The data in Table IV suggest the collapse of intensity in the wings of the continuum with increasing pressure. We find that this pattern pervades as we extend these low pressure studies in a

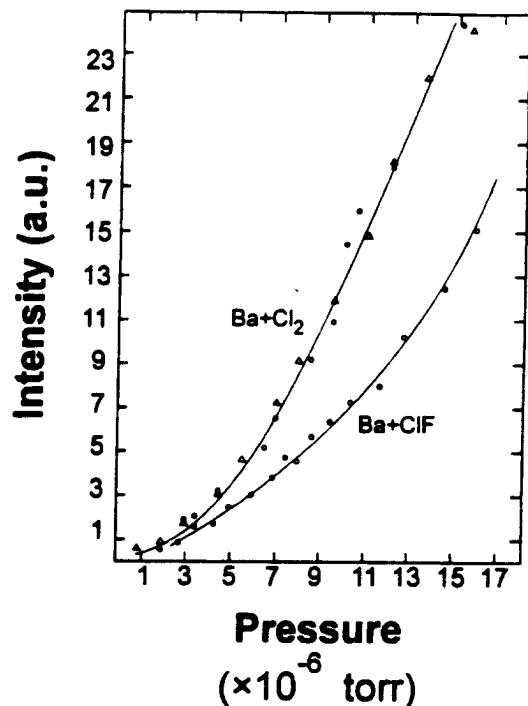


FIG. 5. Chemiluminescent intensity versus oxidant pressure for the reactions  $\text{Ba} + \text{Cl}_2 \rightarrow \text{BaCl}_2^*$  and  $\text{Ba} + \text{ClF} \rightarrow \text{BaClF}^*$ . The results were obtained at a wavelength of 4500 and 4000 Å, respectively, and at a resolution of 10 Å. Pressures were measured with a capacitance manometer. See the text for discussion.

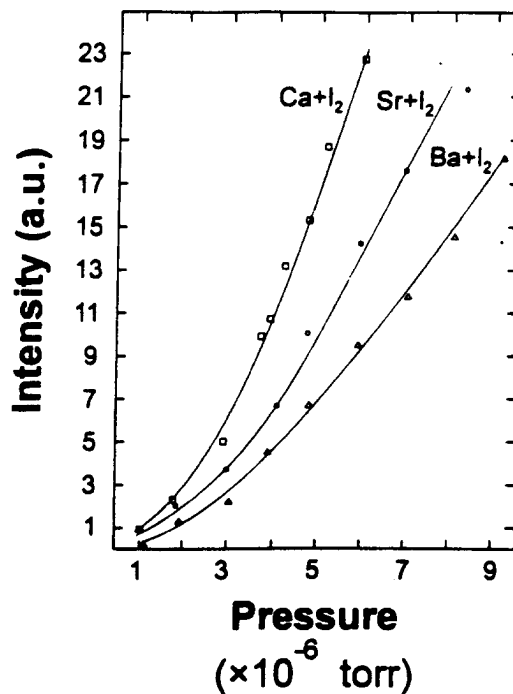


FIG. 7. Chemiluminescent intensity versus oxidant pressure for the reactions  $\text{Ca}$ ,  $\text{Sr}$ ,  $\text{Ba} + \text{I}_2$  run at temperatures to give near matching group IIA metal source fluxes. The results were obtained at a wavelength of 4700 Å and at a resolution of 10 Å. Pressures were measured with a capacitance manometer. See the text for discussion.

controlled manner to the multiple collision pressure regime.<sup>30</sup>

If we consider more closely the pressure dependent behavior indicated by the data of Wren and Menzinger,<sup>10</sup> we note a trend in the onset of the faster than first order pressure dependence. The onset of the nonlinear intensity increase

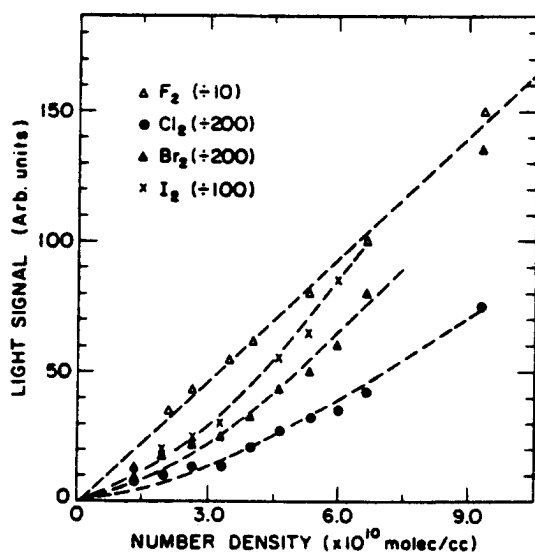


FIG. 6. Chemiluminescent intensity versus oxidant pressure for the reactions  $\text{Ba} + \text{F}_2$ ,  $\text{Cl}_2$ ,  $\text{Br}_2$ , and  $\text{I}_2$  from the data of Wren and Menzinger (Ref. 10). As reinterpreted in the text, dihalide emission is monitored in the  $\text{Cl}_2$ ,  $\text{Br}_2$ , and  $\text{I}_2$  studies whereas monohalide emission is monitored in the  $\text{F}_2$  study. See the text and the Appendix for discussion.

with pressure is most pronounced for the  $\text{Ba} + \text{I}_2$  continuum followed by the continua for  $\text{Ba} + \text{Br}_2$  and  $\text{Ba} + \text{Cl}_2$ , respectively. This trend might be explained by the increased density of states for the heavier product dihalides which promotes a more efficient collisionally stabilized emission. It might also result from the periodic interplay between the ground and low-lying electronic states of the dihalide.

For all of the dihalides which are linear in their ground electronic states, the  $g \leftarrow / \rightarrow g$  electric dipole forbidden nature of the lowest energy transition will lead to a very weak absorption. The results in Table II portend of a clear periodic trend. For the barium dihalides, all of which have bent configurations,  $\text{BaI}_2$  will be influenced by the electric dipole forbidden  $g \leftarrow / \rightarrow g$  transition (for the linear configuration)<sup>35</sup> more than will  $\text{BaBr}_2$  (which should then exceed  $\text{BaCl}_2$ , and  $\text{BaF}_2$ , respectively). The  $\text{BaF}_2$  absorption cross section should exceed the cross sections of all the remaining group IIA dihalides.

The emission spectra for the lowest energy transitions of the group IIA dihalides should also be influenced by the nature of the  $g \leftarrow / \rightarrow g$  selection rule. The excited state radiative lifetimes for the barium halides will be expected to follow the trend  $\tau_R(\text{BaI}_2) > \tau_R(\text{BaBr}_2) > \tau_R(\text{BaCl}_2) > \tau_R(\text{BaF}_2)$ . The expected trend in the radiative lifetimes can be manifest in the observed pressure dependences (Figs. 5–7) for the group IIA–metal halogen reactions. The longer-lived species are expected to display the effects of secondary stabilizing collisions at lower pressures. This appears manifest in Fig. 6 where the  $\text{BaI}_2$  pressure dependent emission intensity rises at a faster rate than that for  $\text{BaBr}_2$  (whose rise is correspond-

TABLE IV.  $\text{BaCl}_2^*$  continuum,  $\text{Ba} + \text{Cl}_2 \longrightarrow \text{BaCl}_2^* + \text{Cl}_2$ . Relative intensities as a function of pressure.

Pressure	$\lambda$ (Å)						
	3000	3553	4327	4659	5000	5765	6318
$3 \times 10^{-5}$	0.26	0.58	1.0	0.97	0.68	0.41	0.34
$4 \times 10^{-5}$	0.13	0.51	1.0	0.89	0.57	0.26	0.18
$4 \times 10^{-5}$	0.14	0.46	1.0	0.89	0.60	0.25	0.18
$5 \times 10^{-5}$	0.17	0.50	1.0	0.83	0.58	0.25	0.18
$5 \times 10^{-5}$	0.16	0.52	1.0	0.92	0.63	0.30	0.19
$6 \times 10^{-5}$	0.13	0.50	1.0	0.91	0.59	0.25	0.16
$6 \times 10^{-5}$	0.12	0.49	1.0	0.89	0.58	0.25	0.16
$7 \times 10^{-5}$	0.11	0.49	1.0	0.89	0.58	0.24	0.14
$7 \times 10^{-5}$	0.10	0.50	1.0	0.90	0.60	0.23	0.15
$8 \times 10^{-5}$	0.08	0.50	1.0	0.88	0.56	0.22	0.13
$8 \times 10^{-5}$	0.09	0.51	1.0	0.88	0.55	0.23	0.13
$9 \times 10^{-5}$	0.08	0.50	1.0	0.90	0.54	0.23	0.11
$9 \times 10^{-5}$	0.08	0.47	1.0	0.85	0.53	0.20	0.11
$10 \times 10^{-5}$	0.08	0.49	1.0	0.86	0.55	0.21	0.16
$10 \times 10^{-5}$	0.07	0.49	1.0	0.86	0.53	0.20	0.11
$2 \times 10^{-4}$	0.07	0.51	1.0	0.86	0.54	0.21	0.10
$2 \times 10^{-4}$	0.07	0.52	1.0	0.87	0.55	0.21	0.10
$3.1 \times 10^{-4}$	0.07	0.49	1.0	0.84	0.53	0.20	0.10
$3.1 \times 10^{-4}$	0.07	0.49	1.0	0.85	0.54	0.19	0.10
$4 \times 10^{-4}$	0.07	0.52	1.0	0.86	0.54	0.20	0.10
$4 \times 10^{-4}$	0.08	0.51	1.0	0.87	0.55	0.20	0.10
$5 \times 10^{-4}$	0.08	0.52	1.0	0.86	0.55	0.20	0.11
$5 \times 10^{-4}$	0.09	0.53	1.0	0.85	0.55	0.20	0.10

ingly faster than that for  $\text{BaCl}_2$ ). A similar trend is manifest in Fig. 7 for the  $\text{CaI}_2$ ,  $\text{SrI}_2$ , and  $\text{BaI}_2$  emission features where the "faster than first order" behavior onsets most sharply for the longer-lived  $\text{CaI}_2$  followed by  $\text{SrI}_2$  and then  $\text{BaI}_2$ .

While it might be argued that the behavior observed for the barium halides corresponds to an enhanced stabilization cross section paralleling an increased density of states, this is an unlikely explanation for the trends observed in Fig. 7 for the  $\text{CaI}_2$ ,  $\text{SrI}_2$ , and  $\text{BaI}_2$  pressure dependences. The data in Fig. 5 for the  $\text{BaCl}_2$  and  $\text{BaClF}$  emission features are also consistent with a dependence on radiative lifetime. Here, the  $\text{BaClF}$  complex is expected to be shorter lived due to the lighter fluorine atom and the loss of symmetry relative to  $\text{BaCl}_2$ .<sup>30,38</sup> The parallel with the periodic trends observed in Table II is striking.

The data presented in Fig. 6 for the  $\text{Ba} + \text{F}_2$  reaction seems inconsistent with this periodically based interpretation and with the observed pressure dependences of the remaining barium reactions. However, it can be demonstrated (Appendix) that the observed linear pressure dependence which corresponds with the seemingly continuous emission feature observed to extend from 6000–7000 Å in the spectrum for the  $\text{Ba} + \text{F}_2$  reaction [Fig. 1(d)] correlates not with  $\text{BaF}_2$  but with a much shorter lived, highly vibrationally-rotationally excited,  $\text{BaF}$  molecule.

### A symmetry constrained electron jump process

The relative intensities of the group IIA dihalide continuum emissions observed for homo- and heteronuclear halogen reactions can be understood within the electron jump harpoon model. Here, we use the correlations outlined in Table V and extrapolate on the simple yet elegant argu-

ments used by Menzinger<sup>14</sup> to explain the metal monohalide chemiluminescent emissions from fluorine and chlorine molecule reactions.

The correlation diagram in Fig. 8 provides a simple description of the reaction channels based upon electronic rearrangements along the reaction coordinate. This simple model, which reduces the four-dimensional hypersurface to two-dimensional energy profiles, can be used to provide a good first order description of the systems of interest because of the strongly covalent and ionic character of the relevant configurations. Within this framework, the location of the intersections,  $R_x$ , of the curves (configurations) of interest and the strength of their coupling<sup>14</sup> can be estimated from Coulomb's law and empirical correlations.<sup>39–41</sup>

We adopt the reasonable proviso that most of the electronic branching for these systems is governed by entrance channel interactions. We realize that at long range, where the Coulomb interaction of charge clouds dominates the multi-

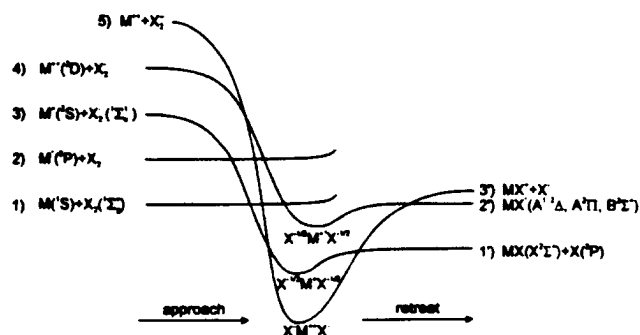


FIG. 8. Correlation of electron configurations for group IIA metal (M)–halogen molecule ( $\text{X}_2$ ) reactive encounters.

TABLE V. States arising from  $M+X_2$  reactant configurations.

	$C_\infty$	$C_{2v}$	$C_{\infty v}$
$M(^1S)+X_2(^1\Sigma_g^+)$	$^1A'$	$^1A_1$	$^1\Sigma$
$M(^2S)+X_2(^2\Sigma_u^+)$	$^1,3A'$	$1,3B_2$	$1,3\Sigma$
$M(^2S)+X_2(^1\Sigma_g^+)$	$^1A'$	$^1A_1$	$^1\Sigma$

pole expansion of the interaction potential, the Harpooning model<sup>42</sup> provides a reliable estimate of the covalent/ionic crossing radius

$$R_x = e^2 / \Delta E_{ci} \quad (3)$$

where  $\Delta E_{ci} = IP - EA$  is the asymptotic separation of covalent  $|c\rangle$  and ionic  $|i\rangle$  configurations and where IP and EA are the effective values of the reacting metal fragment ionization potential and halogen molecule electron affinity. Although the model is expected to fail at shorter range in proportion to the overlap of the fragment electron distributions, it can still provide a reasonable estimate of the inner crossing regions. The correlation diagram is constructed on this basis.

Reactions to produce the dihalide are thought to proceed through an electron jump "outer harpooning" process involving the interaction of the  $M+X_2$  ( $|1\rangle$  in Fig. 8) covalent and  $M^++X_2^-$  ( $|3\rangle$  in Fig. 8) ionic curves. For a  $C_\infty$  or  $C_{\infty v}$  collision geometry, this process involves the strong coupling of  $^1A'$  or  $^1\Sigma$  covalent and ionic potentials (Table V) of the same symmetry, leading to an avoided crossing, harpooning, and the formation of the ground state metal halide. However, if the collision geometry is of  $C_{2v}$  symmetry, the symmetry species of the covalent and ionic curves (Table V) are  $^1A_1$  and  $^1B_2$ , respectively, and the curves for the two states intersect. It is through this intersection and a range of approach angles within a cone of acceptance around the  $X_2$  bisector<sup>43</sup> that the system slips past the outer harpooning region corresponding to the conical intersection of adiabatic states at the  $|1\rangle|3\rangle$  crossing (Fig. 3) and gains access to the "inner harpooning" region.

The crossing involving the ionic configuration  $|3\rangle$  and the doubly ionic configuration  $|5\rangle$  will be avoided as the  $|3\rangle|5\rangle$  interaction between these curves of the same symmetry is thought to be significant. Access to the inner harpooning region thus promotes an avoided crossing leading to the chemiluminescent channels. The low statistical weight of the near  $C_{2v}$  collisions is partly responsible for the chemiluminescent quantum yields in these systems. For the  $M+XY$  reactive encounters, which cannot access a  $C_{2v}$  collision trajectory, the outer harpooning process must always correspond to an avoided crossing which shields the channel for chemiluminescent product formation.<sup>44</sup> As we compare the continua generated for the barium atom-mixed halogen reactions with ICl and IBr with those for the corresponding homonuclear  $Cl_2$ ,  $Br_2$ , and  $I_2$  reactions (Fig. 1), we observe a considerably weaker emission for the mixed halides vs their homonuclear counterparts. However, this difference diminishes for the strontium system (Fig. 2) and is almost completely muted for the calcium system (Fig. 3).

TABLE VI. States arising from  $MX+X_2$  reactant configurations with the MX molecular axis along the perpendicular bisector of the  $X_2$  bond for  $C_{2v}$  symmetry.

	$C_\infty$	$C_{2v}$	$C_{\infty v}$
$MX(^2\Sigma^+)+X_2(^1\Sigma_g^+)$	$^2A'$	$^2A_1$	$^2\Sigma$
$MX^+(^1\Sigma^+)+X_2(^2\Sigma_u^+)$	$^2A'$	$^2B_2$	$^2\Sigma$

We suggest that this behavior is again consistent with the electron jump process. The probability,  $P$ , that there is no change in electronic state during passage through the outer harpooning crossing point,  $R_x$ , can be given approximately by

$$P = \exp(-v_m/v), \quad (4)$$

where  $v_m$  is the characteristic velocity (proportional to  $R_x^2$  and  $\Delta E_x^2$ , the separation between the ionic and covalent curves at the crossing point) and  $v$  represents the initial relative velocity of the colliding alkaline earth metal and halogen molecule. In concert with the alkaline earth ionization potentials, we anticipate  $R_x(\text{Ba}) > R_x(\text{Sr}) > R_x(\text{Ca})$  for a given halogen molecule, implying  $v_m(\text{Ba}) > v_m(\text{Sr}) > v_m(\text{Ca})$ . With  $v_{\text{Ca-X}} > v_{\text{Sr-X}} > v_{\text{Ba-X}}$  we have

$$(v_m/v)_{\text{Ba}} > (v_m/v)_{\text{Sr}} > (v_m/v)_{\text{Ca}} \quad (5)$$

suggesting that the probability of outer harpooning and the formation of the ground state metal halide is greatest for the barium reactions and decreases for the reactions of strontium and calcium, respectively. As the characteristic relative velocities of the reactants at the ionic-covalent crossing increases in traversing the group IIA metals from barium to calcium, the reactions now overcome or tunnel through the barrier to chemiluminescent product formation.

The singly ionic excited configurations  $X^{-1/2}M^+X^{-1/2}$  and  $X^{-1/2}M^+(nd)X^{-1/2}$  are expected to have a substantially reduced binding energy compared with the ground state of the dihalide. This alone should promote an intermediate of considerable spatial extent, facilitating the possibility of collisional stabilization. The symmetry constrained electron jump process signals a dynamic constraint which is not consistent with the two step double harpooning process (1). The dominant participation of this process would require (Table VI) that the highly vibrationally and rotationally excited MX product of an initial  $M+X_2$  reactive encounter maintain axial alignment along the perpendicular bisector of the  $X_2$  bond as the second electron jump process occurs. This is a highly unlikely possibility.

We suggest that the absence of difluoride emission spectra resulting from the calcium, strontium, and barium reactions and the weak difluoride emission continuum observed for the magnesium reaction can also be explained within the framework of the electron jump process. Because the ionization potential<sup>23</sup> of magnesium (7.644 eV) considerably exceeds those of calcium (6.111 eV), strontium (5.692 eV), and barium (5.210 eV), the  $Mg+F_2$  reaction is expected to proceed more slowly as covalent forces come into play and the electron jump process is less efficient. With a less efficient electron jump process and an interaction at closer range, the

probability for fluorine molecule dissociation can be diminished to the extent that the difluoride complex can be formed and collisionally stabilized.

The electron jump model qualitatively explains the observed trends in dihalide emission intensity. More detailed calculations of the couplings at the avoided crossing regions will be needed to place these arguments on a more quantitative base however the framework of collision complex stabilization is established. Refinements will best be accomplished following an initial effort to parameterize dihalide electronic and vibronic structure from optical signatures (energy levels, radiative lifetimes, differential bond angle changes), all of which can also serve to refine ionic models.

## ACKNOWLEDGMENTS

The author gratefully acknowledges the helpful comments of Professor T. C. Devore and Dr. Kangkang Shen and the helpful comments and technical assistance of C. B. Winstead. The assistance of David Grantier and Peter Medley in preparing the figures is gratefully appreciated. David Grantier provided the simulations presented in Appendix A. The support of the Georgia Tech Foundation through a grant from Betty Peterman Gole, the Army Research Office through the Short Term Innovative Research Program, the Air Force Office of Scientific Research and the Army Research Office and AFOSR/SDIO is greatly appreciated.

## APPENDIX: FORMATION OF HIGHLY VIBRATIONALLY EXCITED $\text{BaF}^* B^2\Sigma^+ - X^2\Sigma^+$ FROM THE $\text{Ba} + \text{ClF}, \text{F}_2$ REACTIONS

Some confusion in the interpretation of the dynamics of group IIA-halogen molecule reactions has resulted from the assignment of monofluoride emission features to the difluorides. Menzinger,<sup>45</sup> in studying the reactions of calcium, strontium, and barium with molecular fluorine, assigned an observed 6000–7500 Å feature, resulting from the  $\text{Ba} + \text{F}_2$  reaction, to a  $\text{BaF}_2$  continuum emission on the basis of a conceived minimal correlation with the  $\text{BaF}^* B^2\Sigma^+ - X^2\Sigma^+$  emission system. He noted also the virtual absence of  $\text{CaF}_2$  and  $\text{SrF}_2$  emission features. Engelke<sup>15,46</sup> has identified the  $B^2\Sigma^+ - X^2\Sigma^+$  (~6000–7000 Å) and  $A^2\Pi - X^2\Sigma^+$  (~7500–8800 Å) band systems of BaF resulting from the "crossed beam"  $\text{Ba}(^3D_1) + \text{F}_2$  reaction at pressures less than  $10^{-5}$  Torr.

The  $\text{Ba} + \text{ClF}$  reaction [Fig. 1(c)], like the  $\text{Ba} + \text{F}_2$  system, is characterized by an emission feature extending from 6000 to 7000 Å. It is apparent even in the fast scan of Fig. 1(c) that this is a structured feature and the higher resolution scan depicted in Fig. 9(a) demonstrates that the observed spectrum corresponds to the  $B^2\Sigma^+ - X^2\Sigma^+$  band system of BaF. While this correspondence can be established, the chemiluminescence spectrum differs notably from previously observed emission features for the  $B-X$  system. The chemiluminescence spectrum is dominated by  $\Delta v = +2$  to  $\Delta v = +5$  sequences whereas all previous spectra are dominated by the  $\Delta v = 0$ ,  $v = +1$ , and  $v = -1$  sequence groupings. The reason for this discrepancy can be discerned from the simulation for the  $\text{BaF } B^2\Sigma^+ - X^2\Sigma^+$  transition presented in Fig. 9(b).

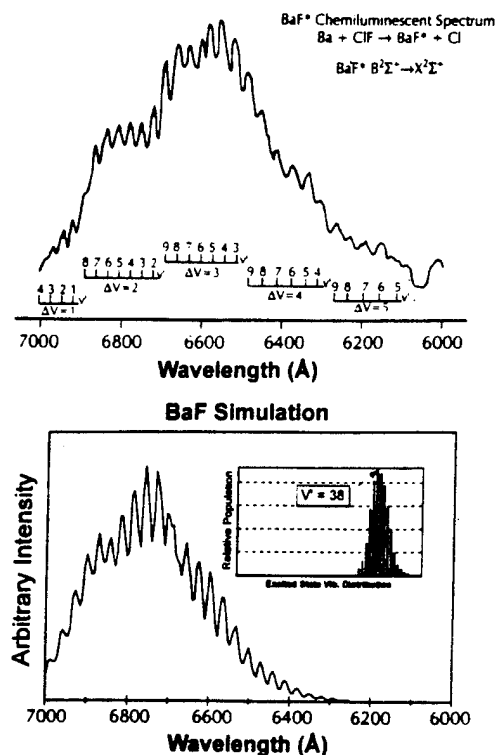


FIG. 9. (a)  $\text{BaF}^* B^2\Sigma^+ - X^2\Sigma^+$  chemiluminescent emission spectrum for the reaction  $\text{Ba} + \text{ClF} \rightarrow \text{BaF}^* + \text{Cl}$  over the pressure range  $1 \times 10^{-5}$  to  $1 \times 10^{-4}$  Torr corresponding to "single collision" conditions. The spectrum is characterized by off-diagonal sequence structure. Bandheads are designated by the excited state vibrational quantum number and all identified sequences correspond to a larger quantum number for the excited state than that for the ground state. (b) Simulation of the  $\text{BaF}^* B^2\Sigma^+ - X^2\Sigma^+$  chemiluminescent emission spectrum for the  $\text{Ba} + \text{ClF} \rightarrow \text{BaF}^* + \text{Cl}$  reaction [Fig. 1(a)]. The simulated spectrum suggests the vibrational distribution inset in the figure peaking at the high excited state vibrational quantum level  $v' = 38$ .

To generate the simulation of Fig. 9(b), we used the BaF molecular constants of Effantin *et al.*<sup>47</sup> A suitable set of Franck-Condon factors was calculated, using standard techniques,<sup>48</sup> from the rotationless RKR potentials of the  $B^2\Sigma^+$  and  $X^2\Sigma^+$  electronic states of the BaF molecule. We considered transitions between the lowest 50 vibrational levels of each state. A Boltzmann rotational temperature close to 800 K was imposed on each upper state vibrational level and chemiluminescent transitions were allowed from populated  $B$  state vibrational levels to the lowest 50 vibrational levels of the ground electronic state.  $\rho$ -type doubling, appropriate for a  $^2\Sigma - ^2\Sigma$  transition,<sup>48</sup> was included in the simulation for both the upper and lower electronic states. The resulting spectrum was appropriately smoothed to simulate a finite bandwidth instrument response in order to facilitate comparison with experimental observations. The upper state vibrational population distribution is clearly non-Boltzmann in character. We find that the BaF spectrum of Fig. 9(a) is well represented by a strongly inverted vibrational distribution peaking at  $\sim v' = 38$ . Transitions involving the lower vibrational levels are strongly diagonal, however, high vibrational excitation fosters the observed sequence deviations.

Because the impact parameter for the electron jump reactions of barium is quite high, we also considered the possibility that the effective potential

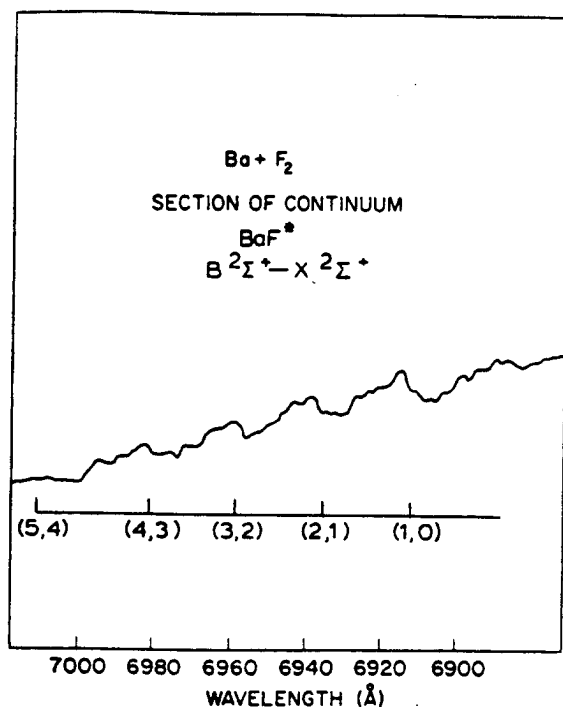


FIG. 10. Section of the  $\text{BaF}^* B^2\Sigma^+ - X^2\Sigma^+$  chemiluminescent emission spectrum for the reaction  $\text{Ba} + \text{F}_2 \rightarrow \text{BaF}^* + \text{F}$ . Based on comparison with Figs. 9(a) and (b), the excited state distribution is expected to peak at a very high vibrational quantum level,  $v'$ . Bandheads are designated  $(v', v'')$ .

$$U_{\text{eff}}(R) = U(R) + \hbar^2 J(J+1)/2\mu R^2$$

for the previous and present spectroscopic studies differs substantially, promoting a deviation from diagonal  $\Delta v = 0$  sequence structure. While a greatly increased rotational excitation causes some deviation, this is by no means sufficient to explain the clear  $\Delta v = +2, +3$  sequence domination depicted and simulated in Fig. 9.

The results obtained for the  $\text{Ba} + \text{ClF}$  reaction portend of the rovibrational distribution we expect for the  $\text{Ba} + \text{F}_2$  reaction which is considerably more exothermic. From a scan (Fig. 10) taken at the long wavelength onset of the dominant seemingly continuous emission [Fig. 1(d)], we recognize features corresponding to the  $\Delta v = +1$  sequence,<sup>49</sup> however, the identification of these features is greatly aided by our knowledge of the observed trends in the  $\text{Ba} + \text{ClF}$  ( $B^2\Sigma^+ - X^2\Sigma^+$ ) emission spectrum. With a larger reaction exoergicity and a comparable if not greater impact parameter, the  $\text{Ba} + \text{F}_2$  reaction should display (1) a more pronounced off-diagonal shift in the  $\text{BaF } B^2\Sigma^+ - X^2\Sigma^+$  emission system as considerably higher vibrational levels are populated and (2) a significant increase in rotational excitation. The experimental scans confirm this result as the rotational excitation is so pronounced that the resolution of vibrational structure is difficult. At wavelengths shorter than 6900 Å, the overlap of vibrational-rotational structure leads to a spectrum of such density that resolution is precluded. There is, however, a clear trend toward emission from the  $\Delta v = +N$  sequences.

The linear pressure dependence reported by Wren and Menzinger<sup>10</sup> for the  $\text{Ba} + \text{F}_2$  reaction is not surprising. Because a  $\text{BaF } B^2\Sigma^+ - X^2\Sigma^+$  fluorescent feature is moni-

tored, the observed pressure dependence with halogen concentration is linear since the radiative lifetime for the  $B^2\Sigma^+$  state of  $\text{BaF}$  is of order  $10^{-8}$  s.<sup>50</sup> The collision frequency at  $10^{-4}$  Torr, the upper limit of the pressure dependent plot, is of order  $10^3/\text{s}$ ; therefore, those  $\text{BaF}^* B^2\Sigma^+$  molecules formed in bimolecular reaction radiate well before suffering secondary collisions.

<sup>1</sup> J. L. Gole, *Opt. Eng.* **20**, 546 (1981).

<sup>2</sup> J. L. Gole and D. R. Grantier, *High Temp. Sci.* (in press).

<sup>3</sup> J. L. Gole, H. Wang, J. S. Joiner, and D. E. Dawson, *J. Chem. Phys.* **102**, 7437 (1995). See also, *Gas-Phase Metal Reactions*, edited by A. Fontijn (North Holland, Amsterdam, 1992).

<sup>4</sup> G. Herzberg, *Molecular Spectra and Molecular Structure I. Spectra of Diatomic Molecules* (Van Nostrand, New York, 1950), p. 443.

<sup>5</sup> J. M. Parson, *J. Phys. Chem.* **90**, 1811 (1986).

<sup>6</sup> T. Kasai, T. Masui, H. Nakane, I. Hanazaki, and K. Kuwata, *Chem. Phys. Lett.* **56**, 84 (1978).

<sup>7</sup> Y. Yoshimura, H. Ohyama, T. Humada, T. Kasai, and K. Kuwata, *Chem. Phys. Lett.* **106**, 271 (1984).

<sup>8</sup> C. D. Jonah and R. N. Zare, *Chem. Phys. Lett.* **9**, 65 (1971).

<sup>9</sup> C. A. Mims and J. H. Brophy, *J. Chem. Phys.* **66**, 1378 (1977).

<sup>10</sup> D. J. Wren and M. Menzinger, *Chem. Phys. Lett.* **27**, 572 (1974).

<sup>11</sup> D. R. Grantier and J. L. Gole, *J. Phys. Chem. Lett.* **98**, 7427 (1994); *J. Chem. Phys.* (to be submitted).

<sup>12</sup> T. C. Devore, R. Kahlscheuer, D. A. Dixon, H. Wang, and C. B. Winstead (in preparation).

<sup>13</sup> W. J. Rosano and J. M. Parson, *J. Chem. Phys.* **84**, 6250 (1986).

<sup>14</sup> M. Menzinger, *Adv. Chem. Phys.* **42**, 1 (1980); in *Gas Phase Chemiluminescence and Chemiionization*, editor A. Fontijn (Elsevier Science, Amsterdam, 1985), pp. 25-66; *Acta Phys. Polonica A* **73**, 85 (1988).

<sup>15</sup> F. Engelke, *Chem. Phys.* **44**, 213 (1979).

<sup>16</sup> D. Wren, Ph.D. thesis, University of Toronto, 1978.

<sup>17</sup> H. C. Brayman, D. R. Fischell, and T. A. Cool, *J. Chem. Phys.* **73**, 4247 (1980).

<sup>18</sup> See, for example, L. H. Dubois and J. L. Gole, *J. Chem. Phys.* **66**, 779 (1977); D. R. Preuss and J. L. Gole, *J. Chem. Phys.* **66**, 880 (1977); **66**, 2994 (1977); G. J. Green and J. L. Gole, *Chem. Phys.* **46**, 67 (1980); **69**, 357 (1982), and references therein.

<sup>19</sup> J. L. Gole, in *Gas Phase Chemiluminescence and Chemiionization*, edited by A. Fontijn (Elsevier Science, New York, 1985), p. 253.

<sup>20</sup> D. M. Lindsay and J. L. Gole, *J. Chem. Phys.* **66**, 3886 (1977); M. J. Sayers and J. L. Gole, *Ibid.* **67**, 5442 (1977); J. L. Gole and S. A. Pace, *Ibid.* **73**, 836 (1980).

<sup>21</sup> A. W. Hanner and J. L. Gole, *J. Chem. Phys.* **73**, 5025 (1980); J. L. Gole and S. A. Pace, *J. Phys. Chem.* **85**, 2651 (1981); J. L. Gole, B. Ohlsson, A. W. Hanner, and E. J. Greene (unpublished).

<sup>22</sup> A. N. Nesmeyanov, *Vapor Pressures of the Elements* (Academic, New York, 1963).

<sup>23</sup> See, for example, NBS Special Publication 505, Bibliography on Atomic Transition Probabilities (1914 through October 1977) and Supplement I (November 1977 through March 1980), U.S. Department of Commerce/National Bureau of Standards, C. E. Moore, *Atomic Energy Levels* (National Bureau of Standards, Maryland, 1949).

<sup>24</sup> See, for example, R. S. Berry and C. W. Reimann, *J. Chem. Phys.* **38**, 1540 (1963); R. S. Berry, *ibid.* **27**, 1288 (1957); W. S. Struve, J. R. Krenos, D. L. McFadden, and D. R. Herschbach, *ibid.* **62**, 404 (1975); R. C. Oldenborg, J. L. Gole, and R. N. Zare, *ibid.* **60**, 4032 (1974).

<sup>25</sup> T. C. Devore and James L. Gole (in preparation).

<sup>26</sup> For  $\text{F}_2^-$  see (a) J. A. Ayala, W. E. Wentworth, and E. C. M. Chen, *J. Phys. Chem.* **85**, 768 (1981); (b) W. A. Chupka, J. Berkowitz, and D. Gutman, *J. Chem. Phys.* **55**, 2724 (1971); (c) for  $\text{ClF}^-$  H. Disper and K. Lacmann, *Int. J. Mass. Spectrom. Ion Phys.* **28**, 49 (1978); (d) for  $\text{Cl}_2^-$  see (a) and H. Disper and K. Lacmann, *Chem. Phys. Lett.* **45**, 311 (1977); (e) A. P. M. Baeda, *Physica* **59**, 541 (1972); (f) for  $\text{Br}_2^-$  see D. L. Baulch, R. A. Cox, P. J. Crutzen, R. F. Hampson, Jr., J. A. Kerr, J. Troe, and R. T. Watson, *J. Phys. Chem. Ref. Data* **11**, 327 (1982), and Ref. (e) above. (g) for  $\text{I}_2^-$  A. P. M. Baeda, J. Averbach, and D. J. Los, *Physica* **64**, 134 (1973).

<sup>27</sup> J. A. Coxon and N. F. Ramsey, *Can. J. Phys.* **54**, 1034 (1976).

<sup>28</sup> L. Wharton, R. A. Berg, and W. Klemperer, *J. Chem. Phys.* **39**, 2023

- (1966); A. Buchler, J. L. Stauffer, W. Klemperer, and L. Wharton, *Ibid.* **39**, 2299 (1963); A. Buchler, J. L. Stauffer, and W. Klemperer, *Ibid.* **40**, 3471 (1964); *J. Am. Chem. Soc.* **86**, 4544 (1964).
- <sup>29</sup> James L. Gole, *J. Chem. Phys.* **58**, 869 (1973).
- <sup>30</sup> J. L. Gole, H. Wang, J. S. Joiner, and D. E. Dawson, *J. Chem. Phys.* **102**, 7437 (1995).
- <sup>31</sup> E. F. Hayes, *J. Phys. Chem.* **70**, 3740 (1966).
- <sup>32</sup> D. R. Yarkony, W. J. Hunt, and H. F. Schaefer, *Mol. Phys.* **26**, 941 (1973).
- <sup>33</sup> R. L. DeKock, M. A. Peterson, L. K. Timmer, E. J. Baerendo, and P. Vernooijs, *Polyhedron* **9**, 1919 (1990).
- <sup>34</sup> J. L. Gole, A. K. Q. Siu, and E. F. Hayes, *J. Chem. Phys.* **58**, 857 (1973).
- <sup>35</sup> Rapid vibrational motion corresponding to a bending mode for the  $\text{MF}_2$  molecule will produce an effective linear molecule whose dipole moment may be near zero. Similarly rapid rotation can produce an effective near zero dipole moment.
- <sup>36</sup> P. J. Dagdigian, H. W. Cruse, and R. N. Zare, *J. Chem. Phys.* **60**, 2330 (1974).
- <sup>37</sup> D. R. Preuss, C. L. Chalek, and J. L. Gole, *J. Chem. Phys.* **66**, 548 (1977).
- <sup>38</sup> The  $\text{BaClF}$  bond angle should also be smaller than that for  $\text{BaCl}_2$ , this further increasing the transition moment.
- <sup>39</sup> R. E. Olson, F. T. Smith, and E. Bauer, *Appl. Opt.* **10**, 1848 (1970).
- <sup>40</sup> R. Grice, D. R. Herschbach, *Mol. Phys.* **27**, 159 (1974).
- <sup>41</sup> J. Los and A. W. Kleyn, in *Alkali Halide Vapors*, edited by P. Davidovits and D. L. McFadden (Academic, New York, 1979).
- <sup>42</sup> R. B. Bernstein and R. D. Levine, *Molecular Reaction Dynamics* (Oxford U.P., New York, 1974).
- <sup>43</sup> T. Carrington, *Accts. Chem. Res.* **7**, 20 (1974).
- <sup>44</sup> Note that the radiative lifetimes associated with the lowest energy  $MXY$  emission band systems ( $\sigma-\pi$  transitions) will be shorter than their  $MX_2$  counterparts ( $\sigma_g-\pi_g$  transitions). Thus the relative  $MXY^*$  excited state production is considerably muted relative to that indicated in Figs. 1-3.
- <sup>45</sup> M. Menzinger, *Can. J. Chem.* **52**, 1688 (1974).
- <sup>46</sup> Engelke also observes a mildly structured emission associated with the  $\text{Mg}-\text{F}_2$  reaction; however, he correlates  $260\text{ cm}^{-1}$  separations in the observed chemiluminescence with a  $277\text{ cm}^{-1}$  frequency assigned to the bending mode of  $\text{MgF}_2$  in rare gas matrices. The bending mode of  $\text{MgF}_2$  is now thought to be considerably lower ( $150-160\text{ cm}^{-1}$ ) casting doubt on the assigned chemiluminescent features.
- <sup>47</sup> C. Effantin, A. Bernard, J. d'Incan, J. Verges, and R. F. Barrow, *J. Molec. Spectrosc.* **145**, 456 (1991).
- <sup>48</sup> See for example, R. N. Zare, *J. Chem. Phys.* **40**, 1934 (1964).
- <sup>49</sup> These features have also been observed by Engelke and correlated incorrectly with the  $\text{BaF}_2$  bending mode.
- <sup>50</sup> H. Wang and J. L. Gole (unpublished).

## APPENDIX XII

"Confirmation of Long-Range Collision Complex Stabilization Through The Controlled Relaxation of High Internal Excitation", J. L. Gole, H. Wang, J. S. Joiner and D. E. Dawson, J. Chem. Phys., 102, 7437 (1995).

# Confirmation of long-range collision complex stabilization through the controlled relaxation of high internal excitation

J. L. Gole, H. Wang, J. S. Joiner, and D. E. Dawson  
*School of Physics, Georgia Institute of Technology, Atlanta, Georgia 30332*

(Received 24 October 1994; accepted 3 February 1995)

A series of controlled multiple collision chemiluminescent and laser induced fluorescent studies confirm the long-range collisional stabilization of high temperature group IIA dihalide complexes of some considerable spatial extent. The relaxation process demonstrates that the pseudocontinuum emissions observed under near single collision conditions [J. Chem. Phys. **102**, 7425 (1995)] correspond to the overlap of a closely spaced, highly excited, rovibronic distribution. Controlled relaxation reveals the first vibrationally resolved electronic emission for the dihalides. The vibronic structure of the observed emission spectra correlates well with expectations based on the molecular electronic structure of the ground and low-lying electronic states of the dihalides. The vibronically resolved emission from the  $\text{Sr} + \text{ICl} \xrightarrow{\text{He}} \text{SrICl}^*$  and mixed halogen  $\text{Sr} + \text{Cl}_2$ ,  $\text{Br}_2 \xrightarrow{\text{He}} \text{SrCl}_2^* + \text{SrBr}_2^*$  reactions provides strong support for the formation of a collisionally stabilized dihalide complex. These results, correlated with near single collision studies, form a basis for the discussion of (1) the kinetics of formation of the dihalide complexes and (2) the implications of long-range collisional stabilization. Current theories may not accurately model these observations. Dihalide complex formation as it influences the energy partitioning to metal monohalide excited states may account for the discrepancies between those monohalide bond strengths determined by mass spectrometry and chemiluminescent techniques. © 1995 American Institute of Physics.

## INTRODUCTION

In the previous paper<sup>1</sup> we considered a series of nearly continuous emission features, generated from group IIA metal-halogen molecule reactions and extending across the visible and ultraviolet regions of the spectrum. We assigned these continua to highly excited group IIA dihalide emitters. These emission features, studied under near single collision conditions in a beam-gas environment, might be attributed to the overlap of a closely spaced highly excited rovibronic distribution. Alternatively they might correspond to a predissociating and broadened level structure or even the manifestation of a fly-by collision.<sup>2</sup> By extending single collision chemiluminescent and laser induced fluorescent studies in a controlled manner to the multiple collision pressure regime<sup>3</sup> we wish to employ the relative rates of  $R-R$  and  $V-V$  relaxation processes. We wish to relax, if possible, the high degree of rotational excitation characteristic of the single collision environment while still preserving the degree of vibrational excitation. Not only does this approach elucidate the single collision process, but also it greatly aids the identification of the chemiluminescent emitter and simplifies laser induced fluorescent evaluations of the reactive environment.

The controlled extension of the study of highly exothermic processes to the multiple collision regime also reveals unexpected efficiencies for the rates of energy transfer among the electronically and highly vibrationally excited states of high temperature molecules.<sup>4-6</sup> Collision induced intramolecular energy transfer proceeds at rates which for certain levels may approach 500 times gas kinetic with cross sections well in excess of  $4000 \text{ \AA}^2$ .<sup>3,4</sup> It appears that both the low-lying electronic states and high vibrational levels of the ground state of simple high temperature molecules interact with a collision partner as if strong interactions are present

over a much larger region of configuration space than might have been previously anticipated.<sup>4-6</sup>

If the single collision dihalide continuum observed at low pressures<sup>1</sup> results from an extremely high rotational excitation, and if this excitation can be relaxed selectively, the identity of the contributing dihalide excited states might be established. Here, we demonstrate the successful relaxation of the continuous dihalide emission features (considered previously) and determine that these continua correspond to the overlap of emission from three transition regions. We establish the discrete nature of the dihalide emissions which contribute to the single collision continuum, obtain the first vibrationally resolved emission spectra for the group IIA dihalides, and confirm the highly efficient R3BR mechanism for their formation.

## EXPERIMENT

### Sources

The multiple collision studies outlined here were carried out in an entrainment device similar to that used previously.<sup>7,8</sup> The Group IIA metals calcium, strontium, and barium, were vaporized from specially designed and capped c.s. grade graphite crucibles at temperatures between 900 and 1200 K producing a vapor pressure between  $\sim 10^{-3}$  and  $10^{-1}$  Torr for most of the experiments considered in the present study. The crucibles were machined to fit inside a commercial tungsten basket heater (R. D. Mathis, Long Beach, CA) which was lightly wrapped with zirconia cloth (Zircar Products, Florida, NY). The Group IIA metal flux was entrained in a helium (HoloX 99.998%) or argon (HoloX 99.99%) buffer gas and transported to the reaction zone. At a suitable point above the flow the halogen molecule oxidants intersected the entrained group IIA metals, entering from a con-

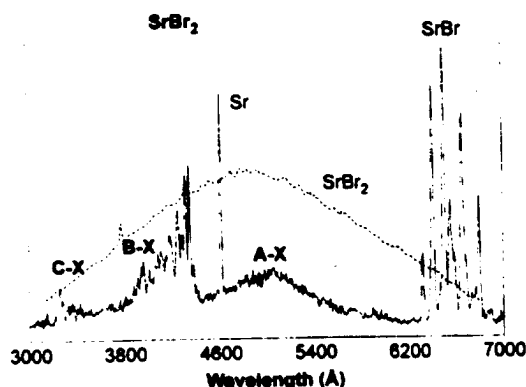


FIG. 1.  $\text{SrBr}_2 + \text{SrBr}$  multiple collision chemiluminescent spectrum taken at a resolution of 10 Å. Formation of the di- and monobromide results from the reactive process  $\text{Sr} + \text{Br}_2 \xrightarrow{h\nu} \text{SrBr}_2 + h\nu_1$  or  $\text{SrBr} + \text{Br} + h\nu_2$  at a background helium pressure of 0.8–1.2 Torr. The dihalide A–X, B–X, and C–X emission regions (see Table I) are indicated in the figure. The near single collision  $\text{SrBr}_2$  spectrum (dashed line) is included for comparison. See the text for discussion.

centric ring injector inlet. Typical operating pressures ranged from 10 to 80 mTorr of oxidant and between 1 and 2 Torr of helium buffer gas.

#### "Detection systems and laser induced fluorescence studies"

Both chemiluminescent and laser induced fluorescent techniques<sup>9</sup> were used to monitor reaction products in the multiple collision pressure regime. The chemiluminescence for the reactions of interest was monitored at right angles to the metal flow. Spectral emissions were dispersed with a 1 m Spex scanning monochromator operated in first order with a Bausch and Lomb 1200 groove/mm grating blazed at 5000 Å. Either RCA 1P28 or 4840 photomultipliers or a dry ice cooled EMI 9808 photomultiplier tube was used to detect the dispersed fluorescence and provide a signal for either a Keithley 417 fast picoammeter or a 417 autoranging picoammeter. The output signal from the picoammeters was then sent either to a Hewlett Packard chart recorder or to a personal computer for storage and subsequent analysis. All spectra were wavelength calibrated with a mercury arc lamp<sup>10</sup> or with respect to group IIA metal atomic emissions.<sup>10</sup>

In order to carry out the laser-induced fluorescence (LIF) experiments, the second harmonic of a Quanta-ray Nd:YAG laser (0.53  $\mu$ ) was used to pump a Spectra-Physics PDL-3 pulsed tunable dye laser system operated with DCM or LDS698 dye. The output of the pulsed dye laser (with a linewidth of 0.07  $\text{cm}^{-1}$  and a pulsewidth of 9 ns) was then either mixed with the fundamental output of the YAG laser or frequency doubled in a frequency mixer (Quanta-Ray WEX-1) to produce uv (in the range 310–410 nm) coherent radiation.

The laser beam was introduced to the reaction chamber in a direction perpendicular to both the reactant flow and detector. The YAG laser was triggered by a digital pulse generator (SRS DG535) with a repetition rate of 15 Hz. The Q-switching signal of the YAG oscillator was used to trigger a boxcar integrator (SRS SR250) for better synchronization.

The fluorescence induced by the uv laser pulse was collected with an RCA 1P28 photomultiplier (2.2 ns rise time) and, through a fast preamplifier (CLC 100 Video Amplifier, 500 MHz), sent to the gated integrator to record the spectrum as a function of the laser frequency. A fast digital oscilloscope (HP 54111D, 0.7 ns rise time) was used to real time monitor and record the fluorescence decay. The integration gate was set to a proper width in the range from 20 to 300 ns, dictated by the nature of the monitored fluorescence decay, with a delay timed such that the gate opened just after the short laser scattering pulse, thus reducing background noise. A personal computer (PC) drove the dye laser stepper motor, scanning the dye laser frequency and acquiring the averaged output data from the boxcar synchronously. In order to achieve a linear scan in wavelength when the dye laser frequency

TABLE I. Vibronic bands observed for  $\text{SrCl}_2$  in the dihalide A–X transition region.<sup>a</sup>

Band number (see Fig. 2)	Wavelength (Angstroms)	Frequency <sup>b</sup> (Vacuum $\text{cm}^{-1}$ )	$\Delta(\text{Frequency})$ ( $\text{cm}^{-1}$ )
1	4387	22 788.2	124
2	4411	22 664.2	117.5
3	4434	22 546.7	111.3
4	4456	22 435.4	120.2
5	4480	22 315.2	99.2
6	4500	22 216.0	117.8
7	4524	22 098.2	116.6
8	4548	21 981.6	115.4
9	4572	21 866.2	114.2
10	4596	21 752.0	113.0
11	4620	21 639.0	121.1
12	4646	21 517.9	119.7
13	4672	21 398.2	127.5
14	4700	21 270.7	117.0
15	4726	21 153.7	124.6
16	4754	21 029.1	123.2
17	4782	20 905.9	104.4
18	4806	20 801.5	119.0
19	4836	20 672.5	111.6
20	4862	20 561.9	121.9
21	4891	20 440.0	

<sup>a</sup>See Table III—Ref. 1 and Fig. 2.

<sup>b</sup>Frequencies are  $\pm 5 \text{ cm}^{-1}$ . Additional poorly resolved features to shorter and longer wavelength,  $\pm 10 \text{ cm}^{-1}$ .

was mixed with the infrared, the scan step size of the dye laser was calculated in real time using the PC. The output frequency of the WEX-1 was calibrated using aluminum atom lines.<sup>10</sup>

### MULTIPLE COLLISION RELAXED DIHALIDE EMISSION SYSTEMS

A successful and controlled extension from the near single collision pressure regime to the multiple collision condition, using primarily helium buffer gas entrainment, provides the means to collisionally relax the dihalide continuum so as to reveal what appear to be three discrete band systems. We obtain the first clear indication that the low pressure continua correspond to a profound rotational excitation associated with bound excited state levels and not with the free-bound transition of a very weakly bound dihalide excited state.<sup>11</sup> The overview spectrum depicted in Fig. 1 for the  $\text{Sr} + \text{Br}_2$  reaction combination is exemplary. From the figure, it is apparent that collisional relaxation produces a collapse in the wings of the near single collision  $\text{SrBr}_2$  dihalide continuum, analogous to that noted previously for  $\text{BaCl}_2$ ,<sup>1</sup> and leads to the observed relaxed spectrum in Fig. 1.

In the  $\text{SrBr}_2$  overview spectrum, the lower energy system (feature), which extends from the fringes of the ultraviolet through the visible, is dominated by a long progression in the bending mode of the  $\text{SrX}_2$  complex. This is clearly apparent in the  $\text{SrCl}_2$  emission spectrum depicted in Fig. 2. The observed feature, cataloged in Table I, would appear to correspond to the analog of the  ${}^1B_2((1a_2)^2(4b_2)(6a_1)) \rightarrow X {}^1A_1((1a_2)^2(4b_2)^2)$  transition in  $\text{BeF}_2$  correlating in linear configuration to a  ${}^1\Pi_g - {}^1\Sigma_g^+$  transition involving  $\sigma_g$  and  $\pi_g$  molecular orbitals. For all of the reactive combinations studied thus far, we find that both group IIA metal and halogen molecule collisions very effectively quench this feature, a fact which is not surprising in view of the anticipated longer lifetime ( $\tau_{\text{radiative}} \geq 10^{-5}$  s) for the excited state emitter.

The more clearly resolved, higher energy,  $B-X$  band system depicted in Fig. 1 is displayed in greater detail for the  $\text{Sr} + \text{Cl}_2$ ,  $\text{Sr} + \text{Br}_2$ , and  $\text{Sr} + \text{ICl}$  reactive encounters in Figs. 3–5, (cataloged in Table II).<sup>8</sup> A weaker, higher energy,  $C-X$  emission system which appears energetically accessible only to the  $\text{Sr} + \text{Cl}_2$ ,  $\text{Br}_2$ , and  $\text{ICl}$  reactions is displayed in greater detail in Fig. 6. The  $B-X$  and  $C-X$  band systems for  $\text{SrCl}_2$  and  $\text{SrBr}_2$  would seem to correspond to the analogs of the electric dipole allowed  ${}^1B_2(\cdots(1a_2)(4b_2)^2(2b_1))$  and  $\cdots(1a_2)^2(4b_2)(2b_1) - X {}^1A_1$  transitions in  $\text{BeF}_2$  (Table III—Ref. 1) which correlate in linear configuration to the allowed  ${}^1\Sigma_u - {}^1\Sigma_g^+$  transition involving the  $\pi_u$  and  $\pi_g$  molecular orbitals of the linear dihalide. This transition, which in adsorption involves primarily a change from  $M-X$  ( $M-X$  and  $M-Y$  for  $\text{SrCl}$ ) nonbonding to  $M-X$  antibonding character, should be dominated by progressions in the  $\text{MX}_2$  (or  $\text{MXY}$  for  $\text{SrCl}$ ) stretching modes. The frequency separations between the observed features are consistent with moderate progressions in the dihalide stretching modes in agreement with this suggestion.

The tentative assignments which we give for the  $A-X$ ,  $B-X$ , and  $C-X$  emission band systems are all consistent with the lowest electric dipole allowed transitions associated

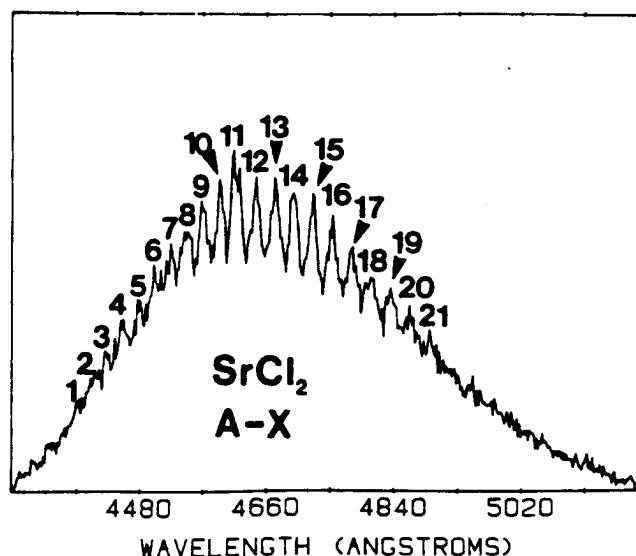


FIG. 2. Multiple collision chemiluminescent spectrum for  $\text{SrCl}_2$  in the dihalide  $A-X$  emission region (see Table III—Ref. 1) taken at a resolution of 10 Å. The emission corresponds to a long progression in the dihalide bending mode. The dihalide emitter is formed via a collisionally stabilized  $\text{Sr} + \text{Cl}_2 \rightarrow \text{SrCl}_2^*$  reactive encounter. The helium gas background pressure ranges from 0.8 to 1.2 Torr. The labeled emission features are cataloged in Table II. See the text for discussion.

with the group IIA dihalide correlation diagram. We favor these assignments over possible vibronically allowed transitions since we find little evidence for alternating intensity patterns associated with the dihalide asymmetric stretching mode.<sup>1</sup> However, it is to be noted that there may be evidence for Fermi resonances in the observed emission patterns. This possibility is now the subject of further study.<sup>12</sup>

### SUPPORT FOR A COLLISIONALLY STABILIZED DIHALIDE COMPLEX

#### The energetics of metal monohalide formation

We have suggested<sup>1</sup> that (1) the periodicity of group IIA dihalide formation, (2) the lack of a difluoride emission associated with the calcium, strontium, and barium systems, and (3) the symmetry effects which are manifest in the mixed verses homonuclear halogen molecule reactions all support the validity of a collisional stabilization mechanism and cast doubt on a two step harpooning mechanism for the formation of the dihalide emitter. The ability to relax while not quenching the near single collision dihalide emission continua, revealing discrete emission features, provides a means for supporting these conclusions.

The results we obtain in a comparative study of the  $\text{Sr}-\text{Cl}_2$ ,  $\text{Sr}-\text{Br}_2$ , and  $\text{Sr}-\text{ICl}$  systems (Fig. 7) and in a study of the mixed  $\text{Sr}-\text{Br}_2 + \text{Cl}_2$  system (Fig. 8) are significant for they demonstrate that the observed dihalide emission results, in large part, from a collisional stabilization process. If dihalide formation occurs via the two step double harpooning mechanism strongly suggested by Menzinger<sup>13</sup> and others the combination of  $\text{Sr}-\text{ICl}$  and  $\text{SrX}-\text{ICl}$  reactive encounters should produce  $\text{SrCl}_2$ ,  $\text{SrCl}$ , and  $\text{SrI}_2$  emission with the

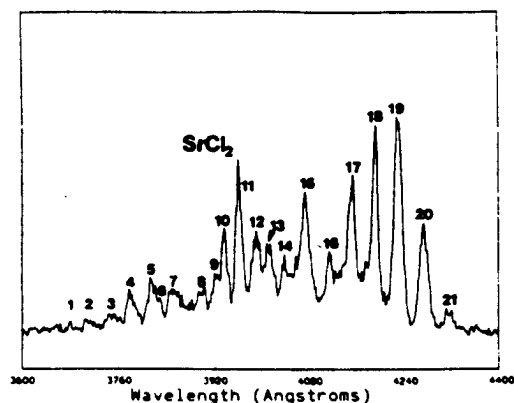


FIG. 3. Multiple collision chemiluminescent spectrum for  $\text{SrCl}_2$  in the dihalide  $B-X$  emission region (see Table III—Ref. 1) taken at a resolution of 10 Å. The dihalide emitter is formed via a collisionally stabilized  $\text{Sr} + \text{Cl}_2 \rightarrow \text{SrCl}_2^*$  reactive encounter. The helium background gas pressure ranges from 0.8 to 1.2 Torr. The spectrum appears to be dominated by dihalide stretching modes. The labeled emission features are cataloged in Table II. See the text for discussion.

strong possibility that the dichloride emission dominates that for the mixed halide and  $\text{SrI}_2$ . If the collisional stabilization mechanism is operative, the observed emission spectrum will correspond to the  $\text{SrICl}$  complex formed in a *dynamically constrained* electron jump process.

The reactions of strontium with  $\text{Cl}_2 + \text{Br}_2$  mixtures of varying relative chlorine and bromine concentration should produce emission from  $\text{SrCl}_2$ ,  $\text{SrBrCl}$ , and  $\text{SrBr}_2$  (Table III) if the two step double harpooning mechanism is operative. If the highly efficient R3BR collisional stabilization process is operative, the observed spectra should consist of the sum of only  $\text{SrCl}_2$  and  $\text{SrBr}_2$  emission features, varying with the relative  $\text{Cl}_2$  and  $\text{Br}_2$  concentration.

A study of the  $\text{Sr}-\text{ICl}$  reaction, with its attendant symmetry based dynamic constraint,<sup>1</sup> must be cautiously pursued for  $\text{SrCl}$  molecules with moderate vibrational excitation, *produced from the relaxation of rapidly emitting SrCl electroni-*

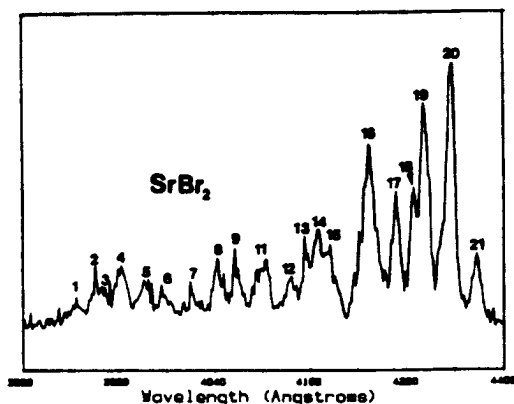


FIG. 4. Multiple collision chemiluminescent spectrum for  $\text{SrBr}_2$  in the dihalide  $B-X$  emission region (see Table III—Ref. 1) taken at a resolution of 10 Å. The dihalide emitter is formed via a collisionally stabilized  $\text{Sr} + \text{Br}_2 \rightarrow \text{SrBr}_2^*$  reactive encounter. The helium background gas pressure ranges from 0.8 to 1.2 Torr. The spectrum appears to be dominated by dihalide stretching modes. The labeled emission features are cataloged in Table II. See the text for discussion.

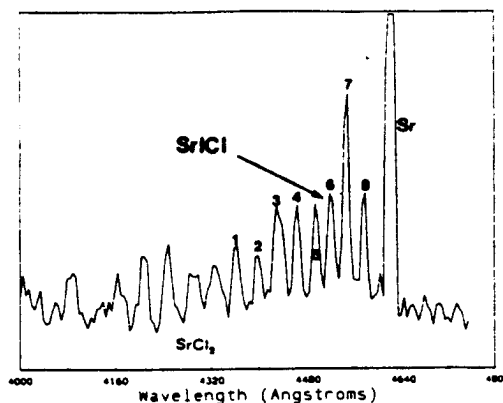


FIG. 5. Multiple collision chemiluminescent spectrum for  $\text{SrICl}$  in the dihalide  $B-X$  emission region (see Table III—Ref. 1) taken at a resolution of 10 Å. The dominant dihalide emitter is formed via a collisionally stabilized  $\text{Sr} + \text{ICl} \rightarrow \text{SrICl}^*$  reactive encounter (some  $\text{SrCl}_2$  contamination is also evident due to the  $\text{SrCl} + \text{ICl} \rightarrow \text{SrCl}_2^* + \text{I}$  reaction). The helium background gas pressure ranges from 0.8 to 1.2 Torr. The spectrum appears to be dominated by dihalide stretching modes. The labeled emission features are cataloged in Table II. See the text for discussion.

cally excited products, can react with  $\text{ICl}$  in a sufficiently exothermic process to produce  $\text{SrCl}_2$  emission features. In fact, under certain conditions, the observed spectral signature for the  $\text{Sr}-\text{ICl}$  reaction can be contaminated by  $\text{SrCl}_2$  emitters (both  $A-X$  and  $B-X$  systems) formed via the reaction of a nearly *thermalized* ground state  $\text{SrCl}$  product with  $\text{ICl}$ .

It is relevant that we choose to evaluate the ultraviolet spectra in the  $B-X$  region corresponding to one of the strongly allowed  $\text{SrX}_2 \ ^1B_2 - X \ ^1A_1$  transitions. The band systems in this region should display a minimal difference between the transition moments for the  $\text{SrX}_2$  ( $X = \text{Cl}, \text{Br}$ ) and corresponding  $\text{SrXY}$  ( $\text{XY} = \text{ICl}$ ) emitters. In monitoring the  $\text{Sr}-\text{ICl}$  reaction, we observe a dominant emission corresponding to the  $\text{SrICl}$  complex both in the  $B-X$  region (Figs. 5 and 7) and at higher energies corresponding to a  $C-X$  band system (Fig. 6) which can be easily populated by the more exothermic  $\text{ICl}$  reaction. The spectrum in Fig. 7 does show some  $\text{SrCl}_2$  contamination at the higher temperatures (higher  $\text{Sr}$  flux) over which the three spectra in the figure were obtained. However, the *dominance of the SrICl emission system*, especially as it results from a symmetry constrained process, is clearly apparent. This dominance signals the formation of  $\text{SrICl}$  in a collisionally stabilized reactive encounter (R3BR) where the formed excited state complex is stabilized by a long range interaction with a second  $\text{ICl}$  molecule.

The collage of dihalide spectra in Fig. 8, which have been obtained for varying mixtures of  $\text{Br}_2$  and  $\text{Cl}_2$ , correspond to sums of emission features resulting exclusively from the dichloride and dibromide with *no evidence* for the mixed halogen ( $\text{SrBrCl}$ ) emitter. This represents a strong confirmation of the highly efficient collisional stabilization mechanism. The comparison which we make is based primarily on the  $B-X$  stretching mode region, again avoiding the possibility of comparing transitions with distinctly different oscillator strengths in the  $A-X$  emission region. We also note that the formation of an  $\text{SrBrCl}$  emitter should lead to a *stronger*  $A-X$  emission feature compared to those for  $\text{SrCl}_2$

TABLE II. Vibronic bands observed for  $\text{SrX}_2$ ,  $\text{SrXY}$  ( $\text{X}=\text{Cl}, \text{Br}$ ;  $\text{Y}=\text{I}$ ) in the dihalide  $B-X$  transition region.<sup>a</sup>

Molecule band number	Wavelength (Angstroms)	Frequency <sup>b</sup> (Vacuum $\text{cm}^{-1}$ )	$\Delta(\text{Frequency})$ ( $\text{cm}^{-1}$ )
<b><math>\text{SrCl}_2</math> (Fig. 3)</b>			
1	3687	27 114.6	
2	3715	26 910.2	204.4
3	3750	26 659.1	251.1
4	3782	26 433.5	225.6
5	3818	26 184.3	249.2
6	(3831)	26 099.4	84.9
7	3852	25 953.2	146.2
8	3900	25 633.8	319.4
9	3923	25 483.5	150.3
10	3940	25 373.5	110
11	3964	25 219.9	153.6
12	3994	25 030.5	189.4
13	4015	24 899.6	130.9
14	4038	24 757.7	141.9
15	4076	24 526.9	230.8
16	4117	24 282.7	244.2
17	4156	24 054.8	227.9
18	4196	23 825.5	229.3
19	4233	23 617.2	208.3
20	4275	23 385.2	232.0
21	4318	23 152.4	232.8
<b><math>\text{SrBr}_2</math> (Fig. 4)</b>			
1	3873	25 812.5	
2	3898	25 646.9	165.6
3	(3905)	25 600.9	46.0
4	3928	25 451.0	149.0
5	3959	25 251.8	199.2
6	3981	25 112.2	139.6
7	4017	24 887.2	225.0
8	4049	24 690.5	196.7
9	4071	24 557.1	133.4
10	4099	24 389.3	167.8
11	4109	24 330.0	59.3
			188.1

TABLE II. (Continued.)

Molecule band number	Wavelength (Angstroms)	Frequency <sup>b</sup> (Vacuum $\text{cm}^{-1}$ )	$\Delta(\text{Frequency})$ ( $\text{cm}^{-1}$ )
12	4141	24 141.9	116.0
13	4161	24 025.9	86.3
14	4176	23 939.6	85.7
15	4191	23 853.9	270.1
16	4239	23 583.8	187.6
17	4273	23 396.2	119.9
18	4295	23 276.3	75.6
19	4309	23 200.7	171.0
20	4341	23 029.7	168.5
21	4373	22 861.2	
<b><math>\text{SrICl}</math> (Fig. 5)</b>			
1	4347	22 997.9	178.4
2	4381	22 819.5	186.0
3	4417	22 633.5	173.0
4	4451	22 460.5	160.2
5	4483	22 300.3	108.9
6	4505	22 191.4	146.8
7	4535	22 044.6	125.7
8	4561	21 918.9	

<sup>a</sup>See Table III—Ref. 1 and Figs. 3, 4, and 5.<sup>b</sup>Frequencies are  $\pm 10 \text{ cm}^{-1}$ .

and  $\text{SrBr}_2$ . The resultant  $\text{SrBrCl}$  emission should appear approximately central to the dichloride and dibromide features in the three intermediate panels of Fig. 8. We find no evidence for this emission.

The lack of an  $\text{SrBrCl}$  emission feature in Fig. 8 would appear to be especially significant when we note that the sum of both  $\text{SrCl}$  and  $\text{SrBr}$  emission features also characterize the monohalide emissions for all of the chlorine-bromine mixtures [compare to  $\text{Sr}+\text{Cl}_2$  (top) and  $\text{Sr}+\text{Br}_2$  (bottom)] depicted in Fig. 8. This implies that both  $\text{SrCl}$  and  $\text{SrBr}$  are available to react with  $\text{Br}_2$  and  $\text{Cl}_2$  to produce the mixed  $\text{SrBrCl}$  dihalide. However, the fast bimolecular  $\text{Sr}+\text{X}_2\rightarrow\text{SrX}+\text{X}$  reactions are not sufficiently exothermic<sup>1</sup> to populate the electronically excited states of  $\text{SrCl}$  or  $\text{SrBr}$ . Likewise, a collision induced transfer from the high vibrational levels of the ground state of  $\text{SrCl}$  or  $\text{SrBr}$ , to form the excited state emitters, can be eliminated as a possibility<sup>14</sup> in the multiple collision environment of the present study not only on energetic grounds, but also on the basis of an expected thermalization of the ground state rovibrational distribution. The data displayed in Figs. 9 and 10 correspond to laser induced fluorescence spectra for  $\text{SrCl}$  and  $\text{SrBr}$  ob-

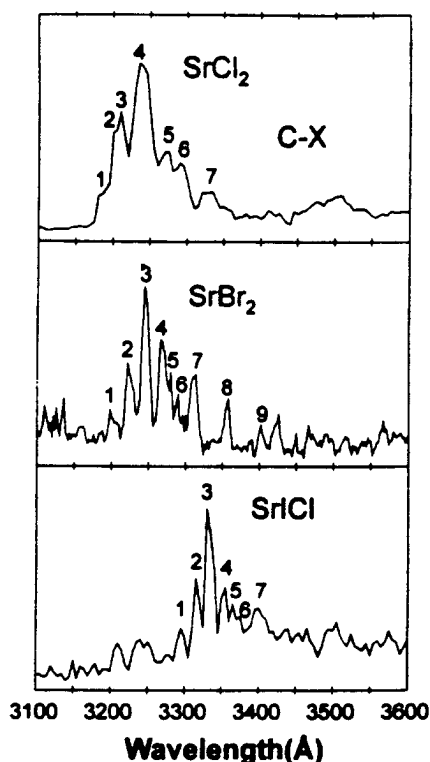


FIG. 6. Collage of multiple collision chemiluminescent emission spectra for  $\text{SrCl}_2$ ,  $\text{SrBr}_2$ , and  $\text{SrCl}$  in the dihalide  $C-X$  emission region (see Table III—Ref. 1) taken at resolutions of 10 Å. The dihalide emitters were formed via the collisionally stabilized  $\text{Sr}+\text{Cl}_2$ ,  $\text{Br}_2$ ,  $\text{ICl}^{\text{tr}}\text{SrCl}_2^*$ ,  $\text{SrBr}_2^*$ ,  $\text{SrCl}^*$  reactive encounters. The helium background gas pressure ranges from 0.8 to 1.2 Torr. The spectra appear to be dominated by dihalide stretching modes although some evidence for short bending mode progressions may be manifest.

tained using a Nd:YAG pumped dye laser system. Fits to the LIF spectra, exemplified by that for the  $\text{SrCl } C^2\Pi-X^2\Sigma^+$  band system in Fig. 11, suggest a thermalized distribution ( $T_{\text{vib}} \sim 450$  K,  $T_{\text{rot}} \sim 450$  K) among the lowest vibrational levels of the ground electronic state of the monochloride and monobromide. As the LIF spectra are taken in the wavelength regions characterized by strong dihalide emission they indicate that either the radiative lifetimes of the dihalide excited states are considerably longer than those of the monohalide or the population of ground state dihalide levels is not significant.

We find a close interplay between the growth of the metal dihalide and metal monohalide emission features displayed in Fig. 8. The considerable increase in the metal dihalide bond energy relative to that of the monohalide, combined with the data displayed in Figs. 9–11, suggests that electronically excited  $\text{SrCl}$  and  $\text{SrBr}$  are formed via the dissociation of a dihalide complex (see following discussion).

The considerations which we outline demonstrate the utility of extrapolating near single collision chemiluminescence studies in a controlled manner to the multiple collision pressure regime. This allows an assessment of the electron jump process which leads to excited state dihalide formation. The results obtained under multiple collision conditions support the conclusions reached in the analysis of the low pres-

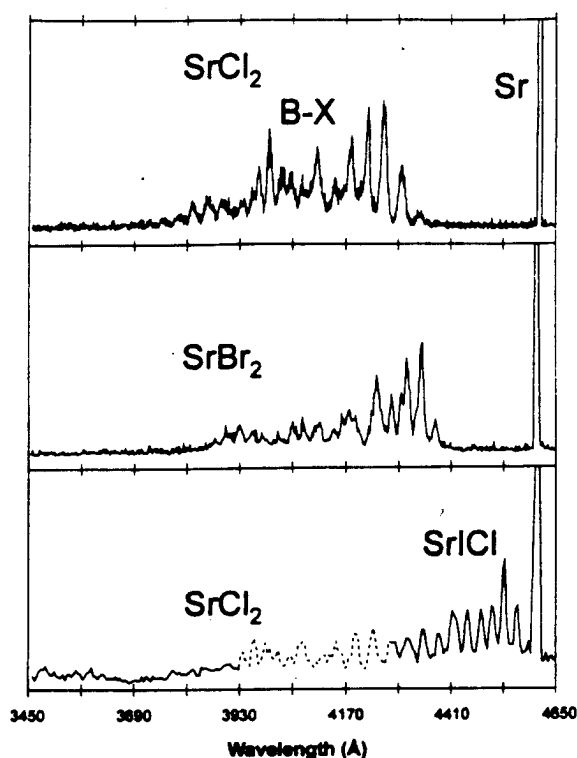


FIG. 7. Comparison of multiple collision chemiluminescent spectra for  $\text{SrCl}_2$ ,  $\text{SrBr}_2$ , and  $\text{SrCl}$  in the dihalide  $B-X$  emission region. The homo- and heteronuclear dihalide emitters are formed via the collisionally stabilized  $\text{Sr}+\text{Cl}_2$ ,  $\text{Br}_2$ ,  $\text{ICl}^{\text{tr}}\text{SrCl}_2^*$ ,  $\text{SrBr}_2^*$ ,  $\text{SrCl}^*$  reactive encounters. The helium pressure ranges from 0.8 to 1.2 Torr. The spectra appear to be dominated by short progressions in the dihalide stretching modes. Note also Figs. 3, 4, and 5 and Table II. See the text for discussion.

sure data and they strongly suggest the probability that an extremely efficient collisional stabilization mechanism represents the dominant means of forming the dihalide excited state. This conclusion is also further supported by the lack of a continuum emission associated with the fluorine based reactions.

## DISCUSSION

### Relaxed (discrete) emission from the $\text{MX}_2$ collision complex

There have been numerous studies<sup>15–22</sup> of the group IIA dihalides, both experimental and theoretical, which suggest the ground state vibrational frequency ranges summarized in Table IV for the  $\text{SrCl}_2$  and  $\text{SrBr}_2$  molecules. There are several comparisons which can be made with the data of Table IV.

It is apparent, as we have suggested previously, that the  $\text{SrCl}_2$  and  $\text{SrBr}_2$   $B-X$  (Table II) and  $C-X$  band systems, which most likely involve a change from  $M-X$  nonbonding to  $M-X$  antibonding character, are dominated by progressions in the stretching modes of the dihalide. A precise interpretation of the level structure for these systems must consider higher order interactions including Fermi resonances and possible vibronic couplings, although the latter do not appear to be strongly manifest in the observed emission fea-

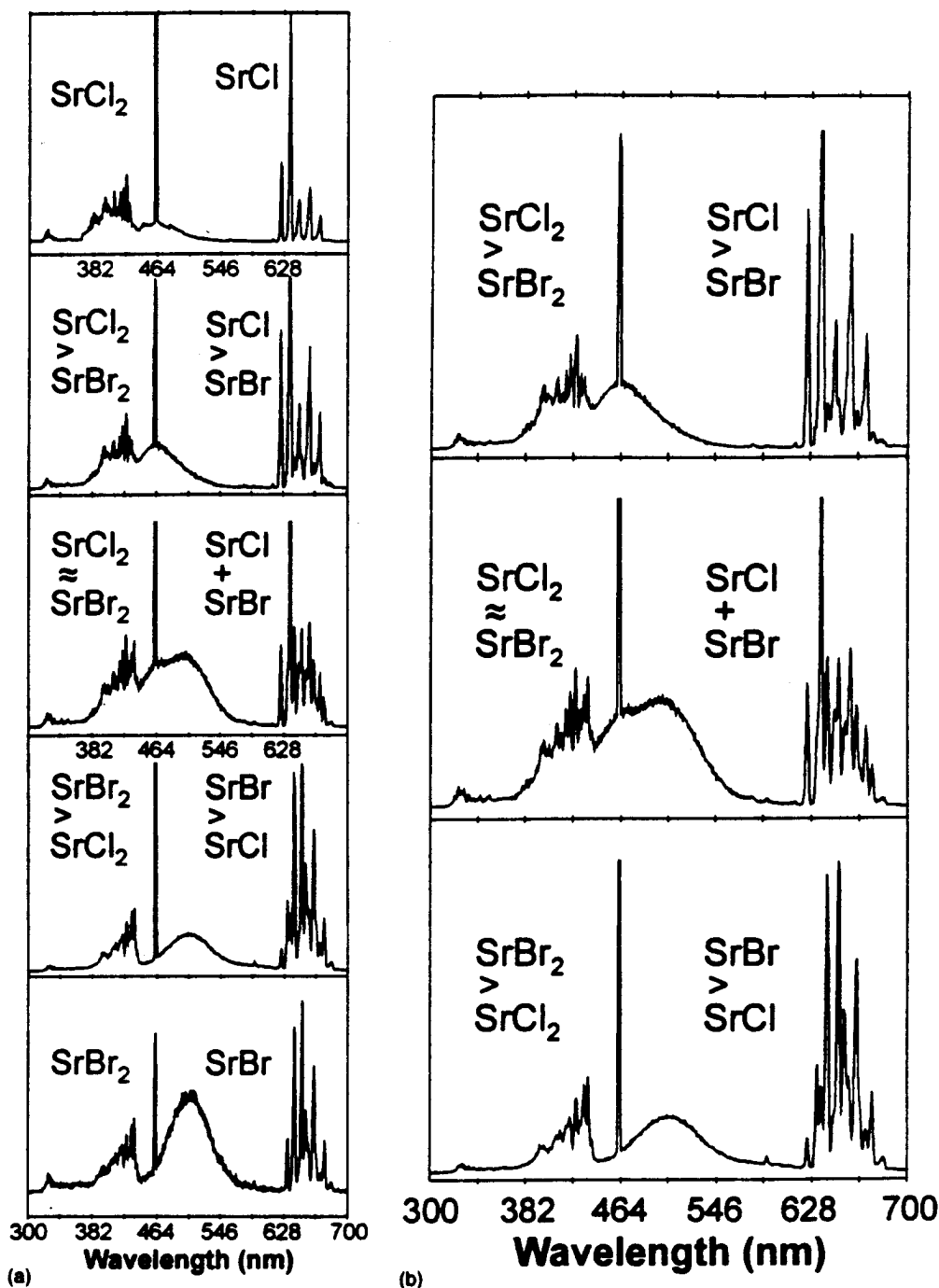


FIG. 8. (a) Collage of multiple collision chemiluminescent emission spectra for reactive mixtures of strontium metal and varying relative concentrations of Cl<sub>2</sub> and Br<sub>2</sub> reactants. The spectra correspond to the sum of metal dihalide and metal monohalide emitters. The dihalide emission features represent combinations of only SrCl<sub>2</sub> and SrBr<sub>2</sub> emitters with no evidence obtained for SrBrCl emission (see Table III). The monohalide emission features represent combinations of SrCl and SrBr formed via the collisionally stabilized process  $\text{Sr} + \text{X}_2 \rightarrow \text{SrX}_2^* \xrightarrow{\text{HCl}} \text{SrX}^* + \text{X}$  where the dihalide is formed as a precursor intermediate to the monohalide. (b) Closeup of inner three panels in (a). See the text for discussion.

tures. Of equal importance may be the dynamics of the forming emitting complex and its relation to the molecular electronic structure of that dihalide state in which it is formed.

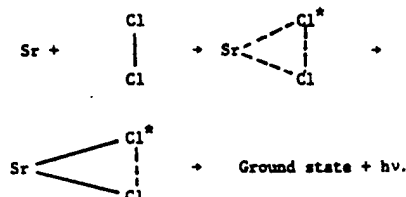
The resolved features for the SrCl<sub>2</sub> A-X band system in Fig. 2 are certainly consistent with a long progression in the bending mode of the SrCl<sub>2</sub> emitter. However, the observed frequency separations for this readily quenched emission feature, which are on the order of 110–120 cm<sup>-1</sup> (Table I),

TABLE III. Mechanisms for mixed Cl<sub>2</sub>+Br<sub>2</sub> reactions with strontium metal.

Collisional stabilization mechanism	
$\text{xSr} + \text{Cl}_2 + \text{Br}_2 \rightarrow \text{SrCl}_2 + \text{SrBr}_2$	
Two step harpooning mechanism	
$\text{Sr} + \text{Cl}_2 \rightarrow \text{SrCl} + \text{Cl}$	
$\text{SrCl} + \text{Br}_2 \rightarrow \text{SrClBr} + \text{Br}$	
$\text{Sr} + \text{Br}_2 \rightarrow \text{SrBr} + \text{Br}$	
$\text{SrBr} + \text{Cl}_2 \rightarrow \text{SrBrCl} + \text{Cl}$	
$\text{SrCl} + \text{Cl}_2 \rightarrow \text{SrCl}_2$	
$\text{SrBr} + \text{Br}_2 \rightarrow \text{SrBr}_2$	

considerably exceed the bending mode frequency for the IIA dihalide, measured as  $\sim 44 \text{ cm}^{-1}$ <sup>18</sup> in rare gas matrices (calculated to be between 13 and  $27 \text{ cm}^{-1}$ )<sup>16,19</sup>. The observed features cannot be attributed to a dihalide stretching mode. A series of relaxation studies suggest that the features associated with the A-X emission system correspond primarily to a progression in the ground state vibrational level structure associated with an emitting complex. The ease with which this band system is quenched is consistent with its anticipated long lifetime,<sup>1,2</sup> and with previous studies of the chemiluminescent emission from long-lived excited electronic states in that the relaxed emission appears localized to the lowest vibrational levels of the upper electronic state.<sup>3,4</sup>

We suggest that the apparent discrepancy between the determined frequency separations and the anticipated dihalide bending mode frequency may reflect the remnants of bonding between the two chlorine atoms substantially increasing the frequency of the vibrational mode corresponding to the bending vibration. The observed A-X band system may correspond to emission from an intermediate complex formed via the approach of strontium to  $\text{Cl}_2$ , viz.,



The emitting complex would appear to correlate with a local minimum on the  $\text{SrCl}_2$  potential surface<sup>23,24</sup> which corresponds to an incomplete rearrangement to the final product dihalide.

If we have observed emission from a highly bent intermediate complex, this further complicates the analysis of the B-X and C-X emission features. As Table IV demonstrates for the normal dihalide ground state geometries, the asymmetric stretch frequency considerably exceeds that of the

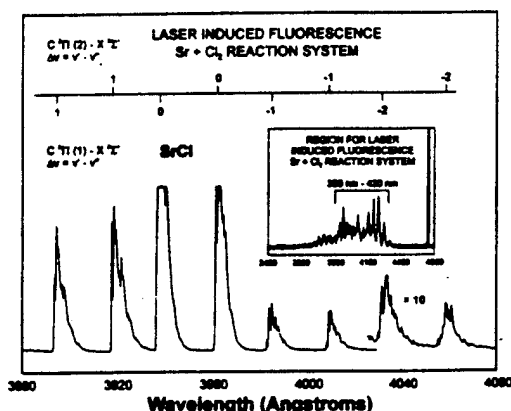


FIG. 9. Laser induced fluorescence spectrum for SrCl obtained by pumping ground state SrCl to the  $\text{SrCl } C^2\Pi$  state. The range of the laser induced fluorescent scan is correlated with a portion of the  $\text{SrCl}_2$  chemiluminescent emission in the B-X region as indicated in the inset of the figure. All features in the LIF spectrum are to be associated with the monochloride suggesting a much higher oscillator strength for the monochloride versus the dichloride B-X (Table II) transitions. Note also Fig. 3 and Table II. See the text for discussion.

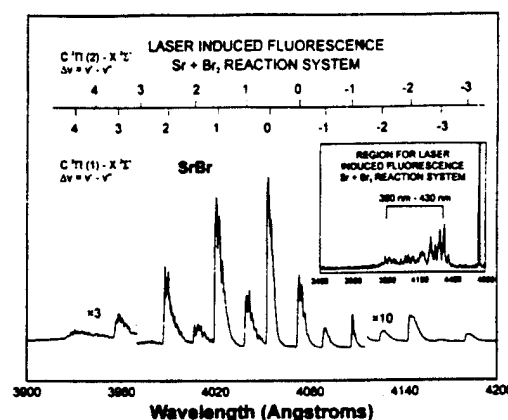


FIG. 10. Laser induced fluorescence spectrum for SrBr obtained by pumping ground state SrBr to the  $\text{SrBr } C^2\Pi$  state. The range of the laser induced fluorescent scan is correlated with a portion of the  $\text{SrBr}_2$  chemiluminescent emission in the B-X region as indicated in the inset of the figure. All features in the LIF spectrum are to be associated with the monobromide suggesting a much higher oscillator strength for the monobromide versus the dibromide B-X (Table II) transitions. Note also Fig. 4 and Table II. See the text for discussion.

symmetric stretch, both of which greatly exceed the bending mode. A preliminary normal mode analysis can be used to suggest that, as the dihalide bends to angles smaller than the equilibrium bond angle, its symmetric stretch frequency increases as the asymmetric stretch frequency decreases.<sup>23</sup> Because the symmetric stretch frequency can approach and exceed the asymmetric stretch frequency for an  $\text{SrCl}_2$  complex formed as a local minimum on the  $\text{Sr}-\text{Cl}_2$  reaction surface, the analysis of the observed features associated with the

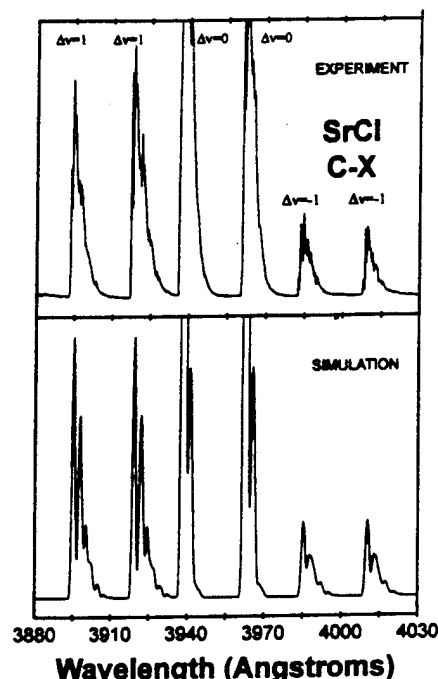


FIG. 11. Fit of  $\text{SrCl } C^2\Pi-X^2\Sigma^+$  laser induced fluorescence spectrum with known ground state and adjusted excited state constants. The vibrational and rotational temperatures are set at 450 K for the simulation. See the text for discussion.

TABLE IV. Ground state vibrational frequencies for SrCl<sub>2</sub>, SrBr<sub>2</sub>.

Dihalide (vibrational mode)	Vibrational frequencies (cm <sup>-1</sup> )
SrCl <sub>2</sub> (ν <sub>1</sub> )	251, <sup>a</sup> 256, <sup>b</sup> 270 <sup>c</sup>
(ν <sub>2</sub> )	19, <sup>a</sup> 20, <sup>b</sup> 44 <sup>d</sup>
(ν <sub>3</sub> )	337, <sup>a</sup> 307, <sup>b</sup> 300 <sup>c</sup>
SrBr <sub>2</sub> (ν <sub>1</sub> )	160, <sup>a</sup> 152, <sup>b</sup> 157 <sup>c</sup>
(ν <sub>2</sub> )	13, <sup>a</sup> 11, <sup>b</sup> 37 <sup>a</sup>
(ν <sub>3</sub> )	267, <sup>a</sup> 242, <sup>b</sup> 263, <sup>c</sup> 223–269 <sup>d</sup>

<sup>a</sup>References 16, 18–22.<sup>b</sup>Reference 17.<sup>c</sup>M. W. Chase, C. A. Davies, J. R. Downey, Jr., D. J. Frurip, R. A. McDonald, and A. N. Syverd, JANAF Thermochemical Tables, J. Phys. Chem. Ref. Data 14 (1985), Suppl. No. 1.<sup>d</sup>Reference 18.

B–X and C–X emission systems becomes more complex. In fact, the nature of the bonding in those excited states formed in reaction may also strongly influence the formation of the dihalide in one or more local minima which subsequently emit radiation. These considerations are the subject of ongoing collaborative study.<sup>23,24</sup>

### "Bond energy determinations"

The formation of a long-lived dihalide complex via the reaction of group IIA metals with chlorine, bromine, and iodine also may have implications for the determination of bond energies using chemiluminescent techniques.<sup>25</sup>

The population of the electronically excited states of SrCl and SrBr from the Sr–Cl<sub>2</sub> and Sr–Br<sub>2</sub> reactions (Figs. 1 and 8) at first seems puzzling<sup>14</sup> until we note the strong synergism between the development of the dihalide emission features and the subsequent increase in intensity of the monohalide emission features. We also realize that the exothermicity of a reactive process forming the dihalide provides sufficient energy to produce the excited states of the monohalide via a dissociative process. For example, under multiple collision conditions, the exothermicity of the reaction



given closely by the difference in the SrCl and Cl<sub>2</sub> molecule<sup>26</sup> bond energies is 39.8 kcal/mol (~13 920 cm<sup>-1</sup>).<sup>1</sup> This is not a sufficient energy to produce the monochloride emission recorded in Fig. 8. The energy available through the process



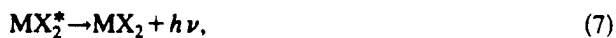
corresponds closely to an increment of order 49.3 kcal/mol [~17 243 cm<sup>-1</sup> = 1/2 AE(SrCl<sub>2</sub>) – D<sub>0</sub><sup>0</sup>(Cl<sub>2</sub>)<sup>26</sup>] where AE(SrX<sub>2</sub>) is the dihalide atomization energy.<sup>1</sup> The significant differential in energy which can be manifest to pump electronically excited monohalide states results from a substantially larger dihalide bond energy. For the Sr–Br<sub>2</sub> system, the energetics<sup>1</sup> yield 33.5 kcal/mol (~11 717 cm<sup>-1</sup>) and of order 49 kcal/mol (~22 600 cm<sup>-1</sup>) for direct metal monohalide formation and dihalide complex dissociation, respectively.

The considerations above might account for the prediction of bond energies significantly higher than those deter-

mined from mass spectrometry<sup>27</sup> as one uses chemiluminescent techniques to evaluate the chlorides, bromides, and iodides. In contrast, the bond energies determined for the calcium, strontium, and barium fluorides, evaluated from direct fluorine molecule reactions which are believed not to proceed through a long-lived complex, are in good agreement with those obtained from mass spectroscopy.<sup>27</sup>

### "Kinetics of formation of the dihalide complex"

Based on the combination of observations made under both single<sup>1</sup> and multiple collision conditions, the pressure dependent behavior monitored under near single collision conditions is indicative of the formation of a readily stabilized group IIA dihalide complex of some considerable spatial extent. A kinetic sequence consistent with both the single and multiple collision data is



where MX<sub>2</sub><sup>\*</sup> represents the nascent dihalide formed in reaction and MX<sub>2</sub><sup>\*</sup> the collisionally stabilized complex.

The potential energy along the reaction coordinate for a general M + X<sub>2</sub> → MX<sub>2</sub><sup>\*</sup> association process certainly requires that the complexes formed via reaction (3) must possess low excess energy and/or high angular momentum in order to survive long enough to emit a photon or suffer a stabilizing collision. We suggest that these criteria may indeed be fulfilled for the group IIA dihalides as they may also be for many other high temperature constituents.

A comparison of the near single collision and multiple collision spectra for the dihalides suggests that a profound rotational excitation may play an important role in the observation of the near continuous emission observed in a beam-gas environment. The energy of the overall rotation for the complex

$$E_R = \hbar^2(J)(J+1)/2\bar{I}, \quad (8)$$

where *J* is the total angular momentum quantum number and  $\bar{I}$  is the average moment of inertia, does not contribute to the nonfixed energy that facilitates the decay of the complex via a return through the M + X<sub>2</sub> entrance channel. Therefore, the funneling of energy into rotation may represent an important aspect of the observed behavior for these systems, lengthening the complex lifetime and enhancing the possibility for stabilization.

The importance of a stabilized long-lived MX<sub>2</sub><sup>\*</sup> intermediate complex is certainly evidenced in the chlorine, bromine, and iodine systems where it can lead to an enhanced excitation of the metal monohalide over and above that which would be obtained in a direct fast bimolecular reactive encounter (metal monofluoride formation). Because the dihalide atomization energy more than doubles the metal monohalide bond energy, the conditions exist which we believe

also facilitate complex formation and stabilization. It is relevant that these conditions may also be present in several other high temperature systems.

The observation of an R3BR process at pressures as low as  $1 \times 10^{-6}$  Torr is surprising.<sup>28,29</sup> A steady state treatment of the mechanism [Eqs. (3)–(7)] gives an expression for the chemiluminescence signal as a function of  $X_2$  density ( $X_2 = Q$ ) which can be shown<sup>30,31</sup> to be consistent with a significant stabilization cross section of order,  $\sigma_5 \sim 3000\text{--}5000 \text{ \AA}^2$ , and a long excited state radiative lifetime ( $\sim 10^{-2}$  s). A long radiative lifetime can be consistent with the group IIA dihalide  $A-X$  transition region (Table I and previous discussion). However, it is to be emphasized that in employing comparisons of the group IIA dihalide  $B-X$  emission region to demonstrate strong evidence for the formation of the dihalides in a collisionally stabilized reactive encounter (R3BR), we have considered transitions which are electric dipole allowed in both absorption and emission. These allowed transitions should be characterized by radiative lifetimes much shorter than  $10^{-2}$  s. The collisional stabilization mechanism [Eqs. (3)–(7)], within an RRKM framework, requires a radiative lifetime well in excess of  $10^{-5}$  s<sup>30</sup> in order that emission from the complex compete favorably with excited state dihalide loss mechanisms. However, the collisional stabilization process would appear to be operative for much shorter lived excited states. If we eliminate the requirement of a long-lived electronic state, this implies a considerably larger stabilization cross section than that conceived by Wren and Menzinger<sup>30</sup> and an extremely long range interaction involving group IIA dihalide excited states and their relaxing collision partner. It is clear that the stabilization process competes favorably with unimolecular decomposition for which RRKM calculations suggest a unimolecular lifetime (averaged over the distribution of energy and angular momentum) on the order of  $\tau_D \sim 10^{-7}$  s.

A large stabilization cross section provides the route for dissipating the energy increments<sup>30</sup> which must be funneled from the freshly forming Group IIA  $MX_2$  complex. The facilitating inelastic events may not be surprising in view of the high level density and large geometrical cross section presented by the strongly vibrating complex. The present studies, strongly dependent on the effective transfer of energy, suggest that the configuration space associated with collisional stabilization and energy transfer far exceeds that which would be associated with rotationally averaged hard sphere collision cross sections. This, of course, raises the question of whether association processes in these systems can be treated in a satisfactory fashion employing some variant of unimolecular rate theory.<sup>32</sup> The key question must be whether dissociative processes, well characterized by RRKM theory, or highly efficient energy transfer dominates the system. The present results, in conjunction with the highly efficient  $V-E$  and  $E-E$  transfers characterizing high temperature molecules in general,<sup>4</sup> would suggest that it is appropriate to consider the expansion of small molecule configuration space to account for a significantly enhanced energy transfer efficiency.

## CONCLUSION

We have outlined the nature of an extremely efficient collisional stabilization process involving intermediate complexes of some considerable extent. We also suggest that complexes which might be characterized by a diffuse excited state electron density, may be present in several environments. The implication of the present results may be broader. The extent of interaction of high temperature molecular complexes, as they form, can considerably exceed that which we normally associate with collisional stabilization and energy transfer processes. High temperature molecules in electronically excited states or in high vibrational levels of their ground electronic states simply are capable of much longer range interactions. An understanding of the formation and interaction of these species must contribute to our ability to control the behavior of systems operating under extreme conditions. A neglect of these phenomena in models of combustion or propulsion systems renders these models unrealistic.

## ACKNOWLEDGMENTS

The authors gratefully acknowledge the helpful comments of Dr. Kangkang Shen and the helpful comments and technical assistance of Mr. C. B. Winstead. The assistance of Mr. David Grantier and Mr. Peter Medley in preparing the figures is gratefully appreciated. Mr. David Grantier provided the simulations presented in the Appendix. The support of the Georgia Tech Foundation through a grant from Mrs. Betty Peterman Gole, the Army Research Office through the Short Term Innovative Research Program, the Air Force Office of Scientific Research, the Army Research Office, the National Science Foundation, and AFOSR/SDIO is greatly appreciated.

## APPENDIX: ESTIMATION OF VIBRATIONAL AND ROTATIONAL TEMPERATURES FOR THE $SrCl X^2\Sigma^+$ GROUND ELECTRONIC STATE (FIGURE 9)

Using molecular constants from Huber and Herzberg,<sup>33</sup> a suitable set of Franck-Condon factors was calculated, using standard techniques,<sup>2</sup> for the rotationless RKR potentials<sup>34</sup> of the  $C^2\Pi_{3/2} - X^2\Sigma_{1/2}$  and the  $C^2\Pi_{1/2} - X^2\Sigma_{1/2}$  electronic transitions of the  $SrCl$  molecule. We considered only the first ten vibrational levels of each state. The rotational constants,  $B_e$ , were extrapolated for the upper and lower states ( $B'_e \sim 0.098$ ,  $B''_e \sim 0.102$ ) from known data on the well characterized Group IIA monohalides. Vibrational ( $v'$ ,  $v'' = 0-9$ ) and rotational distributions ( $J'$ ,  $J'' = 0-19$ ) corresponding to temperatures of 450K were imposed on the ground and electronic state components of the doublet and all transitions to the ten lowest ground state vibrational levels were considered. The resulting simulated spectrum was also smoothed to simulate a finite bandwidth instrument response and facilitate comparison with the experimental results.

<sup>1</sup> J. L. Gole, *J. Chem. Phys.* **102**, 7425 (1995).

<sup>2</sup> R. B. Bernstein and R. D. Levine, *Molecular Reaction Dynamics* (Oxford University, New York, 1974).

<sup>3</sup> G. J. Green and J. L. Gole, *Chem. Phys.* **100**, 133 (1985); R. W. Woodward, J. S. Hayden, and J. L. Gole, *ibid.* **100**, 153 (1985).

- <sup>4</sup>J. L. Gole, in *Gas Phase Chemiluminescence and Chemiionization*, edited by A. Fontijn (Elsevier Science, New York, 1985), p. 253.
- <sup>5</sup>D. M. Lindsay and J. L. Gole, *J. Chem. Phys.* **66**, 3886 (1977); M. J. Sayers and J. L. Gole, *ibid.* **67**, 5442 (1977); J. L. Gole and S. A. Pace, *ibid.* **73**, 836 (1980).
- <sup>6</sup>A. W. Hanner and J. L. Gole, *J. Chem. Phys.* **73**, 5025 (1980); J. L. Gole and S. A. Pace, *J. Phys. Chem.* **85**, 2651 (1981); J. L. Gole, B. Ohlsson, A. W. Hanner, and E. J. Greene (unpublished).
- <sup>7</sup>See Refs. 3 and 4; M. McQuaid, K. Morris, and J. L. Gole, *J. Am. Chem. Soc.* **110**, 5280 (1988).
- <sup>8</sup>J. R. Woodward, S. H. Cobb, K. K. Shen, and J. L. Gole, *JQE* **26**, 1574 (1990), invited paper; K. K. Shen, H. Wang, and J. L. Gole, *JQE* **29**, 2346 (1993).
- <sup>9</sup>H. Wang and J. L. Gole, *J. Chem. Phys.* **98**, 9311 (1993); *J. Mol. Spectrosc.* **161**, 28 (1993).
- <sup>10</sup>See, for example, NBS Special Publication 505, Bibliography on Atomic Transition Probabilities (1914 through October 1977) and Supplement I (November 1977 through March 1980), U.S. Department of Commerce/National Bureau of Standards; C. E. Moore, *Atomic Energy Levels* (National Bureau of Standards, Maryland, 1949).
- <sup>11</sup>J. M. Parson, *J. Phys. Chem.* **90**, 1811 (1986).
- <sup>12</sup>T. C. Devore and James L. Gole (in preparation).
- <sup>13</sup>M. Menzinger, *Adv. Chem. Phys.* **42**, 1 (1980). M. Menzinger, in *Gas Phase Chemiluminescence and Chemiionization*, edited by A. Fontijn (Elsevier Science, Amsterdam, 1985), pp. 25–66; *Acta Phys. Polonica A* **73**, 85 (1988).
- <sup>14</sup>We have found that the careful and controlled extension of chemiluminescent studies from single to multiple collision conditions (see Ref. 3) preserves the maximum internal excitation observed under single conditions with no exceptions. While we observe rotational followed by vibrational relaxation and thermalization, no enhanced excitation is manifest due to energy transfer collisions.
- <sup>15</sup>James L. Gole, *J. Chem. Phys.* **58**, 869 (1973).
- <sup>16</sup>L. Seijo, Z. Barandiaran, and S. Huzinaga, *J. Chem. Phys.* **94**, 3762 (1991).
- <sup>17</sup>J. L. Gole and D. A. Dixon (unpublished results).
- <sup>18</sup>F. Ramondo, L. Bencivenni, C. Nunziante, and K. Hilpert, *J. Mol. Struct.* **192**, 83 (1989).
- <sup>19</sup>M. Kaupp, P. R. Schleyer, H. Stoll, and H. Preuss, *J. Am. Chem. Soc.* **113**, 6012 (1991).
- <sup>20</sup>D. White, G. V. Calder, S. Hemple, and D. E. Mann, *J. Chem. Phys.* **59**, 6645 (1973).
- <sup>21</sup>V. Calder, D. E. Mann, K. S. Seshadri, M. Alleva, and D. White, *J. Chem. Phys.* **51**, 2093 (1969).
- <sup>22</sup>D. E. Mann, G. V. Calder, K. S. Seshadri, D. White, and M. J. Linevsky, *J. Chem. Phys.* **46**, 1138 (1967).
- <sup>23</sup>T. C. Devore and J. L. Gole (work in progress).
- <sup>24</sup>K. Morokuma, J. Bowman, D. A. Kabysch, and J. L. Gole (work in progress).
- <sup>25</sup>M. Menzinger, *Can. J. Chem.* **52**, 1688 (1974).
- <sup>26</sup> $D_0^0(\text{Cl}_2) = 2.479\,367\text{ eV}$  (57.2 kcal/mol) from R. J. Leroy, in *Molecular Spectroscopy*, Vol. 1 (The Chemical Society, London, 1973), p. 113;  $D_0^0(\text{Br}_2) = 1.971\text{ eV}$  (45.5 kcal/mol) from J. A. Horsley and R. F. Barrow, *Trans. Faraday Soc.* **63**, 32 (1967);  $D_0^0(\text{ICl}) = 2.152\text{ eV}$  (49.6 kcal/mol) from W. E. Eberhardt, W. C. Cheng, and H. Renner, *J. Mol. Spectrosc.* **3**, 664 (1959).
- <sup>27</sup>D. L. Hildenbrand, in *Proceedings of the Symposium on High Temperature Metal Halide Chemistry*, Vol. 78-1 (The Electro-Chemical Society, Princeton, New Jersey, 1978), p. 248.
- <sup>28</sup>W. J. Rosano and J. M. Parson, *J. Chem. Phys.* **84**, 6250 (1986).
- <sup>29</sup>F. Engelke, *Chem. Phys.* **44**, 213 (1979).
- <sup>30</sup>D. J. Wren and M. Menzinger, *Chem. Phys. Lett.* **27**, 572 (1974).
- <sup>31</sup>D. Wren, Ph.D. thesis, University of Toronto, 1978.
- <sup>32</sup>P. J. Robinson and K. A. Holbrook, *Unimolecular Reactions* (Wiley Interscience, London, 1972).
- <sup>33</sup>K. P. Huber and G. Herzberg, *Constants of Diatomic Molecules*, Van Nostrand, Princeton, 1979. See also reference 3.
- <sup>34</sup>See for example, R. N. Zare, *J. Chem. Phys.* **40**, 1934 (1964).

### APPENDIX XIII

"What Is The Ionization Potential Of Silicon Dimer?", C.B. Winstead, S.J. Paukstis, and J. L. Gole, Chemical Physics Letters, 237, 81 (1995).

**WHAT IS THE IONIZATION POTENTIAL OF SILICON DIMER?**

**C. B. Winstead, S. J. Paukstis, and J. L. Gole**

**School of Physics  
Georgia Institute of Technology  
Atlanta, GA 30332**

## ABSTRACT

Resonant two photon ionization and laser induced fluorescence spectra of the  $\text{Si}_2 \text{H } ^3\Sigma_u^- - \text{X } ^3\Sigma_g^-$  transition are presented. The ionization behavior of several  $\text{H } ^3\Sigma_u^-$  vibrational levels is investigated using KrF excimer and Nd:YAG laser 4th harmonic radiation. The results of these studies are employed to tightly bracket the silicon dimer ionization potential (7.9-8.1 eV). This evaluation is discussed in relation to previous estimates of the  $\text{Si}_2$  ionization potential reported in the literature.

## INTRODUCTION

Not surprisingly, the study of the structures and properties of small silicon clusters has been an extremely active area of current research interest<sup>1-11</sup>, principally because of silicon's importance in both fundamental and applied science. The discovery of emissive nanometer-scale silicon clusters has further heightened this interest<sup>3</sup>. Within this framework, the measurements reported by Fuke et al. in a recent study<sup>2</sup> of the ionization potentials for silicon clusters,  $\text{Si}_n$  ( $n = 2 - 200$ ), were surprising in that they suggested that the silicon dimer ionization potential was in excess of 8.5 eV, considerably higher than previous evaluations given in the literature<sup>4-11</sup>. This most recent result, in concert with the dimer ionization potentials evaluated from experiment<sup>7-11</sup> and theory<sup>4-6</sup> suggests values ranging from at least 7.3 to in excess of 8.5 eV, although the more recent results of Trevor et al.<sup>10</sup> and Heath et al.<sup>11</sup> establish a lower bound of 7.87 eV for the ionization potential. The evaluation of Fuke et al.<sup>2</sup> is consistent with this lower bound, however it disagrees with a recent value of  $\leq 8.04 \pm 0.13$  eV given by Boo and Armentrout<sup>9</sup>, who obtained their estimate from their measured value of the enthalpy of formation of  $\text{Si}_2^-$  and the JANAF enthalpy of formation of  $\text{Si}_2$ . The ionization potential provides an important link to the understanding of molecular electronic structures, chemical reactivities, and dissociation processes and also serves as a sensitive probe of the accuracy of theoretical calculations which extend from the evaluation of small silicon clusters to surface modeling.<sup>12</sup> Thus the substantial range of I. P. values for even the simplest silicon molecule is a source of concern. In this report, we summarize studies of the dimer ionization potential using a combination of resonant multiphoton ionization techniques (similar to those recently applied to  $\text{Ag}_2$ <sup>13</sup>) to closely bracket the  $\text{Si}_2$

ionization potential.

## EXPERIMENTAL EVALUATION OF THE $\text{Si}_2$ IONIZATION POTENTIAL

### Experimental

The apparatuses which we have used to evaluate the  $\text{Si}_2$  ionization potential have been described in our previous studies of  $\text{Ag}_2$  ionization dynamics<sup>13</sup> and in our studies of metal cluster oxidation<sup>14</sup>. Briefly, the data we report was obtained from the Nd:YAG pumped dye laser induced fluorescence (LIF) of oven produced  $\text{Si}_2$  and resonant two photon ionization (R2PI) of supersonically cooled dimers formed from pulsed (Nd:YAG) laser vaporization. The higher temperature oven based studies produced clusters at temperatures which allowed the observation of an extended rotational structure in the LIF scans. R2PI scans were taken with both KrF excimer (5 eV) and Nd:YAG fourth harmonic (4.66 eV) ionization after initial excitation into the electronically excited  $\text{Si}_2$  H state. The R2PI excitation schemes are depicted in Figure 1. Here color filters were used to reduce the KrF excimer power so that no non-resonant ionization signal was observed. The most abundant isotope of iron has the same mass as the most abundant isotope of  $\text{Si}_2$  (56 amu). Iron is resonantly ionized by KrF excimer radiation, resulting in a large background signal component in the  $\text{Si}^{28}\text{Si}^{28}$  R2PI spectrum. Thus, R2PI spectra were often recorded in the less abundant  $\text{Si}^{28}\text{Si}^{29}$  or  $\text{Si}^{28}\text{Si}^{30}$  mass channels to expedite the evaluation of silicon dimer spectra at a reasonable signal to noise level.

### Results

Figure 2 depicts LIF and R2PI spectra for the  $\text{H } ^3\Sigma_u^- - \text{X } ^3\Sigma_g^-$  transition of  $\text{Si}_2$ . The spectra were obtained using pulsed LIF of oven generated  $\text{Si}_2$ , and R2PI of the dimers generated

from a pulsed laser vaporization source. The R2PI spectrum results from the KrF excimer ionization of  $\text{Si}^{28}\text{Si}^{30}$ , leading to a shift in the bandhead energies between the LIF ( $\text{Si}^{28}\text{Si}^{28}$ ) and R2PI spectra. The shift results from the isotope effect. A close examination of the magnitude of the isotope shifts reveals that the accepted vibrational numbering of the H state is incorrect<sup>15</sup> (lowest level observed in absorption studies is  $v' = 1$  and not  $v' = 0$  as previously assumed<sup>16</sup>). However, this has little effect on the following discussion other than to alter the numbering quoted for the H state vibrational levels.

The  $\text{Si}^{28}\text{Si}^{30}$  H ( $v' = 3$ ) - X ( $v'' = 0$ ) transition lies at  $24841 \text{ cm}^{-1}$  or 3.08 eV. As Figure 2 demonstrates, a 5 eV KrF laser photon is capable of producing ionization in  $\text{Si}_2$  from the H ( $v' = 3$ ) level. This implies an  $\text{Si}_2$  ionization potential less than 8.08 eV (See Figure 1, R2PI scheme (a)). Although the  $v' = 2$  level of the H state is not observed in the R2PI spectrum, it is not certain that this observation results from insufficient energy to produce ionization. Ionization from the  $v' = 2$  level is energetically allowed using an ArF excimer laser (6.4 eV). However, the apparent lowered ionization efficiency from the H  $^3\Sigma_u^-$  state using ArF radiation provides an insufficient signal so that we might observe the less intense (2, 0) and (3, 0) vibrational transitions. In any case, an upper bound is established for the  $\text{Si}_2$  ionization potential.

Figure 3 depicts LIF and R2PI spectra obtained after excitation of the higher energy H ( $v' = 8$ ) - X ( $v'' = 0$ ) transition. Here, both KrF and Nd:YAG fourth harmonic (4.66 eV) ionization were attempted in a R2PI framework (See also Figure 1, R2PI schemes (b) and (c)). The similarity between the LIF and KrF R2PI scans is evident as an H ( $v' = 8$ ) associated signal is observed in both scans. The  $\text{Si}^{28}\text{Si}^{28}$  mass channel was monitored in the R2PI spectra so that a direct comparison with the depicted LIF spectrum could be made. Thus, the small peaks to the

blue of the  $v' = 8$  transition region in the KrF R2PI scan result from fluctuations in the iron atom contaminant levels.

The R2PI spectrum associated with the  $H(v' = 8) - X(v'' = 0)$  transition is readily obtained using KrF ionization. The vertical arrow in Figure 3 locates the bandhead of the H state  $v' = 8$  level at  $26150\text{ cm}^{-1}$  or  $3.24\text{ eV}$ . The Nd:YAG laser fourth harmonic at  $4.66\text{ eV}$ , however, is of insufficient energy to produce ionization from the  $v' = 8$  level (Figure 1, R2PI scheme (c)). This implies a lower bound of  $7.9\text{ eV}$  ( $3.24 + 4.66\text{ eV}$ ) for the ionization potential of  $\text{Si}_2$ . If it were possible to observe the H state vibrational excitation necessary to allow ionization by fourth harmonic radiation, a closer bracketing of the  $\text{Si}_2$  ionization potential could be achieved. However, predissociation of the  $\text{Si}_2$  H state prevents the clear observation of levels higher than  $v' = 8$ . This is evidenced in Figure 4 where LIF reveals the  $H(v' = 8) - X(v'' = 0)$  transition clearly while only a broad fluorescence is observed in the  $v' = 9$  wavelength region, signaling the clear onset of predissociation. The calculated position for the  $H(v' = 9) - X(v'' = 0)$  transition is indicated in the figure. Franck-Condon factors calculated for the H-X transition (using the new vibrational numbering) reveal that the  $(9, 0)$  transition has a larger Franck-Condon factor than the  $(8, 0)$  transition, yet only the broad fluorescence (whose shape is determined primarily by the laser dye curve and not the  $\text{Si}_2$  absorption) is observed.

### Discussion

The experimental results which we have obtained in this study for the first time experimentally bracket the  $\text{Si}_2$  ionization potential between  $7.9$  and  $8.08\text{ eV}$ . This bracketing does not account for field ionization effects, which have previously been shown to be of importance for the accurate determination of ionization potentials<sup>13</sup>. While field ionization was not explicitly

studied here, the electric fields present in the time-of-flight mass spectrometer only raise the ionization potential upper bound by  $\sim 120 \text{ cm}^{-1}$  to 8.1 eV. The determined I. P. range is in agreement with the lower bound established by Trevor et al.<sup>10</sup> and Heath et al.<sup>11</sup> who observed that  $\text{F}_2$  excimer laser photons are of insufficient energy to produce a single photon ionization of  $\text{Si}_2$ , thus establishing an I. P. in excess of 7.87 eV. Our measurements also agree with the I. P. value reported by Boo and Armentrout<sup>9</sup> from the enthalpy of formation of  $\text{Si}_2^-$  ( $8.04 \pm 0.13 \text{ eV}$ ), and with the most recent theoretical prediction of Curtiss et al.<sup>6</sup> (7.94 eV) using the G2 theoretical procedure.

The 7.9 to 8.1 eV range established by our ionization potential measurements is, however, in distinct disagreement with the conclusions of Fuke et al.<sup>2</sup> Using stimulated Raman scattering techniques to generate 7.46, 7.97, and 8.49 eV photons, Fuke et al. report that even an 8.49 eV photon does not possess sufficient energy to single photon ionize  $\text{Si}_2$ . This assertion is based on the very small  $\text{Si}_2$  signals observed when 146 nm (8.49 eV) radiation is used as an ionization source in their time-of-flight mass spectrometer. However, a close examination of Fuke et. al.'s Figure 5 (which shows no dimer signal for 7.46 eV ionization) reveals a small but noticeable dimer ion peak with 7.97 eV ionization, consistent with the current bracketed values.

#### Acknowledgements

We wish to express our appreciation to Dr. Richard Oldenborg of Los Alamos National Laboratory for allowing us the use of the Lambda-Physik EMG102 excimer laser. The support of the Army Research Office through grant number DAAH04-93-G-0195 is also greatly appreciated.

## REFERENCES

1. For example  
K. Raghavachari, Phase Transitions **24-26**, 61 (1990).  
C. C. Arnold and D. M. Neumark, J. Chem. Phys. **100**, 1797 (1994).
2. K. Fuke, K. Tsukamoto, F. Misaizu, and M. Sanekata, J. Chem. Phys. **99**, 7807 (1993).  
K. Fuke, K. Tsukamoto, F. Misaizu, Z. Phys. D **26**, 5204 (1993).
3. S. Hayashi, Y. Kanzawa, M. Kataoka, T. Nagarede, and K. Yamamoto, Z. Phys. D **26**, 144 (1993).
4. K. Raghavachari and V. Logovinsky, Phys. Rev. Lett. **55**, 2853 (1985).
5. K. Raghavachari, J. Chem. Phys. **84**, 5672 (1986) and references therein.
6. L. A. Curtiss, K. Raghavachari, P. W. Deutsch, J. A. Pople, J. Chem. Phys. **95**, 2433 (1991).
7. J. Drowart, G. D. Maria, and M. G. Inghram, J. Chem. Phys. **29**, 1015 (1958).
8. G. Verhaegen, F. E. Stafford, and J. Drowart, J. Chem. Phys. **40**, 1622 (1964).
9. B. H. Boo and P. B. Armentrout, J. Am. Chem. Soc. **109**, 3549 (1987).
10. D. J. Trevor, D. M. Cox, K. C. Reichmann, R. O. Brickman, and A. Kaldor, J. Phys. Chem. **91**, 2598 (1987).
11. J. R. Heath, Y. Liu, S. C. O'Brien, Q. Zhang, R. F. Curl, F. K. Tittel, and R. E. Smalley, J. Chem. Phys. **83**, 5520 (1985).
12. See for example K. D. Brommer, M. Needels, B. E. Larson, and J. D. Joannopoulos, Phys. Rev. Lett. **68**, 1355 (1992), I. Stich, M. C. Payne, R. D. King-Smith, and J. S. Lin **68**, 1351 (1992), N. Binggeli and James R. Chelikowsky, Phys. Rev. B **50**, 11764 (1994).
13. C. B. Winstead, S. J. Paukstis, J. L. Walters, and J. L. Gole, J. Chem. Phys., in press.

14. R. Woodward, P. N. Le, M. Temmen, and J. L. Gole, *J. Phys. Chem.* **91**, 2637 (1987).
15. C. B. Winstead, S. J. Paukstis, and J. L. Gole, in preparation.
16. I. Dubois and H. Leclercq, *Can. J. Phys.* **39**, 3053 (1971).

## FIGURE CAPTIONS

Figure 1: Resonant two photon ionization schemes for  $\text{Si}_2$ . Schemes (a) and (b) use KrF excimer ionization from the  $\text{Si}_2 \text{H } ^3\Sigma_u^-$  ( $v' = 3$ ) and ( $v' = 8$ ) vibrational levels. Scheme (c) depicts attempted Nd:YAG 4th harmonic ionization of the  $\text{H } ^3\Sigma_u^-$  ( $v' = 8$ ) level. See text for discussion.

Figure 2: LIF and R2PI spectra of the  $\text{Si}_2 \text{H } ^3\Sigma_u^-$  ( $v' = 2-5$ ) -  $\text{X } ^3\Sigma_g^-$  ( $v'' = 0$ ) transitions. The R2PI spectrum was obtained in the  $\text{Si}^{28}\text{Si}^{30}$  mass channel to reduce background noise caused by KrF resonant ionization of iron atoms in the  $\text{Si}^{28}\text{Si}^{28}$  mass channel. The shift in the bandhead energies between the LIF and R2PI spectra is caused by the isotope effect. The higher temperature of the oven produced clusters results in the observation of an extended rotational structure. See text for discussion.

Figure 3: LIF and R2PI spectra of the  $\text{Si}_2 \text{H } ^3\Sigma_u^-$  ( $v' = 8$ ) -  $\text{X } ^3\Sigma_g^-$  ( $v'' = 0$ ) transition. KrF excimer radiation produces ionization from the  $\text{H } (v' = 8)$  level, whereas Nd:YAG 4th harmonic does not. Features marked by an asterisk (\*) in the KrF R2PI spectrum result from fluctuations in the background signal caused by KrF resonant ionization of iron atoms. The R2PI spectrum was recorded in the  $\text{Si}^{28}\text{Si}^{28}$  mass channel to provide a direct comparison to LIF spectra. See text for discussion.

Figure 4: LIF spectrum in the wavelength region of the  $\text{Si}_2 \text{H } ^3\Sigma_u^-$  ( $v' = 8-9$ ) -  $\text{X } ^3\Sigma_g^-$  ( $v'' = 0$ ) transitions. While the transition to the ( $v' = 8$ ) level is clearly visible, predissociation obscures the transition to the ( $v' = 9$ ) level. The calculated position of the  $\text{H } (v' = 9)$  -  $\text{X } (v'' = 0)$  transition is

indicated in the figure. See text for discussion.

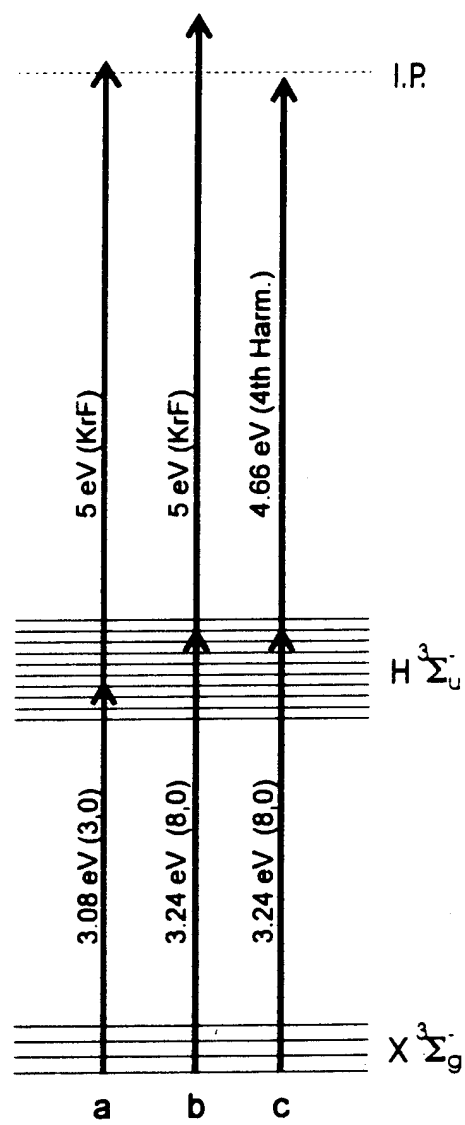


Figure 1

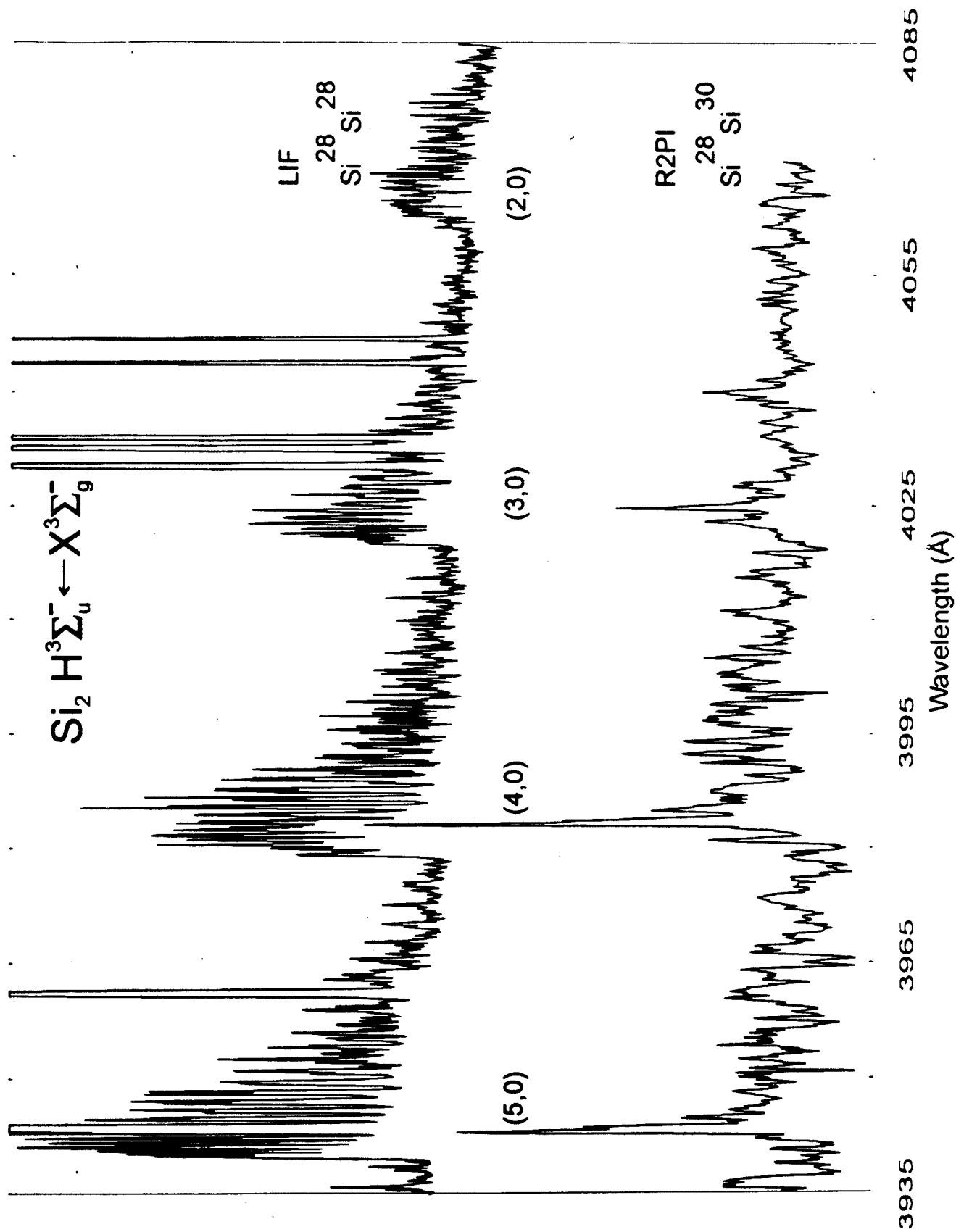


Figure 2

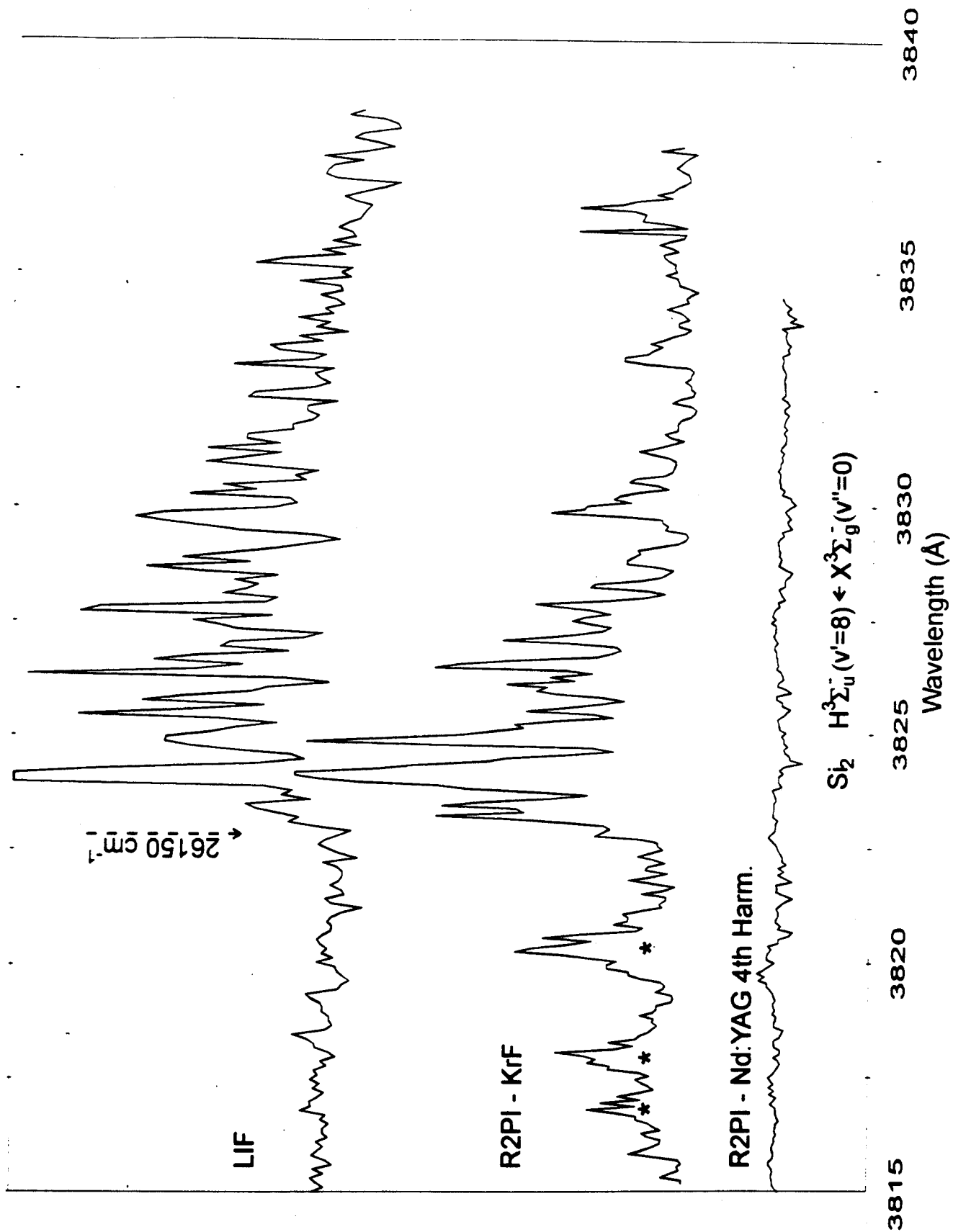


Figure 3

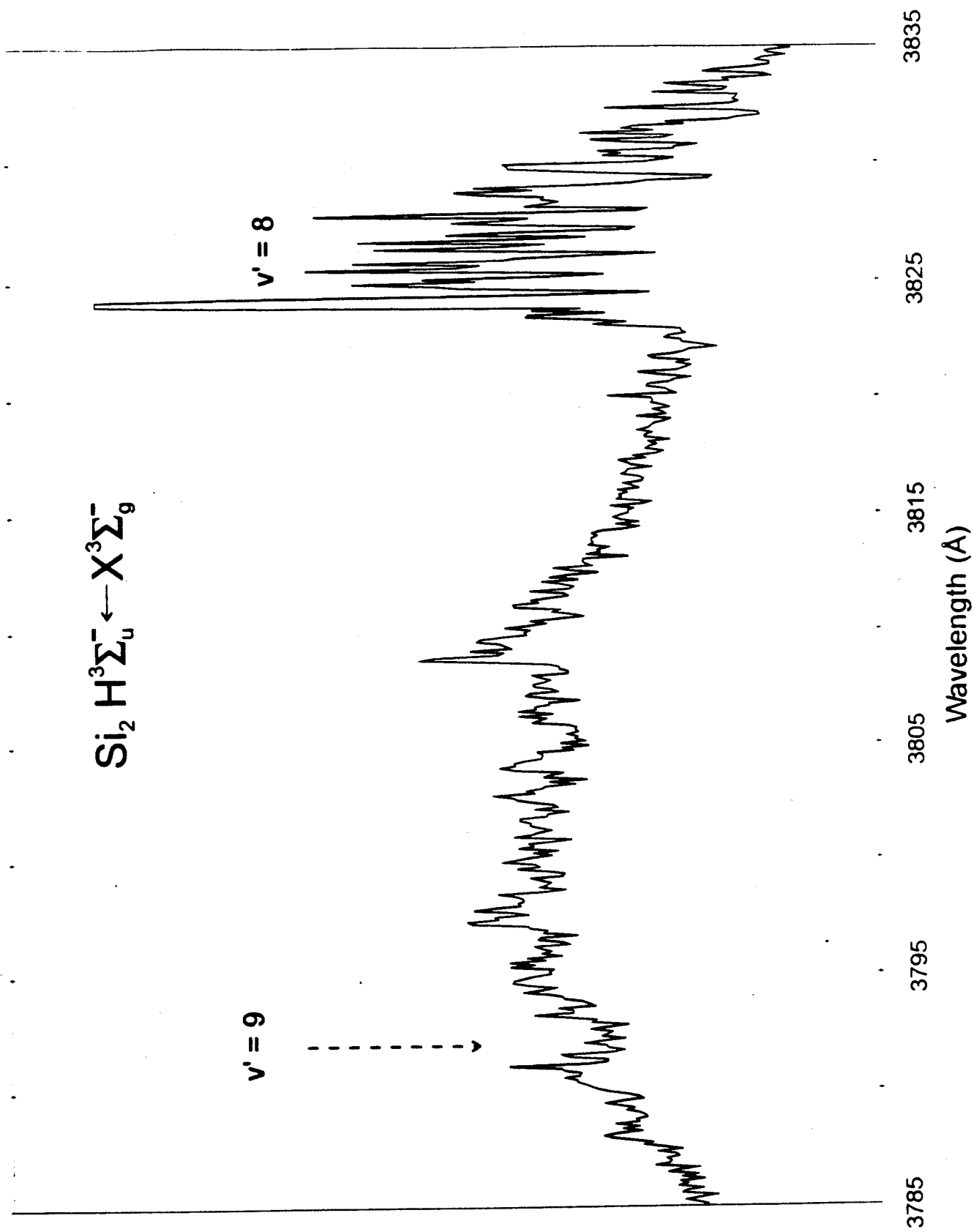


Figure 4

## APPENDIX XIV

"Spectroscopy of the  $H^3\Sigma_u$  Electronic State of  $Si_2$  Using A Combined Laser Vaporization-Rempi And Oven Based LIF Study", C. B. Winstead, S. J. Paukstis, and J. L. Gole, Journal of Molecular Spectroscopy in press.

**SPECTROSCOPY OF THE  $H^3\Sigma_u^-$  ELECTRONIC STATE OF  $Si_2$  USING A  
COMBINED LASER VAPORIZATION-REMPI AND OVEN BASED LIF STUDY**

by

C. B. Winstead, S. J. Paukstis, and J. L. Gole

School of Physics  
Georgia Institute of Technology  
Atlanta, Georgia 30332

**Running Heading:** Laser Spectroscopy of Silicon Dimer

**Proofs to:** Prof. James L. Gole  
School of Physics  
Georgia Institute of Technology  
Atlanta, GA 30332

## Laser Spectroscopy of Silicon Dimer

### Abstract

Laser induced fluorescence and resonant two photon ionization techniques have been combined to study the  $H^3\Sigma_u^-$  state of  $Si_2$ . A measurement of the isotope induced bandhead shifts reveals that the previously accepted vibrational numbering of the  $H^3\Sigma_u^-$  state is incorrect. Revised molecular constants based on the new vibrational numbering scheme are  $T_e = 24151.86$   $cm^{-1}$ ,  $\omega_e = 279.28$   $cm^{-1}$ ,  $\omega_e x_e = 1.99$   $cm^{-1}$ ,  $B_e = 0.17255$   $cm^{-1}$ , and  $\alpha_e = 0.00135$   $cm^{-1}$ . Lower bound measurements of the  $H^3\Sigma_u^-$  radiative lifetime ( $P_T \sim 1500$  mTorr) are reported. Resonant two photon ionization of the  $H^3\Sigma_u^-$  state has allowed the bracketing of the  $Si_2$  ionization potential between 7.9 and 8.1 eV.

## Introduction

Although Downie and Barrow (1) first observed the flame emission spectrum of silicon dimer in 1947, the first extensive study of the dimer was carried out by Douglas in 1955 (2). Using an electric discharge through silane, Douglas was able to identify two band systems associated with the  $X^3\Sigma_g^-$ ,  $D^3\Pi_u$ ,  $H^3\Sigma_u^-$ , and  $L^3\Pi_g$  electronic states. No absolute vibrational numbering was obtained for either of the states active in the  $H^3\Sigma_u^- - X^3\Sigma_g^-$  transition. However, as outlined in Fig. 1, the transitions observed by later investigators (3,4) were used to modify the relative numbering scheme used by Douglas and to determine a suggested absolute H and X state vibrational numbering. Douglas was also the first to suggest that an abrupt termination of the H - X band system following the most intense emission features observed in the spectrum resulted from predissociation.

In examining the absorbing products of the flash photolysis of phenyl and bromosilane, Verma and Warsop (3) observed several additional  $Si_2$  excited state band systems and transitions from the lowest vibrational level of the ground electronic state to the  $H^3\Sigma_u^-$  state. While their observations allowed an absolute vibrational numbering for the  $X^3\Sigma_g^-$  ground state to be established, a relative numbering was still necessary for the  $H^3\Sigma_u^-$  state (whose predissociation was also noted). Verma and Warsop observed a vibrational level one quanta higher in the H state than did Douglas, although this level was diffuse and appeared to be homogeneously perturbed. Like Douglas, Verma and Warsop suggested that the  $Si_2$  ground electronic state corresponded to a  $(\sigma_g 3s)^2(\sigma_u 3s)^2(\sigma_g 3p)^2(\pi_u 3p)^2$  <sup>valence</sup> electron configuration, while the H state was associated with the promotion of a  $\pi_u$  electron to form the  $(\sigma_g 3s)^2(\sigma_u 3s)^2(\sigma_g 3p)^2(\pi_u 3p)^1(\pi_g 3p)^1$  valence configuration. This suggestion was later confirmed in ab initio calculations performed by Peyerimhoff and Buenker (5), who assigned the H state as the lowest-lying  $^3\Sigma_u^-$  state of  $Si_2$ . As noted by Verma and Warsop, the H state dissociates into  $^3P$  and  $^1D$  products, while the  $X^3\Sigma_g^-$  ground state dissociates to two  $^3P$  ground state silicon atoms. The predissociation of the H state provides an upper bound for the ground state dissociation energy of approximately 3.2 eV, in close agreement with the thermodynamic measurements (6) of the ground state bond energy. Thus, the H state predissociation likely results from an interaction with a state arising from the same limit as the ground state dissociation products.

In 1971, Dubois and Leclercq (4) reported the observation of several new vibrational bands of the  $\text{Si}_2 \text{H}^3\Sigma_u^- - \text{X}^3\Sigma_g^-$  band system, again observed in the absorption from silane discharges. Dubois and Leclercq observed an H state vibrational level one quanta lower in energy than that observed by Douglas (2) (Fig. 1), and it was assumed that this vibrational level was indeed the  $v = 0$  level of the H state. This observation provided the basis for the subsequently used H state vibrational numbering. The accepted values (7) for all H state spectroscopic constants ( $T_e$ ,  $\omega_e$ ,  $\omega_e x_e$ ,  $B_e$  and  $\alpha_e$ ) were thus based upon the assumptions that the H state  $v = 0$  level had been observed.

In this manuscript, we demonstrate the value of combining mass selected (time-of-flight) R2PI spectroscopy on cold  $\text{Si}_2$  molecules produced through laser vaporization-adiabatic expansion with a correlated laser induced fluorescence (LIF) spectroscopy on the entrained and cooled  $\text{Si}_2$  molecules generated from an oven based source. While the laser vaporization-supersonic expansion and time-of-flight mass spectroscopy techniques readily provide mass selection, making isotopic labeling simple, the oven based experiments allow the analysis of an extensive rotational structure. Here, we use this combination to revise the vibrational numbering of the  $\text{H}^3\Sigma_u^-$  state. Revised molecular constants have been evaluated based on the new vibrational numbering scheme. The first measurements of  $\text{H}^3\Sigma_u^-$  fluorescence lifetimes (vibrationally resolved) are presented and resonant two photon ionization through the  $\text{H}^3\Sigma_u^-$  state is used to establish an accurate bracketing of the  $\text{Si}_2$  ionization potential.

## Experimental Procedures

### High Concentrations of Silicon Molecules From an Oven-Based Source

An oven based configuration has been used to produce silicon dimers and higher silicon clusters for LIF studies. This source configuration, which has been described in detail elsewhere (8), has previously been applied in the investigation of metal cluster oxidation reactions. In this study, we produced silicon dimer using a crucible (Fig. 2) machined from a high density carbon rod (MicroMech T-6) and half-filled with high purity silicon powder (Johnson-Matthey Electronics, 99.5%). The crucible was heated in a well insulated configuration (Fig. 2 zirconia

cloth, felt, and tubing-Zircar inc., Florida, N.Y.) to temperatures ranging from 1400 to 2000° C using a tungsten basket heater (R. D. Mathis). In order to carry out this experiment, the temperature of the basket heater was increased slowly to 1300° C. At this point, an even slower heating cycle was instituted until the silicon melted (~1380° C). This process of slow heating was used to avoid the insufficient outgassing of the silicon melt (which could lead to the destruction of the silicon basket heater). Once sufficiently outgassed, the temperature of the melt could be raised more quickly. The crucible temperature was monitored using an optical pyrometer (Leeds and Northrup).

The basket heater and crucible were mounted between two water-cooled copper electrodes within a water cooled oven housing (Fig. 2). Carrier gas inlets located in the cap of the housing could be used to create a converging flow region at the cap. Silicon vapor effusing from the crucible was entrained in the carrier gas flow, its concentration increasing as the flow converged. Collisions between the silicon vapor, carrier gas (typically helium), and housing cap cooled and condensed the silicon vapor. The temperature of the housing cap was controlled by circulating water, liquid nitrogen, or dry ice cooled methanol (8). The flow of carrier gas and silicon molecules emerged from the cap into the center of the vacuum chamber containing the oven source, where LIF was used to investigate the  $\text{Si}_2\text{H}$  state. The vacuum chamber was evacuated by a Sergeant-Welch 1397 mechanical vacuum pump, which allowed the attainment of background pressures as low as 10 mTorr.

## Pulsed Laser Induced Fluorescence

Pulsed LIF studies of the  $\text{Si}_2\text{H } ^3\Sigma_u^-$  state were performed using a configuration modified only slightly from that already discussed in the literature (9). Fig. 3 depicts the experimental arrangement used for these investigations. Briefly, a tunable (dye) laser beam entered the vacuum chamber (containing the silicon oven), crossing the flow from the oven source at a right angle. The resulting LIF from the H state was monitored by a blank photomultiplier tube (Hamamatsu R446) mounted as shown on the chamber.

To maximize the collection of the LIF, a 2.5" focal length lens was used to focus the image of the fluorescence zone directly onto a slit in front of the phototube. By scanning the dye

laser through the  $H^3\Sigma_u^- - X^3\Sigma_g^-$  transition wavelength region, a rotationally resolved spectrum of the  $H - X$  transition was obtained. Spectral calibrations were carried out using background atomic fluorescence features excited by the dye laser.

### Dispersed Laser Induced Fluorescence

Each  $Si_2$  feature observed using the total fluorescence technique corresponded to a sum of the fluorescence signals to several ground state levels. To observe the frequency distribution of the total fluorescence signal, a spectrometer was used to disperse the light originating at the fluorescence zone. With the laser frequency set on an  $Si_2$  H state resonance, a wavelength scan of the resulting fluorescence was performed by the spectrometer.

The experimental configuration for dispersed LIF is depicted in Fig. 4. A 1 meter Czerny-Turner spectrometer (SPEX Industries 1704) was used to disperse the LIF which was focused onto the spectrometer using a two lens system. The first lens collimated the light from the fluorescing  $Si_2$  molecules, while the second focused the collimated light onto the entrance slit of the spectrometer. The second lens was chosen in order to match the f numbers of the lens system and spectrometer. The precise alignment of these lenses, the oven configuration, and the spectrometer, was accomplished with a HeNe laser (9(b)). The focal lengths of the lenses and the dimensions of the experiment are indicated in Fig. 4.

### Laser Induced Fluorescence Data Acquisition

The current from the photomultiplier tube monitoring the LIF was amplified by a 20 dB video amplifier (Comlinear CLC100) prior to being sent to a gated boxcar integrator (Stanford Research SR250). A digital oscilloscope (Hewlett-Packard 54111D) was used to view the phototube signal. Although attempts were made to minimize the scattered laser light reaching the phototube, some scattered signal was always visible on the oscilloscope. A rejection of this undesirable scattering was accomplished using the appropriate timing of the gate from the boxcar integrator. In this way, only the exponential decay of the LIF was monitored by the boxcar, integrated during the gate time, and converted into a DC output signal. The boxcar gate was set to a time just after the dye laser firing, this procedure resulting in the rejection of most of

the scattering signal. However, the photomultiplier tube current did not immediately return to its zero level after the laser fired, thus introducing some small scattering signal into the LIF scans. This manifested itself in the observation of a background dye output curve visible only in scans of weak fluorescence features. The averaging of the boxcar integrator, the analog to digital conversion of the boxcar output voltage, and the control of the laser scans were accomplished in the same manner as that described for recent studies of the resonant multiphoton ionization of silver dimer (9(b),10).

## Resonant Two Photon Ionization

Resonant two photon ionization (R2PI) studies of silicon dimer were performed using the precise experimental configuration employed previously in our study of the resonant multiphoton ionization of  $\text{Ag}_2$  (10). Some further discussion of this experimental configuration is presented in a following section.

## Results

### Laser Induced Fluorescence - Oven Based Configuration

A pulsed LIF spectrum of the  $\text{H } ^3\Sigma_u^- - \text{X } ^3\Sigma_g^-$  transition is presented in Fig. 5. Here, the frequency mixed output from a Nd:YAG pumped pulsed dye laser (operating with DCM laser dye) was used to excite  $\text{Si}_2$  molecules produced from an oven source. The resulting fluorescence was monitored using a Hamamatsu R446 photomultiplier tube. Transitions originating from the lowest two vibrational levels ( $v'' = 0$  and 1) of the  $\text{X } ^3\Sigma_g^-$  state to five  $\text{H } ^3\Sigma_u^-$  vibrational levels ( $v' = 2-6$ ) are depicted in the figure. While the rotational features associated with the  $(v',v'') = (6,0)$  and  $(5,0)$  transitions are well-resolved, the  $(4,0)$ ,  $(3,0)$ , and  $(2,0)$  bands are overlapped by the  $(6,1)$ ,  $(5,1)$ , and  $(4,1)$  features. Crucible temperatures in excess of 1500 C were required to obtain a silicon vapor pressure sufficient to produce the necessary concentration of  $\text{Si}_2$ . Flow conditions which raised the vacuum chamber pressure to 1500 mtorr were required to maximize the silicon dimer fluorescence signal. The spectrum in Fig. 5 was also used to outline regions for the dispersed LIF studies which will be the subject of the following discussion. These dispersed

fluorescence results will be described in concert with our consideration of the H state vibrational numbering.

An expanded view of the H ( $v' = 6$ ) - X ( $v'' = 0$ ) fluorescence is shown in Fig. 6, where the individual P and R branches of the rotational structure are denoted. The depicted spectrum was calibrated using the iron atomic fluorescence features visible in the figure. The measured rotational line energies were reproducible to within  $\pm 0.35 \text{ cm}^{-1}$ . A  $^3\Sigma_u^- \rightarrow ^3\Sigma_g^-$  transition belongs strictly to Hund's coupling case *b* (11) so that the quantum number *N* labels the observed rotational transitions. Each rotational feature in the figure is composed of three separate components corresponding to the three vectorial combinations of the *N* vector and the projections of the total spin vector *S*. These components,  $J = N, N-1$ , and  $N+1$ , are not resolved in the spectrum of Fig. 6. For a  $\Sigma \rightarrow \Sigma$  transition, the selection rule  $\Delta N = \pm 1$  thus results in the formation of the P ( $\Delta N = -1$ ) and R ( $\Delta N = +1$ ) branches.

From the labeling of the rotational structure, it is immediately obvious that only odd numbered rotational lines are present in the fluorescence spectrum. Symmetry constraints, associated with the zero nuclear spin of the  $^{28}\text{Si}$  atom and the  $^3\Sigma_g^-$  ground state of silicon dimer, result in the population of only odd numbered ground state rotational levels (for  $^{28}\text{Si}^{28}\text{Si}$  (2,3)). For each *N* level observed, a fit of the measured features in Fig. 6 (using the appropriate combination difference expressions (11)) allowed an evaluation of the  $B_v'$  and  $B_v''$  rotational constants for the upper and lower state vibrational levels associated with the electronic transition. The average measured  $B_v'$  value ( $0.163 \text{ cm}^{-1}$ ) compares favorably with the  $B_v$  value calculated using the H state rotational constants  $B_e$  and  $\alpha_e$  determined from earlier absorption experiments ( $0.164 \text{ cm}^{-1}$ ) (2,3,4). Table I lists the observed and calculated rotational level energies for the H  $^3\Sigma_u^-$  ( $v' = 6$ ) - X  $^3\Sigma_g^-$  ( $v'' = 0$ ) transition. The calculated energies listed in Table I, which effectively reproduce the observed rotational energies, were obtained using the previously accepted vibrational numbering and constants (7). As will be demonstrated, however, the vibrational numbering used to obtain these constants was incorrect, necessitating their revision.

A consequence of the large difference between the H  $^3\Sigma_u^-$  and X  $^3\Sigma_g^-$  rotational constants ( $0.164 \text{ cm}^{-1}$  vs  $0.238 \text{ cm}^{-1}$ ) is the virtual absence of a bandhead structure in Fig. 6. The expected

turn-around in the R branch for the H - X (6,0) transition occurs at the  $N = 2$  rotational level. For  $^{28}\text{Si}^{28}\text{Si}$  the  $N = 0$  and 2 levels are not populated. Therefore the R branch simply begins at  $N = 1$ . As indicated in Table I, the first line encountered on the high energy side of the H ( $v' = 6$ ) - X ( $v'' = 0$ ) transition is the R(1) line. This behavior persists throughout the vibrational bands investigated in the current study. The rapid turnaround of the R branch has important implications for the character of an observed R2PI spectrum and the measurement of the isotope shifts which we describe in a following section.

### **H $^3\Sigma_u^-$ Lifetime Measurements**

Using pulsed dye LIF, we have determined the vibrationally resolved radiative lifetimes for several of the lowest levels of the  $\text{Si}_2$  H  $^3\Sigma_u^-$  electronic state. Fig. 7 depicts the exponential decay of the fluorescence following excitation of the P(7) line of the H ( $v' = 6$ ) - X ( $v'' = 0$ ) transition. The initial scattering signal resulting from the firing of the laser is apparent in the figure, followed by the signal resulting from the fluorescence of the  $v' = 6$  level of the H  $^3\Sigma_u^-$  state. For reliable data collection, sixty-four averages were performed on this fluorescence waveform using a Hewlett-Packard 54111D digital oscilloscope. The depicted waveform was stored in the oscilloscope memory and subsequently transferred through IEEE-488 communications to an I.B.M. compatible computer for further storage and analysis. The measured lifetimes given in Table II were obtained through least squares fitting of the observed waveform to a single exponential function (using the program Peakfit from Jandel Software). Each vibrational level was pumped via a P(3) to P(7) transition.

As is apparent from Table II, the lifetimes of the lower vibrational levels of the H  $^3\Sigma_u^-$  state were determined to be near 100 nanoseconds at  $P_{\text{Total}} = 1500$  mTorr. Because these lifetime measurements were carried out at an elevated pressure, collisional deactivation should lead to a shortening of the measured lifetimes. Thus, these values must be regarded as lower bounds for the H state fluorescence lifetimes. The measured H ( $v' = 5$ ) lifetime of 120ns may signal the perturbation mixing of this level with a longer-lived electronic state. The isotope shift data which we consider in a following section also displays an anomalous behavior for the  $v' = 5$  level.

### Resonant Two-Photon Ionization Spectroscopy of Si<sub>2</sub>

We have employed R2PI spectroscopy to determine the absolute vibrational numbering of the silicon dimer  $H^3\Sigma_u^-$  state and to bracket the dimer ionization potential. A laser vaporization cluster source, time-of-flight mass spectrometer, and pulsed laser system (9,10) were combined to accomplish this study. A silicon rod (Metron, 99.999% purity, 1/2 inch diameter) provided the target sample in a pulsed valve nozzle assembly, with helium serving as the carrier gas. Both stainless steel and aluminum nozzle assemblies were used to house the sample rod and provide a channel for cluster nucleation. The use of the aluminum nozzle assembly was preferred in mass selected studies of silicon dimer because the most abundant isotopes of iron and Si<sub>2</sub> have the same atomic mass, 56 amu. Iron atoms are resonantly ionized by KrF excimer radiation, leading to a large background signal in the Si<sub>2</sub> mass channel. The use of the aluminum nozzle assembly (rather than the iron-rich stainless steel assembly) reduced this iron atom contamination significantly, though it did not remove it entirely.

The resonant two photon ionization spectroscopy of Si<sub>2</sub> was implemented using the techniques which have been described in detail in the literature (9,10). The gate from a boxcar averager was adjusted to coincide temporally with one of the Si<sub>2</sub> isotopic mass channels. Laser radiation from a Nd:YAG pumped pulsed dye laser system was used to excite Si<sub>2</sub> molecules into the  $H^3\Sigma_u^-$  excited electronic state, with subsequent ionization accomplished by photons from an excimer laser or the Nd:YAG laser fourth harmonic. Both pump and ionization laser powers were adjusted so that each laser alone produced no dimer signal. Figure 8 depicts exemplary R2PI spectra obtained for the  $H^3\Sigma_u^- - X^3\Sigma_g^-$  transition of the three dominant Si<sub>2</sub> isotopes. The shift in vibrational energies due to the isotope effect is evident. The output from the Nd:YAG pumped pulsed dye laser, operating with DCM laser dye, was frequency mixed with the Nd:YAG fundamental to provide the appropriate energy photons to excite several H state vibrational levels. Radiation from an excimer laser, operating with an ArF gas mixture (193 nm), ionized the excited state dimer molecules. The spectrum in Fig. 8 shows a progression originating from the lowest vibrational level of the ground electronic state of the internally cold silicon dimer molecules to several excited state vibrational levels. The ready identification and

assessment of the nature of this spectrum is facilitated by the mass selectivity of the R2PI process and the cross correlation of the sparse R2PI with extensive LIF spectra.

### Comparison of R2PI and LIF Spectra

The appearance of spectra obtained using the R2PI of supersonically cooled  $\text{Si}_2$  molecules differed dramatically from those obtained using the LIF of oven produced  $\text{Si}_2$ . In Fig. 9, R2PI and LIF spectra of the  $\text{Si}_2 \text{H}^3\Sigma_u^- - \text{X}^3\Sigma_g^-$  transition are compared. The R2PI spectrum results from the monitoring of the  $^{28}\text{Si}^{28}\text{Si}$  isotopic mass channel. Whereas an extended rotational structure is clearly visible for the LIF scan, only the bandheads are visible for the R2PI scan. The difference in the rotational temperatures for the laser vaporization produced adiabatically expanded and oven produced silicon dimer molecules can be shown to account for the difference in appearance of the R2PI and LIF features.

From the relationship for the distribution of rotational levels, the maximum intensity in a rotational distribution is reached at a rotational level (11)

$$J_{\max} = \sqrt{\frac{kT}{2Bhc}} - \frac{1}{2}. \quad (1)$$

The value of  $J_{\max}$  increases with increasing temperature, as does the total number of rotational levels populated. As opposed to the LIF spectra of oven produced  $\text{Si}_2$ , the bandhead region represents the most intense spectral feature in the R2PI spectrum of supersonically cooled  $\text{Si}_2$ . A comparison with the LIF spectra suggests that the maximum intensity rotational transitions observed in the R2PI spectra can be associated with no greater than the  $N'' = 3$  rotational level. A  $J_{\max} = 3$  (or  $N_{\max}$  for the  $\text{Si}_2 \text{X}$  state) implies a rotational temperature close to 8K (as one might expect for an efficient supersonic expansion). While the  $\text{Si}_2$  molecules produced in the oven source were cooled by collisions with the entraining carrier gas, the extent of cooling was far less than that achieved in a supersonic expansion. The maximum intensity of the bands observed in the LIF spectroscopy of oven produced silicon dimer was typically reached near  $N = 21-25$ , implying a rotational temperature of 300 - 450 K. Rotational temperatures of this magnitude

demonstrate the degree of thermalization achieved in the carrier gas flow, since the required temperature of the Si vapor was achieved with  $T_{\text{oven}} \geq 1500\text{K}$  to produce a sufficient concentration for the efficient detection of silicon dimer. While the production of low temperature molecules for spectroscopy is often desirable to simplify spectral analysis, a combination of moderate and low temperature spectroscopy clearly reveals more information than either technique alone.

## Isotope Shift Measurements and the Absolute Vibrational Numbering of the $\text{H } ^3\Sigma_u^-$ State

Although spectra involving several vibrational levels of the  $\text{H } ^3\Sigma_u^-$  state of  $\text{Si}_2$  have been observed previously, no absolute numbering for the vibrational levels could be established before this study. The spectroscopic constants now employed for  $\text{Si}_2$  are based upon the assumption that the absorption to the lowest observed vibrational level of the  $\text{H } ^3\Sigma_u^-$  state corresponded to the  $v = 0$  level (Fig. 1). Using the isotope effect, we demonstrate that this assumption is incorrect and establish an absolute numbering for the H state vibrational levels. Vibrational and rotational constants are then corrected for the new numbering scheme, establishing a final set of spectroscopic parameters.

For an electronic transition from the ground electronic state, the observed frequencies of the energy levels for two isotopes are given by

$$\nu = \nu_e + \omega'_e \left( v' + \frac{1}{2} \right) - \omega'_e \chi'_e \left( v' + \frac{1}{2} \right)^2 - \omega''_e \left( v'' + \frac{1}{2} \right) + \omega''_e \chi''_e \left( v'' + \frac{1}{2} \right)^2 \quad (2)$$

and

$$\begin{aligned} \nu_i = \nu_e + \rho \omega'_e \left( v' + \frac{1}{2} \right) - \rho^2 \omega'_e \chi'_e \left( v' + \frac{1}{2} \right)^2 \\ - \rho \omega''_e \left( v'' + \frac{1}{2} \right) + \rho^2 \omega''_e \chi''_e \left( v'' + \frac{1}{2} \right)^2, \end{aligned} \quad (3)$$

where  $\rho$  is given by the usual relation involving isotopes and reduced masses,

$$\rho = \frac{v_i}{v} = \sqrt{\frac{\mu}{\mu_i}}, \quad (4)$$

and  $v_e$  represents the zeroth order energy (in  $\text{cm}^{-1}$ ) of the electronically excited state. The magnitude of the shift in vibrational level frequencies measured for two different isotopes of the same molecular species will be given by

$$\begin{aligned} v - v_i = & (1 - \rho)\omega'_e(v' + \frac{1}{2}) - (1 - \rho^2)\omega'_e\chi'_e(v' + \frac{1}{2})^2 \\ & - (1 - \rho)\omega''_e(v'' + \frac{1}{2}) + (1 - \rho^2)\omega''_e\chi''_e(v'' + \frac{1}{2})^2, \end{aligned} \quad (5)$$

where the isotope shift increases as the excited state vibrational excitation increases. Setting  $v'' = 0$  in this equation (since the transitions observed using R2PI all originate in the lowest vibrational level of the ground state) and solving for  $v'$  yields

$$v' = \frac{(1 - \rho)\omega'_e \pm \sqrt{Z}}{2(1 - \rho^2)\omega'_e\chi'_e}, \quad (6)$$

where

$$\begin{aligned} Z = & [(1 - \rho)\omega'_e]^2 \\ & - 4[1 - \rho^2]\omega'_e\chi'_e[\frac{1}{2}(1 - \rho)\omega''_e - \frac{1}{4}(1 - \rho^2)\omega''_e\chi''_e + v - v_i]. \end{aligned} \quad (7)$$

Thus, the measurement of the difference in vibrational frequencies ( $v - v_i$ ) for a given vibrational level may be used to calculate the absolute numbering ( $v'$ ) for the vibrational quanta of the level.

Fig. 10 depicts a high resolution scan for a single vibrational level observed in the 56, 57 and 58 amu mass channels for the H - X transition. The measured isotopic shifts are indicated in the figure. The onset of the bandhead for a given vibrational level serves as a measure of the position of the level, as indicated by the vertical dashed lines in the figure. Although the most accurate value for the position of a vibrational band is given by the origin of the band (determined from the rotational structure), the onset of the H state bandhead provides an excellent approximation given the lack of a rotationally resolved R2PI spectrum (9(b)). The rapid reversal of the R branch rotational structure implies that the band origin and bandhead are of similar energies.

Substitution of the measured shifts from Fig. 10 into the vibrational level equation (Eq. 7) reveals that the depicted level is the  $v = 4$  level of the  $H^3\Sigma_u^-$  state. The vibrational numbering scheme used previously (4,7) labels this level as  $v = 3$ . In Table III, the bandhead positions measured for several vibrational levels are listed as well as the calculated and previously used vibrational numbering. An examination of the table reveals that the previously accepted vibrational numbering for the  $H^3\Sigma_u^-$  state was incorrect. One vibrational level, labeled  $v = 4$  in the old scheme and  $v = 5$  using the new numbering, deviates significantly. Interestingly, the lifetime of this level is measured to be 20% longer than other nearby levels (120 ns vs. 100 ns). A perturbation like those seen to effect other H state vibrational levels could easily explain this observed deviation.

### Correction of the $Si_2$ $H^3\Sigma_u^-$ Spectroscopic Constants

The new vibrational numbering for the  $H^3\Sigma_u^-$  state necessitates a revision of the accepted spectroscopic constants. Table IV lists the old and new spectroscopic constants for the  $H^3\Sigma_u^-$  state, while Table V catalogues calculated vibrational energies using the old and new constants. Because the previously accepted H state vibrational numbering and constants accurately predict the observed H - X transition energies, these earlier constants may be simply updated to account for the correct vibrational numbering. The previously accepted (7) H state constants calculated by Dubois and Leclercq (4) were based upon a vibrational numbering ( $v-1$ ) rather than the correct numbering  $v$ . Accounting for this discrepancy in the vibrational energy equation given by

$$v = T_e + \omega_e \left( v + \frac{1}{2} \right) - \omega_e \chi_e \left( v + \frac{1}{2} \right)^2 \quad (8)$$

reveals that the new constants ( $T_e^{(new)}$ ,  $\omega_e^{(new)}$ , and  $\omega_e \chi_e^{(new)}$ ) are given in terms of the old constants ( $T_e$ ,  $\omega_e$ , and  $\omega_e \chi_e$ ) by

$$\begin{aligned} T_e^{(new)} &= T_e - \omega_e - \omega_e \chi_e \\ \omega_e^{(new)} &= \omega_e + 2\omega_e \chi_e \\ \omega_e \chi_e^{(new)} &= \omega_e \chi_e. \end{aligned} \quad (9)$$

A similar correction applied to the effective rotational constant equation

$$B_v = B_e - \alpha_e \left( v + \frac{1}{2} \right) \quad (10)$$

yields the corrected rotational constants

$$\begin{aligned} B_e^{(new)} &= B_e + \alpha_e \\ \alpha_e^{(new)} &= \alpha_e. \end{aligned} \quad (11)$$

The additional significant figure in the revised value for  $B_e$  clearly does not imply an increased accuracy for the new constants but is necessary to reproduce the previously determined (2) H state  $B_v$  values. Since the new constants are based upon a reevaluation of the previously accepted constants (7), the error associated with the new values is that of the old constants. However, previous reports (2, 3, 4) quote no error analysis for the H state spectroscopic constants. A comparison of the observed and calculated rotational level energies listed in Table I provides some insight into the accuracy of the old and new constants.

### Dispersed Laser Induced Fluorescence

The most dramatic demonstration of the effects of the corrected vibrational numbering and constants can be observed when simulating dispersed LIF spectra. Figures 11(a) and 11(b) depict spectra associated with dispersed LIF from the H state ( $v' = 5$ ) and ( $v' = 6$ ) levels respectively. Also depicted are spectra simulated using both the old and new spectroscopic constants. The Nd:YAG pumped pulsed dye laser system, operating near 3940 Å or 3900 Å, was employed to excite a low rotational level of either the H - X (5,0) or (6,0) transition. The resulting fluorescence was dispersed to obtain features associated with transitions from the H state ( $v' = 5$ ) or ( $v' = 6$ ) level to several ground state vibrational levels. The ( $v' = 5$ ) DLIF spectrum was obtained at approximately 10 Å resolution. The scan was digitized by incrementing the spectrometer wavelength in 1 Å steps between data points. The ( $v' = 6$ ) spectrum was observed at a lower 30 Å resolution while the scan wavelength was increased in 5 Å steps. The intensities of the (5,0) and (6,0) transitions appear artificially large due to scattering from the dye laser beam. Since only one H state rotational level was excited in the DLIF scan, the resulting fluorescence to each ground state vibrational level simply consists of the two lines associated with the P and R emissions from this excited rotational level. The spectrometer resolution was insufficient to resolve these two lines, and thus yielded a single peak for each vibrational transition observed.

Simulations of H - X dispersed fluorescence spectra were performed using both the old and new spectroscopic constants. Franck-Condon factors calculated using each set of constants provided a relative intensity distribution for the simulations. An initial simulation spectrum was constructed where each transition between upper and lower state vibrational levels was represented by a single data point. The intensity of each data point was determined by the calculated Franck-Condon factor. Each point of this initial spectrum was then broadened by a 5-15 angstrom (FWHM) Lorentzian function to simulate the transmission-resolution of the spectrometer. The degree of broadening introduced was determined by the spectrometer resolution for the particular spectrum being simulated. The Franck-Condon factors were calculated using software packages executed on an IBM RISC 6000 computer and the turning points of the excited and ground state  $\text{Si}_2$  vibrational levels were calculated using the RKR

method (12). A spline routine was used to construct a curve representing the upper and lower state potentials. Overlap integrals, using wavefunctions calculated for the vibrational levels of each state, determined the Franck-Condon factors. Table VI lists the results of the Franck-Condon factor calculations using the new H state constants for several H - X transitions.

The new spectroscopic constants clearly reproduce the observed intensity distributions much more accurately than do the old constants. For example, the simulation of the emission from the H ( $v' = 5$ ) level (Fig. 11(a)) using the old spectroscopic constants predicts large intensities for the H - X ( $v', v''$ ) = (5,5), (5,9), and (5,13) transitions. The simulation using the new constants accurately predicts the small intensity of these transitions. Further, the determination of additional spectroscopic constants for the H  $^3\Sigma_u^-$  and X  $^3\Sigma_g^-$  states should improve the quantitative agreement between the simulated and observed intensities.

#### Determination of the Silicon Dimer Ionization Potential

Several researchers over the years have attempted to measure (6,13-16) and calculate (17-19) the Si<sub>2</sub> ionization potential. From the earliest electron impact studies (6) (which may have been plagued by low-lying metastable states) to the more recent photoionization studies, the determined IP values have ranged from 7.3 (6) to in excess of 8.49 eV (16). Several of the most recent attempts to bracket the Si<sub>2</sub> IP using photoionization techniques (13,14,16) have yielded only lower bounds.

In the present study, ionization from the Si<sub>2</sub> H  $^3\Sigma_u^-$  state was investigated using both KrF excimer and Nd:YAG laser 4th harmonic radiation (5.0 eV and 4.66 eV photons, respectively). Fig. 12 depicts the R2PI schemes which have been used to closely bracket the Si<sub>2</sub> IP. Fig. 13 depicts a R2PI spectrum of the H  $^3\Sigma_u^-$  - X  $^3\Sigma_g^-$  transition obtained using the pulsed laser vaporization cluster source and the time-of-flight mass spectrometer. The output from the frequency mixed Nd:YAG pulsed dye laser was used to excite various vibrational levels of the H  $^3\Sigma_u^-$  state which were subsequently ionized using KrF excimer radiation. The depicted spectrum was recorded in the  $^{28}\text{Si}^{30}\text{Si}$  mass channel to avoid the high background signal in the  $^{28}\text{Si}^{28}\text{Si}$  mass channel associated with the KrF resonant ionization of iron atoms. Color filters (Schott BG24) were installed in the excimer laser beam path to reduce the laser power and prevent

observation of a nonresonant  $\text{Si}_2$  ionization signal. Ionization by the 5 eV KrF excimer photons was clearly observed for H state vibrational levels as low as  $v' = 3$ . The  $^{28}\text{Si}^{30}\text{Si}$  H ( $v' = 3$ ) - X ( $v'' = 0$ ) transition lies at  $24841 \text{ cm}^{-1}$  or 3.08 eV, implying a silicon dimer ionization potential of less than 8.08 eV (see Fig. 13, R2PI scheme (a)).

The H ( $v' = 2$ ) - X ( $v'' = 0$ ) transition was not observed in the R2PI spectrum. However, it was not possible to clearly establish whether this observation resulted from an insufficient energy to produce ionization. Ionization from the H ( $v' = 2$ ) level is energetically allowed for a single ArF excimer photon (6.4 eV). However, an apparent lower ionization efficiency for ArF ionization from the  $\text{Si}_2$  H state resulted in an insufficient signal to allow the clear observation of the less intense (2,0) vibrational level transition. Thus, no comparison between ArF and KrF excimer laser ionization of the H ( $v' = 2$ ) level could be made. Nevertheless, the upper bound for the dimer I. P. of 8.08 eV was firmly established by the KrF ionization spectrum.

Figure 14 depicts LIF and R2PI spectra obtained for the higher energy H ( $v' = 8$ ) - X ( $v'' = 0$ ) transition. Here, KrF excimer (5.0 eV) and Nd:YAG 4th harmonic (4.66 eV) lasers provided the second photon for the R2PI experiments (Fig. 13, R2PI schemes (b) and (c)). The similarity between the LIF and KrF ionization R2PI scans is evident, as the H ( $v' = 8$ ) - X ( $v'' = 0$ ) transition is readily observed in both. For the KrF R2PI scan, the  $^{28}\text{Si}^{28}\text{Si}$  mass channel was monitored so that a direct comparison with the LIF scan could be depicted. The small peaks located at slightly shorter wavelengths than the H ( $v' = 8$ ) - X ( $v'' = 0$ ) transition in the KrF R2PI scan thus result from fluctuations in the resonantly ionized iron atom background signal. However, the H ( $v' = 8$ ) - X ( $v'' = 0$ ) transition was readily reproducible using a KrF based R2PI. The bandhead of the H ( $v' = 8$ ) - X ( $v'' = 0$ ) transition was located at  $26150 \text{ cm}^{-1}$ , or 3.24 eV, as is indicated in Fig. 14 by the vertical arrow. The figure clearly indicates that Nd:YAG 4th harmonic radiation is not of sufficient energy to produce ionization from the  $v' = 8$  level (Fig. 13, R2PI scheme (c)). This implies a lower bound of 7.9 eV ( $3.24 + 4.66 \text{ eV}$ ) for the ionization potential of  $\text{Si}_2$ .

The observation of higher lying H state vibrational levels using Nd:YAG 4th harmonic ionization could have resulted in even tighter bracketing the  $\text{Si}_2$  ionization potential. However,

the predissociation of the  $\text{Si}_2$  H state prevented the clear observation of levels higher than  $v' = 8$  (20).

The preceding results bracket the  $\text{Si}_2$  ionization potential between 7.9 and 8.08 eV. This bracketing does not account for field ionization, demonstrated to be important in the previous determination of the  $\text{Ag}_2$  ionization potential (10). While this field ionization was not specifically studied for  $\text{Si}_2$ , the electric fields present in the time-of-flight mass spectrometer can raise the ionization potential upper bound by only  $120 \text{ cm}^{-1}$  to 8.1 eV. Therefore, the ionization potential of  $\text{Si}_2$  lies between 7.9 and 8.1 eV (20).

The measured ionization potential range for  $\text{Si}_2$  (7.9 - 8.1 eV) is in agreement with the previous lower bound established for the dimer I. P. by Trevor et al. (14) and Heath et al. (13), who noted that an  $\text{F}_2$  excimer photon (7.87 eV) was of insufficient energy to single photon ionize  $\text{Si}_2$ . The ionization potential estimate of Boo and Armentrout (15) ( $\leq 8.04 \pm 0.13 \text{ eV}$ ) also falls within this measured range, as does the most recently calculated dimer I. P. value (Curtiss et al. (7.94 eV) (19)). However, the lower bound established by Fuke et al. (16) does not agree with the current bracketing. Fuke et al. (16) used stimulated Raman scattering to generate 7.46, 7.97, and 8.46 eV photons, which were subsequently used to ionize silicon clusters. These researchers suggested that even an 8.46 eV photon was of insufficient energy to single photon ionize  $\text{Si}_2$ . While the reason for the discrepancy in these ionization potential measurements is unclear, it is interesting to note that in Fuke et al.'s Fig. 5, no dimer signal is observed for 7.46 eV ionization. However, a small, but noticeable dimer ionization peak is revealed for 7.97 eV ionization, consistent with the measured I. P. range determined in this study.

### Acknowledgements

We wish to express our appreciation to Dr. Richard Oldenborg of Los Alamos National Laboratory for allowing us the use of the Lambda-Physik EMG102 excimer laser. The support of the Army Research Office through grant number DAAH04-93-G-0195 is also greatly appreciated.

## References

1. A. R. Downie and R. F. Barrow, *Nature* **160**, 198 (1947).
2. A. E. Douglas, *Can. J. Phys.* **33**, 801-810 (1955).
3. R. D. Verma and P. A. Warsop, *Can. J. Phys.* **41**, 152-161 (1963).
4. I. Dubois and H. Leclercq, *Can. J. Phys.* **49**, 3053-3054 (1971).
5. S. D. Peyerimhoff and R. J. Buenker, *Chem. Phys.* **72**, 111-118 (1982).
6. J. Drowart, G. De Maria, and M. G. Inghram, *J. Chem. Phys.* **29**, 1015-1021 (1958),  
G. Verhaegen, F. E. Stafford, and J. Drowart, *ibid.* **40**, 1622-1628 (1964).
7. K. P. Huber and G. Herzberg, "Molecular Spectra and Molecular Structure",  
(Van Nostrand Reinhold, New York, 1979), Vol. IV.
8. (a) R. Woodward, P. N. Le, M. Temmen, and J. L. Gole, *J. Phys. Chem.* **91**,  
2637-2645 (1987). (b) J. L. Gole, in "Advances in Metal and Semiconductor  
Clusters", edited by M. A. Duncan (JAI, Greenwich, 1993), Vol. 1, p. 159-209.
9. (a) H. Wang and J. L. Gole, *J. Chem. Phys.* **98**, 9311-9319 (1993). (b) C. B.  
Winstead, Ph.D. Thesis, The Georgia Institute of Technology, June 1995.
10. C. B. Winstead, S. J. Paukstis, J. L. Walters, and J. L. Gole, *J. Chem.*  
*Phys.* **102**, 1877-1881 (1995).
11. G. Herzberg, "Molecular Spectra and Molecular Structure", (Van Nostrand,  
Reinhold, New York, 1950), Vol. I.
12. R. N. Zare, *J. Chem. Phys.* **40**, 1934-1944 (1964), and references therein.  
G. Herzberg, "Molecular Spectra and Molecular Structure. I. Spectra of  
Diatomic Molecules", 2nd ed. (Krieger, Malabar, 1989). J. L. Dunham,  
*Phys. Rev.* **41**, 721-731 (1932).
13. J. R. Heath, Y. Liu, S. C. O'Brien, Q. Zhang, R. F. Curl, F. K. Tittel,  
and R. E. Smalley, *J. Chem. Phys.* **83**, 5520-5526 (1985).
14. D. J. Trevor, D. M. Cox, K. C. Reichmann, R. O. Brickman, and A. Kaldor,  
*J. Phys. Chem.* **91**, 2598-2601 (1987).
15. B. H. Boo and P. B. Armentrout, *J. Am. Chem. Soc.* **109**, 3549-3559 (1987).

16. K. Fuke, K. Tsukamoto, F. Misaizu, and M. Sanekata, J. Chem. Phys. 99, 7807-7812 (1993).
17. K. Raghavachari and V. Logovinsky, Phys. Rev. Lett. 55, 2853-2856 (1985).
18. B. K. Rao and E. Blaisten-Barojas, Chem. Phys. Lett. 150, 259-262 (1988).
19. L. A. Curtiss, K. Raghavachari, P. W. Deutsch, and J. A. Pople, J. Chem. Phys. 95, 2433-2444 (1991).
20. C. B. Winstead, S. J. Paukstis, and J. L. Gole, "What is the Ionization Potential of Silicon Dimer", Chem. Phys. Lett., in press.

### Figure Captions

Figure 1:  $\text{Si}_2 \text{H}^3\Sigma_u^- - \text{X}^3\Sigma_g^-$  transitions and vibrational numbering assignments used to determine the previously accepted constants for the  $\text{H}^3\Sigma_u^-$  and  $\text{X}^3\Sigma_g^-$  electronic states. See text for discussion.

Figure 2: Oven configuration used to produce  $\text{Si}_2$  molecules. A carbon crucible containing silicon powder is heated to temperatures in excess of 1500 K using a tungsten basket heater. A carrier gas, typically helium, is used to entrain and cool the oven produced silicon vapor.

Figure 3: Experimental configuration used for laser induced fluorescence studies of oven produced molecules. A pulsed dye laser is used to pump molecules produced by the oven source into excited electronic states. The resulting fluorescence is imaged onto a slit and detected by a photomultiplier tube to obtain an excitation spectrum.

Figure 4: Experimental configuration used for dispersed laser induced fluorescence studies. A two lens system focuses the fluorescence resulting from the excitation of the  $\text{H}^3\Sigma_u^-$  state of  $\text{Si}_2$  onto the entrance slit of a spectrometer which disperses the fluorescence.

Figure 5: Laser induced fluorescence spectrum of the  $\text{Si}_2 \text{H}^3\Sigma_u^- - \text{X}^3\Sigma_g^-$  transition. An extended rotational structure is visible for transitions from the lowest two vibrational levels of the ground  $\text{X}^3\Sigma_g^-$  state to five vibrational levels of the  $\text{H}^3\Sigma_u^-$  state. Transitions are labeled ( $v', v''$ ). Features associated with background atomic fluorescence are labeled A\*.

Figure 6: An expanded view of the  $\text{Si}_2 \text{H}^3\Sigma_u^- (v' = 6) - \text{X}^3\Sigma_g^- (v'' = 0)$  transition. The P and R branches of the rotational structure are clearly visible labeled by the numbering scheme given at the

top of the figure. The symmetry of the  $\text{Si}_2$  ground state implies that only odd numbered rotational levels are observed.

Figure 7: Total fluorescence resulting from the excitation of a low-lying rotational level of the  $\text{Si}_2$   $\text{H } ^3\Sigma_u^-$  ( $v' = 6$ ) vibrational level.

The initial scattering signal from the excitation laser is visible in the figure, followed by the exponential decay of the fluorescence.

Figure 8: Resonant two photon ionization spectra for the  $\text{Si}_2$   $\text{H } ^3\Sigma_u^- - \text{X } ^3\Sigma_g^-$  transition recorded in separate isotopic mass channels. The shifts in vibrational energy levels caused by the isotope effect are clearly visible.

Figure 9: Comparison of laser induced fluorescence and resonant two photon ionization spectra for the  $\text{Si}_2$   $\text{H } ^3\Sigma_u^- - \text{X } ^3\Sigma_g^-$  transition. The higher temperature of the oven produced dimers allows the observation of an extended rotational structure in the LIF spectrum.

See text for discussion.

Figure 10: An expanded view of the isotope shifts for the  $\text{Si}_2$   $\text{H } ^3\Sigma_u^-$  ( $v' = 4$ )  $- \text{X } ^3\Sigma_g^-$  ( $v'' = 0$ ) transition. Bandhead energies and measured isotope shifts are indicated in the figure. See text for discussion.

Figure 11: (a) Comparison of experimental and simulated dispersed fluorescence spectra for excitation of the  $\text{Si}_2$   $\text{H } ^3\Sigma_u^-$  state  $v' = 5$  vibrational level. The simulated spectrum obtained using the corrected H state constants clearly reproduces the experimental data more accurately than the simulation obtained using the previously accepted constants. (b) Comparison of experimental and simulated dispersed fluorescence spectra for excitation of the H state  $v' = 6$  vibrational level.

Figure 12: Resonant two photon ionization schemes used to bracket the  $\text{Si}_2$  ionization potential.

Figure 13: R2PI spectrum of the  $^{28}\text{Si}^{30}\text{Si } H^3\Sigma_u^- - X^3\Sigma_g^-$  transition obtained using KrF excimer (5 eV) ionization. Ionization from the  $H(v' = 3)$  vibrational level is clearly observed.

Figure 14: LIF and R2PI spectra of the  $^{28}\text{Si}^{28}\text{Si } H^3\Sigma_u^-(v' = 8) - X^3\Sigma_g^-(v'' = 0)$  transition. While ionization from the  $H(v' = 8)$  vibrational level is observed using KrF excimer (5 eV) ionization, no R2PI signal is obtained using Nd:YAG 4th harmonic (4.66 eV) ionization. Features marked with an asterisk in the KrF R2PI spectrum correspond to fluctuations in the resonantly ionized iron atom background.



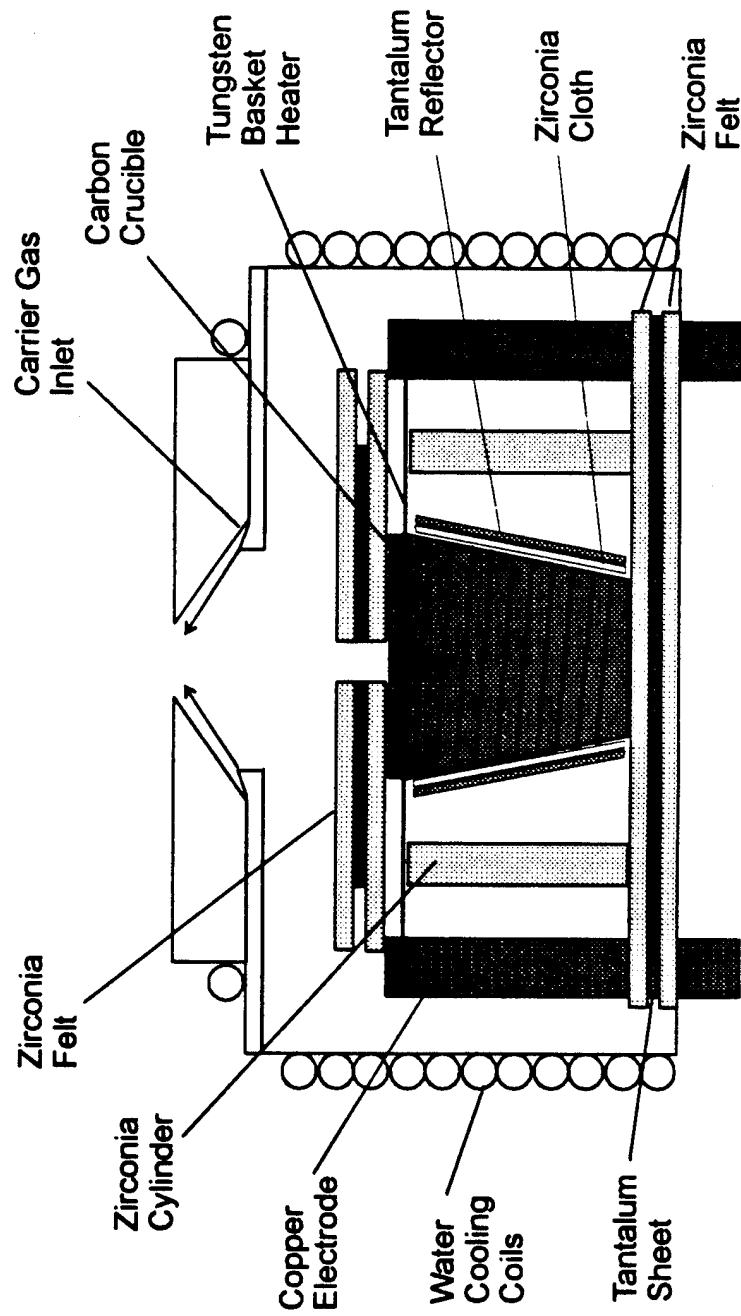


Figure 2

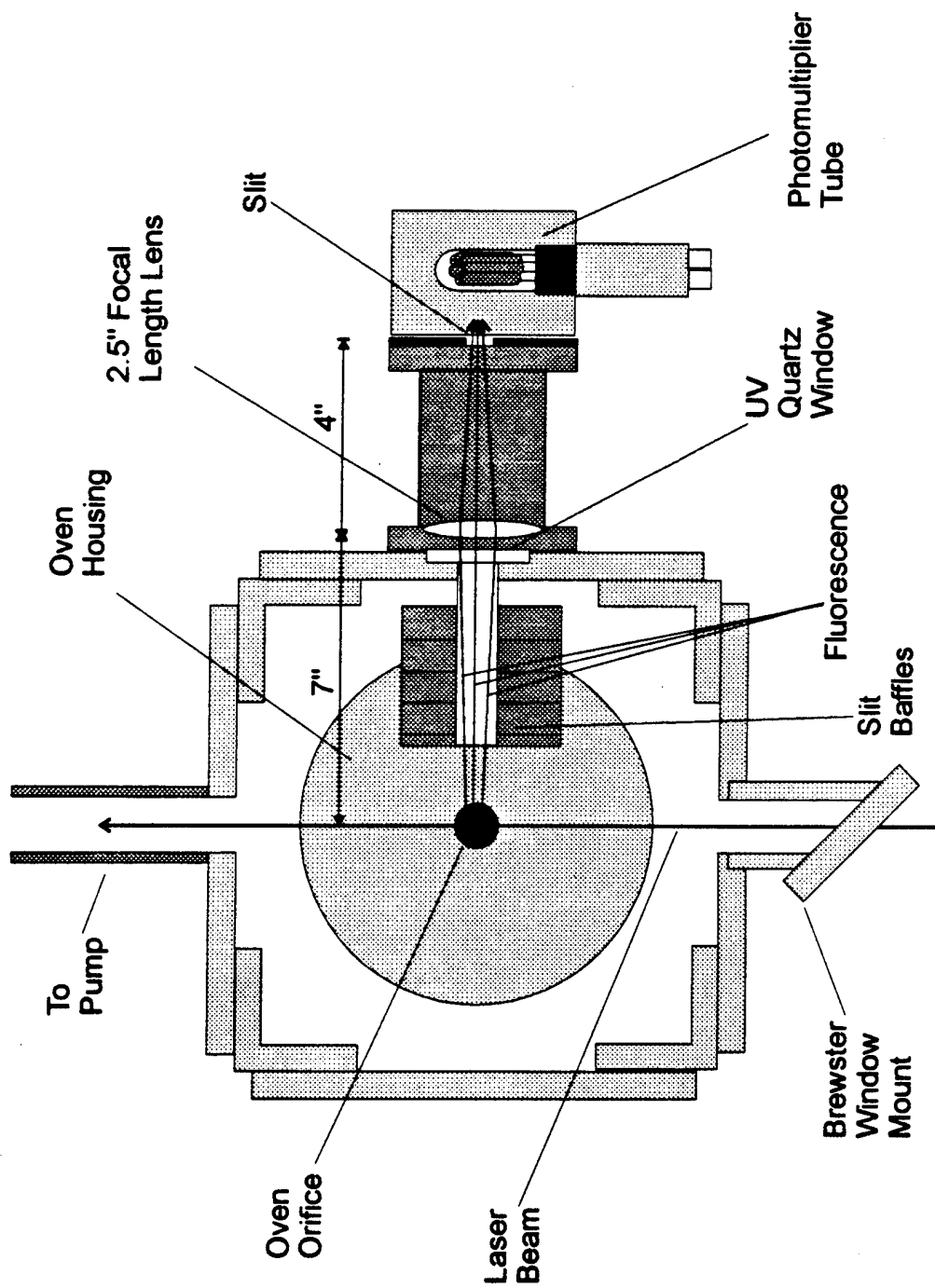


Figure 3

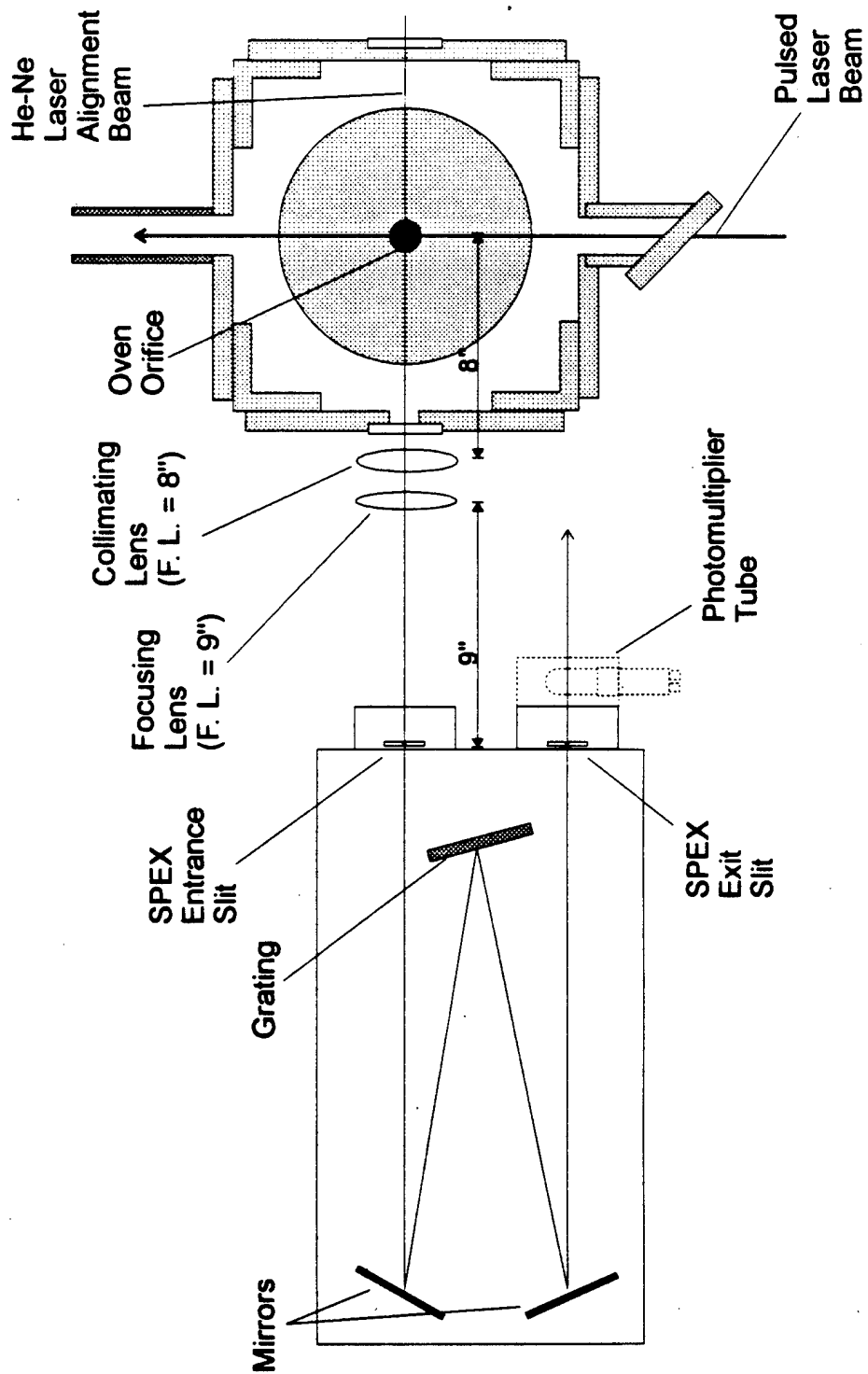


Figure 4

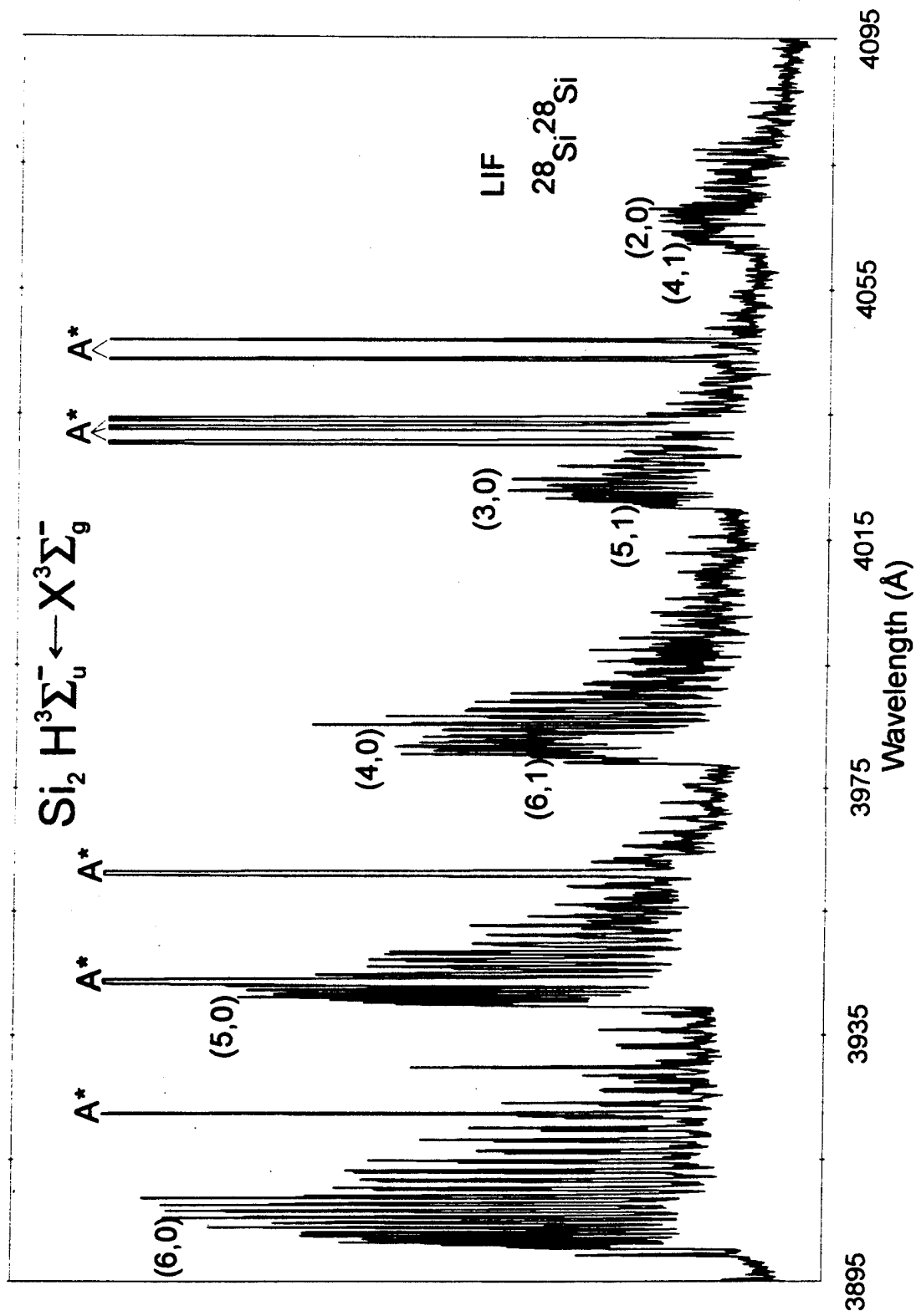


Figure 5

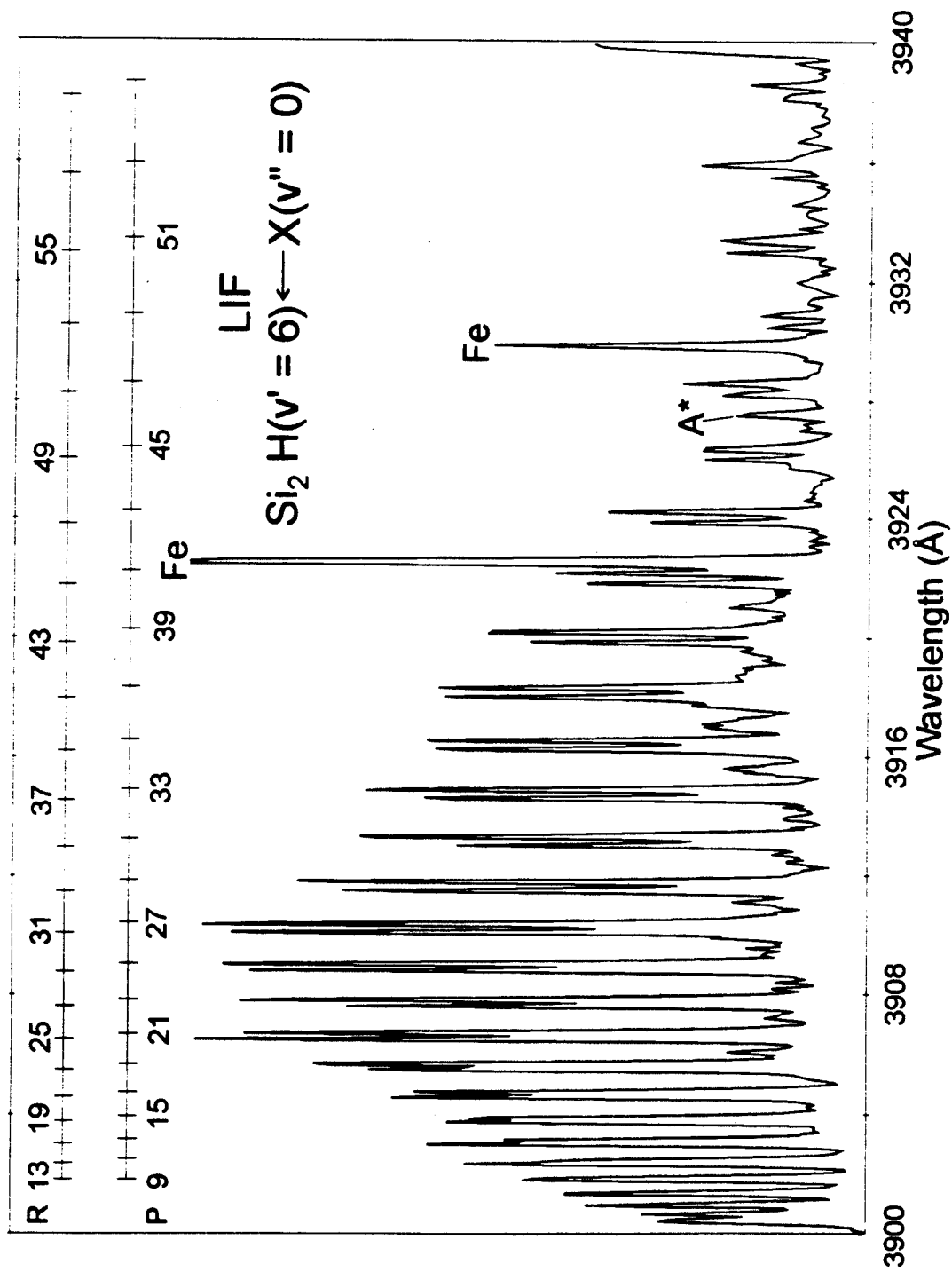


Figure 6

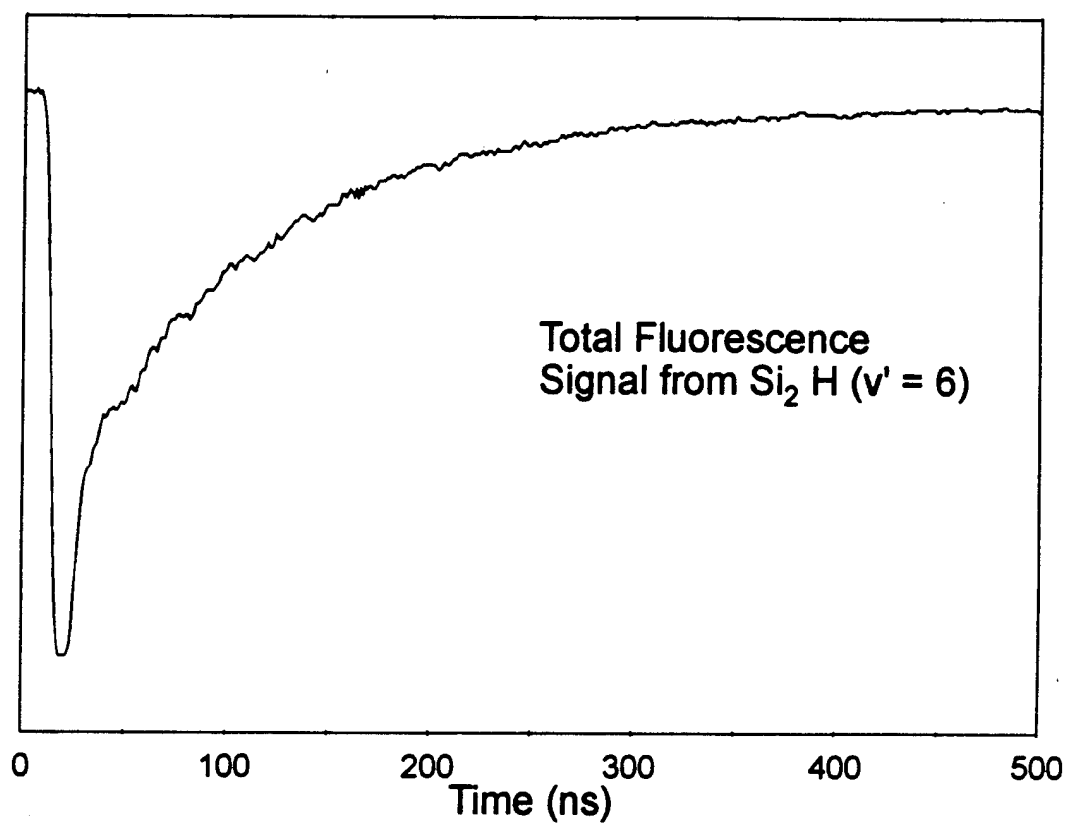


Figure 7

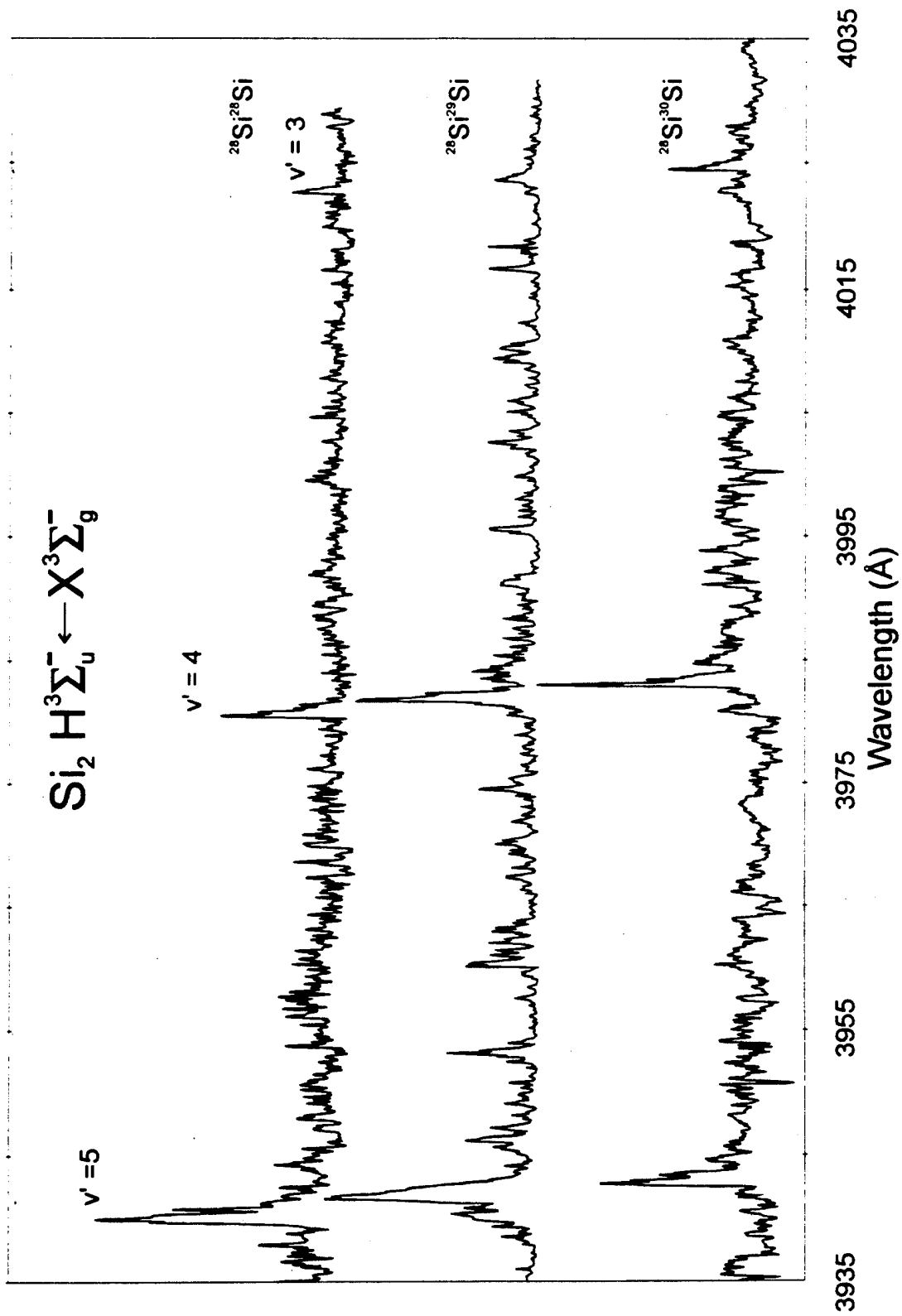


Figure 8

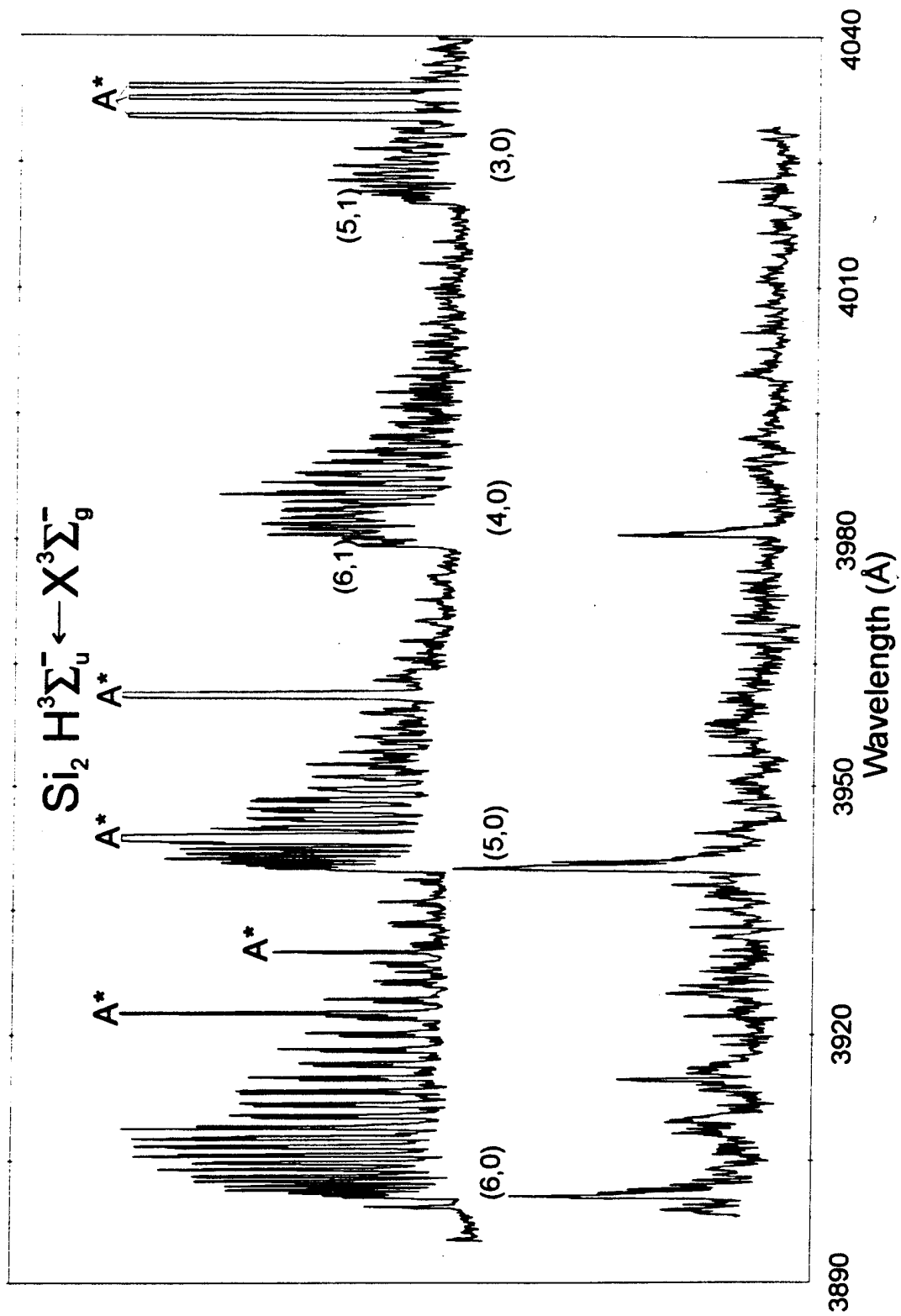


Figure 9

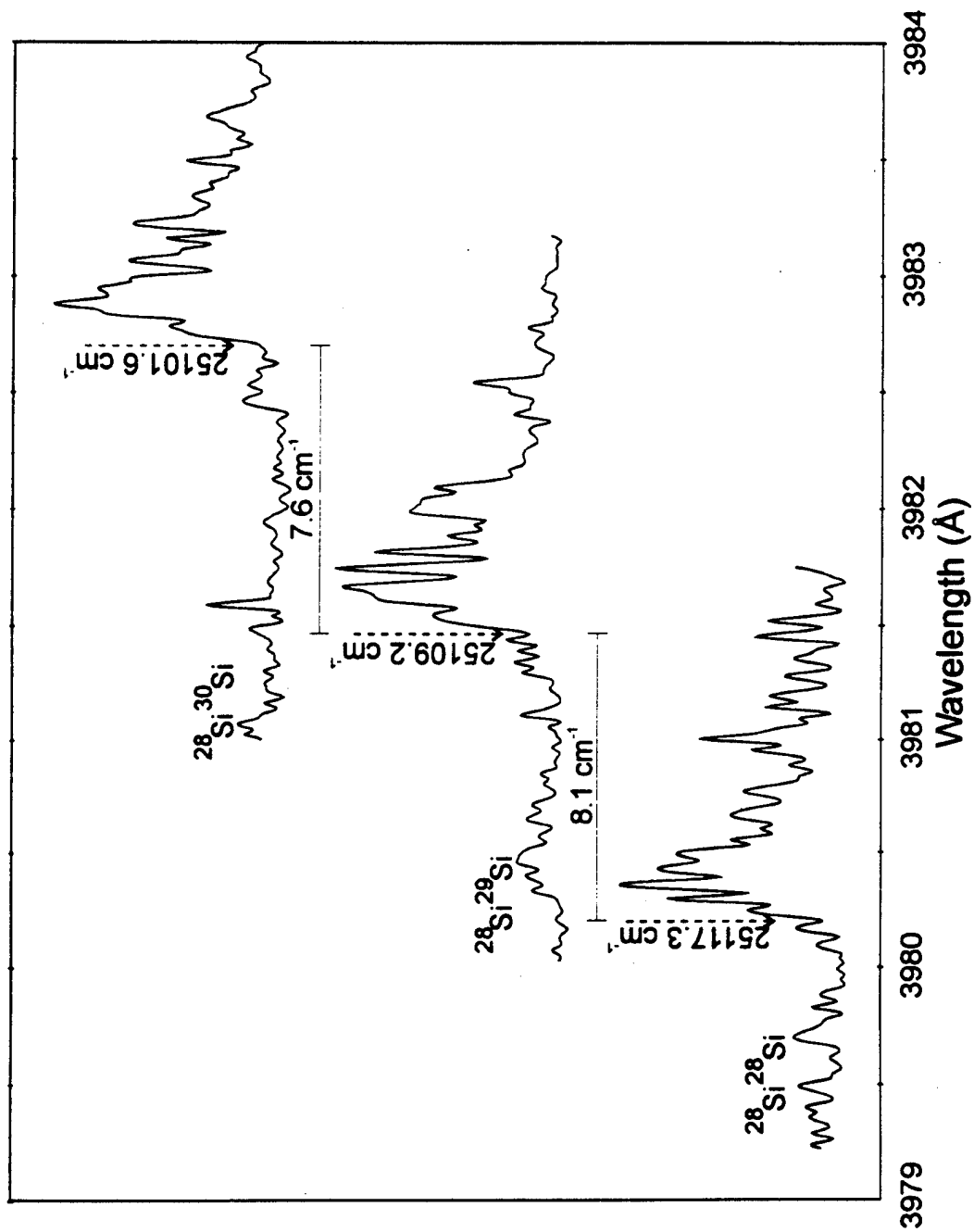


Figure 10

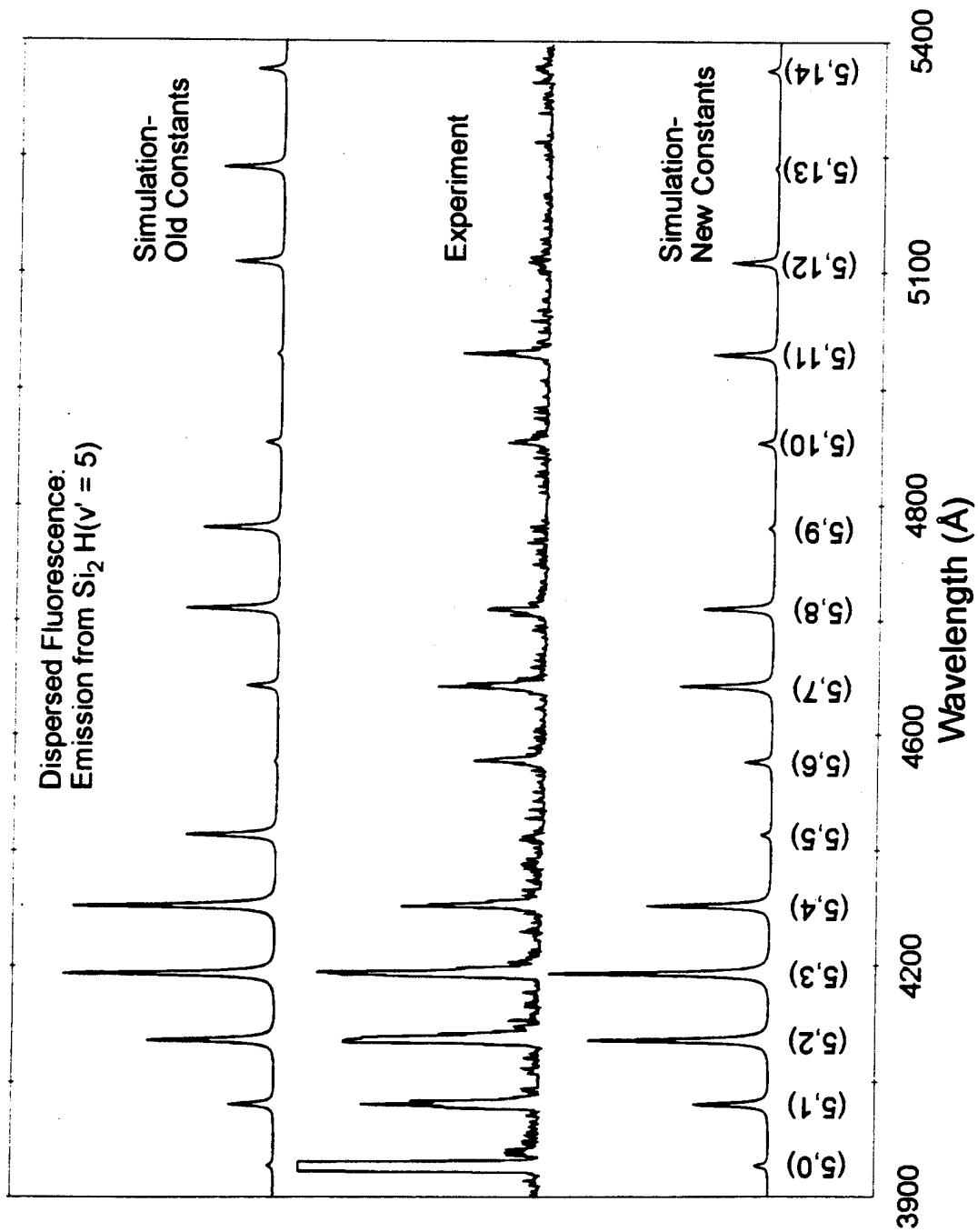


Figure 11(a)

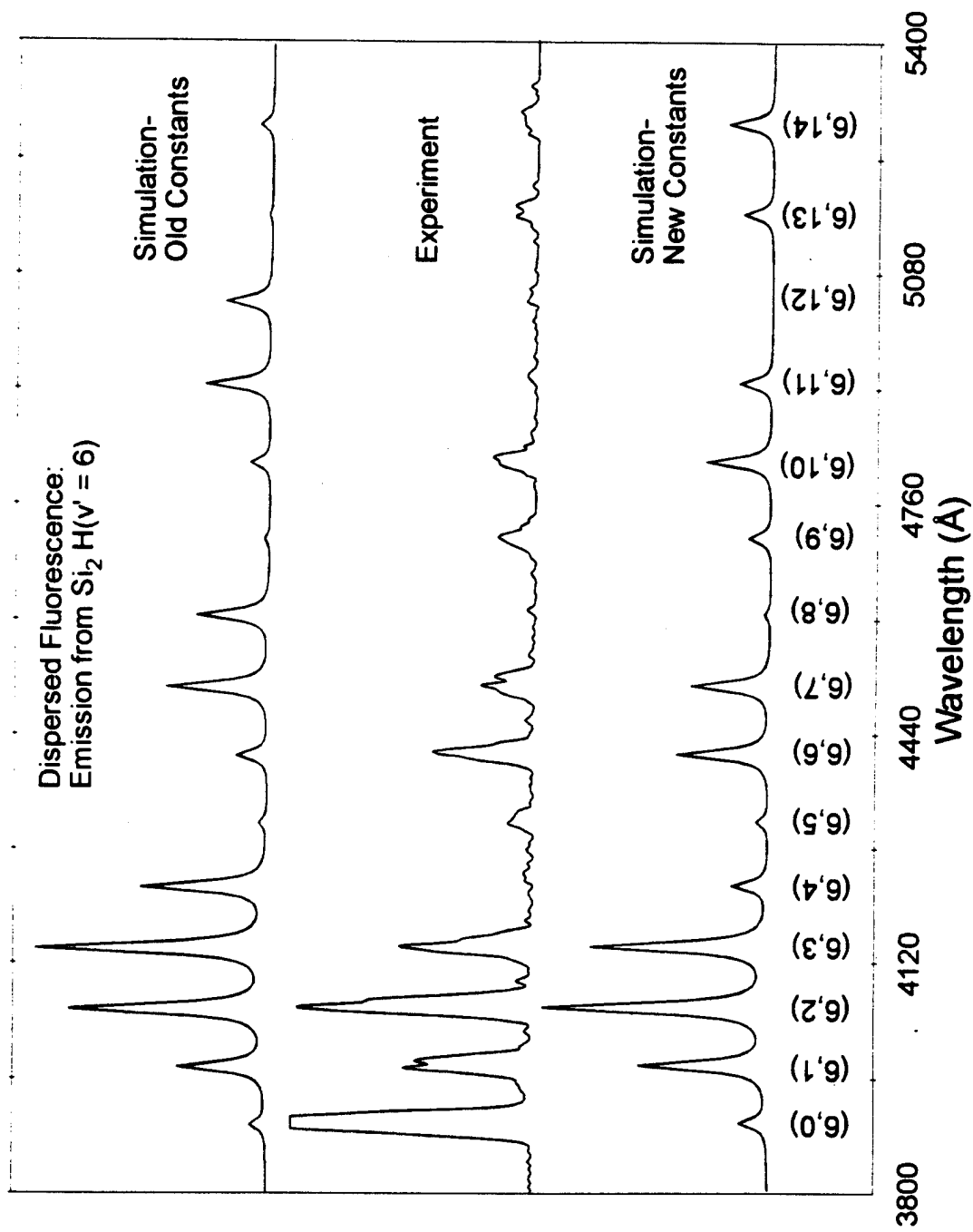


Figure 11(b)

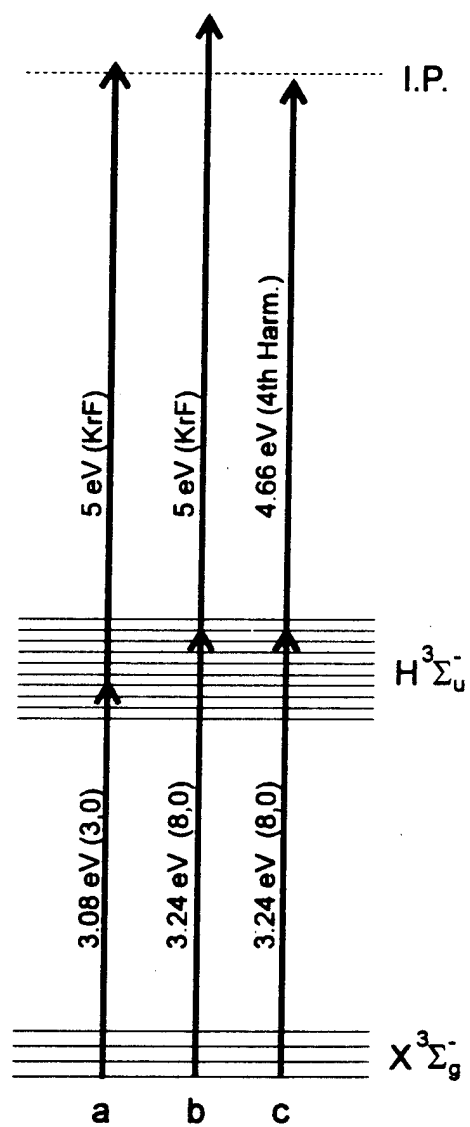


Figure 12

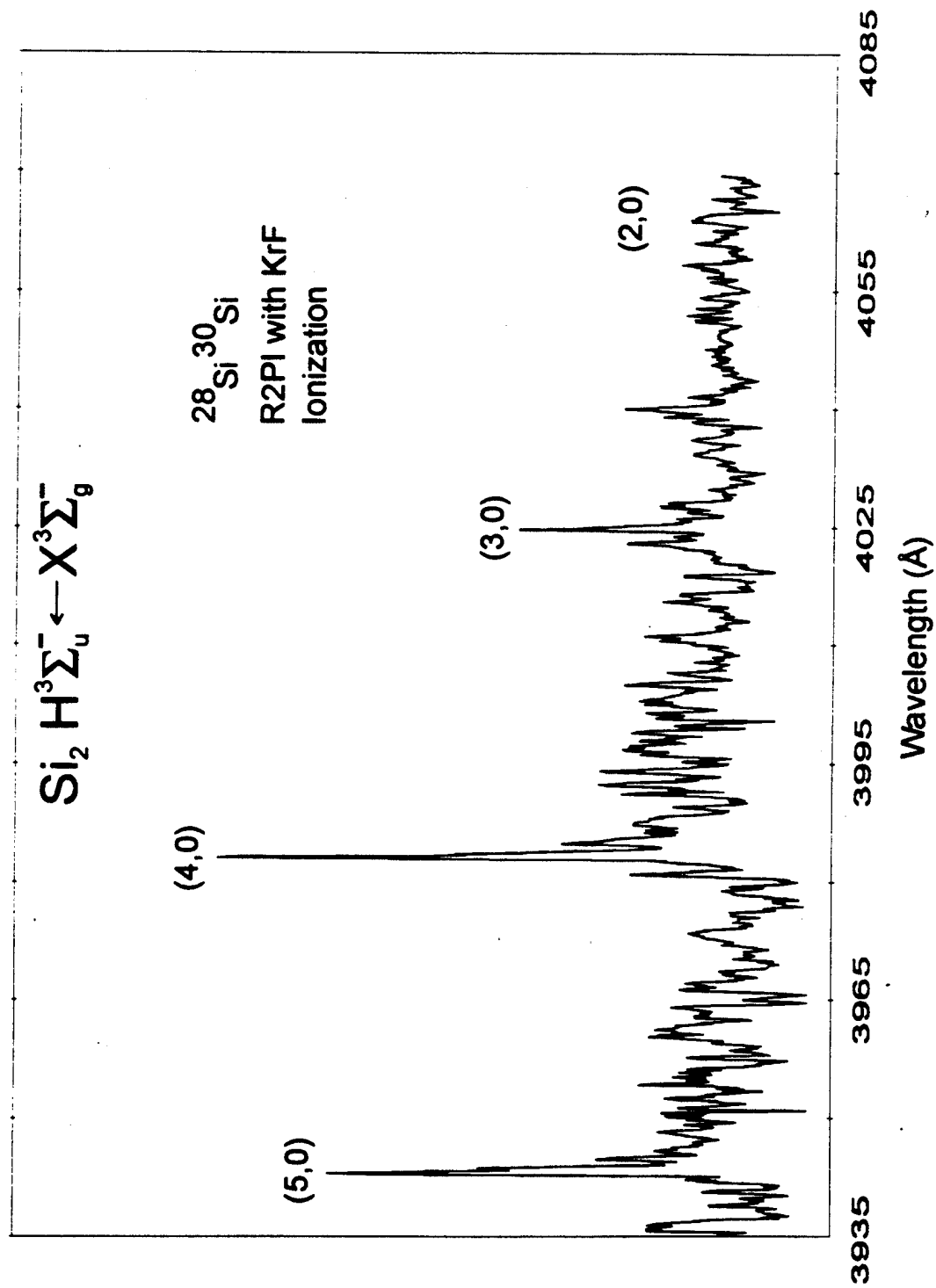


Figure 13

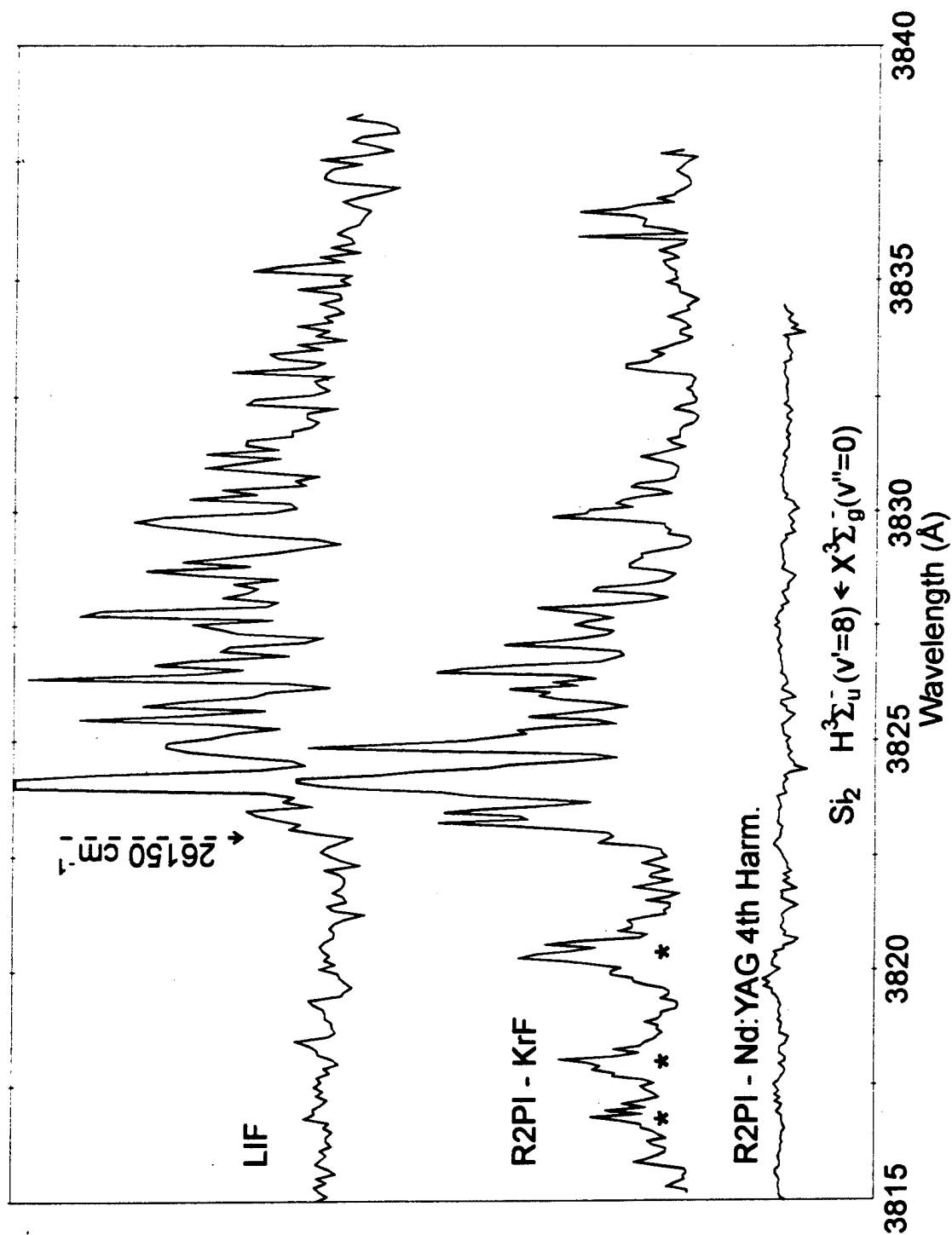


Figure 14

Table I

Observed and Calculated Rotational Energies for the  
 $\text{H } ^3\Sigma_u^- (v' = 6) \leftarrow \text{X } ^3\Sigma_g^- (v'' = 0)$  Transition

N	R Branch ( $\text{cm}^{-1}$ )		P Branch ( $\text{cm}^{-1}$ )	
	Calculated	Observed	Calculated	Observed
1	25628.62	-	25627.63	-
3	25628.53	-	25626.23	-
5	25627.84	-	25624.24	-
7	25626.56	-	25621.64	-
9	25624.68	-	25618.46	25618.56
11	25622.20	-	25614.67	25614.85
13	25619.13	25619.27	25610.29	25610.44
15	25615.46	25615.56	25605.31	25605.4
17	25611.19	25611.46	25599.74	25600.04
19	25606.33	25606.42	25593.57	25594.02
21	25600.87	25601.14	25586.80	25587.20
23	25594.80	25595.16	25579.44	25579.86
25	25588.14	25588.57	25571.47	25571.80
27	25580.88	25581.30	25562.91	25563.17
29	25573.02	25573.44	25553.76	25554.00
31	25564.56	25564.82	25544.00	25544.25
33	25555.50	25555.88	25533.64	25533.91
35	25545.83	25546.12	25522.68	25523.01
37	25535.57	25535.67	25511.13	25511.10
39	25524.70	25525.00	25498.96	25499.18
41	25513.22	25513.63	25486.21	25486.46
43	25501.14	25501.46	25472.84	25473.10
45	25488.46	25488.72	25458.88	25459.13
47	25475.17	25475.37	25444.31	25444.54
49	25461.27	25461.49	25429.13	25429.47

Table II

Fluorescence Lifetimes for the  $H^3\Sigma_u^- \leftarrow X^3\Sigma_g^-$  Transition

$Si_2$ $v$	$H^3\Sigma_u^-$ Lifetimes $\tau(ns)$
2	101±8
3	98±5
4	95±5
5	120±4
6	96±3

Table III

Measured Bandhead Energies and Vibrational Numbering for Isotopically Labeled  $\text{Si}_2\text{H } ^3\Sigma_u^- \leftarrow \text{X } ^3\Sigma_g^-$  Transitions

Previously Accepted Vibrational Numbering $v'$	$^{56}\text{Si}_2$ Band Energy ( $\text{cm}^{-1}$ )	$^{57}\text{Si}_2$ Band Energy ( $\text{cm}^{-1}$ )	$^{58}\text{Si}_2$ Band Energy ( $\text{cm}^{-1}$ )	Calculated $v'$ from $^{56}\text{Si}_2$ - $^{57}\text{Si}_2$ Shift	Calculated $v'$ from $^{56}\text{Si}_2$ - $^{58}\text{Si}_2$ Shift	Calculated $v'$ from $^{57}\text{Si}_2$ - $^{58}\text{Si}_2$ Shift	Correct Vib. Num. $v'$
2	24853.2	24847.4	24841.6	3.04	3.12	3.18	3
3	25117.3	25109.2	25101.6	4.13	4.13	4.09	4
4	25376.5	25366.0	25359.3	5.30	4.50	3.64	5
5	25631.9	25619.9	25608.8	6.08	6.03	5.93	6

Table IV

Comparison of Newly Calculated and Previously Accepted Spectroscopic Constants for the  $\text{Si}_2 \text{H } ^3\Sigma_u^-$  State

$\text{Si}_2 \text{H } ^3\Sigma_u^-$ Constants	Previous ( $\text{cm}^{-1}$ )	Corrected ( $\text{cm}^{-1}$ )
$T_e$	24429.15	24151.86
$\omega_e$	275.30	279.28
$\omega_e x_e$	1.99	1.99
$B_e$	0.1712	0.17255
$\alpha_e$	0.00135	0.00135

Table V

Calculated Energies of  $\text{Si}_2\text{H}^+ \Sigma_u^-$  State Vibrational Levels - Corrected Versus  
Previously Accepted H State Constants

Previous Vibrational Numbering	Calculated Vib. Energies- Previous Constants ( $\text{cm}^{-1}$ )	Corrected Vibrational Numbering	Calculated Vib. Energies- Corrected Constants ( $\text{cm}^{-1}$ )
-	-	0	24291.00
0	24566.30	1	24566.30
1	24837.62	2	24837.62
2	25104.96	3	25104.96
3	25368.32	4	25368.32
4	25627.70	5	25627.70
5	25883.10	6	25883.10
6	26134.52	7	26134.52
7	26381.96	8	26381.96
8	26625.42	9	26625.42
9	26864.90	10	26864.90

Table VI

Franck-Condon Factors ( $\times 10,000$ ) for the  $\text{Si}_2\text{H } ^3\Sigma_u^- \leftarrow \text{X } ^3\Sigma_g^-$  Transition  
Calculated Using Corrected H State Constants

$v'$ $v''$	0	1	2	3	4	5	6	7	8	9
0	0	0	1	5	14	34	69	125	204	302
1	0	3	14	45	108	209	344	491	615	685
2	2	19	74	188	358	542	671	686	572	372
3	12	77	234	464	666	718	574	313	82	0
4	44	216	506	737	714	438	123	0	108	298
5	121	456	776	740	366	40	46	270	402	301
6	271	746	835	399	21	108	376	388	156	2
7	505	949	577	44	125	429	350	64	27	224
8	800	924	182	72	450	353	30	88	315	269
9	1097	645	0	403	427	34	123	358	207	4
10	1313	263	191	555	98	104	385	180	1	192
11	1386	18	536	313	31	400	209	6	246	266
12	1299	67	665	24	332	317	0	263	265	11
13	1087	376	449	94	478	27	227	305	9	159

## APPENDIX XV

"A New and Simple Pyrolysis Source for the Controlled Formation of SiO Metastables", J. Stephens and J. L. Gole, Jour. Applied Physics, submitted.

A New and Simple Pyrolysis Source for the Controlled Formation  
of SiO Metastables

James M. Stephens and James L. Gole

School of Physics  
Georgia Institute of Technology  
Atlanta, Georgia 30332

## ABSTRACT

A simple silane pyrolysis -  $N_2O$  oxidation source which produces silicon monoxide metastables in a controlled and reproducible manner has been developed. The  $SiO$   $b^3\Pi$  metastable state is formed in a ratio exceeding 2200 times that of the remaining  $SiO$  excited states. This source would appear to allow the creation of a long path length medium for the efficient energy transfer pumping of visible chemical laser amplifiers and oscillators. The source may also provide an improved mode for the control and efficient monitoring of  $SiO$  surface deposition processes.

## INTRODUCTION

Silicon monoxide has gained wide acceptance as a thin film material for a large diversity of applications.<sup>1</sup> In complement, in the gas phase, the highly exothermic, high quantum yield,  $\text{Si} + \text{N}_2\text{O} \rightarrow \text{SiO} + \text{N}_2$  reaction, which selectively produces electronically excited SiO metastables<sup>2,3</sup> in the energy range 3-3.5 eV, creates an energy storage medium which can be used to develop chemically driven laser amplifiers and oscillators<sup>4,5</sup> operating in the visible region of the spectrum. Electronic population inversions are created by means of ultrafast near resonant intermolecular energy transfer from the SiO metastables. The SiO metastable storage states are found to efficiently pump amplifying receptor atom transitions in thallium ( $\lambda = 535 \text{ nm}$ ),<sup>4</sup> gallium ( $\lambda = 417 \text{ nm}$ )<sup>4</sup> and sodium ( $\lambda = 569, 616, 819 \text{ nm}$ ).<sup>5</sup> To date, however, these gas phase studies have relied on the direct vaporization of silicon from a long path-length ( $\sim 5 \text{ cm}$ ) oven source configuration followed by subsequent reaction to form metastable SiO.

In order to obviate the need for a high temperature source technology to generate silicon atoms, subsequently oxidized to produce SiO, we have been concerned with an approach for the efficient conversion of gaseous silane ( $\text{SiH}_4$ ) to atomic silicon via a readily controllable thermalization process. However, the development of a simple source which produces SiO metastables in a consistent and reproducible manner, with minimal or non-existent clustering in the gas phase, also has potential application to thin film development. Further, with a high yield gas phase metastable state production, forming a species whose long-lived emission extends well into the ultraviolet region, the potential for the direct in-situ optical monitoring of the SiO concentration above a deposition substrate is vastly improved over that of infrared detectors.

The spectroscopy of the silicon monoxide molecule has been considered by a number of authors. The excited  $a^3\Sigma^+$ ,  $b^3\Pi$ , and  $A^1\Pi$  states of the molecule have been produced in the chemiluminescent reactions of ground state silicon atoms, vaporized directly from an oven source, with  $\text{O}_3$ ,<sup>6</sup>  $\text{N}_2\text{O}$ ,<sup>2,6</sup> and  $\text{NO}_2$ .<sup>3</sup> Limited studies of SiO spectroscopy have also been conducted with silicon produced through various silane decomposition routes. These studies have utilized the electric discharge decomposition of silane<sup>6,7</sup> or shock tube pyrolysis.<sup>8</sup> The results obtained certainly signal the need for a controlled silane based thermal decomposition process which neither produces clustering<sup>9</sup>

nor suffers from those problems attendant to the control of discharge configurations.<sup>1</sup>

In the present study, the pyrolysis of silane is employed to create a gas phase, readily reproducible, metastable SiO concentration in a simple and controlled manner. Silicon atoms formed in the pyrolysis process are reacted with N<sub>2</sub>O to produce two excited states of the SiO molecule. In addition to the SiO b<sup>3</sup>Π metastable state (monitored through the SiO b<sup>3</sup>Π - X<sup>1</sup>Σ<sup>+</sup> inter-combination band system) a much smaller component of emission is also observed to emanate from the short-lived A<sup>1</sup>Π state (A<sup>1</sup>Π - X<sup>1</sup>Σ<sup>+</sup> band system).

In the following section we outline our experimental approach. We then consider the experimental observations as they apply to the formation of SiO metastable pump states and contrast the present observations to results obtained with a high temperature oven based technology. We offer some conclusions on the potential of the present device as a means to generate useful and reproducible SiO concentrations.

## EXPERIMENTAL

The experimental configuration used in this study is depicted in Figure 1(a)-(b). Dilute silane is pyrolyzed upon passage through a ceramic tube heated to temperatures close to 1000°C and converted to silicon atoms which are subsequently oxidized (N<sub>2</sub>O) to SiO.

The pyrolizer consists of a high grade alumina or zirconia tube (Coors Ceramic) ~3/8" O.D. and ~1/4" I.D. cut to a 6" length. Approximately 3' of 0.020" tantalum wire (Rembar) is wound onto a 4" length of the tube, leaving one end free for connection to a gas inlet-Cajon fitting. The wire wrap is secured with a layer of high temperature cement (Cotronics Corp. ultra high temp. adhesive) which also serves the important purpose of providing electrical insulation.

Silane is passed, diluted, to the pyrolizer. A typical silane dilution for the present experiments is of order one percent in argon, obtained by mixing semiconductor grade silane (Matheson 98%) and argon under preselected conditions through an arrangement of mass flow controllers (MKS, Models 247C, 2159A). The flow controllers are calibrated with nitrogen and the appropriate correction factors are applied to generate the desired flows for the silane and argon as they are mixed in a manifold prior to admission to the pyrolizer. The converted mixture enters the vacuum chamber through the pyrolizer.

Typical source flows range from 6 to 15 sccm silane with ~ 1250 sccm argon. It is necessary to dilute the silane in order to alleviate the reaction of its intermediate decomposition products<sup>7-10</sup> with the silane itself and to ensure the complete dissociation to atomic silicon.

Oxidant (N<sub>2</sub>O-Matheson 99.5%) is introduced into the pyrolyzer stream through a separate nozzle (Figure 1), the intersection of the silane/diluent and N<sub>2</sub>O gas streams defining the reaction zone. The oxidant flow is adjusted to give a bright chemiluminescent flame. The overall pressure is monitored with a thermocouple gauge (Veeco TG-70) at the top of the vacuum chamber. Assuming a correction for argon (the dominant gas in the reaction zone), typical monitored pressures ranged from 0.5 to 1 Torr. With the high pumping speed employed in these studies, these values are accurate to within 20%. The mixing zone of Figure 1 is greatly stabilized by a moderate sized (15 cubic feet) ballast separating a 150 cfm pump from the reaction chamber. In order to protect the viewing windows and ports from the condensation of silicon oxide, "self-flushing" optical windows<sup>11</sup> were operated with a protective argon flow.

A 1m SPEX 1702 scanning monochromator operated in first order with a Bausch and Lomb 1200 groove/mm grating blazed at 5000 Å was used to disperse the chemiluminescence from the reaction zone. A Hamamatsu 1P28 photo-multiplier tube was used to detect the dispersed fluorescence and provide the signal to a Keithley 417 autoranging picoammeter whose output was sent to a personal computer for storage and subsequent analysis. All chemiluminescent spectra were wavelength calibrated using a mercury arc lamp, silicon, or aluminum atomic emission features.<sup>12</sup>

#### DECOMPOSITION OF SILANE

Because of its technological importance, an extensive literature has been compiled on the decomposition of the silane molecule.<sup>9-11</sup> Silane is believed to pyrolyze via a two step process:



Reaction (1) has received more study since silylene (SiH<sub>2</sub>) is thought to be an important silicon precursor in the vast majority of silicon deposition processes. However, both Rxns. (1) and (2) must be carefully considered in studying the production of gas phase silicon.

For Reaction (1), symmetry constraints suggest that both silylene and  $H_2$  should be produced in their ground electronic totally symmetric electronic states.<sup>13</sup> The endothermic dissociation produces the hydrogen molecule in its ground state due simply to energetics. The  $H_2$   $1\Sigma_g^+$  ground state resolves to  $1A_1$  under the  $C_{2v}$  point group of silylene. The ground state of silylene is of  $1A_1$  symmetry. If we require that the direct product of the  $H_2$  and  $SiH_2$  symmetries must correlate with the  $1A_1$  ground state of silane, we suggest that  $SiH_2$  should be in its  $1A_1$  ground state.

Francisco and Barnes<sup>14</sup> have argued that Reaction (2) yields  $H_2$  in its ground electronic state accompanied by an electronically excited  $1D$  silicon atom at  $6298.81\text{ cm}^{-1}$ .<sup>12</sup>

## RESULTS AND DISCUSSION

### Observed Emission Spectra

Figure 2 depicts the typical silicon monoxide emission spectrum observed when using a zirconia tube pyrolyzer. The  $SiO$   $A^1\Pi - X^1\Sigma^+$  and  $b^3\Pi - X^1\Sigma^+$  band systems are clearly visible and readily reproduced with the same emission intensity distribution. A moderately strong A-X emission is observed at wavelengths below  $2900\text{ \AA}$  whereas stronger features associated with the  $SiO$   $b^3\Pi - X^1\Sigma^+$  intercombination band system and the formation of the metastable  $b^3\Pi$  state extend from  $2900$  to  $\sim 3350\text{ \AA}$ .

When an alumina tube pyrolyzer is used instead of zirconia, considerable changes are apparent in the observed emission. Figure 3 demonstrates that the  $SiO$   $b^3\Pi - X^1\Sigma^+$ ,  $\Delta v = -1$  sequence  $((v', v'') = (0, 1), (1, 2), (2, 3))$  is obscured by an emission corresponding to the  $2D_{3/2} \rightarrow 2P_{1/2}$  and  $2D_{5/2, 3/2} \rightarrow 2P_{3/2}$  atomic transitions of aluminum. It appears that a small concentration of aluminum atoms leached from the alumina pyrolyzer is excited as the result of a very near resonant (see Table I) collision induced energy transfer involving the metastable  $b^3\Pi$  state of  $SiO$ . This efficient transfer allows the  $SiO$  metastables to readily pump the aluminum atom transitions demonstrating, again, the extremely important capability which has been used to create population inversions among the energy levels of atomic thallium,<sup>4</sup> gallium,<sup>4</sup> and sodium.<sup>5</sup> Here, however, no population inversion is created relative to the terminal  $2P_{3/2, 1/2}$  ground state levels of the aluminum atom.

It is surprising that no emission from the  $SiO$   $a^3\Sigma^+$  state is observed in this current study as we use the outlined pyrolysis sources to produce the

precursor whose oxidation yields the SiO spectrum depicted in Figure 2. By comparison, the SiO spectrum (Figure 4), observed when an oven based source is used to generate silicon atoms, clearly indicates the SiO  $a^3\Sigma^+ - X^1\Sigma^+$  band system to longer wavelength of the  $b^3\Pi - X^1\Sigma^+$  features. We will consider this result in following discussion.

### Relative Populations of $b^3\Pi$ Metastable and $A^1\Pi$ Excited States

The relative populations of the  $b^3\Pi$  and  $A^1\Pi$  states may be estimated by employing the relation<sup>2</sup>

$$N(b^3\Pi)/N(A^1\Pi) \approx 200 \frac{I(b^3\Pi - X^1\Sigma^+)}{I(A^1\Pi - X^1\Sigma^+)} \quad (3)$$

where  $N(b^3\Pi, A^1\Pi)$  and  $I(b^3\Pi - X^1\Sigma^+, A^1\Pi - X^1\Sigma^+)$  represent the populations of the indicated states and the monitored relative intensities of the corresponding transitions. For the silane pyrolysis used to generate the SiO emission spectrum of Figure 2, this ratio typically falls within the range 2200-2500. This is a very conservative estimate. The determined relative intensities are obtained through observation of a limited reaction zone region. Because the radiative lifetime of the SiO  $A^1\Pi - X^1\Sigma^+$  transition is close to 10 ns,<sup>15</sup> emission from the forming  $A^1\Pi$  emitters should be confined almost exclusively to the monitored reaction zone.<sup>16</sup> However, this is not the case for those SiO products formed in the long-lived  $b^3\Pi$  excited state, most of which are lost by diffusion from the reaction zone<sup>16</sup> before they are detected via the  $b^3\Pi - X^1\Sigma^+$  intercombination transition. The ratio we have given for  $N(b^3\Pi)/N(A^1\Pi)$  can be interpreted as a strong lower bound for the branching ratio.

### The Lack of a $^3\Sigma^+$ Metastable Emission

While a clear explanation is not apparent, it is significant that little if any emission is observed from the energetically accessible  $a^3\Sigma^+$  state under the conditions of the present experiment. As Figure 4 suggests, when a substantial concentration of ground state Si( $^3P$ ) atoms is available, both the SiO  $b^3\Pi$  and  $a^3\Sigma^+$  states can be monitored through the b-X and a-X intercombination band systems although the  $a^3\Sigma^+$  state is relaxed primarily to its  $v' = 0$  level. However, the spectrum of Figure 4 is obtained with silicon atoms in the presence of primarily argon carrier whereas the spectrum of Figure 2 is

obtained in the presence of silane and its decomposition products. The latter environment may prove more effective in quenching the  $a^3\Sigma^+$  state.

If the silane decomposition pathway outlined in Rxns (1) and (2) yields primarily excited state Si  $^1D$  atoms, the Si-N<sub>2</sub>O reaction would be expected to yield primarily excited singlet state ( $A^1\Pi$ ) SiO product. If we assume that Francisco and Barnes<sup>14</sup> have correctly assessed the symmetry of the product channels for Rxn. (2), implying strictly singlet silicon formation, the population of the  $b^3\Pi$  state is difficult to rationalize without invoking a mechanism involving, for example, intersystem crossing from the spin favored  $A^1\Pi$  state or high vibrational levels of the ground electronic  $^1\Sigma^+$  state. Alternatively, the absence of the  $a^3\Sigma^+$  state, whose lifetime must greatly exceed that of the  $b^3\Pi$  state,<sup>2</sup> may result from its selective quenching in an environment containing silane and its decomposition products.

Hager et al.<sup>6</sup> discuss the possibility of intersystem crossing from the  $b^3\Pi$  to the  $a^3\Sigma^+$  in order to account for the pressure dependence of their observations of the changing relative emissions from the SiO  $a^3\Sigma^+$  and  $b^3\Pi$  states as a function of pressure in the 2-4 Torr pressure range (primarily helium buffer gas). However, the absence of the  $a^3\Sigma^+ - X^1\Sigma^+$  band system suggests that this mechanism is not operative in the present study and that, in fact, the  $a^3\Sigma^+ - X^1\Sigma^+$  emission is readily quenched in the present reactive environment.

Hager et al.<sup>6</sup> employed a hollow cathode discharge through dilute silane to produce the atomic silicon for their oxidation studies. Their discharge configuration may promote a different decay scheme with which are associated distinctly different symmetry constraints for the allowed states of the product silicon atom. Further, their produced silicon atoms traveled several centimeters under higher buffer gas pressures than did those products employed in the present study before reaction with N<sub>2</sub>O. The collisional quenching of excited state silicon may have been significant, producing ground state  $^3P$  silicon atoms.

### The Useful Extrapolation of the Pyrolysis Configuration

The pyrolysis source we have developed in this study may be useful not only for the formation of a long path length metastable SiO\* source to pump atomic receptors that can be formed into visible chemical laser amplifiers but also as a well defined controllable source of SiO for thin film deposition.

In fact a configuration which we are developing that should serve both these purposes is depicted in Figure 5. Here we operate five pyrolyzers in tandem. In order to develop this source for SiO surface deposition, a future consideration must be the evaluation of the velocity distributions from the individual pyrolyzers.

The pyrolysis source which we have developed may have distinct advantages over discharge sources in that the results we obtain are consistent and readily controllable. Further, we find little or no evidence for clustering in the region immediate to the source. Finally the long-lived SiO metastable emitters might be used to distinct advantage in monitoring a surface deposition process. If the SiO  $b^3\Pi - X^1\Sigma^+$  emission is not strongly quenched in the near vicinity of a deposition substrate, it can represent a ready means of detecting SiO concentration gradients above the substrate. In other words, we have an in-situ optical diagnostic whose sensitivity exceeds that in the infrared by two orders of magnitude. This potential would seem to be worth further consideration.

#### SUMMARY AND CONCLUSION

The efficient gas phase decomposition of silane has been accomplished using a simple, controllable, pyrolysis scheme. The resulting gas phase silicon atoms have been reacted with  $N_2O$  to produce primarily the metastable  $b^3\Pi$  excited state of SiO. This source will be useful to create a long path length medium for the efficient energy transfer pumping (via collisions) of atomic receptor atoms that can be used to form the amplifying medium for a visible chemical laser. Further, the source may provide an additional mode of control for SiO vapor deposition processes both in terms of system stability and in terms of the enhanced ability to detect the SiO metastable emitters in the near vicinity of the deposition substrate. It remains to further characterize the source by evaluating its velocity distribution to aid in the evaluation of the potential uniformity of the deposition process.

The thermolysis process strongly favors production of the SiO  $b^3\Pi$  to the  $A^1\Pi$  excited state in a ratio exceeding 2200/1. Because only one of the energetically accessible metastable triplet states is observed in the present study, the data suggest that a symmetry constrained process may influence the results of the silane pyrolysis. This, however, will require further study.

### **Acknowledgements**

The authors greatly acknowledge helpful discussions with Mr. Douglas Berlin, Mr. David Grantier, and Dr. KangKang Shen. The support of the Georgia Tech Foundation through a grant from Mrs. Betty Peterman Gole, the Army Research Office through grant number DAAH04-93-G-0195, and the Air Force Office of Scientific Research through AFOSR/SDIO are also greatly acknowledged.

## References

1. See for example, G. Hass, J. Am. Ceram. Soc. 33, 353 (1950); G. Siddall, Vacuum 9, 274 (1959); D. B. York, J. Electrochem. Soc. 110, 271 (1963); J. Nishizawa, Y. Horike, M. Hirose, K. Sido, and A. Garscadden, "Fundamental Reactions in Silane Discharges", Proceedings of the Symposium on Dry Process, Honolulu, HI, 22-23 October, 1987.
2. See for example, G. J. Green and J. L. Gole, Chemical Physics 100, 133 (1985), and references therein.
3. R. W. Woodward, J. S. Hayden, and J. L. Gole, Chemical Physics 100, 153 (1985).
4. See for example, J. R. Woodward, S. H. Cobb, K. K. Shen, and J. L. Gole, "A Chemically Driven Visible Laser Transition Using Fast Near Resonant Energy Transfer", in IEEE J. Quantum Electron., Vol. 26, 1574, 1990; J. R. Woodward, S. H. Cobb, and J. L. Gole, "Superfluorescent Chemically Driven Visible Laser Transitions Using Fast Near Resonant Energy Transfer", Proceedings of the Fourth International Laser Science Conference, A.I.P. Conf. Proc. No. 191, Optical Science and Engineering Series 10, p. 63. J. L. Gole, J. R. Woodward, S. H. Cobb, K. K. Shen, and J. R. Doughty, SPIE Proceedings Volume 1397, Eighth International Symposium on Gas Flow and Chemical Lasers, 1990, p. 125.
5. See for example, K. K. Shen, H. Wang, and J. L. Gole, IEEE J. Quantum Electronics, Vol. 29, 2346 (1993).
6. G. Hager, R. Harris, and S. G. Hadley, J. Chem. Phys. 63, 2810 (1975). G. Hager, L. E. Wilson, and S. G. Hadley, Chem. Phys. Lett. 27, 439 (1974).
7. J. M. Jasinski and Jack O. Chu, J. Chem. Phys. 88, 1678 (1988).
8. V. N. Votintsev, I. S. Zaslonko, V. S. Mikheev, and V. N. Smirnov, Kinetics and Catalysis 27, 843 (1986).
9. For a discussion of clustering kinetics and its use see K. A. Littau, P. J. Szajowski, A. J. Muller, A. R. Kortan, and L. E. Brus, J. Phys. Chem. 97, 1224 (1993), and references therein.
10. H. Michels, United Technologies, private communication.
11. W. H. Crumley and J. L. Gole, Rev. Sci. Instruments, Vol. 57, 1692 (1986).
12. C. E. Moore, "Atomic Energy Levels", National Bureau of Standards, 1949.

13. G. Herzberg, "Electronic Spectra of Polyatomic Molecules", D. Van Nostrand Company, New York, New York, 1966.
14. J. S. Francisco and R. Barnes, J. Chem. Phys. 88, 2334 (1988).
15. W. H. Smith and H. S. Liszt, J. Quant. Spectrosc. and Radiative Transfer 12, 505 (1972).
16. In the environment of this experiment, the fraction  $F^*$ , of molecules radiating with lifetime,  $\tau$ , traveling a distance  $d = 5$  cm, drops well below one as the lifetime increases beyond  $10^{-4}$  seconds. \*The fraction of molecules radiating with lifetime,  $\tau$ , traveling a distance  $d$ , at velocity,  $v$ , is  $(1 - e^{-d/v\tau})$ . In measuring the quantum yield, the loss of product fluorescing molecules to the viewing zone must be considered. This certainly affects the SiO triplet states whose lifetimes are likely to exceed  $10^{-3}$  seconds.

Table I

Near Resonances of  $\text{SiO}^*$  ( $b^3\Pi - X^1\Sigma^+$ ) and Select Aluminum Atomic Transitions  
which are Energy Transfer Pumped

Aluminum Atomic Transition	$\text{SiO}(v', v'')$	
	b-X Transitions,	$E(\text{cm}^{-1})^a$
$^2D_{5/2} \rightarrow ^2P_{3/2}$ @ $32324.75 \text{ cm}^{-1}$	(0,1)	278
	(1,2)	59
	(2,3)	-163
$^2D_{3/2} \rightarrow ^2P_{3/2}$ @ $32323.41 \text{ cm}^{-1}$	(0,1)	280
	(1,2)	61
	(2,3)	-161
$^2D_{3/2} \rightarrow ^2P_{1/2}$ @ $32435.45 \text{ cm}^{-1}$	(0,1)	168
	(1,2)	-51
	(2,3)	-273)

a. Molecular level energy - Atomic level energy. Positive quantities denote exothermic energy transfer.

## Figure Captions

Figure 1: (a) Ceramic tube pyrolizer and (b) schematic side and top view of reaction chamber for the study of the silane based formation of silicon monoxide metastable excited states.

Figure 2: (a) Overview of SiO chemiluminescent emission spectra produced as silane is pyrolyzed in a zirconia tube pyrolizer to form atomic silicon which subsequently reacts with  $N_2O$ . The  $SiO^* A^1\Pi - X^1\Sigma^+$  and  $b^3\Pi - X^1\Sigma^+$  band systems are apparent in the figure. (b) Closeup of  $b^3\Pi - X^1\Sigma^+$  intercombination emission showing bands labeled ( $v', v''$ ) where  $v'$  is the upper state vibrational level quantum and  $v''$  is the lower state quantum level. Spectral resolution is  $8 \text{ \AA}$ . See text for discussion.

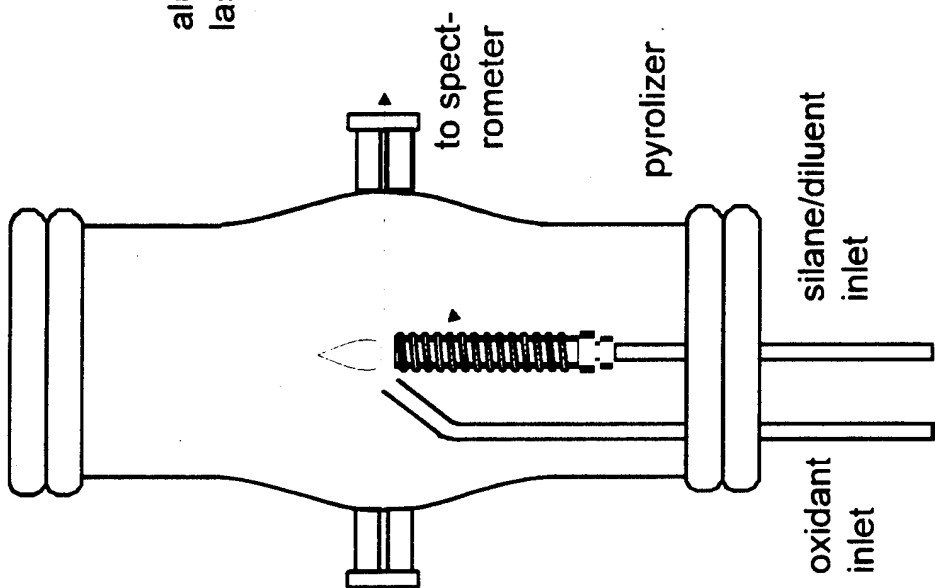
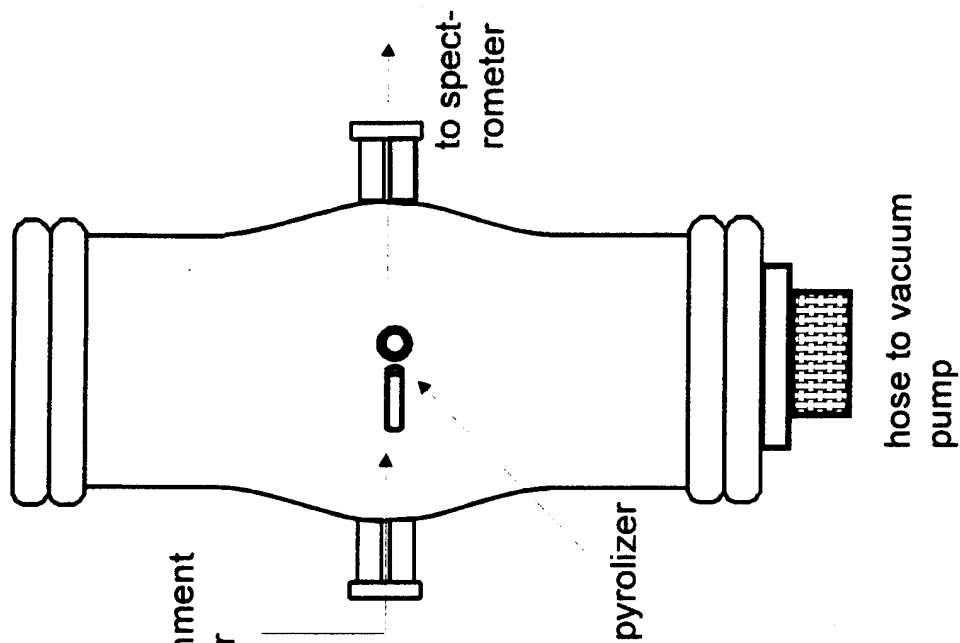
Figure 3: Overview of SiO chemiluminescent emission spectrum (note Figure 2) produced as silane is pyrolyzed in an alumina tube pyrolizer to form atomic silicon which subsequently reacts with  $N_2O$ . Here, in addition, aluminum atoms leached from the pyrolizer are excited by energy transfer. The aluminum  $^2D_{3/2} - ^2P_{1/2}$  and  $^2D_{5/2,3/2} \rightarrow ^2P_{3/2}$  transitions are clearly visible at 3083 and 3094  $\text{\AA}$ . Spectral resolution is  $8 \text{ \AA}$ . See text for discussion.

Figure 4: Overview of SiO chemiluminescent emission spectra produced as silicon atoms obtained from an oven source react with  $N_2O$  to produce the  $SiO^* A^1\Pi$ ,  $b^3\Pi$ , and  $a^3\Sigma^+$  excited states. The  $A^1\Pi - X^1\Sigma^+$ ,  $b^3\Pi - X^1\Sigma^+$ , and  $a^3\Sigma^+ - X^1\Sigma^+$  band systems are apparent in the figure. Spectral resolution is  $8 \text{ \AA}$ . See text for discussion.

Figure 5: Tandem pyrolizer configuration to produce a long path length SiO metastable flame. See text for discussion.

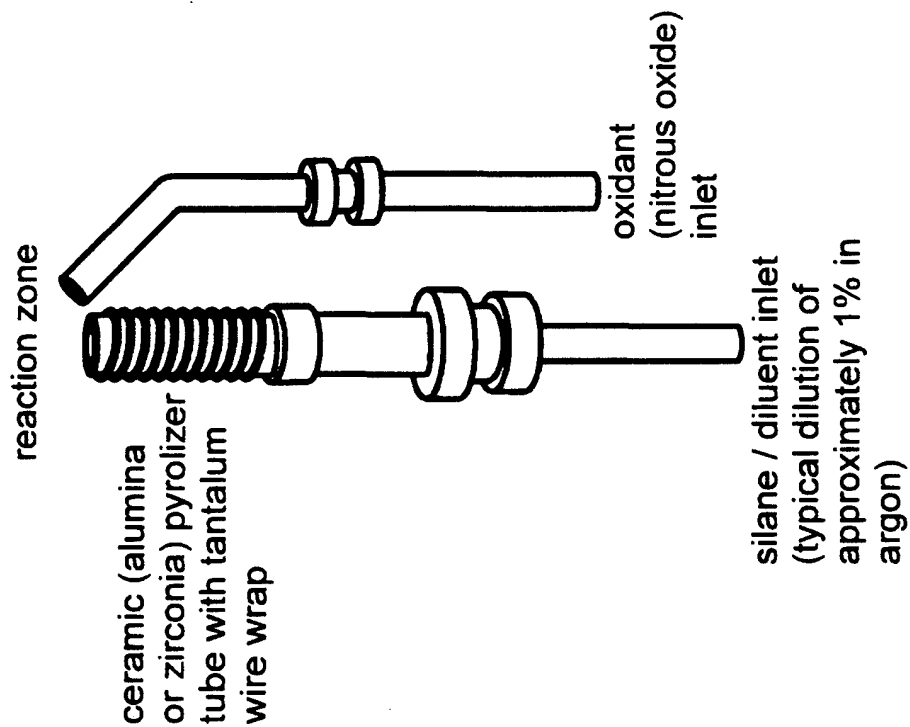
top view

side view



(b)

FIG. 1



(a)

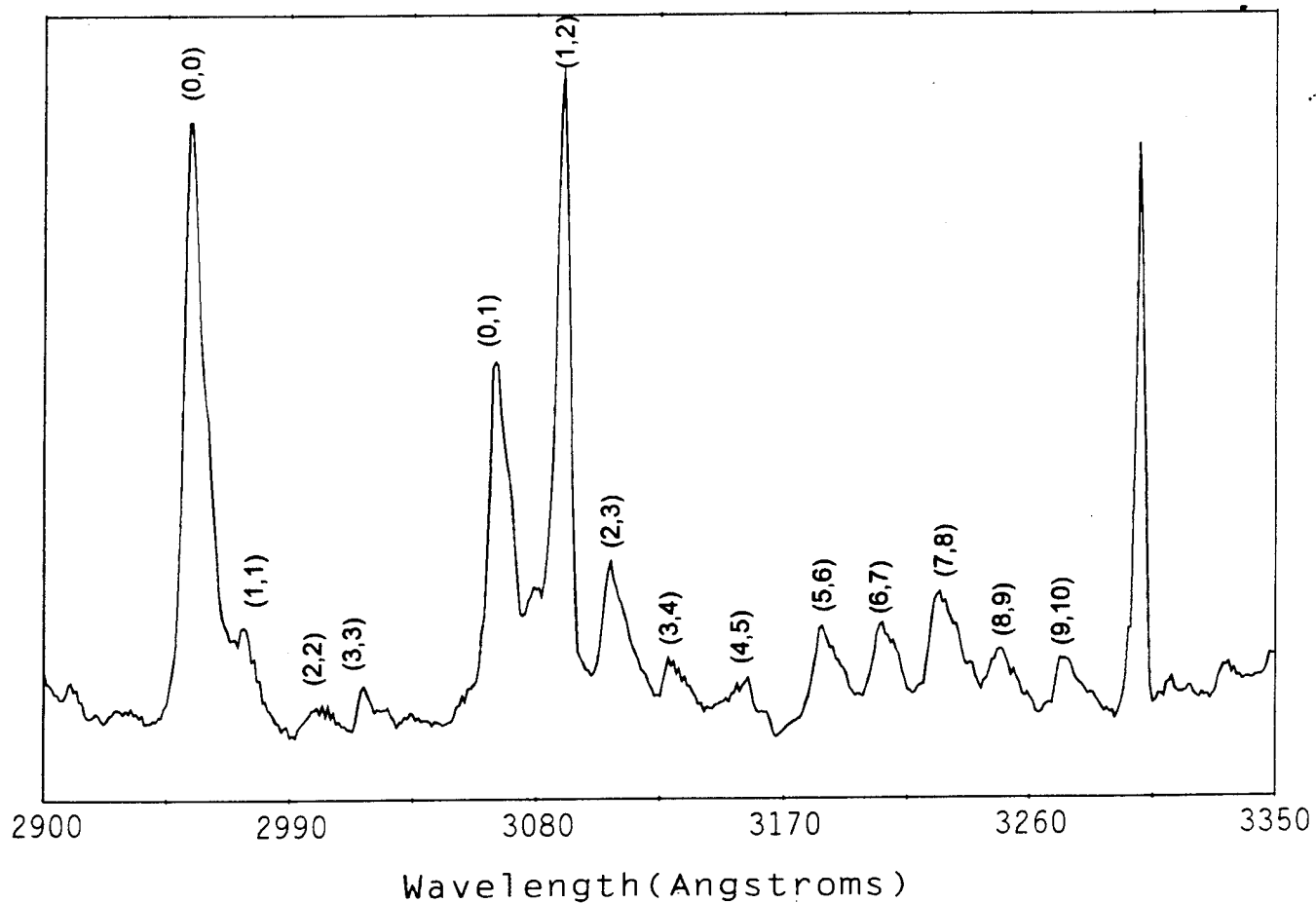
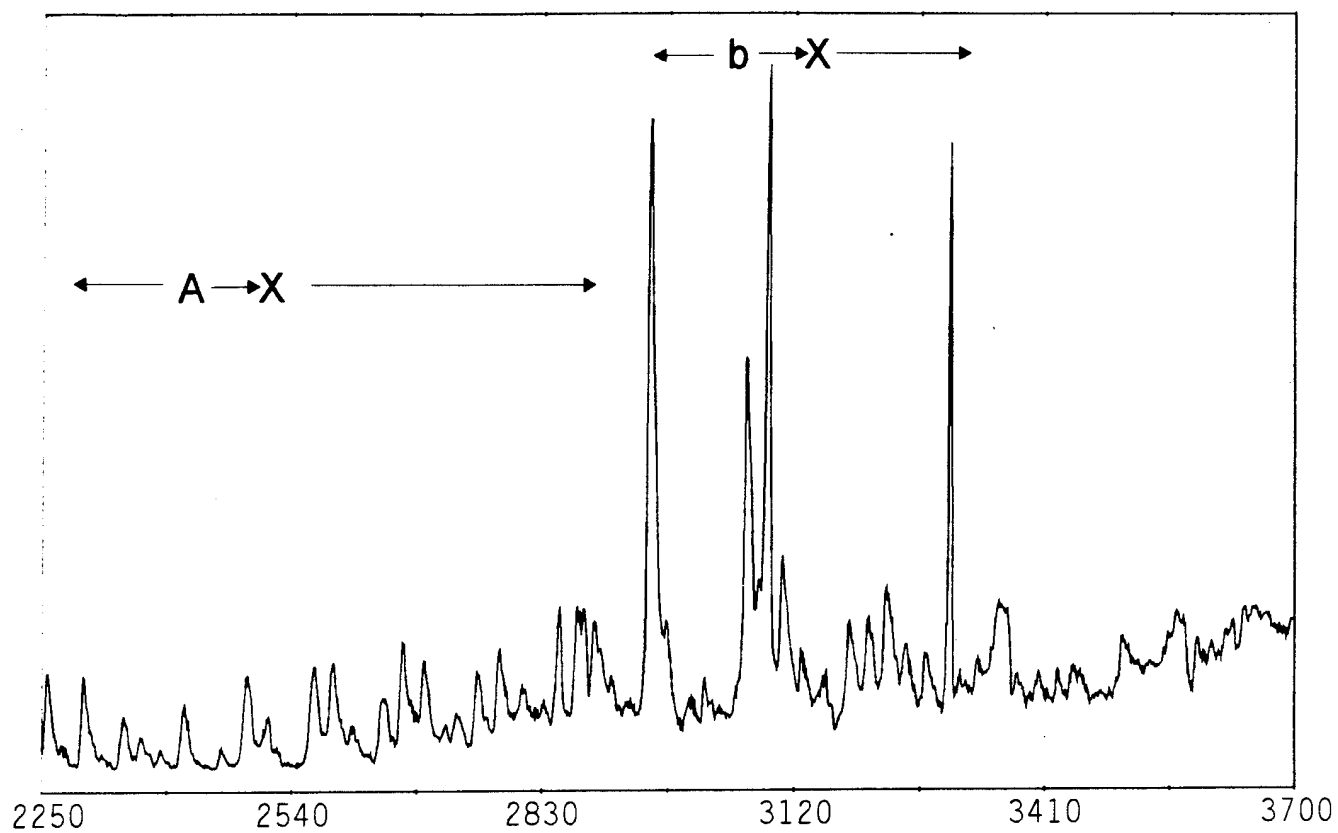


FIG. 2

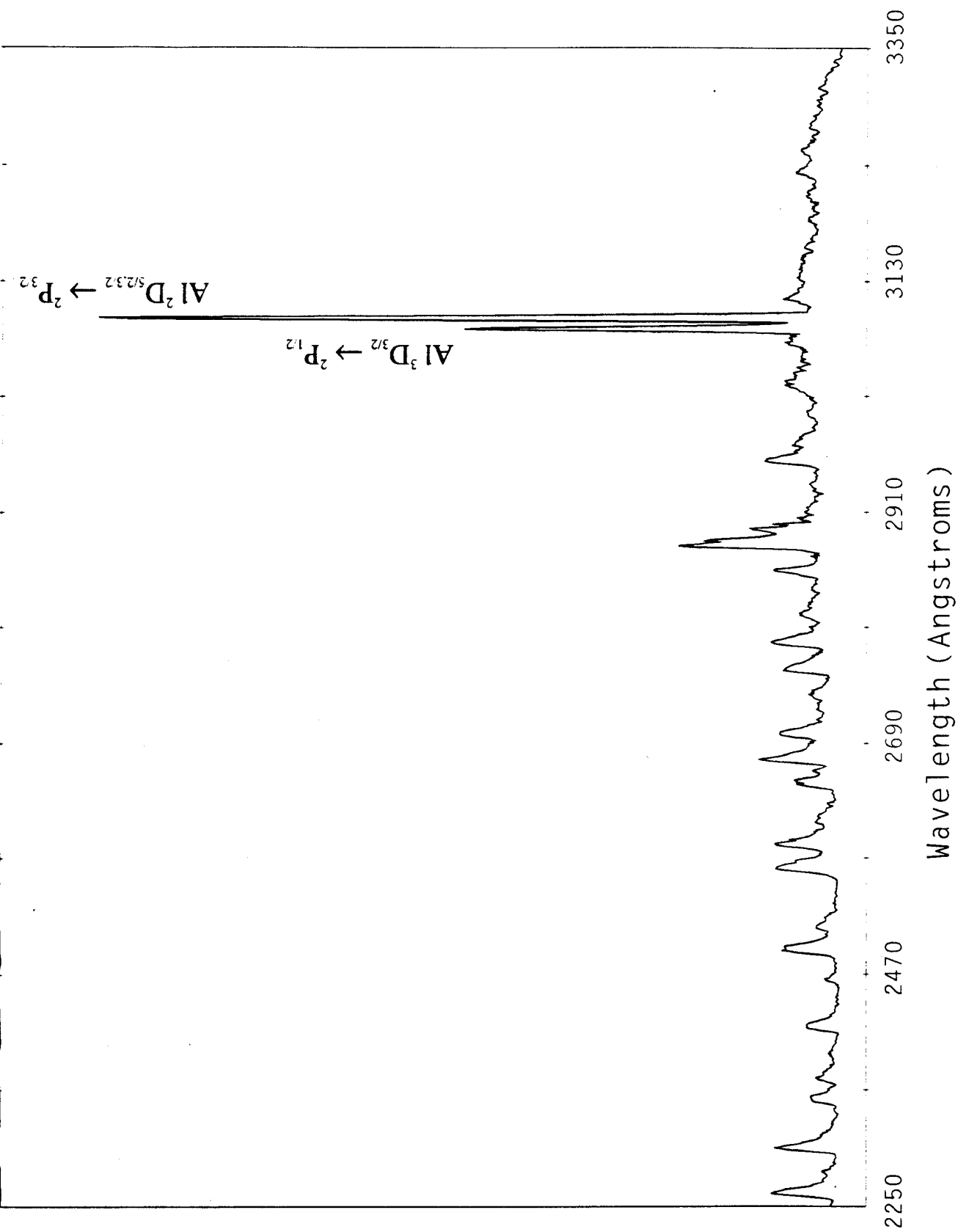


FIG. 3

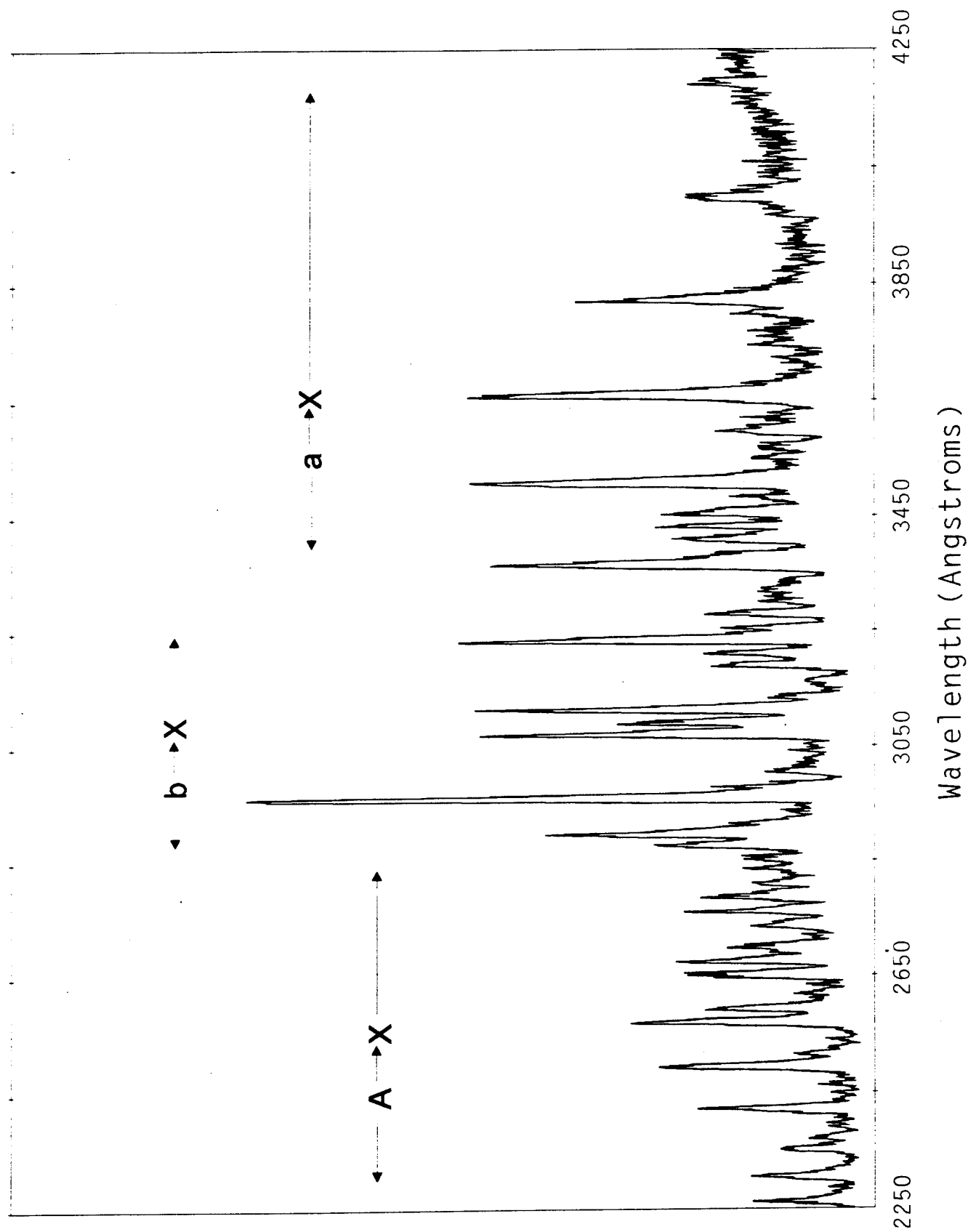


FIG. 4

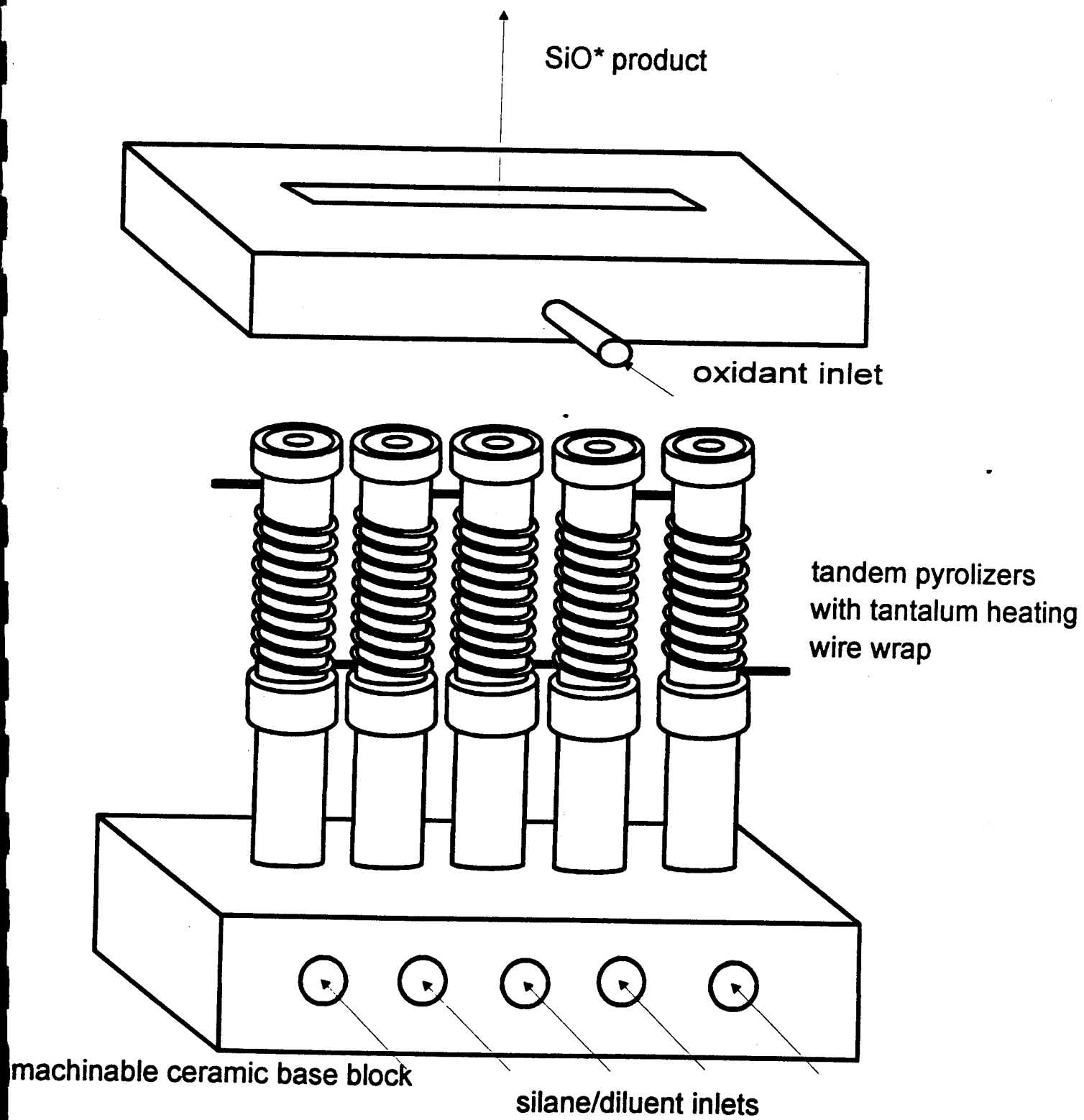


FIG. 5